THE

PHYSICAL REVIEW

Volume Second Series Number 1

JANUARY 1, 1949

Published for the

American Physical Society

by the

American Institute of Physics

Lancaster, Pa. and New York, N. Y.

Suggestions for Contributors

Manuscripts

Send manuscripts to John T. [illegible] Department of Physics, University of Min[illegible], Minneapolis 14, Minnesota.

Each article submitted will in general consist of (a) textual material, i.e., all material which is to be set in type, and (b) drawings or photographs from which zinc etchings or copper halftones will be made. Textual material will consist of an abstract, the body of the paper, tabular material, references, and figure captions. All of this material must be in English, typewritten (except mathematical expressions) double spaced with wide margins (for editorial corrections to the printer) on a durable, white paper, preferably letter size. The original copy, not the carbon, should be submitted.

For general style, spellings, abbreviations, and form, recent issues of this journal should be consulted.

The prime requisite is that the copy shall be clear to the typesetter, who is neither a physicist nor a mathematician.

Abstracts

An abstract must accompany each article. It should be adequate as an index and as a summary. As an index, it should give all subjects, major and minor, concerning which new information is presented. As a summary it should give the conclusions of the article and all numerical results of general interest.

Mathematical Expressions

All but the simplest mathematical expressions should be carefully printed in by hand. Be sure to distinguish between capital and small letters. Indicate clearly superscripts and subscripts by inverted carets and carets, respectively. Avoid complicated superscripts and subscripts. Avoid repetition of a complicated expression by representing it by some convenient symbol. Identify in the margin Greek letters and unusual symbols. Use fractional exponents instead of root signs. Use the solidus (/) for fractions wherever its use will save vertical space.

References

References should appear as footnotes, numbered consecutively, and arranged [illegible]:

[1] A. B. Smith, Phys. Rev. 41, 852 (19[illegible]).
[2] H. Lamb, *Hydrodynamics* (Cambridge University Press, Teddington, England), sixth edition, pp. [illegible].

Tables

All but the simplest tabular material should be organized in tabular form rather than as a part of the running text. Tables may be typewritten on sheets separate from the running text with indications in the margin of the running text where the table is to be inserted. Each table must have a caption which will make the data in the table intelligible without reference to the text. Avoid complicated column headings; if necessary, use symbols which are explained in the table caption.

Figures

Wherever possible figures should be planned for the width of a column of the *Physical Review* (3 inches). A convenient reduction ratio is about 2:1 or 3:1. The original drawings or photographs should therefore be in general about 6 to 9 inches wide and the lettering and symbols should be large enough on the original that when reduced they shall not be less than about $\frac{1}{16}$ in. (~1.5 mm). If the reduction is 3:1, the original lettering should be not less than $\frac{1}{16}$ in. high.

The process of making zinc etchings or copper halftones is a black and white photographic one. Therefore line drawings must be in *india ink* on white paper or tracing cloth. Coordinate paper is not desirable but if used must be blue lined and the coordinate lines which are to show must be inked over.

Photographs should have maximum black and white contrast.

Plan figures to use space efficiently. Avoid wasting space, particularly at the top or bottom.

Identify on the back or other suitable place each original drawing or photograph with the author's name and the figure number. Figures should be numbered consecutively and their approximate position indicated in the margin of the running text. Figure captions should be typed and included with the manuscript (not as part of the figure).

Avoid round and oval photographs.

Alterations

Take great care that each manuscript is typographically accurate. A limited number of alterations in proof are unavoidable, but the cost of making extensive alterations after the article has been set in type will be charged to the author.

Proof and all correspondence concerning papers in the process of publication should be addressed to the Publication Manager, American Institute of Physics, 57 East 55 Street, New York 22, New York.

THE
PHYSICAL REVIEW

A journal of experimental and theoretical physics established by E. L. Nichols in 1893

SECOND SERIES, VOL. 75, NO. 1 JANUARY 1, 1949

Threshold and Resonances in $C^{14}(p,n)N^{14}$ Reaction and Energy Levels of N^{15} *

W. E. SHOUPP, B. JENNINGS, AND K. H. SUN
Westinghouse Research Laboratories, East Pittsburgh, Pennsylvania

(Received September 2, 1948)

The threshold energy required to induce the (p,n) reaction in C^{14} has been measured to be $E_t=0.664\pm0.009$ Mev or a reaction energy of -0.620 ± 0.009 Mev. This reaction is the inverse of the $N^{14}(n,p)C^{14}$ process studied by Hughes and Eggler and their observed reaction energy $Q_{n,p}=0.597\pm0.009$ Mev can be compared with the negative of the reaction energy observed here. Six resonances have been observed in the process at 1.14, 1.30, 1.47, 2.05, 2.21, and 2.65 Mev, three of which can be correlated with those previously observed in the $N^{14}(n,p)$ reaction. The cross section at the first resonance at 1.14 Mev has been measured to be approximately 0.7 barn.

INTRODUCTION

SINCE the first observation of (p,n) reactions by Du Bridge, Barnes, and Buck,[1] measurements have been made of various (p,n) thresholds with the Westinghouse Van de Graaff type of generator as a source of high energy protons.[2,3] Resonances have been found in the excitation functions above the threshold, particularly for Li^7 and Be^9, yielding information about the compound nuclei involved.[4,5] We have extended work of this type by measuring the threshold of the (p,n) reaction of the radioactive isotope C^{14} and, by using both thick and thin target techniques, several resonances attributable to the excited nucleus of N^{15} have been found. From these data it is also possible to place limits on the mass of the neutrino from the threshold measurement and to determine some of the energy levels of N^{15} from the resonances. Some estimate of the cross section for the first (p,n) resonance level can be given.

EXPERIMENTAL

The Westinghouse Van de Graaff high voltage generator[6] was used as a source of high energy protons. The voltage scale used in these experiments is based on the $Li^7(p,n)$ threshold at 1.883 $\pm$0.006 Mev of Hanson and Benedict,[7] and the voltage extrapolation was carried out by a compensating generating voltmeter whose linearity was known to be better than 0.1 percent.[2]

The proton ion current was measured by a current integrator modified slightly from that of Watt[8] and the reaction was carried out within a Faraday cage arranged as in Fig. 1.

* Assisted by the Joint Program of the Office of Naval Research and the Atomic Energy Commission.

[1] L. A. Du Bridge, S. W. Barnes, and J. H. Buck, Phys. Rev. **51**, 995 (1937).

[2] R. O. Haxby, W. E. Shoupp, W. E. Stephens, and W. H. Wells, Phys. Rev. **58**, 1035 (1940).

[3] W. E. Shoupp, B. Jennings, and W. Jones, Phys. Rev. **73**, 421 (1948).

[4] J. E. Hill, and W. E. Shoupp, Phys. Rev. **73**, 931 (1948).

[5] W. J. Hushley, Phys. Rev. **67**, 34 (1945).

[6] W. H. Wells, R. O. Haxby, W. E. Stephens, and W. E. Shoupp, Phys. Rev. **58**, 162 (1940).

[7] A. O. Hanson and D. L. Benedict, Phys. Rev. **65**, 33 (1944).

[8] B. E. Watt, Rev. Sci. Inst. **17**, 334 (1946).

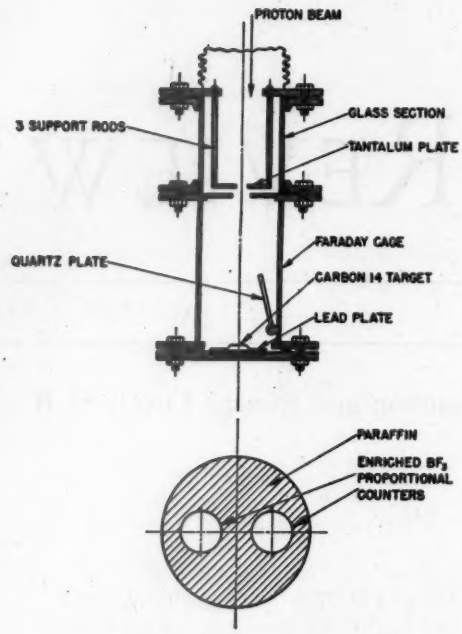

FIG. 1. Arrangement of target, paraffin, and BF_3 proportional counters.

Neutrons produced by this reaction were counted by two large proportional counters filled with boron trifluoride enriched in B^{10} and surrounded by about five centimeters of paraffin. Pulses from the counters were amplified by an Atomic Instrument Company Model 204-A amplifier which operated a pulse discriminator, a scale of 10, and a mechanical recorder.

THICK TARGET RESULTS AND THE THRESHOLD MEASUREMENT

The thick C^{14} target was a one-millimeter layer of $BaCO_3$ powder containing 2.7 percent of the active C^{14}. The thick-target curve (Fig. 2) shows the threshold and resonances up to 3.0 Mev and shows the relative position of threshold and resonance levels. The $C^{14}(p,n)$ reaction energy $Q_{p,n}$ is obtained from the threshold energy E_t since $Q_{p,n}=-(14/15)E_t$. To aid in extrapolating the excitation function to the threshold a method based on a yield equation due to Stephens, Spruch, and Schiff was used.[9] Their work indicates that the neutron yield near the threshold should vary directly with $(E_p-E_t)^{\frac{3}{2}}$, where E_p is the proton energy and E_t the threshold energy.

[9] W. E. Stephens, L. Spruch, and L. I. Schiff, University of Pennsylvania Report, June 1947.

This theoretical relationship involves the assumptions that the capture of a slow neutron by N^{14} (the reverse process) obeys a $1/v$ law and that no resonances exist near the threshold. The latter is justified from the experimental evidence shown in Fig. 3. Plotting the $\frac{2}{3}$ power of the neutron yield against E_p, one obtains a straight line which is extrapolated to the threshold as shown in Fig. 3, apparently justifying the assumptions made. The $C^{14}(p,n)$ threshold obtained in this manner from several thick target runs is 0.664 $\pm$0.009 Mev (see Table I), and the reaction energy $Q_{p,n}$ is -0.620 ± 0.009 Mev.

The energy value for the $C^{14}(p,n)$ reaction $Q_{p,n}$ is equal to the negative of that for the inverse reaction $N^{14}(n,p)$, $Q_{n,p}$. The $Q_{n,p}$ value for this reaction has been measured by a number of investigators with results between 0.55 to 0.71 Mev as summarized by Hornyak and Lauritsen.[10] Recently Huber and Stebler[11] gave a value of 0.63 ± 0.01 Mev from ionization chamber measurements, and Hughes and Eggler[12] have found a value of 0.596 Mev from measuring the length of proton tracks in a cloud chamber. Using the $Q_{p,n}$ value (-0.620 ± 0.009 Mev) obtained in this experiment and taking the value (0.755 $\pm$0.016 Mev) for the neutron-proton mass difference[13] and (14.00751 ± 0.00004 a.m.u.)[14] for the mass of N^{14}, we calculate the mass of C^{14} to be (14.00766 ± 0.00007 a.m.u.). Although this yields practically the same value (14.00767 $\pm$0.00005 a.m.u.)[14] as that derived from the beta-ray energy of C^{14}, it does not involve the assumption of zero neutrino mass.

C^{14} is a neta-emitter and decays according to Eq. (2). Consider then the two reactions,

$$C^{14}+H^1\rightarrow N^{14}+n^1+Q_{p,n}, \quad (1)$$

$$C^{14}\rightarrow N^{14}+Q_{\beta^-}+\nu. \quad (2)$$

Combining these equations we obtain for the neutrino rest mass, ν,

$$\nu=(n^1-H^1)-Q_{\beta^-}+Q_{p,n}. \quad (3)$$

[10] W. F. Hornyak and T. Lauritsen, Rev. Mod. Phys. 20, 191 (1948).
[11] P. Huber and A. Stebler, Phys. Rev. 73, 85 (1948).
[12] D. J. Hughes and C. Eggler, Phys. Rev. 73, 809 (1948).
[13] W. E. Stephens, Rev. Mod. Phys. 19, 19 (1947).
[14] H. A. Bethe, *Elementary Nuclear Theory* (John Wiley and Sons, Inc., New York, 1947).

Using the value $Q_{\beta^-}=(0.155\pm0.002$ Mev)[15] for the maximum beta-ray energy of C^{14} we obtain from Eq. (3)

$$\nu=(0.755\pm0.016)-(0.155\pm0.002)$$
$$-(0.620\pm0.009)\text{ Mev},$$
$$\nu=(-0.020\pm0.027)\text{ Mev}$$

or, if one ignores the negative mass deviation, the neutrino mass is about one percent of that of the electron.

THIN TARGET RESULTS

The thin C^{14} target was prepared by allowing CO_2 containing C^{14} (which was produced at A in Fig. 4) to react with a very thin layer of $Ba(OH)_2$, B which had been sprayed on a

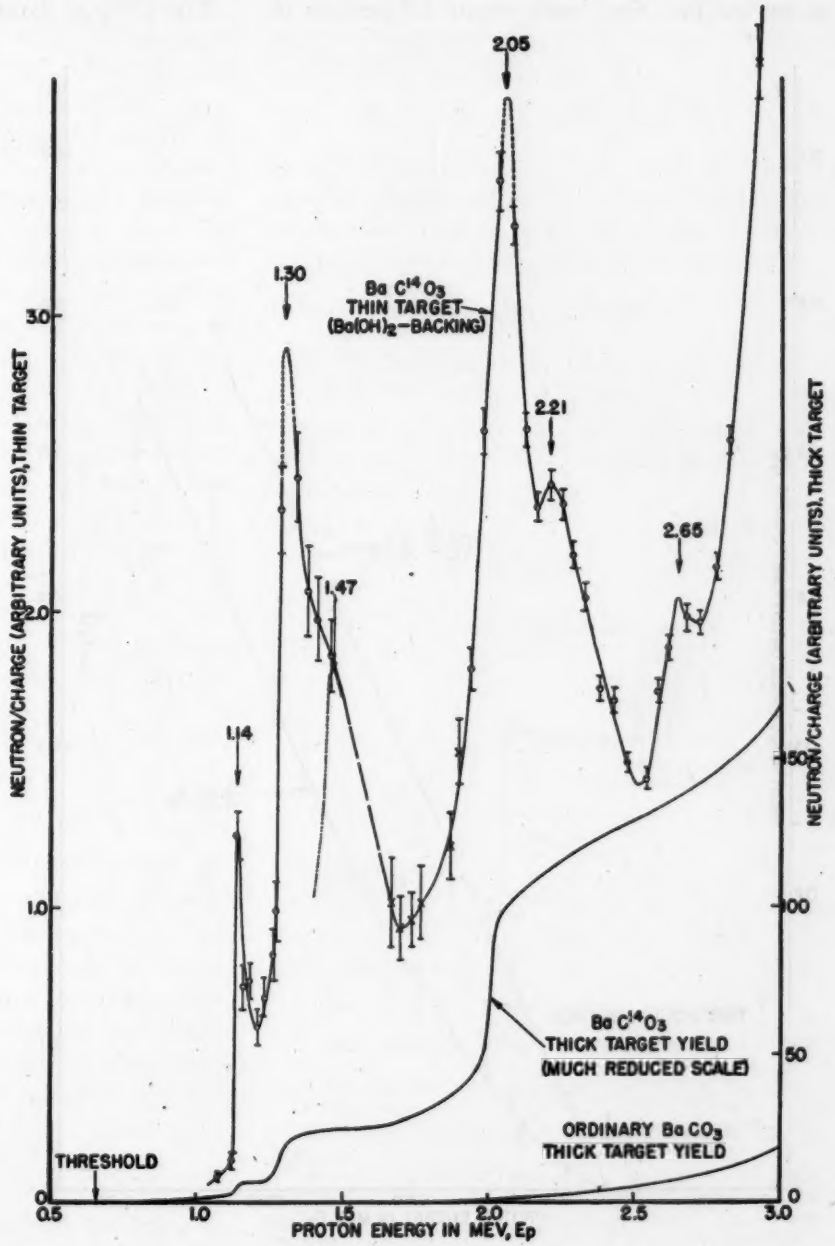

FIG. 2. $C^{14}(p,n)$ resonances.

[15] J. L. Berggren and R. K. Osborn, Bull. Am. Phys. Soc. 23 (2), 46 (1948).

tantalum plate. The reaction at B produces a small amount of $BaCO_3$ containing C^{14}. The amount of C^{14} on the thin target was measured by means of the C^{14} radioactivity with a thin mica window Geiger counter and compared with a $Ra(D+E)$ standard supplied by the National Bureau of Standards. It is found to be 0.26 microcurie per cm². This corresponds to about 4.2×10^{-9} mole of C^{14} per cm², using 5100 years[16] as its half-life. Since only about 2.7 percent of the carbon atoms in the barium carbonate are C^{14}, the thickness of $BaCO_3$ is about 6×10^{-6} cm. Using data on atomic stopping power and range-energy relationship of proton given by Livingston and Bethe[17] and by interpolating a value of atomic stopping power of barium between silver and gold, we obtain an approximate target thickness of 0.003 Mev for a proton energy of 1.14 Mev.

The $C^{14}(p,n)$ excitation function for the thin

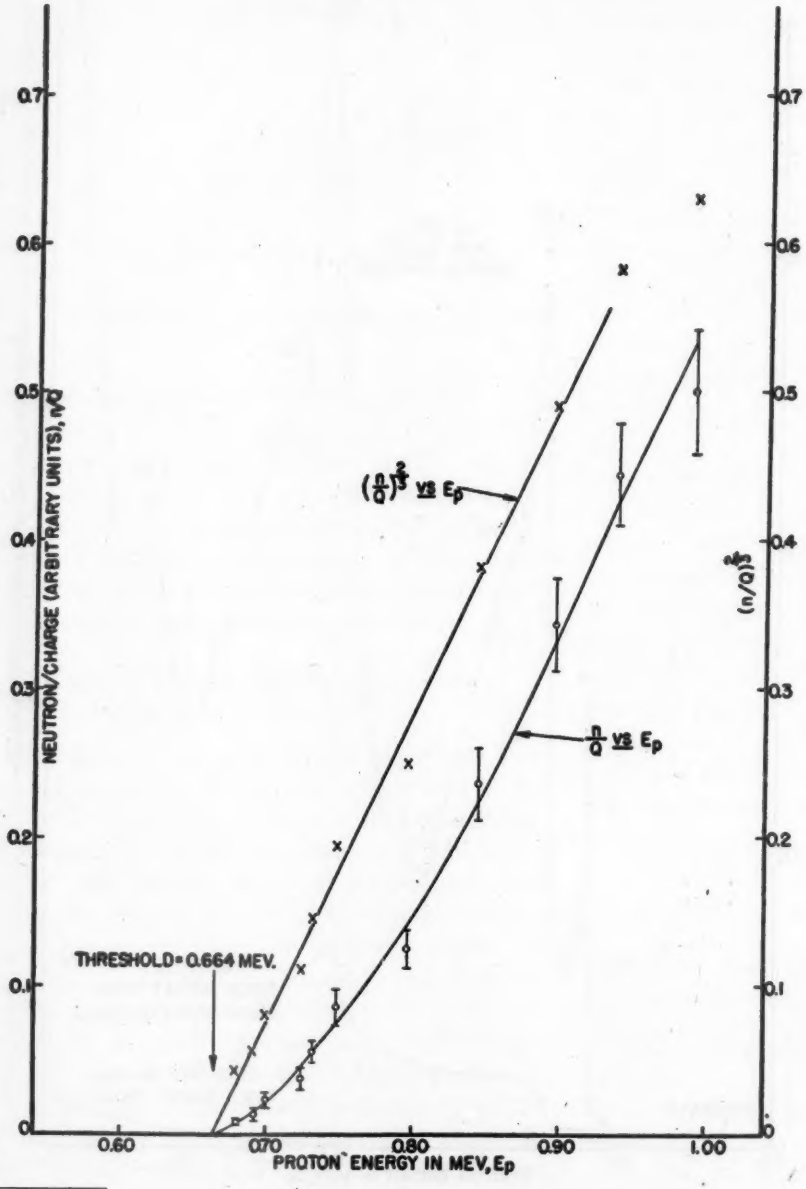

FIG. 3. $C^{14}(p,n)$ threshold ($BaC^{14}O_3$ thick target).

[16] L. D. Norris and M. G. Inghram, Phys. Rev. **73**, 350 (1948).
[17] M. S. Livingston and H. A. Bethe, Rev. Mod. Phys. **9**, 245 (1937).

TABLE I.

	Proton energy Mev	Reaction energy $Q(p,n)$ Mev	Energy levels in $H^1+C^{14}\rightarrow N^{15}$ $[10.14+(14/15)E_p]$ Mev	Energy levels in $n^1+N^{14}\rightarrow N^{15}$ $[10.76+(14/15)E_n]$ Mev
C_{14} threshold	0.664±0.009	−0.620±0.009		
Resonance 1	1.14±0.02		11.21±0.29	11.28
Resonance 2	1.30±0.02		11.35±0.29	11.41
Resonance 3	1.47±0.05		11.51±0.32	
Resonance 4	2.05±0.02		12.06±0.29	12.11
Resonance 5	2.21±0.05		12.21±0.32	
Resonance 6	2.65±0.05		12.62±0.32	

target is shown in Fig. 2. Strong resonances are observed at 1.14, 1.30, and 2.05 Mev and doubtful ones at 1.47, 2.21, and 2.65 Mev.

The existence of a resonance of 1.47 Mev is doubtful because the resolution of our experimental method was not high enough to separate it from the nearby resonance at 1.30 Mev. The small peaks at 2.21 and 2.65 Mev were checked by several independent runs across this voltage range. There is no doubt that the general rise in neutron yield above 2 Mev, found in the thin target results, is due to the backing layer of $Ba(OH)_2$. However, the yield at the first resonance is probably due to the C^{14} target alone and therefore can be used to make a cross section estimate. For the same reason, it is possible to estimate the half-widths of only the first resonance, which is about 0.04±0.01 Mev. This corresponds to a life time of 10^{-19} sec. for the compound nucleus at this level. Also shown in Fig. 2 are the thick target yields for $BaC^{14}O_3$ and ordinary $BaCO_3$ in reduced scale.

When a proton enters a C^{14} nucleus, the compound nucleus, N^{15} is formed:

$$C^{14}+H^1\rightarrow N^{15*}+10.14 \text{ Mev}. \quad (4)$$

An energy of excitation of 10.14 Mev was calculated from the mass data given by Bethe,[14] which are used throughout the paper with the exception that the mass of the neutron and of C^{14} are taken to be 1.00894[13] and 14.00766 a.m.u., respectively. The energy levels of N^{15} corresponding to the resonance energy of the proton E_p in the $C^{14}(p,n)$ reaction may be calculated thus:

$$E_{N^{15}}=10.14+(14/15)E_p \text{ in Mev}. \quad (5)$$

The N^{15} energy levels so obtained are given in Table I and in Fig. 5. which also shows the levels obtained for the inverse reaction $N^{14}(n,p)$ by Barschall and Battat;[18]

$$E_{N^{15}}=10.76+(14/15)E_n \text{ in Mev}. \quad (6)$$

Since the voltage calibration used in the two experiments may not be the same the agreement in absolute value may be fortuitous. However, the agreement in level separation is excellent

$C^{14}(p,n)$ CROSS SECTION

To estimate the cross section it is necessary to know the angular distribution $N(\theta)$ of the emitted neutrons in the laboratory system for the reaction $C^{14}(p,n)N^{14}$. This may be calculated from Eq. (7):

$$N(\theta)=N(\varphi)\{2\gamma\cos\theta + [(1+\gamma^2\cos 2\theta)/(1-\gamma^2\sin^2\theta)^{\frac{1}{2}}]\}. \quad (7)^{**}$$

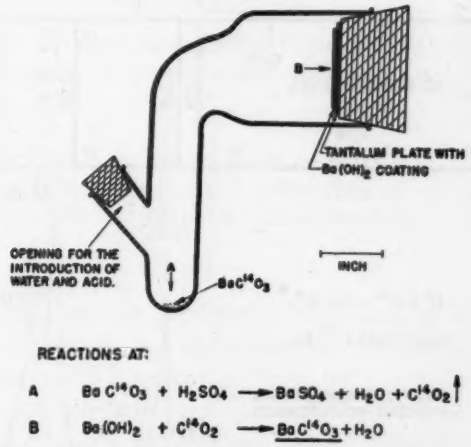
B
TANTALUM PLATE WITH Ba(OH)2 COATING
OPENING FOR THE INTRODUCTION OF WATER AND ACID.
INCH
BaC14O3
REACTIONS AT:
A BaC14O3 + H2SO4 → BaSO4 + H2O + C14O2
B Ba(OH)2 + C14O2 → BaC14O3 + H2O

FIG. 4. Simple apparatus for preparing thin $BaC^{14}O_3$ target.

[18] H. H. Barschall and M. E. Battat, Phys. Rev. **70**, 245 (1946).

** A slightly different form of Eq. (7) is given by C. E. Mandeville [J. Franklin Inst. **244**, 385 (1947)] who, however, does not give Eq. (8). The latter was derived following a similar treatment for recoil nucleus after Livingston and Bethe (reference 17).

Here $N(\varphi)$ is the angular distribution in the center of gravity system and may be assumed for the (p,n) type of reaction to be spherically symmetrical. θ is the angle between the incident and ejected particles in the laboratory system, and γ is given by

$$\gamma=\{M_pM_eE_p/M_rM_c[Q+(M_t/M_c)E_p]\}^{\frac{1}{2}}, \quad (8)^{**}$$

where M_p, M_t, M_e, M_r, and M_c are the masses of projectile, target, ejected particle, recoil nucleus, and compound nucleus, respectively, and Q is the reaction energy. We have also $M_c=M_p+M_t=M_e+M_r$. For the $C^{14}(p,n)N^{14}$ reaction

$$\gamma=[E_p/(196E_p-129)]^{\frac{1}{2}}, \quad (9)$$

where E_p is the proton energy in Mev. At $E_p=1.14$ (the first resonance level in Fig. 2 where the background is negligible), the over-all estimated average number of neutrons per unit solid angle in all directions is about 80 percent of that in the forward direction. The average number of neutrons intercepted by the counters (extending over an angle of about 30 degrees from the proton beam) is estimated to be about 99 percent of that in the forward direction. In

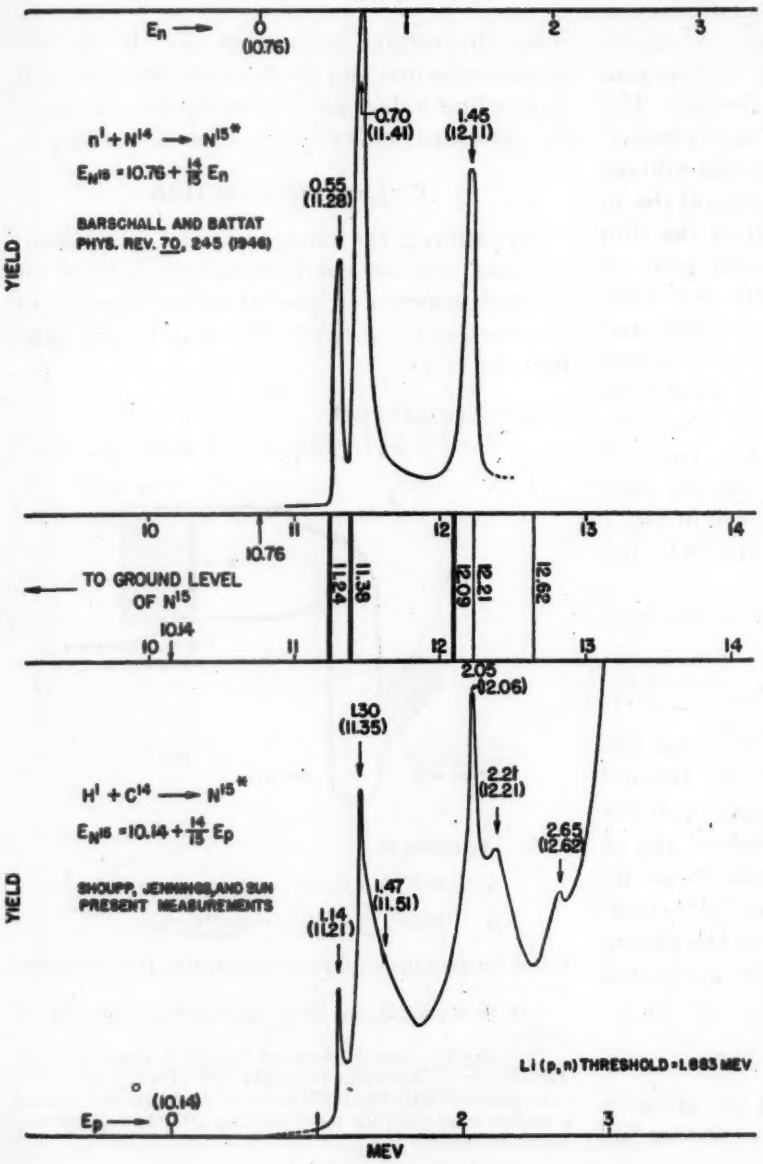

FIG. 5. Energy levels of N^{15}.

order to determine the absolute number of neutrons passing through the proportional counters from the number of recorded counts, spherical neutron sources of known intensity and various energies between 0.03 and 4.25 Mev were placed at the same distance from the counters as was the C^{14} target.[19] In this manner a conversion factor of 0.0028 was estimated and found to be nearly energy independent. The total number of neutrons emitted from the C^{14} target at a given proton voltage and ion current can be determined from the recorded number of neutron counts, the conversion factor, and the angular distribution relationship stated. Knowing the number of C^{14} nuclei in the target area where the beam hits, one calculates the cross section of the process to be about 0.7 barn for the top of the first resonance.

The cross section, $\sigma_{p,n}$, is related to that of the inverse $N^{14}(n,p)C^{14}$ process, $\sigma_{n,p}$, by the principle of detailed balance:[14]

$$\sigma_{p,n}/\sigma_{n,p}=[(2s_n+1)(2s_N+1)/(2s_p+1)(2s_C+1)]\cdot[P_n^2/P_p^2], \quad (10)$$

where s and P denote spin and momentum in the center of gravity system and subscripts denote the individual nuclear particles involved. The spins of n, $p(H^1)$, N^{14}, and C^{14} are known to be $\frac{1}{2}$, $\frac{1}{2}$, 1 and 0,[20] respectively. Since the masses of n and p and of N^{14} and C^{14} are about the same, Eq. (10) becomes

$$\sigma_{p,n}=3[(E_p-E_t)/E_p]\sigma_{n,p}, \quad (11)$$

an equation which involves only quantities measurable in the laboratory system, where E_p and E_t are the proton energy and the threshold energy of the $C^{14}(p,n)N^{14}$ reaction. For E_p at 1.14 Mev and using a vlaue of 0.085 barn for $\sigma_{n,p}$ from Barschall and Battat,[18] $\sigma_{p,n}$ was calculated to be 0.11 barn which is about $\frac{1}{8}$ of that estimated from our experiments.

[19] Boron trifluoride proportional counter calibrated at Argonne National Laboratory by Dr. D. J. Hughes and associates.

[20] F. A. Jenkins, Phys. Rev. **73**, 639 (1948).

PHYSICAL REVIEW VOLUME 75, NUMBER 1 JANUARY 1, 1949

Total Cross Sections of Nuclei for 90-Mev Neutrons*

LESLIE J. COOK, EDWIN M. MCMILLAN, JACK M. PETERSON, AND DUANE C. SEWELL
Radiation Laboratory, Department of Physics, University of California, Berkeley, California

(Received September 1, 1948)

Total cross sections of H, D, Li, Be, C, N, O, Mg, Al, Cl, Cu, Zn, Sn, Pb, and U for 90-Mev neutrons have been measured, using the 184-inch cyclotron as a source and carbon disks as detectors. Experimental details are described, and a brief discussion of some of the theoretical implications of the results is given.

I. INTRODUCTION

DATA on the total cross sections of nuclei for neutrons are of considerable importance, since they furnish the most direct evidence from which the sizes of nuclei can be computed. If a nucleus is thought of as simply an opaque sphere of collision radius R (which includes an "effective radius" of the incident neutron), then the total cross section σ_t is given by:

$$\sigma_t=2\pi R^2, \quad (1)$$

so long as the de Broglie wave-length of the neutron is not too large compared to the nuclear diameter.** Deviations from this simple law can result from several causes. When the neutron energy is only a few Mev, resonance levels in the compound nucleus produce irregular variations in σ_t. At energies of 25 Mev[1] and 14 Mev,[2] the resonances are not very important, as would be expected from the fact that the excitation ener-

* The results of this work were published in a Letter to the Editor, Phys. Rev. **72**, 1264 (1947).

** See the Appendix for fuller discussion.

[1] R. Sherr, Phys. Rev. **68**, 240 (1945).

[2] Amaldi, Bocciarelli, Cacciapuoti, and Trabacchi, Nuovo Cimento **3**, 203 (1946).

gies of the compound nuclei are now of the order of 30 Mev where the levels are presumably close together, and the values obtained by these authors show a regular variation with A. This regularity appears in the form that a plot of R (computed from (1)) against $A^{\frac{1}{3}}$ is a straight line, or at least nearly so. The simple interpretation of this is that nuclear matter has a nearly constant density, so that the true nuclear radius is proportional to the cube root of the number of nucleons; the intercept of the line at $Z=0$ represents the effective neutron radius which must be added. Comparing the data of Sherr at 25 Mev with the more accurate values of Amaldi *et al.* at 14 Mev, it appears that there is probably no significant difference between them. The latter data can be represented rather well by the line:

$$R=(1.3+1.37A^{\frac{1}{3}})\times 10^{-13}\text{ cm}, \qquad (2)$$

which was drawn giving small weight to the values for Be and S, which do not fit on a smooth curve, and ignoring an apparent slight decrease in slope in the region of the heaviest elements. A fuller discussion of the fitting of a curve to these data is given by Amaldi and Cacciapuoti.[3] In any case, the above expression probably gives a good approximation to the actual geometrical radii of nuclei, plus an additive constant representing the effective neutron radius.

One might expect that at higher neutron energies the collision radii would be about the same as at 14–25 Mev, except for a possible slight decrease in the effective neutron radius; actually the results of this paper show that the collision radii for the light elements lie considerably below the line (2), while those for the heavy elements tend to approach it. The interpretation of this fact brings in a new concept, that of nuclear transparency. We say that the effective collision radius as defined by (1) is smaller than the geometrical radius because neutrons have a certain chance of passing through a nucleus without suffering any deflection, and that this chance is greater for the smaller nuclei.

The very lightest nuclei, H and D, do not fit into the scheme discussed above. The deuterium nucleus, because of its small binding energy, can hardly be considered as a close-packed system like the nuclei of mass 4 and above. Both the H and D cross sections decrease with increasing energy much more than those of the other nuclei investigated, as will be seen by comparison of our results with those of Salant and Ramsey,[4] Ageno *et al.*,[5] Sleator,[5a] and Sherr.[1]

II. OUTLINE OF METHOD; NATURE OF SOURCE AND DETECTOR

The cross sections were determined by measuring the attenuation of the neutrons on passing through blocks of various materials, under conditions of good geometry. The neutron source was a $\frac{1}{2}$-inch thick Be target mounted on the probe of the 184-inch cyclotron; deuterons passing through this target produce a neutron beam by the process of "stripping."[6,7] The neutron energy can be estimated from the theory of this process. First, the mean energy of the neutron set free in a stripping process is very nearly half the deuteron energy, which is taken to have an initial average value of 190 Mev;[6] then the energy lost by the deuteron in the target must be taken into account. The estimated loss in traversing the target is 20 Mev; since stripping may occur at any depth, the mean loss to the deuteron before stripping is 10 Mev, and half of this is taken away from the neutron. Therefore the mean neutron energy is $190/2-5=90$ Mev. There is a distribution in energy caused primarily by the internal relative velocity of the particles in the deuteron before stripping, which leads to a momentum distribution for neutrons emitted in the forward direction of the following form:

$$P(p)\sim[1+(p-p_0)^2/M\epsilon_d]^{-2}, \qquad (3)$$

where p is the forward momentum, p_0 its mean value, M the proton mass and ϵ_d the deuteron binding energy. The points where the probability is down to half its maximum value are given by $(p-p_0)^2=(\sqrt{2}-1)M\epsilon_d$; the neutron energies at these points are then given approximately by $E_0\pm[2(\sqrt{2}-1)\epsilon_d E_0]^{\frac{1}{2}}$, where E_0 is the energy

[3] E. Amaldi and B. N. Cacciapuoti, Phys. Rev. **71**, 739 (1947).

[4] E. O. Salant and N. F. Ramsey, Phys. Rev. **57**, 1075 (1940).

[5] Ageno, Amaldi, Bocciarelli, and Trabacchi, Phys. Rev. **71**, 20 (1947).

[5a] W. Sleator, Jr., Phys. Rev. **72**, 207 (1947).

[6] A. C. Helmholz, E. M. McMillan, and D. C. Sewell, Phys. Rev. **72**, 1003 (1947).

[7] R. Serber, Phys. Rev. **72**, 1008 (1947).

corresponding to p_0. This puts the half-value points at 90 ± 12.8 Mev, and makes the half-width of the distribution equal to 25.6 Mev. If the additional spread as a result of the ranges of initial deuteron energies and energy losses is added according to the law for random distributions, the half-width is increased slightly to about 28 Mev. The distribution given by Eq. (3) falls off rapidly for large energy deviations from E_0; for example, it says that only 3 percent of the total number of neutrons have energies below 60 Mev, and 3 percent have energies above 125 Mev.

The neutrons were detected by measuring the activity induced in carbon disks according to the reaction $C^{12}(n,2n)C^{11}$. Details of the counting technique will be discussed later. The way in which the sensitivity of this detector varies with neutron energy is not well known experimentally, but we believe on the basis of theory[8] and experiments checking certain aspects of the theory of this and related processes[9–11] that the cross section is approximately constant above 60 Mev. It is certainly zero below 20 Mev, and may have a peak in the vicinity of 40 Mev. However, the number of neutrons between 20 and 60 Mev is small, and if we suppose that the detector sensitivity is nearly constant for the bulk of the effective neutrons, then the total cross section observed is simply the mean value averaged over the initial energy distribution. If the variation of the total cross section with energy can be represented by a straight line over the intense part of the neutron spectrum, then because of the approximate symmetry of the spectrum the measured cross section would correspond to the value at 90 Mev.

Recent experiments by J. A. Hadley *et al.* and H. F. York (both to be published) furnish some information on the energy distribution of the neutrons and on the carbon $(n,2n)$ excitation curve. Their results indicate that there are probably somewhat more low energy neutrons than are given by Eq. (3) and that the effective mean neutron energy as seen by the carbon detectors may be as low as 80 Mev. Therefore it should be understood that although the energy is given nominally as 90 Mev it would be more correct to say that it lies between 80 and 90 Mev.

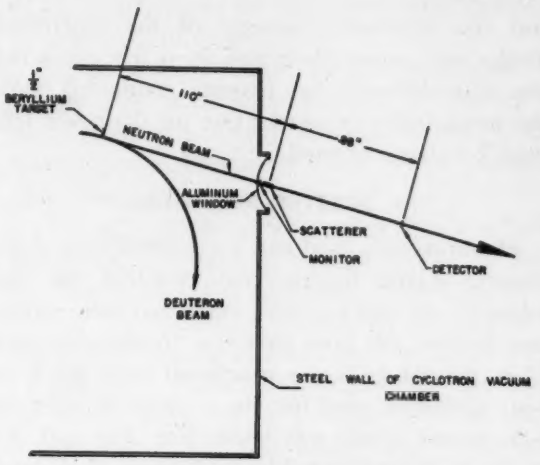

FIG. 1. Plan view of experimental set-up.

A plan view of the experimental set-up is shown in Fig. 1. The monitor, scattering block, and detector were mounted on supports made of thin dural, and were aligned along the axis of the neutron beam. A "neutron window" 32 inches in diameter, spun out of $\frac{1}{8}$-inch aluminum sheet, was set into the vacuum chamber wall, in order to reduce the background of scattered neutrons produced by the steel wall. The monitor and detector were carbon disks of $1\frac{11}{16}$-inch diameter and $\frac{1}{8}$-inch thickness. The alignment was done with the aid of a cathetometer; the axis was located by sighting on the target with the window removed, and the supports were then adjusted until cross-hairs mounted in rings having the same diameters as the scatterer and the carbon disks were on this line. The position of the axis had to be determined only once, since a mark was made on the window at its intersection with the axis, and a set of cross-hairs was fixed in a hole through the concrete cyclotron shield, through which the sighting was done. This procedure allows the achievement of very accurate collinearity. Since the greatest extent of the source is not over $1\frac{3}{4}$ inches and the detector diameter is a little less than that, it is clear that a $1\frac{3}{4}$-inch scatterer would intersect all the effective rays, but for safety a margin was allowed

[8] W. Heckrotte and P. Wolff, Phys. Rev. **73**, 264, 265 (1948).
[9] W. W. Chupp and E. M. McMillan, Phys. Rev. **72**, 873 (1947).
[10] E. M. McMillan and R. D. Miller, Phys. Rev. **73**, 80 (1948).
[11] E. M. McMillan and H. F. York, Phys. Rev. **73**, 262 (1948).

and the standard diameter of the scattering blocks was set at $2\frac{1}{2}$ inches. In a few cases the size was different for reasons connected with the availability of stock, but no diameter less than 2 inches was used.

III. SCATTERING BLOCKS

The materials used can be divided into three classes: solids, liquids, and powders. Of the solids, C, Al, and Cu were machined from stock, and Sn and Pb from castings, to the standard $2\frac{1}{2}$-in. diameter. *U* was machined from stock to 2-in. diameter, and for Be a piece of existing 2-in. round stock was used. For Mg and Zn stacks of rectangular blocks forming 3-in. and 2-in. squares respectively were used. The most difficult to handle was Li, which we obtained in the form of rather rough 2×2×1-in. blocks. These were carefully scraped clean under kerosene, then pressed in a die which brought them into an accurately rectangular shape, wiped free of kerosene and used before appreciable oxidation had occurred. Paraffin was used to get the H cross section by taking the paraffin-carbon difference; $2\frac{1}{2}$-in. disks were machined from clear bubble-free slabs of high quality paraffin and stacked together. The paraffin used was analyzed by the Chemistry Department and found to have a composition corresponding to $CH_{2.08}$.

The dimensions of the solid blocks were measured by micrometers and they were weighed to get the densities. In the case of Be the outer surface of the stock was not machined, so its density was determined by immersion in water. The measured densities are entered in Table I; it will be seen that they correspond very closely to the accepted values, with two exceptions. The density of the carbon is below the theoretical value for graphite, but this is to be expected and there is no doubt of the homogeneity and purity of the material. The density of the lithium is 6 percent high, indicating the presence of impurities. The error in the Li cross section will not be this large, however, since the impurities themselves do some absorbing; the mass absorption coefficients of the elements from Be to Cl are close enough to that of Li that any of these as impurities would give less than 1 percent error in the cross section.

The liquid absorbers were contained in thin-walled aluminum cells $2\frac{1}{2}$-in. in diameter by 11 27/64-in. long, with $\frac{1}{32}$-in. Al ends. One cell was filled with water, one with heavy water, and one was left empty to be used in the initial intensity and background determinations. The water cross section minus that of H gave the O cross section, and a direct comparison of the light and heavy water absorptions gave the D–H difference. One of these cells was also used to contain CCl_4 to measure the Cl cross section. The densities of the liquids were not measured, since their purity was known and the accepted values could be used.

The only powdered substance used was melamine ($C_3H_6N_6$), from which the N cross section was obtained. This was tamped into a $2\frac{1}{2}$-in. Al tube, taking care to get as nearly uniform packing as possible. The bulk density is of no interest; in the computations the surface density obtained from the inner diameter of the tube and the weight of melamine was employed.

IV. EXPERIMENTAL PROCEDURE

The experimental data were taken in a series of 18 runs, each run comprising the measurements taken on any one day or with any one particular experimental set-up. It was necessary to perform the alignment procedure for each run to make sure that the axes of the monitor, the absorber, and the detector lay along a common ray of the neutron beam from the cyclotron. It was not necessary to keep the longitudinal distances the same from run to run, but for convenience they were kept roughly the same, the run-to-run variation being only a few inches at the most.

A typical run took several hours to perform and included as many as 50 separate absorption measurements. Each measurement began with the insertion of a matched pair of carbon disks into the monitor and detector holders, a suitable length of absorbing material having been interposed. (Each pair of the monitor and detector carbon disks was matched in weight to within 0.2 percent.) This arrangement was then exposed to the neutron beam for 1.5 minutes, at the end of which time the carbon disks were taken to another building and the ratio of their activities counted. As the half-life of the induced activity in the carbon disks was only 20.5 minutes, i.e.,

small compared with the length of the run, it was necessary to begin the counting of the pairs of disks while other pairs of disks were being exposed. The time interval between the end of the exposure and the beginning of the counting varied from 4 to 30 minutes and was usually about 10 minutes.

In the first eleven runs absorption curves were plotted from measurements made on various thicknesses of absorbing material. These absorption curves, when corrected for background, were found to be exponential within experimental error as far as they could be followed into the background. This background activity induced in the carbon disks was caused by scattering of the neutron beam from the aluminum window in the cyclotron vacuum chamber, from the aluminum and dural trough which supported the absorber and the monitor disk, and from other neighboring materials. Another contributor to the background was the production of neutrons in parts of the cyclotron other than the $\frac{1}{2}$-inch beryllium target. The magnitude of the background reading was 5 to 6 percent of the activity induced when no absorber was interposed between the two carbon disks. It was measured by inserting a 32-inch length of copper rod in the absorber position; its diameter was equal to that of the usual absorbing samples. In the presence of no background this copper rod would have attenuated the beam to 2.5×10^{-7} of its undisturbed intensity. The substances on which absorption curves were run were paraffin, carbon, aluminum, copper, and lead. Figure 2 shows the absorption curves of copper and aluminum plotted on semi-logarithmic graph paper.

It having been shown in this way that the absorption of the neutron beam was indeed exponential, the remaining runs, upon which the final results were chiefly based, employed single lengths of absorbers and depended on repeated measurements for accuracy. The length of absorber used in each case was about one mean free path. Of course, before the experiment was actually run, it was impossible to tell exactly what length of absorber corresponded to one mean free path, but one could make reasonably good guesses by extrapolation or interpolation from previous measurements on other substances or by a quick run on some arbitrary length of the absorber in question.

For the calculation of the absorbing power of a typical substance, three ratios of detector to monitor activity had to be determined: (1) the ratio with no absorber between the carbon disks (the "blank" measurement), (2) the ratio with the length of absorber whose attenuation is being measured, and (3) the background ratio. Each of these ratios was measured several times to reduce the statistical errors. In the course of the repetitions the blank and the absorber ratios were measured alternately to keep the conditions as closely identical as possible. Not as many determinations of the background ratio were made because its contribution to the probable error was less than those of the other two ratios.

V. COUNTING TECHNIQUE AND CALCULATIONS

The basic measurement is the ratio of the activity of the detector disk to that of the monitor disk; calling this ratio r when the scattering block is in place, r_0 when it is absent, and r_b when the long copper block is in place

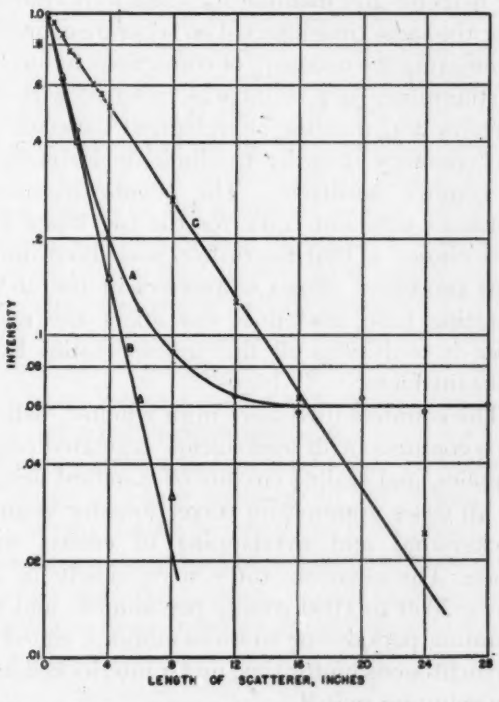

FIG. 2. Some attenuation curves. Curve A (circles): Copper scatterer, neutron background not subtracted. Curve B (triangles): Copper scatterer, background subtracted. Curve C (crosses): Aluminum scatterer, background subtracted.

TABLE I. Measured mean free paths.

Substance	Density ρ g/cm³	Mean free path λ (cm)	$\rho\lambda$ (g/cm²)
H_2O	0.998[a]	32.2	32.1
D_2O	1.105[a]	30.1	33.3
paraffin ($CH_{2.08}$)	0.918	35.3	32.4
melamine ($C_3N_6H_6$)	— [b]	—	34.4
CCl_4	1.595[a]	26.4	42.1
Li	0.567	64.7	36.7
Be	1.85	18.8	34.8
C	1.596	22.7	36.3
Mg	1.735	22.6	39.2
Al	2.711	14.8	40.0
Cu	8.91	5.33	47.5
Zn	7.078	6.94	49.1
Sn	7.28	8.26	60.1
Pb	11.33	6.70	75.9
U	18.8	4.18	78.6

[a] Density from tables. Other values were measured on the samples used.
[b] Only surface density measured on this sample. The individual errors are not given, but should be taken as about ±2 percent of λ and $\rho\lambda$. Corrections for scattering into the detector have been applied.

(background), the following relation holds:

$$(r-r_b)/(r_0-r_b)=\varepsilon^{-l/\lambda}, \qquad (4)$$

where l is the length of the scatterer and λ is the mean free path for the neutrons.

All counts were made concurrently; that is, the detector and monitor activities were counted over the same time interval on separate counters, eliminating the necessity of corrections for decay. Furthermore, each count was repeated with the detector and monitor interchanged between the two counters, in order to eliminate inequalities in counter sensitivity. The counter-to-sample distances were not equal for the two disks, but were chosen so that the ratio r_0 was about unity. This procedure allows more efficient use of the counting time, and does not affect the result since it multiplies all the activity ratios by a constant factor.

The counters used were mica window, bell-jar type counters, with lead shields, regulated power supplies, and scaling circuits of standard design. In all cases appropriate corrections for counter background and overlapping of counts were made. The counting rates were mostly in the range 2000 to 6000 counts per minute, and the counting periods one to three minutes, timed by a synchronous motor time meter interlocked with the counting switch.

The statistical errors may be estimated in the following way. A typical determination of r_0 involves about 5000 counts each on the detector and monitor, and an equal number with the samples interchanged, giving a mean error in r_0 of $1/(5000)^{\frac{1}{2}}=1.4$ percent. Similarly, in measuring r, the detector made about 2000 counts and the monitor about 5000, giving an error in r of $[\frac{1}{2}(1/5000+1/2000)]^{\frac{1}{2}}=1.9$ percent. Since the determination of r_b contributes a negligible error, and $l/\lambda\sim 1$, then according to (4) the error in a single determination of λ is just $((1.4)^2+(1.9)^2)^{\frac{1}{2}}=2.4$ percent. Finally, for each substance the determination was repeated about ten times, so that the mean statistical error in the final value for λ is a little less than 1 percent. It was found that the spread among individual determinations, even when made on different days or with different counters, corresponded to that expected from the counting statistics.

Where the cross-section values are derived from differences, as in the cases of H, D, O, N, and Cl, the errors are of course greater than those of the individual measurements. In taking the differences $CH_{2.08}-C$ and D_2O-H_2O, samples of nearly equal attenuation were used, and the readings were alternated between the samples. The numbers of separate determinations of these differences were 30 and 20 respectively.

The errors in the length and density measurements are believed to be less than 0.5 percent. Another possible source of error, the back-scattering of neutrons from the absorber into the monitor, was found to be negligible in a special experiment designed to measure this effect. The errors given with the final results are

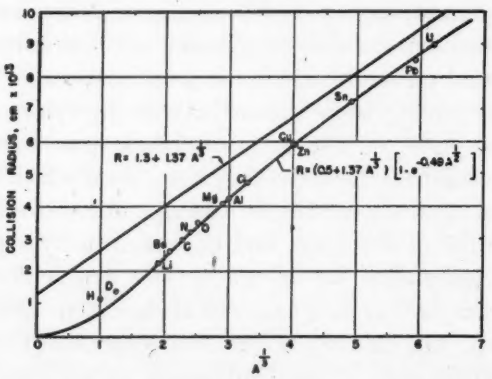

FIG. 3. Collision radii R, computed from the measured cross sections by Eq. (1), plotted against cube roots of mass numbers. The straight line represents an approximation to data obtained by other observers at 14–25 Mev; the curve is from an empirical formula fitted to the 90-Mev points, not including H and D.

the mean statistical errors, plus 1 percent added to allow for other unsuspected sources of error.

VI. CORRECTION FOR SCATTERING INTO DETECTOR

In spite of the very good geometry of this experiment, the errors arising from scattering of neutrons into the detector by the heavier elements are not quite negligible, on account of the small angular spread of the diffraction patterns at this neutron energy. Therefore, corrections were made for this effect, computed as outlined in the Appendix. The largest correction for this effect was 3 percent.

VII. RESULTS

The results are collected in Tables I and II.

VIII. DISCUSSION

The cross sections from Li to U can be compared with the results at lower energy, as given in Eq. (2), by plotting R against $A^{\frac{1}{3}}$. Such a plot is given in Fig. 3. It is apparent that the values lie on a smooth or nearly smooth curve, and can therefore be fitted by an empirical equation. Such an equation is:

$$R=(0.5+1.37A^{\frac{1}{3}})[1-\exp(-0.49A^{\frac{1}{3}})] \times 10^{-13}\text{ cm}. \quad (5)$$

This is plotted on the figure, and the values are also entered in the last column of Table II. The form of this equation has no theoretical basis, but it may be useful for purposes of interpolation. The deviations of some of the points from the smooth curve are hardly statistically significant. After completing the measurements described above, some attenuation values were obtained with the same detectors and absorbers, but using the collimated neutron beam which emerges through a 2-inch hole in the concrete cyclotron shield. The values obtained were for carbon $\sigma_t=0.556\pm0.013$, and for copper $\sigma_t=2.13\pm0.04$. The two carbon values are in excellent agreement; the two copper values lie above and below the empirical curve, making us believe that the deviations from this curve are not significant.

It will be noted that the 90-Mev values tend to approach the lower energy values for large A, but become increasingly smaller than the latter as A becomes smaller. This is attributed to the transparency of the nucleus, the probability of penetration without collision becoming greater as the nuclear diameter becomes less compared to the mean free path of the neutrons in nuclear matter. This mean free path, computed using the measured H and D cross sections, is consistent with the degree of transparency shown by the other elements. Since a more complete discussion will be given in a paper to be published by the theoretical group of the Radiation Laboratory, these relations will not be developed further here.

As pointed out in Section II, the effective mean energy of the neutrons may be below the nominal value of 90 Mev by as much as 10 Mev. The energy is thus known with less accuracy than the cross sections. This uncertainty is not very important in making a theory to correlate the various cross sections, where one is dependent chiefly on internal consistency of the data, but it is important in comparing the cross sections with computed absolute values, or with values measured at other energies. In the cases of H and D which may be compared with theoretical calculations based on assumed nuclear force laws, the fact that the nominal energy of 90 Mev is possibly a little too high should be taken into account.

TABLE II. Total cross sections.

Substance	σ_t cm$^2\times10^{24}$	A mean mass no.	$A^{\frac{1}{3}}$	R cm$\times10^{13}$	R' cm$\times10^{13}$
H	0.083±0.004	1	1	1.15±0.03	0.72
D[a]	0.117±0.005	2	1.26	1.36±0.03	1.11
Li	0.314±0.006	6.94	1.91	2.24±0.02	2.26
Be	0.431±0.008	9	2.08	2.62±0.02	2.58
C	0.550±0.011	12	2.29	2.96±0.03	2.97
N	0.656±0.021	14	2.41	3.23±0.05	3.19
O	0.765±0.020	16	2.52	3.49±0.05	3.39
Mg	1.03 ±0.02	24.32	2.90	4.05±0.04	4.07
Al	1.12 ±0.02	27	3.00	4.22±0.04	4.25
Cl	1.38 ±0.03	35.46	3.29	4.69±0.05	4.74
Cu	2.22 ±0.04	63.57	3.99	5.94±0.05	5.85
Zn	2.21 ±0.04	65.38	4.03	5.93±0.05	5.90
Sn	3.28 ±0.06	118.70	4.92	7.22±0.07	7.21
Pb	4.53 ±0.09	207.21	5.92	8.49±0.08	8.60
U	5.03 ±0.10	238	6.20	8.95±0.09	8.99

[a] The difference D–H has an error of ±0.003. The collision radius R is computed from Eq. (1); R' is the corresponding value given by the empirical Eq. (5). The errors given are the statistical mean errors plus 1 percent.

ACKNOWLEDGMENTS

The authors wish to thank Professor E. O. Lawrence for his encouragement in this work, the cyclotron operating crew for their assistance

in making the runs, and Miss Alice Dodson for her help in computing the data. This paper is based on work performed under Contract No. W-7405-eng-48 with the Atomic Energy Commission in connection with the Radiation Laboratory, University of California.

APPENDIX. CORRECTION FOR DIFFRACTION EFFECTS

In interpreting fast neutron scattering experiments, it has generally been assumed that the diffraction of the neutron waves by the nucleus accounts for a part of the total cross section equal to the projected collision area of the nucleus. This is a very reasonable assumption in cases where the neutron wave-length is short compared to the nuclear diameter, since the diffracted intensity is mostly in the forward direction and the situation approximates that of diffraction by a disk-like obstacle. Comparison with the well-known equivalent optical problem shows that the total diffracted flux is indeed equal to the flux intercepted by the obstacle, and that its angular distribution is given by:

$$d\sigma_d/d\omega=\left[\frac{RJ_1(kR\sin\theta)}{\sin\theta}\right]^2 \tag{6}$$

where $d\sigma_d/d\omega$ is the cross section per unit solid angle for diffraction at the angle θ, R is the collision radius of the nucleus, k is 2π times the reciprocal of the neutron wave-length, and J_1 is a Bessel function.

The total cross section σ_t should then be made up of the integrated cross section σ_d for diffraction plus an equal amount to take care of the neutrons that actually strike the nucleus, giving the usually assumed relation:

$$\sigma_t=2\sigma_d=2\pi R^2. \tag{7}$$

This should be strictly valid when $kR\gg1$, if the nucleus can be considered as an opaque obstacle. If the nucleus is partially transparent, as is apparently the case for lighter nuclei at 90-Mev neutron energy, the situation is more complicated, and both the magnitude and angular distribution of the diffraction can be altered. One can however still treat (7) as a definition of R in these cases, and use the diffraction formula (6) as a first approximation, with the understanding that the R so defined may be smaller than the actual nuclear radius.

In the cases to be considered here, we are dealing with 90-Mev neutrons, for which $k=2.15\times10^{13}$ cm^{-1}; the collision radius found for the uranium nucleus is 9.0×10^{-13} cm, giving $kR=19$. According to Eq. (6) the diffraction pattern for uranium falls to half intensity at $\theta=0.085$ radian, while the patterns for other elements will be wider.

At small values of θ, the diffraction per unit solid angle is given approximately by the first two terms in the series expansion for the Bessel function, thus:

$$d\sigma_d/d\omega\sim1/4k^2R^4[1-1/8(kR\sin\theta)^2]^2. \tag{8}$$

With the above preliminaries we can estimate the intensity diffracted into the detector in a typical attenuation experiment, set up as in Fig. 1. The method of calculation is similar to that of reference (2), appendix II. The source and detector are treated as points, since they subtend angles small compared to the width of the central diffraction peak. Because of the similarity of the treatment to that already published by Amaldi *et al.*,[2] only the result is given here. The intensity I_d diffracted into the detector, in terms of the intensity I that would be seen there in the absence of diffracted neutrons, is given by:

$$\left.\begin{aligned} I_d&=I(l/\lambda)(K-K^2)(1+l/8\lambda),\\ K&=(1/16\pi)k^2a^2(1/x_1+1/x_2)^2\sigma_t,\end{aligned}\right\} \tag{9}$$

where a is the radius of the scatterer, x_1 and x_2 are the distances from the center of the scatterer to the source and detector, l is the length of the scatterer, and λ is the mean free path of the neutrons in the scatterer. The term in K^2 comes from the second term of (8) and the term in $(l/8\lambda)$ from double scattering processes; their smallness indicates that higher order approximations are not necessary. Numerically we find for example in the case of lead $k=2.15\times10^{13}$ cm^{-1}, $a=1.25$ in., $x_1=110$ in., $x_2=88$ in., $\sigma_t=4.5\times10^{-24}$ cm^2, giving $K=0.027$. The relative error in λ is simply the error in the intensity times λ/l, and is therefore equal to I_d/I from (9) without the factor l/λ, giving an error of $0.027(1+1/8)=3.0$ percent. For lighter elements the error is obviously smaller, and for uranium it is smaller because the radius of the scattering block was only one inch.

In order to check the approximate validity of the formula used in making this correction, measurements were made of the scattering from rings of Cu and Pb placed around a long copper rod which intercepted the direct beam. Although not very precise because of the relatively high background, these results verified the computed scattering with sufficient accuracy for the purpose of making this small correction.

On Simultaneous Beta-Gamma Emission from Nuclei*

CONRAD L. LONGMIRE**
University of Rochester, Rochester, New York
(Received August 30, 1948)

The possibility of simultaneous beta-gamma-emission as an alternative process for strongly forbidden beta-decay is investigated. The lifetime of the compound transition is estimated, and the beta- and gamma-spectra are given. Combinations of spin and parity for which the compound transition would not be obscured by the ordinary beta transition are listed.

ACCORDING to the Fermi theory of beta-decay, there are (for all but the tensor form of nucleon-electron-neutrino interaction) some beta-transitions which are highly forbidden even though the spin change is small.[1] The forbiddenness may be said to come from having the wrong parity instead of a large spin change. Examples of such transitions are 0→0 "yes" for the scalar and polar vector interactions, and 0→0 "no" for the axial vector and pseudoscalar interactions. ("Yes" and "no" refer to parity change.) The transitions cited are, in fact, absolutely forbidden.

Suppose there are two nuclei, just right for beta-decay, except that the transition between ground states falls in the class just mentioned. Suppose also that the residual nucleus has no excited states low enough to allow ordinary beta-decay followed by a nuclear gamma-ray. The question then arises whether the transition between ground states could take place if a gamma-ray were emitted by the nucleus simultaneously with the electron and neutrino. Such a transition can be thought of as occurring by means of the virtual transitions and intermediate states of second order perturbation theory, as shown in Fig. 1. In such a process, the ordinary selection rules do not apply to the over-all transition. In the particular example of Fig. 1, the ordinary beta-ray selection rules apply between the initial nucleus and the intermediate nucleus, and the gamma-ray selection rules apply between the intermediate nucleus and the final nucleus. The total available energy will be shared by the electron, the neutrino, and the photon, and there will be a strict coincidence among all these "particles." (This latter property would distinguish experimentally the present process from that in which the electron emits bremsstrahlung on its way out of the atom. This bremsstrahlung cannot help circumvent selection rules.)

We are interested in cases where the lifetime of the compound beta-gamma-transition is observable and is equal to or less than the lifetime of the direct beta-transition between ground states. Since the compound transition is inherently weaker (by a factor of about 10^9) than ordinary beta-transitions, the net forbiddenness of the compound transition must be much less than that of the direct transition, in order for the effect not to be obscured. Gamma-rays abhor large spin changes as much as do beta-rays. It follows that the net forbiddenness of the compound beta-gamma-transition will be appreciably less than that of the direct beta-transition only when the latter is strongly forbidden for reasons of parity rather than large spin change. An examination of the selection rules[1] shows that the only interesting cases are the absolutely forbidden transitions with small spin change.

It is clear that the compound transition would have the shortest lifetime when the beta-part is allowed and the gamma-ray is electric dipole. Unfortunately, this combination cannot occur,

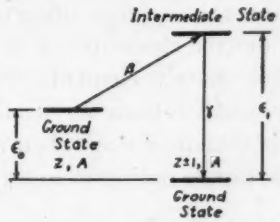

FIG. 1. Example of compound beta-gamma-transition

* Part of work on Doctoral Thesis.
** National Research Predoctoral Fellow; now at Department of Physics, Columbia University, New York, New York.
[1] E. J. Konopinski and G. E. Uhlenbeck, Phys. Rev. 60, 313 (1941).

TABLE I. Absolutely forbidden beta-transitions and their beta-gamma-alternatives.*

Form of interaction	Over-all transition	Best alternatives
Scalar	0→0 yes	$(0+)\xrightarrow{\beta 1f}(1-)\xrightarrow{\gamma MD}(0-)$
	0↔1 no	$(0+)\xrightarrow{\beta 0f}(0+)\xrightarrow{\gamma MD}(1+)$
	0↔1 no	$(0+)\xrightarrow{\beta 1f}(1-)\xrightarrow{\gamma ED}(1+)$
	0↔2 yes	$(0+)\xrightarrow{\beta 1f}(1-)\xrightarrow{\gamma MD}(2-)$
Polar Vector	0↔0 yes	$(0+)\xrightarrow{\beta 1f}(1-)\xrightarrow{\gamma MD}(0-)$
Tensor	No absolutely forbidden transitions	
Axial Vector	0↔0 no	$(0+)\xrightarrow{\beta 0f}(1+)\xrightarrow{\gamma MD}(0+)$
	0↔0 no	$(0+)\xrightarrow{\beta 1f}(1-)\xrightarrow{\gamma ED}(0+)$
Pseudoscalar	0↔0 no	$(0+)\xrightarrow{\beta 1f}(1+)\xrightarrow{\gamma MD}(0+)$
	0↔1 yes	$(0+)\xrightarrow{\beta 0f}(0-)\xrightarrow{\gamma MD}(1-)$
	0↔1 yes	$(0+)\xrightarrow{\beta 1f}(1+)\xrightarrow{\gamma ED}(1-)$
	0↔2 no	$(0+)\xrightarrow{\beta 1f}(1+)\xrightarrow{\gamma MD}(2+)$

* Notation: $0f$ = allowed, $1f$ = first forbidden; ED = electric dipole, MD = magnetic dipole.

for any form of interaction, when the ordinary beta-transition between ground states is absolutely forbidden. The best that can be had is an allowed beta-ray with a magnetic dipole gamma-ray, and the next best is a first-forbidden beta-ray with an electric dipole gamma-ray. This is shown in Table I, which lists absolutely forbidden beta-transitions and their best compound alternatives. In the alternative transitions, all parities may be reversed, and the order of the beta- and gamma-parts may be reversed with suitable modification of the intermediate state.

In estimating the lifetime of the compound transition, there is a large uncertainty in the gamma-ray matrix elements. It is known that electric dipole matrix elements for nuclei are considerably smaller than for a single charged particle;[2] this weakness was taken into account. For magnetic dipole radiation experimental data are lacking. For this case the matrix element of

$$\sum_i \left(\frac{e_i}{e}\mathbf{L}_i+\mu_i\boldsymbol{\sigma}_i\right)$$

was set equal to unity. (Here e_i is the charge of the i'th nucleon, μ_i is its magnetic moment in nuclear magnetons, $\mathbf{L}_i$ is its angular momentum in units of $\hbar$, and $\boldsymbol{\sigma}_i$ is its Pauli spin operator.) There are also the usual uncertainties in the beta-ray matrix elements.

Table II contains the numerical values of the estimated lifetimes, calculated on the assumption that the total energy available is 2 Mev. Only the two best combinations of the beta- and gamma-forbiddenness are considered. Although the net forbiddenness is the same for both cases (magnetic dipole is one degree more forbidden than electric dipole), the transition involving the electric dipole gamma-ray has a longer lifetime because of the weak oscillator strength (assumed to be 1/50) for electric dipole radiation. In calculating the lifetimes, full strength was assumed for the beta-ray matrix elements.

The approximate dependence of the lifetime τ on ϵ_0, the energy available, is

$$1/\tau\sim\epsilon_0^{\beta+2s}$$

where β is the normal exponent for the beta-ray part, and

$$s=1 \text{ for electric dipole,}$$
$$s=2 \text{ for magnetic dipole.}$$

The differential electron-gamma-spectrum, for transitions in which the beta-part is allowed, is given by

$$Id\epsilon_e d\epsilon_\gamma = I_0\frac{\epsilon_\gamma^{2s-1}}{(\epsilon_1-\epsilon_\gamma)^2}\times[(\epsilon_0-\epsilon_e-\epsilon_\gamma)^2\epsilon_e(\epsilon_e^2-1)^{\frac{1}{2}}]d\epsilon_e d\epsilon_\gamma$$

where $d\epsilon_e$ is the energy range for the electron and

TABLE II. Lifetimes of compound transitions.

Beta-ray	Gamma-ray	Estimated lifetime
Allowed	magnetic dipole	10^6 years
First forbidden	electric dipole	4×10^7 years

[2] H. A. Bethe, Rev. Mod. Phys. 9, 221 (1937); also Phys. Rev. 55, 434 (1939).

$d\epsilon_\gamma$ that for the gamma-ray. The quantity in square brackets is the usual expression for an allowed beta-transition. I_0 is a constant which depends on ϵ_0 and ϵ_1 (through the matrix elements) but not on ϵ_e and ϵ_γ, so that the shapes of the spectra are given exactly by this formula. However, for a forbidden beta-part, the quantity in square brackets must be replaced by the ordinary energy-function appropriate to the degree of forbiddenness.

The author is grateful to the National Research Council for financial aid, and to Professor R. Marshak for suggesting and guiding the work reported here.

PHYSICAL REVIEW VOLUME 75, NUMBER 1 JANUARY 1, 1949

The Fission of Thorium with Alpha-Particles

AMOS S. NEWTON
Radiation Laboratory, University of California, Berkeley, California
(Received September 27, 1948)

The fission distribution of fission of thorium with alpha-particles of average energy 37.5 Mev has been measured by the chemical method. The distribution found shows that the characteristic dip in the fission yield mass spectrum has been raised to within a factor of two of the peaks compared to a factor of 600 in slow neutron fission of U^{235}. The raise in the dip has caused a corresponding lowering in fission yield of these elements at the peaks. The cross section for fission of thorium with 37.5-Mev alphas was found to be about 0.6 barn, and the threshold for fission was found to be 23 to 24 Mev.

I. INTRODUCTION

SOON after the discovery of fission, Meitner[1] and Bretscher and Cook[2] found differences in the decay of various chemical fractions separated from uranium irradiated with slow neutrons and thorium irradiated with fast neutrons, respectively, and suggested that a difference existed in the distribution of fission products in the two cases. In 1940, Turner[3] suggested that the distribution in various modes of fission should be investigated. The fact that elements such as tin, cadmium, palladium, and silver[4] were found in fast neutron and deuteron fission of uranium and thorium before they were found in slow neutron fission of uranium suggested that the middle region of the distribution was raised as the energy of the incident particle was increased.

Since the compound nucleus formed in the fission of thorium with alpha-particles is U^{236}, the same compound nucleus formed in the fission of U^{235} with neutrons, it is of interest to study the fission of thorium with alphas and compare the resulting distribution of fission products with that found with uranium with slow[5] and thorium with fast[6] neutrons. Any difference between the various results where the same compound nucleus is formed must be due to differences in energy content and possible differences in distribution of the nucleons in the compound nucleus at the time of fission.

II. EXPERIMENTAL METHODS

Of the various methods available for studying the fission process, the method of chemically isolating the fission products with added carrier and determining the fission yield of each isotope seemed most suitable.[7] The method of studying the energy distribution of fission fragments in an ionization chamber, as used by Jentschke[8] and

[1] L. Meitner, Nature **143**, 637 (1939).
[2] K. Bretscher and L. G. Cook, Nature **143**, 559 (1939).
[3] L. A. Turner, Rev. Mod. Phys. **12**, 9 (1940).
[4] Y. Nishina, K. Kimura, T. Yasaki, and M. Ikawa, Nature **146**, 24 (1940); Phys. Rev. **58**, 660 (1940); Phys. Rev. **59**, 323 (1941); Phys. Rev. **59**, 667 (1941).
[5] "Nucleii formed in fission," Plutonium Project, J. Am. Chem. Soc. **68**, 2411 (1946); Rev. Mod. Phys. **18**, 513 (1946).
[6] A. Turkevich, private communication. Presented at A.A.A.S. Meeting, Chicago, December, 1947.
[7] H. L. Anderson, E. Fermi, and A. V. Grosse, Phys. Rev. **59**, 52 (1941).
[8] W. Jentschke, Zeits. f. Physik **120**, 165 (1943).

Flammersfeld, Jensen and Gentner,[9] is not particularly suited for the present problem because of the difficulties inherent in using an ionization chamber in the presence of the alpha-beam.

The thorium used in the bombardment was special purity thorium metal produced by the group at the Atomic Research Institute at Iowa State College. In a long bombardment, designated as Bombardment *A*, of 3020 μah of 39-Mev helium ions (impinging energy as estimated by Dr. J. G. Hamilton) on the Crocker Laboratory cyclotron, a 3⅛-inch diameter thorium backing plate ⅛ inch thick was used. After bombardment a radioautograph of the disk was made to determine the active area. The activity was then removed by milling thin layers from the active area, using a milling set-up in which the millings could be quantitatively collected. Eleven layers, varying from 1 to 3 mils in thickness, were removed from this target so the fission product distribution and the excitation curve for fission could be determined. The milling removed about 95 percent of the total beta- and gamma-activity from the target. In addition to this, three shorter bombardments of 24-hour, 2-hour, and 4-hour duration, designated as bombardments *B*, *C*, and *D*, respectively, were obtained on thorium foils of thickness about 30 mg/cm² using the interceptor set-up of the Crocker cyclotron. In these cases it was assumed that all of the 2-cm² area of the interceptor received bombardment.

The technique used in determining the fission yields was the standard chemical technique as used on the Plutonium Project. The bombarded sample was dissolved in either hydrochloric or nitric acid, a small amount of ammonium fluosilicate being added as a catalyst. The solution was diluted to a known volume and stored in Lusteroid tubes inside a glass tube to prevent loss of activity by adsorption on glass and evaporation of the solution. Aliquots were taken for determination of each desired element. In each fraction, carrier was added for the element to be separated, and the element chemically separated and decontaminated from other activities. The element was then precipitated in a suitable form, weighed, and the chemical yield determined. The samples were mounted on cardboard, covered with Cellophane, and counted on the second shelf of a standard counter set-up. Corrections were made in the counting rate for coincidences, geometry, and absorption to obtain the disintegration rate of the sample. Decay curves were taken to characterize all activities, and absorption curves were taken where possible. If absorption curves could not be taken, absorber corrections were made on the basis of published absorption curves for that activity which were known to have been taken on similar equipment. In order to obtain the fission yield the activities were all extrapolated back to a given time shortly after the end of the bombardment. Since the cyclotron irradiations were irregular, in order to integrate the bombardment and correct for saturation of shorter-lived materials during the bombardment, the bombardment history was treated in small time intervals. The microampere hours of bombardment in each time interval were then allowed to "decay" to some comparison time with the half-life of the activity being considered. At the comparison time the effective irradiations from each time interval were summed to give a total effective bombardment at that time. If the increments were longer than 5 percent of the half-life of the isotope, corrections were made for saturation during each increment.

Since neither the absolute fission yield of a fission product produced in the fission of thorium with alpha-particles nor the fission cross section are known, the cross section for the formation of each isotope which is the product of the fission yield and cross section for fission has been calculated by the equation:

$$\sigma_{\text{F.P.}} = \sigma_f \times \text{F.Y.} = \frac{(\text{atoms F.P.})(\text{area target})}{(\text{atoms Th})(\mu\text{ah})(1.13\times 10^{16})},$$

where the term (μah) refers to the effective μah of bombardment at the time of comparison, and the factor 1.13×10^{16} converts μah to the number of helium ions striking the target.

Variations in the cross section for various bombardments have not been normalized to any given value; since the values of $\sigma_f \times$F.Y. have been calculated on an absolute basis there is no *a priori* reason for normalizing the values to any given value of the barium, the element with which comparisons are usually made. Since there

[9] A. Flammersfeld, P. Jensen, and W. Gentner, Zeits. f. Physik 120, 450 (1943).

are inaccuracies in estimating the total bombardment and the distribution of the bombardment, variations can be expected when long and short-lived periods are compared in any one bombardment. In general, the results are probably correct to within a factor of two when comparisons are made between different bombardments.

III. ISOTOPES STUDIED

In all bombardments the 300-hr. Ba^{140} was separated in order to offer a rough check on the bombardment. The chemical methods used in the isolation were modifications of those developed for the fission products by the Plutonium Project. These will be described in detail by the individual authors,[10] so only the general methods will be described here.

1. *Zinc* was separated by precipitation as $ZnHg(CNS)_4$, which was dissolved in dilute nitric acid, and mercuric and bismuth sulfide scavenging precipitations were made. Zinc sulfide was precipitated, dissolved in hydrobromic acid, and fumed twice to dryness. From a sodium hydroxide solution, ferric hydroxide and barium carbonate scavenging precipitates were made. Zinc sulfide was precipitated, dissolved, and the zinc finally precipitated as $ZnHg(SCN)_4$. The final yield of carrier added was only 10 percent, and only a small activity was found which could not be identified as the 49-hr. Zn^{72}. An initial observed activity of 250 c/m decayed with a 3-hr. period, followed by a period longer than 5 days, and could conceivably be silver contamination. An upper limit of 50 c/m of the 49-hr. period could have been present and not resolved, setting an upper limit of 8×10^{-29} for the value of $\sigma_f\times$F.Y. for mass 72.

2. *Arsenic* was separated to study the chain Ge^{77} $\xrightarrow{12\text{ hr.}}$ As^{77} $\xrightarrow{40\text{ hr.}}$ Se^{77} (stable). The arsenic was separated about 24 hours after bombardment, so 75 percent germanium had decayed to arsenic. Since in uranium fission the independent yield of members of this chain is nearly all 40-hr. As^{77},[11] it is believed the result found represents >95 percent of the chain. Arsenic and germanium were separated by precipitation as the sulfide from $6N$ HCl. Germanium was distilled from HCl and $KClO_3$. Then arsenic was distilled as arsenic trichloride from concentrated hydrochloric acid containing cuprous chloride with antimony, tellurium, and tin as holdback carriers. Arsenic sulfide was precipitated from the distillate and redistilled. The arsenic was weighed as As_2S_3. The yield of carrier was 40 percent, and an observed activity of 50 c/m decayed to less than 5 c/m with a 40-hr. half-life. It was assumed to be all arsenic. Since no absorption curve could be taken, the activity was extrapolated to zero absorber on the basis of absorption curves of Steinberg and Engelkemeier.[11] The activity found gives a value of $\sigma_f\times$F.Y. of 2.8×10^{-29}.

3. *Bromine* was isolated by extraction with carbon tetrachloride after oxidation with permanganate. The extract was decontaminated from iodine by oxidation with sodium nitrite and extraction of the iodine with carbon tetrachloride. The bromine was then oxidized by permanganate and extracted. Two such decontamination cycles were run, and the bromine was then precipitated as silver bromide.

The 2.4-hr. Br^{83} was found and identified, it being found with a $\sigma_f\times$F.Y. of 5.69×10^{-27} and 4.83×10^{-27} in two determinations. A search for the 35-hr. Br^{82}, a shielded isotope, from a larger sample was not successful, the low activity found being resolvable into 22-hr. and 8-day curves which were probably iodine contamination. A maximum of $\frac{3}{4}$ of the observed 22-hr. period might have been 35-hr. activity and not resolved, placing the maximum value of $\sigma_f\times$F.Y. at 1.85×10^{-29}.

4. *Strontium* was isolated by precipitation of strontium and barium nitrates from fuming nitric acid. After two nitrate precipitations a ferric hydroxide decontamination precipitate was made. Barium was separated by precipitating as barium chromate from an acetate buffered solution. The strontium was precipitated from an ammoniacal solution as $Sr(C_2O_4)\cdot H_2O$ with ammonium oxalate.

The 9-hr. Sr^{91}, 2.7-hr. Sr^{92}, 53-day Sr^{89}, and 25-yr. Sr^{90} periods were studied. The 53-day Sr^{89} was observed in both bombardments *A* and *B*. Two values of $\sigma_f\times$F.Y., 3.3×10^{-28}, and 2.25×10^{-26}, respectively, were found. The 25-yr. Sr^{90} was measured by extracting the 60-hr. Y^{90} daughter

[10] Plutonium Project Record, Vol. 9B (to be issued).
[11] E. P. Steinberg and D. W. Engelkemeier, PPR Vol. 9B, No. 7.2.1 (to be issued).

after allowing a strontium sample to equilibrate with the daughter. This gave a value of $\sigma_f \times$F.Y. of 2.16×10^{-26} for the 25-yr. Sr^{90}. The 9.7-hr. Sr^{91} was observed directly after allowing the 2.7-hr. Sr^{92} and its daughter to decay. The absorption correction used included an estimation of the effect of the 40 percent branching to an excited state of Y^{91} and the 9 percent conversion of the Y^{91} gamma-ray. A value of 2.08×10^{-26} was found for $\sigma_f \times$F.Y. for this isotope. The 2.7-hr. Sr^{92} decaying to a 3.5-hr. Y^{92} was found by subtraction of the 9-hour and 53-day periods. The observed curve was compared to a synthetic growth and decay curve for the two isotopes and found to fit quite well, the assumption being made that the two isotopes were counted with equal efficiency. A value of 2.23×10^{-26} was found for $\sigma_f \times$F.Y. of Sr^{92}.

5. *Zirconium* was separated by precipitation as barium fluozirconate after precipitation of lanthanum fluoride. The barium fluozirconate was dissolved in boric acid, reprecipitated, dissolved, and barium sulfate precipitated. The zirconium was then precipitated with cupferron and ignited to ZrO_2 for weighing and mounting.

The 65-day Zr^{95} was separated several months after bombardment *A*, counted, and an absorption curve taken immediately to eliminate effects caused by the growth of the 35-day columbium daughter. The activity observed was corrected back to the comparison time on the basis of the published half-life of 65 days. Two samples separated from the same bombardment gave values of $\sigma_f \times$F.Y. of 1.94×10^{-26} and 1.79×10^{-26}.

The 17-hr. Zr^{97} was counted after equilibration with the 75-min. daughter Cb^{97}. The observed activity of the parent plus the daughter gave values $\sigma_f \times$F.Y. of 1.98×10^{-26} and 2.09×10^{-26} for the yield of Zr^{97}.

6. *Molybdenum* was separated by extraction with ether after oxidation with bromine. The ether was washed with hydrochloric acid and evaporated. The residue was taken up in nitric acid and oxalic acid to complex the columbium, and α-benzoin oxime to precipitate molybdenum added. The precipitate was fumed with perchloric acid, made basic with ammonia, and two ferric hydroxide scavenging precipitates made. Molybdenum was then again precipitated with α-benzoin oxime after acidification. The α-benzoin oxime precipitate was dissolved in perchloric acid, and silver molybdate precipitated from an acetate buffered solution.

The 67-hr. Mo^{99} was observed and decayed to below background with no tailing of the curve. No growth of the 6.6-hr. Tc^{99} daughter was observed through the 7.5 mg of absorber present. From the observed activity a value of $\sigma_f \times$F.Y. of 1.81×10^{-26} was calculated.

7. *Ruthenium* was separated from bombardment *A* some six months after bombardment, at which time only the 1-yr. Ru^{106} was found. The separation was made by distillation of ruthenium tetroxide from perchloric acid and sodium bismuthate. The ruthenium tetroxide was collected in sodium hydroxide, reduced with alcohol, and the oxide separated. This was dissolved in hydrochloric acid and reduced with magnesium to ruthenium metal.

An absorption curve of the ruthenium showed the presence of no radiation other than the 4-Mev beta from the Rh^{106} daughter. The decay was followed over several months, and no activity shorter than 330 days was seen. A value of $\sigma_f \times$F.Y. of 2.27×10^{-26} was calculated for Ru^{106}.

8. *Palladium* was precipitated with dimethylglyoxime from a diluted nitric acid solution of the thorium. The dimethylglyoxime precipitate was dissolved in nitric acid, and made basic with ammonia and silver iodide precipitated from the ammonia solution. The solution was then acidified with hydrochloric acid, and palladium was again precipitated with dimethylglyoxime. In one experiment the palladium was mounted and counted, and, in a second, the palladium dimethylglyoxime precipitate was dissolved in nitric acid and aliquots of this solution periodically milked for silver after equilibration for one day. The palladium solution was stored in Lusteroid to avoid adsorption of silver by glass, which occurs to considerable extent when silver is present only in tracer quantities. The chemical yield of palladium was determined on that portion of the palladium solution not used for milkings.

The gross decay curve of palladium is not too useful, since two isotopes of palladium, Pd^{109} and Pd^{112}, are present with half-lives of 13.4 hr. and 21 hr., respectively. The final portion of the palladium gross decay curve was extrapolated back on a 21-hr. line. Using the absorption data

of Seiler[12] for the 3.2-hr. Ag^{112} and 21-hr. Pd^{112}, $\sigma_f \times$F.Y. for the 21-hr. Pd^{112} was calculated to be 1.6×10^{-26} in bombardment *B*. In bombardment *D* the palladium was milked for its 3-hr. silver daughter, and the yield was calculated to be 0.8×10^{-26}.

9. *Silver* was separated by precipitation as silver chloride which was dissolved in ammonia, and two ferric hydroxide scavengings were made. Silver sulfide was then precipitated, dissolved in nitric acid, and the purification repeated. The silver was finally precipitated as silver chloride. The 7.5-day Ag^{111} was the only isotope found after decay of the 3.2-hr. Ag^{112}. A value of 1.32×10^{-26} was found for $\sigma_f \times$F.Y. for Ag^{111}.

10. *Cadmium* was separated as the sulfide, dissolved in acid, made ammoniacal, and hydroxide scavengings made with ferric and lanthanum hydroxides. From acid solution silver chloride was precipitated. From 2*M* HCl solution palladium and antimony sulfides were precipitated. The cadmium was finally precipitated as cadmium ammonium phosphate.

From bombardment *A*, the 43-day Cd^{115} period was separated and found to have a $\sigma_f \times$F.Y. of 1.01×10^{-27}. From a short bombardment both the 2.3-day Cd^{115} and the 43-day Cd^{115} were separated, and the 43-day isomer was found to give a value of 1.28×10^{-27} for $\sigma_f \times$F.Y. The decay of the 2.3-day isomer through the 4.5-hr. In^{115} and the fact that the gamma-ray from the 4.5-hr. In^{115} is 49 percent converted[13] was considered in calculating the fission yield of the 2.33-day cadmium. Two values of $\sigma_f \times$F.Y. obtained were 1.32×10^{-26} and 1.43×10^{-26} for this isomer.

11. *Tin* was separated as stannic sulfide. This was dissolved in concentrated acid, and an antimony sulfide scavenging was made from hot 2*N* HCl. From sodium hydroxide solution, ferric hydroxide, cadmium hydroxide, and columbic oxide were precipitated, followed by a second ferric hydroxide scavenging. In an acid solution the antimony sulfide scavenging was repeated. The tin was precipitated as metastannic acid from boiling nitric acid containing ammonium nitrate to which had been added a few drops of ruthenium carrier. The metastannic acid was ignited to SnO_2 and mounted on thin mica or glass and covered with Cellophane.

The isotopes of tin are in a rather confused state. On the Plutonium Project[5] periods of 62 hours, 10 days, and 130 days were found. Grummit and Wilkinson[14] found a 7-day and a 17-day period in place of the 10-day. Recently the 62 hour has been changed to 26 hour,[15] and is apparently identical with an isotope reported earlier by Livingood and Seaborg.[16] Lindner and Perlman[17] have recently shown this isotope to be Sn^{121} by deuteron bombardment of the separated tin isotope, Sn^{120}, and have further shown that no other period than the 26-hour one is formed by deuteron bombardment of Sn^{120}. Therefore, the 26-hr. period is the only long-lived isotope at mass 121. This leaves the 10 day, or 7 and 17 day, and the 130 day to be placed at Sn^{123} and Sn^{125}. Already at Sn^{125} is a 9-minute period which is apparently the parent of the 2.7-yr. Sb^{125}.[18] Further, Wilkinson[19] found that no antimony activity could be milked from any of the longer-lived tin isotopes they observed in the fission of U^{235} with slow neutrons.

In a long bombardment, tin was separated about six months after bombardment and only the 130-day period observed, decaying with a 130-day period over two half-lives. From a shorter bombardment, a 26-hr. period, a period of about 7.5 days, and two longer periods were found. The longer periods have not yet been resolved, but apparently one is the 130-day period and the other may have a half-life of about 20 days. The aluminum absorption curve of the 7.5 day, plus a small amount of the longer periods, had a Feather range of 1230 mg/cm² (2.5 Mev) which checks the reported energy of 2.6 Mev for the 10-day period[20] and is considerably greater than the 1.8-Mev energy reported by Grummit and Wilkinson for their 7- and 17-day periods.

Values of $\sigma_f \times$F.Y. have been calculated for the 26-hr., 7.5-day, and 130-day periods, the values

[12] J. A. Seiler, PPR Vol. 9B, No. 7.21 (to be issued).
[13] J. M. Lawson and J. M. Cork, Phys. Rev. **57**, 982 (1940).
[14] W. E. Grummit and G. Wilkinson, Nature **158**, 163 (1946).
[15] E. P. Steinberg, private communication.
[16] J. J. Livingood and G. T. Seaborg, Phys. Rev. **54**, 775 (1938).
[17] M. Lindner and I. Perlman, Phys. Rev. **73**, 1124 (1948).
[18] C. W. Stanley and L. E. Glendenin, PPR Vol. 9B, No. 7.23 (to be issued).
[19] G. Wilkinson, private communication (April, 1948).
[20] J. A. Seiler, PPR Vol. 9B, No. 7.26.1 (to be issued).

found for the 26-hr. period being 1.09×10^{-26} and 0.98×10^{-26} in one bombardment and 0.62×10^{-26} in another. For the 7.5-day period values of 0.64×10^{-26} and 0.59×10^{-26} were found in one bombardment, and 0.78×10^{-26} and 0.91×10^{-26} in another bombardment. The 130-day period gave a value of $\sigma_f\times$F.Y. of 0.76×10^{-26}, an average of five values for the same solution. For the reasons given in the above discussion both the 7.5-day and 130-day periods have been tentatively placed at mass number 123.

12. *Antimony* was separated by precipitation as the sulfide, after oxidation and reduction of the carrier to ensure exchange. The sulfide was dissolved in nitric acid and fumed with sulfuric acid. The antimony was electrolyzed in 4–6 *N* H_2SO_4 from a lead cathode to give stibene, which was collected in silver nitrate solution as silver antimonide. This was treated with hydrochloric acid, and antimony was precipitated as the sulfide from the supernatant. The yields in this separation were poor, but according to Wilkinson[19] the antimony is very pure. The sulfide is not a desirable method of weighting antimony, and probably contains considerable impurities, making the results low.

Some 12 months after bombardment *A*, antimony was separated to obtain the 2.7-yr. Sb^{125}. The activity found has decayed a few percent over a period of four months. The aluminum absorption curve contained two beta-components, the more energetic of which gave a Feather range of 300 mg/cm² (0.75 Mev). The activity had a gamma-ray, of energy about 0.5 Mev as estimated from a lead absorption curve on 80 gamma c/m. This is in agreement with the published data for this isotope.[5] A calculation of $\sigma_f\times$F.Y. for this isotope gave values of 0.69×10^{-26} and 0.73×10^{-26}.

13. *Tellurium* was separated by evaporating the sample plus carrier with HBr several times, taking up in HCl and reducing the tellurium with sulfur dioxide. The tellurium was then dissolved in nitric acid, and ferric hydroxide scavengings were made from ammonia solution, after which the sample was precipitated twice more as tellurium metal with sulfur dioxide from hydrochloric acid solution.

The gross tellurium decay curve is quite complex and could not be resolved. However, from the growth of 2.4-hr. iodine a value of $\sigma_f\times$F.Y. for the 77-hr. Te^{132} of 1.44×10^{-26} was calculated. Milking a purified tellurium sample for iodine was not successful, since the iodine radio-chemical exchange was not quantitative from the tellurium solution because of complexing of iodine and tellurium. Following the activity of 2.4-hr. iodine separated periodically from aliquots of the original sample also gave poor results because of poor exchange of the iodine carrier. However, from the highest points on the curve obtained by periodic separations of the 2.4-hr. iodine, a value of 0.9×10^{-26} for $\sigma_f\times$F.Y. of the 77-hr. tellurium was obtained.

14. *Iodine* was separated by oxidizing the sample plus carrier with sodium hypochlorite in sodium carbonate solution to periodate, acidifying this, and reducing the iodine with hydroxylamine to free iodine which was extracted with carbon tetrachloride. The iodine was re-extracted into dilute sulfurous acid, re-oxidized with sodium nitrite and nitric acid, and re-extracted into carbon tetrachloride. Three such extraction cycles were run, and the iodine was then precipitated as silver iodide from nitric acid solution. The activity of the 8-day iodine was observed in samples separated after all the 22-hr. iodine had decayed, so no interference from the 5.3-day xenon daughter of the 22-hr. iodine occurred. The values of $\sigma_f\times$F.Y. were fairly consistent at 0.9×10^{-26}, 0.7×10^{-26}, and 0.8×10^{-26}. However, considering the scatter of points in the activity of the 2.4-hr. iodine observed in these same samples, it is probable that complete exchange with the carrier was not achieved.

15. *Cesium* was separated by precipitation of cesium perchlorate on dilution with alcohol after fuming with perchloric acid. The cesium perchlorate was dissolved, made basic with ammonia, and two ferric hydroxide scavenging precipitates made. The solution was evaporated, the beaker flamed to eliminate ammonium ion, and cesium again precipitated as the perchlorate which was mounted.

About 12 months after bombardment *A* the 33-yr. Cs^{137} was separated. The aluminum absorption curve showed the presence of two beta-components, the visual range and the Feather range of the more energetic being about 350 mg/cm² (0.9 Mev). A gamma-ray is present, to

the extent of about 0.65 percent, which has an energy of about 0.9 Mev. This compares well with the published data, and a comparison of the observed aluminum absorption curve with that of Glendenin and Metcalf[21] showed them to be parallel. A calculation of $\sigma_f \times$F.Y. for the 33-yr. Cs^{137} gives a value of 5.1×10^{-26} in each of two samples. Since this value is higher than that of any other mass number, the cesium in one sample was redissolved and run through another series of purification steps, including hydroxide scavenging and sulfide scavenging. No change occurred in the specific activity of the sample, indicating no significant amount of impurities were present.

In bombardment *D*, cesium was separated to study the 13-day Cs^{136}, a shielded isotope. Two samples gave values of $\sigma_f \times$F.Y. of 9.0×10^{-28} and 9.3×10^{-28}.

16. *Barium* was separated by precipitation of the chloride from a concentrated hydrochloric acid and ether solution. After three such precipitations, a ferric hydroxide scavenging precipitate was made, and the barium reprecipitated as the chloride. The 300-hr. Ba^{140} was observed in all bombardments. The equilibrium mixture of 300-hr. barium and its 40-hr. lanthanum daughter was counted, and from this the activity of the barium was calculated. The values of $\sigma_f \times$F.Y. found were 2.44×10^{-26}, 1.96×10^{-26}, 1.73×10^{-26}, and 2.15×10^{-26} in bombardments *A*, *B*, *C*, and *D*, respectively.

17. *Cerium* was separated by first separating the thorium as the iodate from 5*N* nitric acid. Then a cerium hydroxide followed by a cerium fluoride precipitation was made. The fluoride was dissolved in boric acid and ceric iodate precipitated in the presence of lanthanum hold-back carrier. The precipitation of ceric iodate was repeated, and then a zirconium iodate scavenging precipitation was made. The cerium was precipitated as the hydroxide and finally precipitated as cerous oxalate.

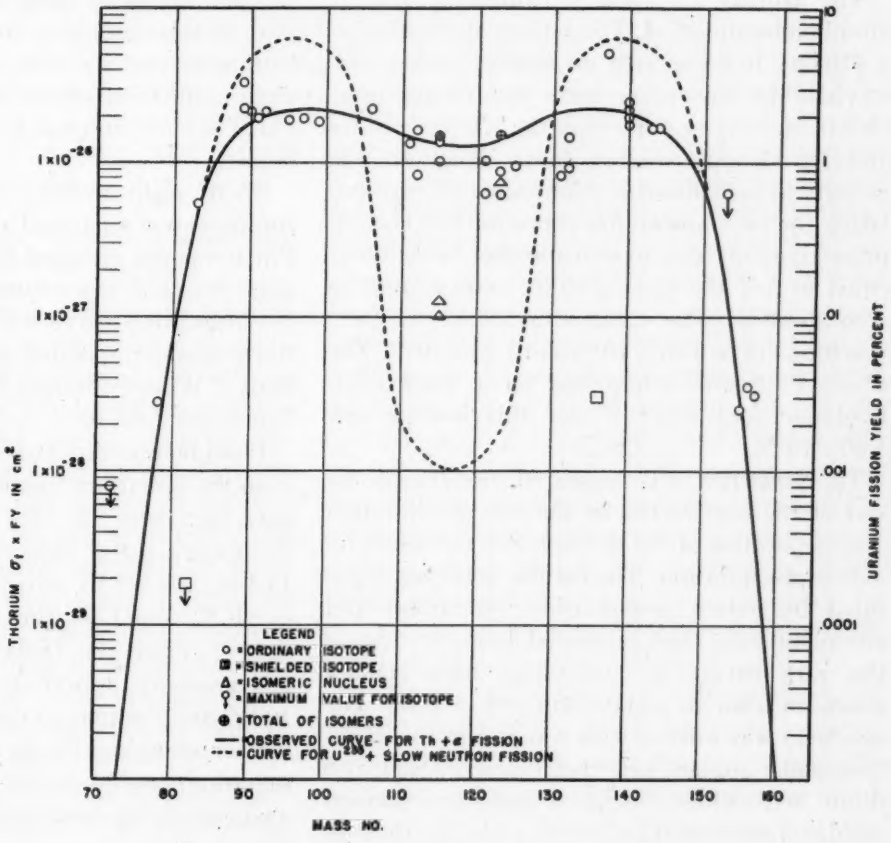

FIG. 1. Fission yield spectrum of thorium for fission with 38-Mev helium ions compared to that of U^{235} for fission with slow neutrons.

[21] L. E. Glendenin and R. P. Metcalf, PPR Vol. 9B, No. 7.39.1 (to be issued).

TABLE I. Values of $\sigma_f \times$F.Y. for various isotopes found in the bombardment of thorium with 37.5-Mev helium ions.

Isotope	Bombardment	$\sigma_f \times$F.Y. (cm²)	Isotope	Bombardment	$\sigma_f \times$F.Y. (cm²)
Zn^{72}	*B*	$<8\times10^{-29}$	Sn^{123}?(130d)	*A*	0.71×10^{-26}
As^{77}	*D*	$\sim2.8\times10^{-29}$	Sn^{123}?(130d)	*A*	0.65×10^{-26}
Br^{82}	*C*	$<1.85\times10^{-29}$	Sn^{123}?(130d)	*A*	0.85×10^{-26}
Br^{82}	*C*	5.69×10^{-27}	Sn^{123}?(130d)	*A*	0.77×10^{-26}
Br^{80}	*C*	4.83×10^{-27}	Sn^{123}?(130d)	*A*	0.79×10^{-26}
Sr^{89}	*A*	3.34×10^{-26}	Sb^{125}	*A*	0.89×10^{-26}
Sr^{89}	*B*	2.25×10^{-26}	Sb^{125}	*A*	0.93×10^{-26}
Sr^{90}	*A*	2.16×10^{-26}	I^{131}	*D*	0.98×10^{-26}
Sr^{91}	*B*	2.08×10^{-26}	I^{131}	*D*	0.68×10^{-26}
Sr^{92}	*B*	2.23×10^{-26}	I^{131}	*D*	0.82×10^{-26}
Zr^{95}	*A*	1.94×10^{-26}	Te^{132}	*B*	1.44×10^{-26}
Zr^{95}	*A*	1.79×10^{-26}	Te^{132}	*D*	0.91×10^{-26}
Zr^{97}	*D*	2.09×10^{-26}	Cs^{134}	*D*	3.0×10^{-28}
Zr^{97}	*D*	1.98×10^{-26}	Cs^{134}	*D*	3.1×10^{-28}
Mo^{99}	*B*	1.81×10^{-26}	Cs^{137}	*A*	5.15×10^{-26}
Ru^{106}	*A*	2.27×10^{-26}	Cs^{137}	*A*	5.15×10^{-26}
Ag^{111}	*B*	1.32×10^{-26}	Ba^{140}	*A*	2.44×10^{-26}
Pd^{112}	*B*	$\sim1.65\times10^{-26}$	Ba^{140}	*A*	2.47×10^{-26}
Pd^{112}	*D*	0.83×10^{-26}	Ba^{140}	*B*	1.96×10^{-26}
Cd^{115}(2.33d)	*B*	1.43×10^{-26}	Ba^{140}	*C*	1.74×10^{-26}
Cd^{115}(2.33d)	*B*	1.32×10^{-26}	Ba^{140}	*C*	1.72×10^{-26}
Cd^{115}(43d)	*A*	1.01×10^{-27}	Ba^{140}	*D*	2.23×10^{-26}
Cd^{115}(43d)	*B*	1.28×10^{-27}	Ce^{143}	*B*	1.66×10^{-26}
Sn^{121}	*B*	0.62×10^{-26}	Ce^{144}	*A*	1.67×10^{-26}
Sn^{121}	*C*	1.09×10^{-26}	Ce^{144}	*A*	1.73×10^{-26}
Sn^{121}	*C*	0.98×10^{-26}	Sm^{153}	*B*	6.3×10^{-27}
Sn^{123}?(7.5d)	*C*	0.98×10^{-26}	Eu^{155}	*A*	2.5×10^{-28}
Sn^{123}?(7.5d)	*C*	0.78×10^{-26}	Eu^{156}	*B*	3.5×10^{-28}
Sn^{123}?(7.5d)	*B*	0.64×10^{-26}	Eu^{157}	*B*	3.1×10^{-28}
Sn^{123}?(7.5d)	*B*	0.59×10^{-26}			

The 270-day Ce^{144} was separated six months after bombardment *A*. The activity decayed with a 270-day half-life with no shorter periods observed. The absorption curve showed the presence of no activity other than the 270-day cerium and its 17-min. praseodymium daughter, the activity at zero absorber determined by extrapolating the beta-absorption curve for the 17-min. praseodymium back to zero absorber being about equal to half the total activity extrapolated to zero absorber. The value of $\sigma_f \times$F.Y. for Ce^{144} was found to be 1.67×10^{-26} and 1.73×10^{-26}. The 33-hr. Ce^{143} was determined on a short bombardment and $\sigma_f \times$F.Y. for this isotope was 1.66×10^{-26}.

18. *Samarium* was separated along with the rest of the rare earths by fluoride precipitation after separation of the thorium and zirconium by iodate precipitation. The cerium was then separated by iodate precipitation. Samarium and europium were then separated from the rest of the rare earths by extraction with sodium amalgam from an acetate buffered solution. The amalgam was washed with water, and the samarium and europium were then extracted back into dilute hydrochloric acid. Three such sodium amalgam extraction cycles were run, lanthanum hold-back carrier being added in each case. The samarium and europium were then separated by reducing the europium with amalgamated zinc and precipitating samarium hydroxide with ammonia while the europium was in the reduced state. The samarium was further purified by precipitation from added inactive europium in a second cycle. The samarium was finally precipitated as the oxalate.

In bombardment *B* the 47-hr. Sm^{153} was studied. The activity found contained a 4.5-hr., a 45-hr., and 13-day periods, so the sample was undoubtedly contaminated with praseodymium, neodymium, and probably lanthanum. The 45-hr. component observed was probably composed of a mixture of 40-hr. lanthanum and 47-hr. samarium, so the value of $\sigma_f \times$F.Y. for this period, 0.6×10^{-26}, represents only a maximum value, and is probably considerably lower since the 13-day activity was quite pronounced indicating considerable impurities.

19. *Europium* was separated by isolating a rare earth fraction and separating europium from the rare earths by reduction with amalgamated zinc. In this case, after the first separation more lanthanum carrier was added, and two more decontamination cycles from other rare earths run. The europium was finally precipitated as the oxalate.

About eight months after bombardment *A*, europium was separated and a low activity found which was not removed by further decontamination cycles and was assumed to be the 2-yr. Eu^{155}. No absorption curve was possible, and the activity was extrapolated to zero absorber on the basis of Winsberg's data.[22] The value of $\sigma_f \times$F.Y. found was 2.5×10^{-28}.

From bombardment *B* the europium separated from the samarium fraction previously described gave activities of 15.4 hours and 15 days. Winsberg's data[22] was used to extrapolate the 15.4-hr. period to zero absorber. The value of $\sigma_f \times$F.Y. found for the 15.4-hr. Eu^{157} was 3.12×10^{-28}. From the 15-day portion of the curve, and assuming the activity to be the daughter of a 10-hr. Sm^{156} parent as stated by Winsberg,[22] and further assuming that no significant separation of samarium and europium occurred in the sodium amalgam extraction, a process requiring several

[22] L. E. Winsberg, PPR Vol. 9B, No. 7.56.3 (to be issued).

TABLE II. Excitation data on fission products of thorium with helium ions.

Layer	Mg/cm² Th in layer	$\sigma_f \times$F.Y. of fission products in layer (10^{-28} cm²) Ce^{144}	Ba^{140}	$Sn^{123?}$(130d)	Cd^{115}(43d)	Ru^{106}	Sr^{89}	Specific gross β^- activity in layer c/m/mg Th
1	46.2	1.67 1.73	2.44 2.45	0.75 (av. of 5 values)	0.101	2.27	3.34	8.63×10^5
2	47.4	1.20	1.9	0.356 0.361	0.046	1.38	2.17	6.02×10^5
		1.23	1.53	0.364 0.377				
3	38.6	0.852 0.835	1.31 1.38	0.22	0.032	0.54	1.8	3.66×10^5
4	74.4	0.223 0.225	0.27 0.32	0.036	0.0049	0.16	0.37	9.57×10^4
5	71.3	0.00995	0.0115	0.0017	0.0018	0.0057	0.016	2.74×10^3
6	29.1	0.0041	0.0086	0.0012	0.00017	0.0021	0.0054	1.22×10^3
7	4.78	0.0034	0.0052	0.00082		0.0018	0.0040	1.09×10^3
8	46.1	0.0028	0.005	0.00094		0.0015	0.0039	9.4×10^2
9	29.3	0.0021	0.0039	0.00075		0.00095	0.0033	8.0×10^2
10	126.3	0.0011	0.0030	0.00016 0.00025		0.00061	0.0015	4.8×10^2
11	18.3	0.0024	0.0024	0.00012		0.00039		3.3×10^2

hours, a value of $\sigma_f \times$F.Y. for the chain of mass 156 was calculated to be 3.5×10^{-28}.

IV. THE FISSION YIELD SPECTRUM AND THE CROSS SECTION FOR FISSION

The values of the yields of the various fission products investigated at an average alpha-energy of 37.5 Mev have been tabulated in Table I. These are plotted in Fig. 1, in which the distribution of yields of isotopes formed in the bombardment of thorium with 37.5-Mev helium ions has been compared to that obtained from the slow neutron fission of U^{235}. Despite the spread of the points, it is at once apparent that the spectrum is quite different in the middle region of the distribution. Instead of a factor of 600 in yield between the peaks and the minimum as in slow neutron fission of U^{235}, there is only a factor of about two in the depth of the dip in the fission of thorium with 37.5-Mev helium ions.

It is also seen that the shielded isotopes Br^{82} and Cs^{136} were both formed in very low yield compared to the unshielded isotopes. The value of unshielded Cs^{137} is far off the drawn curve, and there is no obvious explanation. This isotope was taken from only one long bombardment, but other long-lived isotopes, e.g., Sr^{90}, give more reasonable values. It may be that another isotope is present, e.g., 2.3-yr. Cs^{134}, in about 10 percent abundance relative to Cs^{137}, though from the results with slow neutron fission where the 2.3-yr. Cs^{134} has not yet been detected this appears to be improbable. A second explanation is that the half-life of the Cs^{137} is about 15 to 20 years rather than 33 years. Since the Cs^{137} absorption curve contains two components, it would be difficult to find 10 percent of a shorter-lived isotope by absorption measurements, and the half-life of any second isotope must be long enough to make its detection by decay over a few months impossible with ordinary counting methods.

In Fig. 1 the sum of isomeric nuclei have been plotted. The isomers of Cd^{115} and the assumed isomers of Sn^{123} have been summed to give the total yield of those masses. No account was taken in the curve for the possible existence of any other tin isotope.

A summation of the values of $\sigma_f \times$F.Y. over

the entire curve, and assuming the total fission yield to add up to 200 percent, a value for the cross section of thorium for fission with 37.5-Mev helium ions of 0.58 ± 0.1 barn is found. The probable error of 0.1 barn is estimated from the distribution of points and the types of weighted curves which could be drawn through those points other than the one drawn. This gives a value of about 2.8 percent for the fission yield of Ba^{140}.

V. THE FISSION EXCITATION CURVE OF THORIUM WITH ALPHA-PARTICLES

The layers separated in the milling of the thorium disk used in bombardment *A* were analyzed separately for Ba, Sr, Sn, Ce, Ru, and Cd; hence it is possible to obtain a rough excitation curve for the fission of thorium by helium ions.

In Table II the measured yields are expressed as $\sigma_f \times$F.Y. for the isotopes studied in each of the various layers of thorium together with the specific beta-activity of that layer. This data is plotted on a logarithmic scale in Fig. 2. It is seen that fission continues to occur well beyond the range of the impinging 39-Mev alphas, which in thorium is about 340 mg/cm², and this is probably due to a slight deuteron contamination of the alpha-beam, to fast neutron fission, or to a combination of the two effects.

In the first 200 mg/cm² of the thorium the distribution does not appear to shift a great deal since the isotopes studied maintain their relative positions and remain in approximately the same proportions to each other and to the gross specific activity. The proportion of the 43-day cadmium

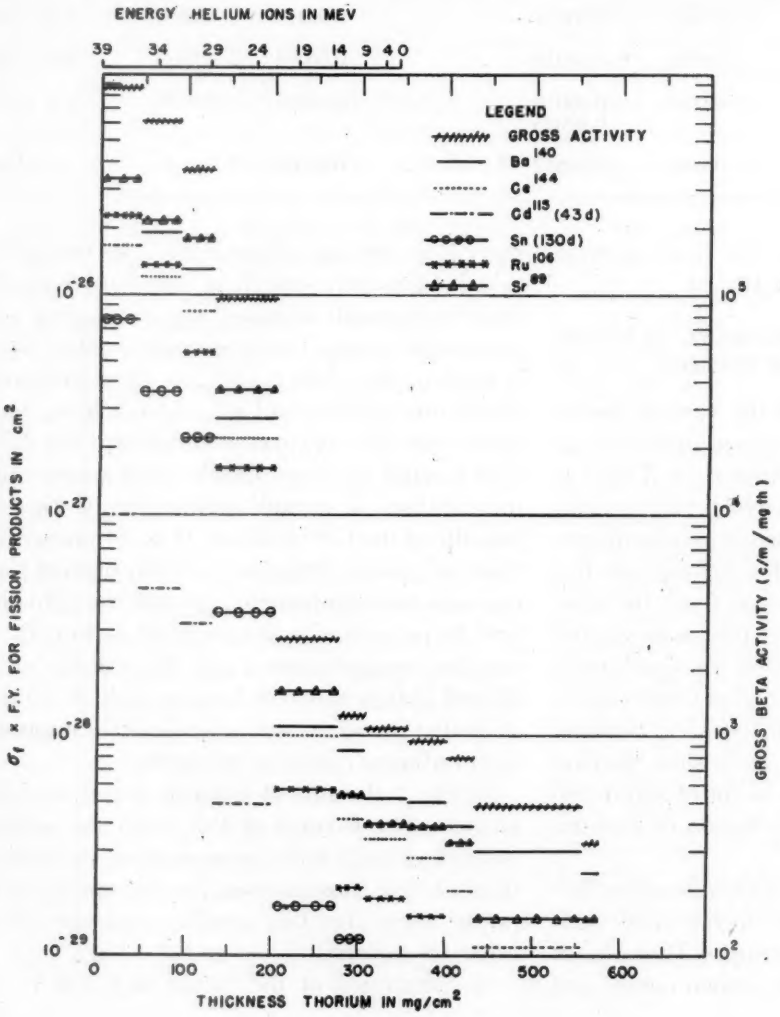

FIG. 2. Yield of some fission products from thorium+helium ions.

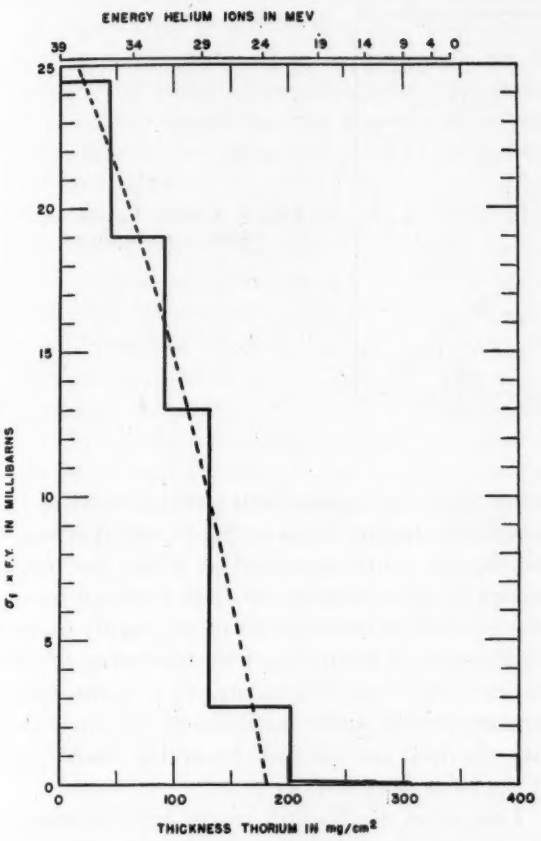

FIG. 3. Excitation curve of gross beta-activity in thorium target.

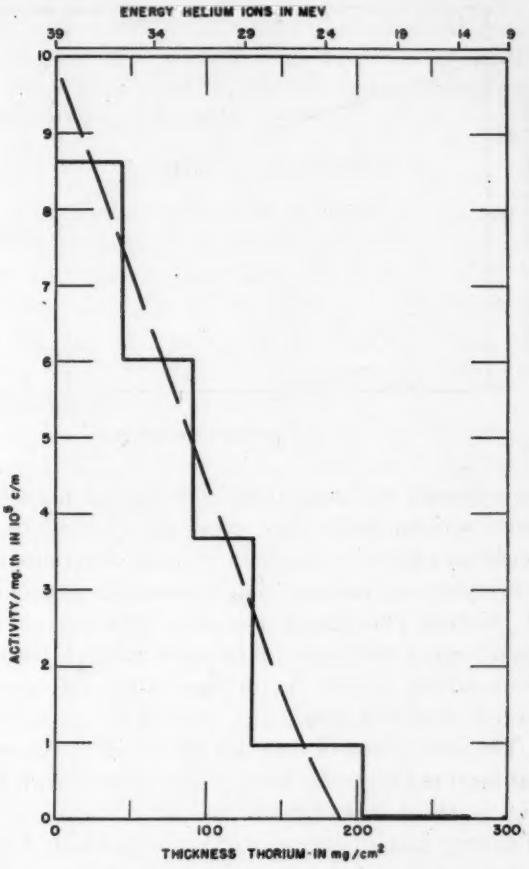

FIG. 4. Excitation curve of barium activity in thorium target.

does decrease somewhat, but whether this is significant or not is doubtful since the yield becomes so low. Below 200 mg/cm² the relative positions are maintained, except in the case of strontium which shifts from a position above barium to one below. In the first four layers Sr^{89} has an abnormally high yield compared to the other isotopes, since it is not expected to be above barium, if the two halves of the curve are symmetrical. The presence of krypton or rubidium impurities in the thorium target to produce Sr^{89} by particle reactions is not likely, and impurities of strontium or yttrium, while more likely as impurities, would require a neutron or deuteron flux of fairly high intensity to raise the yields of Sr^{89} to the values found.

In Figs. 3 and 4 the specific gross beta-activity and the $\sigma_f \times$F.Y. found for barium have been plotted against the thickness of thorium and an excitation curve drawn. The threshold for the alpha-reaction is found to be 23 to 24 Mev, and the cross section for fission is 0.6 barn at an average energy of 37.5 Mev, as found in the preceding section, the gross beta-curve indicating the higher value. This difference might be due to the presence of some long-lived beta-emitters formed at the higher alpha-energies by a process other than fission. These values differ somewhat from those reported by Jungerman and Wright,[22] who found a threshold of about 21 Mev and a cross section at 38 Mev of about 1.5 barn. From the data in this paper, the difference in threshold is probably not significant since too few points were taken to adequately define the curve near the threshold. The difference in cross section indicates that the beam measurements in this experiment may be in error or that the effect of different products of uranium and thorium in the

[22] J. Jungerman and S. C. Wright, Phys. Rev. **74**, 150 (1948).

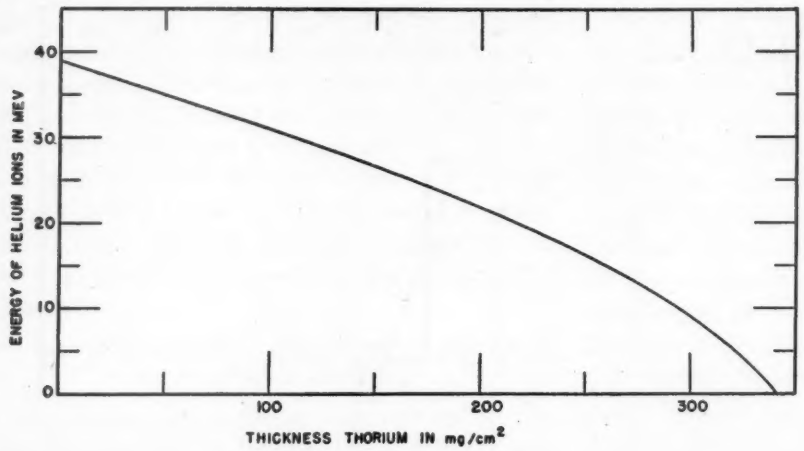

FIG. 5. Energy loss of 39-Mev helium ions in thorium.

experiments of Jungerman and Wright may be more serious than they expected. James[24] has made an extensive study of particle reactions in this region and believes that the number of atoms of thorium undergoing fission at this energy is about equal to those undergoing particle reactions which would be in line with the cross section reported here.

The conversion of thorium thickness to energy has been made on the basis of the curve shown in Fig. 5, which was obtained by integrating a rate of energy loss *vs.* energy curve for thorium. This latter curve was obtained by extrapolating data calculated by the theoretical group at the University of California Radiation Laboratory for the rate of energy loss of alpha-particles in lead, silver, copper, and aluminum to thorium, the extrapolation being made graphically at several energies by plotting $-dE/dx$ against $1/Z$ and extrapolating to thorium along a smooth curve.

VI. DISCUSSION

The distribution curve found for the fission of thorium with energetic alphas confirms a long standing suspicion that the isotopes in the center of the distribution are produced more abundantly in fission by highly energetic particles than is the case in slow neutron fission of U^{235}. In the case of fission of bismuth with 400-Mev alphas, the fission is apparently entirely symmetrical,[25,26] and the primary fission products formed have an n/p ratio which is constant and equal to that of the fissioning nucleus. Goeckermann and Perlman[26] ascribe the supra threshold at which the fission occurs with decreasing the time between formation by boiling off neutrons of the highly excited nucleus which fissions and the fissioning of that nucleus into two fragments, to a point where rearrangement of the nucleons in the nucleus to give the most energetically favorable distribution of nucleons does not occur.

This same mechanism might be occurring in the fission of thorium with alpha-particles. In this case the compound nucleus U^{236} would be formed in a highly excited state and boil off some neutrons. However, this intermediate nucleus would still be in an energy state far more excited than that of the corresponding nucleus in fission of U^{235} by slow neutrons, and might therefore split much faster and before rearrangement to the most energetically favorable distribution of nucleons could occur. Therefore, one might expect a constant n/p ratio to be found for the primary fission products in this case, as was found in bismuth fission. However, with thorium this n/p ratio is probably that of U^{234} or U^{233}, i.e., $\sim$1.53, since only a few neutrons need be boiled off before a nucleus is reached where fission occurs. Hence even if the products have a constant n/p ratio of 1.53, this will not be observed in the distribution curve since nuclei in the fission product region with this n/p ratio still are well above the line of stability and are all beta-emitters. Since the isotopes used in determining the distribution curve are all near the stability line, the primary products will still not be seen, and the only ob-

[24] R. A. James, private communication, August, 1948.
[25] I. Perlman, R. H. Goeckermann, D. H. Templeton, and J. J. Howland, Phys. Rev. **72**, 352 (1947).
[26] R. H. Goeckermann and I. Perlman, Phys. Rev. **73**, 1127 (1948).

servable difference in this respect between fission of thorium with helium ions and U^{235} with slow neutrons would occur in the length of the chains between the primary products and the stable nuclei, those chains on the heavy side of the distribution curve being shortened. This has not been investigated.

The depth of the dip in the mass yield curve must be related to the excess excitation in the fissioning nucleus. The results with slow neutron fission of U^{235}, where the factor in yield between dip and peaks of the distribution curve is about 600, fast neutron fission of thorium where the factor is 6 is about 10, and fission of thorium with 37.5-Mev helium ions where the factor was found to be only about 2, indicate that there is a definite relation between the excitation of the nucleus and the occurrence of symmetrical fission. While the results at alpha-energies lower than 37.5 Mev do not give a complete picture of the distribution at these energies, enough is given to indicate that the dip is always much shallower than that found in slow neutron fission of U^{235}.

ACKNOWLEDGMENTS

The author wishes to express his thanks to Professor I. Perlman and Professor G. T. Seaborg for valuable suggestions and criticisms, to Dr. N. Ballou for aid in separating samarium and europium, and to Dr. J. G. Hamilton and the crew of the Crocker Laboratory cyclotron for making the bombardments.

This work was performed at the Radiation Laboratory, University of California, Berkeley, California under the auspices of the Atomic Energy Commission.

PHYSICAL REVIEW VOLUME 75, NUMBER 1 JANUARY 1, 1949

A Note on the One-Electron States of Diatomic Molecules

HENRY A. ERIKSON AND E. L. HILL
Department of Physics, University of Minnesota, Minneapolis, Minnesota
(Received July 26, 1948)

The explicit formulation of an integral of the motion is given for a single electron moving in the field of two fixed nuclei, for both the classical and the quantum mechanical cases. The corresponding quantal operator together with the Schrödinger Hamiltonian and the operator for the component of the orbital angular momentum of the electron about the internuclear axis form a complete set of commuting observables of the problem. This supplies the dynamical interpretation of the separation parameter of the energy equation.

I. INTRODUCTION

IT is well known that the equations of motion of the electron moving in the field of two fixed nuclei are separable in elliptic coordinates in both classical and quantum mechanics. In the latter case the separability of the Schrödinger equation falls under Case VII of Eisenhart's classification.[1] The separated differential equations have been studied in detail for the special case of the hydrogen molecular ion (H_2^+) by Burrau,[2] Wilson,[3] Teller,[4] Hylleraas,[5] and others.

The purpose of the present note is to establish the form of a general integral for the problem. While the use of this integral is implicit in all of the work which has been done on the two-center problem, back to that of Euler,[6] its explicit formulation and dynamical significance have not been given previously, to our knowledge. The possession of the integral does not give one any information which cannot be derived from the separation of the variables in the Schrödinger equation, but it is of theoretical interest as an important example of the use of first integrals in quantum mechanics. Actual examples of this

[1] L. P. Eisenhart, Phys. Rev. **74**, 87 (1948).
[2] Ø. Burrau, K. Danske Viden. Selskab **7**, Nr. 14 (1927).
[3] A. H. Wilson, Proc. Roy. Soc. London **A118**, 617 (1928); **A118**, 635 (1928).
[4] E. Teller, Zeits. f. Physik **61**, 458 (1930).
[5] E. Hylleraas, Zeits. f. Physik **71**, 739 (1931).
[6] E. T. Whittaker, *Analytical Dynamics* (Cambridge University Press, Cambridge, 1927), third edition, p. 97.

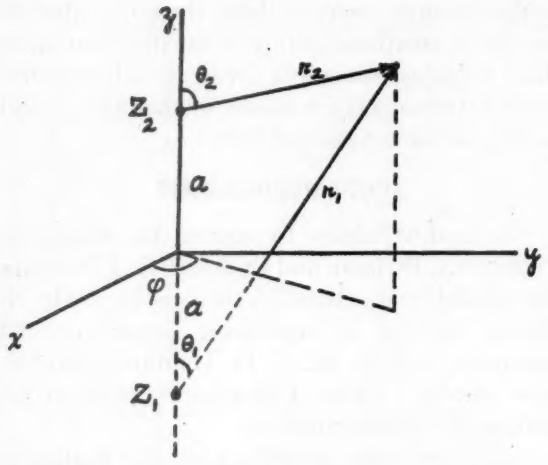

FIG. 1. Coordinate system for the two-center problem.

type are rather difficult to discover for the Schrödinger equation.[7]

II. THE CLASSICAL INTEGRAL

The basic cartesian reference system S is chosen as indicated in Fig. 1, the origin being at the midpoint between the nuclei. We let $\mathbf{L}'$ and $\mathbf{L}''$ be the orbital angular momentum vectors of the electron as referred to the two nuclei 1 and 2 respectively as origins. A short calculation from the Newtonian equations of motion of the electron shows that the following quantity is an integral of the motion[8]

$$\Omega_c \equiv \mathbf{L}' \cdot \mathbf{L}'' + 2me^2a(Z_1 \cos\theta_1 - Z_2 \cos\theta_2), \quad (1)$$

that is, we have $d\Omega_c/dt = 0$ as a consequence of the equations of motion of the particle. The notation in Eq. (1) is as indicated in Fig. 1, with m as the electronic mass. A curious feature of this expression is that it involves the angular momentum vectors of the electron computed about two different points. For vanishing internuclear distance this reduces to the square of the angular momentum about the origin of the system S.

III. THE QUANTUM MECHANICAL INTEGRAL

We wish to formulate expression (1) as a self-adjoint linear operator Ω which will satisfy the identical commutation relation

$$[\mathcal{H}, \Omega] \equiv \mathcal{H}\Omega - \Omega\mathcal{H} = 0, \quad (2)$$

with the Schrödinger energy operator $\mathcal{H}$, the latter being

$$\mathcal{H} \equiv -\frac{\hbar^2}{2m}\nabla^2 - \frac{Z_1e^2}{r_1} - \frac{Z_2e^2}{r_2}. \quad (3)$$

This is the standard condition which, when satisfied, assures one that the wave functions of the stationary states of the system can be arranged to be simultaneous eigenfunctions of the two operators $\mathcal{H}$ and Ω; i.e., the wave functions will satisfy the two simultaneous equations

$$\mathcal{H}\psi = E\psi, \quad \Omega\psi = \bar{\omega}\psi, \quad (4)$$

where E and $\bar{\omega}$ are eigenvalues of the two operators.

Calculation shows that this can be accomplished by the usual simple procedure of taking the symmetrized form of Eq. (1)

$$\Omega \equiv \tfrac{1}{2}\hbar^{-2}(\mathbf{L}' \cdot \mathbf{L}'' + \mathbf{L}'' \cdot \mathbf{L}') + \gamma(Z_1 \cos\theta_1 - Z_2 \cos\theta_2), \quad (5)$$

with

$$\gamma = 2me^2a/\hbar^2 = 2a/a_0, \quad (6)$$

where a_0 is the Bohr radius.

The angular momentum operators in (5) can be formulated in terms of the corresponding operators in the reference system S by the relations

$$\begin{aligned} L_x' &= L_x + iha\partial_y, & L_x'' &= L_x - iha\partial_y, \\ L_y' &= L_y - iha\partial_x, & L_y'' &= L_y + iha\partial_x, \\ L_z' &= L_z, & L_z'' &= L_z. \end{aligned} \quad (7)$$

On insertion of these expressions into (5) we find that

$$\Omega \equiv \hbar^{-2}L^2 + a^2(\nabla^2 - \partial_z^2) + \gamma(Z_1 \cos\theta_1 - Z_2 \cos\theta_2). \quad (8)$$

The proof of the commutation relation (2) is a somewhat onerous task, but since it requires only elementary techniques it will not be given here. The work is perhaps performed most readily with the expressions (3) and (5) for the operators, but can also be carried out with the formulations in terms of elliptic coordinates given below.

We give for reference the forms of the operators in terms of elliptic coordinates (ξ, η, φ) defined by the relations

$$r_1 = a(\xi + \eta), \quad r_2 = a(\xi - \eta). \quad (9)$$

[7] J. M. Jauch and E. L. Hill, Phys. Rev. **57**, 641 (1940).

[8] An attempt to find the remaining integrals of the problem in explicit form by the standard procedures of classical theory (reference 6, p. 323) fails by reason of the appearance of elliptic integrals.

The transformation of the energy operator follows readily from the usual formula for the laplacian operator in curvilinear coordinates, and yields the result

$$\mathcal{H}\equiv-\frac{\hbar^2}{2ma^2}\left\{\frac{1}{\xi^2-\eta^2}\frac{\partial}{\partial\xi}\left[(\xi^2-1)\frac{\partial}{\partial\xi}\right]+\frac{1}{\xi^2-\eta^2}\frac{\partial}{\partial\eta}\left[(1-\eta^2)\frac{\partial}{\partial\eta}\right]+\frac{1}{(\xi^2-1)(1-\eta^2)}\frac{\partial^2}{\partial\varphi^2}\right\}-\frac{e^2}{a}\frac{(Z_1+Z_2)\xi-(Z_1-Z_2)\eta}{\xi^2-\eta^2}. \quad (10)$$

The transformation of the operator Ω is more laborious, but again it requires only elementary techniques and will not be given here. The result is

$$\Omega\equiv\frac{1-\eta^2}{\xi^2-\eta^2}\frac{\partial}{\partial\xi}\left[(\xi^2-1)\frac{\partial}{\partial\xi}\right]-\frac{\xi^2-1}{\xi^2-\eta^2}\frac{\partial}{\partial\eta}\left[(1-\eta^2)\frac{\partial}{\partial\eta}\right]+\left[\frac{1}{\xi^2-1}-\frac{1}{1-\eta^2}\right]\frac{\partial^2}{\partial\varphi^2}+\gamma\frac{(Z_1+Z_2)\xi(1-\eta^2)+(Z_1-Z_2)\eta(\xi^2-1)}{\xi^2-\eta^2}. \quad (11)$$

The operators $\mathcal{H}$, Ω, and $L_z\equiv-i\hbar\partial_\varphi$ which gives the component of orbital angular momentum of the electron about the internuclear axis, thus form a complete set of commuting observables defining the stationary states of the system.

The Schrödinger equation with the energy operator (10) permits separation of the variables with the wave function written in the form

$$\psi(\xi,\eta,\varphi)=F(\xi)G(\eta)\exp(i\Lambda\varphi), \quad (12)$$

with

$$\Lambda=0,\ \pm1,\ \pm2,\ \cdots.$$

Considered by itself, the operator Ω allows separation into individual equations for the functions $F(\xi)$ and $G(\eta)$ alone only for Σ-states ($\Lambda=0$). Nevertheless, we can employ it to give a dynamical interpretation of the separation parameter in the Schrödinger equation, by the introduction of the operator

$$\mathfrak{A}=-\Omega-2ma^2\mathcal{H}/\hbar^2. \quad (13)$$

When the operator $\mathfrak{A}$ is applied to a complete wave function of the form (12), which is a solution of the Schrödinger equation for an energy eigenvalue E, we find that

$$\mathfrak{A}\psi=A\psi \quad (14)$$

where A is the separation parameter of the Schrödinger equation.[9] The operator $\mathfrak{A}$ of Eq. (13) thus gives us the interpretation of the separation parameter in terms of the dynamical operators of the problem.[10]

[9] H. A. Bethe, *Handbuch der Physik*, (Edwards Brothers, Ann Arbor, 1943) second edition, vol. 24, part 1, p. 530.

[10] The explicit formulation of the operator of Eq. (13) is made following a remark of the referee who suggested its use as part of the set of commuting observables instead of Ω. While this is quite possible, it leads to no particular simplification since the separated form of the Schrödinger equation shows that the eigenvalues E and A both appear in each of the two separated equations.

Note on the Bremsstrahlung Produced by Protons

JOHN L. POWELL*
Department of Physics, University of Wisconsin, Madison, Wisconsin
(Received September 21, 1948)

The bremsstrahlung produced by protons is discussed on the assumption that the anomalous magnetic moment can be described in terms of a Pauli type interaction with the electromagnetic field. The result of a perturbation theoretical calculation of the cross section is given, and a comparison is made to the approximate method of Weizsäcker and Williams. Reasons are given for the failure of the Weizsäcker method in special cases.

IN calculations concerning the radiative energy loss of mesons of spin $\frac{1}{2}$[1] it has been shown that the bremsstrahlung cross section increases rapidly with increasing energy if the particle has an anomalous magnetic moment of the Pauli type.[2] The assumption that the *proton* is correctly described by Pauli's equation is admittedly questionable. However, it is of interest to apply the calculations to the proton, inasmuch as the bremsstrahlung produced by primary cosmic particles may be of importance in accounting for the production of showers.

The aforementioned calculations were based upon the approximate method of Weizsäcker and Williams,[3] although it has been found that this approximation can lead to error in cases for which small impact parameters are important.[4] On the other hand, the method is known to give a correct result for the Dirac particle with no anomalous moment. The question therefore arises as to whether the method is applicable in the case of the Dirac particle (proton?) with arbitrary moment. It is the purpose of this note to compare the Weizsäcker-Williams result to a straightforward calculation by the method of perturbation theory and to point out that the approximate procedure can give misleading results in this problem, in particular for the case of the pure Coulomb field.

We assume that the only interaction between proton and nucleus arises from the electrostatic field of the nuclear charge, and that it is of the form

$$H' = e\Phi - i\lambda \frac{e\hbar}{2Mc}\beta\boldsymbol{\alpha}\cdot\nabla\Phi.$$

(Φ = spherically symmetric potential of nuclear electrostatic field, $\boldsymbol{\alpha}$, β = Dirac matrices, $\lambda(e\hbar/2Mc) = 1.79$ nuclear magnetons.) The time dependent perturbation theory may be applied, in the manner described by Heitler,[5] to the calculation of the cross section for bremsstrahlung. For convenience, we restrict the discussion to proton energies which are large compared to Mc^2. For the pure Coulomb field, ($\Phi = Ze/r$) one obtains the result

$$d\sigma = dk\lambda^4 Z^2\alpha(e^2/Mc^2)\{E_0/(Mc^2)^2\}F(k/E_0), \quad (1)$$

where $d\sigma$ = total cross section for emission of a quantum in the energy range $(k, k+dk)$, α = fine structure constant, and E_0 = initial energy of proton. The function F, defined by

$$F(x) = -\tfrac{1}{3}\{(4-x)(1-x)^2\ln(1-x) + x[6(1-x)+x^2]\ln x + x(1-x)\}$$

is zero for $x=0$ and $x=1$ and has the maximum value 0.67 for $x \approx 0.26$. Integrating, one obtains for the energy loss cross section

$$\Sigma = \int_0^{E_0} k\,d\sigma = \frac{5}{36}\lambda^4 Z^2\alpha(e^2/Mc^2)^2\{E_0^3/(Mc^2)^2\}$$

This result is remarkable for its very strong dependence upon E_0, as compared to the case of the electron ($\lambda = 0$), for which[6]

$$\Sigma_{(\lambda=0)} = Z^2\alpha(e^2/Mc^2)^2 4E_0[\ln(2E_0/Mc^2) - \tfrac{1}{3}].$$

* Now at Institute for Nuclear Studies, University of Chicago, Chicago, Illinois.
[1] S. B. Batdorf and R. Thomas, Phys. Rev. **59**, 621 (1941).
[2] W. Pauli in Handbuch d. Physik (Julius Springer, Berlin, 1933), Vol. XXIV/1, p. 233.
[3] C. F. v. Weizsäcker, Zeits. f. Physik. **88**, 612 (1934); E. J. Williams, Phys. Rev. **45**, 729 (1934).
[4] R. F. Christy and S. Kusaka, Phys. Rev. **59**, 405 (1941).
[5] W. Heitler, *Quantum Theory of Radiation* (Oxford University Press, New York, 1944), p. 161.
[6] See reference 5, p. 172.

However, this behavior is characteristic of the Coulomb field and is essentially a result of the divergence of Φ for $r\to 0$. When this divergence is removed by the introduction of a nuclear radius, Σ is found to depend less strongly upon the energy. Thus, if one carries through the perturbation calculation for a potential Φ which is Ze/r for $r>a$ but approaches a value $\approx Ze/a$ for $r=0$, one obtains

$$d\sigma = dk\cdot\lambda^4 IZ^2(e^2/Mc^2)^2(e^2/aMc^2) \times\{(1-k/E_0)/Mc^2\}, \quad (2)$$

where I is a number of order unity which depends upon the detailed shape of the function assumed for Φ. For the energy loss cross section, this gives

$$\Sigma = \tfrac{1}{6}\lambda^4 IZ^2(e^2/Mc^2)^2(e^2/aMc^2)(E_0^2/Mc^2).$$

The introduction of the nuclear radius therefore reduces the energy dependence of the cross section by a factor $\sim 1/E_0$.

The formula (1) is essentially that derived by Batdorf and Thomas[1] by the Weizsäcker-Williams method, in which the problem is treated in the coordinate system in which the proton is at rest, and the scattering of the virtual quanta in the contracted Coulomb field is calculated from the Compton scattering cross section. The total cross section is expressed as an integral over the impact parameters r, extending from $r_{\min}$ to $r_{\max}$. The lower limit for the integration, which enters on account of the semiclassical nature of the method, is an essential feature and must be at least as large as the Compton wave-length of the proton. Equation (2) is obtained if one takes $r_{\min}=a$, which amounts to the neglect of impacts within the nuclear radius. The above calculation shows, however, that it is precisely for these small radii that one obtains significant contributions to the cross section for the pure Coulomb field.

It must be concluded, therefore, that the formula (1) represents the actual situation only to the extent that the nuclear field can be considered to be produced by a static distribution of charge. In a realistic treatment of the problem, fluctuations of nuclear charge density would have to be considered, and the problem of individual proton-proton collisions within the nucleus would therefore present itself. Also, in close collisions with nucleons, the specifically nuclear forces would come into play and would influence the production of radiation. Finally, the recoil of the nucleons, which has been neglected in the above, would have the effect of reducing the cross section.

It should be noted that the Weizsäcker-Williams approximation gives a complete answer in the case of a particle of normal moment (e.g., the electron). The reason for this difference in the two problems is easily understood. The neglect of small impact parameters implies the neglect of Compton scattering of the high energy virtual quanta characteristic of this region. For the electron this is justified by the small Compton cross section for quanta of energy greater than Mc^2. For the Pauli particle, however, the Compton cross section increases linearly with the energy in the extreme relativistic limit (see Appendix), so that the contributions from virtual quanta of high energy are of decisive importance. Since the Weizsäcker-Williams method in its customary form does not apply to the region in the immediate neighborhood of the nucleus, it does not take proper account of these high energy quanta, and cannot be used to obtain formula (1). The approximate result is in agreement with the formula (2) for the "cut-off" Coulomb field, since for this field the high energy quanta are present with negligible intensity.

ACKNOWLEDGMENTS

It is a pleasure to acknowledge discussions with Professor R. G. Sachs, who suggested this problem. Financial support was received from the Eastman Kodak Fellowship in Physics at the University of Wisconsin and from the Wisconsin Alumni Research Foundation.

APPENDIX, COMPTON SCATTERING FORMULAE

The differential cross section for Compton scattering by a Pauli particle of magnetic moment $(1+\lambda)eh/2Mc$ is[7]

$$\begin{aligned} d\sigma = d\Omega\tfrac{1}{2}(e^2/Mc^2)^2(k^2/k_0^2)\{&[k_0/k+k/k_0-\sin^2\theta] \\ &+\lambda[(2k_0k/M^2c^4)(1-\cos\theta)^2] \\ &+\lambda^2[(k_0k/M^2c^4)\{4(1-\cos\theta)+\tfrac{1}{2}(1-\cos\theta)^2\}] \\ &+\lambda^3[(k_0k/M^2c^4)\{2(1-\cos\theta)+\sin^2\theta\}] \\ &+\lambda^4[(k_0k/2M^2c^4)(1+\tfrac{1}{2}\sin^2\theta)]\}, \end{aligned}$$

[7] Compare W. Pauli, Rev. Mod. Phys. 13, 203 (1941), and reference (1), where this result is derived for the special case $\lambda=-1$. Note also that the expression given by Pauli in Table III, formula III, should be corrected to read

$$d\Omega(\gamma-1)^4(e^2/Mc^2)^2\frac{1}{4}\frac{k}{k_0}\left(\frac{k}{Mc^2}\right)^2(1+\tfrac{1}{2}\sin^2\theta)+\cdots.$$

where e and M are the charge and mass of the scatterer, k_0 and k are the initial and final quantum energies, and θ is the scattering angle. The first term is the Klein-Nishina formula, and the remaining terms arise from the "Pauli part" of the magnetic moment. The total cross section is

$$\sigma=\pi(e^2/Mc^2)^2\Big[\Big\{-\frac{(2+2\gamma-\gamma^2)}{\gamma^3}\ln(1+2\gamma)+\frac{4}{\gamma^2}+\frac{2(1+\gamma)}{(1+2\gamma)^2}\Big\}+\lambda\Big\{\frac{2}{\gamma}\ln(1+2\gamma)-\frac{4(1+3\gamma)}{(1+2\gamma)^2}\Big\}$$
$$+\lambda^2\Big\{\frac{1}{2\gamma}\ln(1+2\gamma)-\frac{(1+3\gamma-8\gamma^2)}{(1+2\gamma)^2}\Big\}+\lambda^3\Big\{-\frac{1}{\gamma}\ln(1+2\gamma)+\frac{2(1+3\gamma+4\gamma^2)}{(1+2\gamma)^2}\Big\}$$
$$+\lambda^4\Big\{-\frac{1}{4\gamma}\ln(1+2\gamma)+\frac{(1+3\gamma+4\gamma^2+2\gamma^3)}{2(1+2\gamma)^2}\Big\}\Big],\quad(\gamma=k_0/Mc^2).$$

In the extreme relativistic limit, the term in λ^4 is dominant:

$$\sigma\approx\pi(e^2/Mc^2)^2(\gamma/4).$$

It is this term which leads, by the method of Weizsäcker and Williams, to formula (2) above.

PHYSICAL REVIEW VOLUME 75, NUMBER 1 JANUARY 1, 1949

Radiations of Uranium Y*

G. B. KNIGHT AND R. L. MACKLIN
K-25 Research Laboratories, Carbide and Carbon Chemicals Corporation, Oak Ridge, Tennessee
(Received May 24, 1948)

The radioactivity of UY (Th_{231}) has been re-investigated. Samples were prepared by growth from U_{235} largely freed of U_{238}, and absorption, decay, and coincidence experiments were run. The presence of the 210-kev beta-ray was re-confirmed, and a 35-kev gamma-ray 82 percent converted in the L shell was discovered. The half-life of UY was determined as 25.5 hours.

INTRODUCTION

URANIUM Y is the second member of the naturally occurring actinum series of radioactive isotopes. It rapidly approaches equilibrium with the parent U_{235}, having a half-life of about one day, and is isotopic with thorium, ionium, and UX_1. Since UX_1 is formed at a considerably greater rate from the U_{238} in natural uranium, it is not possible to prepare UY in radioactively pure form from this source. Thus, despite its discovery by Antonoff[1] in 1911, relatively little work has been reported on its radioactive properties.

The International Radium Standards Commission[2] reported in 1931 a half-life of 24.6 hours and a beta-ray absorption coefficient of about 300 cm^{-1} in aluminum. This absorption coefficient, reported by Kirsch,[3] corresponds to an energy of 200 kev on the basis of recent range-energy-absorption curves of Libby.[4] Gratias and Collie[5] redetermined the half-life in 1932, arriving at a value of 24.0 hours after discounting a 25.4-hour determination obtained by an electroscope method. These authors give references to several earlier investigations of the half-life. In 1937 Erchova[6] reported extensive absorption measurements on UY. She found two components of the radiation with absorption coefficients of 19.6 and 216 cm^2 per gm. These were both considered as beta-radiation and correspond[4] to beta-ray energies of 160 kev and 0.6 Mev. (The more penetrating component, if considered as electromagnetic radiation, would have an energy of about 11 kev.)

In 1945 at the Metallurgical Laboratories in

* This document is based on work performed under Contract No. W-7405-Eng-26 for the Atomic Energy Commission by Carbide and Carbon Chemicals Corporation, at Oak Ridge, Tennessee. It was originally reported in October, 1947 and declassified in April, 1948.

[1] G. N. Antonoff, Phil. Mag. **22**, 419 (1911), and **26**, 1058 (1913).

[2] Int. Rad. Stds. Comm., Rev. Mod. Phys. **3**, 427 (1931).

[3] G. Kirsch, Wien Ber. IIa **129**, 309 (1920).

[4] W. F. Libby, Anal. Chem. **19**, 2 (1947).

[5] O. Gratias and C. H. Collie, Proc. Roy. Soc. **A135**, 299 (1932).

[6] Z. V. Erchova, J. de phys. et rad. **8**, 501 (1937).

Chicago[7] a few samples of UY were examined under the direction of Ghiorso and Jaffey. These samples were derived from nearly pure U_{235} but, unfortunately, were contaminated with Pa_{233}. Several components of the radiation based on absorption measurements were reported. The 0.2-Mev beta-ray was observed together with a weaker component reported as a 50–60-kev beta-ray. The 1.45-mg/cm² half-thickness for absorption of the latter is, however, quite close to the value for the 3-kev *M*-shell x-rays. The Chicago group proposed two decay schemes. One involved a branched beta-decay with 67 percent of the UY atoms emitting a 60-kev beta-ray and a 140-kev gamma-ray in cascade. This was rejected because no such gamma-ray could be detected in sufficient intensity. The other decay scheme called for two consecutive highly converted low energy gamma-rays following the 0.2-Mev beta-ray. The observed intensity ratio of 2 of the weak components

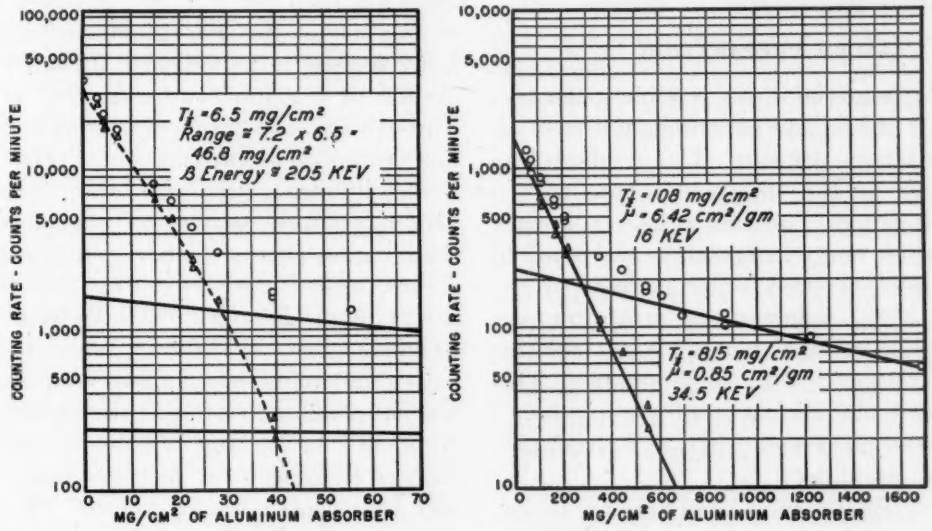
COUNTING RATE - COUNTS PER MINUTE
MG/CM² OF ALUMINUM ABSORBER
T½ = 6.5 mg/cm²
Range = 7.2 x 6.5 = 46.8 mg/cm²
β Energy = 205 KEV
T½ = 108 mg/cm²
μ = 6.42 cm²/gm
16 KEV
T½ = 815 mg/cm²
μ = 0.85 cm²/gm
34.5 KEV

FIG. 1. Uranium Y absorption data, sample 1.

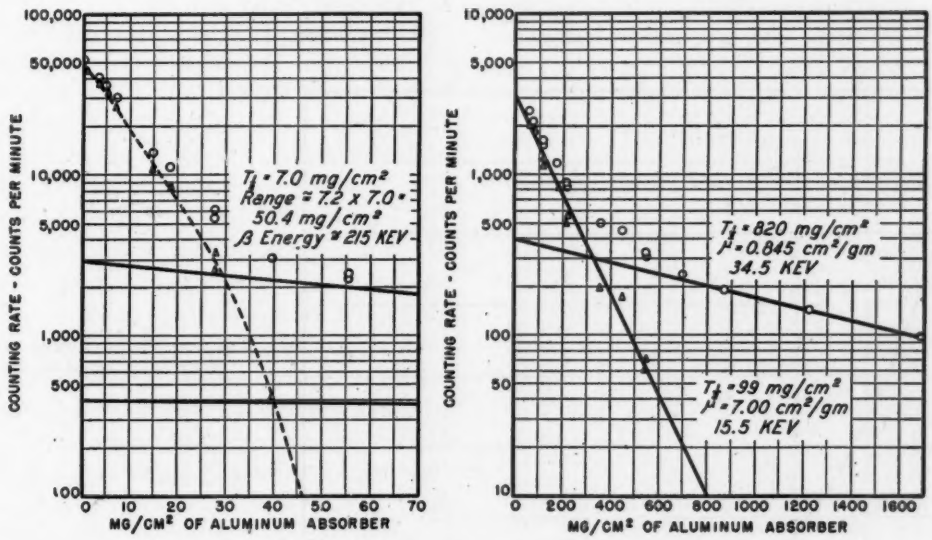
COUNTING RATE - COUNTS PER MINUTE
MG/CM² OF ALUMINUM ABSORBER
T½ = 7.0 mg/cm²
Range = 7.2 x 7.0 = 50.4 mg/cm²
β Energy = 215 KEV
T½ = 820 mg/cm²
μ = 0.845 cm²/gm
34.5 KEV
T½ = 99 mg/cm²
μ = 7.00 cm²/gm
15.5 KEV

FIG. 2. Uranium Y absorption data, sample 2.

[7] Chicago University Metallurgical Laboratory Progress Report for May, 1945, CN 3001.

TABLE I. Uranium Y half-life data.

Half-life of UY (hours)	Weight
25.664	148.1
25.391	283.7
25.822	94.2
25.118	49.4
25.128	2.5

and the 0.2-Mev beta-ray required the proposal of two weak gammas in cascade. This mechanism was considered improbable.

SAMPLE PREPARATION

As starting material it was possible to use U_{235} largely freed of U_{238} and exceptionally free of all other radioactive elements. The residual U_{238} evolves UX_1, another thorium isotope with a 24-day half-period. For this reason a growth period of from one to three days was used in order to effect an even larger increase in the $UY/(UX_1+UX_2)$ disintegration rate ratio over the equilibrium ratio. Values above 200 for this ratio were obtained with some samples. This compares with the normal equilibrium value of 0.023 and the maximum value 0.56 attainable with natural uranium.

The UY samples were isolated from the parent U_{235} at the end of each growth period with 5 mg of LaF_3 as a carrier precipitate. The precipitations were carried out in 50-ml centrifuge tubes lined with hard wax. The precipitate was carefully washed and deposited in a thin uniform film on a one-inch disk of Whatman No. 2 filter paper. The sample was then mounted for counting. For coincidence experiments a few hundredths of a milligram of LaF_3 precipitate with adsorbed UY were deposited directly on a thin (1 mg/cm²) aluminum foil.

MEASUREMENTS

In connection with another program, samples of UY were found to exhibit a more penetrating radiation than the 0.2-Mev beta-ray. Upon investigation of the absorption coefficient the *L* x-ray seemed to be indicated along with a suggestion of a gamma-ray estimated at 25 kev. Through the cooperation of Clinton Laboratories more complete absorption curves (Figs. 1 and 2) were obtained with thin mica window-type Geiger counters. Analyses of the components of these curves show a 35-kev gamma-ray, 16-kev *L*-shell x-rays, and a 210-kev beta-ray. The energy of the beta-ray was calculated from the formulae given by Libby.[4] While these semi-logarithmic plots show appropriate convexity, it was not possible to estimate the maximum range accurately or to run Feather analyses. The counter efficiencies for such low energy gamma and x-rays are not well known. The probable values of the counting efficiencies for the rays found will be discussed later in connection with the proposed decay scheme.

An attempt to check the half-life on one

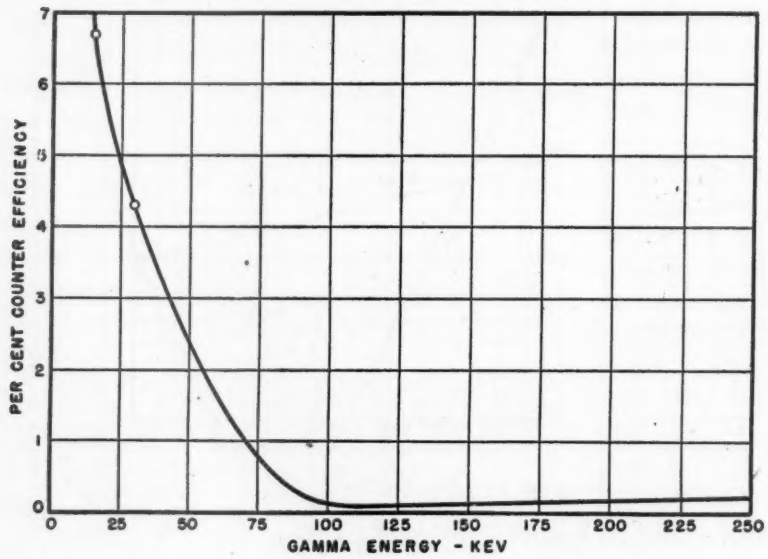

FIG. 3. Approximate counter efficiencies for gamma-rays.

sample gave a value of 25.4 hours. As this was higher than the values reported in the literature, a series of five samples was prepared and their activities followed with two thin wall Geiger counters. Samples of natural uranium were counted daily as operating standards. The data were resolved into three components: a constant activity caused by cosmic rays, counter contamination and U_{235} traces in the sample, a UX_1 and UX_2 activity assumed to decrease with a 24.6-day half-life, and the UY activity. Each of these components was evaluated from the appropriate data by the method of least squares. The activity measurements after 14 days decay were used to evaluate the constant and the UX_1+UX_2 activities. From these the background rates during the first ten days were predicted together with their uncertainties. The net rates during the first ten days of decay were then used to calculate the UY half-life and initial activity. Each rate was weighted in the calculation as the reciprocal of the quantity counting variance plus coincidence correction variance plus background variance. The half-lives obtained from each sample (each an average of the values on the two counters) are given in Table I together with their relative weights as calculated from the fit of the data about the least squares exponential decay curves.

The weighted average half-life is 25.51 hours. The samples were shown to differ among themselves more than expected from the fit of the data to the least squares curves, and hence the confidence belt is calculated from the scatter of half-lives determined from each sample. The limit of error at the 95 percent confidence level arrived at in this manner is 0.93 hour. The corresponding probable error is 0.23 hour.

Through the cooperation of Mr. Francis McGowan of Clinton Laboratories it was possible to run coincidence measurements on one of the samples. The beta-gamma-coincidences were not sufficiently delayed, however, to permit their being counted with the delay circuits available (~ 1 μ-sec.). The apparent immediate coincidence rate includes a back-scattering effect of not well-known magnitude. Thus the data warrant only the conclusion that the half-life of Pa^*_{231} toward emission of the 35-kev gamma is less than one microsecond.

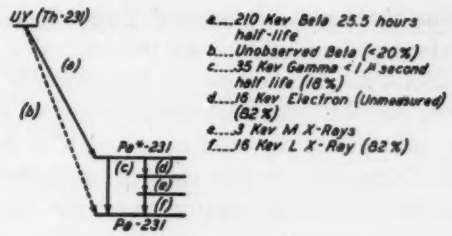

FIG. 4. Decay scheme of uranium Y.

DISCUSSION

The average value of 210 kev of the UY β-particle energy reported here is in substantial agreement with the 0.2-Mev value reported by most previous investigators. The possibility of a pair of beta-rays differing in maximum energy by 35 kev has not been entirely ruled out by the present experiments due to low counting rates and consequent poor precision near the end of the range. The high yield of gamma-rays (q.v.i.), however, indicates that the stronger beta would be present to an extent considerably less than 20 percent of the total. This suggests the supervention of a forbidden transition over the simple beta-decay without gamma-emission.

While the absorption curves of the beta-ray component shown in Figs. 1 and 2 display typical curvature, the two weaker components adhere closely to straight lines in the logarithmic activity plots. From the linear absorption, energies of 16 and 35 kev have been computed for the two

TABLE II. Estimation of counter efficiencies based on equality of beta- and gamma-emission rates. Average extrapolated counting rates observed: Beta: 41,200 counts/min.; x-ray: 2290 counts/min.; gamma: 322 counts/min.

16-kev x-ray		Unconverted 35-kev gamma-ray		Percent of gamma-rays converted in L shell
Assumed counter efficiency	Photons through counter per minute	Photons through counter per minute	Derived counter efficiency	
0.060	38167	3033	0.106	93
0.061	37541	3659	0.088	91
0.062	36935	4265	0.076	90
0.063	36349	4851	0.066	88
0.064	35781	5419	0.059	87
0.065	35231	5969	0.054	86
0.066	34697	6503	0.050	84
0.067	34179	7021	0.046	83
0.068*	33676	7524	0.043*	82
0.069	33188	8012	0.040	81
0.070	32714	8486	0.038	80

* Best fitting values (see Fig. 3).

components found. The exact average absorption coefficient to be expected for the several $L-M$ transitions is complicated by two factors. The relative $L\alpha$, $L\beta$, etc., intensities found in x-ray work are caused by excitation with a broad range of energies. In the case of excitation by conversion of a single gamma-ray not too far removed in energy from the L limit, a quite different distribution of relative intensities might result. In addition, the high intensity of a component near the $M-N$ transition energy as observed at Chicago suggests the possibility of an appreciable Auger (auto-ionization) effect which would lead to a further modification of the L x-ray spectrum. A value of 15.5–16.0 kev for the average seems a quite reasonable expectation, in view of the foregoing, for the average L-shell, x-ray energy of protoactinium. Thus the less penetrating electromagnetic component is thought to be the L x-ray resulting from conversion of a 35-kev gamma-ray.

The efficiencies of the counters used in these experiments increase regularly above approximately 0.2 Mev. A rough estimate in that range equates the numerical values of the percent efficiency and the energy in Mev. A minimum efficiency of about 0.1 percent is reached in the neighborhood of 100–150 kev, below which the efficiency rises rather sharply. At 25 kev an efficiency of perhaps 5 percent is to be expected. If both the 16-kev and 35-kev components had a 5 percent counter efficiency, the average extrapolated intensities at the counter would be 45,800 and 6440 c/m, respectively. This compares with an average beta-intensity of 41,200 c/m and indicates that each beta-emission is accompanied by one gamma-ray which often suffers conversion in the L-shell of the atom. Setting the emission rates of gamma-photons and beta-particles equal, it is possible to find values of the counter efficiencies at 16 and 35 kev which best fit the expected efficiency *vs.* energy curve. As can be seen from Table II, the required efficiency at 35 kev for this equality varies more rapidly than the assumed efficiency at 16 kev. The best fitting efficiencies appear to be 6.8 percent at 16 kev and 4.3 percent at 35 kev. These values are plotted with the expected curve in Fig. 3.

The percent conversion is shown not to depend very strongly upon the choice of efficiencies. The value of 82 percent for the best fitting efficiencies is also relatively insensitive to the possible presence of a small beta-ray component unaccompanied by gamma-radiation mentioned above in connection with the beta-ray absorption curves. This high conversion value in the L shell suggests that multipolar radiation of at least quadruple order is involved. Exact calculations are complicated by the relativistic effects in such a heavy nucleus as thorium and by the energetically excluded K conversion.

The decay scheme suggested by these experiments is summarized in Fig. 4.

CONCLUSION

The half-life of UY has been computed as 25.51 hours with a limit of error at the 95 percent confidence level of 0.93 hours. The beta-ray energy was found by absorption measurements to be 210 kev. A gamma-ray of 35 kev was found, about 82 percent converted in the L shell.

Experiments on the Effect of Atomic Electrons on the Decay Constant of Be^7

E. SEGRÈ AND C. E. WIEGAND
Radiation Laboratory, Department of Physics, University of California, Berkeley, California

(Received September 7, 1948)

In an attempt to detect a possible influence of the atomic electrons on the radioactive decay constant of Be^7 we have measured $\lambda_{BeO}-\lambda_{Be}$ and found $(-3.0\pm1.8)10^{-4}\lambda_{Be}$. We also describe a method to measure mean lives of radioactive substances in a time short compared with the mean life.

I. INTRODUCTION*

THE decay constant of a radioactive substance undergoing orbital electron capture is proportional, according to current beta-decay theories, to the electron density at the nucleus $|\psi(0)|^2$. This fact seems to afford a possibility of altering the nuclear decay constant λ by acting on the atomic electrons; e.g., if it were possible to completely strip a nucleus of all its electrons, it clearly could not decay by orbital electron capture and such a radioactive nucleus, as long as it stays stripped, is stable.

In a light element it does not seem impossible to achieve by chemical means an alteration of $\psi(0)$ sufficiently large to affect in a measurable way the decay constant. The most promising nucleus with which to observe this effect is Be^7 which decays by orbital electron capture with a half-period of 52.9 days, the decay being followed by the emission of a 455-kev gamma-ray.[1] In this atom the contribution to $|\psi(0)|^2$ due to the two $1s$ electrons according to Hartree[2] is, in certain units, 106.62; the contribution due to the $2s$ electrons is 4.25, making a total of 110.87. For the ion Be^{++} $|\psi(0)|^2$ according to the same author is 107.96. From these data one would expect that the decay constant of the atom would be 1.027 times greater than that of the ion. A 2.7 percent variation of the decay constant would be easily observable, but, of course, it is not very practical to keep Be^7 in a doubly ionized state for months. Another possibility that we have considered is to have the Be in a metallic state at high temperature and rely on the thermal expansion of the metal to diminish $|\psi(0)|^2$; the effect achievable in this way is, however, too small to be measured.

We finally decided to compare the decay constant of Be^7 with that of Be^7O, hoping that the change in $|\psi(0)|^2$ induced by the different chemical structure might effect λ in a detectable way. Unfortunately, a precise estimate of the variation of $\psi(0)$ in passing from beryllium metal to beryllium oxide is not available. Professor F. Seitz has kindly pointed out to us the following crude estimates: "Consider first an atom of Be gas; according to Hartree's results the ratio of the density of $2s$ electrons to $1s$ electrons near the nucleus of Be in free space is $1.86/55.9=0.033$. Now the radius of the sphere having the same volume as the beryllium atom in the metal is $2.37a_0$ (a_0 is the Bohr radius $=0.531$A). The charge outside this radius in the free atom is $1.041e$, all of which is associated with the $2s$ wave functions. This charge must be packed inside the sphere in going to the metal so that ψ^2 near the nucleus for the $2s$ electron would just about double. Thus the electron density near the nucleus should be raised by about three percent. The more accurate work of Herring and Hill[3] gives closely the same value.

"The spacing between O and Be in BeO is $1.64\text{A}=3.09a_0$. The accepted 'radius' of the oxygen ion (O^{--}) is $1.32\text{A}=2.49a_0$. Now Hartree's treatment of the neutral oxygen atom gives about $0.2e$ outside the sphere having the radius $3.09a_0$ and about $0.4e$ outside the sphere

* A preliminary account of this work and of the results obtained was given at the 276th and 380th meetings of the Am. Phys. Soc. [Phys. Rev. **71**, 274 (1947); **73**, 743 (1947)] and in MDDC 1098. Work on the same subject has also been reported by R. Bouchez, R. Daudel, P. Daudel, and R. Muxart, J. de phys. et rad. **8**, 336 (1947).

[1] For the half-life see J. E. Hill, Phys. Rev. **57**, 567 (1940) and this paper; for the gamma-ray see K. Siegbahn, Arkiv. Mat., Astr. Fys. **34B**, 6 (1946).

[2] D. R. Hartree and W. Hartree, Proc. Roy. Soc. **149**, 210 (1935). See also W. Hartree, *ibid.* **150**, 9 (1935) for a second calculation taking into account the exchange effect. We have used the first numbers because the comparison for the Be^{++} is given only in the earlier paper.

[3] C. Herring and A. C. Hill, Phys. Rev. **58**, 132 (1940).

of radius $2.49a_0$. Hartree's results are notable in not drawing the electrons sufficiently close to the nucleus, so the true values for the neutral atom are somewhat smaller. However, this decrease is compensated by the fact that the oxygen in BeO is regarded as the double charged negative ion for which the charge outside any given sphere is certain to be larger than for the neutral atom, even if treated on the basis of Hartree's theory.

"Now in a very rudimentary theory, the charge outside either one of the two radii mentioned in the preceding paragraph would become associated with the Be^{++} ion. This charge would enter the $2s$ state and would be contained inside the ionic radius, which is taken as approximately $0.6a_0$ (i.e., the difference between the radius of the oxygen ion, namely, $2.49a_0$, and the Be—O spacing in the oxide, namely, $3.09a_0$). Now in the free beryllium atom the amount of $2s$ electron inside this radius is only $0.032e$. This is obtained from Hartree's wave functions. Hence, according to the rudimentary picture, the amount of $2s$ electron inside the "ionic radius" is increased from $0.032e$ to a value between from $0.2e$ to $0.4e$ in going from the gas to the oxide, that is, by a much larger factor than in going from the gas to the metal.

"This rudimentary picture can be looked upon in other ways. The fact that the oxygen atom contains so much charge outside the ionic radius, or outside the radius corresponding to the Be—O distance for that matter, means that the outer shell electrons on the oxygen ion in the BeO crystal also belong to the Be atom. In other words, the binding is a mixture of ionic and homopolar electron structures. Thus one can say that the result of binding is to add four electrons to the beryllium atom in the shell of total quantum number 2. This could increase the density of ψ^2 for the $2s$ electrons in the vicinity of the nucleus. It will be highly accidental if this increase is the same to within ten percent as that incurred in the metal."

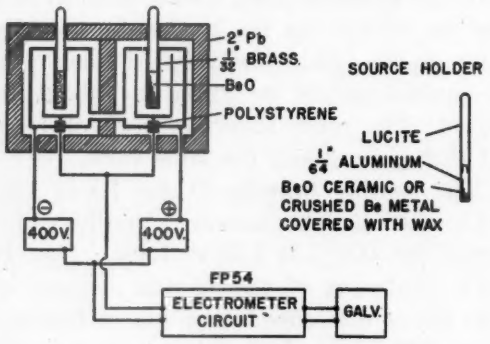

FIG. 1. Schematic diagram of balanced ionization chambers.

In view of the admitted uncertainty of these estimates, we decided to perform the experiment pushing the precision as much as reasonably feasible with the sources at our disposal.

The final result obtained is

$$\lambda_{BeO}-\lambda_{Be}=(-3.0\pm1.8)10^{-4}\lambda_{Be}.$$

It is remarkable that the change in λ is so small and whether this result is caused by an accidental compensation of various effects or has some other reason can be shown only by further experiments using different pairs of compounds or other ways of affecting $\psi(0)$. We plan to perform some of these experiments.

II. EXPERIMENTAL

A. Preparation of the Sources

The Be^7 was prepared by proton bombardment of lithium with the Crocker cyclotron. It is obviously of vital importance that the substance used be radioactively pure because otherwise the results may be falsified by different amounts of radioactive impurities, with half-lives different from Be^7, going into the metal and oxide. Accordingly, the following procedure was adopted: the lithium target was dissolved in dilute hydrochloric acid, 0.1 g of beryllium, and 10 mg each of Cu, Co, and Zn added. Sulfides were precipitated in 0.3 molar hydrochloric acid and discarded. The solution was evaporated and the residue dissolved in 12 molar sodium hydroxide. Hydrogen sulfide was added and the precipitate discarded. The solution was then acidified and the beryllium was precipitated from it by ammonium hydroxide. This operation was repeated several times. Subsequently the beryllium hydroxide was converted to the basic acetate, dissolved in chloroform, the chloroform solution extracted repeatedly with water, and finally the beryllium in the chloroform layer was reconverted to hydroxide.** This hydroxide showed only gamma-ray activity.

** These operations were performed by Dr. R. F. Leininger and Mr. G. Johnson.

The hydroxide was further diluted with normal beryllium and converted to oxide. A fraction of this oxide was converted to a button of solid beryllium metal by members of the Atomic Research Institute of the Iowa State College, to whom we are greatly indebted for their kind cooperation. This button was broken into pieces with a hammer and half of it, in the metallic state, made our sample M, the other half, reconverted to oxide, was our sample $C2$. Sample $C1$ was obtained from the part of the oxide that had not been converted to metal. The comparisons occurred among $C1$, $C2$, and M. The initial gamma-ray activity of the sources was approximately equivalent to that of 45 micrograms of radium.

B. Radioactivity Measurements

For a comparison of λ_C and λ_M the decay constants of the oxide and the metal, we have used a differential method. The advantages over a separate measurement of λ_C and λ_M are several: it is possible to measure the samples at the same time and by interchanging them minimize systematic errors; the readings on the difference of the activities are always small and with ionization chambers are much more convenient to take than the readings on the activities; the time of observation is used more efficiently and it is practical to use considerably stronger samples than for single readings.

If two samples of metal and oxide have decay constants λ_M and λ_C and their initial activities $M(0)$ and $C(0)$ are approximately equal, we have

$$\delta = M(t) - C(t) = [M(0) - C(0)]^{-\lambda t} + C(0)t\Delta\lambda e^{-\lambda t}, \quad (1)$$

where $\Delta\lambda = \lambda_C - \lambda_M$ and $\lambda = \lambda_M$. We can rewrite (1):

$$\delta e^{\lambda t} = M(0) - C(0) + C(0)(\Delta\lambda/\lambda)(t/\tau), \quad (2)$$

where $\tau = 1/\lambda$ is the mean life of Be^7.

Experimentally we measure $\delta(t)$ and using (2) we obtain from it $\Delta\lambda/\lambda$. In the ideal case that $M(0) - C(0) = 0$, the maximum of δ is obtained at a time $t = \tau$ and the best time for measuring is $t = 2\tau$, i.e., the time at which the ratio between δ and its fluctuation caused by the statistical nature of the radioactive decay is maximum.

The apparatus used is schematically shown in Fig. 1. It consists of two argon-filled ionization chambers made as nearly equal as possible. The pressure in the chambers was 135.6 cm of Hg at 23°C and the density of the gas was kept constant to one part in a thousand. The two chambers were interconnected by a small copper tube to keep their pressures equal. The room in which the apparatus was located, although not temperature-controlled, was well shielded thermally. The collecting electrodes of the two chambers were connected together and to the input of a conventional electrometer circuit using a General Electric type FP-54 plyotron. The circuit was operated by the rate of drift method. The collecting potential for the chambers was taken from a dry cell battery pack delivering potentials of +400 volts and −400 volts. The polarities of the collection voltages were chosen so that the ionization current in one chamber opposed the ionization current in the other chamber. Thus, equal samples placed in the chambers would cause no drift of the galvanometer of the electrometer circuit. The samples were rigidly mounted in aluminum holders that fitted snugly into the central cavity of the ionization chambers, and we checked that possible small accidental differences in the geometry of the arrangement would not affect the results. This was done by verifying that the influence of artificial changes of geometry much larger than the changes to be expected in various runs was negligible. With this differential arrangement very small differences in the activities of two large samples can be measured. Our measuring procedure was as follows: we placed the M sample in chamber 1 and the C sample in chamber 2; the rate of drift of the galvanometer

TABLE I.

(Mar. 21, '47) Time	Duration, seconds	Sample in Ch 1	Sample in Ch 2	p mm sec.$^{-1}$	q mm sec.$^{-1}$
11.50	600	—	—	Background	+0.118
12.02	600	M	$C1$	+0.367	
12.12	600	$C1$	M		−0.133
12.23	600	M	$C2$	+0.047	
12.34	600	$C2$	M		+0.175
12.44	600	M	$C1$	+0.323	
12.55	600	$C1$	M		−0.158
13.06	600	M	$C2$	+0.033	
13.16	600	$C2$	M		+0.237
...	...	...	...	...	...
...	...	...	...	...	...

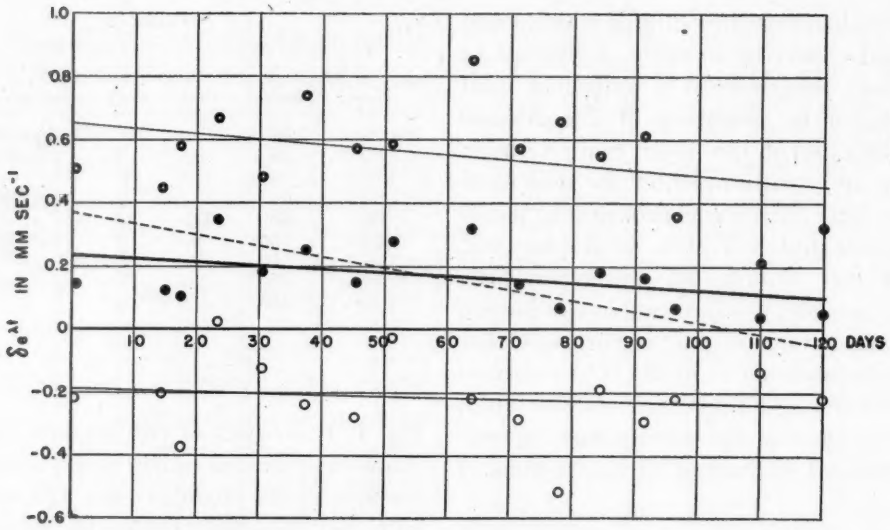

FIG. 2. Observed difference of activities of Be and BeO corrected for decay. $\delta e^{\lambda t}=M-C+M(\Delta\lambda/\lambda)(t/\tau)$ in mm sec.$^{-1}$. (1) Open circles: Be metal−BeO No. 1. (2) Open double circles: Be metal−BeO No. 2. (3) Solid circles: averages of (1) and (2). $M(0)\cong C(0)=270$ mm sec.$^{-1}$. Solid lines are best fits to experimental points. $\Delta\lambda/\lambda=-10^{-3}$ would give dotted straight line.

is then

$$p=MS_1-CS_2, \tag{3}$$

where S_1, S_2 are the sensitivities of chambers 1 and 2, respectively, and are very nearly equal. If we now interchange the samples, we have a rate of drift q

$$q=CS_1-MS_2, \tag{4}$$

from which

$$p+q=(M+C)(S_1-S_2), \tag{5}$$

$$p-q=(M-C)(S_1+S_2)\cong 2\delta S_1. \tag{6}$$

If the apparatus has a spontaneous rate of drift, which in practice, however, was extremely small, it cancels out in forming the expression (6) from the observations.

In our experiment, initially the sample of beryllium metal put in chamber 1 gave 270 mm sec.$^{-1}$ drift of the galvanometer, i.e., $M(0)S_1=270$ mm sec.$^{-1}$; when balanced with a sample of oxide in chamber 2 we obtained $p-q=0.5$ mm sec.$^{-1}$. As an example, observations from an actual run of comparisons between M and C are listed in Table I. Calculations were made by the standard least square procedure from the complete set of observations of that day. We obtained

$$2(M-C1)=0.463\pm0.038 \text{ mm sec.}^{-1},$$
$$2(M-C2)=-0.299\pm0.066 \text{ mm sec.}^{-1}$$

(the errors are standard deviations).

Observations extending over 120 days were finally calculated and plotted in Fig. 2. The value of λ adopted in the calculation is 1.309×10^{-2} day^{-1} corresponding to a half-life of 52.93 days. (For this value see Section IV.)

From the plot of Fig. 2 (all observations have approximately equal precision) we find $\Delta\lambda/\lambda=(-1.38\pm2.5)10^{-4}$ for the comparison M, $C1$; $\Delta\lambda/\lambda=(-4.76\pm3.0)10^{-4}$ for the comparison M, $C2$. If we use all the observations trusting that $C1$ and $C2$ are both free of radioactive impurities, we obtain

$$\Delta\lambda/\lambda=(-3.0\pm1.8)10^{-4}.$$

We must conclude that the $\Delta\lambda/\lambda$ observed is comparable with the error of observation and small compared with what one would expect barring accidental compensations in the change of $\lambda(0)$ between oxide and metal.

III. RADIOACTIVE FLUCTUATIONS

It is interesting to check the fluctuations on the balance of the instrument over a certain time

T. Suppose the instrument were exactly balanced with two sources each giving A mm sec.$^{-1}$ rate of drift, and call $\langle v^2 \rangle$ the average of the square of the deflections obtained in many measurements, each extending over a time T. Call d the deflection of the galvanometer produced by an elementary ionization process; then $A/d = \nu$ is equal to the number of elementary ionization processes produced by one source per second. We have then, according to the laws of fluctuations of radioactive decay,

$$\langle v^2 \rangle_{Av} = 2\nu T d^2 = 2ATd. \tag{7}$$

These quantities are all directly measurable with the exception of d. However, d can be estimated from the capacity of the chambers and the roughly calculated ionization produced by a 455-kev gamma-ray in our chamber; if all the energy of the gamma-ray is spent in the chamber, we have $d = 0.015$ mm and this is clearly an upper limit. In a series of measurements we had $A = 270$ mm sec.$^{-1}$, $\langle v^2 \rangle_{Av} = 1800$ mm^2, and $T = 600$ sec., from which we obtain using (7) $d = 0.006$ in reasonable agreement with the estimate, if one takes into account that only a small fraction of the gamma-ray energy of each quantum is transformed into ionization in the chamber.

IV. A RAPID WAY OF MEASURING LONG HALF-LIVES

Another application of our differential ionization chamber arrangement is the rapid measurement of radioactive periods, provided one has rather strong and radioactively pure sources.

If we balanced at time 0 the substance to be measured with a practically constant source (radium), the unbalance δ at time t is in good approximation for $\lambda t \ll 1$:

$$\delta = A\lambda t, \tag{8}$$

where A is the initial activity of the source. If we can measure A and δ with comparable relative precision, Eq. (8) gives λ.

In the case of Be^7 if $\lambda t = 5 \times 10^{-3}$ and A is equivalent to the activity of 100 micrograms of radium, it is easy to determine λ to ± 10 percent with our apparatus, and this result could be bettered for longer life substances. Thus, for example, we have measured $T_{\frac{1}{2}}$ of Be^7 taking observations intermittently over a period of about 5 hours and found 51.3 ± 11 days.

Using the data obtained by intermittent observations over a period of 28 hours we find 52.4 ± 1.3 days. Our best value for $T_{\frac{1}{2}}$ of Be^7, 52.93 ± 0.22 days, was obtained by comparison with a constant radium source extending over a period of 127 days. The standard error is obtained from the consistency of the measurements, but it must be borne in mind that it is possible that the measurement was affected by some slight systematic error.

Similarly, the half-life of Y^{90} was determined in three days and gave 108 days. Co^{60} was also measured intermittently (2 hours total measuring time, 0.6 mg Ra equivalent source) for 8 days and gave 5.08 years. This method could certainly be used also for much longer half-lives, such as radium itself, if one used as balancing substance uranium in equilibrium with its products. It is, however, essential that the substance to be measured be radioactively pure.

This work was done under the auspices of the Atomic Energy Commission.

The Secondary Emission of Electrons by High Energy Electrons

J. G. TRUMP AND R. J. VAN DE GRAAFF
Massachusetts Institute of Technology, Cambridge, Massachusetts

(Received September 20, 1948)

The secondary emission of electrons from tungsten, steel, aluminum, and graphite was studied as a function of the energy of the bombarding primary electrons in the range from 30 kilovolts to 340 kilovolts. The ratio of secondary to primary electrons was found to diminish with increasing primary energy and to increase with the atomic number of the target material. Thus, with aluminum the ratio diminished from 0.25 at 50 kilovolts to 0.17 at 200 kilovolts, while with tungsten it diminished from 0.73 to 0.62 in the same voltage range. Study of the energy distribution of the secondary electrons showed a percentage with energies less than 20 volts. Most of the remainder had energies greater than the available 800-volt repressor potential and resulted mainly from elastic nuclear scattering, particularly in the case of targets of high atomic number.

INTRODUCTION

IN the course of experiments directed primarily at investigating the mechanisms of voltage breakdown in high vacuum,[1] the opportunity arose to measure the emission of electrons from a number of materials under impact by steady streams of high energy electrons. Constant voltages up to 700 kilovolts developed by an air-insulated electrostatic generator were brought into an 18-inch diameter vacuum chamber through an evacuated porcelain bushing. By means of a corona loading device, the voltage could be held steady to about one percent at any value in this range. The vacuum chamber was constructed mostly of polished stainless steel parts and was maintained at pressures of 10^{-5} mm Hg or better by means of a mercury diffusion pump with a liquid air trap in series.

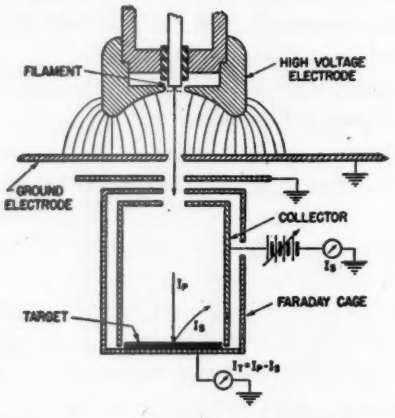

FIG. 1. Electrode arrangement for measuring secondary electron emission.

The electrode arrangement for measuring the secondary electron emission under high energy electron bombardment is shown in Fig. 1. The accelerating voltage was applied between the upper electrode and the steel ground plane, their geometry being such that the electrons from the 7-mil tungsten filament passed through the axial hole in the ground plane and on toward the Faraday cage beneath. A grounded intermediate diaphragm with slightly larger aperture was used to collect scattered electrons and further shield the target system. Within the Faraday cage, an insulated collector of steel was positioned to receive most of the secondaries emitted from the target. The potential of this collector relative to ground could be varied from +800 to −800 volts. Targets in the form of tungsten, steel, aluminum, and graphite disks were successively placed at the bottom of the Faraday cage. In these experiments, the energy of the bombarding electrons was varied over the range from about 30 kilovolts to 340 kilovolts. The targets were smooth and chemically cleaned, and their emission characteristics became stable after a short period of electron bombardment. The emission measurements were made with primary electron currents of about 10 microamperes; no changes caused by the heating of the target were noted.[2]

The curves in Fig. 2 show the ratio of secondary to primary electrons for tungsten, steel, aluminum, and graphite as a function of primary

[1] J. G. Trump and R. J. Van de Graaff, "The insulation of high voltages in vacuum," J. App. Phys. 18, 327–332 (1946).

[2] Treolar and Landun, Proc. Phys. Soc. 50, 625 (1938).

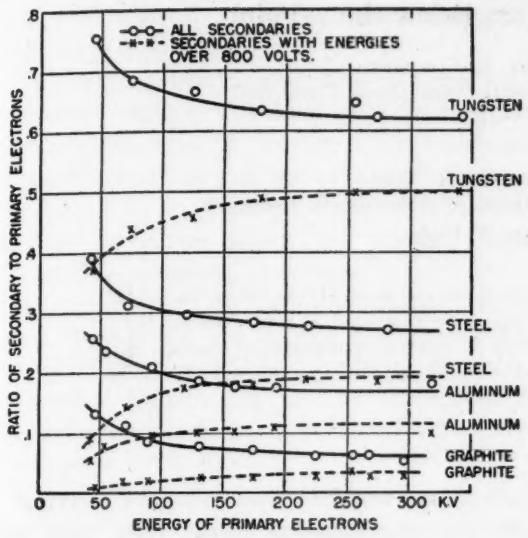

FIG. 2. Secondary emission of electrons by electrons with energies up to 340 kv.

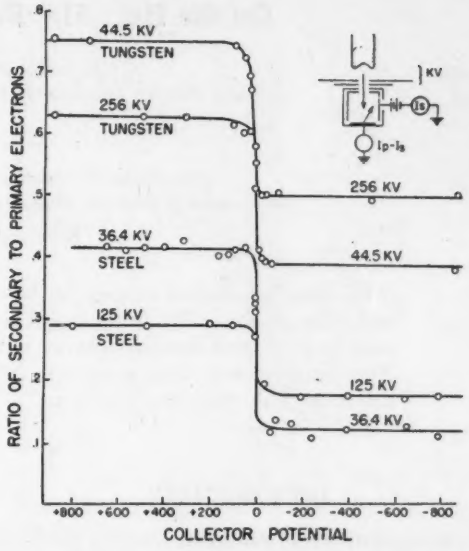

FIG. 3. Variation of secondary emission with collector potential.

energies from 30 kilovolts to 340 kilovolts. The descending curves include all of the secondaries, while the ascending curves include only those secondaries with energies in excess of 800 volts. The low energy secondaries actually lay almost entirely in the region of less than 20 volts, as can be seen from the variation of secondary emission with collector voltage given in Fig. 3. No adjustment was made in these curves for secondary electron emission from the walls of the collector by impact of secondaries from the target. It would be desirable in experiments of this kind to employ collectors of low atomic number such as beryllium or carbon in order to minimize these higher order effects.

These data show that the electron emission under high energy bombardment includes a considerable proportion of energetic electrons. These result mainly from elastic nuclear scattering rather than from electron-electron scattering or inelastic nuclear scattering.[3] This proportion increases with the energy of the bombarding primaries and has the expected marked dependence on atomic number. Low energy secondaries account for nearly 50 percent of the emission from tungsten and 90 percent of the emission from graphite at primary energy of 50 kilovolts, but the percentage of the low energy secondaries diminishes with increase in primary energy. Above 200 kilovolts all of the curves become substantially constant. In all cases, the ratio of the total secondary to primary electrons was well under unity and decreased with increasing bombarding energy. These results do not appear to be inconsistent with the emission peaks and values found by other investigators at lower energies.[4]

This work was performed some years ago as part of the experimental study of vacuum insulation, particularly the mechanisms for the emission of electrons, positive ions, and photons from electrodes subjected simultaneously to high voltages and high electric fields. The authors take pleasure in acknowledging the assistance of J. R. Maull in making some of the measurements.

[3] R. J. Van de Graaff, W. W. Buechner, and H. Feshbach, "Experiments on the elastic single scattering of electrons by nuclei," Phys. Rev. 69, 452–459 (1946).

[4] Bruining and DeBoer, Physica 5, 17 and 901 (1938).

On the He^3-He^4 Equilibrium below the λ-Point

C. T. LANE AND HENRY A. FAIRBANK
Sloane Physics Laboratory, Yale University, New Haven, Connecticut*

AND

L. T. ALDRICH AND ALFRED O. NIER
*Department of Physics, University of Minnesota,** Minneapolis, Minnesota*

(Received September 27, 1948)

Previous experiments attempting to establish the distribution of He^3 between the liquid and vapor phases of He^4, in the region below the λ-point, are discussed. It is pointed out that, because of the non-classical behavior of liquid helium II, customary methods of analysis fail. New measurements, using an entirely different kind of technique, are reported, and the results compared with prior determinations.

INTRODUCTION

IN two recent papers Daunt, Probst, and Smith[1] and Rollin and Hatton[2] have reported new measurements on the distribution of the He^3 isotope between the liquid and vapor phases of He^4, with special emphasis on the region below the λ-point. In an earlier communication[3] we reported a series of measurements on this subject, the results of which indicated that the concentration of He^3 in the vapor in equilibrium with the liquid fell to an unmeasurably small value, shortly after passing the λ-point, in the case of solutions produced from helium gas having a concentration of He^3/He^4 of about 1.2×10^{-6}. Although both the above-mentioned groups of investigators worked with samples having a different concentration range than this, and rendering comparison difficult, it nevertheless appears that the different experiments yield quite different results.

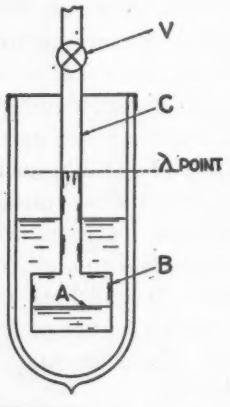

FIG. 1. Schematic arrangement of apparatus previously used for static equilibrium measurements.

Since the publication of our paper we have continued our investigation of this matter by a new approach, obtaining results also at variance with our old ones and bringing to light a number of factors unique to this problem, the neglect of which, in our opinion, is bound to lead to incorrect measurements. Since some of these "masking effects" also appear to have been neglected in the work of Daunt and collaborators and in that of Rollin and Hatton as well as in our prior work, the purpose of this paper is to discuss these various effects and report on our new measurements wherein they have been minimized.

Equilibrium measurements on two component liquid-gas systems have occupied the attention of chemists for many years, and a considerable amount of technique has been devised for this purpose. In the more closely allied problem dealing with gaseous mixtures at low temperatures, several methods have been employed.[4] In our original work[3] we made use of the so-called "static method," and this was also employed by Daunt and collaborators in their more recent measurements.[1] This static method has been used with success in many previous investigations[4] and, at the time we employed it, there seemed no *a priori* reason why it should not work equally

* Assisted by the Office of Naval Research.
** Assisted by the joint program of the Office of Naval Research and Atomic Energy Commission.

[1] J. G. Daunt, R. E. Probst, and S. R. Smith, Phys. Rev. 74, 495 (1948).
[2] B. V. Rollin and J. Hatton, Phys. Rev 74, 508 (1948).
[3] H. A. Fairbank, C. T. Lane, L. T. Aldrich, and A. O. Nier, Phys. Rev. 73, 729 (1948); 71, 911 (1947).
[4] For a description of these various methods see M. Ruhemann, *The Separation of Gases* (Clarendon Press, Oxford, 1940), Ch. II.

well in the special case where the substance was an isotopic mixture.

The reasons why neither this nor any other "classical" method can lead to correct equilibrium measurements in the case of He^3-He^4 have emerged gradually and are of some interest in themselves. In principle it is due to the extremely unusual properties which the solvent, liquid helium *II*, possesses, properties shared by no other known liquid. In the liquid helium *I* region, where the solvent has normal liquid properties, the before-mentioned classical methods of analysis are entirely satisfactory, as the agreement between the results of Daunt and collaborators[1] and of our prior work[3] shows.

We, therefore, now propose to discuss these masking effects and the steps we have taken, in the new measurements, to render such effects less harmful.

MASKING EFFECTS

(a) Figure 1 shows, in schematic fashion, the kind of arrangement used in the classical static method of equilibrium analysis. A bulb *B* containing the liquefied gas under investigation is immersed in a cryostat containing a refrigerant whose temperature may be controlled; in the present instance it is liquefied well helium. Connecting *B* to the outside of the cryostat is a tube *C*, usually small in diameter. The initial charge of the isotopic mixture *A* is condensed in *B* via *C*, and this latter also serves to remove samples of the vapor in *B* for analysis. Tube *C* contains a stopcock *V*. The tube leaving *V* is connected to an evacuated break-seal bulb (not shown) in which the gas sample is collected. The liquid and vapor in *B* are held at the desired temperature for a period of time (around 15 minutes in our earlier work), and then *V* is momentarily opened and a sample of gas, coming substantially from the vapor space of *B*, is collected in the break-seal bulb. Since no information exists with regard to the "equilibrium time" for the passage of He^3 atoms from vapor to liquid and *vice versa*, we have no recourse but to leave liquid and vapor in isothermal contact for a time which we guess to be much greater than this probable equilibrium time.

During this period, a film of liquid creeps up the sides of bulb *B* and tube *C* (indicated by arrows in Fig. 1) and, upon reaching a temperature equal to the λ-point, evaporates. Since *V* is closed, this evaporated gas, perforce, has to return down the tube and recondense at the surface of the liquid *A* in the bulb *B*, the heat of condensation being carried away by the outer bath. Now the gas produced from this creeping film is probably pure He^4, and hence the isotope equilibrium in *B* is being continually disturbed by the presence of He^4 fed by the film. Just how much a disturbance this amounts to is hard to say—it may be considerable if the amount of film evaporating per second is large and the equilibrium time mentioned before is long. In any event, it is evident that it would be highly desirable to suppress, in some way, this film. This, Rollin and Hatton have attempted to do but have introduced a second masking effect which may be even more serious. This film dilution effect has, of course, been recognized for some time as being objectionable in this kind of work involving helium *II*. We stressed its importance in our earlier work[3] and attempted to make some allowance for it. However, very recently, some new measurements[5] on the volume rate of flow of this film have been reported. They are widely divergent from the earlier results of Daunt and Mendelssohn,[6] which we had used, and in such a direction as to make the dilution effect possibly much more serious than we had supposed.

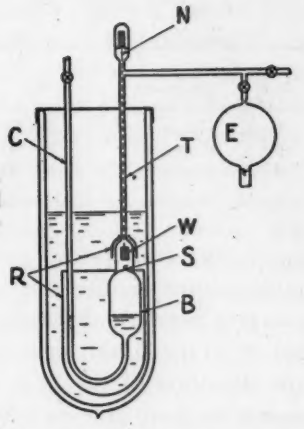

FIG. 2. Schematic diagram of arrangement used in the present measurements.

(b) The reason for this second effect arises from a discovery by us which was subsequent to

[5] K. R. Atkins, Nature 161, 925 (1948).
[6] J. G. Daunt and K. Mendelssohn, Proc. Roy. Soc. A170, 423 (1939); 170, 439 (1939).

TABLE I. Summary of experimental data.

Run	Apparatus	C_0	Temp.	Equilibrium time	Sampling time	C_v	C_L	C_v/C_L
1	Glass	1.2×10^{-6}	1.8°K	31 min.	~20 sec.	35×10^{-6}	0.6×10^{-6}	58
2	Copper	1.1×10^{-6}	1.8°K	30 min.	~2 sec.	27.8×10^{-6}	0.63×10^{-6}	44
3	Glass	36.5×10^{-6}	1.8°K	31 min.	~20 sec.	1350×10^{-6}	13.9×10^{-6}	97

our earlier equilibrium work. We found[7] that a temperature gradient in bulk liquid helium *II* exerts a ponderamotive force on He^3 atoms dissolved in the liquid, such that the latter travel in the direction of the heat flow. In these experiments we were able to raise the concentration of the He^3, at the surface of the liquid subjected to the temperature gradient, by a factor of several hundred with very small temperature gradients. It is probable then that the creeping film, in addition to dilution, will likely produce a large disturbance in the equilibrium as a result of this heat flush effect. Thus, again referring to Fig. 1, the heat of condensation of the film gas at the surface *A* will flow mainly through the bottom surface of bulb *B* to the outer bath. This will drive the He^3 to the bottom of the bulb leaving the surface *A*, where the equilibrium exchange is taking place, denuded of He^3.

It is clear then that if we are to make reliable measurements, we must avoid the creeping film and, in addition, avoid, as far as possible, temperature gradients in the liquid under study. The experiments which we are about to discuss are a considerable improvement in this respect over previously reported work.

NEW MEASUREMENTS

Figure 2 is a schematic diagram of the arrangement used in the present work. A charge of helium gas containing He^3 (usually around 2 liters S.T.P.) is condensed in the glass bulb *B* via the capillary filling tube *C*. The upper end of *B* is closed by a small glass tip *S*, above which hangs a small gold weight *W* suspended from the outside of the cryostat by a thread *N*. The capillary *T* containing the thread *N* has a side arm outside the cryostat which goes to the vacuum system and the usual break-seal collection bulb *E*. Aluminum foil radiation shields *R* are placed as shown, and the level of the outer bath of helium is kept well above the weight *W* at all times during the experiment.

Typical procedure is then as follows. The outer bath temperature is set at 1.8°K, and the contents of *B* allowed to remain at this temperature for about 30 minutes. Weight *W* is then dropped and seal *S* broken. Simultaneously, the stopcock to vessel *E*, which has been previously evacuated, is momentarily opened (for a few seconds) and a sample of the vapor in *B* collected. At the end of the experiment the apparatus was dismantled, and the size of the orifice created by breaking *S* determined. In all runs this hole was less than 1 mm in diameter.

It is clear that this technique greatly reduces the masking effects previously discussed. Since all parts of the apparatus are always below the λ-point, the film in bulb *B* is static—it does not evaporate until the seal *S* is broken. Since the sampling is extremely rapid, and since the amount of film is limited by the small orifice created at *S*, the film effect is reduced many orders of magnitude over such effect in previous experiments. To all intents and purposes, then, we have effectively suppressed the creeping film. In so doing we have also largely eliminated the concomitant heat flush effect.

It must be pointed out, however, that the heat flush effect has not been entirely suppressed. First there is a heat flush caused by film evaporating in the side arm *C*—this we have minimized in another version of the experiment presently to be described. Perhaps more serious is the heat flush caused by sampling. Thus, when the sample is withdrawn at *E*, a momentary drop in pressure occurs in the vapor space of *B*, and this in turn causes evaporation from the liquid surface in *B*. In consequence, this surface cools, and hence heat is directed towards it carrying He^3. During sampling therefore, the surface is richer in He^3 than it should be if true equilibrium, obtained. It

[7] C. T. Lane, H. A. Fairbank, L. T. Aldrich, and A. O. Nier, Phys. Rev. 73, 256 (1948).

will be noted that this effect is just the reverse of that produced by the evaporating film in the earlier experiments.

In order to ameliorate these last two conditions somewhat we modified the apparatus such that bulb B (except seal S) and filling capillary C were made of copper instead of glass, the former having a much higher thermal conductivity than the latter. In this case we would expect the temperature gradients in the liquid in B to be dissipated much more rapidly and the resulting heat flush effects reduced.

In all we have taken four runs with this apparatus, three with the glass bulb, and one with the copper, and all at the same temperature, which was in the vicinity of 1.8°K. In the first run taken a rather unexpected difficulty arose. Referring again to Fig. 2, in this run, the weight W was suspended by a fine constantan wire, and the surrounding tubing was highly evacuated. Upon dropping W, after 30 minutes, the outside helium bath rose suddenly in temperature as judged by the oil manometer reading the vapor pressure of this bath. It was apparent that, even after 30 minutes, weight W had not come into thermal equilibrium with the outer bath because of the heat fed by the supporting wire and the high vacuum surrounding W. Upon rupture of seal S the escaping vapor established heat interchange to the outer bath, and this temperature rise reacted unfavorably on the whole system. In subsequent runs, as reported here, we eliminated this difficulty by using an insulating thread (Nylon) instead of the wire and by surrounding W with helium gas at approximately 10^{-2}-mm Hg pressure for heat exchange. This exchange gas was pumped off just prior to sampling, but, in any event, its amount was so small as to be of negligible importance as far as contaminating the sample was concerned.

RESULTS AND DISCUSSION

The experimental data collected in three runs is summarized in Table I. Under the column "apparatus" we have noted whether the bulb B was of Pyrex glass or copper. The third column headed C_0 gives the ratio of He^3/He^4 in the gas used to produce the liquid and vapor phases. Runs 1 and 2 used Airco atmospheric helium, while the gas used in run 3 was enriched by the use of a thermal diffusion column. In the final column appears the ratio of He^3/He^4 in the vapor (C_v) to the same quantity in the liquid (C_L). As was done previously,[3] C_0 and C_v were measured with the mass spectrometer and C_L computed from the mass balance and composition balance equations.

A comparison of these present results, and those given previously by us,[3] shows a very great discrepancy. Thus at 1.8°K, with Airco helium, our prior measurements gave $C_v/C_L<0.04$. Again, at the higher concentration range, Daunt and collaborators,[1] using a method very similar to that used in our prior work, found $C_v/C_L\cong 3$ at 1.8°K, whereas our new measurement (run 3) gives $C_v/C_L=97$. However, both these differences are in the right direction since, as we stressed previously, the effect of the creeping film both by dilution and heat flush is to lower the values of C_v/C_L. The fact that the C_v/C_L ratio appears to be a function of concentration, as suggested by London and Rice,[5] and confirmed by Daunt and collaborators,[1] is also suggested by our present results.

Comparison of the present work and that of Rollin and Hatton[2] is rendered difficult partly because of the fact that the latter investigators are working in a much higher concentration range and also because the method they use appears to be an "open" evaporational process[4] rather than a static equilibrium measurement. It is true, of course, that we have elements of open evaporation in our measurements during the sampling process also. Thus, during sampling, we have a certain amount of evaporation at the surface of

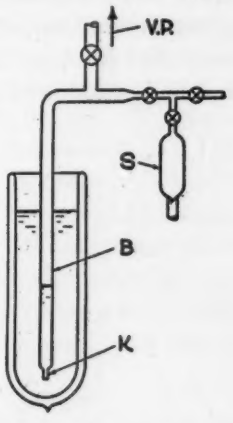

FIG. 3. Type of apparatus which yields non-equilibrium values.

[5] F. London and O. K. Rice, Phys Rev. 73, 1189 (1948).

the liquid in bulb B which should lead to a higher concentration of He^3 in the vapor than is proper due to the heat flush effect, a fact which has already been mentioned. We tried to minimize this in run 2 by using high thermal conductivity copper to equalize sudden temperature differences and also by making the equivalent vapor space in B (reduced to S.T.P.) much larger than the size of our sample. The fact that the amount of evaporation at the surface of the liquid in B was small was evidenced by the fact that no noticeable drop in temperature of the outer bath was observed during the sampling process. The only way to avoid completely this sampling error would be to have a helium *II* tight valve just above the liquid in B which could be closed during sampling. Such a valve is most difficult to construct. In the Rollin and Hatton experiment rather complex heat flux effects must be present, and it is difficult to see how their method could lead to anything approaching correct equilibrium values.

In this connection the following experiment bears a certain similarity to the one of Rollin and Hatton and is, we believe, subject to the same criticism as far as providing a correct equilibrium value. Referring to Fig. 3, a glass tube B has a capillary section at its lower end which is provided with a Kovar metal tip K. This is immersed in a bath of liquid helium, and B is charged with about 3 cm^3 of condensed Airco helium. The latter had a concentration of He^3/He^4 of 0.93×10^{-6}. The bath temperature was set at 1.6°K, and the liquid in B was pumped by a medium capacity pump via V.P. The temperature of the liquid in B, therefore, fell somewhat below the bath temperature, and heat flowed into B via the metal end K. After about 15 minutes the liquid in B had evaporated until only about 1.6 percent of the liquid originally present in B remained in K. This remaining liquid in K was now vaporized and collected in S for analysis. Two things are wrong with this experiment as far as an equilibrium measurement is concerned.

(a) The heat flush effect is continuously transporting He^3 atoms to the evaporating surface of the liquid in B, consequently this surface is not in He^3 equilibrium with the liquid as a whole.

(b) Apart from this, one cannot be sure that the evaporating vapor is in thermodynamic equilibrium with the parent liquid.

However, if one, for the moment, assumes that thermodynamic equilibrium between the liquid and evaporating vapor is in fact approached, then one can estimate C_v/C_L for this case. It is easy to show that

$$\log C_i/C_f=[(C_v/C_L)-1]\log M_i/M_f,$$

where the subscripts i and f refer to initial and final conditions, and M and C refer, respectively, to the liquid mass and the He^3/He^4 concentration. The results were

$$M_i/M_f=62,$$
$$C_i/C_f=93\times10^{-8}/3\times10^{-8}=31,$$

whence

$$C_v/C_L=1.9.$$

According to the views expressed in this paper, we cannot regard this last result as having any meaning insofar as it bears on the problem of the He^3-He^4 equilibrium. It seems to us that this kind of experiment and, to a lesser extent, that of Rollin and Hatton deal essentially with non-equilibrium processes.

Finally, we should like to express our appreciation for the assistance given to the low temperature phase of the work by Mr. Charles Reynolds.

Gamma-Rays from Deuteron Reactions

DAVID E. ALBURGER*
*Sloane Physics Laboratory, Yale University,** New Haven, Connecticut*
(Received September 28, 1948)

Gamma-rays from Na, Mg, Al, Si, P, S, and PbO_2 targets under cyclotron bombardment by 3.7-Mev deuterons have been measured by coincidence absorption of Compton electrons. With PbO_2, Al, and Mg Compton distributions were also obtained by means of a thin lens magnetic spectrometer. Correlation of several of the measured values can be made with excited states of N^{14}, O^{17}, and Si^{28} as obtained from other information. The predominant gamma-rays have moderately large energy, being 8.8 Mev in one case, indicating a preference for direct transitions from states of high excitation to the ground state of the product nucleus.

I. INTRODUCTION

NUCLEAR energy levels appearing during the bombardment process are revealed by gamma-radiation. In analogy with atomic and molecular spectroscopy, the measurement of gamma-ray energies can give spacings, transition probabilities, and other information pertaining to levels in the nucleus.

Correlation of gamma-ray data with levels obtained by other methods should be possible. This has been done[1] in the bombardment of a few very light elements. However, for product nuclei above nitrogen few gamma-rays have been accurately determined. Some recent work[2,3] along this line has been done in which gamma-ray energies associated with the alpha-particle bombardment of Na, Mg, Al, Si, P, and S, were obtained by absorption in lead and by coincidence absorption of Compton electrons. Agreement was found in several cases with existing information and there was, in addition, some evidence for the presence of selection rules.

During this alpha-particle work a few rough measurements were made at the cyclotron tuning resonance for deuterons and with an aluminum target gamma-rays of moderately high energy were observed. A program of coincidence absorption using the deuteron beam was therefore carried out on the same series of target elements. In the course of this work a thin lens magnetic spectrometer became available and was adapted to measure energies of gamma-rays from targets under cyclotron bombardment. This was applied to several cases which will be described.

II. EXPERIMENTAL METHODS

The experimental arrangement for coincidence absorption measurements has been described previously.[3] This consists of two thin window beta-ray counters placed on a line with the target. Gamma-rays formed in the target produce Compton electrons in the end wall of the first counter which can traverse both counters and give coincidences. The absorber thickness placed between the counters which just reduces the yield to the random coincidence rate is the maximum Compton electron range and from this the incident gamma-ray energy may be calculated.

Relatively high gamma-ray intensities were available in deuteron bombardment and a means was sought to overcome the large random coincidence rate found with the elementary circuit[4,3] used at first. A double coincidence circuit of medium resolution designed[5] by Professors Schultz and Pollard was convenient for this purpose. This employs two 10-megacycle blocking oscillators triggered by the initial pulse rise. Coincidences formed between the narrow rectified oscillator output pulses make the resolving time essentially independent of counter pulse width. In a test using two Geiger counters at a chosen

* Now at Brookhaven National Laboratory, Upton, New York.
** Assisted by the office of Naval Research under Contract N6ori-44.
[1] W. F. Hornyak and T. Lauritsen, Rev. Mod. Phys. **20**, 191 (1948).
[2] E. Pollard and D. E. Alburger, Phys. Rev. **72**, 1196 (1947).
[3] D. E. Alburger, Phys. Rev. **73**, 1014 (1948).
[4] A. B. Martin, Phys. Rev. **72**, 378 (1947).
[5] H. L. Schultz and E. Pollard, Rev. Sci. Inst. **19**, 617 (1948).

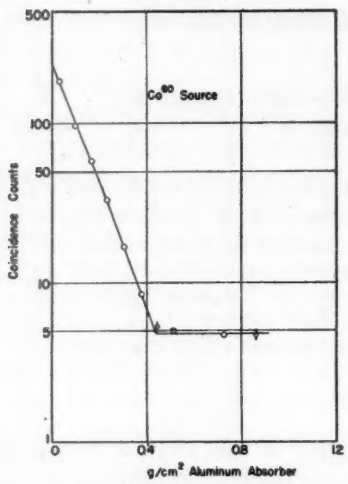

FIG. 1. Coincidence absorption calibration using a Co^{60} source.

counting level, only three random coincidences per minute were recorded in comparison with 100 per minute from the older circuit.

Because of the increased measuring accuracy made possible by higher intensities and improved coincidence counting equipment as compared with previous work[3] using alpha-particles a recheck on the coincidence absorption method became desirable. Co^{60} was available for this purpose. This emits two gamma-rays which have been reported[6] by Deutsch, Elliott, and Roberts to have energies of 1.10 Mev and 1.30 Mev. More recent values given[7] by Jensen, Laslett, and Pratt are 1.16 Mev and 1.32 Mev. Using the same geometry and counting level as in the cyclotron experimental data of Part III the curve in Fig. 1 was obtained. This has an extrapolated maximum range of 0.440 g/cm² of aluminum, although the point at 0.446 g/cm² is probably slightly above the random coincidence rate. From the Feather relation,[8]

$$R(\text{g/cm}^2\text{Al}) = 0.543E(\text{Mev}) - 0.160,$$

a maximum gamma-ray energy of 1.31 ± 0.02 Mev may be calculated using the 0.440 g/cm² range to obtain the electron energy and adding the correct value for the back-scattered quantum. The agreement seems to indicate that this formula is more suitable in the present application than the modified Feather relation published[9] by Bleuler and Zünti.

Additional measurements were made with a thin lens magnetic spectrometer of conventional design[10] adapted as shown in Fig. 2 to observe gamma-rays from cyclotron targets. The beam is deflected through an extension tube and strikes the target which is mounted on the spectrometer radiator for large solid angle in the production of secondary electrons. The tin baffle restricts the beam to a limited portion of the target. A vacuum connection through holes in the spectrometer end plate eliminates foils from the path of the beam which might otherwise result in undesirable gamma-radiation. The energy distribution of electrons from the radiator is measured in the usual fashion. Spaced iron shielding rings are provided to reduce the defocusing effect of the stray cyclotron magnetic field without appreciably affecting the characteristics of the lens. A more complete description of this shielding method is given[11] elsewhere.

To facilitate cyclotron tuning the beam current is read directly from the insulated target-radiator holder by means of a galvanometer. Because of low currents and fluctuations in intensity it was

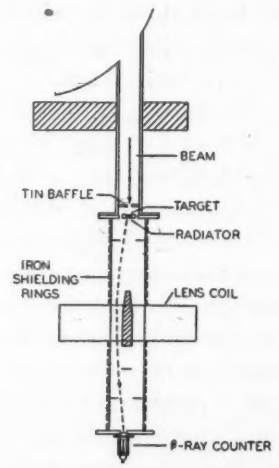

FIG. 2. Experimental arrangement for measuring energies of gamma-rays from targets under cyclotron bombardment. A thin-lens spectrometer has been adapted to obtain secondary electron distributions.

[6] M. Deutsch, L. G. Elliott, and A. Roberts, Phys. Rev. **68**, 193 (1945).
[7] E. N. Jensen, L. J. Laslett, and W. W. Pratt, Phys. Rev. **73**, 529 (1948).
[8] N. Feather, Proc. Camb. Phil. Soc. **34**, 599 (1938).
[9] E. Bleuler and W. Zünti, Helv. Phys. Acta. **19**, 137 (1946).
[10] M. Deutsch, L. G. Elliott, and R. D. Evans, Rev. Sci. Inst. **15**, 178 (1944).
[11] D. E. Alburger, Rev. Sci. Inst. **19**, 474 (1948).

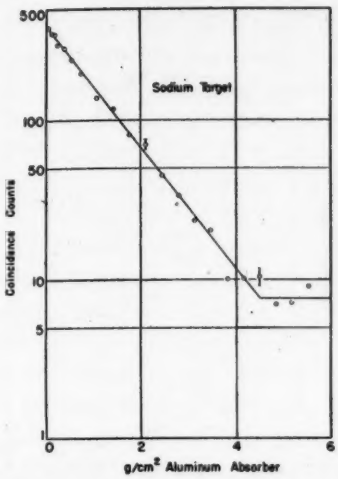

FIG. 3. Coincidence absorption of Compton electrons due to gamma-rays from sodium under deuteron bombardment.

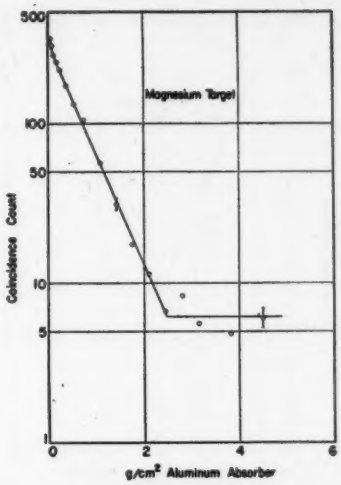

FIG. 4. Coincidence absorption, gamma-rays from Mg+D^2.

found most suitable to integrate the beam with a monitor gamma-ray counter (not shown) placed near the target and to refer the yield from the spectrometer at each point to a fixed number of monitor counts. Calibration of the spectrometer was taken from the Compton distribution of Co^{60} gamma-rays. A value of 97 gauss-cm per ampere was obtained.

III. EXPERIMENTAL RESULTS

Coincidence absorption curves for gamma-rays resulting from the deuteron bombardment of Na, Mg, Al, Si, P, and S, are shown in Figs. 3–8. In all cases the separation between counter bases was $1\frac{1}{2}$ inches and coincidences have been referred to 16,000 counts in the first counter. Beam currents of the order of 0.005 microampere were sufficient to operate at the desired counting level.

The curve for sodium in Fig. 3 is nearly linear with an end point at 4.5 g/cm² corresponding to an 8.8±0.6-Mev gamma-ray. An estimate of the cross section for this reaction compared with the formation of Na^{24} could be made. The run was restricted to three hours in order to prevent the build-up of excessive radioactivity and during this time the first or monitor counter recorded a total of 1.7×10^6 counts (about 160/sec.). At the end of bombardment and with the cyclotron turned off, the net rate in the same counter due to 2.8 Mev Na^{24} gamma-rays was about 8.0 per second. From a calculation using a decay constant 1.3×10^{-5} sec.$^{-1}$, this corresponds to the formation of 0.6×10^6 Na^{24} nuclei—not allowing for solid angle and absolute counter efficiency. To compare this yield with the 1.7×10^6 reactions resulting in 8.8-Mev gamma-rays, a factor of about 3 must be introduced because of the increase of counter efficiency with gamma-ray energy.[12] On the same basis 1.8×10^6 Na^{24} nuclei have therefore been formed. The cross sections for these two processes are thus about equal. However, it is unlikely that the 8.8-Mev gamma-ray is produced during the formation of Na^{24},

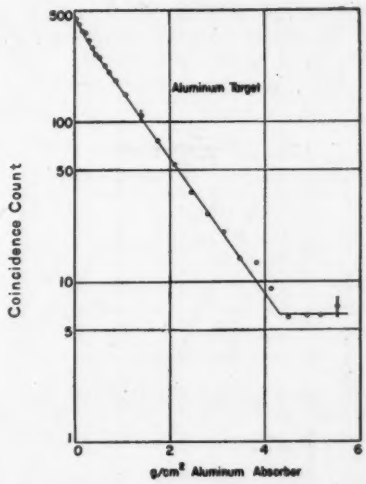

FIG. 5. Coincidence absorption, gamma-rays from Al+D^2.

[12] Bradt, Gugelot, Huber, Medicus, Preiswerk, and Scherrer, Helv. Phys. Acta 19, 77 (1946).

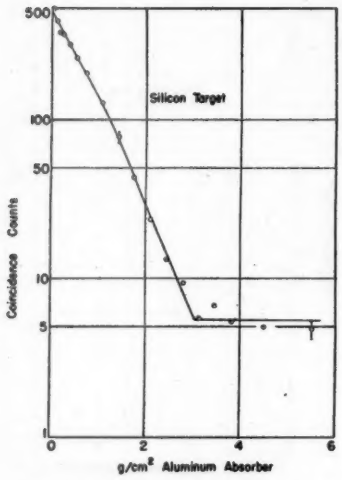

FIG. 6. Coincidence absorption, gamma-rays from Si+D².

since the Q-value for this reaction is less than 5 Mev.

Figure 4 for magnesium has an end point at 2.5 g/cm² Al, giving a gamma-ray energy of 5.1±0.3 Mev. A slight increase in yield below 0.2 g/cm² Al indicates a weak gamma-ray of less than 0.9 Mev.

The aluminum target yield in Fig. 5 shows a predominant gamma-ray energy of 8.5±0.5 Mev from the 4.3-g/cm² Al maximum electron range. A slight break occurs at 0.55-g/cm² Al as seen more clearly with a straight edge, and corresponds to a gamma-ray energy of 1.5±0.2 Mev.

Curves for Si, P, and S given in Figs. 6, 7, and 8 show end points of 3.1, 3.1, and 3.0 g/cm² Al. The first two are from 6.2±0.3-Mev gamma-rays and the third from a 6.0±0.3-Mev gamma-ray.

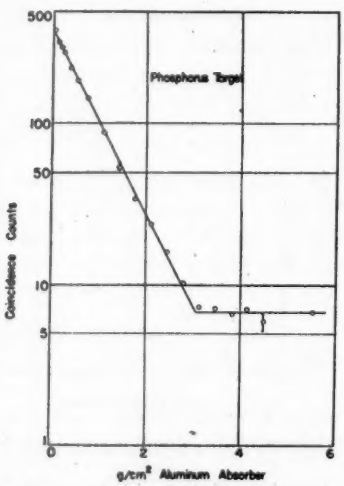

FIG. 7. Coincidence absorption, gamma-rays from P+D².

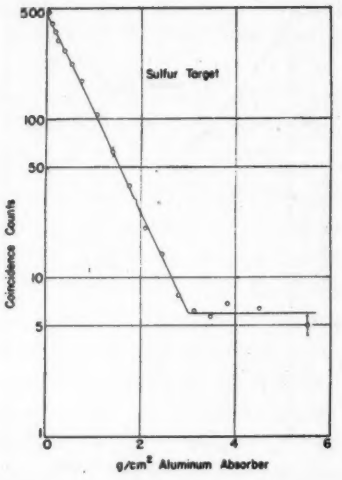

FIG. 8. Coincidence absorption, gamma-rays from S+D².

For an initial test of the spectrometer method described in Part II, cases were considered which might yield simple gamma-ray spectra within the 4-Mev measuring range of the instrument. The $O^{16}(dp)O^{17}$ reaction has been studied recently by Pollard and Davison[13] and by Heydenburg and Inglis.[14] Proton groups to the ground state and first excited state of the O^{17} nucleus at 0.87 Mev have been found. In the absence of other excited states or competing processes, a single gamma-ray energy could be expected.

The Compton electron distribution found with a PbO_2 target mounted on a thick copper radiator is shown in Fig. 9. Because of high background from the main cyclotron chamber and low intensity from the target, a net yield of only 17 percent at the maximum was obtained—giving the statistics indicated at 32.5 amperes. Considerably more shielding was used than shown in Fig. 2. A dashed line has been drawn in Fig. 9 to separate out poorly resolved variations above 40 amperes. The gamma-ray producing the main peak with the inflection point indicated is 0.90 ±0.05 Mev and is thus in agreement with the first excited state of O^{17}. With the present data it is not felt that any significance can be attached to the region of the curve above 40 amperes.

[13] E. Pollard and P. W. Davison, Phys. Rev. **72**, 736 (1947).
[14] N. P. Heydenburg and D. R. Inglis, Phys. Rev. **73**, 230 (1948).

To further study this spectrum coincidence absorption measurements were made on the same target. The combined data for several runs is shown in Fig. 10. Two ranges seem to be present at 0.23 g/cm² Al and at 1.92 g/cm² Al which correspond to 0.90±0.15 Mev and 4.0±0.3 Mev gamma-rays, respectively. There may also be a component of 2.1±0.3 Mev at 0.85 g/cm² Al.

Several other targets were tried under deuteron bombardment, aluminum giving the curve in Fig. 11. This spectrum extends beyond the range of the instrument as to be expected from the coincidence absorption data of Fig. 5. The upper portion has been extended back with a dashed line and subtracted from the experimental points resulting in the curve below. The $H\rho$ value at the inflection point yields a gamma-ray energy of 1.72±0.08 Mev, which is a somewhat more accurate determination than the coincidence absorption measurement of Fig. 5. The expected deviation in points is indicated at 45 amperes. A slight variation seems to occur at 110 amperes which could indicate the presence of a 3.0±0.2 Mev gamma-ray.

With magnesium the Compton distribution in Fig. 12 was obtained and is apparently the unresolved composite resulting from several gamma-rays. A maximum energy of 4.9 Mev at about 175 amperes is in essential agreement with the coincidence absorption curve of Fig. 4. Spectrometer curves for the remaining targets were not taken.

IV. DISCUSSION

A summary of the gamma-ray energies measured is given in Table I together with the probable reaction in cases where correlations can be made.

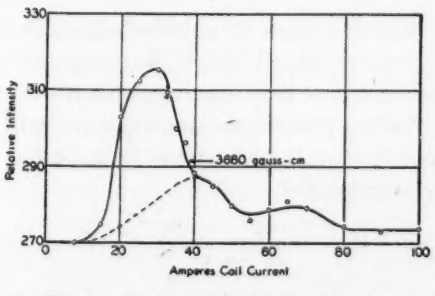

FIG. 9. Compton electron distribution from a thick copper radiator due to gamma-rays from PbO_2+D^2 as measured by the arrangement in Fig. 2.

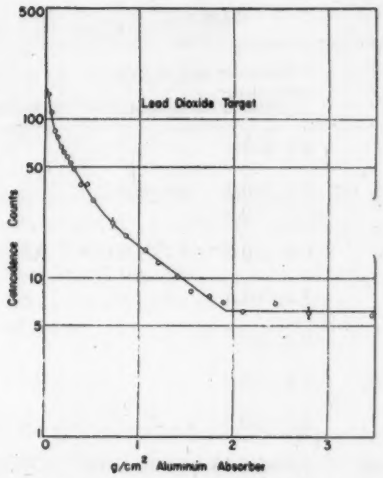

FIG. 10. Coincidence absorption, gamma-rays from PbO_2+D^2. The end point at about 0.23 g/cm² Al corresponds to the prominent peak in Fig. 9.

The first excited state of Si^{28} has been found from radioactivity measurements of Bleuler and Zünti[15] and by Barkus[16] to be at 1.8 Mev. This level is further confirmed[17] by Peck using photographic methods to study the $Al^{27}(dn)Si^{28}$ reaction. He obtains a first excited state at 1.7±0.3 Mev and other levels ranging up to 9.7 Mev at the same bombarding energy used in the present work. His levels are consistent with a Q-value[18] of 9.4 Mev for the dn reaction and could also account for the 8.5-Mev gamma-radiation observed here. The 1.72-Mev gamma-ray has therefore been assigned in Table I to Si^{28}.

In the spectrum from PbO_2 the agreement of the 0.90-Mev gamma-ray with the first excited

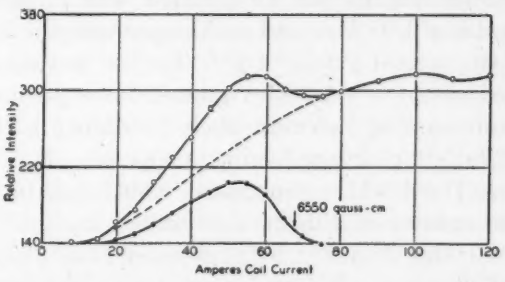

FIG. 11. Compton distribution, gamma-rays from Al+D². The 6550$H\rho$ component agrees with the break at 0.55 g/cm² Al in the curve of Fig. 5.

[15] E. Bleuler and W. Zünti, Helv. Phys. Acta **20**, 195 (1947).
[16] W. H. Barkas, Phys. Rev. **72**, 346 (1947).
[17] R. A. Peck, to be published.
[18] Q-values have been calculated from masses given by Mattauch and Flügge, Physik. Zeits. **44**, 181 (1943).

TABLE I.

Target	Gamma-ray energy (Mev) Coincidence absorption	Spectrometer	Probable reaction
Sodium	8.8 ±0.6		
Magnesium	5.1 ±0.3 <0.9	4.9 max.	
Aluminum	1.5 ±0.2	1.72±0.08 3.0 ±0.2?	$Al^{27}(dn)Si^{28}$
	8.5 ±0.5		
Silicon	6.2 ±0.3		
Phosphorus	6.2 ±0.3		
Sulfur	6.0 ±0.3		
Lead dioxide	0.90±0.15 2.1 ±0.3? 4.0 ±0.3	0.90±0.05	$O^{16}(dp)O^{17}$ $O^{16}(d\alpha)N^{14}$

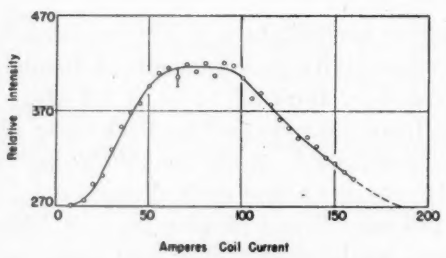

FIG. 12. Compton distribution, Mg+D^2.

state of O^{17} seems fairly certain. Other levels have not been reported in the *dp* reaction although Burcham and Smith have found[19] excited states of O^{17} at 0.83, 2.95, 3.77, and 4.49 Mev from $F^{19}(d\alpha)O^{17}$. The 4.0-Mev gamma-ray might then be due to the *dp* reaction which has a *Q*-value of 1.95 Mev and could agree with the 3rd or 4th excited states of O^{17}. The *dn* process is ruled out by a −1.7-Mev ground state *Q*-value. The remaining and most likely possibility is the $O^{16}(d\alpha)N^{14}$ reaction having a *Q*-value of 3.13 Mev. The 4.0-Mev gamma-ray would then be in good agreement with the first excited state of N^{14} at 4.0 Mev found[20,3] by Stuhlinger from alpha-particle resonances producing slow neutrons in $B^{11}(\alpha n)N^{14}$. The intermediate and questionable gamma-ray of 2.1 Mev is in rough agreement with radiation of 2.3 Mev observed[21] by Sherr, Muether, and White in the positron decay of O^{14} and might therefore be caused by another level in N^{14}.

The shape of an unresolved coincidence absorption curve depends on the geometry used and the energies and relative intensities present. An estimate of what could be expected with the present arrangement for a single energy may be made from Fig. 1 since the radiation from Co^{60} is roughly monoenergetic. A slight concavity to the coordinates in the logarithmically plotted absorption curve is to be noted. The presence of other gamma-ray components of less than half the energy and of comparable intensity causes a pronounced convexity to the coordinates in the resultant curve as illustrated in Fig. 10 for PbO_2.

This qualitative feature may be applied to the curves for Na, Mg, Al, Si, P, and S, which are nearly linear, excepting for additional yields at low absorption in Mg and Al. Silicon most closely exhibits the shape expected for a single component. The general conclusion to be drawn from these six cases is that at least 30–50 percent of the radiation consists of the highest energy components and that smaller intensities of lower energy gamma-rays are probably present. In view of low lying level spacings of the order of 1 Mev or less obtained by other methods in this region of the periodic table, the predominance of these energies indicates a preference for direct transitions from states of high excitation. The processes producing these gamma-rays will have to be determined from further particle reaction level data, by comparing particle and gamma-ray excitation curves, or by performing coincidence experiments between particles and gamma-rays.

The author wishes to acknowledge the assistance given by Mr. William Bateson, who constructed the thin lens spectrometer used in this work. Many valuable discussions were held with Professor Ernest Pollard whose suggestions were greatly appreciated.

[19] W. E. Burcham and C. L. Smith, Proc. Roy. Soc. A168, 176 (1938).
[20] Stuhlinger, Zeits. f. Physik 114, 185 (1939).
[21] R. Sherr, H. R. Muether, and M. G. White, Bull. Am. Phys. Soc. 23, No. 7, A4 (1948).

The Cosmic-Ray Intensity above the Atmosphere*

A. V. GANGNES, J. F. JENKINS, JR., AND J. A. VAN ALLEN
Applied Physics Laboratory, Johns Hopkins University, Silver Spring, Maryland
(Received September 24, 1948)

In a series of flights of Aerobee and V-2 rockets at geomagnetic latitude $\lambda=41°$N, single Geiger counters and Geiger counter telescopes have been employed to measure the total intensity of cosmic rays above the appreciable atmosphere. The directional intensity j, averaged over the upper hemisphere, is found to be 0.120 ± 0.009/sec./cm²/steradian, constant from 55-km altitude to the highest altitude reached of 161 km. This result is an experimental upper limit to the primary intensity of charged particles at this latitude.

I. INTRODUCTION

IN a previous report,[1] we presented measurements on the counting rate of a single Geiger counter from ground level to 161 kilometers in altitude. (See Fig. 1, reproduced from reference 1.) It was found that a substantially flat plateau intensity exists above about 55 km.

An interpretation of the plateau counting rate in terms of charged particle intensity was given.

This paper contains further comments on the previous results and a description of subsequent single counter and coincidence telescope measurements, made at high altitude by means of the new American sounding rocket, the Aerobee, and by means of another V-2.

Inasmuch as a single Geiger counter is perhaps the most sensitive practical indicator of either an attenuation or multiplication of the cosmic-ray intensity, it seems justified to consider the experimental figure of 55 km as the upper bound of the appreciable atmosphere in cosmic-ray considerations. This is especially true for a cylindrical counter with axis approximately vertical; for such a counter has its maximum sensitivity to rays entering the atmosphere at grazing incidence and, hence, traversing the greatest path length in the atmosphere. In what follows, we shall refer to measurements above this altitude as having been made "above the atmosphere."

All results herein have been obtained in rockets fired from the White Sands Proving Ground, Las Cruces, New Mexico. Although in some flights as much as 1° of latitude is traversed, the geomagnetic latitude of the launching site, $\lambda=41°$N, is adopted for convenience since there is no indication that present results justify more refined consideration.

No determination of the quantitative importance of secondaries emerging from the earth's atmosphere has been made. Rossi[2] has recently contributed an illuminating discussion of the nature of this problem.

II. REMARKS ON THE SINGLE GEIGER COUNTER MEASUREMENTS IN V-2 NO. 30 FIRED ON JULY 29, 1947

In reference 1, it was assumed that the inner ends of the glass skirt which surrounded the 3-mil anode wire of the Geiger counter defined the effective length of the counter. This length was 15.2 cm. Subsequently, we have determined the effective length of tubes from the same batch by the experimental method of Street and Woodward.[3] A typical curve (for the actual counter flown in V-2 No. 35 described in Section III) is shown in Fig. 2. The experimental effective length is 13.5 cm. In accordance with the universal finding of other workers, the effective diameter has been taken, as before, as the internal diameter of the metal wall of the counter, 2.38 cm. Thus, ascribing the mean plateau counting rate of 22.4 counts/second to a cosmic-ray flux isotropically distributed over the upper hemisphere, zero over the lower hemisphere, a revised value for the directional intensity

$$j=0.13/\text{sec.}/\text{cm}^2/\text{steradian}$$

is obtained.

* This work was supported by the Navy Bureau of Ordnance under Contract NOrd 7386.

[1] J. A. Van Allen and H. E. Tatel, Phys. Rev. **73**, 245 (1948).

[2] B. Rossi, Rev. Mod. Phys. **20**, 537 (1948).

[3] J. C. Street and R. H. Woodward, Phys. Rev. **46**, 1029 (1934); K. Greisen and N. Nereson, Phys. Rev. **62**, 316 (1942); S. A. Korff, *Electron and Nuclear Counters—Theory and Use.* (D. Van Nostrand Company, Inc., New York, 1946), pp. 138, 139.

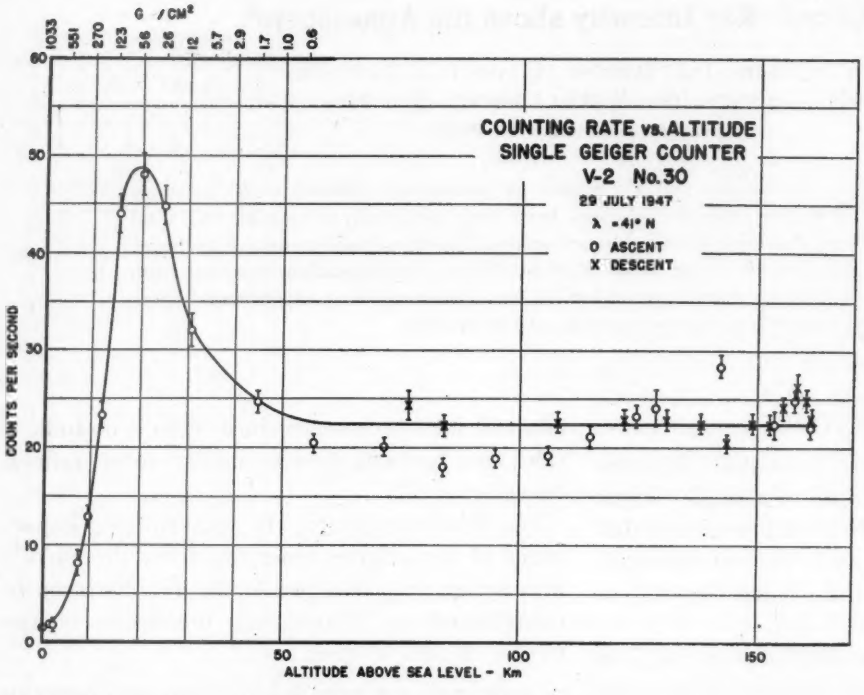

FIG. 1. Counting rate of a single Geiger counter as a function of altitude.

III. SINGLE COUNTER DATA FROM THE FLIGHT OF V-2 NO. 35 FIRED ON MAY 27, 1948

In V-2 No. 35, a single counter of the same batch as the one of V-2 No. 30 was used. Its physical location in the rocket was identical with that of reference 1. But in this case, the coincidence bundle of counters was considered no longer necessary and only one scale-of-eight circuit was used. Missile-borne electronics, telemetering, timing, missile tracking, etc. were similar to the previous flight.

The counting rate was determined in preflight tests on the ground at White Sands (altitude 1.22 km above sea level, pressure 890 g/cm²) as 1.72±0.06/sec. with counter axis horizontal. In the 90 seconds just preceding take-off, a rate of 1.60±0.10/sec. was recorded over the telemetering system; during this latter period the counter axis was vertical.

The rocket was fired at 7:16 A.M. on May 27, 1948. Fuel cut-off was accomplished at 64 seconds after launching; at this time, the velocity was 1400 m/sec., inclination of the trajectory 8° to the vertical, altitude 39.6 km above sea level. Summit altitude of 140 km was attained at 210 seconds. Explosive break-up of the missile was

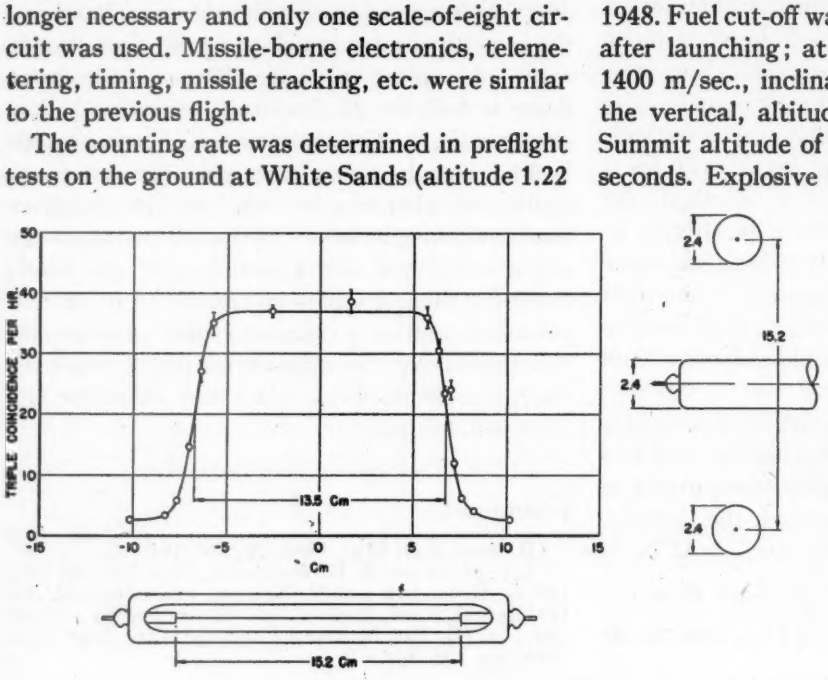

FIG. 2. Schematic arrangement for determining effective length of a Geiger tube for fast particles and plot of results for the single tube used in V-2 No. 35.

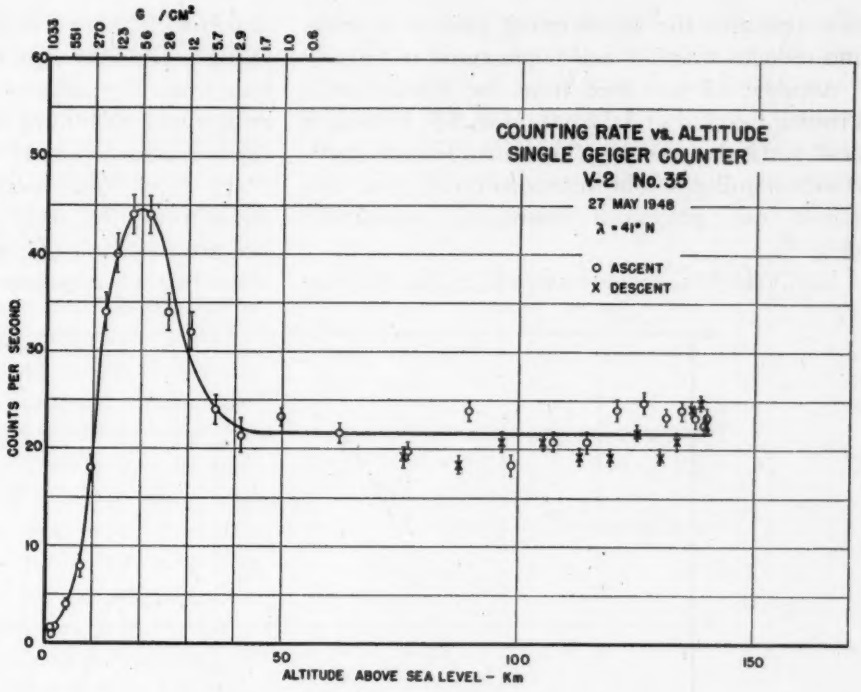

FIG. 3. Counting rate as a function of altitude of a single Geiger counter carried in a V-2 rocket.

performed at 341.6 seconds. The roll period of the missile during its unpowered flight was 50 seconds; the missile axis departed from the near-vertical direction very slowly, probably not exceeding a zenith angle of 90° up to 335 seconds. Precise information on this aspect of the flight will not be available for several months. Tracking by photo-theodolite, radar, and photo-telescopes was very good throughout flight. An exceptionally clean telemetering record was obtained, making possible continuous reading of data from 90 seconds before take-off to 335 seconds of flight time.

Figure 3 exhibits the counting rate of the single counter as a function of altitude above sea level.

The counting rate curve resembles in all important respects the one obtained in V-2 No. 30. The counting rate at the Regener-Millikan-Pfotzer maximum appears slightly lower and the average plateau counting rate is likewise slightly lower, being 21.6 ± 0.2/sec., based on 5736 counts in the time interval 70–335 seconds. A detailed analysis of the distribution of time intervals between successive scale-of-eight pulses showed excellent agreement with the statistical theory of Alaoglu and Smith,[4] thus giving further confidence in the flight operation of the Geiger counter and the scaling circuit.

[4] L. Alaoglu and N. M. Smith, Jr., Phys. Rev. **53**, 832 (1938).

IV. SINGLE COUNTER DATA FROM THE FLIGHT OF AEROBEE A5 ON MARCH 5, 1948

The Aerobee is a new American rocket specifically designed for use in upper atmospheric investigations. It has been developed for the Navy Bureau of Ordnance and the Office of Naval Research by the Aerojet Engineering Corporation and the Douglas Aircraft Company under the technical supervision of the Applied Physics Laboratory of the Johns Hopkins University. By means of it, a useful payload of 70 kg of equipment can be transported to an altitude of about 115 km. The equipment is contained in a thin ogival-shaped aluminum nose cone at the forward end of the rocket.

Radio transmission of data is provided by a small 85-mc telemetering set of six channels, developed by this laboratory. The system of tracking, timing signals, etc. is similar to that used for the V-2's, except that, thus far, no radar beacon has been carried by the Aerobee.

The firing of the Aerobee is conducted by the U. S. Naval Unit, White Sands Proving Ground. The Physical Science Laboratory of the New Mexico College of Agriculture and Mechanic

Arts operates the telemetering ground stations and reduces tracking and telemetered records.

Aerobee A5 was fired from the White Sands Proving Ground at 3:51 P.M. March 5, 1948 on a near-vertical trajectory. The altitude-time curve is shown in Fig. 4. The instrumentation cone contained two pieces of cosmic-ray equipment (Fig. 5).

(a) A single Geiger counter (11 in Fig. 5) of the same batch as used in V-2's Nos. 30 and 35 was located on a fiber structure near the point of the nose cone. Precautions were taken, as before, to reduce to a minimum the amount of material in the immediate vicinity of the counter.

(b) A pair of crossed wide-angle triple-coincidence telescopes, *AOB* and *XOY*, was located in the after portion of the nose cone. The axes of these two telescopes were at right angles to each

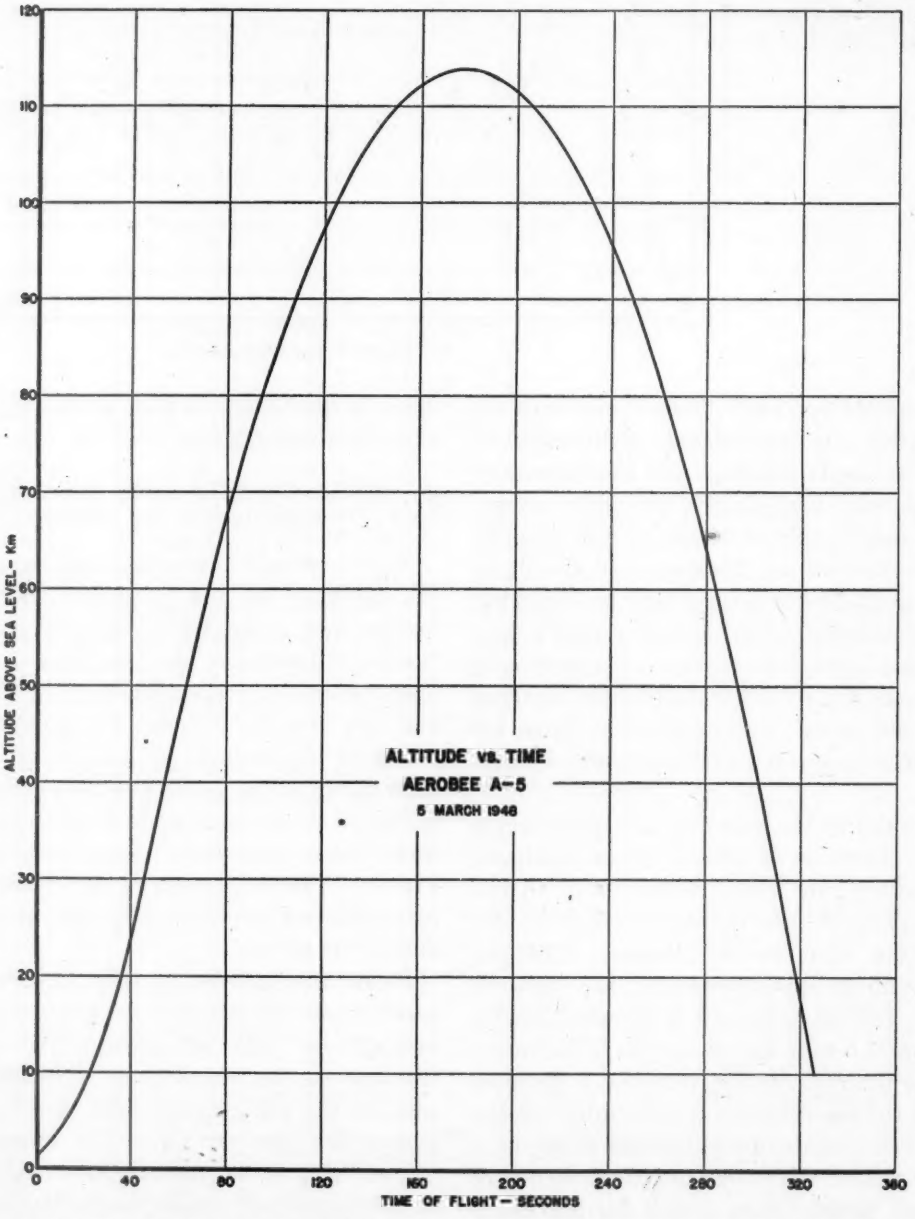

FIG. 4. Plot of altitude above sea level *vs.* time for Aerobee A5. This curve is based in part on external tracking data and in part on cosmic-ray data as discussed in the text. Disintegration of the rocket structure occurred at altitude 10 km on the descending branch of the curve.

other; the plane of their axes included the axis of the rocket. The inclination of the telescope axes was 45° to the rocket axis.

Necessary batteries, electronic chasses, etc., occupied the remaining volume of the cone. Three arrays of 1P42 photoelectric cells were located in the periphery of the rocket to measure, by means of the sun, azimuth and zenith angles during flight.

At fuel exhaustion, which occurred 48 seconds after launching, the zenith angle of the rocket axis was 10°; the roll period was 1.13 seconds. Thereafter, the roll period maintained a constant value; the longitudinal axis of the rocket precessed with a period of about sixty seconds in an approximate cone of about 15° half-angle. This angular motion, with the nose generally upward, persisted until about 260 seconds flight time. Beginning at about this time, the axis of the rocket assumed a larger and larger zenith angle. Complete inversion had occurred and the axis had become parallel to the trajectory with the nose downward by about 290 seconds.

A complete telemetering record was obtained from 55 seconds before take-off to 326 seconds flight time, with the exception of a total of 11.5 seconds during the inversion period. This loss of signal was presumed a result of nulls in the radiation pattern of the rocket-borne antenna. At 326 seconds, altitude 10 km, the missile broke up and no data were obtained beyond this time.

A plot of the counting rate of the single Geiger counter *vs.* altitude above sea level is shown in Fig. 6. For the first time we were successful in "closing the curve" back through the maximum at about 20 km.

The photo-theodolites provided a good knowledge of the trajectory almost to fuel burn-out; but the velocity at fuel burn-out and, therefore, the complete trajectory were not accurately determined. Figure 6 was prepared by first plotting the counting rate data *vs.* time of flight. This curve was then folded so as to bring the maxima into coincidence. The altitudes of the counting rate maxima on the ascending and descending portions of the trajectory were *assumed* the same. With due regard for the variation of g with altitude and for aerodynamic drag, the altitude-time curve of Fig. 4 was then arrived at by trial and error calculation. The curve so produced was well within the determination of it provided by the tracking data. (This is believed to be the first practical application of cosmic-ray data to the determination of a rocket trajectory.) Finally, the counting rate *vs.* time of flight curve was converted to an altitude basis (Fig. 6) by the use of Fig. 4.

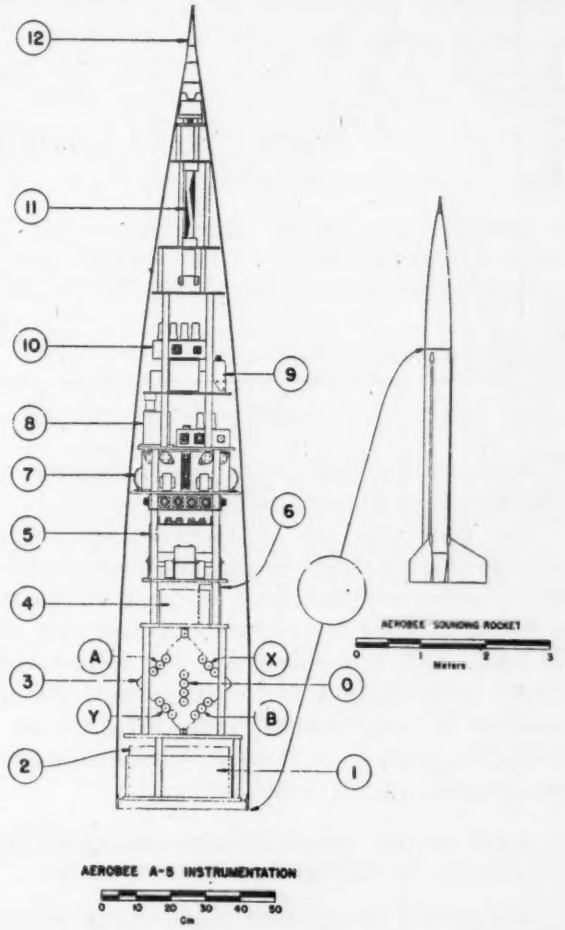

FIG. 5. Arrangement of equipment in Aerobee A5. The instrument cone is shown in large scale and the relationship of the cone to the entire rocket is indicated by the smaller drawing on the right. *A*, *O*, *B*, *X*, *Y* are individual Geiger counter trays of the cosmic-ray telescopes *AOB* and *XOY* and associated guard counters. 11 is the single Geiger counter whose output pulses were transmitted. Other principal items of equipment are as follows: 1, telescope coincidence circuits; 2, telemetering sub-carrier audio modulator; 3, telescope assembly; 4, emergency fuel cut-offreceiver; 5, lead storage batteries; 6, rf-telemetering transmitter; 7, dynamotors and filters for B^+ supply to circuits; 8, motor and commutator for commutating orientation photo-cells; 9, high voltage battery for Geiger counters; 10, scale-of-eight circuit; 12, telemetering antenna, insulated from body of missile. Sea-level atmospheric pressure maintained by aluminum nose cone 1.0 mm thick. Arrays of photo-cells not shown, but located aft of nose cone in forward skirt of rocket structure.

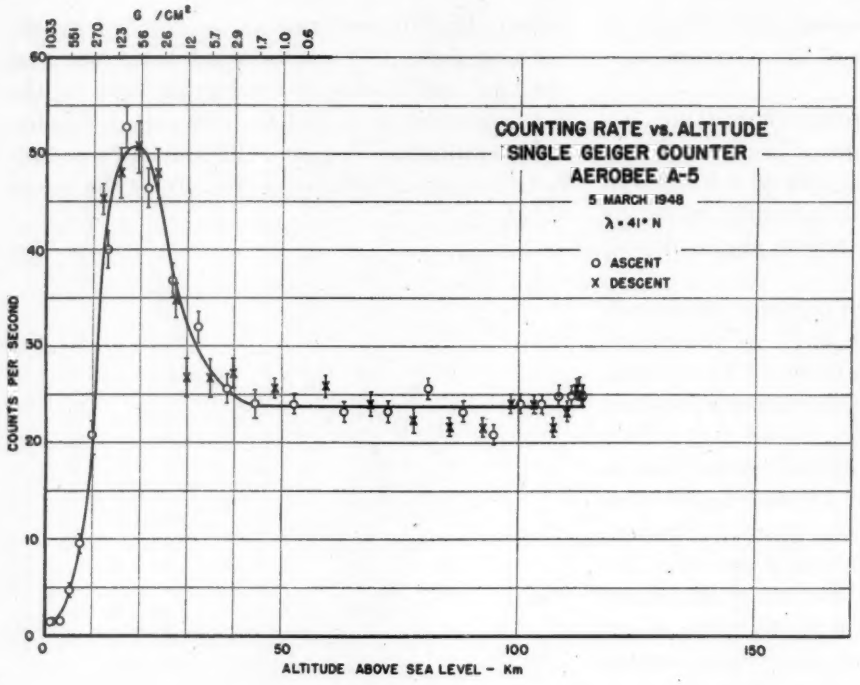

FIG. 6. Counting rate as a function of altitude of a single Geiger counter carried in an Aerobee rocket.

Again, substantially the same counting rate *vs.* altitude curve was obtained.

The counting rate of 1.45 ± 0.11/sec. was recorded during the 55 seconds previous to take-off. A peak counting rate of 51/sec. occurred at a 19-km altitude and a mean plateau rate of 23.7 ± 0.2/sec. was found for 227 seconds of record in the period 60 to 300 seconds. As in previous sections, the error indicated is the statistical probable error. Possible systematic errors are discussed in a later section.

V. COINCIDENCE TELESCOPE MEASUREMENTS IN FLIGHT OF AEROBEE A5—MARCH 5, 1948

The general arrangement of the two threefold coincidence telescopes is shown in Fig. 5. A more detailed view of the geometry of the counters is contained in Fig. 7. The aluminum nose cone of the rocket, which surrounded all the instrumentation, had a thickness of 1.0 mm. The Geiger tubes in the telescope were of the same batch as those used in the single counter apparatus discussed in previous sections. Thus, an average traversal of the telescope involved penetration through about 0.4 g/cm² of Al and 4.0 g/cm² of Cu. The perpendicular separation between midplanes of counter trays X and Y or A and B was 17.2 cm. The respective telescopes XOY and AOB were as nearly identical as practical.

The following coincidences were formed electronically with standard type circuits with a resolving time $\tau=10\mu s$,

AOB
XOY
AOB (X and/or Y) *or* XOY (A and/or B).

The latter type coincidence requires simultaneous passage of at least two particles through the telescope array.

On the telemetered record (8 cm/sec.) additional identification of the multiple particle events was accomplished with a resolving time of about 0.007 sec. Thus, it was possible to list coincidences in the following five categories,

(1) AOB
(2) AOB (X or Y)
(3) XOY
(4) XOY (A or B)
(5) $XOYAB$.

In order to interpret the telescope counting rate in terms of directional intensity, it is necessary to calculate the geometric factor for the telescope. The counting rate N of an idealized threefold coincidence set of three parallel rect-

angular plane counters of effective length l, width a, separation between outer planes s is given by

$$N/e^3j=(a^2l/s)\ \text{arc}\ \tan(l/s), \qquad (1)$$

for a/s small, e absolute efficiency of each counter, j directional intensity in particles/sec./cm²/steradian, constant over the aperture of the telescope and "downward" only. The wide-angle telescope AOB (or XOY) may be considered as composed of nine simple component telescopes (refer to Fig. 7) with a/s small. First, formula (1) was applied to each of the component telescopes; then a correction[5] for the actual cylindrical shape of the counters was calculated analytically and added to the first approximation. The nine corrected factors were then summed to give the geometric factor for the entire telescope. The result for isotropic intensity (applicable to plateau counting rate above the atmosphere) was

$$N/e^3j=28.1\pm0.7\ \text{cm}^2\ \text{steradian}, \qquad (2)$$

in which N is observed coincidences/sec., j is in particles/sec./cm²/steradian, and e is the counting efficiency of each tray. The value of e includes the intrinsic efficiency and the loss of counts as a result of counter dead time; it is, therefore, dependent on the counting rate. On the high altitude plateau $e^3=0.96$; at the Pfotzer maximum, 0.92; on the ground, 0.98. The error indicated in Eq. (2) is believed to be such as to almost certainly encompass the true value of the geometric factor.

For the interpretation of preflight counting rates of the telescope in a laboratory on the ground, the geometric factor for the telescope is somewhat lower than that computed above. Utilizing the theorem of Greisen[5] and assuming that at White Sands for any azimuth $j(\theta)=j(0°)\cos^2\theta$, where θ is the zenith angle, we find for the axis of our telescope vertical

$$N(0°)/e^3j(0°)=25.1\pm0.7\ \text{cm}^2\ \text{steradian}, \qquad (3)$$

and for the axis of the telescope at $\theta=45°$,

$$N(45°)/e^3j(45°)=25.7\pm0.7\ \text{cm}^2\ \text{steradian}. \qquad (4)$$

At altitudes intermediate between ground level and 55 km, the geometric factor for the telescope will lie between the value of Eq. (3) and that of Eq. (2) because of progressive change of zenith angle distribution from $\cos^2\theta$ to approximately isotropic. No detailed quantitative interpretation of data at intermediate altitudes is given in this paper.

Accidental coincidences were estimated by the formulas of Schiff[6] taking into account all possible modes of generation of accidental coincidences. The principal contribution comes from events of the type: true coincidence of OY overlapping an unrelated count of tray X. On the high altitude plateau, it was estimated that

$$(\Delta N)_{XOY}=0.04\ \text{accidentals/sec.} \qquad (5)$$

The rate of accidental fourfold electronic coincidences and the rate of incorrect identifications on the telemetered record were estimated to be negligible.

In the preflight runs, all classes of accidentals were negligible.

Table I contains a summary of preflight telescope data and directional intensities $j(0°)$ and $j(45°)$ calculated from them with the use of formulas (3) and (4). Agreement of the calculated intensities with accepted values[2] is satisfactory.

In flight, the counting rates (1)–(2)–(5) and

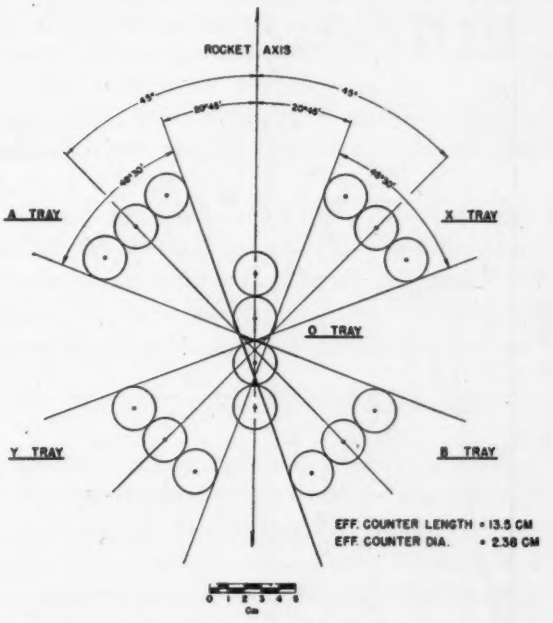

FIG. 7. Scale drawing of end view of telescope. Perpendicular distance between trays A and B or between X and Y 17.2 cm.

[5] Compare K. Greisen, Phys. Rev. **61**, 212 (1942).

[6] L. I. Schiff, Phys. Rev. **50**, 88 (1936).

TABLE I. Ground data with telescopes *XOY* and *AOB*—White Sands Proving Ground.

$\lambda = 41°N$ Nominal pressure 890 g/cm² Alt. 1.22 km

Nominal telescope zenith angle	Observed counting rates Av. (1)–(2)–(5) and (3)–(4)–(5)	Av. (2) and (4)	(5)
0°	19.9±0.4/min.	1.0±0.2/min.	0.8±0.2/min.
45°	10.9±0.2	0.6±0.1	0.3±0.1

Calculated intensities:
$j\,(0°) = 0.0135 \pm 0.0006$/sec./cm²/steradian
$j\,(45°) = 0.0072 \pm 0.0003$/sec./cm²/steradian

TABLE II. High altitude plateau data.

Category	No. of counts
(1)	975
(1)–(2)	808
(1)–(2)–(5)	666
(3)	1046
(3)–(4)	842
(3)–(4)–(5)	700

Rate of Telescope *AOB*, less all recorded multiple particle events = 2.91±0.07/sec.
Rate of Telescope *XOY*, less all recorded multiple particle events = 3.06±0.08/sec.
Average net rate per telescope = 2.99±0.05/sec.

(3)–(4)–(5) *vs.* time of flight were statistically indistinguishable. The averages of these two counting rates *vs.* altitude are plotted in Fig. 8, using Fig. 4 to convert time to altitude. The peak of this curve occurs at about 16 km, somewhat lower than for the single counter curves; likewise, the plateau appears to commence at an altitude of about 40 km. Both of these differences from the single counter curves may be reasonably attributed to the restricted range of zenith angles around 45° in which the telescope would accept counts. Thus, the effective amount of atmospheric material "above" the telescope is less, at every altitude, than that "above" a single counter.

Table II summarizes plateau data for 228.5 seconds during the period 60–300 seconds.

VI. DISCUSSION OF DATA

Referring to Sections II, III, and IV, it is seen that there are certain minor differences among the single counter results of the three flights. There is a temptation to identify these differences with the recent results of the California Institute of Technology group[7] on the fluctuations of cosmic-ray intensity within the atmosphere. However, because of possible systematic differences of effective counter length and spurious counts during the various flights, we do not believe that

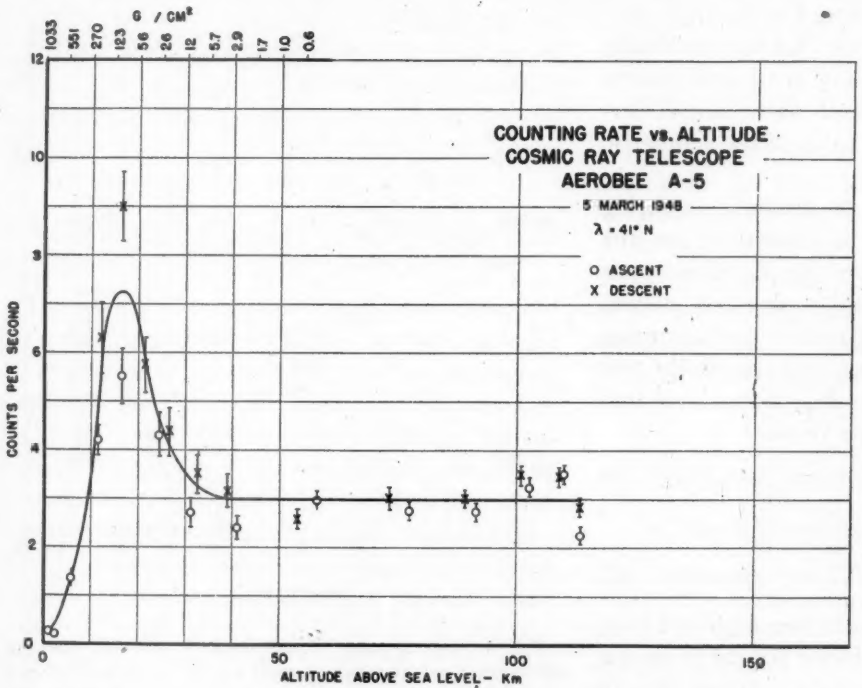

FIG. 8. Counting rate as a function of altitude of a cosmic-ray telescope carried in an Aerobee rocket.

[7] A. T. Biehl, R. A. Montgomery, H. V. Neher, W. H. Pickering, and W. C. Roesch, Rev. Mod. Phys. **20**, 353, 360 (1948).

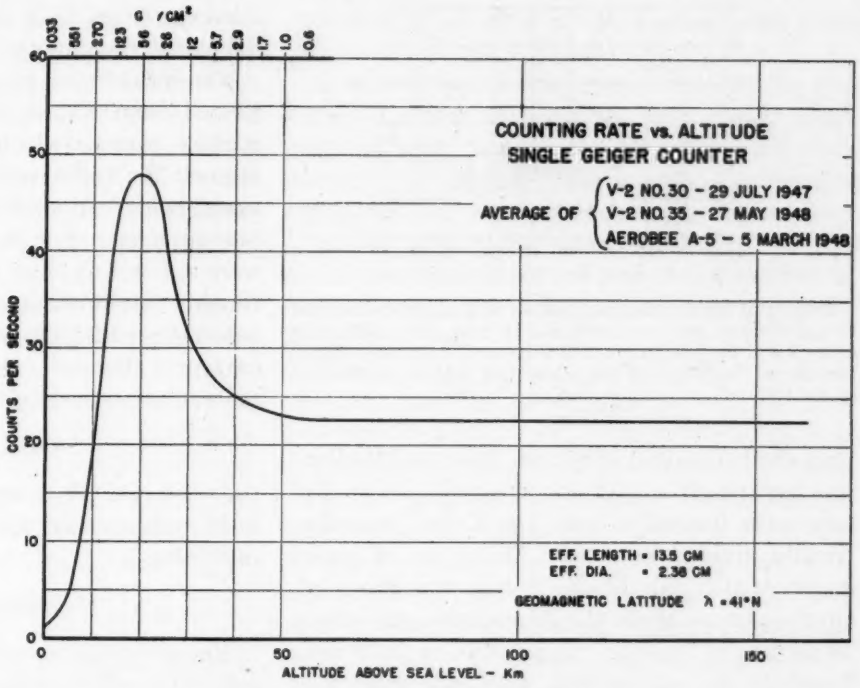

FIG. 9. Smoothed composite curve of all single counter data.

our single counter data justify such refined consideration. The three sets of data have, therefore, been combined into a single smooth curve (Fig. 9).

There do appear to be significant undulations in the individual plateau data of the separate flights. In each case, these undulations are generally correlated with the zenith angle of the rocket axis. In reference 1, it was proved that in a hemispherically symmetric field of flux, the counting rate of a single counter is independent of orientation; further, it was found experimentally that the extraneous influence of material in the rocket was negligible for our arrangement so that neither a reduction resulting from shadowing nor an augmentation caused by multiplication could occur in any orientation of the rocket. It is, therefore, suggested that the observed undulations, if indeed significant, constitute evidence for the lack of hemispherical constancy of the directional intensity above the atmosphere. A semi-quantitative idea of the directional, i.e., telescopic, properties of a single cylindrical counter may be obtained from Fig. 10, in which is plotted the counting rate per unit uniform flux per unit solid angle of a conical field of flux of half-angle α, the axis of the cone lying along the axis of the counter. As is well known, a cylindrical counter is considerably more sensitive to flux perpendicular to its axis than to flux parallel to its axis. Further discussion of this question is deferred until a subsequent report on the azimuthal and zenith angle dependence of intensity above the atmosphere, as obtained by detailed analysis of the telescope data from the flight of Aerobee A5. Section V of this paper deals only with the over-all summary of the telescope data.

The average plateau counting rate from Fig. 9 is 22.6/sec. If this rate be ascribed to a directional cosmic ray intensity of charged particles j, uniform over the upper hemisphere, zero over the lower hemisphere, then we calculate

$$j = 0.131 \pm 0.005/\text{sec.}/\text{cm}^2/\text{steradian}$$

as a final result of this series of measurements.

We now proceed to discussion of the telescope measurements. Minimizing the amount of material in the vicinity of a single counter is of essential importance in obtaining true intensity measurements in the upper atmosphere and above the atmosphere; in measurements with telescopes, surrounding material is even more troublesome. In early V-2 flights of this laboratory, a telescope

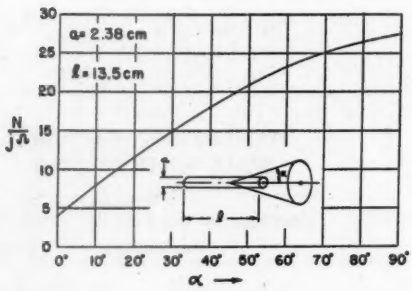

FIG. 10. Plot of counting rate N of a single cylindrical Geiger counter per unit uniform flux j per unit solid angle of a conical field of flux of half angle α. The field of flux is considered "solid" with the center line parallel to the axis of the counter.

patterned after that of Schein, Jesse, and Wollan[8] was used; each tray of our telescope consisted of two tubes instead of one. The C tray was electrically divided into two. Also a set of guard counters alongside of the B tray was provided. On the plateau above the atmosphere, only about 15 percent of "in-line" events ABC or BCD were found to be *unassociated* with side counts or double counts in the split tray.[9] The rate of multiple particle events increases very rapidly in the upper atmosphere, approximately as $\exp(-h/150)$ where h is the pressure in g/cm.[2] These events seem to be primarily a result of bursts from the primaries themselves.[8–11] Inasmuch as a typical path through the above-mentioned telescope was 100 g/cm² of lead for a ray from any direction, not necessarily within the solid angle of the telescope, it is not surprising that this is so. The *NRL* group has reported a similar situation in their high altitude measurements with leaded telescopes.[12–18] In the Aerobee telescope (Figs. 5, 7), a special effort was made to reduce the amount of proximate material.

The measure of success in this effort may be judged from Table II of Section V. Multiple particle events (which are, of course, of great interest for their own sake in other investigations) were reduced far below their previous predominance. Yet the telescope measurements were still not as clean as would be desired, since roughly one-third of AOB or XOY events were associated with guard counts. The average rate of category (1) and category (3) events on the plateau, disregarding the guard counts, is

$$4.42\pm0.07/\text{sec.}$$

per telescope. The average *net* rate per telescope, after subtraction of all recorded associated multiples, is

$$2.99\pm0.05/\text{sec.}$$

Bursts caused by particles whose paths lie outside of the telescope geometry spuriously increase the counting rate of the telescope; bursts caused by particles whose paths lie within the telescope geometry are properly included in the "true" rate of the telescope. Thus, it may reasonably be believed that the true rate of such a telescope in free space lies between the two rates just calculated. Inasmuch as most of the nearby material lay outside of the solid angle of the telescope, we have chosen the *net* rate as the best experimental determination of the true rate of the telescope in free space. At the worst, this rate is probably not more than a few percent too low. Using the geometric factor of Section V and making the minor corrections for inefficiency and accidentals, we have finally

$$j=0.109\pm0.006/\text{sec./cm}^2/\text{steradian}$$

from the telescope measurements on the plateau.

As described in Section IV, the angular motion of the telescope axes on the plateau was, in detail, rather complicated; in over-all view, however, it is felt that the upper hemisphere was scanned with reasonably uniform weight. Thus, the above

[8] M. Schein, W. P. Jesse, and E. O. Wollan, Phys. Rev. **57**, 847 (1940). See also M. Schein, E. O. Wollan, and G. Groetzinger, Phys. Rev. **58**, 1027 (1940); and especially M. Schein, M. Iona, Jr., and J. Tobin, Phys. Rev. **64**, 253 (1943); and for a general summary M. Schein and D. J. Montgomery, *Problems in Cosmic Ray Physics*, (1946), Princeton lectures.

[9] J. A. Van Allen, H. E. Tatel, and R. P. Petersen, *High Altitude Research Using the V-2 Rocket* (Applied Physics Laboratory, Johns Hopkins University Report No. 81, edited by L. W. Fraser and E. H. Siegler), pp. 62–64.

[10] H. E. Tatel and J. A. Van Allen, Phys. Rev. **73**, 87 (1948).

[11] J. A. Van Allen, Sky and Telescope **VII**, 7 (1948).

[12] S. E. Golian, E. H. Krause, and G. J. Perlow, Phys. Rev. **70**, 223 (1946).

[13] S. E. Golian, E. H. Krause, and G. J. Perlow, Phys. Rev. **70**, 776 (1946).

[14] G. J. Perlow and J. D. Shipman, Jr., Phys. Rev. **71**, 325 (1947).

[15] S. E. Golian and E. H. Krause, Phys. Rev. **71**, 918 (1947).

[16] G. J. Perlow, Phys. Rev. **72**, 173 (1947).

[17] E. H. Krause and S. E. Golian, Phys. Rev. **72**, 173 (1947).

[18] G. J. Perlow, Phys. Rev. **73**, 1218 (1948).

determination refers to the average directional intensity over the upper hemisphere. As before, we have here tacitly assigned any flux from the lower hemisphere to the upper hemisphere.

The directions of the two telescopes *AOB* and *XOY* were rapidly interchanged in flight by the rotation of the rocket. Their average counting rates were within reasonable statistical agreement (Table II).

The intensity result from the single counters is probably a little high because of spurious counts; the intensity result from the telescopes is probably a little low due to excessive subtraction of multiple particle events. Therefore, lacking a better procedure, we have arbitrarily combined with equal weight the final single counter determination of $j=0.131\pm0.005$ and the telescope determination of $j=0.109\pm0.006$. Thus,

$$j=0.120\pm0.009/\text{sec.}/\text{cm}^2/\text{steradian}$$

is our best value for the average directional intensity above the appreciable atmosphere in the 55–161-km altitude band at geomagnetic latitude $\lambda=41°$N. The assigned error is intended to indicate the values between which we believe the true average intensity almost certainly lies.

VII. GENERAL DISCUSSION

Our value of $j=0.120\pm0.009/\text{sec.}/\text{cm}^2/\text{steradian}$ is an experimental upper limit to the average directional intensity of *charged* cosmic-ray primaries at the latitude of these experiments. From the systematic studies of the latitude effect[19] by Millikan and associates, it is already known that the primary intensity of charged particles is indeed of this order of magnitude.

Secondaries emerging from the atmosphere and executing orbits in the earth's magnetic field undoubtedly contribute in some measure to the measured intensity above the atmosphere.

It has often occurred to others and to us that the extraneous secondaries should be easily absorbable. Some of our results and the results of Perlow and Shipman[14] with leaded telescopes have been so interpreted. Yet the complexity of the counting situation in leaded telescopes in the high atmosphere (see Section VI) has led us to a considerable caution in conclusions from such apparently straightforward results.

It may be mentioned that Primakoff[20] has obtained a series of counting rate curves with balloon-borne telescopes containing different amounts of absorber. His curves for telescopes containing various thicknesses of lead from 0 to 10 cm converge to the same counting rate at the top of the atmosphere and lead to the conclusion that the easily absorbable component is negligible at about 37 km.

In view of the conflicting evidence, we feel that there is, thus far, no satisfactory experimental determination of the importance of secondaries.

Low energy (for example 10^7) γ-radiation would produce a much greater counting rate in a single counter than in a coincidence telescope. Since the intensity results by the two distinct methods are, with due regard for the probable magnitude and sign of systematic errors, in substantial agreement, it may be concluded that there is no significant contribution of such γ-rays. However, an intensity of the order of $1/\text{sec.}/\text{cm}^2/\text{steradian}$ would probably escape detection.

It is not clear that such an argument can be used to exclude important contributions from γ-rays of energies like 10^9 ev. A telescope such as that used in the Aerobee flight would have a detection efficiency for γ-rays of this energy similar to that of a single counter. This detection efficiency would be only a few percent; however, there seems to be no basis for excluding a large intensity of γ-rays of such energy.

Auxiliary experiments with detectors of high γ-ray efficiency are planned.

Appreciable intensities of γ-rays of energies greater than 5×10^9 ev appear to be ruled out by the experiment of Hulsizer.[2]

In consideration of the general theory of the effect of the earth's magnetic field on the trajectories of charged particles passing through it, it may be concluded that the intensity plateaus observed in rocket flights of up to 160-km peak altitude are *not* of indefinite extension. The portion of the intensity resulting from charged primaries will, at all geomagnetic latitudes below

[19] See, for example, the excellent summary of L. Janossy, *Cosmic Rays* (Oxford University Press, London, 1948).

[20] Second semi-annual report of the work of the Bartol Research Foundation of the Franklin Institute under Contract N6ori-144 with the Office of Naval Research, September 15, 1947.

say 50°, slowly rise with increasing altitude—approaching asymptotically, at "altitudes" many times the radius of the earth, the free space intensity in the astronomical vicinity of the earth. At all latitudes, except at $\lambda=90°$, the contribution of secondaries—"cosmic-ray albedo" of the earth's atmosphere—should progressively diminish with increasing altitude due to their inability to escape from the earth's magnetic field.

Comparisons with related work of other investigators will now be made. Biehl, Montgomery, Neher, Pickering, and Roesch[7] have recently reported vertical intensity measurements at various latitudes. The highest altitude point (38 g/cm²) on their curve 2 for Fort Worth, Texas, $\lambda=41.7°$N yields a vertical intensity $j=7.7$/min./cm²/steradian or 0.13/sec./cm²/steradian, almost identical with our value above the atmosphere. It is, of course, not known how much farther the curve of Biehl *et al.* would have continued to fall if the balloon had risen higher.

It may be noted that the zenith angle dependence of total intensity within the atmosphere[21, 22] combines with the directionality of a single vertical counter to cause a single counter curve to peak at a considerably higher altitude and to likewise level at a considerably higher altitude than the curve for a vertical narrow angle telescope.

Pfotzer's original measurements[23] with a vertical coincidence telescope may be noted. His corrected counting rate at the highest altitude attained (27 g/cm²) was 125 counts in 4 minutes. A reasonable extrapolation of his curve to zero pressure would be 115 counts in 4 minutes. The geometric factor for his telescope can be roughly figured as

$$A_1A_2/r^2=(4.5)^2(5)^2/(12)^2=3.5 \text{ cm}^2 \text{ steradian}.$$

Thus, the extrapolated intercept would correspond to a vertical intensity of approximately 0.14/cm²/sec./steradian, at $\lambda=49°$.

Primakoff[20] and co-workers have made similar measurements; however, we have not been able to find a description of the geometry of their telescope.

[21] W. F. G. Swann, Rev. Mod. Phys. **11**, 242 (1939).
[22] J. F. Jenkins, Bull. Am. Phys. Soc. **23**, No. 3 1948, Washington Meeting Abstract EA3.
[23] G. Pfotzer, Zeits. f. Physik **102**, 23. 40 (1936).

It may be noted that all the above-quoted results are subject to a greater extraneous contribution of secondaries than are the rocket measurements.

Golian and Krause[15] in a V-2 telescope experiment have found a ratio of intensity above the atmosphere to vertical sea level intensity of 11.5 for the "total" radiation and 9.0 for the "hard" component.

Our corresponding ratio for the total intensity is

$$0.120/0.011=11.$$

VIII. CONCLUSION

By means of single Geiger counters and coincidence telescopes of Geiger tubes carried by rockets to high altitudes at geomagnetic latitude $\lambda=41°$N, a constant value of cosmic-ray intensity above 55 km has been clearly demonstrated. An upper limit to the directional intensity of charged cosmic-ray primaries, averaged over the upper hemisphere, has been determined. This upper limit is $j=0.120\pm0.009$/sec./cm²/steradian.

IX. ACKNOWLEDGMENTS

The conduct of experiments in rockets involves operations on such an extensive scale that it is very difficult indeed to give adequate credit to all participants.

We are, first of all, deeply indebted to the U. S. Navy Bureau of Ordnance for support of this work, and in particular for the sponsorship of the development of the Aerobee sounding rocket. The opportunity for making measurements in the V-2's is due the generosity of the U. S. Army Ordnance Department and the White Sands Proving Ground. Time signals and missile tracking for the V-2 and the Aerobee are provided by the Ballistic Research Laboratory of the Aberdeen Proving Ground and by the U. S. Army Signal Corps Engineering Laboratories. Special instrumentation cones and telemetering service for the V-2's are furnished by the Naval Research Laboratory.

The Aerobee was developed and built by the Aerojet Engineering Corporation and the Douglas Aircraft Company. The U. S. Naval Unit of the White Sands Proving Ground is in charge of field operations in firing the Aerobee.

We have been assisted in field work by the

Naval Unit, the Army Technical Section, and the General Electric Group, all of the White Sands Proving Ground. The Physical Science Laboratory of the New Mexico College of Agriculture and Mechanic Arts has carried a major share of the technical field work for the Aerobee in the conduct of preflight telemetering tests, flight telemetering, and in the reduction of tracking and telemetered data.

Within the Applied Physics Laboratory, we are particularly indebted to our director, Dr. R. E. Gibson, for continuing support; to Messrs. T. W. Sheppard, G. Melton, and R. O. Robinson of the Telemetering Group; to Mr. J. F. R. Floyd for assistance and advice with rocket problems; and to our immediate associates Messrs. L. W. Fraser, F. W. Loomis, R. O. Ostrander, R. J. McEvitt, and J. Vincent Smith.

This series of experiments was originally planned in conjunction with Dr. H. E. Tatel, now at the Department of Terrestrial Magnetism of the Carnegie Institution.

PHYSICAL REVIEW VOLUME 75, NUMBER 1 JANUARY 1, 1949

The Properties of Cosmic Radiation at Very High Altitudes*

MARTIN A. POMERANTZ
Bartol Research Foundation of The Franklin Institute, Swarthmore, Pennsylvania

(Received September 10, 1948)

The variation of the vertical cosmic-ray intensity as a function of altitude has been investigated in a series of free-balloon ascents with standardized quadruple-coincidence-counter trains containing various amounts of interposed absorber, to a maximum thickness of 7.5 cm Pb. The curves thus obtained converge at the "top of the atmosphere." A maximum occurs in the curve with 4 cm of Pb, but disappears with 6 cm of Pb. Cosmic-ray absorption curves at various altitudes above that corresponding to an atmospheric pressure of 250 mm of Hg are plotted from the data, as are integral and differential distributions-in-range. The relative stopping powers of carbon and lead are also available from the data.

Disturbing effects such as those arising from side showers and scattering appear to be negligible. An extrapolation procedure, which leads to results consistent with those of other experiments, provides a new picture of the composition of the cosmic rays in the atmosphere. With heavier particles ($P+M$) displaying a maximum intensity at a higher altitude than electrons (E), the conclusions drawn from the present investigation are compatible with a primary radiation consisting of protons (and possibly heavier nuclear particles) producing mesotrons which subsequently give rise to the electronic component.

Comparison of the results reported here with those of Schein and Allen indicate an absorption of primaries, by a process other than ionization, in thicknesses of Pb between 7.5 and 18 cm.

I. INTRODUCTION

ONE of the most widely used methods of investigating the nature and properties of cosmic-ray particles is based upon measurements of their absorption in matter. Although this technique has been pursued extensively near sea level, at great depths, and on mountain peaks, no experiments designed to obtain data of this type have been performed, even at altitudes accessible to aircraft. In the course of investigations of mesotron production, conducted by Schein, Wollan, and Groetzinger[1] in airplanes, and of the latitude effect of the penetrating component by Bhabha, Aiya, Hoteko, and Saxena,[2] and by Gill, Schein, and Yngve,[3] *intensity vs. altitude* curves have been determined with various counter arrangements embodying several different thicknesses of interposed lead. However, the authors do not regard the results as being

* These investigations have been supported by the Office of Naval Research. Although the observations reported here were obtained at geomagnetic latitude 52°N, considerable experience in the techniques was obtained during The Joint National Geographic Society—Army Air Forces Eclipse Expedition to Bocaiuva, Brazil, during May, 1947.

[1] M. Schein, E. O. Wollan, and G. Groetzinger, Phys. Rev. 58, 1027 (1940).
[2] Bhabha, Aiya, Hotenko, and Saxena, Phys. Rev. 68, 147 (1945).
[3] P. S. Gill, M. Schein, and V. Yngve, Phys. Rev. 72, 733 (1947).

amenable to the deduction of cosmic-ray absorption curves.

In free balloon ascents, Schein, Jesse, and Wollan[4] have obtained *intensity vs. altitude* curves for the cosmic rays capable of penetrating various large thicknesses of lead. Their published results appear to indicate equality of intensity from altitudes as low as that corresponding to 350 mm of Hg upward to 20 mm with 8 cm and 18 cm of Pb interposed in their counter trains. However, owing to statistical uncertainties at the lower altitudes and the variation of the geometrical arrangements with which the data were obtained, the authors attributed significance only to comparison at the very highest altitudes attained,[5] and regarded the close agreement there among the points for different lead thicknesses as constituting very strong evidence for the absence of primary electrons. Ehmert[6] has also measured the intensity of particles penetrating 9 cm of Pb, but the scatter of his points prevented him from drawing any conclusion other than one to the effect that there was a general constancy of intensity between 100 and 16 mm. Finally, using a shield of 10 cm of Pb, Dymond[7] conducted several flights, the results of which were not reported in detail. Only a general statement that a maximum of about nine times the sea-level intensity exists at 16 km was published.

A number of investigations of the variation with altitude of the total vertical cosmic-ray intensity have been reported previously.[8–10] The curves of Pfotzer,[11] obtained with a threefold coincidence counter arrangement, extended to altitudes of 10 mm.

In lieu of the desired data, quantitative comparisons frequently have been made of the results obtained by different investigators. This procedure could be subject to considerable error for several reasons. Principally, the geometrical differences introduce uncertainties in the method of reduction of the data to a common scale. In some instances, the curves have been fitted at high altitudes, in others at sea level. The change in the zenith angle distribution of intensity as a function of altitude, demonstrated by the experiments of Swann, Locher, and Danforth,[9] may vitiate comparisons based simply upon solid angle corrections, and the results obtained may depend upon the altitude at which the data are normalized. In some instances, where data are fitted near the top of the atmosphere, apparent agreement is attained merely as a consequence of the choice of scales, which are usually such as to mask the discrepancies at lower altitudes.

In principle, an idealized experiment whereby the desired ends might be realized is one in which a single apparatus with optimum geometrical arrangement is maintained at each of a number of high altitude stations for long periods of time. At each station various thicknesses of absorber would be interposed cyclically in the counter train, and the corresponding counting rates recorded. It is currently impossible to achieve this situation at altitudes exceeding those accessible to B-29 airplanes (<40,000 feet). However, the practical equivalent may be attained by sending aloft a number of identical instruments, each containing a different fixed thickness of absorber, and comparing the results. By utilizing standard sets, the counting rates of which are in agreement to within a rather small statistical uncertainty in both preflight and postflight runs, it is possible to compare counting rates directly without recourse to an arbitrary normalization.

II. EXPERIMENTAL PROCEDURE

A. Apparatus

Each individual apparatus contained a train of four G-M counters arranged to record vertical quadruple coincidences. The geometrical disposition of the counters was identical in all flights, which differed only in the amount of absorber interposed in the counter train.

The individual counters were 20 cm in length ×1 cm in diameter. The problem of determining the average path length through a vertical coincidence counter train, of importance in selecting

[4] M. Schein, W. P. Jesse, and E. O. Wollan, Phys. Rev. **59**, 615 (1941).
[5] This fact was not explicitly stated in reference 4, but was expressed in a private communication from M. Schein to the author.
[6] A. Ehmert, Zeits. f. Physik **115**, 320 (1940).
[7] E. G. Dymond, Nature **144**, 782 (1939).
[8] E. Regener and G. Pfotzer, Nature **136**, 718 (1935).
[9] W. F. G. Swann, G. L. Locher, and W. E. Danforth, Nat. Geog. Soc. Cont. Tech. Papers, Stratosphere Series No. 2, 13 (1936); J. Frank. Inst. **221**, 275 (1936); Phys. Rev. **51**, 389 (1937).
[10] T. H. Johnson, Phys. Rev. **54**, 151 (1938).
[11] G. Pfotzer, Zeits. f. Physik **102**, 23 (1936).

TABLE I. Summary of flight histories.

Flight no.	Date	Absorber thickness and composition	Rate of ascent**—feet per minute	Maximum altitude—feet	Length of time at maximum altitude—hours	Rate of descent**—feet per minute	Landing point	Air miles from launching site	Duration of radio contact—hours
	1947								
1A	July 17	2.5 cm Pb	865	95,000	*NL*	560	Riegelsville, Pa.	50	4¾
2A	July 22	0	660	95,000	6	—	Belmont, N. Y.	325	10½
3A	July 26	7.5 cm Pb	665	90,000	10¾	—	Lewisville, Ohio	350	13⅓
5A	Aug. 7	3.5 cm Pb	985	128,000	*NL****	770	Pleasant Gap, Pa.	145	6
8A	Sept. 3	7.5 cm C	370 to 68,000′ then 45 to 88,000′	88,000	68,000–88,000′ for 7 hours	1500	Peacedale, R. I.	230	10⅓
9A*	Sept. 9	4.0 cm Pb	550	85,000	*NL*	1200	West Grove, Pa.	23	4⅓
10A	Sept. 16	0	500	70,000	4	—	Bucksport, Maine	465	8
13A	Oct. 4	6.0 cm Pb	550	92,000	*NL*	450	Holmdel, N. J.	70	6
14A†	Oct. 25	7.5 cm C	530	85,000	*NL*	640	Not recovered	—	5
	1948								
15A	June 3	3.0 cm Pb	400	92,500	*NL*	1150	Shellsville, Pa.	100	4
17A	June 10	1.0 cm Pb	270	88,000	*NL*	1200	Not recovered	—	5
19A	June 24	4.0 cm Pb	530	95,000	*NL*	950	Pine Hill, N. J.	25	4¾

* Flight 9A contained an out-of-line counter for shower detection.
** Ascent and descent rates are approximate values at high altitudes.
*** *NL* indicates that, as a consequence of the particular inflation schedule selected, the flight did not level off.
† Flight 14A utilized the same instrument as Flight 8A.

an optimum geometry, has been treated by E. E. Witmer and the author.[12] The dimensions of the present apparatus are such that the average path length through the absorber is 7.3 percent greater than the thickness of the slabs for a $\cos^2\theta$ distribution of intensity with zenith angle, and 9.5 percent greater for an isotropic distribution. For present purposes, an intermediate value has been used in computing the absorber thicknesses when expressed in g/cm². Thicknesses stated in cm are measured values. The wall thickness of the Cu cylinders was 0.008″ and of the glass envelopes 0.063″. Thus, to produce a fourfold coincidence, a vertically-incident particle is required to penetrate a total of 4.2 g/cm² (1.3 g/cm² Cu and 2.9 g/cm² of glass). The filling consisting of a mixture of 86 percent argon and 14 percent butane at a total pressure of 12 cm of Hg provided stable self-quenching operation. Avoidance of the more commonly used organic vapors resulted in a counting rate plateau exceeding 200 volts (as measured in the balloon-borne instrument itself) which was independent of temperature over a range between −60°C and +50°C. The net efficiency of the counters, as determined in the customary manner, exceeded 99 percent.

Radio signals indicating the atmospheric pressure, temperature within the apparatus, and cosmic-ray events were continuously transmitted to the ground station where the information was recorded on paper tape by means of a high speed direct-inking recording oscillograph arrangement. Details regarding the complete balloon-borne apparatus, as well as a description of the ground station equipment will be given elsewhere.[13] It should be stated here, however, that the resolving and recovery times were sufficiently short to eliminate the necessity for applying corrections to the observed counting rates, such as were required, for example, in Pfotzer's experiments.

Furthermore, with no adjustment of the data, the absorption curve obtained on the basis of ground runs with different instruments, each containing a fixed amount of lead, agreed well with that measured with a single apparatus in which the lead thickness was varied.

B. Free Balloon Ascents

This series comprised a total of 18 flights. The weight of the instruments ranged between 4.3 kg and 5.9 kg, depending upon the amount of absorber. Flight plans varied considerably, and a summary of the vital statistics of representative ascents is embodied in Table I. Details regarding ballooning techniques and procedures

[12] E. E. Witmer and M. A. Pomerantz, Phys. Rev. **73**, 651 (1948); J. Frank. Inst. **246**, 273 (1948).

[13] M. A. Pomerantz, to be published in Rev. Sci. Inst.

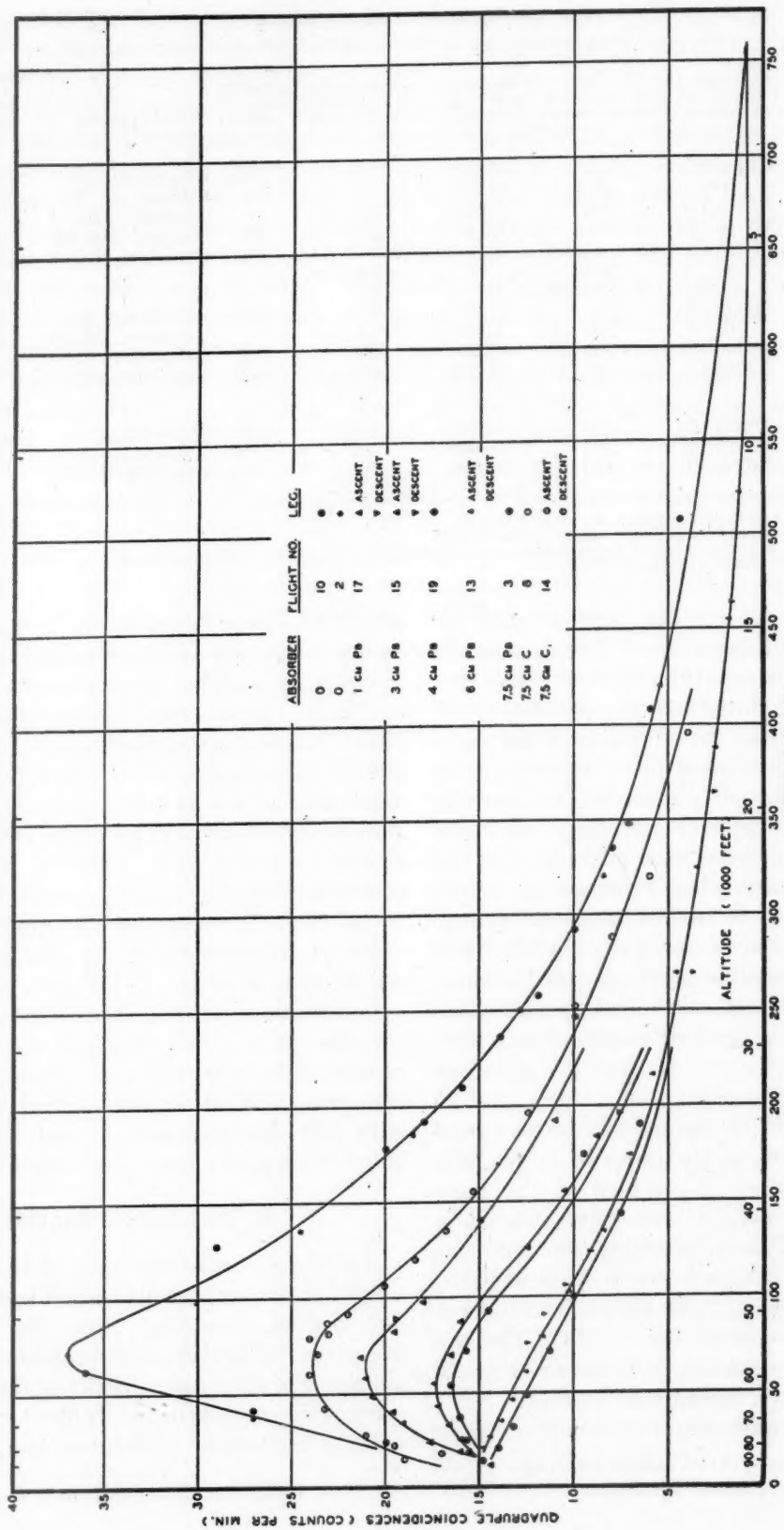

FIG. 1. *Intensity vs. altitude* curves for cosmic rays capable of penetrating various thicknesses of absorber. The actual quadruple-coincidence counting rates require no instrumental corrections, and are plotted directly as a function of atmospheric pressure.

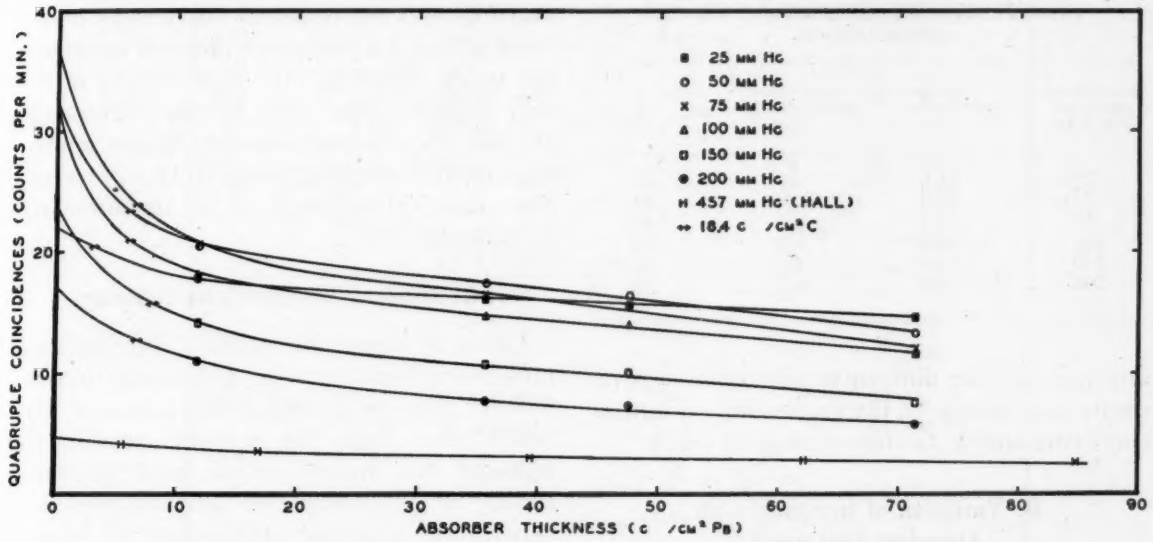

FIG. 2. Absorption in lead of cosmic-ray particles at various altitudes. A point representing the counting rate at the altitude indicated, with a constant thickness of interposed carbon, is plotted on each curve.

will also be omitted for the present. It is worth mentioning, however, that remarkable temperature constancy was maintained inside the apparatus by means of the well-known "greenhouse effect."

III. EXPERIMENTAL RESULTS

The experimental results will first be presented, and only the salient empirical features indicated. Detailed discussion of the implications thereof will be relegated to a later section.

A. Variation of Intensity With Altitude

The combined results are plotted in Fig. 1. The degree of reproducibility is best revealed by the agreement among the various flights having the same interposed absorber. Table I indicates, for each flight, whether the instrument was original or recovered, and it is seen that the agreement of data plotted in Fig. 1 is satisfactory in either case.

It is difficult to make general statements regarding the statistical uncertainties of the results. At altitudes lower than those corresponding to a pressure of 250 mm, the data are not significant.[14] This is a consequence of the combination of the briefness of the time interval spent by the apparatus in the regions of higher atmospheric pressure, and the low counting rates. An indication of the number of counts involved in any particular instance may be deduced on the basis of information contained in Table I. From the stated ascent and descent rates, and the counting rate at any point, a good approximation to the desired standard deviation may be obtained.

It is seen, as might be expected where true primaries are predominant, that the various curves obtained with thicknesses of lead up to 7.5 cm interposed in the counter train converge at the "top of the atmosphere."

A pronounced maximum exists in the *intensity vs. altitude* curves for interposed thicknesses up to 3 cm of Pb, becomes less definite with 4 cm,[15] and disappears with 6 cm.

Data of Pfotzer[11] and of Schein, Jesse, and Wollan[4] have been compared, but are not plotted on the graph here. In both instances, when the normalization is performed at the point of maximum intensity and no attempt is made to take

[14] Measurements at airplane altitudes have been obtained recently with standard sets in B-29 flights sponsored jointly by the Air Forces and the National Geographic Society. Observations up to 14,250 feet were also made on Mt. Evans this summer. This program will make available cosmic-ray absorption curves obtained under standardized conditions at altitudes from sea level to the "top of the atmosphere." The results of the experiments conducted at the lower altitudes will be published shortly.

[15] This is in agreement with observations of the Chicago group. A maximum with 4 cm of Pb occurred at about 60 mm Hg pressure, according to a private communication from M. Schein.

TABLE II. Experimental values of S_C/S_{Pb} at various altitudes.

Atmospheric pressure—mm of Hg	Carbon thickness—g/cm²	Equivalent lead thickness—g/cm²	S_C/S_{Pb}
25	14.0	3.0	.21
50	14.0	6.0	.43
75	14.0	6.6	.47
100	14.0	6.0	.43
150	14.0	8.0	.57
200	14.0	6.4	.46

into account the differences among the instruments (see Section I), the shapes of the resulting curves are similar to their analogs in Fig. 1.

B. Variation of Intensity with Absorber Thickness

Utilizing the smooth curves of Fig. 1, a change in the parameter from *absorber thickness* to *altitude* affords a determination of the variation of counting rate with absorber thickness at any desired altitude. The results are shown in Fig. 2. Data obtained by D. B. Hall[16] on Mt. Evans are included for comparison. Approximate values of the relative stopping powers[17] of carbon and lead (S_C/S_{Pb}) are obtained by locating on each curve of Fig. 2 a point with ordinate corresponding to the counting rate with 7.5 cm of C at that altitude. The value of the corresponding abscissa then is the amount of lead which is equivalent in stopping power to 18.4 g/cm² of C. The numerical values of S_C/S_{Pb} are summarized in Table II.

C. Integral Distributions-in-Range

Figure 3 shows the integral distribution-in-range at various altitudes. The points (obtained directly from the corresponding points of Fig. 2 rather than from the smooth curves), thus represent the fraction of the total vertical intensity at the designated altitude capable of penetrating absorber thicknesses at least as great as the value of the corresponding abscissa. It is to be noted that the slopes in the region 200 mm − 50 mm are rather similar at larger absorber thicknesses. The absorption coefficients between 4 and 6 cm of Pb have values of approximately 0.008 − 0.006 cm²/g, as compared with 0.003 cm²/g from Hall's measurements over a similar absorber thickness interval much lower in the atmosphere.

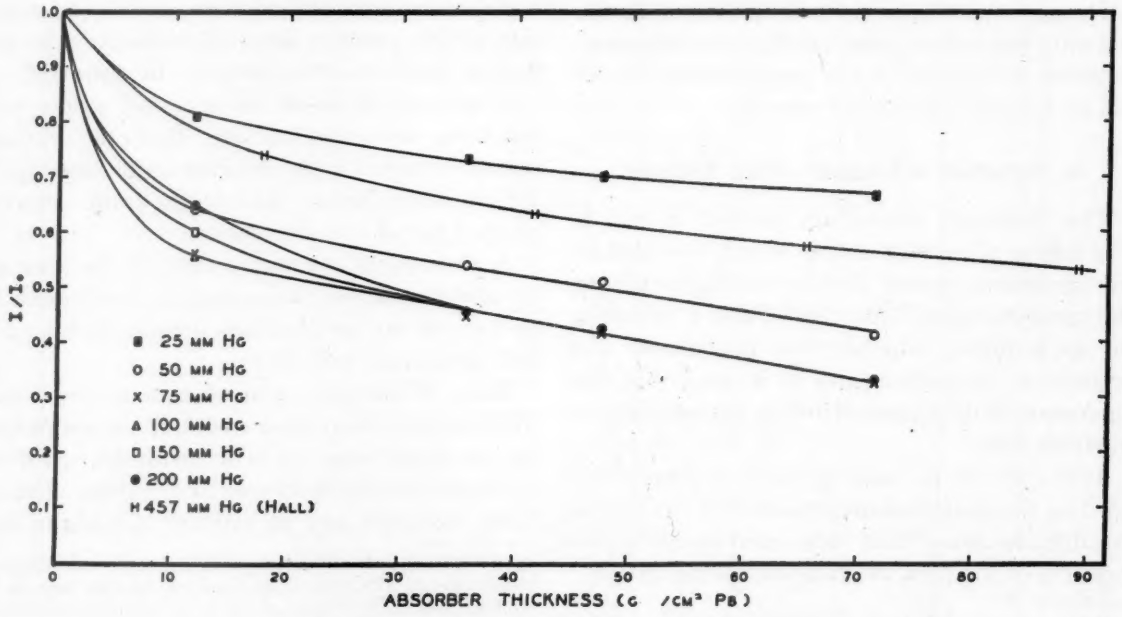

FIG. 3. Integral distributions-in-range at various altitudes.

[16] D. B. Hall, Phys. Rev. 66, 321 (1944).
[17] For a definition of S_C/S_{Pb} see, e.g., M. A. Pomerantz, Phys. Rev. 57, 3 (1940).

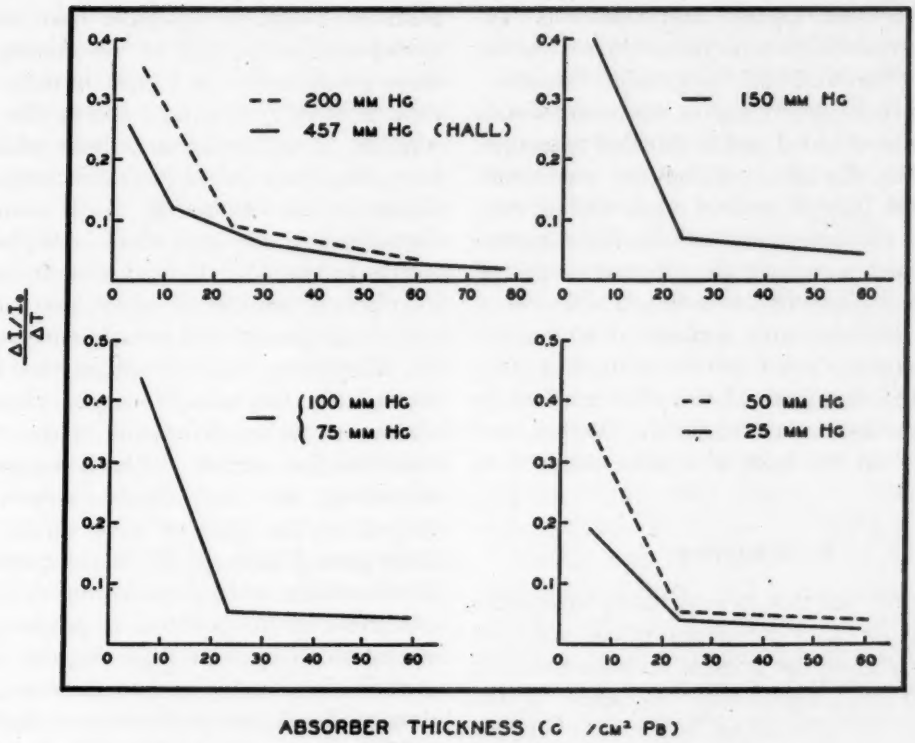

FIG. 4. Differential distributions-in-range at various altitudes.

D. Differential Distributions-in-Range

Differential distributions-in-range, computed directly from the points shown in the integral plots, are given in Fig. 4. Here, the units of the ordinates are *percent of total intensity per cm of Pb.* Values of the abscissa represent the corresponding average ranges, expressed in g/cm². The manner in which the composition of the cosmic radiation changes in the atmosphere is evident in this diagram.

It is striking that as the altitude increases upwards from sea level, the intensity of the soft component (defined in terms of range in Pb) also increases. At about 100 mm, a decrease sets in, until near the top of the atmosphere the particles actuating the apparatus are practically all primaries.

IV. EFFECTS OF SHOWERS AND SCATTERING

A. Showers

Either a determination of the effects of side showers or elimination of their effects is essential in any coincidence-counter measurements of cosmic rays. Various methods have been invoked for accomplishing this, and data bearing upon the present situation already exists.

In the present flights, specific precautions were taken to reduce shower effects to an absolute minimum. No heavy material was placed above or alongside the counters. In the interests of instrumental simplicity the inclusion of side-counter anticoincidence arrangements in the standard sets was avoided. It was considered preferable to ascertain the shower contribution (appreciable accidental coincidences having already been precluded) in a separate flight. This was accomplished with an apparatus which was standard except for the position of one of the counters, which was placed just out of line. Although the lead was interposed in a manner which was expected to be characterized by the maximum probability for the manifestation of shower phenomena, the highest out-of-line rate amounted to only about 5 percent of the lowest corresponding in-line rate. Hence the influence of showers upon these absorption measurements is negligible.

The first experiments embodying shielding banks of anticoincidence counters were per-

formed by Swann, Locher, and Danforth.[9] Intensity measurements were obtained within the gondola of the National Geographic Society—U. S. Army stratosphere flights, and comparisons of results with shielded and unshielded telescopes revealed that the effect of showers was small. Johnson and Barry[18] arrived at a similar conclusion as a consequence of balloon flight experiments in which a counter was alternately shifted from an out-of-line to an in-line position in a coincidence counter train inclined at 60 degrees from the vertical. Neher and Pickering[19] likewise indicated the smallness of the shower effect in balloon experiments, as did Schein, Wollan, and Groetzinger[1] on the basis of results obtained in airplanes.

B. Scattering

Despite the fact that it is virtually impossible to arrive at an exact evaluation of the influence of scattering upon the present measurements, it is essential that cognizance be taken of the limitations this disturbing effect may impose upon the interpretation of some of the data. Although the scattering situation is not necessarily more severe here than in other coincidence counter experiments, it has often been entirely disregarded, occasionally under circumstances in which it is perhaps capable of accounting for observed effects.

The principal justification for regarding as small the contamination arising from scattering in the present absorption measurements is based upon the experimental fact that within statistical uncertainties the *counting rate vs. altitude* curves obtained with a particular absorbing layer are independent of the latter's position in the counter train. The magnitude of the effect of scattering is a function of the geometrical arrangement, and it was hence considered desirable to alter this factor as much as possible in different flights having the same total thickness of lead, and to look for discrepancies.

Several qualitative arguments relating to scattering may be mentioned. In the first place, the scattering effect of a block of material upon particles which would have been stopped by absorption anyway is of no consequence. Of those particles having ranges initially exceeding that defined by the lead block, the most susceptible to scattering are those which emerge from the block with just sufficient energy to penetrate the remaining G-M counter walls. Consequently, the rays which could be scattered out of the beam by the lead, thereby introducing a spurious additional absorption, have high energies in general and, consequently, small average scattering angles.[20] Moreover, it can be shown that for each of certain classes of ray which can be scattered out of the train exact compensation occurs. This is caused by the scattering, into the effective solid angle subtended by the train, of rays which would not have passed through all four counters in the absence of the scattering medium. A quantitative treatment of the problem is precluded by lack of precise information regarding the composition of the cosmic radiation and the energy distributions of the various components at high altitudes.

The presence of scattering effects may become somewhat more serious in measurements of the relative stopping powers of carbon and lead. Caution must be exercised in drawing conclusions from this type of data, owing to the fact that the scattering in carbon is negligible in comparison with that in lead.

V. ANALYSIS OF EXPERIMENTAL CURVES

A. Extrapolation of Counting Rate *vs.* Absorber Thickness Curves

It has been assumed previously that data obtained with coincidence-counter trains containing 8 cm of Pb represent the intensity of mesotrons.[21] This evidently involves the assumption, now completely untenable, that all particles incapable of penetrating this thickness are not mesotrons, but are electrons exclusively. The present experiments permit a somewhat more accurate evaluation of the relative intensities of the electron (E) and proton plus mesotron ($P+M$) components.[22]

[18] T. H. Johnson and J. G. Barry, Phys. Rev. **57**, 245 (1940).
[19] H. V. Neher and W. H. Pickering, Phys. Rev. **61**, 407 (1942).
[20] E. J. Williams, Proc. Roy. Soc. **A169**, 531 (1939).
[21] This assumption has been made by many authors. See, e.g., M. Schein, W. P. Jesse, and E. O. Wollan, Phys. Rev. **57**, 847 (1940).
[22] The $P+M$ component is here construed as including all nonelectronic charged particles having sufficient energy to penetrate the apparatus (see Section IIA). It embraces

This is accomplished by an extrapolation to zero absorber thickness of the straight lines through the three points in Fig. 2 representing the larger absorber thicknesses. This is the customary procedure used for separating the soft and hard components at low altitudes where, however, the absorber thicknesses are somewhat greater. The assumptions involved here are (1) that the intensity of electrons capable of penetrating more than 35 g/cm² of Pb[23] is relatively small, and (2) that the $P+M$ intensity varies linearly with the absorber thickness. For purposes of the present discussion, the results are not extremely sensitive to these admittedly arbitrary assumptions. It can easily be seen that a small admixture of high energy electrons would not significantly alter the values of extrapolated counting rates. Furthermore, factors which would compensate for the above are doubtless operative. Firstly, should scattering be important in removing slow mesotrons from the incident beam, it is clear that the M intensity might be higher than is indicated by the extrapolation. Secondly, the location of the maximum of the $P+M$ momentum distributions may correspond to a small range in lead at high altitudes, thereby vitiating the straight-line extrapolation. In the light of the present state of our knowledge, it seems probable that, if anything, the $P+M$ intensity has been underestimated.

Finally, the extrapolation leads to results which are entirely in accord with the existing experimental data gathered in airplane flights and on mountain peaks. The experiments of Hall[16] at an altitude corresponding to 458 mm of Hg revealed that the E intensity penetrating 3.5 cm of Pb amounts to approximately 8 percent of the corresponding $P+M$ intensity. Furthermore, at that station, an extrapolation analogous to that performed here yields results within 10 percent of those obtained by a more elegant method of distinguishing mesotrons from electrons based upon a shower-production criterion. Auger[24] concluded, from an analysis of aluminum and lead absorption curves, that electrons having a range exceeding 2.5 cm of Pb comprise 8 percent of the total, or 11 percent of the $P+M$ intensity at 490 mm, lending additional support to assumption (1). Rossi, Sands, and Sard[25] have measured the increase with altitude of the intensity of mesotrons stopped in 2″ of Al, utilizing an apparatus wherein these particles are identified by the occurrence of delayed disintegration electrons. Although comparison can only be rough because of statistical uncertainties, their ratios with respect to sea level of the intensity of slow mesotrons at different altitudes (range interval $=2.2$ g/cm² -13.8 g/cm²; momentum $=0.6\times10^8-1.2\times10^8$ ev/c; energy $=17\times10^6-56\times10^6$ ev) are in accord with those computed from the present data on the basis of extrapolation.

Herzog and Bostick[26] have reported that at 233 mm of Hg the slow mesotrons (range $=0.75$ cm Pb) amounted to 9 percent of the fast particles, a value in agreement with that computed from the extrapolated data at the same altitude. Indeed, the excellency of the agreement must be regarded as fortuitous.

These agreements have been cited primarily for the purpose of demonstrating that this admittedly arbitrary extrapolation procedure is actually not very radical. It leads to results which are consistent with those of other experiments which, by revealing the presence of many slow heavy particles, have already necessitated a revision of the prevalent concepts regarding the relative intensities of the so-called "soft" and "hard" components of cosmic radiation at very high altitudes.

B. Relative Intensities of E and $P+M$ Components as a Function of Altitude

The previous representation of cosmic-ray intensities in the atmosphere[27] was determined by subtracting from Pfotzer's[11] curve of the total vertical intensity as a function of pressure that obtained by Schein, Jesse, and Wollan[4] with 8 cm of Pb. The latter was regarded as characteristic of the mesotron intensity, and the difference was

mesotrons of various types (π, μ, etc.), secondary protons, primary protons, and heavier nuclear primaries and secondaries.

[23] According to calculations by Bhabha, $E=3\times10^8$ ev for such electrons. H. J. Bhabha, Proc. Ind. Acad. Sci. **XIX**, 23 (1944).

[24] P. V. Auger, Phys. Rev. **61**, 684 (1942).

[25] B. Rossi, M. Sands, and R. F. Sard, Phys. Rev. **72**, 120 (1947).

[26] G. Herzog, Phys. Rev. **59**, 117 (1941) and G. Herzog and W. H. Bostick, Phys. Rev. **59**, 122 (1941).

[27] See reference 21.

attributed to electrons. Data on showers, obtained by Regener and Ehmert,[28] were shown as following closely the E curve. In this scheme, the intensity at the maximum and, in fact, at all high altitudes except near the top of the atmosphere was attributed almost entirely to electrons.

The new picture, based upon the results of the extrapolation described above, is shown in Fig. 5. It will be noticed that the E intensity now obtained by subtracting from the total intensity that of the more relevant $P+M$ component determined as described above is now less than that of the latter. The maximum of the $P+M$ curve occurs at an altitude of 60 mm of Hg, as compared with about 78 mm for the electrons. Furthermore, the agreement between the shower measurements and curve E is preserved.

It should be emphasized that the results plotted in Fig. 5 apply only to particles having energies exceeding the minimum for penetration of the apparatus (see Section IIA). Thus, mesotrons having energies less than 2×10^7 ev are excluded. Considering ionization losses alone, it follows that electrons with energies less than approximately 7×10^6 ev are not included. There may be a high intensity of such low energy electrons, and their numbers might easily be comparable with those of the other components. The relative intensities based upon the extrapolation procedure may be influenced near the top of the atmosphere by the fact that shower equilibrium has not been established.

VI. COMPARISON WITH RESULTS AT LARGE ABSORBER THICKNESSES

The uncertainties in the comparison of data obtained under different conditions have already been cited. Nevertheless, in view of the importance of exhausting the possibilities of existing data, it is appropriate to attempt a comparison of the present results with those of Schein and Allen[29] for larger thicknesses of absorber. For this purpose, the normalization evidently should be performed at sea level. The principal uncertainty then concerns possible differences between the results obtained with two different apparatuses arising from the change with altitude of the zenith angle distribution law. Calculations cited previously[12] afford a means for evaluating such effects. The average zenith angles of rays

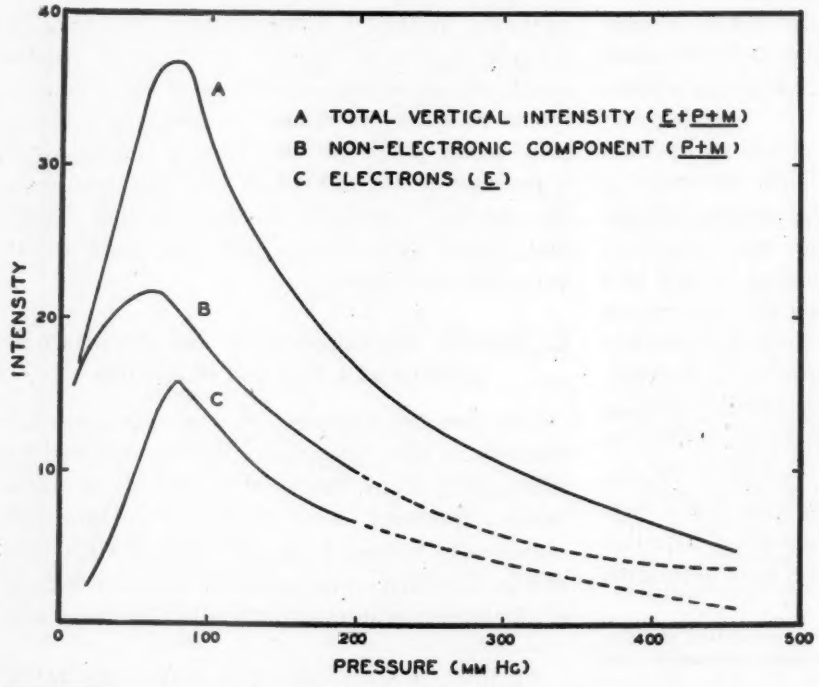

FIG. 5. Variation with altitude of total vertical intensity ($E+P+M$), heavy component intensity ($P+M$) as defined in reference 22, and electron intensity (E) on the basis of the present experiments. The shower intensity (not plotted) follows the E curve closely.

[28] E. Regener and A. Ehmert, Zeits. f. Physik **111**, 501 (1939).
[29] Professor Schein has very kindly provided the author with this unpublished data obtained in collaboration with F. Allen.

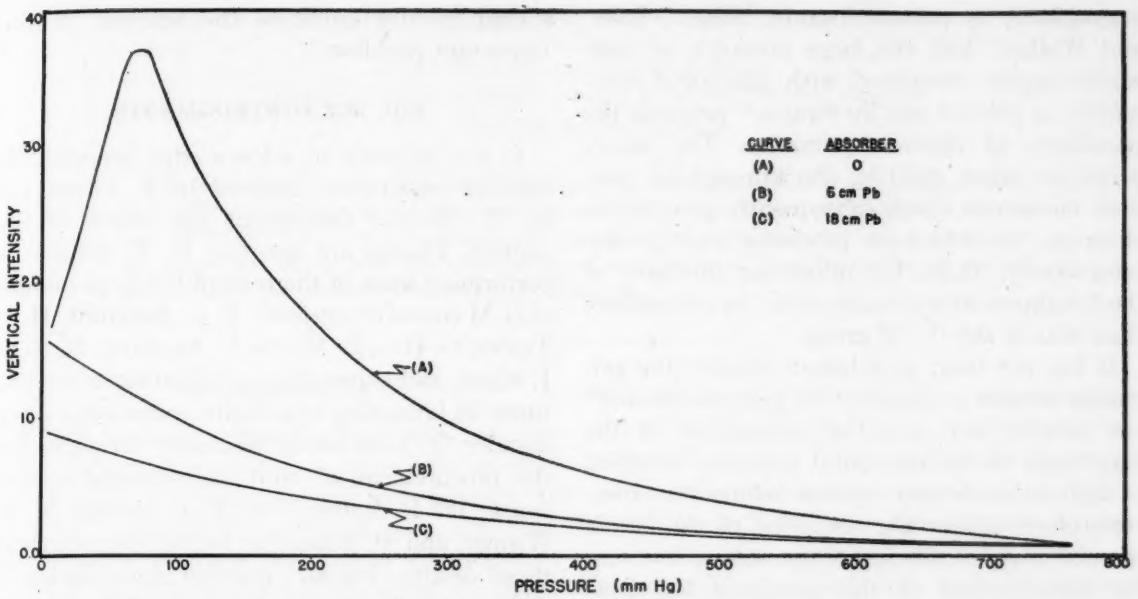

FIG. 6. *Intensity vs. altitude* curves with 0, 6, and 18 cm of Pb. The points of Schein and Allen, with 18 cm Pb, have been fitted to the others at 760 mm of Hg, in conjunction with absorption measurements at sea level.

capable of actuating the two counter trains are 20° and 10°, respectively, for a $\cos^2\theta$ distribution. In the case of the geometrical arrangements here being compared, these values are not very sensitive to the type of distribution law. In fact, for an isotropic distribution the average angles would be altered by less than 2°. Hence, a comparison appears warranted.

Figure 6 shows the resulting curves. Some absorption of the primary radiation appears to occur at thicknesses between 7.5 and 18 cm of Pb, even at the top of the atmosphere. It is possible that in these thicknesses, which are already comparable in superficial mass to one-tenth of an atmosphere, primaries having the minimum energy necessary to penetrate the earth's magnetic field (2.6 Bev for protons at 52° geomagnetic latitude) are completely stopped. Quantitatively, such a primary could conceivably lose all of its energy by the production of a number of mesotrons, none of which are sufficiently energetic to penetrate the remaining lead. For example the total energy of 2.6×10^9 ev could be transformed into 10 mesotrons of $\mu c^2=10^8$ ev each having a k.e.$=1.6\mu c^2$, corresponding to a range in lead of approximately 100 g/cm². Other modes of transformation might lead to a similar result. However, it is necessary to account for the absorption by some process other than ionization.

This is the first experimental evidence for the stopping of primary particles by an absorber interposed within a particle-detecting instrument. It is obviously of the utmost importance to perform similar experiments with absorbers having different atomic numbers, in order to obtain additional information regarding the nature of the primary interaction.

With smaller lead thicknesses, conditions are such that, as indicated by the convergence of the curves in Fig. 1, either the primary or its progeny created in the apparatus itself always has sufficient residual range to actuate the coincidence train.

The convergence also provides experimental evidence precluding the presence near the "top of the atmosphere" of an appreciable upward and outwardly directed component having sufficient energy to penetrate the counter train (see Sections IIA, and VB).

VII. CONCLUSIONS

The data presented above are in accord with a theory of cosmic radiation based upon the hypothesis that the primaries are heavy particles. The absorption characteristics at the top of the

atmosphere, as pointed out by Schein, Jesse, and Wollan,[4] and the large intensity at high zenith angles, compared with azimuthal symmetry, as pointed out by Swann,[30] preclude the possibility of electron primaries. The heavy primaries, upon entering the atmosphere, produce mesotrons which subsequently give rise to electrons (by knock-on processes and by disintegration). Thus, the maximum intensity of the E component occurs deeper in the atmosphere than that of the $P+M$ group.

It has not been established whether the primaries consist exclusively of protons. Swann[31] has pointed out that the explanation of the magnitude of the horizontal intensity observed at high altitudes also requires helium primaries. Heretofore neither the resolution of the $P+M$ components near the top of the atmosphere, nor the identification of the primaries has been feasible experimentally. Devices now in operation, such as particle-discriminating G-M counter systems[32] and balloon-borne cloud chambers[33] should greatly facilitate the solution of this important problem.

[30] W. F. G. Swann, Rev. Mod. Phys. **11**, 242 (1939); Phys. Rev. **59**, 770 (1941).
[31] W. F. G. Swann, J. Franklin Inst. **236**, 1 (1943).
[32] M. A. Pomerantz and F. L. Hereford—unpublished.
[33] R. B. Leighton and C. D. Anderson, Bull. Am. Phys. Soc. Houston Meeting, Nov. 1947; Freier, Lofgren, Ney, Oppenheimer, Bradt, and Peters, Phys. Rev. **74**, 213 (1948); a balloon-borne cloud chamber has also been developed by T. H. Johnson and R. P. Shutt.

VIII. ACKNOWLEDGMENTS

It is a pleasure to acknowledge herewith the valuable assistance rendered by F. Green and D. W. Watson throughout the course of this project. Thanks are also due M. V. Scherb for performing some of the tests of the large number of G-M counters required; F. L. Hereford, H. C. Taylor, G. Hay, P. Morris, D. Seymour, R. Kerr, J. Kane, and others for participating at various times in launching and flight operations; Commander G. Vaux for so efficiently arranging for the procurement of vital instrumental components; W. E. Ramsey, W. F. G. Swann, E. E. Witmer, and M. Schein for helpful discussions of these results. Finally, grateful appreciation is expressed to the National Geographic Society for cooperation in connection with certain phases of this program of cosmic-ray investigations through its Committee on Research, Dr. Lyman J. Briggs, Chairman.

The Absorption Spectrum of Dense Lithium Vapor

CH'EN SHANG-YI AND CHANG CHIH-SAN
Institute of Physics, National Academy of Peiping, Peiping, China
(Received August 11, 1948)

Thirty-five new lines or diffuse bands appeared in the neighborhood of the principal series lines of lithium absorption spectrum were measured. The temperature of the absorption tube was 850–1040°C. He, Ne, and A were used to lessen the speed of distillation of lithium to the cooler part of the tube. The appearance and the position of these lines or bands are not influenced by the nature of the foreign gas employed.

INTRODUCTION

THE absorption spectra of all alkali vapors, except that of lithium, have been studied by Kuhn,[1] Ny and Weng,[2] and others.[3] In addition to the molecular bands many new lines or diffuse bands were observed in the neighborhood of the principal series lines when the vapor density was high. These new lines were classified empirically according to their relative positions with respect to the principal series lines and were interpreted as resulting from loosely bound diatomic molecules. The corresponding observation for lithium was made in the present work.

EXPERIMENT

The experimental arrangement was essentially the same as that of Ny and Weng[2] except that wide slit diaphragms were inserted into the absorption tube placed near the borders of the heating coil and the water coolings at both ends to reduce the speed of convection in the tube. The absorption tube was heated by Chromel A pyrometric ribbon and the temperature was measured by the Pt-PtRd thermocouple. Hilger E-1 quartz spectrograph was used throughout the experiment. For the first member of the principal series an 100-w incandescent lamp was used; while for the rest members of the series a hydrogen discharge tube was used as the background of the spectrum. Eastman III-F and Eastman III-O plates were used. Observations were made when the absorption tube was heated to 850–1000°C with 50°C steps. The time of exposures varied from 15 to 30 min. When the absorption tube was heated to 1020°C or 1040°C, the time of exposure had to be increased to one hour.

Since the temperature difference between the hot part at the middle and the cool part at both ends of the absorption tube was very high for lithium, foreign gas must be added to lessen the speed of distillation of the alkali. Nitrogen and hydrogen react readily with lithium at these temperatures rendering no lithium absorption lines observable. Separate observations were made when the pure He, A, or Ne with pressures 22, 21, and 18 cm Hg, respectively, was admitted into the absorption tube to determine whether

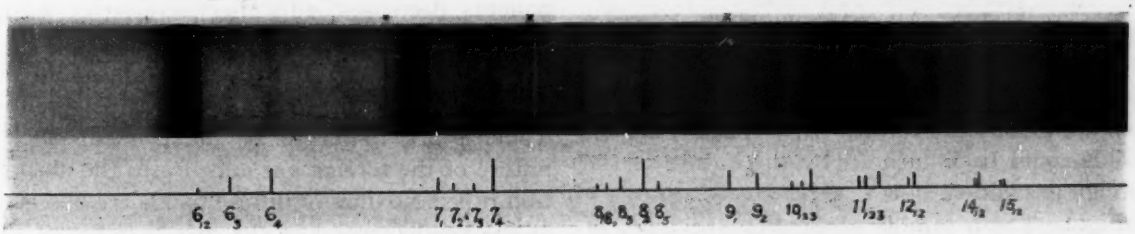

FIG. 1. The absorption spectrum of dense lithium vapor ($T=1040$°C). The lines marked by × are due to impurities.

[1] H. Kuhn, Zeits. f. Physik **79**, 782 (1932).
[2] Ny Tsi-ze and Weng Wen-Po, Comptes Rendus **202**, 1428; **203**, 429; **203**, 860 (1936).
[3] Datta and Chakravaty, Ind. J. Phys. **7**, 273 (1932); Ny Tsi-ze and Choong Shin-Piaw, J. de phys. et rad. **6**, 203 (1935).

TABLE I. New lines or diffuse bands appeared in the absorption spectrum of dense lithium vapor.

$2S-mP$	New lines or bands	Appearance at $T=1040$ °C	Marks	Temp. of absorption tube °C	$2S-mD$ calc'd A	$2S-mS$ calc'd A
6707.8 (1)						3675.7
3232.6 (2)						
	3257.5(?)	*Id*	$_12$	910		
	3254.0(?)	*Id*	$_22$	910	3196.6	2856.3
2741.3 (3)						
	2736.2	*fd*	3_1	910		
	2734.7	*fs*	3_2	910		
2562.5 (4)					2730.5	2611.7
	2560.4	*Fd*	4_1	1040		
	2558.9	*fs*	4_2	910		
	2557.5	*iS*	4_3	910	2557.7	
2475.3 (5)						2500.1
	2472.9	*id*	5_1	940	2472.7	
	2472.2	*id*	5_2	940		
2425.7 (6)						2441.9
	2424.1	*fd*	6_{12}	1020		
	2419.8	*fD*	6_3	1020	2424.3	
	2414.	*iD*	6_4	1020		
2394.5 (7)						
	2390.8	*fd*	7_1	1020	2393.0	
	2389.5	*Fd*	7_2	1020		
	2386.7	*Fd*	7_3	1020		
	2384.4	*ID*	7_4	990		
2373.8 (8)					2372.9	
	2370.8	*Fd*	8_1	1040		
	2369.7	*Fd*	8_2	1040		
	2367.5	*fD*	8_3	990		
	2364.7	*Id*	8_4	990		
	2363.4	*Fd*	8_5	1040		
2359.3 (9)						
	2354.2	*id*	9_1	990		
	2350.	*iD*	9_2	990		
2348.4(10)						
	2346.3	*Fd*	10_1	1020		
	2345.5	*Fd*	10_2	1020		
	2343.9	*is*	10_3	990		
2340.4(11)						
	2338.1	*fd*	11_1	1035		
	2337.	*fd*	11_2	1030		
	2335.2	*fD*	11_3	1020		
2334.2(12)						
	2332.	*fd*	12_1	1040		
	2331.3	*is*	12_2	1020		
2328.9(13)						
2325.1(14)						
	2324.1	*Fd*	14_1	1040		
	2323.5	*fs*	14_2	1020		
2321.8(15)						
	2320.5	*Fd*	15_1	1040		
	2320.	*Fs*	15_2	1040		
2319.2(16)						

the appearance or positions of these lines or bands could be influenced by the nature of the foreign gas added.

Figure 1 is a sample absorption spectrum of lithium when the temperature of the absorption tube was at 1040°C. The new lines or bands are marked by a sketch underneath.

Corresponding observations on the absorption spectrum of potassium at temperatures 500–640°C were repeated for comparison with Ny and Weng's measurements.

RESULTS

The results of measurement are given in Table I. The first column gives the wave-length of lithium principal series. In column 2 the first two lines marked (?) are situated in superposition with the very sharp and strong molecular absorption bands. The meanings of the letters in column 3 are as follows:

i=fairly intense	I=intense
f=faint	F=very faint
s=sharp	S=very sharp
d=diffuse	D=very diffuse

These letters serve to describe very briefly the appearance of these lines or diffuse bands in the spectrogram taken at a temperature of 1040°C.

Because of faintness and diffuseness, wave-length values of the lines or diffuse bands could not be determined with great accuracy, so the decimal figures are not very reliable except those for very sharp lines. The lines or diffuse bands are marked by M_n with M indicating the member of the series lines, and n the ordinal number of the lines or bands counted from the Mth member in the direction of decreasing wave-lengths. The values given in column 5 are the temperatures at which the lines or bands start to appear in the spectrogram. These lines or bands will indeed become more intense when the absorption tube is heated to a still higher temperature.

Lines 3_1, 3_2; 4_2, 4_3; 5_1, 5_2; and even 6_{12} appeared very much like a doublet system with the shorter wave-length component a little stronger and sharper than the longer wave-length one. The separations between the doublet components decreases with the decrease in wave-length.

It is to be noted that the appearance and the positions of all these lines or bands as given in Table I are found to be independent of the nature of the foreign gas added into the absorption tube.[4] No lines or diffuse bands are observed in the neighborhood of the first member of the series.

In the last two columns are listed the calcu-

[4] The diffuse bands λλ2552, 2470, 2422.5, and 2392.7, which appeared as a result of the presence of He, are not listed in Table I.

lated wave-lengths of $2S-mD$ and $2S-mS$ transitions. Some of the values of $2S-mD$ are very close to observed lines but not with the $2S-mS$ values. Forbidden lines may be expected to appear when the alkali vapor density is high.

A spectrogram of potassium absorption spectrum was taken. Ny and Weng's data[2] are confirmed by the present measurements, except that one additional faint line is observed at λ3429 at temperature 710°C.

Finally the authors wish to thank Dr. Ny Tsi-ze for his interest in the experiment.

PHYSICAL REVIEW VOLUME 75, NUMBER 1 JANUARY 1, 1949

Isotope Shifts in Uranium Spectra

L. E. Burkhart, George Stukenbroeker, and Sam Adams
Clinton Engineer Works, Carbide and Carbon Chemicals Corporation, Oak Ridge, Tennessee

(Received July 19, 1948)

A study is made of the isotopic shift of U^{238}, U^{235}, and U^{233} in the emission spectrum of uranium. The shift is sufficient to allow quantitative determination of the concentration of the components of a mixture of the uranium isotopes by routine spectrographic analysis. Data show comparative values obtained by mass spectrometer and spectrograph.

INTRODUCTION

THE separation of the isotopes of uranium affords an excellent opportunity to study the isotope shifts in its spectrum. Shifts had been observed by D. D. Smith and D. R. Long in these laboratories in noting the difference in normal standards, chiefly the U^{238} isotopes and the enriched U^{235} samples on the same plate. This work extends the study to include U^{233}. The arc and the spark were used to produce the spectra of these isotopes, and a large number of shifts were observed at a dispersion of 2.47A per millimeter.

DISCUSSION

The explanation of the isotope effect is not simple, and no attempt is made to explain it here. The shifts in the uranium isotopes are so great that they were recognized in ordinary emission spectrographic analysis. An effort is made here to observe as many as can be obtained under the prescribed conditions and sample size. The difference of the nuclear radius, difference in the building up of the nucleus, or perhaps something peculiar to the uranium type elements, may contribute to this easily observed isotope shift.

The shifts observed in U^{235} and U^{233} by direct emission spectra were obtained on a 15,000-line Jarrell-Ash grating spectrograph. This Wood grating gives a strong second order spectrum with a dispersion of 2.47A per millimeter. One hundred micrograms of U_3O_8 were selected as sample size for obtaining the arc spectra, and this was mixed with 500 micrograms of powdered graphite. A uniform burning was obtained for a period of 45 seconds at 4 amperes direct current. However, currents up to 7 amperes may be used.

The spark spectrum was obtained by use of the Dietert Multisource with a spark produced with settings of 20 microfarads, 25 microhenries and 5.4 ohms. Five hundred micrograms of U_3O_8 mixed with a drop of cellulose acetate in acetone were placed in shallow copper electrodes and then dried. The sample was then sparked for 45 seconds using a 103-0 plate. A careful check was made throughout the 2500A–5000A region. The search did not disclose any appreciable differences between the spark and the arc spectra of uranium. The same lines shifted, and the amounts of shift were the same as for the arc spectra. The spectra obtained by the standard spark supply showed fewer lines but no greater shift than the arc spectra.

The region covered in the arc spectrum study

TABLE I. Frequency of recurrence of shifts.

Position in the spectrum	No. of lines
2500–2600A	18
2600–2700	57
2700–2800	109
2800–2900	140
2900–3000	174
3000–3100	94
3100–3200	56
3200–3300	35
3300–3400	75
3400–3500	61
3500–3600	28
3600–3700	18
3700–3800	14
3800–3900	7
3900–4000	16
4000–4100	6
4100–4200	9
4200–4300	11
4300–4400	10
4400–4500	7
4500–4600	4
4600–4700	7
4700–4800	16

was from 2500A to 8800A. Eastman S.A. No. 2 plates were used for second order plates in the region from 2500 to 4950A. Eastman 1F plates were used for the 4500 to 7300 setting, and a 1N plate for the 6000A to 8800A region, these observations being in the first order.

A large number of shifts were observed, and a total of more than 900 shifts were counted from 2500A to 8800A. A distribution of the occurrence is shown in steps of 100A in Table I. Only two lines, 6101.74 and 6465.0, were observed to exhibit a shift above 4800A. A sample size greater than 100 micrograms shows a larger number of lines and a larger number of shifts. The sample is small in order to compare the spectra of the three isotopes of uranium with a minimum amount of background.

The amount of shift was measured by calibrating the rate of sweep by the scanning motor on a densitometer by measuring the time interval between the minima of known lines. The speed of the sweep was determined to be 0.0179A per second for a second order spectrum. A number of the lines measured are shown in Table II. The largest single shift is in line 4244.37A.

It is of interest to note that in every case observed where there is a shift between the U^{238} and U^{235}, there is also a shift of the U^{233}. This shift is always in the same direction, i.e., toward the ultraviolet or shorter wave-length, in the progression of U^{238} to U^{233}. Even though there is some correlation between the mass difference and the direction of the shift, there does not seem to be any correlation between the mass difference and the amount of the shift. This is indicated on examination of Table II. As is apparent in lines 2, 3, 6, and 7, the shift is greater between U^{235} and U^{233} (mass difference of 2) than between U^{238} and U^{235} (mass difference of 3); while in the cases of the other lines listed in Table II, the greatest

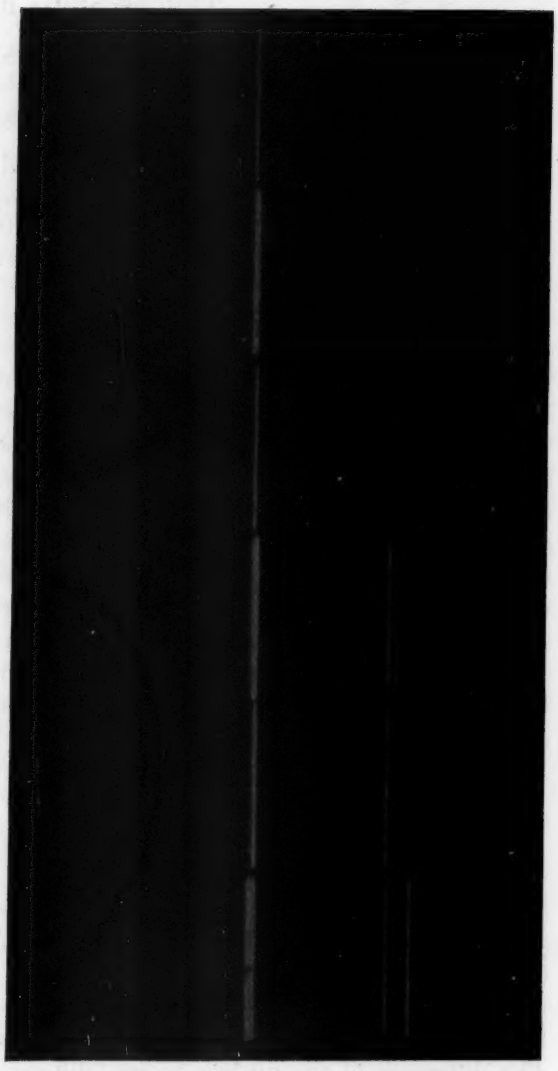

A B

FIG. 1. Line *A* is the uranium 4241.67A line; line *B* is the uranium 4244.37A line. Reading from top to bottom, these spectra are of (1) U^{238}, (2) a mixture of U^{238} and U^{235}, (3) U^{235}, (4) a mixture of U^{235} and U^{233}, (5) U^{233}, and (6) a mixture of U^{238} and U^{233}.

TABLE II. Observed shifts in representative lines.

U^{238} line		$U^{238}-U^{235}$ shift		$U^{235}-U^{233}$ shift		$U^{238}-U^{233}$ shift	
A	cm^{-1}	A	cm^{-1}	A	cm^{-1}	A	cm^{-1}
2565.406	38980.18	0.075	1.14	0.070	1.06	0.145	2.20
2802.157	35686.79	0.018	0.23	0.020	0.25	0.038	0.48
3313.94	30121.02	0.016	0.14	0.036	0.33	0.052	0.47
3633.29	27523.26	0.104	0.79	0.064	0.48	0.168	1.27
3670.072	27247.42	0.009	0.06	0.009	0.07	0.018	0.13
3890.364	25704.53	0.036	0.24	0.055	0.36	0.091	0.60
3944.130	25354.13	0.057	0.37	0.091	0.58	0.148	0.95
4244.372	23560.61	0.248	1.37	0.125	0.70	0.373	2.07
4252.426	23515.98	0.168	0.93	0.089	0.49	0.257	1.42
4365.553	22906.60	0.208	1.09	0.073	0.38	0.281	1.47
4609.864	21692.61	0.077	0.36	0.054	0.26	0.131	0.62

shift is for the difference between U^{238} and U^{235}. Figure 1 is a photograph of a section of a plate which shows the shifts of the 4244.37A line and the reference line 4241.67A. The identities of the isotopes and mixtures are shown in the caption of Fig. 1.

On the basis of data obtained on mixtures of these isotopes, it becomes apparent that it is possible to assign quantitative values to the concentration of these components in mixtures of uranium isotopes. A sample of data of the spectrographic determination of the U^{235} content in a series of samples is given in Table III. These determinations were made by D. D. Smith. The values obtained by the conventional method of assay are listed in column 2, which shows how well the two methods agree.

TABLE III. Comparison of assay methods.

Sample No.	Spectrometer	Spectrograph	Deviation
1	30.5	30.2	+0.3
70	28.6	29.2	−0.6
83	28.3	29.5	−1.2
KJ-1	13.2	12.8	+0.4
2	13.2	12.0	+1.2
*Q*10	5.9	6.4	−0.5
*Q*5	0.61	1.0	—
		Average deviation	0.7

CONCLUSION

On examination of spectra taken, the following general observations may be made: (1) that any line showing a shift between U^{238} and U^{235} also shows a shift between U^{235} and U^{233}, (2) that the direction of shift of lighter isotopes is toward the shorter wave-length, (3) that there is no correlation between the amount of shift and atomic weight, and (4) that quantitative determination of the concentration of uranium isotopes may be made by emission spectrographic methods.

This document is based on work performed under Contract No. W-7405-eng-26 for the Atomic Energy Commission at the Carbide and Carbon Chemicals Corporation, Oak Ridge, Tennessee.

The *K* Spectra of Element 61

L. E. BURKHART, W. F. PEED, E. J. SPITZER
Clinton Engineer Works, Carbide and Carbon Chemicals Corporation, Oak Ridge, Tennessee
(Received July 26, 1948)

The $K\alpha_1$, $K\alpha_2$, $K\beta_1$, and $K\beta_2$ lines of the x-ray spectra of element 61 were obtained from 1.5 mg of sample of the chloride salt. The sample was fused on a copper target and bombarded with electrons from a 70-kv source. Wave-length measurements were made from a microphotometer tracing of the film. After one exposure of the sample, neodymium and samarium were added to the target and the spectrum of the three elements was recorded to show the position of element 61 in the periodic table.

INTRODUCTION

X-RAY spectra have been widely used in establishing positive identification of the elements from the time of Moseley's first investigations. It is known that x-ray spectra are simple and that wave-lengths can be readily calculated from the Moseley law.

Previous workers in the field of rare earth chemistry have made many unsuccessful attempts to isolate the missing rare earth element of atomic number 61. All early work was done on naturally occurring material and, at best, only traces contaminated by neighboring elements were collected.

The *K* lines of the x-ray spectrum of a sample of element 61 supplied by Mr. G. W. Parker and Mr. P. M. Lantz of Oak Ridge National Laboratory have been recorded and the $K\alpha_1$, $K\alpha_2$, $K\beta_1$, and $K\beta_2$, lines appear in their appropriate places in the simple x-ray spectra. The photographs shown herein leave no doubt as to the identity of the material.

SPECTROGRAPH

A transmission type x-ray spectrograph was used. A complete *K* spectra of the material on the target is recorded on the film on both sides of the center line passing through the target and crystal. A calcite crystal $15\times30\times2.5$ mm was used as a diffracting medium. The crystal was located with the 15×30-mm face parallel to the film and equidistant from the target and the slit. The 15-mm edge was fixed in a vertical position. The crystal was cut with the (100) planes (Rhombohedral System) normal to the 15×30-mm edge and parallel to the 15-mm edge. In this type spectrograph the crystal is not oscillated.

A demountable target x-ray tube with a body made of 4-inch Pyrex pipe fittings was used. The anode was made of copper, with the face cut at a 20° angle to the axis through the center of the crystal and the film of the spectrograph; a recess $\frac{1}{8}$-inch wide, $\frac{1}{16}$-inch deep and $\frac{1}{2}$-inch long was cut in the target face to hold the sample. The filament assembly consisted of a tungsten helix mounted in a copper shield profiled to give a line focus of electrons on the anode. During operation, the tube was pumped continuously with a 6-inch oil diffusion pump and a $1\frac{1}{2}$-hp Kinney pump. Normal tube operating pressure was from 2×10^{-5} to 5×10^{-6} mm of mercury. A power supply capable of delivering 130 kv, center grounded was used. High voltage was measured with two calibrated 2-ma meters and series resistors in the high voltage direct current circuit. The meters were connected so as to measure filament-to-ground and anode-to-ground voltages. Tube emission current was measured with a 7.5-ma meter connected in the negative high voltage circuit.

EXPERIMENTAL METHOD

The sample presumed to be element 61, was loaded on the target by evaporating a solution of the chloride salt into the $\frac{1}{8}\times\frac{1}{2}$-inch recess milled in the target face. Heat was supplied with an infra-red lamp. Drying of the sample was completed by baking the target in a vacuum desiccator. When completely dry, the target was heated with a torch to fuse the sample to the target face.

After a spectrogram of pure element 61 was recorded, 1.3 mg of Nd_2O_3 and 1.3 mg of Sm_2O_3 were added to the target, using the same general

method of target-loading to provide reference lines, which is shown in Film *B*. The vacuum drying and fusing steps were omitted. Exposure conditions for Fig. 1 are shown in Table I.

A densitometer trace was made of Film *B* on a Leeds and Northrup microphotometer using 2 mm per minute film travel and 2 inch per minute chart speed. Both film and chart on the microphotometer are driven by synchronous motors. The distance on the densitometer chart from a line on one side of center to the corresponding line on the other side of center which is proportional to the wave-length of the line was measured with an accuracy of 1 part in 9000.

In the calculations, $\frac{1}{2}$ of the distance between corresponding peaks divided by the distance from the slit to the film plane is equal to tangent θ. From this measurement, $\sin\theta$ was determined and the wave-length was then calculated by means of Bragg's law. The distance from the slit to the film plane was measured with an inside micrometer and converted to the same units of distance as the microphotometer chart. Because of the paper wrapping which was used to protect the

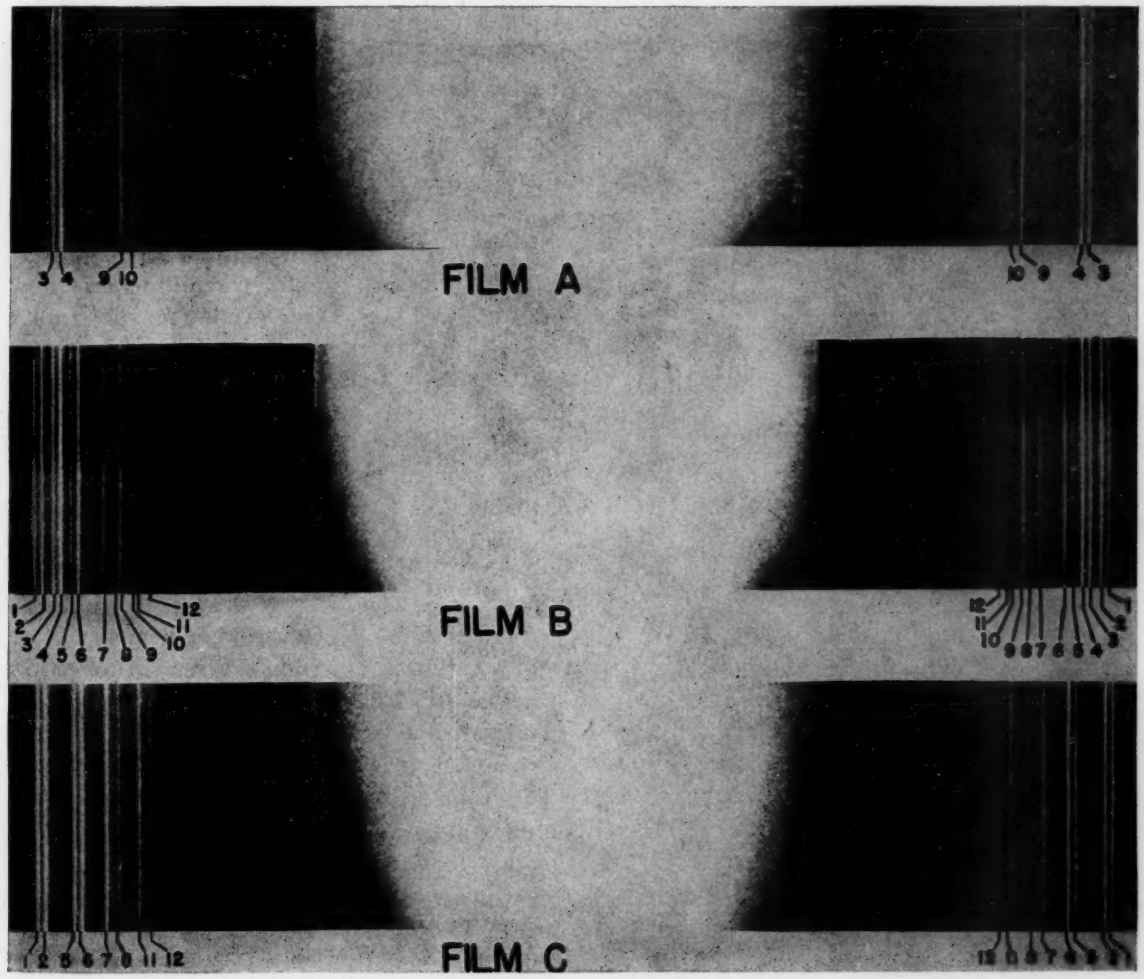

FIG. 1. *K* series x-ray spectra. Film *A*, element 61; film *B*, neodymium, element 61, samarium; film *C*, neodymium, samarium.

Line Identification

1 ND $K\alpha 2$	4 61 $K\alpha 1$	7 ND $K\beta 1$	10 61 $K\beta 2$
2 ND $K\alpha 1$	5 SM $K\alpha 2$	8 ND $K\beta 2$	11 SM $K\beta 1$
3 61 $K\alpha 2$	6 SM $K\alpha 1$	9 61 $K\beta 1$	12 SM $K\beta 2$

TABLE I.

Film	Exposure time, ma hours	Voltage, kv
A	6.5	70
B	11.5	70
C	5.0	80

film from exposure to visible light, the possible error in this measurement is 1 part in 3500.

It was originally intended to use lines of neodymium and samarium as standards of wave-length and to determine the wave-lengths of lines of element 61 by interpolation between these standards. It was observed, however, that there is a discrepancy between the wave-lengths of neodymium and samarium as measured in this laboratory and those reported in the *International Critical Tables*.[1] This difference is shown in Table II.

FIG. 2. In the above figures the lines reading left to right are: Nd $K\alpha 2$, Nd $K\alpha 1$, 61 $K\alpha 2$, 61 $K\alpha 1$, Sm $K\alpha 2$, Sm $K\alpha 1$, Nd $K\beta 1$, Nd $K\beta 2$, 61 $K\beta 1$, 61 $K\beta 2$, Sm $K\beta 1$, Sm $K\beta 2$.

[1] *International Critical Tables*, Vol. VI, p. 39.

TABLE II.

Line	Wave-lengths XU Reported in ICT	Observed
Nd$\alpha 2$	335.96	335.74
Nd$\alpha 1$	331.31	330.95
Sm$\alpha 2$	313.20	312.66
Sm$\alpha 1$	308.54	307.75

Possible errors in this work which have not been investigated are: (1) variations in film dimensions and (2) variations in the interplanar spacing of the calcite crystal which was used. The value of d was taken as 3029.04 XU at 18°C in order to keep these results as consistent as possible with those previously reported. Errors resulting from the change in the d of calcite are negligible, since the linear coefficient of expansion of calcite is 1.02×10^{-5} per degree centigrade.[2] No allowance has been made for film shrinkage or for the Ross effect.[3]

DISCUSSION OF RESULTS

Photographic prints of three films are shown in Fig. 1. Film *A* shows the *K* spectrum of element 61. In the original film, all four lines, K_{α_2}, K_{α_1}, K_{β_1}, and K_{β_2}, are visible and no other impurities were detected.

Film *C* shows the spectrum of neodymium, element 60, and samarium, element 62. The large gap between corresponding lines of these two elements clearly shows, as has been shown before, that an element of atomic number 61 should exist.

Film *B* shows the spectrum of element 61 after additions of neodymium and samarium. Comparison with Film *C* shows that the lines of element 61 fall between the lines of the reference elements as is predicted by Moseley's law.

Exposures of element 61 were made at a maximum voltage of 70 kv to eliminate the possibility of interference by second order lines. Osmium (K_{β_2} wave-length = 168.75, second order wave-length 337 XU), is the longest wave-length that will interfere with any of the elements shown in Fig. 1. Threshold voltage for osmium is 74 kv and, therefore, there is no possibility of inter-

[2] J. A. Bearden, J. App. Phys. 12, 402 (1941).

[3] C. E. K. Mees, *The Theory of the Photographic Process* (The Macmillan Company, New York, 1942), p. 907.

ference from second order lines of the elements of higher atomic number.

Figure 2 shows one end of Film *B* with a densitometer trace which more clearly shows the relative position of the lines and their resolution.

Because of the very large grain size of the high speed film which was used, the β_1 and β_3 doublet lines were not resolved. Predicted wave-lengths of element 61 were calculated by calculating screening constants from the Moseley lay for elements 58, 59, 60, 62, 63 and 64 and determining the value of the screening constant for element 61 graphically. Wave-lengths of reference lines were taken from the *International Critical Tables*.[4] The measured and calculated wave-lengths of the lines of element 61, together with the possible interfering lines, are shown in Table III.

TABLE III.

Element 61 *K* spectra lines	Wave-lengths XU Measured	Calculated	Possible interfering lines
α_2	323.68	324.27	La β_1 327.26
α_1	319.02	319.60	La β_2 319.66
β_1	282.00	282.99	Nd β_2 285.73 Tb α_2 282.94 Tb α_1 278.19 Dy α_2 275.64
β_2	275.03	275.33	Sm β_1 272.50

CONCLUSIONS

The *K* lines of the x-ray spectrum of element 61 have been recorded and their wave-lengths measured. Agreement between measured and calculated wave-lengths is shown in Table III. The spectra and the controlled conditions under which they were obtained is conclusive evidence that the material is element 61. Film *A* in Fig. 1 indicates that the sample was very pure.

The authors wish to acknowledge the assistance of C. E. Normand and A. C. Eckert for their many suggestions while the spectrograph was in its early stages of development, and to thank L. G. Lankford for the excellent machine work in construction of the spectrograph and tube components.

This document is based on work performed under Contract W-7405-eng-26 for the Atomic Energy Commission by Carbide and Carbon Chemicals Corporation, at Oak Ridge, Tennessee.

[4] *International Critical Tables*, Vol. VI, Pp. 39 and 40.

The Electrostatic Interaction and Low Energy Particles in Alpha-Radioactivity

MELVIN A. PRESTON
The University, Birmingham, England
(Received August 6, 1948)

In α-decay, after the particle has been emitted, the asymmetrical electric field of the residual nucleus can cause the α-particle to alter its total energy in conjunction with a change in the state of the nucleus. Since the ability of a particle to penetrate the potential barrier increases rapidly with its energy, the number of particles of each possible energy finally escaping will not be in accord with the decay constants predicted by the Geiger-Nuttall law.

It is found that the effect is not important (a quantitative estimate is given), except in the case where the difference between the energies of the two states is less than about 500 kev.

The investigation allows a theoretical study of the experiments in which W. Y. Chang found anomalous fine structure in the α-spectra of Po and Ra. It is found that very improbable assumptions are required to reconcile these experimental results with the theory presented here, and we have been unable to see how any additional effects connected with the nucleus could alter this conclusion.

I. INTRODUCTION

THE existence of groups of low energy α-particles in the decay spectra of polonium[1] and radium[2] has been reported by Chang. Although these groups have weak intensity compared with the main line in each case, their strength is greater than that shown on the Geiger-Nuttall curve by factors up to 10^6 in the case of Po and 10^4 for Ra. This divergence cannot be accounted for within the framework of the standard theory of α-radioactivity on the ground of non-zero angular momenta of the emitted particles, since improbably high nuclear spins would be involved.[1,2] A number of proposed explanations of the phenomenon are listed in Chang's papers. Some of these are concerned with possible mechanisms within the nucleus, but one theory which is discussed at some length in this second paper seems fairly probable and can be treated mathematically without introducing any speculation about the exact nature of nuclear forces, other than that they are of short range. This explanation supposes that after the α-particle has been emitted it can still interact with the residual nucleus and thus, by altering the nuclear state, change its own energy. Since the ease with which a charged particle can penetrate the potential barrier increases very rapidly with the energy of the particle, changes of this energy during the flight of the α-particle will clearly have some effect on the relative probabilities of its emission with the various possible energies.

After the α-particle has left the region where nuclear forces act (i.e., the nucleus), the most important mechanism which would produce such an interaction is the force acting on the particle due to the asymmetry of the motion of electric charges in the residual nucleus. It is the details of such a process that are studied here.* (Bremsstrahlung has been shown to be unimportant by Dancoff.[3])

There are two cases to be considered. We assume always that the parent nucleus is in its ground state. In the normal case, in the absence of the Coulomb barrier, the probabilities of decay to the various states of the product nucleus are of the same order because the energy of the α-particle is considerably greater than the energy differences between nuclear states. However, the energy of the α-particle has such a great effect on the penetrability of the Coulomb potential barrier that the most probable process is the emergence of the particle with its greatest possible energy, leaving the daughter nucleus in its ground state. If we now take into account the interaction mentioned above, the high energy α-particle, after penetrating part of the barrier, can excite the nucleus to a higher state and lose energy itself, finally appearing as a low energy particle. This appears to be the type of process

[1] W. Y. Chang, Phys. Rev. **69**, 60 (1946).
[2] W. Y. Chang, Phys. Rev. **70**, 632 (1946).

* This possibility was first suggested to the author by Professor Peierls, who in turn attributes it to a remark made some years ago by Professor Gamow.

[3] S. M. Dancoff, Metallurgical Project Report, *Short Range Alphas in Natural Radioactivity.*

envisaged by Chang in his second paper; its probability would have to be greater than that of direct decay to the corresponding excited states. Such a process should occur in the decay of all α-emitters; hence, all should have a low energy group for each excited state of the residual nucleus. However, we shall see that the effect is not, in general, great enough to be distinguished from the direct decay, and is certainly not sufficient to account for the lines observed by Chang.

The second case is one in which, for some reason connected with nuclear structure, the direct decay to the ground state of the daughter nucleus is forbidden. The nucleus is left in an excited state, and the α-particle begins its career with the corresponding low energy. However, because of the interaction, the nucleus can now fall to its ground state, imparting the extra energy to the α-particle instead of emitting a γ-ray. This process will also clearly affect the relative probabilities of emission. With our present knowledge of the constitution of heavy nuclei, it does not seem possible to assess with any certainty the likelihood of the ground state transition being forbidden. It is not forbidden by any of the usual selection rules, such as angular momentum or parity, because these would make equally improbable the transition after emission. Nevertheless the "accidental" vanishing of a usually appreciable factor might make the direct transition improbable. However, we shall see in any case that this process is also incapable of explaining Chang's results.

Indeed, we shall see that there appear to be considerable difficulties attached to any theoretical explanation of Chang's spectra, and the indications are that, whatever the reason for the results, it is not to be found in an effect associated with the polonium or radium nuclei.* In this connection we may also mention that Zajac, Broda, and Feather[4] have re-investigated the γ-radiation from polonium and have found no γ-rays to correspond to the levels suggested by Chang.

* *Note added in proof:* This conclusion has also been indicated by direct experiments on polonium reported by Dr. W. G. Wadey in Phys. Rev. **74**, 1846 (1948).

[4] B. Zajac, E. Broda, and N. Feather, Proc. Phys. Soc. **60**, 501 (1948).

II. GENERAL THEORY

To describe the system formed by the α-particle and the nucleons which comprise the residual nucleus and to allow for the electrical interaction mentioned in the introduction, we employ a many-body wave function, Ψ, which satisfies

$$[-(\hbar^2/2m)\nabla_r^2+V(r)+H_\xi+U(\mathbf{r},\xi)-E]\Psi(\mathbf{r},\xi)=0. \quad (2.1)$$

This is written to describe the relative motion, with origin at the centroid of the residual nucleons. m is the reduced mass (practically that of the α-particle). $\mathbf{r}$ is the position vector of the α-particle, ξ denotes all the coordinates (including spin, etc.) of all the other nucleons, ∇_r^2 denotes the Laplacian operator on $\mathbf{r}$, and H_ξ is the Hamiltonian of the other nucleons. E is the total complex energy, i.e., its imaginary part is $-\frac{1}{2}i\hbar\lambda$, where λ is the total decay constant. $V(r)$ is the potential function for the α-particle which is generally used in theories of α-decay. Outside the nucleus $V=2Ze^2/r$, and inside it forms a well of some shape which we shall not need to specify—in fact we do not even use the assumption that it can be expressed as a function of r inside the nucleus. U is the potential due to the nuclear charge asymmetry. For $r>r_0$ (the nuclear radius),

$$U=\sum_i(2e^2)/(|\mathbf{r}-\mathbf{r}_i|)-2Ze^2/r$$

$$=2e^2\sum_i\sum_{k=1}^{\infty}(r_i^k/r^{k+1})(2/2k+1)^{\frac{1}{2}}P_k(\cos\Theta_i), \quad (2.2)$$

where the sum $\sum_i$ is over all the protons in the product nucleus, Θ_i is the angle between $\mathbf{r}$ and $\mathbf{r}_i$, and P_k is a normalized Legendre function. The form of U for $r<r_0$ is also immaterial to our discussion.

The states of the residual nucleus can then be specified by a complete set of normalized orthogonal eigenfunctions $u_m(\xi)$, and the total wave function Ψ can be expanded as a series in these functions.

$$(H_\xi-E_m^{(N)})u_m(\xi)=0, \quad (2.3a)$$

$$\int u_m u_m^* d\xi=1, \quad (2.3b)$$

$$\Psi=\sum_m\phi_m(\mathbf{r})u_m(\xi). \quad (2.4)$$

Then substituting for Ψ in (2.1), multiplying by u_n^*, and integrating over ξ, we find

$$[-(\hbar^2/2m)\nabla^2+V(r)-(E_n^{(N)}-E)]\phi_n(\mathbf{r}) = -\sum_m \phi_m(\mathbf{r})U_{nm}(\mathbf{r}), \quad (2.5)$$

where

$$U_{nm}(\mathbf{r})=\int u_n^*(\xi)U(\mathbf{r},\xi)u_m(\xi)d\xi. \quad (2.6)$$

Also $E-E_n^{(N)}=E_n$, the complex energy of the nth α-particle group. We take it that the states are enumerated so that each $\phi_n(\mathbf{r})$ corresponds to a fixed angular momentum l_n of the α-particle.** Thus

$$\phi_n(\mathbf{r})=r^{-1}f_n(r)\sum_{M=-l_n}^{l_n} c_M \times P_{l_n}^M(\cos\theta)\exp(iM\varphi). \quad (2.7)$$

We now apply the addition theorem for spherical harmonics to the factor $P_k(\cos\Theta_i)$ in (2.2), put this result in (2.6), and find for $U_{nm}(\mathbf{r})$ the following expression:

$$2\sum_{k=1}^{\infty} r^{-(k+1)}\Big\{C_{k0}^{nm}P_k(\cos\theta) +2\sum_{s=1}^{k}P_k^s(\cos\theta)\Big(C_{ks}^{nm}\cos s\varphi +S_{ks}^{nm}\sin s\varphi\Big)\Big\}, \quad (2.8)$$

where

$$C_{k0}^{nm}=(2/2k+1)\int u_n^*e^2\sum_i r_i^k P_k(\cos\theta_i)u_m d\xi, \quad (2.9)$$

$$C_{ks}^{nm},\ S_{ks}^{nm}=(2/2k+1)\int u_n^*e^2\sum_i r_i^k \times P_k^s(\cos\theta_i)\begin{matrix}\cos\\ \sin\end{matrix} s\varphi_i u_m d\xi, \quad (2.10)$$

and $(r_i, \theta_i, \varphi_i)$ are the coordinates of the ith proton in the nucleus. Then, substituting (2.7) in (2.5), multiplying through by $P_{l_n}^M(\cos\theta)\sin\theta \times\exp(-iM\varphi)$, integrating over θ and φ for each M, and adding the resulting equations, we get

$$\frac{\hbar^2}{2m}\left(\frac{d^2}{dr^2}f_n-\frac{l_n(l_n+1)}{r^2}f_n\right)-(V(r)-E_n)f_n =2\sum_m\sum_{k=1}^{\infty} f_m a_k^{nm}/r^{k+1}. \quad (2.11)$$

The quantities a_k^{nm} are each a sum of quantities which depend on integrals of the form

$$\int_{-1}^{1} P_{l_m}^M(\mu)P_{l_n}^{M'}(\mu)P_k^{|M-M'|}(\mu)d\mu.$$

Since these integrals vanish unless $l_m+l_n>k>|l_m-l_n|$, we have the general equations

$$\frac{d^2f_n}{dr^2}+\left\{\frac{2m}{\hbar^2}(E_n-V)-\frac{l_n(l_n+1)}{r^2}\right\}f_n =\sum_{m=0}^{N-1}f_m\sum_{k=|l_m-l_n|}^{l_m+l_n}A_k^{nm}/r^{k+1} \quad k\neq 0,\ n=0,1,\cdots(N-1). \quad (2.12)$$

N is the total number of nuclear states whose interactions are considered.

In the particular case when one of l_m or l_n is zero, there is only one possible value of k, and the summation over k on the right-hand side of (2.12) reduces to just one term.

A_k^{nm} consists of terms of the form C_{k0}^{nm}, C_{kM}^{nm}, and S_{kM}^{nm} multiplied by constants which depend on the c_M's of (2.7). If we take a statistical average over M of the values of $|C_{k0}^{nm}|$, $|C_{kM}^{nm}|$, and $|S_{kM}^{nm}|$, and call this $|Q_k^{nm}|$, we can then treat the problem simply as if M were zero and write

$$A_k^{nm}=(2m/\hbar^2)2^{\frac{1}{2}}Q_k^{nm}. \quad (2.13)$$

Equations (2.12) are a set of N simultaneous linear second-order equations for the functions f_n. There are thus $2N$ sets of independent solutions, a certain linear combination of which describes our problem. For large r, the equations become independent, and all the f_n's tend to functions proportional to $\exp(\pm ik_n r)$. However, the solutions must represent particles leaving the nucleus; hence we must take for f_n those solutions

** This is true if the parent nucleus has zero spin. Po and Ra are even-even nuclei. If the spin is not zero (2.4) should be replaced by $\Psi=\sum_{m,l}c_{ml}\phi_{ml}u_m$, where each ϕ_{ml} has a fixed angular momentum. However, there will clearly be a later averaging process over the c_{ml} which can affect the results only by an unimportant numerical factor.

which tend to $a_n \exp(ik_n r)$, where a_n is a complex constant. Then the ratios between the quantities $v_n|a_n|^2$ are the relative intensities of the lines in the α-particle spectrum. The condition that all the f_n's should represent outgoing waves at infinity has thus provided N of the $2N$ (complex) conditions needed to determine the particular linear combination of solutions which applies to our problem. The remaining N conditions depend on the nucleus.

The values of the f_n's at r_0 give the relative probabilities of an α-particle of each energy E_n being at the edge of the nucleus, i.e., the relative probabilities of decay if there were no potential barrier. The other conditions could be N homogeneous equations involving these functions; to determine these would require extensive knowledge of intranuclear behavior. However, we shall use our N conditions at infinity, start with the functions $f_n = a_n \exp(ik_n r)$, and integrate the equations inwards. Then the f_n's at r_0 appear as functions of the a_n's; if one set is known the other can be determined. We shall find that a good deal can be discovered without very exact knowledge of the $f_n(r_0)$.

Strictly speaking, of course, our problem is one with given boundary conditions in which we must find the eigenvalues E_n. These eigenvalues are complex; the real part is the energy of the escaping particle and the imaginary part is proportional to the decay constant. Thus the eigenvalues are usually experimentally known, and it is simpler to discuss the problem as above, using this knowledge.

We have mentioned that $f_n(r_0)$ appear as functions of a_n's. So, of course, do df_n/dr at $r=r_0$. If we assume all f_n and df_n/dr given as initial conditions at r_0, we can integrate outwards from r_0 to infinity and find the a_n's. We might therefore attempt to solve the problem by taking "reasonable" initial values, such as the presence originally of only the high energy particles (i.e., $f_0(r_0)=1$, all other $f_n(r_0)=0$), and then applying perturbation theory. There are two objections to this procedure. Firstly, the initial values must represent the physical fact that only outgoing waves are present. Slight errors in these values would be equivalent to a small admixture of the solution which at infinity represents an incoming wave. Inside the potential barrier this solution grows exponentially as r is increased, and hence appreciable amounts of outgoing wave might appear in the solution at large r, for relatively small initial errors.

In the second place, the perturbation technique itself turns out to be invalid here. Dancoff[3] has studied this problem by perturbation methods and has paid particular attention to the case in which the energy difference between the interacting states is small ($\lesssim$500 kev). He found excitation probabilities greater than unity and pointed out that while this may indicate that the effect is appreciable for these energies, it also means that the perturbation theory is unreliable. The present author also originally used a perturbation theory which required that $|f_n| \ll |f_0|$. Although this condition holds at r_0 and at infinity, it was found that at certain intermediate points $|f_n|$ was as much as 100 times greater than $|f_0|$ in some cases.

We have developed a method for integrating outward which avoids these difficulties, but it is more laborious than the inward integration used in this paper, and is no more reliable (except perhaps when the differences between the energies of the states is small).

III. METHOD OF SOLUTION

Consider that set of M functions f_n which satisfy the N-equations (2.12) with the boundary conditions that, at $r=\infty$, $f_j \sim a_j \exp(ik_j r)$ and $f_n = df_n/dr = 0$, if $n \neq j$. Call these functions f_{nj}. For a fixed j, f_{nj} constitute a set of solutions of (2.12); as j runs through all values from 0 to $N-1$, we obtain N linearly independent sets. We form by a combination of these solutions another set of solutions f_n defined by

$$f_n = \sum_{j=0}^{N-1} f_{nj}, \quad n=0, 1, \cdots (N-1). \tag{3.1}$$

These functions are the functions which provide the solution of our problem. Firstly, they have the correct asymptotic behavior for

$$f_{nn} \sim a_n \exp(ik_n r), \tag{3.2}$$

$$f_{nj} = df_{nj}/dr = 0 \quad \text{if} \quad j \neq n, \tag{3.3}$$

and, therefore, by (3.1), $f_n \sim f_{nn}$. Secondly, the N constants a_n are still at our disposal and can be fixed as discussed in the previous section.

Consider now the set j. Let $E_j=\frac{1}{2}mv_j^2$,

$$k_j=mv_j/\hbar,\ x=k_jr,\ \kappa_j=4Ze^2/\hbar v_j,$$
$$\gamma_{nj}=1/\gamma_{jn}=k_n/k_j. \tag{3.4}$$

Since f_{jj} is the only non-zero function of the set at $x=\infty$, we employ a perturbation method for integrating inwards. Thus, treating $|f_{nj}|\ll|f_{jj}|$ and neglecting f_{nj} on the right-hand side, (2.12) becomes

$$d^2f_{nj}/dx^2+\{\gamma_{nj}^2-\gamma_{nj}\kappa_n/x-l_n(l_n+1)/x^2\}f_{nj}$$
$$=f_{jj}\sum_{k=|l_n-l_j|}^{l_n+l_j}B_k^{nj}/x^{k+1} \tag{3.5}$$
$$=F_{nj}(x)f_{jj}. \tag{3.6}$$

Here $B_k^{nj}=A_k^{nj}k_j^{k-1}$. A_k^{nj} contains in Q_k^{nj} a factor of the order of r_i^k where r_i is a position of a proton in the nucleus. Now k_jr_i is of order 1. Hence B_k^{nj} contains the factor $r_i^kk_j^{k-1}$ which is of order r_i. Even after multiplication by $me^2/\hbar^2$, this is still small. Also x is always greater than unity and is about 10 only a short distance from the nucleus. Thus in the equation satisfied by f_{jj} itself, *viz.*,

$$d^2f_{jj}/dx^2+\{1-\kappa_j/x-l_j(l_j+1)/x^2\}f_{jj}$$
$$=f_{jj}\sum_{k=1}^{2l_j}B_k^{jj}/x^{k+1}, \tag{3.7}$$

the terms on the right-hand side are, in general, negligible compared to $l_j(l_j+1)/x^2$, and may be neglected. (If $l_j=0$, the right-hand side is zero.) However, the solution to be developed below allows for the effect of the right-hand side to be estimated if desired.

We define the confluent hypergeometric function $X_n(x)$ as follows:

$$d^2X_n/dx^2+\{1-\kappa_n/x-l_n(l_n+1)/x^2\}X_n=0, \tag{3.8}$$
$$X_n\sim\exp i(x+\eta_n),\quad\text{as}\quad x\to\infty. \tag{3.9}$$

The constant η_n is defined in Eq. (4.5).

From (3.7) and (3.2), we see that (except for the small right-hand side of (3.7))

$$f_{jj}=a_jX_j. \tag{3.10}$$

We use this value in the right-hand side of (3.6) and also with

$$f_{nj}(x)=v_{nj}(x)X_n(\gamma_{nj}x). \tag{3.11}$$

Then

$$v_{nj}(\infty)=(dv_{nj}/dx)_\infty=0. \tag{3.12}$$

Using (3.6), (3.11), (3.10), and (3.8) and simplifying, the equation for v_{nj} becomes, if we suppress the suffixes on v, γ, and F,

$$X_n(\gamma x)v''(x)+2\gamma X_n'(\gamma x)v'(x)=a_jF(x)X_j(x). \tag{3.13}$$

The $'$ denotes differentiation with respect to the argument of the function. This can be written

$$(d/dx)\{X_n^2(\gamma x)v'(x)\}=a_jF(x)X_j(x)X_n(\gamma x),$$

and, therefore,

$$v'(x)=a_jX_n^{-2}(\gamma x)\int_\infty^x F(t)X_j(t)X_n(\gamma t)dt$$

and

$$v(x)=a_j\int_\infty^x\Big\{X_n^{-2}(\gamma t)\int_\infty^t F(u)X_j(u)$$
$$\times X_n(\gamma u)du\Big\}dt. \tag{3.14}$$

The lower limits are determined by the boundary conditions (3.12). Thus the functions f_{nj} and hence, by (3.1), f_n have been found in terms of certain hypergeometric functions.

If it is desired to take account of the correction to f_{jj} caused by the non-vanishing of the right-hand side of (3.7), a similar procedure can be used giving

$$f_{jj}=a_jX_j\Big\{1+\int_\infty^x dtX_j^{-2}(t)$$
$$\times\int_\infty^t\sum(B_k^{jj}/x^{k+1})X_j^2(u)du\Big\}. \tag{3.15}$$

The integral is always a small quantity compared to unity, for B_k^{jj} is of the order 10^{-4} or less and the remainder of the integral is at most 10. (The method of evaluation is indicated in the next section.)

The expression (3.14) can be further simplified by introducing

$$g_n(x)=\int^x X_n^{-2}(t)dt, \tag{3.16}$$

where the additive constant is to have a convenient value, to be chosen later. Then, inte-

grating (3.14) by parts, we find

$$v_{nj}(x)=a_j\gamma_{jn}\int_\infty^x\{g_n(\gamma_{nj}x)-g_n(\gamma_{nj}t)\}\times F_{nj}(t)\mathrm{X}_j(t)\mathrm{X}_n(\gamma_{nj}t)dt. \quad (3.17)$$

This equation expressed a formal solution of the problem. Its usefulness depends on a number of things. Firstly, we must be satisfied that the perturbation solution is close to the actual solution. Secondly, for (3.17) to be valuable, we must have manageable explicit expressions for the hypergeometric functions which appear. Thirdly, since f_{nj} are found approximately, there is a danger that the sum $\sum_j f_{nj}(=f_n)$ is such that the terms largely cancel, leaving only a remainder of the order of the errors of individual terms. We must ensure that this is not so.

IV. EVALUATION OF THE SOLUTION

The problem has been formulated in terms of a complex energy E which represents the decay process. However, in the numerical calculations which we are about to outline, we ignore the imaginary part of E. This is justified, since the imaginary part is so small that it does not have any appreciable effect on the values of the functions considered in this section.

The first step in the evaluation of (3.17) is to obtain an explicit expression for $\mathrm{X}_n(x)$. This function depends on κ_n, which is usually about 50. Thus we want the asymptotic formulae for large κ_n. These have been obtained in a number of papers. We shall use the particular result[5] that, when $l=0$,

$$\mathrm{X}=(\cot\alpha)^{\frac{1}{2}}\exp(\omega), \quad (4.1)$$

$$\omega=\kappa(\alpha-\cos\alpha\sin\alpha), \quad (4.2)$$

and

$$\cos^2\alpha=x/\kappa. \quad (4.3)$$

Suffixes have been dropped. (The term of X in $\exp(-\omega)$ which appears inside the barrier is quite negligible for the calculation in this paper.) These equations were developed primarily for the region where $x<\kappa$. However, it can be seen that this restriction is not essential to their derivation, and the expression (4.1) equally represents the hypergeometric function for large x. This may also be checked directly. The exact definition is

$$\mathrm{X}=\exp(-\tfrac{1}{2}\kappa\pi)(\kappa\pi)^{-\frac{1}{4}}\times\Gamma(1+\tfrac{1}{2}i\kappa)W_{-\frac{1}{4}i\kappa,\frac{1}{4}}(-2ix), \quad (4.4)$$

where W is Whittaker's function. (Compare Eq. (4.1) with Eqs. (3.18) and (3.2) of reference 5 and the definition of W.[6])

Using the known asymptotic expansion for W (see reference 6, p. 343), it can be checked that, for x tending to infinity and κ large, both (4.1) and (4.4) have the same expression, *viz.*,

$$\exp(ix-\tfrac{1}{2}i\kappa\log x+i\eta)\{1+0(1/x)\},$$

where

$$\eta=\eta_n=\tfrac{1}{4}\pi+\tfrac{1}{2}\kappa_n(\log\kappa_n-1-\log 4). \quad (4.5)$$

Thus when $l_n=0$, we shall use (4.1) for X_n.

When $l_n>0$ it is most convenient to employ a suitable recursion formula to estimate X_n.[7] For example, if $l_n=1$,

$$\mathrm{X}_n=C(1/x+\tfrac{1}{2}\kappa_n-d/dx)(\cot\alpha_n)^{\frac{1}{4}}\exp(\omega_n)\doteq C(\tfrac{1}{2}\kappa_n+\tan\alpha_n)(\cot\alpha_n)^{\frac{1}{4}}\exp(\omega_n). \quad (4.6)$$

As $x\to\infty$, $\tan\alpha_n\to -i$. Hence, for the correct infinity behavior, we choose C so that

$$\mathrm{X}_n=(1-2i/\kappa_n)^{-1}(1+2\tan\alpha_n/\kappa_n)\times(\cot\alpha_n)^{\frac{1}{4}}\exp(\omega_n). \quad (4.7)$$

Equation (4.6) cannot be used near $x=\kappa$, for there $d\mathrm{X}/dx$ is not equal to the derivative of the approximate expression for X, which is actually the first term of a semiconvergent series.[5] However, when x is of the order of κ, the centrifugal term is very small compared with $1-\kappa/x$ (except, of course, in the actual limit), and hence the solutions are almost independent of l_n in this region. Thus even when x is near κ, (4.7) gives X_n with only a slight error, since when α approaches zero, X_n behaves, aside from the constant factor, as if l_n were zero.

The correcting factor in (4.7) is never very different from 1, since, at the nuclear radius, $\tan\alpha_n/\kappa_n\sim 0.05$ and it decreases to zero at the boundary of the potential barrier; then it becomes imaginary and its magnitude changes from zero to about 0.02 as x goes to infinity. Thus, in calculating the integrals (3.17) and

[5] M. A. Preston, Phys. Rev. **71**, 865 (1947).

[6] E. J. Whittaker and G. N. Watson, *Modern Analysis* (Cambridge University Press, London, 1946), p. 340.

[7] L. Infeld, Phys. Rev. **59**, 743 (1941); also see reference 5, Eq. (5.2).

TABLE I. Values of I.

$r\times10^{13}$ cm	I_{n0}^-	I_{n0}^+	I_{0n}^-
8.27	$4.1+9.6i$	0.24	5.7
9.36	$3.4+10.6i$	0.26	6.0
10.0	$2.9+11.2i$	0.27	6.1
11.5	$1.6+12.4i$	0.31	6.2
16.0	$-2.9+15.5i$	0.38	6.3

(3.16), the effect of this term can be represented by a constant mean value which is not very different from one.

If l_n is not too much greater than one, considerations very similar to these will still apply.

Now

$$d/dx(\tfrac{1}{2}\exp(-2\omega))=\exp(-2\omega)\tan\alpha.$$

Therefore, we may define

$$g_n(x)=\tfrac{1}{2}\rho_n'\exp(-2\omega_n), \tag{4.8}$$

where ρ' is the mean value factor, almost unity, which we have just discussed. Then

$$g_n(\gamma_{nj}t)=\tfrac{1}{2}\rho_n'\exp\{-2\gamma_{jn}\kappa_j(\beta_{nj}-\cos\beta_{nj}\sin\beta_{nj})\} \tag{4.9}$$

$$=\tfrac{1}{2}\rho_n'\exp(-2\Omega_{nj}), \tag{4.10}$$

where

$$\cos\beta_{nj}=\gamma_{nj}\cos\alpha_j=\gamma_{nj}(t/\kappa_j)^{\frac{1}{2}}. \tag{4.11}$$

Substituting these explicit forms of g_n, X_n, X_j in the expression (3.17) for v_{nj}, we find

$$v_{nj}(k_jr)=v_{nj}(x)=\tfrac{1}{2}a_j\gamma_{jn}\rho_{nj}(\cot\alpha_0\cot\beta_0)^{\frac{1}{2}}\times\exp(\omega_0-\Omega_0)\sum_k B_k^{nj}\times\{I_{nj}^-(k)-I_{nj}^+(k)\}/x^{k+1}, \tag{4.12}$$

$$v_{jn}(k_nr)=\tfrac{1}{2}a_n\rho_{jn}(\cot\alpha_0\cot\beta_0)^{\frac{1}{2}}\times\exp(\Omega_0-\omega_0)\sum_k B_k^{nj*}\times\{I_{jn}^-(k)-I_{jn}^+(k)\}/x^{k+1}, \tag{4.13}$$

where

$$I_{nj}^+(p-1)=I_{jn}^+(p-1)=\int_{k_jr}^{\infty}\exp(\Omega-\Omega_0+\omega-\omega_0)(x/t)^p\times(\cot\alpha\cot\beta\tan\alpha_0\tan\beta_0)^{\frac{1}{2}}dt, \tag{4.14}$$

$$I_{nj}^-(p-1)=\int_{k_jr}^{\infty}\exp(-(\Omega-\Omega_0)+\omega-\omega_0)(x/t)^p\times(\cot\alpha\cot\beta\tan\alpha_0\tan\beta_0)^{\frac{1}{2}}dt, \tag{4.15}$$

$$I_{jn}^-(p-1)=\int_{k_jr}^{\infty}\exp((\Omega-\Omega_0)-(\omega-\omega_0))(x/t)^p\times(\cot\alpha\cot\beta\tan\alpha_0\tan\beta_0)^{\frac{1}{2}}dt. \tag{4.16}$$

Here we have written Ω, ω, β, α for Ω_{nj}, ω_j, β_{nj}, α_j and have denoted by subscript $_0$ the value of any quantity when $t=x=k_jr$. These integrals are to be found by numerical methods. If $E_n<E_j$, I_{jn}^- as it stands can be evaluated for a given value of k_jr; its integrand is a decreasing exponential. However, I_{nj}^- has an increasing exponential integrand inside the potential barrier, and in the external regions where it is oscillatory, the amplitude of the oscillations is of the same order of magnitude as the value of the integrand near the end of the barrier. However, the integral is convergent since, as $t\to\infty$, this amplitude goes to zero like t^{-p}. To evaluate I_{nj}^- numerically it is therefore necessary to transform it. This can be done by the substitution of the complex variable

$$u=2i\ \text{arc}\cos\{\gamma_{nj}(t/\kappa_j)^{\frac{1}{2}}\}. \tag{4.17}$$

It can then be seen that in the u-plane the path of integration can be taken as the line parallel to the real axis from $u=i\beta_0$ to $u=\infty+i\beta_0$. On this path, both real and imaginary parts of the integrand have a rapidly decreasing exponential behavior. The numerical work is laborious, but the results are reliable.

To find the numerical value of I_{nj}^+ either the method for I_{jn}^- or that for I_{nj}^- can be used.

V. APPLICATION TO POLONIUM

As an example, we apply the considerations of the previous sections to the case of polonium, where Chang has reported twelve low energy radiations. We consider first the simplified case of a spectrum of two lines—those connected with the ground state and a typical excited state. For the latter, we have taken the line labeled α_9 by Chang. Thus the energies are $E_0=5.303$ and $E_n=E_9=4.111$ Mev. Then, in the notation of the previous sections, we have, ignoring the

effect of all states but these two,

$$f_0=f_{00}(k_0r)+f_{0n}(k_0r), \quad f_{nn}=a_nX_n(k_nr),$$
$$f_n=f_{n0}(k_nr)+f_{nn}(k_nr), \quad f_{n0}=v_{n0}(k_0r)X_n(k_nr),$$
$$f_{00}=a_0X_0(k_0r), \quad f_{0n}=v_{0n}(k_nr)X_0(k_0r).$$

We shall study this case on the assumption that the transition is "dipole,"*** that is $p=2$ and $l_0=0$, $l_n=1$. Then $X_0=(\cot\alpha)^{\frac{1}{2}}e^{\omega}$, where $\cos^2\alpha=k_0r/\kappa_0$, and $\omega=\kappa_0(\alpha-\cos\alpha\sin\alpha)$. Also $X_n=\{\kappa_n+2\tan\beta)/(\kappa_n-2i)\}(\cot\beta)^{\frac{1}{2}}e^{\Omega}$, where $\cos^2\beta=k_nr/\kappa_n$, $\Omega=\kappa_n(\beta-\cos\beta\sin\beta)$. Then we have

$$v_{n0}(k_0r)=\tfrac{1}{2}a_0\gamma_{0n}\rho_{n0}(\cot\alpha_0\cot\beta_0)^{\frac{1}{2}}\exp(-(\Omega_0-\omega_0))\times B_1^{n0}\{I_{n0}^{-}(1)-I_{n0}^{+}(1)\}/(k_0r)^2$$

and

$$v_{0n}(k_nr)=\tfrac{1}{2}a_n\rho_{0n}(\cot\alpha_0\cot\beta_0)^{\frac{1}{2}}\exp(\Omega_0-\omega_0)\times B_1^{n0*}\{I_{0n}^{-}(1)-I_{n0}^{+}(1)\}/(k_0r)^2.$$

The values of the integrals I have been calculated and are shown in Table I. The meaning factors ρ_{n0} and ρ_{0n} can be seen to lie between 0.95 and 1.05. We shall replace them by unity. We also write

$$B_1^{n0}=A_1^{n0}=(2m/\hbar^2)2^{\frac{1}{2}}Q_1^{n0}=(2^{5/2}me^2/3\hbar^2)R, \quad (5.1)$$

where R is of the same order as, e.g.,

$$C_{10}^{n0}=\int u_n^*\Sigma r_i\cos\theta_i u_0 d\xi.$$

We then find

$$f_0(r_0)=X_0(a_0+a_n\exp(i\delta)R^*B),$$
$$f_n(r_0)=X_n(a_n\exp(i\delta)+a_0RD), \quad (5.2)$$

where r_0 is the nuclear radius and a_0, a_n are real. The values of the known quantities in Eqs. (5.2) are shown in Table II. Note that B and D, which represent the effect of the electrostatic interaction, are not sensitive to the value of the nuclear radius. Since the effect is an extra-nuclear one, occurring over distances large compared with r_0, this is a satisfactory result. We may also note the justification of the perturbation methods. If the perturbation calculation is justified, it is necessary that $|RDX_n|\ll X_0$ and $|R^*BX_0|\ll X_n$. By its definition (5.1) $|R|$ is certainly less than 10^{-12}, the greatest possible distance of a proton from the center of the nucleus; hence these inequalities hold.

*** In γ-ray transition dipole and quadrupole effects are of approximately equal importance; however, in the long-range effects considered here we may expect the dipole to predominate.

TABLE II. Parameters in Eqs. (5.2).

$r_0\times10^{13}$ cm	X_0	X_n	B	D
8.27	6.0×10^{13}	5.1×10^{17}	4.1×10^{14}	$(0.4+1.0i)10^7$
9.36	6.6×10^{13}	5.1×10^{16}	3.4×10^{14}	$(0.3+1.0i)10^7$
10.0	2.0×10^{13}	1.5×10^{16}	3.0×10^{14}	$(0.2+1.0i)10^7$

Next, let us consider the effect of assuming for a_0 and a_n the values given by Chang.[1] Since the squares of these quantities are proportional to the respective partial decay constants, we have $a_n/a_0\doteq7\times10^{-3}$. ($\lambda_0=2.8\times10^{-12}$, $\lambda_0=5.9\times10^{-8}$ sec.$^{-1}$.) Now $|DR|<10^{-5}$; thus $|a_0DR|\ll a_n$. Therefore $f_n=a_n\exp(i\delta)X_n$. Also $|R^*Ba_n|$ is at most of the order of a_0, but since 10^{-12} is probably a high value for $|R|$, the term $a_n\exp(i\delta)R^*B$ does not alter f_0 very much. Hence $|f_n/f_0|\doteq a_nX_n/a_0X_0\doteq10^2$. This means that the probability of decay with energy E_n is much greater (10^2) than with energy E_0, *in the absence of the barrier*. At first sight, this might appear to be the explanation of Chang's results; *viz.*, the emission of an α-particle with energy E_0 is a forbidden process as compared to the emission with energy E_n, but a transition from E_n to E_0 takes place outside the nucleus. However, we shall see that these assumptions are in contradiction with the observed absolute intensity of the α-particles.

By the conservation theorem, we have, for the general case of N states,

$$\frac{\partial}{\partial t}\int\sum_0^{N-1}\phi_m\phi_m^*dv=-\frac{\hbar}{2im}\int\Sigma(\phi_m^*\,\mathrm{grad}\phi_m-\phi_m\,\mathrm{grad}\phi_m^*)\cdot\mathbf{n}d\sigma,$$

where the integrations are over the volume and surface of a sphere of large radius and ϕ_m is defined by Eq. (2.4). Now the energy is complex so that $\sum\phi_m\phi_m^*$ contains a factor $\exp(-\lambda t)$ and the rate of charge of the volume integral is $-\lambda\int\sum\phi_m\phi_m^*dv$. This integral can be split into two parts, one over the region inside the nucleus and one over the region outside, i.e.,

$$\int\sum\phi_m\phi_m^*dv=\sum_m(I_i^m+I_0^m)=\sum I_i^m+\int_{r_0}^{\infty}\sum|f_m|^2dr.$$

However, $|\phi_m|$ decreases very rapidly outside the nucleus, so $\sum I_0^m$ can be neglected. For the surface integral, since the sphere is large, we can use the asymptotic expression for ϕ_m. The result is

$$\lambda = \sum_m v_m |a_m|^2 / \sum_m I_i^m. \tag{5.3}$$

In the case we have been considering where only two levels are concerned,

$$\lambda = v_0 a_0^2/(I_i^0 + I_i^n), \quad \text{since} \quad v_n a_n^2 \ll v_0 a_0^2.$$

We must now consider the integrals I_i^0 and I_i^n which involve the behavior of the wave functions inside the nucleus. It is reasonable to make these functions and their derivatives continuous at the nuclear boundary. We have seen that with Chang's intensities, $|f_n/f_0| \sim 10^2$, and we may also note that f_n'/f_n and f_0'/f_0 are of comparable magnitude. Thus whatever the explicit internal expression of the wave functions, it is clear that $I_i^n \gg I_i^0$. Hence, with Chang's relative intensities

$$\lambda = v_0 a_0^2/I_i^n = (v_0 a_0^2/v_n a_n^2)(v_n/\mathfrak{g}_i^n), \tag{5.4}$$

when $\mathfrak{g}_i^n$ is the internal integral in the standard theory without interaction. (The function f_n differs from X_n, which corresponds to it in the standard theory of radioactivity, only by the factor a_n.) But since $a_0 \gg a_n$, the partial decay constant $\lambda_n \doteq (v_n a_n^2/v_0 a_0^2)\lambda$. Hence $\lambda_n = v_n/\mathfrak{g}_i^n = \lambda_n^0$, where λ_n^0 is the partial decay constant on the standard theory. Thus, when interaction is allowed for, the partial decay constant is practically unchanged from that expected on the standard theory.

In other words, although we may assume suitable conditions to obtain the *relative* intensities found by Chang, the total decay constant, which is determined from the partial one by the ratio $v_0 a_0^2/v_n a_n^2$, is much less than the experimental value. For example, if we take the nuclear radius 8.3×10^{-13} cm (which on the standard one-body theory fits the experimental data for the intense main line[5]), we find that if $a_n/a_0 \doteq 7\times10^{-3}$, then $\lambda \doteq 5\times10^{-14}$ sec.$^{-1}$, whereas the experimental value is 6×10^{-8} sec.$^{-1}$. Of course with a larger radius we can increase the value of λ. Taking $r_0 = 11.5\times10^{-13}$ cm, we find $\lambda \doteq 1.5\times10^{-9}$ sec.$^{-1}$ and with $r_0 \doteq 12.5\times10^{-13}$ we find that λ is about the observed value. However, the nuclear radius as a parameter in the one-body model is always less than 10^{-12} cm and, using the law $r_0 = R_0 A^{\frac{1}{3}}$, we would expect about 9×10^{-13} cm for polonium. A radius such as 12.5×10^{-13} cm would imply a most unusual extension of the region where nuclear forces hold.

The above arguments are not essentially altered if we allow for the emission of particles in more than one low energy state which can interact with the nucleus and acquire the energy of the main line. Equations (5.2) are then replaced by

$$f_0/\chi_0 = a_0 + \sum_1^{N-1} a_m e^{i\delta_m} R_m^* B_m,$$

$$f_m/\chi_m = a_0 R_m D_m + a_m e^{i\delta_m}, \quad m = 1, 2, \cdots (N-1).$$

Now as the difference between E_0 and E_m decreases, D_m increases and so presumably does R_m. However, for m great enough, we have as before $|a_0 D_m R_m| \ll a_m$, if we use Chang's intensities. Also B_m decreases with $E_0 - E_m$; hence $|a_m R_m^* B_m|$ remains of the same order as a_0 or less for all m. Thus it still follows that $|f_m/f_0| \gg 1$, at least for m large enough. Thus we can still reduce (5.3) to an equation similar to (5.4), *viz.*,

$$\lambda \doteq v_0 a_0^2 / \sum_M^{N-1} a_m^2 \mathfrak{g}_i^m,$$

where M is the lowest value of m for which $|f_m/f_0| \gg 1$ is valid. That is

$$\lambda \doteq v_0 a_0^2 \Big/ \left(\sum_M^{N-1} a_m^2 v_m/\lambda_m^0 \right) < (v_0 a_0^2/v_n a_n^2)\lambda_n^0,$$

where n is some value of $m > M$. Thus, just as before, λ is much less than the experimental value, unless a large radius is taken.

To summarize, we may say that Chang's results can be explained with our model only on the basis of two assumptions: that the direct transition to the ground state is (more or less) forbidden and electrostatic interactions occur after the α-particle has left the nuclear region and that the radius of this region must be much larger ($\sim$25 percent) than it is in the case of other radioactive elements. This latter assumption would involve us in many new difficulties. It is to be noted that any explanation involving strictly nuclear behavior does not affect this

point; it could only alter the ratio (f_0/f_n) at r_0. Coupled with the inability of Zajac, Broda, and Feather[4] to find γ-rays which would confirm Chang's results, these theoretical arguments would suggest that the source of the lines observed by Chang was not in the polonium nucleus.

VI. GENERAL DISCUSSION

We may consider what the effect of the electrostatic interaction will be in a general case. Considering again for simplicity the case of only one level in addition to the ground state, Eqs. (5.2) can be solved for a_0 and a_n. The result is

$$\begin{aligned} a_0 &= f_0/\mathrm{X}_0 - R^*Bf_n/\mathrm{X}_n, \\ a_n e^{i\delta} &= f_n/\mathrm{X}_n - DRf_0/\mathrm{X}_0. \end{aligned} \tag{6.1}$$

In general the quantities $|f_0|$ and $|f_n|$, which as indicated in Section III determine the probabilities of decay in the absence of the potential barrier, will be of the same order since E_0-E_n is small compared with the total energy of the escaping particle. In (6.1) the terms f_0/X_0 and f_n/X_n represent the effect of the barrier in the standard theory and the other terms R^*Bf_n/X_n and RDf_0/X_0 introduce the corrections due to the interaction after emission. If we assume $|f_0| \doteq |f_n|$ we see that the interaction alters a_0 by a fractional amount $|R^*B\mathrm{X}_0/\mathrm{X}_n|$ and alters a_n by the fraction $|RD\mathrm{X}_n/\mathrm{X}_0|$. To form some idea of the magnitude of these changes we may consider the case of polonium for which we have worked out numerical values. Taking $R=10^{-12}$, we shall obtain upper limits for the effect. Then $|R^*B\mathrm{X}_0/\mathrm{X}_n| < 10^{-2}$ and $|RD\mathrm{X}_n/\mathrm{X}_0| < 10^{-1}$. Since the decay constants involve a_n^2, these correspond to changes of certainly less than 2 percent in λ_0 and 20 percent in λ_n. Thus the upper limit of the effect is a 20 percent change in the decay constant of the state of lower α-particle energy. When it is remembered that the dependence of λ on energy is logarithmic, it will be realized that even this upper limit does not give a very large effect. The above calculations are for $E_0-E_n=1.2$ Mev.

As E_0-E_n decreases, the effect of the interaction becomes more pronounced. In fact as this difference gets small it can be confirmed that the ratio $|R^*B\mathrm{X}_0/\mathrm{X}_n|$ becomes greater than one (although $|DR\mathrm{X}_n/\mathrm{X}_0|$ probably decreases slightly). However, when this happens we have clearly violated a condition for the validity of the perturbation assumptions implied in the use of Eq. (3.5). Nevertheless, we are led to suspect that when the energy difference is of the order of 500 kev or less the interaction with the nucleus after emission may appreciably affect the relative intensities of the two α-particle groups. As we have indicated above, it is this region of energy differences to which Dancoff[3] has paid particular attention, and his results also indicate that the effect is probably fairly large. In some of the elements which have a fine structure in the α-spectrum, the lower energy α-particles do not obey the Geiger-Nuttall law very exactly. This has been attributed to a non-zero value of the angular momentum quantum number l. We now see that if the energy levels are separated by less than about 500 kev (e.g., RaC) the partial decay constants may be altered by the electrostatic interaction also. It is not easy to separate these two causes, since there are at present few independent estimates of either l or R, but they may have effects of roughly the same order of magnitude, changing λ_n by a factor of about 2 or 3.

We may also consider, briefly the effect when the ground state transition is accidentally more or less forbidden, i.e., $|f_0| \ll |f_n|$. Then (6.1) becomes $a_n \exp(i\delta) = f_n/\mathrm{X}_n$ and $a_0 = f_0/\mathrm{X}_0 - R^* \times \mathrm{Ba}_n \exp(i\delta)$. Thus, if $|f_0|$ is very small a line may appear with intensity $|R^*Ba_n|^2$, which would be less than that expected for energy E_0. On the other hand, if $|f_0|$ is somewhat larger, there may be destructive interference making a_0 vanish, and what would have been a line with abnormally low intensity disappears entirely. There does not appear to be any example of either of these processes in the present experimental data.

It is a pleasure to record my appreciation of many stimulating discussions with Professor R. E. Peierls which have been of the greatest help in this investigation.

Measurement of the Radioactive Decay Constant of ThC′ Using a Coincidence Method*

F. W. VAN NAME, JR.**
*Sloane Physics Laboratory,*** *Yale University, New Haven, Connecticut*

(Received September 27, 1948)

The radioactive half-life of ThC′ has been measured using a delayed coincidence circuit of high resolution. A theory of the effect on the coincidence rate of variations in pulse formation in counters has been developed and compared with experiment. The radioactive decay constants of ThC′ have been found to be:

$$T=(2.2\pm0.1)\times10^{-7}\text{ sec.},$$
$$\lambda=(3.15\pm0.14)\times10^{6}/\text{sec.}$$

INTRODUCTION

WARTIME research applied to coincidence circuits has improved the resolution possibility considerably. A circuit built at this Laboratory by Schultz and Beringer[1] has a resolving time of the order of 10^{-8} sec. Since the half-life of ThC′ is approximately 2.5×10^{-7} sec., it should be possible to use this circuit to measure directly the radioactive constant of ThC′, and at the same time investigate the capabilities of the circuit.

The first direct measurement of the half-life of ThC′ was made by Dunworth[2] in 1939. He measured the number of coincidences between electrons from ThC and subsequent alphas from ThC′ as a function of the resolving time of the coincidence circuit. From the data he inferred a value of $(3\pm1)\times10^{-7}$ sec. for the half-life of ThC′. In 1943 Bradt and Scherrer[3,4] used the same integral method, but included theoretical consideration of the effect of variations in time of formation of pulses in gas-filled counters on the coincidence rate. They found the value $(2.6\pm0.4)\times10^{-7}$ sec. for the half-life of ThC′.

EXPERIMENTAL PROCEDURE

In the present experiment the counters were placed front-to-front with the source in between. Electrons from ThC enter one channel, to be called channel No. 1, which counts only electrons. The corresponding voltage pulses are then passed down a delay line consisting of a helical coil forty-five centimeters long. An electromagnetic pick-up coil receives the pulses at adjustable time delays up to the total delay of the line. The delay line was calibrated and found to be uniform, with a delay of one microsecond for 26.3 cm of line. Alphas from ThC′ enter the second channel, to be called channel No. 2, which counts only alphas, and the corresponding voltage pulses are delayed a small, fixed amount. The pulses from the two channels, after these time delays, then arrive at the discriminator, which will register a count if the two pulses arrive with a time difference less than approximately 10^{-8} sec. The problem is to determine the half-life of ThC′ from the observed coincidence rate *versus* relative delay curve, including in the theory the effect of variations in pulse formation in the counters.

Two preliminary experiments were also performed, similar to those described by Schultz and Beringer. The resolving time of the electronic circuit, independent of the characteristics of the counters, was measured by stimulating both channels simultaneously with a pulse from a single counter and measuring the coincidence rate as a function of relative delay. The resolving time used was found to be 1.3×10^{-8} sec. The effect of pulse variations was determined by placing the counters in line and close together,

* Part of a dissertation presented to the Faculty of the Graduate School of Yale University in candidacy for the degree of Doctor of Philosophy.

** Now at Franklin and Marshall College, Lancaster, Pennsylvania.

*** Assisted by the Joint Program of the Office of Naval Research and the Atomic Energy Commission.

[1] H. L. Schultz and E. R. Beringer, Rev. Sci. Inst. 19, 424 (1948).

[2] J. V. Dunworth, Nature 144, 152 (1939).

[3] H. Bradt and P. Scherrer, Helv. Phys. Acta 16, 251 (1943).

[4] H. Bradt and P. Scherrer, Helv. Phys. Acta 16, 259 (1943).

so that a single particle could traverse both axially, and again measuring the coincidence rate *versus* delay curve.

The source used was the active deposit of thorium on an aluminum foil one-half inch in diameter. The counters were conventional cylindrical counters filled with 20 cm pressure of argon and operated in the proportional region. The capacity-neutralized preamplifiers were similar to those described by Schultz and Beringer, and the main amplifier, delay circuits, and discriminator are the same as in their article. The recording circuit, power supplies, and auxiliary equipment were conventional in design.

THEORETICAL CONSIDERATIONS OF COINCIDENCE RATE

Any theory of coincidence rates in this type of experiment must begin by measuring or assuming a distribution of the individual times of pulse formation about their mean value. Bradt and Scherrer assumed this distribution to be Gaussian. For mathematical simplicity, the author has assumed a triangular distribution about the mean. In this connection, Madansky and Pidd[5] have measured the time delay distribution of a cylindrical counter, with a result which is roughly triangular. However, the test of the assumed distribution will be the agreement of the results of the theory with experiment.

Consider first the preliminary experiment in which the counters are placed close together and in line, both being sensitive to alphas. Let an alpha pass through both counters at time zero, and let D be the delay in channel No. 1 relative to channel No. 2. Then the probability that the pulse from counter No. 1 will arrive at the discriminator between t and $t+dt$ is assumed to be given by the triangular distribution:

$$d\alpha_1=[A-|t-D|]dt/A^2. \tag{1}$$

In the above expression, A is the half-width of the distribution, measured in centimeters, length of delay line employed. Similarly, the probability that the pulse from counter No. 2 will arrive at the discriminator between t and $t+dt$ is given by:

$$d\alpha_2=[A-|t|]dt/A^2. \tag{2}$$

[5] L. Madansky and R. W. Pidd, Phys. Rev. **73**, 1215 (1948).

Since the electronic resolving time, R, is known to be small compared to the half-width of the counter pulse distribution, A, the probability of a coincidence is given by:

$$C=2R\int d\alpha_1 d\alpha_2. \tag{3}$$

Performing the integration and letting $x=|D/A|$:

$$C=\frac{2R}{A}\left[-\frac{1}{2}x^3-x^2+\frac{2}{3}\right] \quad 0\leqslant x\leqslant 1, \tag{4a}$$

$$C=\frac{2R}{A}\left[-\frac{1}{6}x^3+x^2-2x+\frac{4}{3}\right] \quad 1\leqslant x\leqslant 2. \tag{4b}$$

Figure 1 shows a set of experimental data fitted to the above theory for the case of a single alpha-particle traversing both counters placed close together. The value of A was chosen to be 2.9 cm of delay line, corresponding to 1.10×10^{-7} sec. The fit is well within the statistical counting error of 5 percent for all points, and thus from these preliminary data the assumed distribution seems to be satisfactory. Unfortunately, counter No. 2 would not count electrons satisfactorily, so the companion experiment could not be performed for the case of an electron passing through both counters simultaneously.

Now let channel No. 1 count only electrons from ThC and channel No. 2 count only alphas from ThC′. Consider an electron emitted by ThC

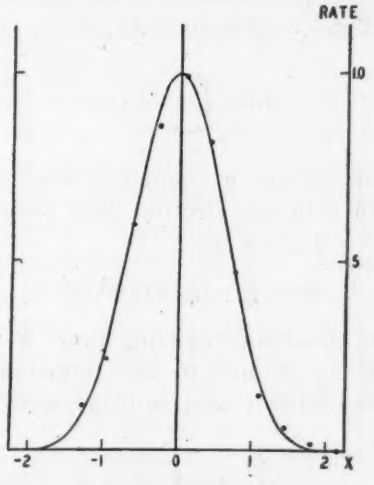

FIG. 1. Coincidence rate *versus* delay curve for the case of a single alpha traversing both counters placed close together.

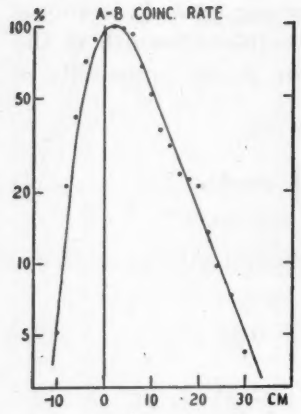

FIG. 2. Coincidence rate *versus* delay curve for the case of electron pulses from ThC delayed relative to alpha-pulses from ThC′.

at radioactive time, t', equal to zero. Then the probability of emission of the following alpha between t' and $t'+dt'$ is

$$d\alpha=\lambda e^{-\lambda t'}dt'. \tag{5}$$

The probability of the pulse arriving at the discriminator from channel No. 2 between t and $t+dt$ as a result of an alpha emitted between t' and $t'+dt'$ is found by combining Eqs. (1) and (5) (applied to channel No. 2), as follows:

$$d^2\alpha=\lambda e^{-\lambda t'}dt'[A-|t-t'|]\frac{dt}{A^2}. \tag{6}$$

However, the alpha could have been emitted at some other time satisfying $(t-A)\leqslant t'\leqslant(t+A)$ and still have its pulse arrive at the discriminator at time t. Thus, the probability of receiving a pulse at the discriminator from channel No. 2 between t and $t+dt$ is given by

$$d\alpha=\int_{t-A}^{t+A}d^2\alpha. \tag{7}$$

We now assume a triangular distribution of half-width B for the electron pulse variations in counter No. 1 given by

$$d\beta=[B-|t-D|]dt/B^2. \tag{8}$$

Since the electronic resolving time, R, is small compared to A and B, the probability of a coincidence with a relative delay setting, D, is given by

$$C=2R\int d\alpha d\beta. \tag{9}$$

The limits are determined by the fact that the electron pulse in channel No. 1 certainly arrives at the discriminator between $D-B$ and $D+B$. However, in setting up the limits it must also be remembered that the alpha is never emitted before the electron. Thus, the limits must be determined for various ranges of D and the corresponding integral found.

For large values of D, such that $D\geqslant(A+B)$, we find, on integration of Eq. (9), that the coincidence rate is:

$$C=\frac{8Re^{-\lambda D}}{\lambda^3A^2B^2}(\cosh\lambda A-1)(\cosh\lambda B-1). \tag{10}$$

Equation (10) shows that the coincidence rate decreases exponentially with delay for large values of delay. This is the important result of the theory, since it permits a direct measurement of the half-life of ThC′ from data for large delays. For smaller delays the calculation of C is straightforward, but tedious, and will not be given here.

The shape of the curve is determined by A, B, and λ, where $\lambda=0.693/T$. A has already been determined to be 2.9 cm of delay (1.10×10^{-7} sec.) from Fig. 1. Plotting data for large values of D gives a value of 0.1195/cm (3.15×10^6/sec.) for λ. Since B could not be determined, a value of 10.0 cm (3.80×10^{-7} sec.) was chosen for B. From other work at this Laboratory, this value seems reasonable, and in any event the shape of the curve is not strongly affected by small errors in B.

Using these values of the constants, Fig. 2 was plotted and compared with experimental data. The fit is seen to be fairly good. The half-life of ThC′ is found from the straight-line portion of the curve, covering four half-lives, to be 5.8 cm (2.21×10^{-7} sec.). The writer feels that the slope can be determined to within 1 cm over four half-lives, giving a probable error in the half-life of 0.25 cm.

CONCLUSION

The radioactive decay constants of ThC′ thus determined using a delayed coincidence technique are found to be:

$$T=(2.2\pm0.1)\times10^{-7}\text{ sec.}$$
$$\lambda=(3.15\pm0.14)\times10^6/\text{sec.}$$

These results agree with earlier measurements but are thought to be more accurate.

From the theory developed above it is seen that the present circuit cannot be used to measure nuclear time intervals much less than 10^{-7} sec., because of the then relatively large effect of variations in pulse formation.

In conclusion the author wishes to express his thanks to Professor H. L. Schultz and Professor E. R. Beringer for suggesting this problem and allowing the author the use of their equipment. It is also a pleasure to acknowledge a fellowship grant from the Swarthmore College Chapter of Sigma Xi during part of this work.

PHYSICAL REVIEW VOLUME 75, NUMBER 1 JANUARY 1, 1949

Observation of the Ferro-Electric Barkhausen Effect in Barium Titanate

R. R. NEWTON,* A. J. AHEARN, AND K. G. MCKAY
Bell Telephone Laboratories, Murray Hill, New Jersey

(Received August 23, 1948)

Conductivity pulses were observed immediately after a single crystal of barium titanate was placed in an electric field, but died out in a few seconds. Several experiments were designed to test the hypothesis that these pulses were caused by the Barkhausen effect. From the experiments, the volume of a Barkhausen region and the apparent velocity of a domain wall could be estimated.

WHEN a single crystal of barium titanate grown by B. Matthias[1] was placed between electrodes and inserted in the equipment used by Wooldridge, Ahearn, and Burton[2] for the observation of alpha-conductivity in diamond, it was found that conductivity pulses appeared immediately upon application of an electric field, even when no alpha-radiation was present. These pulses were quite large, and did not die out for some seconds after application of the field. They were almost all in the same direction; this direction reversed when the direction of the applied field was reversed. Perhaps one pulse in a thousand was in the wrong direction.

In order to observe this effect, it is necessary that the crystal be in a vacuum (about 10^{-2} mm). At atmospheric pressure, application of the required field gives rise to a large amount of noise, which drowns out the effect described above. This noise is readily distinguishable experimentally from the effect in question, since the former does not die out with time.

Polarizing microscope studies[3] had shown that the barium titanate crystal used had domain structure, and that, upon application of an electric field, favorably oriented domains grew at the expense of less favorably oriented ones. It therefore seemed reasonable to assume that the pulses observed were a manifestation of the ferro-electric analog to the well-known Barkhausen effect.[4] This analog has been observed for rochelle salt by Mueller,[5] and has been postulated to account for discontinuities in hysteresis loops[6] of potassium dihydrogen phosphate and barium titanate.

In order to identify the effect conclusively, we undertook the following series of essentially qualitative experiments: (a) a measure of the largest conductivity pulses, (b) a measure of the total charge transferred by all the pulses following an application of field, (c) a measure of the duration of the individual pulses, that is, the length of time during which charge is moving, and (d) a search for a Curie point (suggested to the authors by G. C. Danielson), that is, a

---

* Now at University of Tennessee, Knoxville, Tennessee.

[1] B. Matthias, Phys. Rev. **73**, 808 (1948).

[2] D. E. Wooldridge, A. J. Ahearn, and J. A. Burton, Phys. Rev. **71**, 913 (1947).

[3] B. Matthias and A. von Hippel, Phys. Rev. **73**, 1378 (1948).

[4] H. Barkhausen, Physik. Zeits. **20**, 401 (1919).

[5] H. Mueller, Phys. Rev. **47**, 175 (1935).

[6] A. von Arx and W. Mantle, Helv. Phys. Acta **17**, 299 (1944); B. Zwicker and P. Scherrer, Helv. Phys. Acta **17**, 346 (1944); A. de Bretteville, Jr., Phys. Rev. **73**, 807 (1948).

temperature at which the effect disappears more or less abruptly.

When the detailed study of the phenomenon was begun, it was found that more reliable results were obtained by reversing the field than by changing from zero to some finite value. Accordingly, when voltages are given in what follows, it is to be understood that the voltage across the crystal is changed from a plus to a minus (or vice versa) voltage of the size given.

Since the response of the amplifier is slow, the amplifier functions as an integrating device, and hence the pulse height is a measure of the total charge transferred during a pulse. From the known characteristics of the circuit used, it was computed that the largest pulses were equivalent to the transfer of 8.5×10^6 electrons all the way across the crystal. From this, we can compute the effective volume of a Barkhausen region, that is, the volume of crystal within which the direction of spontaneous polarization would have to reverse in order to give the observed motion of charge.

Let P be the polarization existing within a domain, let A be the cross section of a Barkhausen region, and l its length. The region then has equal and opposite charges of amount PA on its end faces, so that on reversing the voltage, a charge $2PA$ travels the distance l. If Q is the charge measured by the external circuit, and L the distance between electrodes, we have, on the assumption of uniform field within the crystal:

$$Q=2PA(l/L)=2Pv/L,$$

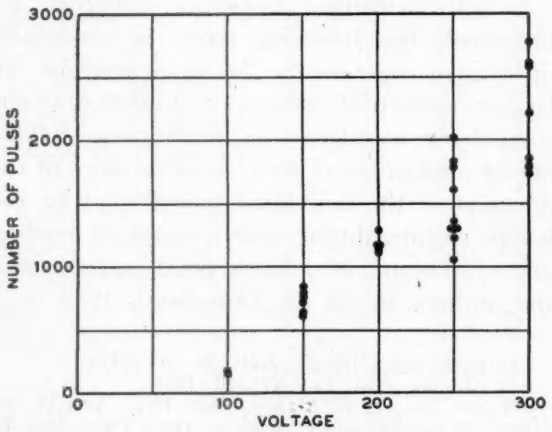

FIG. 1. Number of pulses obtained on reversal of voltage as a function of voltage.

where v is the volume of the Barkhausen region. Using[7] $P=16\times10^{-6}$ coul./cm², and the measured $L=0.15$ cm, we get

$$v=5\times10^{-9}\text{ cm}^3.$$

This seems to be a reasonable order of magnitude for the largest v involved.

In order to measure the total charge transferred by all the pulses following a change of field, the size distribution of the pulses was determined roughly by counter methods. The average pulse was estimated to be about one-fifth of the largest, or

$$\text{average } v=10^{-9}\text{ cm}^3.$$

At 300 volts, or a field of $300/0.15=2000$ volts/cm, the total number of pulses, averaged over about fifteen observations, was 2200. Hence,

$$\text{total volume change}=2200\times10^{-9}=2.2\times10^{-6}\text{ cm}^3.$$

The total volume of the crystal is 5.6×10^{-4} cm³, so that the fraction of the total volume which changed polarization discontinuously is

$$2.2\times10^{-6}/5.4\times10^{-4}=0.4\text{ percent.}$$

The variation of total number of pulses counted as a function of voltage is shown in Fig. 1. The number seems to be a linear function of voltage over the range studied, although the function does not pass through the origin. If we make the large extrapolation to 4500 volts by this linear relation, and assume that the average pulse size is constant, we get a total volume change of 6 percent. This should be compared with the figure of 7.5 percent deduced by Mason,[8] for the same field strength, from electrostriction studies.

For measuring the duration of the individual pulses, a video amplifier was used which gave a time resolution of less than 0.05 μsec., and a gain of 90 db. A free running calibrated sweep was used, giving time scales from 0.3 to 5 μsec. per inch. The input characteristics of the amplifier were such that the pulses were again integrated, and the recovery from a pulse had a time constant of 100 μsec. Thus the pulses gave in the oscilloscope what was essentially a step-

[7] J. K. Hulm, Nature 160, 127 (1947).
[8] W. P. Mason, Phys. Rev. 72, 869 (1947).

function whose rise time equals the duration of the pulse. These rise times were estimated visually, without adopting a precise definition of rise time.

With the high sweep speeds used, only a few pulses occurred while the oscilloscope beam was on the screen, so that at most, one, and frequently zero pulses, could be observed upon each voltage change. About forty pulses were observed visually with duration generally about 1 μsec., but ranging from 0.2 μsec. to greater than 6 μsec. The distribution of pulse height and duration are given in Fig. 2. The data suggest, but are far from demonstrating, a rough correlation between size and duration. For the data which were actually recorded, the pulses which gave an upward deflection had a noticeably longer average duration than those which gave a downward deflection. It is quite possible, however, that this was caused by the unavoidable subjective elements involved in selecting the pulses which were recorded.

If the volume involved is about 10^{-9} cm³, the distance which the polarizing disturbance has to travel is about 10^{-3} cm. If the time required is about 1 μsec., we have

$$\text{velocity of propagation} \approx 10^{3} \text{ cm/sec.}$$

This is a relatively low velocity, and its value may be significant.

Most of the pulses appeared smooth, but a few (perhaps 1 percent to 10 percent) showed structure. Two were observed which rose steeply at first, and then broke sharply into a portion of much slower rise. Several were observed to have three ripples, which seemed to be quite smooth and regular.

Finally, the search for a Curie point was undertaken. In order to heat the crystal in vacuum, a small heater filament was placed on one side of it, and a thermometer on the other side. The thermometer tells only whether the crystal is warming or cooling, but does not tell its temperature. The resistance of the crystal was also measured in these experiments. The temperature was adjusted by varying the current through the filament.

When large filament currents were used, considerable noise appeared on the oscilloscope, and the apparent resistance of the crystal fell to a quite low value (about 20 megohms). We attributed these effects to gas released from the filament. In order to avoid them, we tried using filament currents just large enough to hold the thermometer reading steady. Under these conditions the circuit was quiet, and the indicated resistance of the crystal stayed above 500 megohms. At a thermometer reading of about 70°C, no conductivity pulses were observed. With the thermometer reading 5° lower, many pulses were observed. This critical point was passed through several times in both directions, always with the same results. Finally, the temperature was lowered slowly to room temperature, and the response observed frequently. The response (measured by visual observation of oscilloscope activity) passed through a maximum at a temperature roughly halfway between the Curie point and room temperature. The existence of this maximum, at which the activity was considerably larger than at room temperature or just below the Curie point, was confirmed by passing through it several times in either direction. The observations are not good enough to say whether it is spread over a narrow or a wide temperature range.

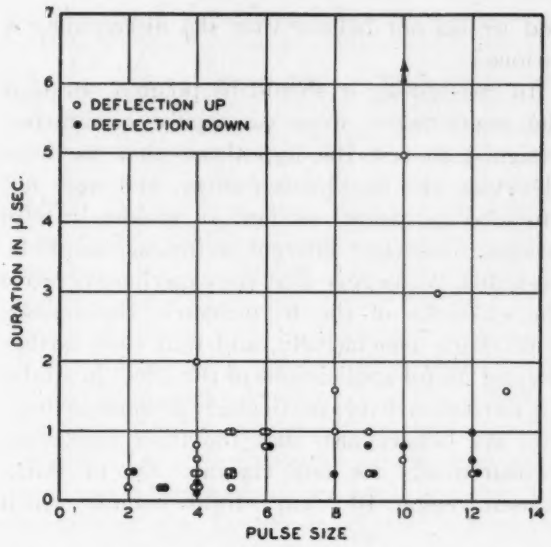

FIG. 2. Duration of pulses against pulse size on an arbitrary scale.

The thermometer reading (70°C) at the Curie point does not agree at all with the known Curie point at 120°C. Because of the geometry, however, we expect the thermometer reading to be much lower than the crystal temperature,

and we do not believe that the discrepancy is serious.

In concluding, it should be pointed out that the experiments were essentially qualitative, designed to test the hypothesis that we were observing the Barkhausen effect, and were not intended as careful studies. In making careful studies, somewhat different techniques would be desirable. We believe that the experiments prove the existence of the ferro-electric Barkhausen effect fairly conclusively, and that they further suggest useful applications of the effect in studying ferro-electricity, particularly in barium titanate. We believe also that the three important measurements for one crystal: size of Barkhausen region 10^{-9} cm^3, total volume which changes orientation discontinuously ≈ 0.4 percent of crystal (at 2000 volts/cm), and velocity of propagation $\approx 10^3$ cm/sec., are correct as to order of magnitude.

We do not believe that the photographs in Fig. 1 of de Bretteville's letter[6] support the conclusion that he was observing Barkhausen jumps. They seem to us more consistent with the hypothesis that his crystal contained regions of different coercive forces. Further, our data do not support his remark that ferro-electric domains are larger than ferro-magnetic ones. In the crystal which we used for most of our tests, the volume of a domain was certainly less than 10^{-3} cm^3, while ferromagnetic domains are frequently as large as 10^{-3} cm^3 or more.

PHYSICAL REVIEW VOLUME 75, NUMBER 1 JANUARY 1, 1949

A Calculation of the Changes in the Conductivity of Metals Produced by Cold-Work*

J. S. KOEHLER
Department of Physics, The Carnegie Institute of Technology, Pittsburgh, Pennsylvania
(Received August 20, 1948)

The increase in the electrical resistance of severely cold-worked metals has been calculated by assuming that the important change which occurs during cold-work is the introduction of large numbers of Taylor dislocations. The results obtained are as follows: The calculated increase in the electrical resistance of polycrystalline copper is in good agreement with the measured value. In case single crystals are considered, the calculations show that there is a decided dependence of the dislocation resistance on the orientation of the electric field relative to the crystallographic axes. In copper the ratio of the largest dislocation resistance to the smallest is 8. This ratio is large for materials having a small Poisson's ratio. It is found that if the dislocations are not too closely clustered no interference effects will occur. The detailed calculations for copper assume that clustering is unimportant. Measurements on single crystals are in progress.

I. INTRODUCTION

IT is found experimentally that if a metal is severely cold-worked its electrical resistance increases by several percent. The available data are summarized in Table I.[1] In the table $\Delta\rho$ is the change in the electrical resistance produced by cold-work, and ρ is the electrical resistance of the annealed metal at room temperature. It should be noted that except for the data on tungsten the specimens used were polycrystals of undetermined purity.

It is the aim of this paper to calculate theoretically the magnitude of this effect and to calculate the dependence of $\Delta\rho$ upon the orientation of the electric field with respect to the various crystallographic axes in a single crystal. The calculation will be made by assuming that the important change which occurs during cold-work is the introduction of a large number of dislocations[2] of the type shown in Fig. 1. It will

* This research was supported by Contract N6ori-47 with the Office of Naval Research. Some of the work was done while the author was a Westinghouse Research Fellow in 1941.

[1] E. Schmid and W. Boas, *Kristallplastisität* (Verlag Julius Springer, Berlin, 1935), p. 214.

[2] F. Seitz, *The Physics of Metals* (McGraw-Hill Book Company, Inc., 1943), p. 88, references to original work are given.

also be assumed that the standard quantum-mechanical methods of calculating resistivities are applicable to this problem.

An experimental investigation of the increase in the electrical resistance of pure metallic single crystals resulting from cold-work is in progress in the Physics Department at the Carnegie Institute of Technology. The measurement swill be made at low temperatures where the dislocation scattering will produce an appreciable contribution to the total resistance.

II. INTRODUCTION—THE RELAXATION TIME AND THE RESISTIVITY

Consider a metal containing N electrons per unit volume. Suppose that each electron can move freely for a mean time $2t$, after which it suffers a collision and its momentum is destroyed, t is called the "relaxation time." The resistivity is then given by:[3]

$$\rho = m/(Ne^2t), \tag{1}$$

where m is the mass of the electron and e is its charge. It can be shown[4] that this equation is still valid if quantum mechanics is used; the classical and quantum treatments differ in their calculation of t.

It will also be assumed that Matthiesson's rule is valid so that

$$\rho = \rho_{\text{thermal}} + \rho_{\text{dislocation}}, \tag{2}$$

where each kind of resistance is related to its characteristic relaxation time by an equation of type (1). These assumptions lead to the result that

$$\Delta\rho/\rho = \rho_{\text{dislocation}}/\rho_{\text{thermal}} = t_{\text{thermal}}/t_{\text{dislocation}}. \tag{3}$$

Since t_{thermal} has been calculated theoretically,[5] a comparison with experiment can be made when $t_{\text{dislocation}}$ has been calculated. The calculation of $t_{\text{dislocation}}$ is the principal aim of this paper.

A short discussion of the assumptions will be given before proceeding. According to present theoretical ideas,[6] the procedure adopted above should be valid in two temperature regions: First in the range where the temperature is large compared with the Debye Θ of the material, and second in the range where the temperature is small compared with the Debye Θ. Deviations from Matthieson's rule, if they occur at all, should appear at temperatures in the vicinity of the Debye Θ. The experimental data available[7] indicates that Matthiesson's rule is valid over a wide range of temperatures, including the range containing the Debye Θ of the material in question. Deviations are sometimes found at very low temperatures. The experimental tests include cases where the temperature independent part of the resistance was primarily produced by impurities and other cases where it was caused by plastic strains. In Table II some results of experimental tests of the rule have been assembled.[7] In this table Matthiesson's rule has been used to calculate ρ_T(obs.), the "observed" thermal portion of the resistivity, and this thermal resistivity has been adjusted so that it takes the value one at zero degrees centigrade. The calculated values of the thermal resistivity ρ_T(calc.) were obtained by using Grüneisen's semi-emperical expression. Note that the "observed" data has been made to fit the calculated values at zero degrees absolute and at zero degrees centigrade. The proof of the Matthiesson rule stems from the fact that not just one set of results gives an "observed" thermal resistance in agreement with "Grüneisen's relation, but that several sets of data all give thermal resistivities in agreement with the relation. The values of ρ_D give the ratio of the temperature independent part of the resistance to the total resistance at zero degrees centigrade for the particular specimen in question. Similar data has been obtained on other materials.[7–9] The data given in Table II also show that the thermal

TABLE I.*

	Cu	Ni	W	Ag	Pt	Mo
$\Delta\rho/\rho$	0.02	0.08	0.50	0.03	0.06	0.18

* See reference 1.

[3] N. F. Mott and H. Jones, *The Theory of the Properties of Metals and Alloys* (Oxford University Press, London, 1936), p. 241.
[4] See reference 3, p. 247 and following pages.
[5] F. Seitz, *Modern Theory of Solids* (McGraw-Hill Book Company, Inc., 1940), p. 517, and following pages.
[6] A. Sommerfeld and H. Bethe, *Handbuch der Physik* (Verlag Julius Springer, Berlin, 1933), Vol. 24, p. 554.
[7] E. Gruneisen, *Handbuch der Physik* (Verlag Julius Springer, Berlin, 1928), Vol. 13, p. 21.
[8] W. J. DeHaas and G. J. VanDenBerg, Physica 4, 683 (1937).
[9] W. J. DeHaas and J. DeBoer, Physica 1, 609 (1934).

resistance can be calculated with good accuracy using Grüneisen's expression.

III. THE INTEGRAL EQUATION GIVING THE RELAXATION TIME

Consider an electron in the crystal lattice in a state specified by the wave number $\mathbf{k}$, where $|k|=2\pi/\lambda$ and λ is the wave-length of the electron. This electron may be scattered by any deviation of the potential from a periodic potential. In such a scattering process the wave number changes from $\mathbf{k}$ to some new value $\mathbf{k}'$.

It is assumed that the Fermi distribution function $f_0(\mathbf{k})$ describes the way in which the conduction electrons are spread over the various allowed energy states in the absence of an external electric field. The Fermi function is:

$$f_0(\mathbf{k})=1/\exp(E-\zeta/KT)+1, \tag{4}$$

where E is the energy of the stationary state associated with wave number $\mathbf{k}$, ζ is the energy of the most energetic electrons when the absolute temperature T is zero, and K is Boltzmann's constant. It is assumed that the electron in state $\mathbf{k}$ has an energy E given by:

$$E=E_0+\alpha k^2. \tag{5}$$

The Fermi function gives the fraction of states having energy E which are occupied; thus the number of electrons which occupy the region $dk_x dk_y dk_z$ in k space is:[10]

$$(2/8\pi^3)f_0(\mathbf{k})dk_x dk_y dk_z. \tag{6}$$

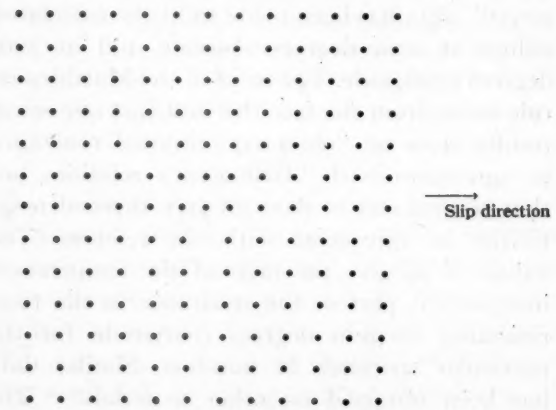

FIG. 1. A schematic diagram of a positive Taylor line dislocation. Atomic planes above and below the plane of the figure are identical with the plane shown. A negative dislocation would be present if the extra atomic plane would appear in the lower portion of the figure rather than in the upper part as shown.

If an external electric field $\mathbf{\varepsilon}$ acts, then it can be shown that the $\mathbf{k}$ vector of each electron changes; the time rate of change is[10]

$$d\mathbf{k}/dt=-e\mathbf{\varepsilon}/\hbar, \tag{7}$$

where $-e$ is the charge on the electron and $\hbar$ is Planck's constant over 2π. The entire Fermi function therefore drifts in $\mathbf{k}$ space, and the time rate of change of the Fermi function produced by the field $\mathbf{\varepsilon}$ is

$$(df/dt)_{\text{field}}=f_0[\mathbf{k}-(e\mathbf{\varepsilon}/\hbar)dt]-f_0(\mathbf{k})/dt$$
$$=-\partial f_0/\partial k[e(\mathbf{\varepsilon}\cdot\mathbf{k})/\hbar k], \tag{8}$$

where k represents the magnitude of $\mathbf{k}$. Note that $f_0(\mathbf{k})$ depends only on the magnitude of k and not on its direction. The second expression for $(df/dt)_{\text{field}}$ is valid only because $f_0(\mathbf{k})$ is a spherically symmetric function in $\mathbf{k}$ space.

In Section II it was shown that it is admissible to calculate the thermal and the dislocation contributions to the resistance separately. We therefore shall attempt to calculate the dislocation contribution by supposing that in a specimen at temperature T a large number of dislocations exist (where it is supposed that the temperature influences the Fermi distribution but that no thermal oscillation of the lattice occurs). In the presence of the external field $\mathbf{\varepsilon}$ the Fermi distribution will drift in k space until a steady state is reached in which the increase in the momentum of the electrons per second produced by the field is equal to the loss per second produced by collisions with the distorted lattice in the vicinity of the dislocations. This balance is described by

$$(df/dt)_{\text{field}}+(df/dt)_{=\text{collisions}}=0. \tag{9}$$

The first term in this equation has already been calculated; an expression for the second term will now be obtained.

The decrease in $f(\mathbf{k})$ per second produced by collisions which change $\mathbf{k}$ to some other value $\mathbf{k}'$ is given by the product of:

(a) The fraction of states k originally filled, i.e., $f(\mathbf{k})$.

(b) The sum of the transition probabilities $P(\mathbf{k}\mathbf{k}')dS'$ to all other states of the same energy multiplied by the probability that the state in question is unoccupied, i.e., by $\{1-f(\mathbf{k}')\}$.

[10] See reference 3, p. 259.

The increase in $f(\mathbf{k})$ per second produced by collisions which change $\mathbf{k}'$ to $\mathbf{k}$ is given by the product of:

(a) The fraction of unoccupied states $\mathbf{k}$, i.e., $\{1-f(\mathbf{k})\}$.
(b) The sum of the transition probabilities $P(\mathbf{k}'\mathbf{k})dS'$ from all other states of the same energy multiplied by the probability that they are filled, i.e., by $f(\mathbf{k}')$.

In the above dS' is the element of area on a sphere in $\mathbf{k}$ space which is associated with the state $\mathbf{k}'$. The sphere gives the end points of all $\mathbf{k}'$ vectors associated with states which have the same energy as the state $\mathbf{k}$. The probability per unit time $P(\mathbf{k}\mathbf{k}')dS'$ that an electron in state k makes a transition to a region dS' having the same energy is given by Mott[11] as

$$P(kk')dS'=\frac{V|\,V(kk')\,|^2dS'}{4\pi^2\hbar(dE'/dk')}.$$

Thus the net change in the Fermi function per second as a result of collisions is

$$(df/dt)_{\text{collisions}}=[1-f(k)]\int f(k')P(k'k)dS'$$

$$-f(k)\int[1-f(k')]P(kk')dS',$$

where the first term gives the change produced by transitions into $\mathbf{k}$ and the second gives the change resulting from transitions out of $\mathbf{k}$. Note that since the dislocations constitute a static perturbation, the collisions are elastic and energy is conserved by the electron in a collision. Note also that the Fermi functions in the last equation are the distorted functions appropriate for the distribution which exists when the balance is achieved. Since the collisions are elastic, one finds that

$$|\,V(kk')\,|^2=|\,V(k'k)\,|^2. \qquad (10)$$

The expression for the rate of change in the Fermi function produced by collisions can therefore be written as

$$(df/dt)_{\text{collisions}}=V/4\pi^2\hbar(dE/dk)$$

$$\times\int\{f(k')-f(k)\}\,|\,V(kk')\,|^2dS'. \qquad (11)$$

[11] See reference 3, p. 251.

TABLE II. Experimental data on Mattiesson's rule.

T degrees Kelvin	Gold, $\Theta=190°K$ Onnes* $\rho_D=0.00210$ ρr(obs.)	Meissner* $\rho_D=0.00039$ ρr(obs.)	Northrup* $\rho_D=0.04$ ρr(obs.)	DeHaas** $\rho_D=0.01575$ ρr(obs.)	ρr(calc.)	T degrees Kelvin	Henning* $\rho_D=0.0016$ ρr(obs.)	Henning* $\rho_D=0.0033$ ρr(obs.)	Platinum, $\Theta=230°K$ Meissner* $\rho_D=0.0016$ ρr(obs.)	Onnes* $\rho_D=0.0098$ ρr(obs.)	$\rho_D=0.000375$ ρr(obs.)	ρr(calc.)
4.2		0.00001			0.000015	1.63					0.0000040	0.0000002
6.78				0.000068	0.000087	2.39					0.0000085	0.0000008
7.57				0.000098	0.000135	3.12					0.0000148	0.0000022
11.18	0.00044			0.000545	0.00064	4.23			0.00004		0.0000282	0.0000074
12.1	0.00061				0.00088	5.47					0.0000520	0.0000207
14.3	0.00150			0.001729	0.00172	7.60					0.0001214	0.0000770
18.08	0.0036			0.004590	0.00439	9.60					0.0002626	0.0001963
20.4	0.0060	0.0060		0.007384	0.00692	14.20				0.00093		0.000940
57.8	0.1315				0.131	15.17					0.001369	0.00122
68.1	0.177				0.174	17.9				0.0027		0.0024
75.2	0.207				0.204	18.08					0.002700	0.0025
80.0		0.2249			0.225	20.44	0.0044		0.0044	0.0044	0.004322	0.0039
81.8		0.2317			0.232	56.5				0.1015		0.1020
90.1	0.270				0.268	68.4				0.1515		0.1513
91.5		0.275			0.273	90.1	0.2441					0.2448
169.3	0.592				0.589	90.3			0.2432	0.2454		0.2457
373.7		1.402			1.405	197.1	0.6935					0.6934
573.1			2.244		2.25	373.1		1.3927				1.3941
773.1			3.164		3.18	373.8			1.3966			1.3968
1073.1			4.77		4.79	473.1		1.7738				1.7739
1273.1			6.03		6.03	573.1		2.1431				2.3261

* See reference 7. ** See reference 8.

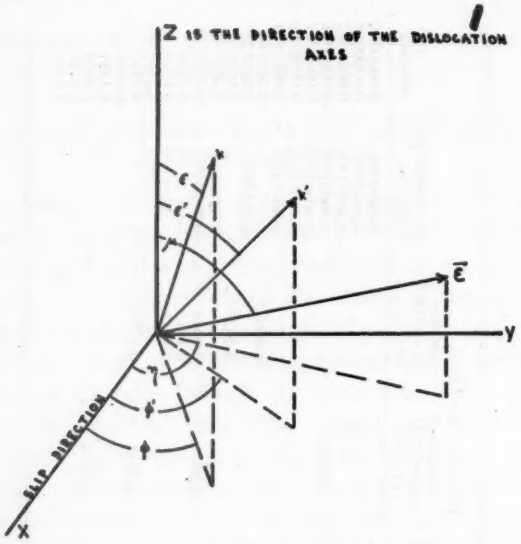

FIG. 2. Diagram showing the scattering geometry. The xy plane is the slip plane; the dislocation axes are parallel to z; k and k' are the wave number vectors of an electron before and after scattering; ε is the electric field.

This expression can be written in terms of the Fermi function for the case where no field is present by introducing the notion of the relaxation time. Consider a metal single crystal containing a large number of dislocations which have their axes parallel. If a field ε is suddenly applied, the Fermi function will drift in k space until collisions establish the balance mentioned. The resultant distortion produced in the Fermi function will depend on the orientation of the field relative to the dislocations and on the direction of motion of the electron under consideration relative to the dislocations. Figure 2 shows the important directions involved in the problem. The xz plane is the slip plane. Using the angles just introduced, Eq. (8) becomes

$$(df/dt)_{\text{field}} = -(e\varepsilon/\hbar)(\partial f_0/\partial k) \times \{\sin\epsilon\cos\phi\sin\mu\cos\eta + \sin\epsilon\sin\phi\sin\mu\sin\eta + \cos\epsilon\cos\mu\}. \quad (12)$$

In addition, using the fact that $f_0(\mathbf{k})$ is a spherically symmetric function in $\mathbf{k}$ space,

$$f(\mathbf{k}) = f_0[\mathbf{k} - t(\mathbf{k},\varepsilon)e\varepsilon/\hbar] = f_0(k) - (e(\varepsilon\cdot\mathbf{k})/\hbar k)(\partial f_0/\partial k)t(\mathbf{k},\varepsilon), \quad (13)$$

where $t(\mathbf{k},\varepsilon)$ is the relaxation time associated with dislocation scattering. t depends on $\mathbf{k}$ and on the direction of ε. A similar expression can be written for $f(\mathbf{k}')$. Inserting the angles, one finds

$$f(\mathbf{k}) = f_0(\mathbf{k}) - (e\epsilon/\hbar)(\partial f_0/\partial k)t(\mathbf{k},\varepsilon) \times \{\sin\epsilon\cos\phi\sin\mu\cos\eta + \sin\epsilon\sin\phi \times\sin\mu\sin\eta + \cos\epsilon\cos\mu\}. \quad (14)$$

The integral equation obtained by inserting (11), (12), (14), and a similar equation for $f(\mathbf{k}')$ into Eq. (9) is

$$\sin\epsilon\cos\phi\sin\mu\cos\eta + \sin\epsilon\sin\phi\sin\mu\sin\eta + \cos\epsilon\cos\mu = V/4\pi^2\hbar(dE/dk)\int |V(kk')|^2 dS' \cdot[t(\mathbf{k},\varepsilon)\{\sin\epsilon\cos\phi\sin\mu\cos\eta + \sin\epsilon\sin\phi\sin\mu\sin\eta + \cos\epsilon\cos\mu\} - t(\mathbf{k}',\epsilon)\{\sin\epsilon'\cos\phi'\sin\mu\cos\eta + \sin\epsilon'\sin\phi'\sin\mu\sin\eta + \cos\epsilon'\cos\mu\}]. \quad (15)$$

Note that since energy is conserved in a collision $k=k'$. The integration $\mathbf{k}'$ will therefore be over the surface of a sphere in $\mathbf{k}$ space.

The integral Eq. (15) will eventually be used to determine the relaxation time for dislocation scattering $t(\mathbf{k},\varepsilon)$.

IV. THE EVALUATION OF THE MATRIX ELEMENT GIVING DISLOCATION SCATTERING

The matrix element will first be evaluated for a dislocation pair which have their axes parallel to the z axis. The positive dislocation is located at $x=0$, $y=+R/2$; the negative dislocation is at $x=0$, $y=-R/2$. The displacements produced by the pair at a point x,y are[12]

$$\begin{aligned} u_x &= A\{\tan^{-1}((y-R/2)/x) - \tan^{-1}((y+R/2)/x)\} \\ &\quad + 2Bx\{(y-R/2)/x^2 + (y-R/2)^2 \\ &\quad - (y+R/2)/x^2 + (y+R/2)^2\}, \\ y_y &= -C\log(x^2+(y-R/2)^2/x^2+(y+R/2)^2)^{\frac{1}{2}} \\ &\quad - 2Bx^2\{1/x^2 + (y-R/2)^2 \\ &\quad - 1/x^2 + (y+R/2)^2\}, \end{aligned} \quad (16)$$

where

$$A = \lambda/2\pi, \quad B = (\lambda/8\pi)(m/(m-1)), \quad C = (\lambda/4\pi)((m-2)/(m-1));$$

λ is the unit crystallographic slip distance, i.e., it is the smallest interatomic distance encountered

[12] J. S. Koehler, Phys. Rev. 60, 398 (1941).

considering atoms lying along the slip direction. m is the reciprocal of Poisson's ratio.

Let $\mathbf{a}_j$ be a vector from the origin of our coordinates to the lattice position of the jth positive ion. The potential in which the valence electrons move in a perfect crystal is taken to be

$$V(\mathbf{r})=\sum_j V_j(\mathbf{r}-\mathbf{a}_j). \quad (17)$$

The potential of a single ion, $V_j(\mathbf{r}-\mathbf{a}_j)$ is taken to be screened Coulomb field, i.e.,

$$V_j(\mathbf{r}-\mathbf{a}_j)=-Ze^2\exp(-q|\mathbf{r}-\mathbf{a}_j|)/|\mathbf{r}-\mathbf{a}_j|, \quad (18)$$

where Ze is the charge of the ion and q is the screening constant. According to Mott[13] the value of q for copper lies between 1.8×10^8 and 3.3×10^8 cm^{-1}.

If all of the ions experience displacements, then the deviation of the resulting potential from that which occurs in a perfect crystal is approximately:

$$\Delta V(\mathbf{r})=-\sum_j \mathbf{u}_j\cdot\operatorname{grad} V_j(\mathbf{r}-\mathbf{a}_j), \quad (19)$$

where $\mathbf{u}_j$ is the displacement of the jth ion. Using this as the perturbation, the matrix element associated with the scattering produced by dislocations is

$$V(kk')=-1/V\int \exp(-ik'\cdot r)\times\left(\sum_j u_j\cdot\operatorname{grad} V_j(\mathbf{r}-\mathbf{a}_j)\right)\exp(i\mathbf{k}\cdot\mathbf{r})dv, \quad (20)$$

where V is the volume of the crystal and where the electronic wave functions associated with the states k and k' have been assumed to be free electron wave functions. The integration is over the entire crystal. Exchanging summation and integration and using as variable in the resulting integral $(\mathbf{r}-\mathbf{a}_j)$, one obtains

$$V(kk')=-1/V\sum_j \exp(-i(\mathbf{k}'-\mathbf{k})\cdot a_j)\int \exp(-i\mathbf{k}'\cdot(\mathbf{r}-\mathbf{a}_j))\mathbf{u}_j\cdot\operatorname{grad} V_j\times\exp(ik\cdot(\mathbf{r}-\mathbf{a}_j))dv. \quad (21)$$

Since all of the dislocations considered have their axes parallel to z, and since each dislocation therefore produces displacements which are perpendicular to z, the resulting u_{iz} is zero. Equation (21) can therefore be written:

$$V(kk')=\sum_j \exp(-i\mathbf{K}\cdot\mathbf{a}_j)[u_{xj}P+u_{yj}Q] \quad (22)$$

where $\mathbf{K}=(\mathbf{k}'-\mathbf{k})$ and

$$P=1/V\int \exp(-i\mathbf{k}'\cdot\mathbf{r})(\partial/\partial X)\times\{Ze^2\exp(-qr)/r\}\exp(i\mathbf{k}\cdot\mathbf{r})dv=(4\pi iZe^2/V)K_x/(q^2+K^2). \quad (23)$$

Also,

$$Q=(4\pi iZe^2/V)(K_y/(q^2+K^2)). \quad (24)$$

The sum over j can now be converted into an integral. The deflection at each successive atom is assumed to vary slowly with j. Then

$$V(kk')=1/V_0\int \exp(-i\mathbf{K}\cdot\mathbf{a})[u_xP+u_yQ]da, \quad (25)$$

where V_0 is the volume associated with one atom, and the integral extends over the entire crystal.

Let us calculate in detail the value of the matrix element $v(kk')$ for the case where the displacement u is that produced by a single pair of dislocations. This matrix element is given by (25) if the displacements (16) are used. The integrations can be done using Bierens De Haan, and one finds

$$|v(kk')|^2=\frac{(16\pi^2)^2Z^2e^4|\delta(K_z)|^2\sin^2(K_yR/2)}{V^2V_0^2(q^2+K^2)^2}\times\left[\frac{A^2K_x^2}{K^4}+\frac{C^2K_y^2}{K^4}-\frac{16BCK_x^2K_y^2}{K^6}\right], \quad (26)$$

where the delta-function $\delta(K_z)$ is given by

$$\delta(K_z)=\int_0^{V^{\frac{1}{3}}}\exp(i\mathbf{K}\cdot\mathbf{z})dz=\frac{\{\exp(iV^{\frac{1}{3}}K_z)-1\}}{iK_z}. \quad (27)$$

The appearance of this delta-function means that only those transitions occur in which k_z equals k_z'. The possibility that interference might occur between the wave scattered from the positive dislocation and the wave scattered by the negative dislocation is manifest in Eq. (26) by the presence of the factor $\sin^2(K_yR/2)$. Assuming a

[13] See reference 3, pp. 88 and 294.

uniform distribution throughout the solid, the dislocations in a severely cold-worked metal are separated by distances of the order of 10^{-6} cm.[14] In the case of copper, $K_y/2$ can take values from zero to 1.36×10^{8} cm^{-1}. Thus as the direction and magnitude of K are varied the argument of the sine goes through many periods while the rest of the matrix element is changing only slightly. It is therefore appropriate to put the average value of $\sin^2(K_yR/2)$ into the expression when dealing with metals. It is interesting to note that these diffraction effects could be of importance if one were discussing the dislocation resistance of a semi-conductor in which the wave-length of the current carriers was about 10^{-6} cm. Experiments on such materials might yield information on the way in which dislocations are distributed in the solid. Diffraction effects might also conceivably occur in a metal if the dislocations were clustered along the slip bands, but this seems rather improbable.[15] If the average value of the sine square is used, then the matrix element appropriate for a large number of dislocation pairs is

$$|V(kk')|^2=n\langle|v(kk')|^2\rangle_{Av}, \tag{28}$$

where the averaged value of the matrix element has been used. n is the total number of dislocation pairs in the specimen.

V. THE SOLUTION OF THE INTEGRAL EQUATION

Inserting (28) and (26) into the integral equation as given by (15), one obtains

$$\sin\epsilon\cos\phi\sin\mu\cos\eta+\sin\epsilon\sin\phi\sin\mu\sin\eta+\cos\epsilon\cos\mu=32\pi^2Z^2e^4n/VV_0^2(dE/dk)\hbar$$

$$\int dS'|\delta(K_z)|^2/(q^2+K^2)^2\cdot(A^2K_x^2/K^4+C^2K_y^2/K^4-16BCK_x^2K_y^2/K^6)$$

$$\times[t(\mathbf{k}\varepsilon)\{\sin\epsilon\cos\phi\sin\mu\cos\eta+\sin\epsilon\sin\phi\sin\mu\sin\eta+\cos\epsilon\cos\eta\}$$

$$-t(\mathbf{k}'\varepsilon)\{\sin\epsilon'\cos\phi'\sin\mu\cos\eta+\sin\epsilon'\cos\phi'\sin\mu\sin\eta+\cos\epsilon'\cos\eta\}]. \tag{29}$$

The integrations can be carried out as follows. In the first place the presence of the delta-function enables one to reduce the integration from a two-dimensional integration to a one-dimensional integration. Since all quantities except the delta-function vary slowly with k_z', the value of the rest of the integrand at the position of the maxima of the delta-function can be used with the integrated value of $|\delta(K_z)|^2$. The result of integrating ϵ' from 0 to π is

$$\int dS'|\delta(K_z)|^2=k^2\int\sin\epsilon'd\epsilon'd\phi'|\delta(K_z)|^2$$

$$=4\pi kV^{\frac{1}{3}}d\phi'. \tag{30}$$

It is next assumed that the relaxation time can be written in the following form:

$$t(\mathbf{k},\varepsilon)=a_0+a_2\cos2\phi+a_4\cos4\phi+a_6\cos6\phi+\cdots+b_2\sin2\phi+b_4\sin4\phi+b_6\sin6\phi+\cdots. \tag{31}$$

The symmetry of the problem leads one to believe that sine terms and cosines containing odd multiple of ϕ will not be needed. It should be noted that the coefficients a_{2i} depend on ϵ, on k, and on the field ε. The integration of Eq. (29) can be facilitated by introducing the angle u defined as follows:

$$u=\tfrac{1}{2}(\phi'-\phi). \tag{32}$$

When this is done and when the results of Eqs. (30) and (31) are used, the integral equation becomes

[14] See reference 12, p. 410.

[15] Diffraction effects would probably only be observable if $KyR/2$ varied from zero to about 15. This would produce about 10 oscillations in the scattering probability as the electric field was shifted from the plane $\eta=0$ to the plane $\eta=90°$. The value of R for this limiting case is only 11×10^{-8} cm. Since this is only four times the smallest interatomic distance in copper, it seems unlikely that such pairs will be formed. This can be seen as follows: A dislocation pair having the separation mentioned in copper can only be separated if an external stress of 260 kg/mm^2 is applied. The tensile strength of polycrystalline copper is 22.6 kg/mm^2. If most of the dislocations in a cold-worked copper specimen had the separation distance mentioned, it would be impossible to account for the extensive plastic deformation which occurs prior to fracture.

$$(1)\cos\phi+(2)\sin\phi+(3)=\frac{\mathbf{A}}{\pi\sin^6\epsilon}\int_0^\pi \frac{du[A^2\sin^2(u+\phi)+C^2\cos^2(u+\phi)-16BC\sin^2(u+\phi)\cos^2(u+\phi)]}{\sin^2u[s^2+\sin^2u]^2}$$

$$\times[+2a_0(1)\sin u\sin(u+\phi)-2a_0(2)\sin u\cos(u+\phi)+a_2(1)\{\sin u\sin(u+\phi)+\sin 3u\sin 3(u+\phi)\}$$
$$+a_2(2)\{\sin u\cos(u+\phi)-\sin 3u\cos 3(u+\phi)\}+2a_2(3)\sin 2u\sin 2(u+\phi)$$
$$+a_4(1)\{\sin 3u\sin 3(u+\phi)+\sin 5u\sin 5(u+\phi)\}+a_4(2)\{\sin 3u\cos 3(u+\phi)-\sin 5u\cos 5(u+\phi)\}$$
$$+2a_4(3)\sin 4u\sin 4(u+\phi)+\cdots+b_2(2)\{\sin u\sin(u+\phi)-\sin 3u\sin 3(u+\phi)\}$$
$$-b_2(1)\{\sin u\cos(u+\phi)+\sin 3u\cos 3(u+\phi)\}-2b_2(3)\sin 2u\cos 2(u+\phi)+b_4(2)\{\sin 3u\sin 3(u+\phi)$$
$$-\sin 5u\sin 5(u+\phi)\}-b_4(1)\{\sin 3u\cos 3(u+\phi)+\sin 5u\cos 5(u+\phi)\}-2b_4(3)\sin 4u\cos 4(u+\phi)+\cdots], \tag{33}$$

where

$\mathbf{A}=2\pi^4Z^2e^4n/V^2V_0^2\alpha k^6\hbar$, $s^2=q^2/4k^2\sin^2\epsilon$, $(1)=\sin\epsilon\sin\mu\cos\eta$, $(2)=\sin\epsilon\sin\mu\sin\eta$, $(3)=\cos\epsilon\cos\mu$.

Since (33) is an identity in ϕ the coefficients of $\cos n\phi$ must be equal.

Coefficient of $\cos\phi$:

$$4(1)\sin^6\epsilon/\mathbf{A}\pi=2a_0(1)d_1\{3A^2+C^2-8BC\}+a_2(1)\{d_1(3A^2+C^2-8BC)-d_3(A^2-C^2+4BC)\}$$
$$+a_4(1)\{-d_3(A^2-C^2+4BC)+d_5 4BC\}+a_6(1)d_5 4BC+b_2(2)\{d_1(3A^2+C^2-8BC)$$
$$+d_3(A^2-C^2+4BC)\}+b_4(2)\{-d_3(A^2-C^2+4BC)-d_5 4BC\}+b_6(2)d_5 4BC.$$

Coefficient of $\cos 3\phi$:

$$0=-2a_0(1)d_3\{A^2-C^2+4BC\}+a_2(1)\{-d_3(A^2-C^2+4BC)+2(d_1+d_3+d_5)(A^2+C^2-4BC)\}$$
$$+a_4(1)\{2(d_1+d_3+d_5)(A^2+C^2-4BC)-(d_3+d_5+d_7)(A^2-C^2)\}+a_6(1)\{-(d_3+d_5+d_7)$$
$$\times(A^2-C^2)+(d_5+d_7+d_9)4BC\}+\cdots+b_2(2)\{-d_3(A^2-C^2+4BC)-2(d_1+d_3+d_5)$$
$$\times(A^2+C^2-4BC)\}+b_4(2)\{2(d_1+d_3+d_5)(A^2+C^2-4BC)+(d_3+d_5+d_7)(A^2-C^2)\}$$
$$+b_6(2)\{-(d_3+d_5+d_7)(A^2-C^2)-(d_5+d_7+d_9)4BC\}+\cdots.$$

Coefficient of $\cos 5\phi$:

$$0=+2a_0(1)d_5 4BC+a_2(1)\{+d_5 4BC-(d_3+d_5+d_7)(A^2-C^2)\}+a_4(1)\{-(d_3+d_5+d_7)(A^2-C^2)$$
$$+2(d_1+\cdots+d_9)(A^2+C^2-4BC)\}+a_6(1)\{2(d_1+\cdots+d_9)(A^2+C^2-4BC)$$
$$-(d_3+\cdots+d_{11})(A^2-C^2)\}+b_2(2)\{+d_5 4BC+(d_3+d_5+d_7)(A^2-C^2)\}$$
$$+b_4(2)\{-(d_3+d_5+d_7)(A^2-C^2)-2(d_1+\cdots+d_9)(A^2+C^2-4BC)\}$$
$$+b_6(2)\{2(d_1+\cdots+d_9)(A^2+C^2-4BC)+(d_3+\cdots+d_{11})(A^2-C^2)\}+\cdots.$$

Coefficient of $\cos 7\phi$:

$$0=+a_2(1)\{(d_5+d_7+d_9)4BC\}+a_4(1)\{+(d_5+d_7+d_9)4BC-(d_3+\cdots+d_{11})(A^2-C^2)\}$$
$$+a_6(1)\{-(d_3+\cdots+d_{11})(A^2-C^2)+2(d_1+\cdots+d_{13})(A^2+C^2-4BC)\}+\cdots$$
$$-b_2(2)\{(d_5+d_7+d_9)4BC\}+b_4(2)\{+(d_5+d_7+d_9)4BC+(d_3+\cdots+d_{11})(A^2-C^2)\}$$
$$+b_6(2)\{-(d_3+\cdots+d_{11})(A^2-C^2)-2(d_1+\cdots+d_{13})(A^2+C^2-4BC)\}+\cdots. \tag{34}$$

$$\vdots$$

Coefficient of $\sin\phi$:

$$4(2)\ \sin^6\epsilon/A\pi = 2a_0(2)d_1\{A^2+3C^2-8BC\}+a_2(2)\{-d_1(A^2+3C^2-8BC)-d_3(A^2-C^2-4BC)\}$$
$$+a_4(2)\{+d_3(A^2-C^2-4BC)+d_5 4BC\}-a_6(2)d_5 4BC+b_2(1)\{+d_1(A^2+3C^2-8BC$$
$$-d_3(A^2-C^2-4BC)\}+b_4(1)\{-d_3(A^2-C^2-4BC)+d_5 4BC\}+b_6(1)d_5 4BC.$$

Coefficient of $\sin 3\phi$:

$$0=-2a_0(2)d_3(A^2-C^2-4BC)+a_2(2)\{d_3(A^2-C^2-4BC)+2(d_1+d_3+d_5)(A^2+C^2-4BC)\}$$
$$+a_4(2)\{-2(d_1+d_3+d_5)(A^2+C^2-4BC)-(d_3+d_5+d_7)(A^2-C^2)\}+a_6(2)\{(d_3+d_5+d_7)(A^2-C^2)$$
$$+(d_5+d_7+d_9)4BC\}+\cdots+b_2(1)\{-d_3(A^2-C^2-4BC)+2(d_1+d_3+d_5)(A^2+C^2-4BC)\}$$
$$+b_4(1)\{+2(d_1+d_3+d_5)(A^2+C^2-4BC)-(d_3+d_5+d_7)(A^2-C^2)\}$$
$$+b_6(1)\{-(d_3+d_5+d_7)(A^2-C^2)+(d_5+d_7+d_9)4BC\}+\cdots.$$

Coefficient of $\sin 5\phi$:

$$0=+2a_0(2)d_5 4BC+a_2(2)\{-d_5 4BC-(d_3+d_5+d_7)(A^2-C^2)\}+a_4(2)\{+(d_3+d_5+d_7)(A^2-C^2)$$
$$+2(d_1+\cdots+d_9)(A^2+C^2-4BC)\}+a_6(2)\{-2(d_1+\cdots+d_9)(A^2+C^2-4BC)$$
$$-(d_3+\cdots+d_{11})(A^2-C^2)\}+\cdots+b_2(1)\{+d_5 4BC-(d_3+d_5+d_7)(A^2-C^2)\}$$
$$+b_4(1)\{-(d_3+d_5+d_7)(A^2-C^2)+2(d_1+\cdots+d_9)(A^2+C^2-4BC)\}$$
$$+b_6(1)\{+2(d_1+\cdots+d_9)(A^2+C^2-4BC)-(d_3+\cdots+d_{11})(A^2-C^2)\}+\cdots.$$

Coefficient of $\sin 7\phi$:

$$0=+a_2(2)\{(d_5+d_7+d_9)4BC\}+a_4(2)\{-(d_5+d_7+d_9)4BC-(d_3+\cdots+d_{11})(A^2-C^2)\}$$
$$+a_6(2)\{+(d_3+\cdots+d_{11})(A^2-C^2)+2(d_1+\cdots+d_{13})(A^2+C^2-4BC)\}+\cdots$$
$$+b_2(1)\{(d_5+d_7+d_9)4BC\}+b_4(1)\{+(d_5+d_7+d_9)4BC-(d_3+\cdots+d_{11})(A^2-C^2)\}$$
$$+b_6(1)\{-(d_3+\cdots+d_{11})(A^2-C^2)+2(d_1+\cdots+d_{13})(A^2+C^2-4BC)\}+\cdots, \quad (35)$$

where the d_i are the following functions of s:

$$d_1=\tfrac{1}{2}(1+2s^2/s^3\{1+s^2\}^{\frac{1}{2}}),$$
$$d_3=-2/s\{1+s^2\}^{\frac{1}{2}}+\tfrac{3}{2}(1+2s^2/s^3\{1+s^2\}^{\frac{1}{2}}),$$
$$d_5=16-\tfrac{1}{2}(20+32s^2/s\{1+s^2\}^{\frac{1}{2}})+\tfrac{1}{2}(\{5-16s^4\}\{1+2s^2\}/s^3\{1+s^2\}^{\frac{1}{2}}),$$
$$d_7=(112+128s^2)-32+\tfrac{1}{2}(56+224s^2+192s^4/s\{1+s^2\}^{\frac{1}{2}})+\tfrac{1}{2}(\{7-112s^4-128s^6\}\{1+2s^2\}/s^3\{1+s^2\}^{\frac{1}{2}}),$$
$$d_9=(432+1152s^2+768s^4)-(288+256s^2)+96-\tfrac{1}{2}(120+864s^2+1728s^4+1024s^6/s\{1+s^2\}^{\frac{1}{2}})$$
$$+\tfrac{1}{2}(9-432s^4-1152s^6-768s^8\{1+2s^2\}/s^3\{1+s^2\}^{\frac{1}{2}}). \quad (36)$$

In general,

$$d_{2i+1}=1/\pi\int_0^\pi du\,\sin(2i+1)u/\sin u\{s^2+\sin^2 u\}^2. \quad (37)$$

If s is much less than one, then

$$d_{2i+1}=2i+1/2s^3. \tag{38}$$

If s is much greater than one,

$$d_{2i+1}=\tfrac{1}{2}/s^4-(i+2)/2^{2i+1}s^{2i+6}+0/s^{2i+8}+\cdots. \tag{39}$$

Equations (34) constitute the requirement that the drift of the Fermi function produced by the x component of the field by balanced by collisions. Equations (35), if satisfied, guarantee that the drift produced by the y component of the field will be balanced by collisions. Sines and cosines of even multiples of ϕ also appear in the integral equation. The equations obtained by considering these terms govern the drift produced by the z component of the field. We have supposed that all dislocation pairs have their axes parallel to z. In this case if thermal scattering is neglected there will be a steady drift of the Fermi function in the k_z direction, i.e., the equation which governs the drift produced by the z component of the field cannot be satisfied.

Equations (34) and (35) are solved for the coefficients a_{2i} and b_{2i}, and the resulting relaxation time is averaged over all directions of $\mathbf{k}$, since electrons traveling in all directions are present. The relaxation time $\bar{t}$ which results will depend only on the orientation of the field direction relative to the array of dislocations. It can be seen from (31) that only a_0 will contribute to $\bar{t}$, since the other contributions average out. The $\bar{t}$ then gives the dislocation resistance when used in Eq. (1). The method used in practice to carry through these calculations will be described in the next section where the averaged relaxation time is calculated numerically for copper.

VI. THE NUMERICAL EVALUATION OF t FOR COPPER

It is assumed that copper has one valence electron per atom. The effective mass of this valence electron is taken to be just the mass of a free electron.[16] The width in energy of the filled portion of the Fermi band is[17] 7.04 ev. This, together with the values just quoted, gives $k=1.36\times10^{+8}$ cm^{-1} and $\alpha=6.095\times10^{-28}$ erg cm^2. The other numerical constants used are given in Table III. The values of the first three constants are taken from a paper by Koehler.[18] The density of dislocation pairs is chosen to give the correct value for the energy stored in copper during work hardening. The pairs are assumed to be uniformly distributed. The value of V_0 is that given by Mott and Jones.[19] The thermal portion of the electrical resistivity is the value quoted in the *Handbook of Chemistry and Physics* (Chemical Rubber Publishing Company, Cleveland, Ohio) (30th edition, 1947).

There are two cases in which the value of a_0 can be calculated simply. If the electric field vector lies in the xz plane, η equals zero, and since $(2)=\sin\epsilon\sin\mu\sin\eta$ is also zero, the coefficients of the b_{2i} terms in (34) vanish; similarly, the coefficients of the a_{2i} terms in (35) vanish. Equations (35) are then a set of linear homogeneous equations in the b_{2i}s. Since the determinant of the coefficients is not, in general, zero, the coefficients b_{2i} must be zero in this case. Equations (34) can then be solved for the a_{2i}s—in particular for a_0. The fact that the b_{2i} should all vanish can also be seen from the symmetry conditions which exist in this case. The symmetry of t is determined by that of the matrix element and by the orientation of the field with respect to the dislocations. In the case under discussion it is easily seen that t should be an even function of ϕ, and hence all the sine terms must be zero. Substituting the numerical values into (34) one obtains the following equations for the case where η is zero:

$$\begin{aligned}
T&=+1.048090a_0+0.094359a_2\\
&\quad -0.302463a_4+0.127223a_6,\\
0&=-0.859372a_0+0.815058a_2\\
&\quad +0.278139a_4-0.581710a_6,\\
0&=+0.254447a_0-0.839382a_2\\
&\quad +1.247998a_4+0.590756a_6,\\
0&=+0.384895a_2-1.238952a_4+1.556807a_6.
\end{aligned} \tag{40}$$

The terms in a_8 and in higher coefficients are assumed to be unimportant for the determination of a_0. Solving this, one finds that

$$a_0=+0.974020T, \text{ when } \eta=0, \tag{41}$$

where

$$T=16\pi\sin^6\epsilon/A\lambda^2.$$

[16] See reference 5, p. 153.
[17] See reference 5, p. 146.
[18] See reference 12, pp. 409 and 410.
[19] See reference 3, p. 318.

TABLE III. Constants used in calculations on copper.

m = reciprocal of Poisson's ratio = 2.941
λ = unit slip distance = 2.552×10^{-8} cm
n = density of dislocation pairs (when highly cold-worked) = $1/2(\pi R^2) = 2.906\times10^{11}$ cm^{-2}
V_0 = volume occupied by one atom = $1/N = 1.1708\times10^{-23}$ cm^3
q = the screening constant for the atomic potential in which the electron moves = 2.5×10^8 cm^{-1} (Mott* gives $1.8\times10^8 \leqslant q \leqslant 3.3\times10^8$ cm^{-1})
$s^2 = \dfrac{q^2}{4k^2(\sin^2\epsilon)_{Av}} = q^2/2k^2 = 1.692$
$d_1 = +0.22549$
$d_3 = +0.32836$
$d_5 = +0.34629$
$d_7 = +0.35235$
$d_9 = d_{11} = d_{13} = d_{15} = d_{17} = 1/s^4 = 0.349301$
ρ_{thermal}(observed 20°C) = 1.692×10^{-6} ohm cm = 1.889×10^{-18} e.s.u. (sec. cm^{-3})

* See reference 13.

Similarly, if the electric field lies in the yz plane η is 90° and (1) = $\sin\epsilon \sin\mu \cos\eta$ is zero. In this case the coefficients of the b_{2i} terms in (35) vanish and Eqs. (34) become a set of linear homogeneous equations in the b_{2i} which are again zero. In this case, as before, t should be an even function of ϕ, and again symmetry conditions enable us to understand the vanishing of the coefficients b_{2i}. Substituting numerical values into (35), the following equations are obtained for the case where η is 90°:

$$\begin{aligned}
T &= +0.199172a_0 - 0.288000a_2 \\
&\quad + 0.315637a_4 - 0.127223a_6, \\
0 &= -0.376828a_0 + 1.433158a_2 \\
&\quad - 2.211349a_4 + 1.351500a_6, \\
0 &= +0.254447a_0 - 1.093828a_2 \\
&\quad + 3.181208a_4 - 3.838450a_6, \\
0 &= +0.384895a_2 - 2.008742a_4 + 4.804501a_6, \qquad (42)
\end{aligned}$$

where T has the value previously given. The value of a_0 in this case is

$$a_0 = +8.037938T, \text{ when } \eta = 90°. \qquad (43)$$

It is more difficult to solve the equations for other values of η. Because of the symmetry of the problem, the complete dependence of $\dot{t}$ on η is known if its behavior from 0° to 90° has been obtained. We have also solved the equations for the case where $\eta = 45°$. Some simplification then occurs because (1) equals (2). The equations which result are:

$$\begin{aligned}
T &= +1.048090a_0 + 0.094359a_2 + 0.953731b_2 \\
&\quad - 0.302463a_4 - 0.556909b_4 \\
&\quad + 0.127223a_6 + 0.127223b_6, \\
T &= +0.199172a_0 - 0.288000a_2 - 0.088828b_2 \\
&\quad + 0.315637a_4 - 0.061191b_4 \\
&\quad - 0.127223a_6 + 0.127223b_6, \\
0 &= -0.859372a_0 + 0.815058a_2 - 1.674430b_2 \\
&\quad + 0.278139a_4 + 2.211349b_4 \\
&\quad - 0.581710a_6 - 1.351500b_6, \\
0 &= -0.376828a_0 + 1.433158a_2 + 1.056330b_2 \\
&\quad - 2.211349a_4 + 0.278139b_4 \\
&\quad + 1.351500a_6 - 0.581710b_6, \\
0 &= +0.254447a_0 - 0.839382a_2 + 1.093828b_2 \\
&\quad + 1.247998a_4 - 3.181208b_4 \\
&\quad + 0.590756a_6 + 3.838450b_6, \\
0 &= +0.254447a_0 - 1.093828a_2 - 0.839382b_2 \\
&\quad + 3.181208a_4 + 1.247998b_4 \\
&\quad - 3.838450a_6 + 0.590756b_6, \\
0 &= +0.384895a_2 - 0.384895b_2 - 1.238952a_4 \\
&\quad + 2.008742b_4 \\
&\quad + 1.556807a_6 - 4.804501b_6, \qquad (44)
\end{aligned}$$

where the first, the third, the fifth, and the seventh equations are from (34). The others are from (35). Solving these equations one finds that

$$a_0 = +2.518534T, \text{ when } \eta = 45°. \qquad (45)$$

The angular dependence of the average relaxation time can now be determined. The symmetry of the problem is such that $\partial\dot{t}/\partial\eta$ is zero at $\eta = 0$ and at $\eta = 90°$. $\dot{t}$ can therefore be written in the following form:

$$\dot{t} = a_0(\mu\eta) = T\{\alpha_0 + \beta_0 \cos 2\eta + \gamma_0 \cos 4\eta + \delta_0 \cos 6\eta + \cdots\}. \qquad (46)$$

Since the matrix element contains terms in $\cos 4\eta$ but does not contain more rapidly oscillating terms, one would expect that the first three coefficients in (46) would be large in comparison with higher coefficients. It is assumed here that δ_0 and higher coefficients are negligible. The values of a_0 given in (45), (43), and (41) then suffice to calculate the coefficients; they are:

$$\begin{aligned}
\alpha_0 &= +3.498157, \\
\beta_0 &= -3.531951, \qquad (47) \\
\gamma_0 &= +1.007815.
\end{aligned}$$

The value of the dislocation resistance can now be calculated. The value of **A** is found using

the expression given below (33). The result is used to obtain T which is given by the relation below (41). The average value of $\sin^6\epsilon$ is inserted in the expression for T (i.e., 15/48). The dislocation resistance is then obtained by substituting from (46) and (47) into (1). The result for copper is

$$\Delta\rho = 1.491\times10^{-20}/(1.000 - 1.010\cos2\eta + 0.288\cos4\eta) \text{ e.s.u.} \quad (48)$$

It should be noted that $\Delta\rho$ does not depend on μ, the angle between the field direction and the dislocation axes. This can be qualitatively understood as follows: As μ decreases from 90° towards zero the magnitude of the matrix element and hence the scattering probability decrease and become zero when μ is zero. On the other hand, the time spent in the perturbed regions around the dislocations by the electrons which contribute the largest part of the dislocation resistance (i.e., the electrons moving along the field direction) increases as μ decreases; this times goes to infinity when μ is zero. Thus the two effects tend to cancel out.

The dependence on η is most interesting. The values of the dislocation resistance in the slip direction, at $\eta=45°$, and perpendicular to the slip direction in copper are

$$\Delta\rho_{\eta=0°} = 5.37\times10^{-20} \text{ e.s.u.},$$
$$\Delta\rho_{\eta=45°} = 2.09\times10^{-20} \text{ e.s.u.},$$
$$\Delta\rho_{\eta=90°} = 0.648\times10^{-20} \text{ e.s.u.}$$

The ratio of the extreme values is

$$\Delta\rho_{\eta=0°}/\Delta\rho_{\eta=90°} = 8.30.$$

This means that the dislocation resistance depends sensitively on the direction of the electric field. The ratio of the extreme values depends on Poisson's ratio for the material and is large for materials having a low value of Poisson's ratio.

In a polycrystalline material all values of η are equally likely. If the relaxation time is averaged over η and is then used in (1), the result obtained is appropriate for comparison with the experimental results on polycrystals mentioned in the introduction. In the case of copper the result is

$$\langle\Delta\rho\rangle_{Av} = 1.491\times10^{-20} \text{ e.s.u.}$$

The averaged dislocation resistance in highly cold-worked copper is therefore calculated to be slightly less than 1 percent of the thermal portion of the electrical resistance at 20°C. Experimentally, (see ρ_{thermal} in Table III) the dislocation resistance amounts to 2 percent of the thermal resistance at room temperature. Considering the complexity of the calculation, the agreement is remarkable.

The treatment given here is incomplete in two respects. First, similar calculations should be made assuming that the electrons are scattered by screw type dislocations.[20] Second, studies should be made to determine just what kind of three-dimensional dislocation arrays are present in the various types of crystals when they undergo certain simple kinds of plastic strain, such as simple glide in one slip direction on one slip plane.

In conclusion I would like to thank Professor Frederick Seitz for suggesting the problem and for numerous helpful discussions. I would also like to thank Mr. John Pittenger and Miss Nancy Michener for help with the numerical calculations.

[20] J. M. Burgers, Proc. K. Akad. Amst. 42, 263, 378 (1939).

Magnetic Susceptibility of Zinc at Liquid Helium Temperatures

S. G. SYDORIAK* AND J. E. ROBINSON
*Sloane Physics Laboratory, Yale University,** New Haven, Connecticut*
(Received September 20, 1948)

The de Haas-van Alphen effect in zinc has been investigated at 4.2°K by measuring the couple on a zinc crystal in a uniform magnetic field. The data obtained give the dependence of the susceptibility both on field strength and on orientation of the crystal relative to the direction of the field. The susceptibility is found to be isotropic in the main cleavage plane. The experimental results are compared to the theory of Blackman and Landau, with which their main features are in qualitative agreement.

Detailed examination, however, indicates discrepancies in (a) the phase of the periodicity, and (b) the shape and amplitude of the envelope of the oscillations, in that the theoretical envelope as interpreted from the data at low fields decreases too slowly at high fields. From the comparison we estimate that the electrons responsible for the effect have a chemical potential $E_0=0.02$ electron volts, a transverse effective mass $m_1=0.01m_0$ (where m_0 is the free electron mass), and a ratio of transverse mass to longitudinal mass $m_1/m_3=0.01$. From these values, the specific heat of these electrons is estimated to be 0.1 percent of the measured electronic heat, and their number to be 2×10^{-6} per atom. Comparison of these results to the work of Marcus on zinc and Shoenberg on bismuth has also been made.

INTRODUCTION

IN 1930 de Haas and van Alphen[1] found that at very low temperatures the diamagnetic susceptibility of a bismuth single crystal depends on the field at which the measurement is made. With increasing field the susceptibility rose and fell periodically with ever increasing amplitude. They made further measurements in 1932[2] and in 1936 Shoenberg and Uddin[3] studied the effect in still greater detail, especially in regard to the influence of temperature and impurities. Definitive measurements on bismuth were made by Shoenberg[4] in 1939. The effect was observed for a variety of crystal orientations and for temperatures ranging from 20°K to 2.1°K but principally at 4.2°K.

In bismuth it is found that susceptibility is independent of the field only when the field is along the trigonal axis, 3. Along a binary axis, 2, and along axis 1, perpendicular to 3 and 2, the susceptibility depends on the field, the periodicity being different for each of these axes.

An attempt to discover the effect in a single crystal of antimony[5] was not successful, but low temperature magnetic measurements on many other metals[2] are not conclusive since the measurements were made with polycrystals.

In 1947 the effect was discovered by J. A. Marcus[6] of this Laboratory in zinc. He investigated the range of temperatures down to 14°K and found that for zinc it is the susceptibility in the direction of the hexagonal axis, χ_3, which is dependent on the magnetic field. He was able to observe the periodic field dependence at temperatures as high as 64°K, provided there was a component of the field in the 3-direction.

In a direction perpendicular to the hexagonal axis, the susceptibility was found to be field independent, having the constant value $\chi_1=-0.15\times10^{-6}$ for all fields and for temperatures from 100°K down to the minimum he observed, at 14°K. In this paper we have extended the measurements on zinc into the liquid helium region and also to a wider range of magnetic field. Shoenberg found many features of his results in remarkable agreement with the theory developed by the successive contributions of Peierls,[7] Blackman,[8] and Landau.[9] Our results for zinc bear a similar relation to these theories. Like Shoenberg, we find certain discrepancies. The simpler symmetry of zinc facilitates comparison of theory and experiment.

* Now at Los Alamos Scientific Laboratory, Los Alamos, New Mexico.
** Assisted by the Office of Naval Research.
[1] W. J. de Haas and P. M. van Alphen, Comm. Phys. Lab. Leiden, Nos. 208d, 212a (1930).
[2] See Reference 1, Nos. 220d, 225b (1932).
[3] D. Shoenberg and Z. M. Uddin Proc. Roy. Soc. A156, 687, 701 (1936).
[4] D. Shoenberg, Proc. Roy. Soc. A170, 341 (1939).
[5] D. Shoenberg and M. Z. Uddin, Proc. Camb. Phil. Soc. 32, 499 (1936).
[6] J. A. Marcus, thesis, Yale University (1947); Phys. Rev. 71, 559 (1947).
[7] R. Peierls, Zeits. f. Physik 80, 763 (1933).
[8] M. Blackman, Proc. Roy. Soc. A116, 1 (1938).
[9] L. Landau, by private communication to Shoenberg. See reference 4.

EXPERIMENTAL PART

For the accurate measurement of field dependent susceptibilities the body force (Faraday) method is unsatisfactory because of the necessary gradient of the magnetic field. We shall see that at liquid helium temperatures a 5 percent change in field may cause a shift from a peak of positive susceptibility to a peak of negative susceptibility. Now with a crystal of zinc such as we have used, having dimensions of the order of 6 mm, the electromagnet and Foex pole pieces available here for use in a body force measurement and used by Marcus provide a field which increases by 5 percent from the top of the specimen to the bottom. With this apparatus we would evidently observe only a greatly smoothed out version of the effect.

Although it would be possible to reduce the gradient by use of other pole pieces, this could be done only at a considerable sacrifice of sensitivity.

I. Principle of the Torsion Method

We have, therefore, following Shoenberg,[4] used a torsion method. The turning couple $\mathbf{C}$ acting on a body with magnetization $\mathbf{I}$ and mass m is given by

$$\mathbf{C}=m\mathbf{I}\times\mathbf{H}, \tag{1}$$

i.e.,

$$\frac{\mathbf{C}}{m}=(I_2H_3-I_3H_2)\mathbf{i}+(I_3H_1-I_1H_3)\mathbf{j}+(I_1H_2-I_2H_1)\mathbf{k}. \tag{2}$$

In the present investigation we are dealing with an hexagonal close-packed structure and shall take the 3 axis along the hexagonal axis [000.1]. The other two crystal axes then lie in the principal or cleavage plane [000.1]. The two-crystal orientations we have used are depicted in Fig. 1. In Fig. 1(a) the hexagonal axis is horizontal (its elevation, $\beta=0$) while in Fig. 1(b) it is vertical. We shall be principally concerned with arrangement (*a*).

The horizontal magnetic field may be set at any angle ϕ to the hexagonal axis. The 2 axis and 1 axis are in the cleavage plane, which is vertical in Fig. 1(a). Equation (2) is then

$$C=(\chi_3-\chi_2\cos^2\theta-\chi_1\sin^2\theta)mH^2\sin\phi\cos\phi, \tag{3}$$

where θ is the elevation of the 2 axis, which is in the hexagonal plane.

The corresponding equation applying to the case of vertical hexagonal axis ($\beta=90°$) is

$$C'=(\chi_1-\chi_2)mH^2\sin\phi'\cos\phi', \tag{4}$$

where ϕ' is the angle between H and the 2 axis. It is well known that at room temperatures there is no magnetic anisotropy in the cleavage plane; i.e., $\chi_1=\chi_2$. Hence, the measurement corresponding to Fig. 1(a) gives us the differential susceptibility $(\chi_3-\chi_1)$ directly since then Eq. (3) reduces to

$$C=(\chi_3-\chi_1)mH^2\sin\phi\cos\phi, \tag{5}$$

if $\chi_1=\chi_2$. It is necessary, however, to verify that $\chi_1=\chi_2$ at liquid helium temperatures.

Although the torsion method gives us only a difference of susceptibilities, $(\chi_3-\chi_1)$, this does not introduce any difficulty in the application of the theory, particularly since only χ_3 is field dependent while χ_1 has the constant value of -0.15×10^{-6} for all fields. In addition to the fact that a constant field is used, other advantages of this method over the body force method are that torsion apparatus is inherently more stable than a microbalance. Finally, we shall see that ferromagnetic impurities can be readily detected by noting the effect of rotating the field relative to the crystal at room temperature. The apparatus described below makes it possible to measure $(\chi_3-\chi_1)$ at fields down to 1 kilogauss in a field which varies less than 0.1 percent over the 0.6 cm specimen.

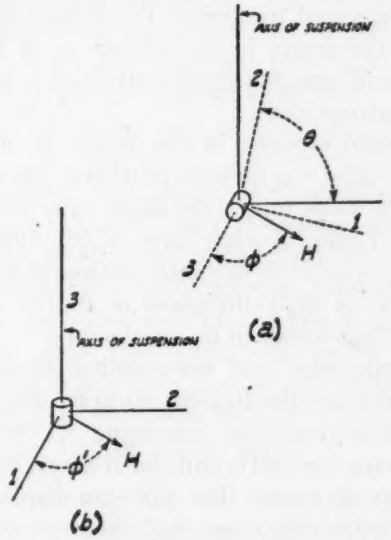

FIG. 1. Crystal orientations used in the experiment.

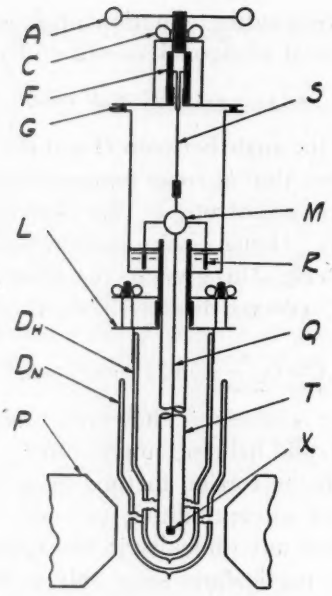

FIG. 2. Schematic diagram of the torsion balance.

II. Apparatus

A schematic diagram of the torsion balance and cryostat are shown in Fig. 2. A single torsion wire has been used in the present investigation.

A mirror M, damping ring, R, dipping in Octoil, and a rigid glass or quartz suspension S are attached to the lower end of the torsion wire. The specimen X is attached to the rigid suspension by means of Duco cement.

A vertical slit illuminated by a 60-watt half-silvered G. E. candlebulb and a traveling microscope were used to observe the deflection of the mirror, the image being focused by a 1-meter focal length lens (not shown) attached over a hole in the balance case.

A critical element in the design is the glass tube T. Since it is necessary to leave the balance mounted while filling the flask with helium in another room, T must have a minimum heat capacity in order to minimize the loss of liquid on assembly. A wall thickness of 0.015″ with a $\frac{1}{2}$″ O.D. was found to be satisfactory.

The specimen and surrounding Dewars are placed between the 10.2-cm diameter flat poles of an electromagnet, the gap being 5.1 cm. With this spacing the field is uniform in the region of the center to the extent that a 0.5-cm displacement toward either pole raises the field about 0.05 percent, while moving parallel to the pole face lowers the field about 0.15 percent. In all our measurements the sample was aligned on the axis of rotation of the magnet to within 0.5 mm.

A maximum field of about 8.5 kilogauss is attainable with our magnet when the coils are in parallel with a 220-volt battery but the necessary maximum current of 25 amperes can be maintained for only a few minutes as the magnet warms up and the batteries polarize.

Mechanical devices for adjusting the suspension are indicated by letters on the left-hand side of Fig. 1. A is an arm by which the zero setting of the mirror can be adjusted and C is a wing nut for controlling its elevation. These operations can be performed in the course of an experiment without breaking the vacuum, the seal being a flexible rubber tube F. Neoprene gasket G seals this suspension adjustment device to the body of the balance. In the front of the balance is a rectangular hole (not shown) covered by the galvanometer lens previously mentioned.

When the superstructure is lifted off, everything comes out of the balance, including the oil tub (not shown). Sealed to the helium flask is the lid L. Three bolts solidly fixed to the lid make possible a rapid attachment and reproducible alignment of the filled helium flask. This is important because of the close tolerances allowed in the region of the pole pieces. When alignment is not good the Dewar may touch the bottom of tube T, displacing it sidewards to the point where it touches the crystal. The nitrogen flask is attached in a somewhat similar fashion to the lid L but with its top end open to the atmosphere.

Choice of the torsion wire presented a problem which was not immediately apparent. At liquid helium temperatures eddy currents in the zinc crystal are very large and persistent. In consequence, if the magnet is rotated while the field is on, the specimen follows the motion of the magnet almost in step. The torsion wire is then subjected to a twist far greater than ever occurs during room temperature measurements, the result being a semipermanent set which lasts an hour or so. That is, there occurs a sudden change in the zero field reading θ_0 of the traveling microscope followed by a very gradual return toward the initial zero reading. In one experiment with a 0.003-in. diameter Nichrome wire this change in zero reading was greater than the effect being

looked for, and it was necessary to reduce the magnet current to zero before each change in the magnet position—a time consuming operation, since the magnet must then be remagnetized at maximum current for each reading. The necessity for remagnetization will be explained later in the section on magnet calibration.

To reduce this semipermanent set a ribbon suspension, S, was finally used. A 0.0063-in. diameter Nichrome wire flattened to $0.0013'' \times 0.016''$ is free of the trouble for twists up to 20 degrees. Nichrome and phosphor bronze are found to be suitable materials when flattened. Tungsten is very poor. A strip of platinum rolled from round wire is also poor. A piece of gold galvanometer strip was found to be less satisfactory than nichrome. Quartz is by far the best material of those tested but is not entirely satisfactory because of its fragility.

The torsion wire was calibrated by timing 100 oscillations of a brass bar attached to the bottom end. The torsion constants, expressed in dyne-cm per cm deflection of the slit image were found to be 0.1524 for the round wire used for the first four helium runs and 0.360 for the flat strip used thereafter. These numbers correspond to an optical arm (slit to mirror to microscope) of 193.4 cm.

The oil used for damping is a frequent source of trouble and might better be replaced by electromagnetic damping. On one occasion a sticky coagulant formed in the oil, caused perhaps by the presence of impurities such as dust or particles of sealing wax. The effect was to cause the zero reading to depend on the direction of the prior deflection. For a time the phenomenon was confused with mechanical hysteresis in the suspension, but on changing the oil the trouble disappeared.

The most persistently annoying aspect of oil damping is the necessity of careful and prolonged outgassing before beginning measurements, particularly when these are made at very low temperatures. On one occasion when the temperature of the helium bath was being reduced, a sudden onset of outgassing caused the image to dart off scale at regular intervals. The reduction in temperature was also reducing the pressure inside the balance case to some extent, thus creating a condition more favorable for outgassing. Direct observation of the oil through the lens window verified that outgassing was taking place.

Several pump oils and manometer oils were tested and all except Octoil were found to be completely unsatisfactory, in that outgassing persisted for a very long time after an exposure to the atmosphere. Attempts to speed up outgassing by application of heat were found to be unsatisfactory because of the danger of cracking the oil.

III. Specimens

The zinc crystal used in this investigation was made by J. A. Marcus, by the Bridgman method[10] of slowly lowering a glass tube containing the molten and outgassed metal through a temperature gradient. The crystal has a weight of 0.6058 g. The metal is "Hilger Spectroscopic," 99.99 percent pure.

IV. Cryogenic Technique

In preparation for a liquid helium run the suspension is carefully aligned on the magnet axis of rotation and the balance is evacuated. Helium gas is admitted to a pressure of 1 mm of mercury to provide thermal contact to the specimen.

Following the procedure in use in this laboratory for some time in connection with Pyrex Dewar flasks[11] the interspace of D_H is evacuated and refilled with 1 mm Hg of air before each run. The air is for the purpose of rapid cooling of the inner wall and contents of the flask down to the temperature of the liquid nitrogen flask D_N. When liquid helium is admitted to D_H, this air freezes and the interspace is then at high vacuum, providing excellent thermal insulation.

While the helium flask is being filled in an adjoining room, the tube T surrounding the specimen is cooled with liquid nitrogen. When all is ready, this nitrogen Dewar is replaced as rapidly as possible by the filled helium flask. By this procedure we gain the advantage of avoiding movement of the specimen after alignment. When properly done the volume of liquid helium evaporated is less than the volume displaced by the tube, with the result that the liquid level is higher after assembly than before.

[10] P. W. Bridgman, Proc. Am. Acad. Arts. Sci. 60, 305 (1925).

[11] C. T. Lane and H. A. Fairbank, Rev. Sci. Inst. 18, 522 (1947).

However, the transfer time is quite critical. In a side experiment done with liquid nitrogen it was estimated that the tube warmed up from 77°K to about 145°K during a 10-second exposure to the atmosphere. It was observed that for exposures of slightly more than 10 seconds ice became visible on the surface of the precooled tube. It appears plausible that ice formation is an important factor in the rapid warming up of the tube. If so, the success of the transfer operation should depend critically on the humidity as well as on the transfer time.

Large variations were, in fact, noted in the volume of liquid helium lost in actual practice. Removal of the precooling flask and insertion of D_H actually takes about 10 seconds. The volume of liquid helium lost was as little as 4 cc on one occasion and as much as 40 cc on another, the average loss for seven experiments being 20 cc. Thus the latent heat of the evaporating liquid averaged 60 joules and was as little as 12 joules on one occasion. It is also interesting to note that the heat removed from tube T on immersion is considerably greater than 12 joules, indicating that the heat exchange between the escaping vapor and the tube is the principal factor in cooling down the tube.

V. Magnet Calibration

Because of hysteresis of the magnet, it is essential that the same procedure be followed during a calibration run and in all subsequent measurements. The invariable procedure was adopted of approaching a desired magnet current from above—from the maximum current attainable. If approached from below, the field may differ by as much as 0.1 kilogauss.

To make this procedure possible, a suitable array of rheostats and resistors for adjusting the magnet current were carefully chosen. They meet the requirement that continuous reduction of current is possible without back tracking.

It suffices to calibrate the field at a single value of magnet current by the ordinary method employing a ballistic galvanometer, together with an observation of the couple acting on the crystal at room temperature at the same magnet current. Since it is well known that diamagnetic susceptibilities are independent of field at ordinary temperatures, other fields can now be measured simply by measuring the couple (proportional to the deflection, $\Delta\theta$, of the mirror) at other values of magnet current.

In measurements on feebly magnetic substances it is important to be sure that ferromagnetic impurities are not present in significant amounts and to apply appropriate corrections for unavoidably small amounts of such impurities. Hence, a well-known method of Honda's[12] is frequently used to correct body force measurements for the effects of such impurities. When the observed susceptibility is plotted as a function of reciprocal field, the result is a straight line whose slope is proportional to the impurity and which intersects the axis at the true diamagnetic susceptibility. It is easy to show that this method is applicable to the torsion measurements as well. The couple acting on a specimen with a ferromagnetic impurity of moment **M** is

$$C=k\Delta\theta=\Delta\chi mH^2\sin\phi\cos\phi+MH\sin\phi', \quad (6)$$

where ϕ' is the angle between **M** and **H** and k the torsion constant. Dividing by $mH^2\sin\phi\cos\phi$ we have what we may call the "observed differential susceptibility,"

$$\Delta\chi_{\text{obs}}=\Delta\chi+\left(\frac{M\sin\phi'}{m\sin\phi\cos\phi}\right)\frac{1}{H}. \quad (7)$$

Since any ordinary ferromagnetic impurity will be saturated in fields of the order of a few hundred gauss, M will be a constant in fields covering the usable range of our balance. In this case, a "Honda plot" of the observed differential susceptibility as a function of $1/H$ would be a straight line whose intercept at infinite field would give the true differential susceptibility of the diamagnetic material.

If, however, the ferromagnetic impurity is localized somewhere high up on the suspension where the field is far less than H or if it is extremely "hard" magnetically, M will depend on H and the Honda plot cannot then be used to correct for the impurity.

Inspection of Eq. (6) suggests another procedure which is in some respects superior. It will be evident that a 360° rotation of the field causes the diamagnetic term to go through 2 cycles while the ferromagnetic term goes through only one. It

[12] K. Honda, Ann. d. Physik 32, 1048 (1910).

is therefore possible to separate out the diamagnetic term. Thus, by averaging the balance deflections ($\Delta\theta$) at any pair of angles ϕ and $\phi+180$ it is seen that the impurity term is eliminated. Knowing the field at which this data was taken one can then make a correction for the impurity at any other value or orientation of the field, provided it can be assumed that the impurity is saturated. The advantage of this procedure over a Honda plot is that the latter is applicable only to the particular crystal orientation at which the data was taken. Furthermore, the Honda plot requires a complete field calibration by the cumbersome and not very precise search coil procedure.

Figure 3 shows the results of an analysis of this type. Since the data shown in (*a*) is for the case of crystal axis nearly vertical the amplitude of the diamagnetic term is quite small and the over-all angle characteristic is badly distorted by the effect of the suspension, shown in (*b*). No analysis of the data on the "suspension alone" is needed, since it is obviously ferromagnetic. When its effect is subtracted from (*a*) and this is analyzed*** for components, it is seen that there may be a slight ferromagnetic impurity in the crystal itself, but its amplitude is scarcely greater than the experimental errors in the points. Thus we see the crystal is substantially free from impurity, although the effect of the suspension itself is not negligible. Even when the crystal is oriented for maximum couple the suspension can cause an error of 1.5 percent in the susceptibility. The other features of Fig. 3 will be discussed later.

*** We assume three possible contributions to the deflection of the crystal alone:

(1) a one-cycle term resulting from ferromagnetic impurity,

(2) a two-cycle term, present if the hexagonal axis is not accurately vertical,

(3) a three-cycle term, present if $\chi_1 \neq \chi_2$.

The resultant crystal deflection is then

$$\theta(\phi) = a\sin(\phi+\alpha)+b\sin(2\phi+\beta)+c\sin(3\phi+\gamma),$$

where ϕ is the azimuth, and α, β, γ are phase constants. Averaging deflections for pairs of angles ϕ and $(\phi+\pi)$,

$$\tfrac{1}{2}\{\theta(\phi)+\theta(\phi+\pi)\} = b\sin(2\phi+\beta).$$

The two-cycle term is then subtracted from $\theta(\phi)$, yielding a table of values for

$$\theta'(\phi) = a\sin(\phi+\alpha)+c\sin(3\phi+\gamma).$$

Further trigonometric manipulation gives

$$\tfrac{1}{3}\{\theta'(\phi)+\theta'(\phi+\tfrac{2}{3}\pi)-\theta'[\phi+(\pi/3)]\} = c\sin(3\phi+\gamma).$$

Subtracting the three-cycle term from $\theta'(\phi)$ then leaves the one-cycle term, and completes the analysis.

Several glass and quartz suspensions of various diameters were tested in the balance, but all displayed a significant magnetic anisotropy, although this did not always have a strictly ferromagnetic angle characteristic as in Fig. 3(b). Although the anisotropy was found to decrease with the diameter of the rod, only a limited reduction in diameter was permissible because of the rigidity requirement. The anisotropy was unaffected by cleaning the suspension or by subjecting it to temperatures high enough to soften the glass or quartz.

We are now prepared to discuss the actual magnet calibration in further detail. Several measured values of H in the range from 4.2 to 6.5 kilogauss were compared to previously observed deflections (at the same magnet current) of the standard crystal, zinc *A*, used in these measurements and the ratio $\Delta\theta/H^2=(0.978\pm0.010)\times10^{-6}$ was obtained. The small spread in the points would appear to indicate that very little impurity was present. Actually, however, analysis of several angle characteristics revealed an impurity which had the effect of reducing $\Delta\theta$ by nearly 1 percent over the entire range of fields at which the calibration was made.

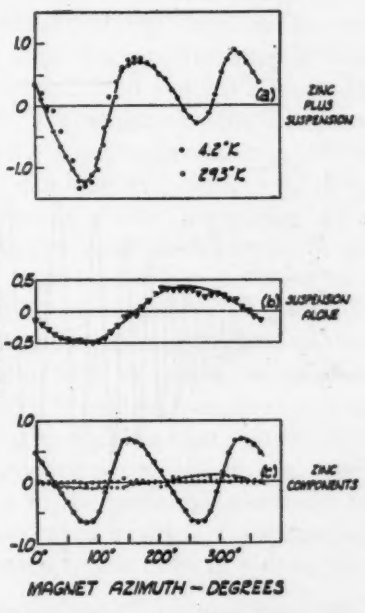

FIG. 3. Angle characteristic with hexagonal axis vertical. By comparison, at the field strength of 5500 gauss at which these measurements were made, the maximum deflection with hexagonal axis horizontal is 29 mm.

TABLE I. Room temperature values of $\chi_3-\chi_1$ for zinc.

Author	$(\chi_3-\chi_1)\times10^6$
Present work	−0.0476
Marcus[a]	−0.045
McLennan, Ruedy, and Cohen[b]	−0.045
Rao[c]	−0.053

[a] See reference 6.
[b] J. C. McLennan, R. Ruedy, and E. Cohen, Proc. Roy. Soc. A121, 9 (1928).
[c] S. R. Rao, Proc. Ind. Acad. Sci. 4, 186 (1936).

VI. Experimental Results

The room temperature value of the differential susceptibility $\Delta\chi=\chi_3-\chi_1$ as measured by us, together with the results of previous investigators on zinc, is given in Table I. It should be noted that the other three determinations cited were all separated measurements of χ_3 and χ_1 and hence ours is inherently the more accurate.

In deriving Eq. (5) we have assumed that $\chi_1=\chi_2$ at 4.2°K as well as at room temperature. Figure 3 shows that this is indeed the case, there being no difference between the data at 293° and 4.2°K. In this connection it should be pointed out that, for the orientation at which the data in Fig. 3 were taken, namely, that shown in Fig. 1(b), we should expect a 3-cycle component in C if $\chi_1\neq\chi_2$. For the orientation corresponding to Fig. 1(a) we should have, as has already been mentioned, a 2-cycle term. Added to both of these would be a 1-cycle term if ferromagnetic impurities were present. The results of a complete analysis on the crystal itself are shown in Fig. 3(c), for the orientation corresponding to Fig. 1(b). The prominent two-cycle term is interpreted as an indication that the hexagonal axis was not accurately vertical.

The slight impurity component has been previously mentioned. It is evident that no three-cycle term (designated by × marks) is present. Hence, $\chi_1=\chi_2$ at 4.2°K.

A. Field Dependence at 4.2°K

Figure 4 shows the de Haas-van Alphen effect at 4.2°K, $\phi=45°$. We have obtained the scale on the right for χ_3 by adding Marcus' value $\chi_1=-0.150\times10^{-6}$ to our observed values of $(\chi_3-\chi_1)$ assuming the value of χ_1 to be constant down to 4.2°K. We see on this scale that a number of the peaks are actually paramagnetic. Although this is not at variance with the theory, it has not been previously observed, either in bismuth or in zinc.†

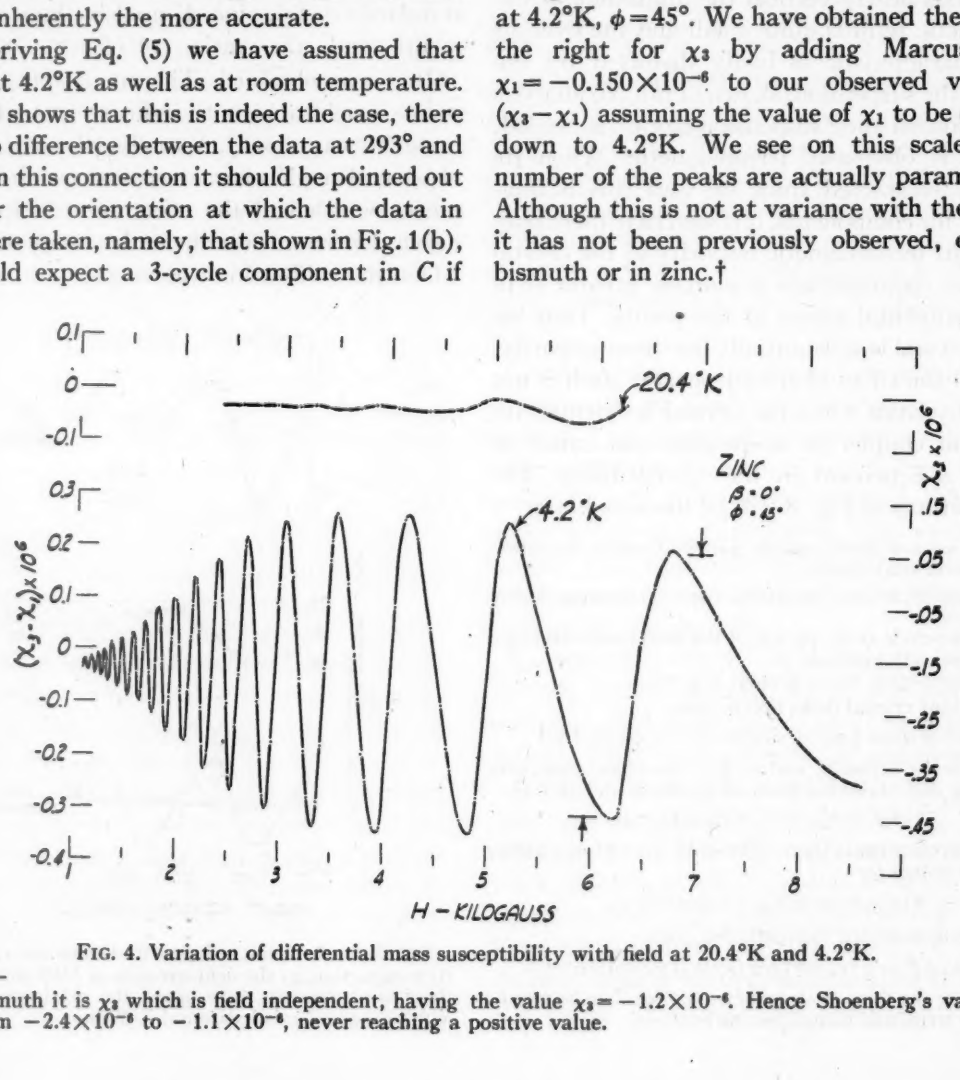

FIG. 4. Variation of differential mass susceptibility with field at 20.4°K and 4.2°K.

† In bismuth it is χ_3 which is field independent, having the value $\chi_3=-1.2\times10^{-6}$. Hence Shoenberg's value of χ_1 ranges from -2.4×10^{-6} to -1.1×10^{-6}, never reaching a positive value.

It is also worthy of note that the amplitude is decreasing at high fields, in agreement with theoretical expectations. Shoenberg was unable to reach fields sufficiently high to produce this effect in bismuth, while the earlier observations of de Haas and van Alphen at fields up to 35 kilogauss are not conclusive because of the necessary field inhomogeneity in their set-up.

Finally, it should be pointed out that the prominent asymmetry of the peaks at the higher fields is an artifact which is due to the circumstance that the large couples obtained at high fields displace the crystal to a new position. As a result of the sharpness of the angle characteristic, to which we shall presently refer, the susceptibility is markedly different in the new orientation and peaks of susceptibility are therefore displaced.

The displacement of two of the peaks at high field was determined at the conclusion of the experiment whose results are shown in Fig. 4. In each case the crystal was purposely displaced to the extent that it would actually be at $\phi=45°$ when maximally deflected. The true locations of the two highest peaks for $\phi=45°$ were thus found to be 6.98 and 5.97 kilogauss with minor changes in amplitude. The theory actually predicts symmetrical peaks when the abscissa is in units of reciprocal field strength. On this basis, if we consider the peaks to originate at the value of the mean susceptibility, extremes of susceptibility would be expected at 6.90 and 5.95 kilogauss, in substantial agreement with the above experimental observation.

B. Angle Characteristic at 4.2°K

With a constant field of 2360 gauss, which by coincidence corresponds to one of the peaks in the field dependence, the angle characteristic shown in Fig. 5 was obtained. Because of the persistent eddy currents present at this low temperature, to which reference has already been made, the specimen approaches its equilibrium position very slowly and at some particular orientations two or three minutes are required to reach equilibrium, in comparison to the normal time of about 4 seconds.

Since the couple is very small near $\phi=0$ and near 90°, some parts of the curve have been omitted or shown by dashes—but there was no evidence of oscillations in these regions.

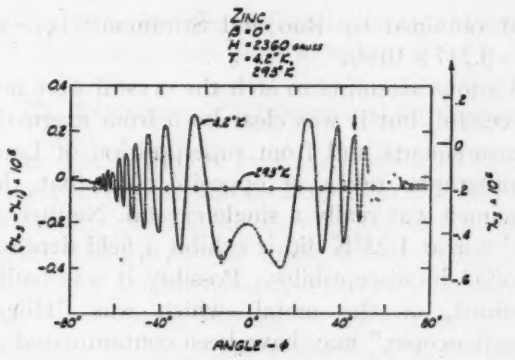

FIG. 5. Variation of differential mass susceptibility with angular orientation at constant magnetic field.

Referring to the χ_3 scale shown in the figure we note that there are several paramagnetic peaks, while most are diamagnetic. Thus there are some directions of field relative to crystal axes in which the crystal appears to be paramagnetic while it is diamagnetic in intervening regions. An angular variation from para- to diamagnetic susceptibility is not unprecedented and has been observed at room temperature by Browne and Lane[13] in dilute solutions of tin in antimony.

C. Cadmium and Thallium

A crystal was briefly tested at temperatures down to 1.65°K, but no field dependence of susceptibility was observed. The magnetic anisotropy was found to be much greater than at room temperature by a factor of 5 at 2.0°K and a factor of 6 at 1.65°K. Unfortunately, the direction of the crystal axes was not known so only a lower limit to $(\chi_3-\chi_1)$ can be given, being -0.111×10^{-6} at room temperature. Our lower limit is slightly greater than the result of McLennan, Ruedy, and Cohen†† (-0.101×10^{-6}), and almost twice that of Rao and Subramaniam[14] (-0.060×10^{-6}).

It is well known that impurities or strain in a single crystal tend to reduce its magnetic anisotropy, and it is evident from the large spread in observed susceptibilities that extraordinary precautions are necessary. While our result with cadmium is in the favorable direction, this was not the case with a single crystal of thallium whose anisotropy was only 40 percent of that of

[13] S. H. Browne and C. T. Lane, Phys. Rev. 60, 895 (1941).

[14] S. R. Rao and K. C. Subramaniam, Phil. Mag. 21 609 (1936).

†† See Table I, reference b.

that obtained by Rao and Sriraman[15] ($\chi_3-\chi_1=-0.247\times10^{-6}$).

Various attempts to etch the crystal were not successful, but it was clear both from magnetic measurements and from superposition of Laue photographs taken of opposite ends that the specimen was really a single crystal. Neither at 4.2° nor at 1.25°K did it exhibit a field dependence††† in susceptibility. Possibly it was badly strained, or the metal, which was "Hilger Spectroscopic," may have been contaminated in the handling. Since Shoenberg has shown that as little as 0.01 percent impurity in bismuth is sufficient to eliminate the field dependence completely, a negative result should not be considered as conclusive unless the purity of the specimen is verified after completion of the experiment.

THEORETICAL PART

I. Introductory

Analysis of the data will be based on Landau's formulation[9] of the theory. Landau's extension of the theory was purely mathematical; the physics was brought to its present stage of development by Blackman.[8] It is essentially a free electron theory, and attributes the effect to a small fraction of the valence electrons which is contained in one or more Brillouin zones. The majority of the valence electrons are assumed to populate other zones, which do not contribute to the oscillating part of the susceptibility, but serve as reservoirs of electrons. These other electrons are then presumed to contribute to the total susceptibility in the more usual manner: e.g., through spin paramagnetism and ordinary Landau diamagnetism.

In outline, Blackman's argument runs as follows. For metals exhibiting the de Haas-van Alphen effect, there exist one or more Brillouin zones in which only the very lowest electronic states are filled. The energies of the electrons occupying these states (hereinafter called the d.H.-v.A. electrons) can then be expressed as a quadratic function of their momenta, and in that sense they may be considered free. Under the influence of a magnetic field, the d.H.-v.A. electrons execute Larmor precession about the lines of force, and their motion in a plane perpendicular to the field is quantized. This quantization gives rise to the spectacular oscillating susceptibility. Motion parallel to the field is not quantized; this permits continuous variation of the susceptibility with field strength. It is assumed that the d.H.-v.A. electrons supply only a negligible portion of the total electronic specific heat, so that their chemical potential E_0 is sensibly constant. Furthermore, they have a highly anisotropic effective mass, from which arises the anisotropy of the effect. It turns out that if E_0 and the effective mass in at least one direction are abnormally small, the theory predicts an appreciable field dependence of the susceptibility at low temperatures.

In the case of bismuth,[8] it was necessary to assume that three zones of trigonal symmetry contribute to the effect. Further, Shoenberg[4] found it necessary to assume that the tensor giving the effective mass in these zones was skewed with respect to the crystal axes, and to use four components of the tensor to fit the data. In zinc, however, the data may be accounted for in terms of a single zone having the full symmetry of the hexagonal crystal. In consequence, Landau's explicit expression for the couple reduces for zinc to a form much simpler than for bismuth. The greater part of this analysis will be a detailed comparison of the periodicity and envelope of the observed oscillations to the predictions of the theory. The principal experimental parameters to be determined are the components of the effective mass tensor and E_0. From these parameters can be calculated the specific heat of the d.H.-v.A. electrons, and this compared to the measured electronic heat. Finally, the present work will be compared to previous work on zinc, and to results for bismuth insofar as is possible.

II. Theoretical Predictions

Since the susceptibility is isotropic in the main cleavage plane, we may assume there to be only two different effective masses: m_1 perpendicular and m_3 parallel to the hexagonal axis. The simplest assumption is then that the d.H.-v.A. electrons in zinc are contained in a single zone of

[15] S. R. Rao and S. Sriraman, Proc. Roy. Soc. A166, 325 (1938).

††† Since thallium is superconducting at this temperature, the measurements were, of course, made in fields greater than the critical threshold.

hexagonal symmetry and have an ellipsoidal energy surface:

$$E=\frac{1}{2m_1}(p_1^2+p_2^2)+\frac{1}{2m_3}p_3^2. \tag{8}$$

Landau's formula then gives, for not too strong fields,

$$\chi_3-\chi_1=(m_1-m_3)f(\beta H), \tag{9}$$

where

$$f(\beta H)=A\left\{\frac{\pi^2}{6}\left(\frac{k}{E_0}\right)^{\frac{1}{2}}-\frac{1}{(T)^{\frac{1}{2}}}\left(\frac{2\pi^2kT}{\beta H}\right)^{\frac{1}{2}}\times\exp\left(-\frac{2\pi^2kT}{\beta H}\right)\sin\left(\frac{2\pi E_0}{\beta H}-\frac{\pi}{4}\right)\right\}, \tag{10}$$

$$\left.\begin{aligned}A&=\frac{\sqrt{2}e^2E_0}{2\pi^4c^2\hbar(k)^{\frac{1}{2}}m_1(m_3)^{\frac{1}{2}}},\\ \beta&=\frac{e\hbar}{cm_1(m_3)^{\frac{1}{2}}}(m_1\sin^2\phi+m_3\cos^2\phi)^{\frac{1}{2}}.\end{aligned}\right\} \tag{11}$$

The principal susceptibilities are given by

$$\left.\begin{aligned}&\chi_1=-m_1f(\beta_1H),\quad \beta_1=\frac{e\hbar}{c(m_1m_3)^{\frac{1}{2}}},\\ &\chi_3=-m_3f(\beta_3H),\quad \beta_3=e\hbar/cm_1.\end{aligned}\right\} \tag{12}$$

Since the amplitude of the envelope varies with the numeric $2\pi^2kT/\beta H$, the fields for which χ_1 and χ_3 have maximum envelope amplitude are in the ratio

$$H_1/H_3=\beta_3/\beta_1=(m_3/m_1)^{\frac{1}{2}}.$$

The observations of Marcus showed no oscillations in χ_1 for fields up to 8.25 kilogauss. Since the oscillations in χ_3 have appreciable amplitude for fields as low as one kilogauss, m_1/m_3 must be very small. Therefore, in discussing the field dependence we may write

$$\beta=(e\hbar/cm_1)\cos\phi.$$

If m_1/m_3 is sufficiently small, the approximation will also be valid in discussing the angle dependence except at very high angles. Equation (9) is then symmetrical in H and $\cos\phi$, and the field and angle characteristics may be analyzed by nearly equivalent procedures. Moreover, it should be possible to bring the two characteristics into coincidence by treating each as dependent on $H\cdot\cos\phi$ rather than on H or $\cos\phi$.

III. Evaluation of Experimental Parameters

In calculating the parameters we need be concerned only with the oscillating term in the susceptibility; consideration of the constant term which obtains at low fields will be postponed. From the periodicity of the experimental curves we can determine β/E_0. From examining the envelope we determine β and m_3A. In addition, the ratio m_1/m_3 can be estimated roughly from the periodicity of the angle characteristic. Wherever possible, calculations will be made independently for the angle and field dependences.

A. Periodicity of the Oscillations

1. Field dependence.—Inspection of (10) shows that the oscillations should vanish whenever

$$\frac{2\pi E_0}{\beta H}-\frac{\pi}{4}=r\pi \quad r=0, 1, 2, 3\cdots \tag{13}$$

We take the points where the curve crosses the line of average susceptibility to be those which satisfy Eq. (13). Plotting the reciprocals of the fields‡ at these points against integers should give a straight line of slope

$$b_h=\frac{\beta}{2E_0}$$

whose intercept on the axis of integers gives the phase constant. The choice of integers is somewhat arbitrary, but in any event r must be an even integer at the last crossover.‡‡ A good straight line is indeed obtained (Fig. 6), giving a slope $b_h=0.0223$ kilogauss^{-1}, but the phase turns out to be 0 instead of $-\pi/4$. The discrepancy is similar to that found by Shoenberg for bismuth.

2. Angle dependence.—We first write (13) in

‡ Corrections have been made in the field dependence calculations for a small ferromagnetic impurity which evidently occurred high on the suspension. The correction amounted to lowering the observed field strength by less than 2 percent at the lowest fields, and was negligible above 4 kilogauss.

‡‡ Since $m_3>m_1$, the sign of the oscillating term follows that of $+\sin[(2\pi E_0/\beta H)-(\pi/4)]$. The slope at the last crossover is negative, and the slope of $\sin(1/x)$ is negative at $r=1/x$ only if r is even. This is exactly opposite to the situation for bismuth.

TABLE II.

	$e\hbar/2cm_1E_0$
Angle dependence, negative ϕ	0.0340
Angle dependence, positive ϕ	0.0331
Field dependence, run 1	0.0324
Field dependence, run 2	0.0316

the form

$$\frac{1}{t\cdot\cos\phi}-\text{constant}=\frac{e\hbar H}{2cm_1E_0}r, \qquad (13a)$$

where

$$t=\left(\frac{m_1}{m_3}\tan^2\phi+1\right)^{\frac{1}{2}}.$$

Plotting $1/\cos\phi$¶ against integers for the crossovers of the angle characteristic should give a line which is straight at low angles but which curves upward at high angles because of the factor t. In Fig. 7 are plotted the values of $1/\cos\phi$, and $1/t\cdot\cos\phi$ for various assumed values of m_1/m_3, the data being taken from the oscillations for $\phi<0$. It can be seen that m_1/m_3 must be of the order of magnitude 1/100, since larger values lead to a downward curvature at high angles. Although the deviations at high angles from the straight line fitted to low angle points are small, they are appreciably larger than could be accounted for by experimental error in measuring ϕ. The integers were chosen by identifying the maximum at 45.6 degrees on the angle characteristic with that at 2.38 kilogauss in the field characteristic. We obtain the value 0.0802 for the slope $b_\phi=e\hbar H/2cm_1E_0$. A similar calculation for positive angles yields $b_\phi=0.0781$.

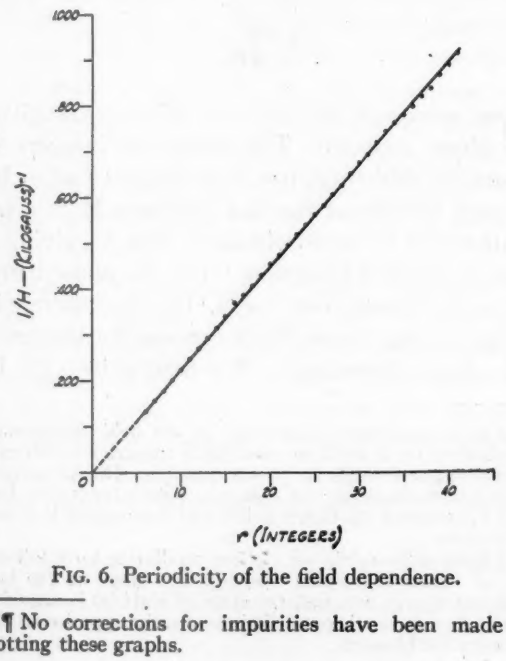

FIG. 6. Periodicity of the field dependence.

¶ No corrections for impurities have been made in plotting these graphs.

3. Comparison of angle and field dependence.—To compare the periodicity of the angle and field dependence we plotted $1/H\cdot\cos\phi$ against integers for each set of crossovers. The slope of each line obtained is $e\hbar/2cm_1E_0$; the results are given in Table II. (We have included the preliminary measurements of the field dependence in this comparison, indicated as run 1.) The angle and first field characteristics were taken without removing the crystal from the suspension, but the crystal was removed and reset before the second and more complete field dependence was obtained. In addition, the angle characteristic is not quite the same for negative and positive ϕ. Since the field characteristics were taken at $\phi=+45°$, the closer agreement between the values of $e\hbar/2m_1E_0$ given by the angle periodicity for $\phi>0$ and by the first field run is to be expected. The difference between the periodicities of the two field runs could be accounted for by a difference in orientation of 1 degree in resetting the crystal. Within the limits of experimental uncertainty, therefore, the angle and field dependent periodicities are in extremely good agreement. Their linearity suggests strongly that the spacing of the Larmor energy levels is accurately proportional to field.

B. Shape and Absolute Breadth of the Envelope

1. Field dependence.—If we let F be the absolute magnitude of the envelope, Eq. (9) gives

$$\log F+\tfrac{3}{2}\log H=-d_1\frac{1}{H}+\log d_1^{\frac{1}{2}}d_2, \qquad (14)$$

where we have set

$$d_1=\frac{2\pi^2kT}{\beta}, \quad d_2=\frac{m_3A}{(T)^{\frac{1}{2}}}.$$

Plotting the left member of (8) against $1/H$ should then give a straight line of slope $-d_1$, d_2 being determined by the intercept on the axis of

abscissae. The constants d_1 and d_2, together with b_h, are then sufficient to determine the effective masses and E_0. We have

$$\left.\begin{aligned} m_1&=wd_1\cos\phi \\ (m_3)^{\frac{1}{2}}&=vd_1^{\frac{1}{2}}d_2b_h\cos\phi \\ E_0&=u/(d_1b_h) \end{aligned}\right\}, \tag{15}$$

where

$$\left.\begin{aligned} u&=\pi^2kT=5.74\times10^{-15} \\ v&=\frac{ch^2}{\pi^2e(2kT)^{\frac{1}{2}}}=3.52\times10^{-12} \\ w&=\frac{eh}{4\pi^3ckT}=1.47\times10^{-33}. \end{aligned}\right\} \tag{16}$$

Following this procedure for the more complete field characteristic, we get the curve of Fig. 8. A straight line is not obtained; the observed amplitude of the envelope falls off more rapidly with increasing field than the theory predicts. The curve is most nearly linear at low fields (high $1/H$), and a straight line was fitted to the low field points in order to determine d_1 and d_2. The best fit gives $d_1=9.61\times10^{3}$ and $d_2=1.51\times10^{-5}$, and leads finally to

$$\begin{aligned} m_1&=0.011m_0, \\ m_3&=6.5m_0, \\ E_0&=0.017 \text{ electron volts}, \end{aligned}$$

where m_0 is the free electron mass. Because of the scattering of the data at low fields, several different straight lines were drawn through the low end of the curve in Fig. 8 to investigate the effect of the fit on the calculated values of the experimental parameters. As could be expected from Eqs. (15), the values of m_1 and E_0 are relatively insensitive to the fit. All possible fits give $m_1=0.01m_0$, and E_0 does not change order of magnitude. The value of m_3 varies from $2m_0$ to $10m_0$. This large sensitivity to the fit makes it impossible to get an accurate estimate of the value of m_3.

Shoenberg also found a discrepancy in the envelope for bismuth, but one which is opposite to that for zinc. He plotted $\log F/T+\frac{3}{2}\log H$ *versus* T/H at constant temperature, obtaining curves for several different temperatures. All plots showed a slight upward curvature at high fields, whereas our curvature at high fields is downward. The departure of the experimental points in Fig. 8 from the straight line fitted at low

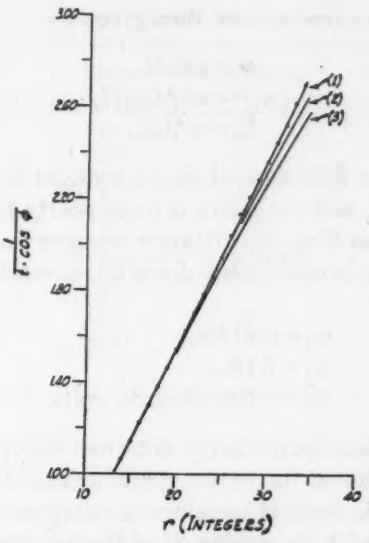

FIG. 7. Periodicity of the angle dependence. (1) $m_1/m_3=0$, (2) $m_1/m_3=1/100$, (3) $m_1/m_3=1/50$.

fields indicates that at the observed envelope maximum the theoretical amplitude is too high by a factor of at least two.

2. Angle dependence.—The envelope of the angle characteristic may be analyzed by the same procedure used for the field characteristic, Eq. (14) being replaced by

$$\log F+\tfrac{3}{2}\log(t\cdot\cos\phi)=-d_3(1/t\cdot\cos\phi)+\log d_3^{\frac{1}{2}}d_2, \tag{14a}$$

where

$$d_3=4\pi^3ckTm_1/ehH.$$

Since we cannot estimate m_1/m_3 accurately, the values of $t\cdot\cos\phi$ for high angles were chosen from consideration of the periodicity of the maxima and minima of the angle dependence. The experi-

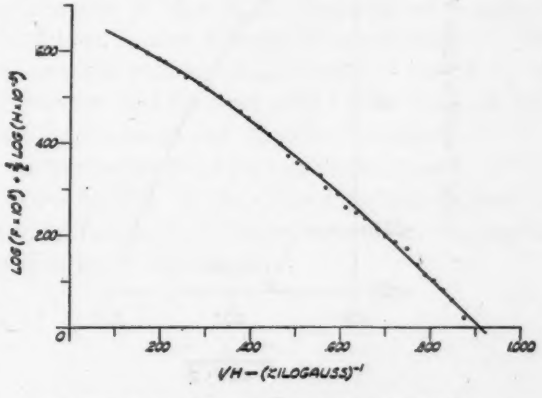

FIG. 8. Variation of envelope with field.

mental parameters are then given by

$$\begin{aligned} m_1 &= w d_3 H, \\ (m_3)^{\frac{1}{2}} &= v d_3^2 d_2 b_\phi H, \\ E_0 &= u/d_3 b_\phi. \end{aligned} \tag{15a}$$

As for the field dependence, a straight line is not obtained, and the curve is most nearly linear for low angles (Fig. 9). Fitting a straight line to the low angle points yields $d_3=4.69$, $d_2=5.48\times10^{-6}$ and

$$\begin{aligned} m_1 &= 0.018 m_0, \\ m_3 &= 7.1 m_0, \\ E_0 &= 0.008 \text{ electron volts.} \end{aligned}$$

The discrepancy is the same as before, and can be considered for either characteristic as failure of the theoretical envelope to decrease rapidly enough with increasing $H_3=H\cos\phi$. Because of the greater number of oscillations observed in the field dependence and the greater scattering of experimental points at high angles in the angle dependence, the values of the parameters calculated from the field characteristic are more accurate, and will be used in further calculations.

IV. Specific Heat

From Eq. (8), the number of electronic states of energy less than E in a crystal volume V is

$$(8\pi V/3h^3) m_1 (m_3)^{\frac{1}{2}} (2E)^{\frac{3}{2}}.$$

The number of electrons per atom which are responsible for the effect is then

$$n(E_0) = \frac{8\pi V}{3h^3} m_1 (m_3)^{\frac{1}{2}} (2E_0)^{\frac{3}{2}}. \tag{17}$$

Using the values of m_1 and E_0 calculated in section III, and taking $m_1/m_3=0.01$,

$$n = 2\times10^{-6} \text{ per atom.}$$

As for bismuth, the number is very small. The electronic specific heat is then

$$C_e = aT = \frac{8\pi^3 k^2}{3h^3} V m_1 (2m_3 E_0)^{\frac{1}{2}} T. \tag{18}$$

Using the same values of the parameters as above gives for the linear coefficient of T, $a=1\times10^{-7}$ cal. mole^{-1} deg.$^{-2}$. The value given by Burton,[16] obtained from threshold field measurements, is $a=1.6\times10^{-4}$ cal. mole^{-1} deg.$^{-2}$. Allowing for the largest possible values of the parameters consistent with any kind of a fit to the data, the d.H.-v.A. electrons can account for only about 0.1 percent of the measured electronic heat, so that Blackman's assumption is indeed valid for zinc. Such a check was not possible in the case of bismuth, where no measurements of the electronic heat exist.

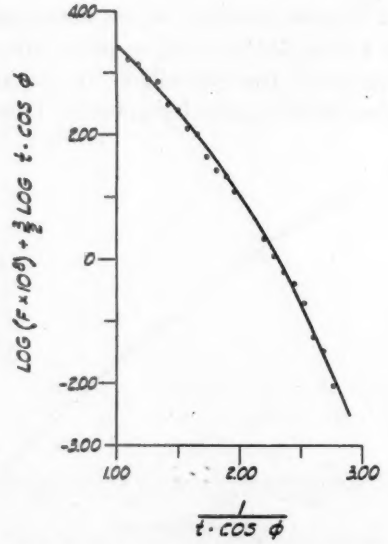

FIG. 9. Variation of envelope with angular orientation.

V. Low Field Constant Susceptibility

From Eq. (12), the principal susceptibilities at very low fields are

$$\kappa_1 = -m_1 A \frac{\pi^2}{6} (k/E_0)^{\frac{1}{2}}, \quad \kappa_3 = -m_3 A \frac{\pi^2}{6} (k/E_0)^{\frac{1}{2}}. \tag{19}$$

In terms of the constants employed in fitting the data,

$$\begin{aligned} \kappa_3 &= -(\pi/6) d_2 (d_1 b_h)^{\frac{1}{2}}, \\ \kappa_1 &= -(\pi/6)(m_1/m_3) d_2 (d_1 b_h)^{\frac{1}{2}}. \end{aligned}$$

Substitution of the numerical values gives (using $m_1:m_3=1:100$)

$$\kappa_3 = -4\times10^{-6}, \quad \kappa_1 = -0.04\times10^{-6}.$$

Although considerable uncertainty attaches to these values because of the discrepancy in the envelope, in any case the calculated value of $-\kappa_1$

[16] Burton, Grayson Smith, and Wilhelm, *Phenomena at the Temperature of Liquid Helium* (Reinhold Publishing Corporation, New York, 1940), p. 348.

is less than the observed $+0.15\times10^{-6}$, and that of $-\kappa_3$ larger than the observed $+0.18\times10^{-6}$. In the case of bismuth, both calculated values were smaller than the experimental, and Blackman inferred that the major part of the constant diamagnetic susceptibility was due to other "free" electrons which do not contribute appreciably to the de Haas-van Alphen effect. Such an explanation cannot suffice for zinc. At all temperatures down to 4.2 degrees, the total susceptibility of crystalline zinc is less than that of the free ions.[17] If the ion core susceptibility then be assumed independent of the crystal structure, it follows that the valence electrons most probably have a net paramagnetic effect. In view of the highly anomalous temperature dependence of χ_3 found by Marcus,[6] more cannot be said at this time.

VI. Comparison with Previous Work

An extensive comparison of the results of the present work with the data obtained by Marcus is not possible, but a rough comparison of the periodicity can be made. In Table III are given the fields at which extremes and crossovers of the oscillations were found by Marcus at 14°K and 20°K, together with the components of field along the hexagonal axis for which the present work indicates the same extremes and crossovers occur at 4.2°K. All measurements were made on the same crystal. (Values in braces were obtained by extrapolation of the periodicity from low fields.) The argument of the periodic term of $f(\beta H)$ is not a function of temperature, so that the extremes and crossovers theoretically should occur at the same H_3 at all temperatures. The rough agreement shown in Table III is fairly good, considering the difference in experimental method. Although the data at the higher temperatures are too meager to permit accurate calculation of $\beta/2E_0$, it is certainly of the same order of magnitude at all three temperatures. (A crude estimate gives a spread of about 50 percent of the value at 4.2°K.) The paucity of data at 14° and 20°K and the bizarre temperature dependence[6] of χ_3 prohibit comment on the envelope.

TABLE III.

r	Extremes of the oscillations 4.2°K	14°K	20°K
7	4.21		4.13
6	4.88		4.85
5	(5.74)	5.62	5.64
4	(7.07)	6.74	7.15
3	(9.19)	9.85	9.83
	Cross-overs of the oscillations		
7	4.52		4.45
6	5.32	5.02	5.16
5	(6.27)	6.31	6.21
4	(7.91)	8.12	8.20

VII. Validity of the Theoretical Formulae

It is, of course, important to ascertain whether or not the discrepancies reported in the preceding sections can have their origin in the mathematical approximations made by Landau in deriving (10). One of us has undertaken an investigation of the validity of these approximations for zinc at the temperatures and fields employed in obtaining the data. While the analysis is not yet completed, we have satisfied ourselves that the mathematics alone cannot account for the discrepancies.

ACKNOWLEDGMENTS

The experimental problem was suggested to one of us (S.G.S.) by Professor C. T. Lane, and I wish to thank him for his interest in the progress of the work. The participation of Mr. T. R. McGuire in all of the low temperature measurements and of Mrs. S. M. Sydoriak on numerous occasions is also gratefully acknowledged. The theoretical problem was suggested to J.E.R. by Professor Lars Onsager, and I wish to thank him for his guidance and continued interest.

The experimental part was submitted by S.G.S. to the faculty of the Yale Graduate School in partial fulfillment of requirements for the degree of Doctor of Philosophy.

[17] The value -0.235×10^{-6} for free ion susceptibility is given by Mott and Jones, *Properties of Metals and Alloys* (Clarendon Press, Oxford, 1936), p. 211.

The Magnetic Internal Conversion Coefficient*

S. D. DRELL
Physics Department, University of Illinois, Urbana, Illinois

(Received September 16, 1948)

The magnetic internal conversion coefficient for K-electrons is rederived with the Dirac current for the electron introduced into the electron-nucleus interaction matrix. Beyond resolving a discrepancy found in the literature, the formula obtained indicates magnetic conversion to be an effect of importance comparable with electric conversion. Its influence on the total conversion coefficient, on the K- to L-shell conversion ratio, and on the lifetimes of isomeric levels is discussed.

I. INTRODUCTION

CONVERSION of magnetic multipole radiation by K-electrons is a relativistic effect depending upon the spin of the electrons. This was first pointed out by Dancoff and Morrison,[1] who gave a relativistic calculation of the magnetic internal conversion coefficient neglecting binding (Born approximation). Recently, Goertzel and Lowen,[2] and Berestetzky[3] have independently calculated this effect on the basis of the Pauli two-component theory of the spinning electron. In the limit of weak binding and soft β-rays ($v_{el} \ll c$, $Ze^2/h\nu_{el} \ll 1$), their result disagrees with the formula of Dancoff and Morrison by a factor $l/(2l+1)$, where the final state of the ejected conversion electron possesses l units of orbital angular momentum. This discrepancy is here shown to be due to the extremely singular character of the magnetic multipole potential. It is resolved by introducing the four-component Dirac current for the electron into the electron-nucleus interaction matrix.

An important consequence of these calculations is that magnetic conversion contributes more significantly than previously appreciated. This is particularly evidenced for soft γ-rays in the neighborhood of the K-electron threshold, since magnetic conversion approaches a large finite value, whereas electric K-conversion vanishes at threshold. Large magnetic conversion can be expected to have an appreciable effect on the total conversion coefficient and on isomeric lifetimes. Of principal concern to the experimentalist will be its influence on the K- to L-shell conversion ratio.

II. CALCULATION

The number of electronic transitions per second from a state o in the K-shell to a continuum state f resulting from magnetic multipole radiation is given for two electrons in the K-shell:[4]

$$N_f d\Omega = (2\pi e^2/\hbar)\,|\,\text{M.E.}\,|^2 d\Omega,$$

where

$$\text{M.E.} = \sum_{\text{spin}} \int dv(\psi_f^* \alpha \psi_o)\cdot \mathbf{A} = \frac{1}{ec} \sum_{\text{spin}} \int dv \mathbf{j}_{fo}\cdot \mathbf{A}. \quad (1)$$

ψ_f is normalized to unit energy, the $(\alpha_1, \alpha_2, \alpha_3)$ are the four-component Dirac spin matrices, and the spin sum extends over final and initial spin states. With Dirac's equation we make the familiar[5] decomposition of the current density,

$$\mathbf{j}_{fo} = (e\hbar/2im)(\psi_f^* \beta\, \mathbf{grad}\psi_o - \psi_o^* \beta\, \mathbf{grad}\psi_f) + (e\hbar/2m)\,\mathbf{curl}(\psi_f^* \sigma \beta \psi_o) - (ie\hbar/2mc)(\partial/\partial t)(\psi_f^* \alpha \beta \psi_o). \quad (2)$$

The first term of (2) is the Schrödinger current. It does not contribute to flux of s-electrons into the continuum because of magnetic multipole radiation, as is seen from the following symmetry considerations. An electron will make a transition

* Assisted by the joint program of the Office of Naval Research and Atomic Energy Commission.

[1] S. M. Dancoff and P. Morrison, Phys. Rev. **55**, 128 (1939).

[2] G. Goertzel and I. S. Lowen, Phys. Rev. **67**, 203 (1945).

[3] V. Berestetzky, J. Phys. USSR. **10**, 137 (1946).

[4] Cf. reference 1. The notation of Dancoff and Morrison is used. Berestetzky has given (J. Phys., USSR. **11**, 85 (1947)) a group theoretical argument showing the gauge in which the scalar potential vanishes to be appropriate for magnetic multipole radiation.

[5] E. L. Hill and R. Landshoff, Rev. Mod. Phys. **10**, 87 (1938).

from the K-shell with zero units to a state with l units of orbital angular momentum upon absorbing a 2^l-pole quantum.[6] The potential of a magnetic 2^l-pole is proportional to Y_l^m, and thus transforms under rotation as a $(2l+1)$-dimensional representation of the rotation group. On the other hand, the Schrödinger current density for this transition transforms as $Y_{l+1}^{m'}$. The angular integral of the product of these two factors vanishes. In terms of parity conservation, the electron parity change accompanying this transition is $(-)^l$, whereas the field of a magnetic 2^l-pole has parity $(-)^{l+1}$. The second term may be identified as the magnetic dipole current associated with the electron spin. The third term is the electric dipole current. It may be neglected in consistency with the accuracy of these calculations. The $\boldsymbol{\alpha}$-matrices mix large and small components of the wave functions and the time derivative is proportional to the energy difference ($\ll mc^2$) between initial bound and final continuum states of the electron.

Introducing (2) into (1), carrying out one partial integration, and employing Gauss's theorem, we obtain for the perturbing matrix element,

$$\text{M.E.} = (\hbar/2mc)\sum_{\text{spin}}\left[\int dv(\psi_f^*\boldsymbol{\sigma}\beta\psi_o)\cdot\mathbf{H} + \int_\Sigma d\boldsymbol{\Sigma}\cdot(\psi_f^*\boldsymbol{\sigma}\beta\psi_o\times\mathbf{A})\right]. \quad (3)$$

$\mathbf{H}=\text{curl}\mathbf{A}$ is the magnetic field strength, and the bounding surface Σ consists of two spheres whose radii approach infinity and zero. Laplace's equation is valid in the annular region between the two spheres which is appropriate for the internal conversion problem.[1]

The first term of (3) gives just the contribution to the magnetic conversion coefficient at low energies as calculated with the Pauli theory. There will be no contribution from the second term because of the surface at infinity. Because of the extremely singular character of the potential $\mathbf{A}$ there will be one from the small sphere about the origin. A magnetic 2^l-pole has parity $(-)^{l+1}$. It induces transitions of s-electrons with $\frac{1}{2}$ unit of total angular momentum to final continuum states of type (a), with $(l-1)$ units of orbital angular momentum and $(l-\frac{1}{2})$ units of total angular momentum, and of type (b), with $(l+1)$ units of orbital angular momentum and $(l+\frac{1}{2})$ units of total angular momentum. Investigation of the behavior of the wave functions and of the magnetic multipole potential for small arguments shows that the surface term in (3) contributes to transitions to continuum states of type (a) from a small sphere about the origin. A regular solution of the coulomb field problem, representing a state of $(l-1)$ units of orbital angular momentum, behaves as r^{l-1} near the origin. Since the singular potential caused by a magnetic 2^l-pole diverges[6] as $r^{-(l+1)}$, the integrand approaches a finite limit as the inner boundary shrinks to zero radius.

To calculate matrix element (3) we limit ourselves to the two large components of the electronic wave functions. This is permitted since the $(\boldsymbol{\sigma}\beta)$ matrices mix large with large and small with small components. The result will be accurate for $v_{el}/c\ll 1$ and will thus serve as a first-order relativistic approximation. The wave functions are for the K-shell:

$$\psi_o=(a^3/\pi)^{\frac{1}{2}}e^{-ar}\begin{pmatrix}1\\0\end{pmatrix},$$

and for the continuum state with l-units of orbital angular momentum:

$$\psi_{l+\frac{1}{2},\,l,\,\frac{1}{2}}=R_l\begin{pmatrix}\sqrt{(l+1)/(2l+1)}\,Y_l^0\\-\sqrt{(l)/(2l+1)}\,Y_l^1\end{pmatrix}, \quad \text{(Type a)},$$

$$\psi_{l-\frac{1}{2},\,l,\,\frac{1}{2}}=R_l\begin{pmatrix}\sqrt{(l)/(2l+1)}\,Y_l^0\\\sqrt{(l+1)/(2l+1)}\,Y_l^1\end{pmatrix}, \quad \text{(Type b)},$$

where

$$R_l=(2mp/\pi\hbar^2)^{\frac{1}{2}}\{|\Gamma(l+1+in)|/(2l+1)!\}e^{\ln\pi}\times(2pr)^l e^{ipr}F(l+1-in,\,2l+2,\,-2ipr),$$

the Y_l^m are normalized spherical harmonics, F is the confluent hypergeometric function, $a=Z\alpha mc/\hbar$, $\alpha=e^2/\hbar c$, $n=a/p=Z\alpha/[2\nu-(Z\alpha)^2]^{\frac{1}{2}}$, where ν is the γ-ray energy in units of mc^2, and $p=1/\hbar$ times the momentum of the ejected

[6] Cf. W. Heitler, Proc. Camb. Phil. Soc. 32, 112 (1936) for derivation of the multipole fields which appear in reference (1). He shows the quantized electric or magnetic 2^l-pole field to represent a light quantum with angular momentum $L\hbar$. Berestetzky has given an alternate derivation in (4).

electron. A simplification may be achieved, as Berestetzky[4] pointed out, by immediately setting to zero, m, the z axis projection of the angular momentum of the emitted multipole radiation. The flux of electrons from the K-shell is independent of the axis orientation. The potential for a 2^l magnetic multipole reads then:[1]

$$A_z=0, \quad A_\pm=A_x\pm iA_y=-b_l Y_l^{\pm 1} f_l(kr).$$

b_l measures the magnetic multipole moment, k is $1/\hbar$ times the momentum of the quantum, and radial function $f_l(kr)$ is $H_{l+\frac{1}{2}}^{(1)}(kr)/(kr)^{\frac{1}{2}}$, where $H_{l+\frac{1}{2}}^{(1)}(kr)$ is the Hankel function of the first kind. In the radial integrations, $f_l(kr)$ is replaced by its most singular term:[7]

$$(\Gamma(l+\tfrac{1}{2})/i\pi)(2^{l+\frac{1}{2}})/(kr)^{l+1}.$$

The magnetic conversion coefficient for two K-electrons is obtained by dividing the electronic flux N_e, calculated from (1) for magnetic 2^l-pole radiation, by the corresponding flux of quanta from the atom,[1]

$$|b_l|^2/\pi^2\hbar k \text{ quanta/sec.}$$

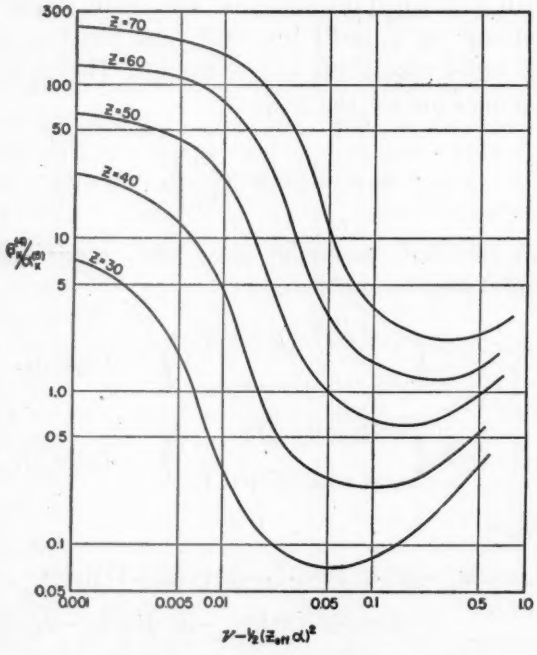

FIG. 1. Graph of the ratio of the K-shell conversion coefficient for 2^4-pole magnetic radiation to the coefficient for 2^4-pole electric radiation *vs.* the kinetic energy of the ejected electron in units of mc^2.

[7] Dancoff and Morrison point out that this is accurate to $(v_{el}/c)^2$.

That this ratio is the experimentally determined quantity is demonstrated by Taylor and Mott.[8] They show that, because of direct interaction between the electrons and nucleus, the flux of "observable" quanta which appear external to the atom is equal, with an error of the order of magnitude of the fine structure constant, to the flux which a bare nucleus would emit upon undergoing the same multipole transition.

The result for the magnetic conversion coefficient for two K-electrons, due to 2^l-pole magnetic radiation, is

$$\beta_K^{(l)}=\frac{l(l+2)}{(2l+1)(l+1)}\left(\frac{\nu^2}{4}\right)\alpha_K^{(l+1)}+2Z^3\alpha^4\left(\frac{2}{\nu}\right)^{l+\frac{1}{2}}$$
$$\times\frac{l+1}{2l+1}\cdot\frac{\pi n}{(1+n^2)^{l-\frac{1}{2}}}\cdot\frac{\prod_{i=1}^{l-1}(i^2+n^2)}{[\Gamma(l)]^2(1-e^{-2\pi n})}$$
$$=\frac{l(l+2)}{(2l+1)(l+1)}\left(\frac{\nu^2}{4}\right)\alpha_K^{(l+1)}$$
$$+\frac{2^{2l+4}\pi\alpha(l+1)}{(Z\alpha)^{2l}(2l+1)[\Gamma(l)]^2}$$
$$\times\frac{n^{2l+4}\prod_{i=1}^{l-1}(i^2+n^2)}{(1+n^2)^{2l+1}(1-e^{-2\pi n})}, \quad (4)$$

where ν is the γ-ray energy in units of mc^2, and $\alpha_K^{(l+1)}$ is the electric conversion coefficient for two K-electrons due to $2^{(l+1)}$-pole electric radiation.[9] For $l=1$,

$$\prod_{i=1}^{l-1}(i^2+n^2)=1.$$

The first term in (4) is the principal contribution given by the Pauli theory.[2,3] For low Z it approaches[10] the limiting expression

$$\{l/2l+1\}Z^3\alpha^4(2/\nu)^{l+\frac{1}{2}}.$$

The second term in (4) is just the contribution

[8] H. M. Taylor and N. F. Mott, Proc. Roy. Soc. A142, 215 (1933).

[9] The author has learned in a private communication that R. J. Bessey has performed this calculation using four-component wave functions. His result is similar to ours.

[10] Cf. formula (15), p. 128 of reference 1.

due to the second term in (3) from a small sphere about the origin. In the limit of low $Z(n\to o)$ this surface term approaches

$$\{l+1/2l+1\}Z^3\alpha^4(2/\nu)^{l+1}.$$

Formula (4) thus agrees with the result of Dancoff and Morrison (Eq. (20), p. 129 of reference 1) for low Z. Condition $v_{el}/c\ll 1$ limits the validity of this result.

An alternate derivation of (4) indicates clearly the failure of the Pauli theory. By decomposition of the Dirac equation into two two-component equations,[5] one can express the small components, X_i, of the wave function in terms of the large ones Φ_i,

$$X_i=(c\sigma\cdot\mathbf{p})/(2mc^2+Ze^2/r)\Phi_i, \qquad (5)$$

where $\mathbf{p}$ is the momentum operator and σ the 2×2 Pauli spin matrices. Introduction of (5) into (1) gives, in place of (3),

$$\text{M.E.}=\hbar/2mc\sum_{\text{spin}}\Big[\int dv\Phi_f^*\sigma\cdot\mathbf{H}\Phi_o + 2emc^2\int dv\Phi_f^*(\sigma\cdot((Ze/r^3)\mathbf{r}\times\mathbf{A}))/((2mc^2+Ze^2/r)^2)\Phi_o\Big]. \qquad (6)$$

Direct evaluation of (6) yields the identical result (4). In the reduction of the Dirac to the Pauli theory one usually neglects the second term of (6) relative to the first term as a second-order correction reduced in the ratio of v_{el}/c. This is an erroneous procedure to adopt in this case because of the extremely singular nature of the magnetic multipole potential, which necessitates preservation of the singular term in the energy denominator.

III. DISCUSSION

The importance of the second term in (4) extends beyond its purely academic significance in removing the discrepancy from the literature. It dominates in formula (4), particularly for elements of medium Z, and indicates magnetic K-conversion to be an effect fully as important as electric K-conversion.

This is exemplified in Figs. 1 and 2. The electric coefficients were obtained from the calculations

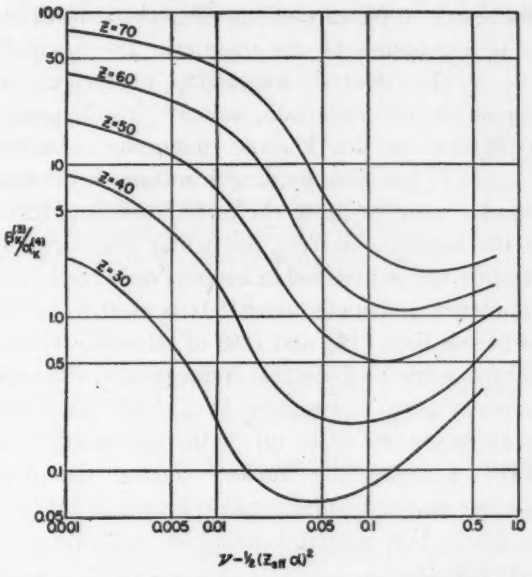

FIG. 2. Graph of the ratio of the K-shell conversion coefficient for 2^8-pole magnetic radiation to the coefficient for 2^4-pole electric radiation *vs.* the kinetic energy of the ejected electron units of mc^2.

of Hebb and Nelson.[11] Their shielding correction for the K-shell was also employed.[12]

Whereas electric K-conversion vanishes as we approach the K-shell threshold $(n\to\infty)$, the magnetic coefficient approaches the large finite value

$$\beta_K^{(l)}=2^{2l+4}\pi\alpha(l+1)/((Z\alpha)^{2l}(2l+1)[\Gamma(l)]^2).(n\gg l)$$

Since the L-shell threshold is one-fourth the K-shell binding energy for the same value of nuclear charge Z, electric L-shell conversion is predominant[11] in this energy region. However, the large magnetic conversion will influence the experimentally observed K to L-shell conversion ratio quite appreciably, and will contribute significantly to the total conversion coefficient.

This contribution will be reflected in the lifetimes of isomeric levels. One may write for the rate of decay, R, of a nucleus from a metastable to ground state[13]

$$R\propto\sum_{l=|J-J'|}^{J+J'}|\sigma_l|^2(1+\alpha^{(l)}) + \sum_{l'=|J-J'|}^{J+J'}|b_{l'}|^2(1+\beta^{(l')}), \qquad (7)$$

[11] M. H. Hebb and E. Nelson, Phys. Rev. **58**, 486 (1940).
[12] From the calculations of J. C. Slater, Phys. Rev. **36**, 57 (1930), we take for the K-shell, $Z_{eff}=Z-0.30$.
[13] M. H. Hebb and G. E. Uhlenbeck, Physica **5**, 605 (1938).

where σ_l is a measure of the electric 2^l-multipole, $b_{l'}$ is a measure of the magnetic $2^{l'}$-multipole, $\alpha^{(l)}$ is the electric conversion coefficient for 2^l-pole electric radiation, and $\beta^{(l')}$ the magnetic coefficient for the $2^{l'}$-pole magnetic radiation. $\mathbf{J}$ and $\mathbf{J}'$ are the quantum numbers of total angular momentum of the initial and final states of the nucleus. Barring particular nuclear symmetries, one is justified in keeping only the lowest permitted multipole order.[14] It is seen from (4), and from Eqs. (14) and (20) of reference 1, that the magnetic and electric conversion coefficients increase with l, roughly as $(1/v)^l$. Since the γ-ray intensity falls off with increasing l as $(k\delta)^{2l}$, δ being the nuclear radius, the total number of ejected electrons decreases as $(k\delta/v^{\frac{1}{2}})^{2l} \approx (p\delta)^{2l}$. For electron energies <1 Mev, $p\delta \approx 1/100$.

By the parity selection rule there corresponds to a given parity change and l value a minimum electric and magnetic multipole.[1] For a "parity allowed" type of transition the lowest allowed multipoles are electric 2^l and magnetic 2^{l+1}, so that (7) reduces to

$$R_{\text{P.A.}} = R_o(1+\alpha^{(l)}), \tag{8}$$

where R_o is the decay rate due to pure γ-emission alone. We have neglected in (8) $|b_{l+1}|^2$ as reduced relative to $|\sigma_l|^2$ by $(k\delta)^4$, and[15]

$$|b_{l+1}|^2\beta^{(l+1)}/|\sigma_l|^2\alpha^{(l)} \approx (k\delta)^4\cdot(\beta^{(l+1)}/\alpha^{(l+2)})\cdot(\alpha^{(l+2)}/\alpha^{(l)}) \approx (k\delta)^4/v^2 \approx (p\delta)^4.$$

For "parity forbidden" transitions, $l'=l-1$ in (7). Electric 2^l-pole amplitude, $|\sigma_l|^2$, and magnetic $2^{(l-1)}$-pole amplitude, $|b_{l-1}|^2$, are of the same order of magnitude. Their relative numerical values will be determined by a nuclear form factor, f, which is a function of the charge-current distribution in the nucleus. f tells what percent of the nuclear transitions to ground level give rise to electric radiation. We may write $|\sigma_l|^2 = fR_o$; $|b_{l-1}|^2 = (1-f)R_o$. In these terms, (7) become

$$R_{\text{P.F.}} = R_o(1+f\alpha^{(l)}+(1-f)\beta^{(l-1)}).$$

One would expect f to be usually in the neighborhood of $\frac{1}{2}$.[16]

This result makes more ambiguous the interpretation of internal conversion data. First of all, one cannot know in advance whether the transition is parity allowed or forbidden. Secondly, if parity forbidden, a precise formula to compare with an internal conversion coefficient would appear hard to come by without further knowledge of f.

The relation between isomeric lifetimes and internal conversion coefficients has been investigated in detail by P. Axel and S. M. Dancoff.[17]

It is a pleasure to acknowledge my indebtedness to Professor S. M. Dancoff for suggesting this problem and for his friendly guidance and constructive criticisms during its progress. I also wish to thank Professor A. Nordsieck for helpful comments. Thanks are due Mr. Gerald P. Beck, who performed the computations for the graphs.

[14] A detailed argument appears in reference 1, pp. 123–124.

[15] One sees from the graphs that the deviation of the ratio $\beta^{(l+1)}/\alpha^{(l+2)}$ from one does not destroy the validity of this argument.

[16] However, recent unpublished experiments by Professors Hill and Scharff-Goldhaber on Te^{125} indicate $f=.05$ in order to account for the large observed K- to L-shell conversion ratio with a parity forbidden $l=4$ transition. The calculated ratio is too small by a factor of ten if only electric conversion is considered.

[17] To be published.

Periods of Motion in Periodic Orbits in the Equatorial Plane of a Magnetic Dipole

ANTONIO ROMERO JUÁREZ
Institute of Physics, University of Mexico, Mexico City, Mexico

(Received August 19, 1948)

The differential equations of motion of an electrically charged particle in the equatorial plane of a magnetic dipole are solved in a way that time appears directly. The period of motion for periodic orbits is then found, and an application to cosmic radiation is made. For electrons moving in the equatorial plane of the magnetic field of the earth the periods in seconds have been determined.

I. INTRODUCTION

A STUDY of the periodic orbits of a charged particle in the equatorial plane of a magnetic dipole has already been made.[1] The work cited is concerned principally with the geometry of these orbits. Nevertheless, since these authors did not compute the actual periods, it seems worth while to do so. In the other works[2] there is introduced a function σ which defines a conformal transformation of the meridian plane. The introduction of the function σ is necessary when we are treating the general problem,[3] in which case there is at present no other method of solution than numerical or mechanical integration. The problem treated in this paper can be solved in terms of elliptic functions, and the use of σ, whose knowledge as a function of time implies one more integration, is not required.

II. THE EQUATIONS OF MOTION

From the general equations of motion[4] one easily finds the following equations for the equatorial plane:

$$m/Mq[(d^2\rho/dt^2)-\rho(d\varphi/dt)^2] = -(1/\rho^2)(d\varphi/dt), \quad (1)$$

$$(m/Mq)(1/\rho)(d/dt)[\rho^2(d\varphi/dt)] = (1/\rho^3)(d\rho/dt), \quad (2)$$

where ρ and φ are the polar coordinates. From the principle of the conservation of energy one finds, furthermore:

$$(d\rho/dt)^2+\rho^2(d\varphi/dt)^2=v^2. \quad (v=\text{constant}). \quad (3)$$

[1] C. Graef and S. Kusaka, J. Math. and Phys. **17**, 43 (1938).
[2] J. Lifshitz, J. Math. and Phys. **21**, 94 (1942).
[3] G. Lemaître and M. S. Vallarta, Phys. Rev. **49**, 719 (1936).
[4] G. Lemaître and M. S. Vallarta, Phys. Rev. **43**, 87 (1933).

Let us take for the unit of length the length c_1 defined by Störmer and given by equation

$$c_1=(M|q|/mv)^{\frac{1}{2}} \text{ cm}, \quad (4)$$

in which M is the magnetic moment of the dipole in electromagnetic units, q the charge of the particle in the same units, v its velocity, and m its transverse mass. If one writes

$$\rho=c_1r, \quad (5)$$

$$v=c_1(ds/dt), \quad (6)$$

then the equations of motion become

$$(d^2r/ds^2)-r(d\varphi/ds)^2=-(1/r^2)(d\varphi/ds), \quad (7)$$

$$(1/r)(d/ds)[r^2(d\varphi/ds)]=(1/r^3)(dr/ds), \quad (8)$$

$$(dr/ds)^2+r^2(d\varphi/ds)^2=1. \quad (9)$$

It is seen from the last equation that s is the length of arc measured along the orbit.

III. INTEGRATION OF THE EQUATIONS OF MOTION

A first integral of Eq. (8) is

$$r^2(d\varphi/ds)+(1/r)=2\gamma_1, \quad (10)$$

where γ_1 is a constant.

From (9) and (10) one obtains

$$s=\pm\int(r^4-4\gamma_1^2r^2+4\gamma_1r-1)^{-\frac{1}{2}}r^2dr. \quad (11)$$

The right-hand side of this is an elliptic integral which can be expressed in terms of Legendre canonical forms. For this purpose we use

$$y^2=1+(2\gamma_1/r)-(1/r^2). \quad (12)$$

Without loss of generality one can choose the

TABLE I. Values of the period in seconds t for some values of the number l of loops and the number n of turns, for electrons moving in the equatorial plane of the magnetic field in the neighborhood of the earth. If the greatest common divisor of l and n is d, then the orbit has d identical orbits.

n \ l	1	2	3	4	5	6	7	8	9	10
1	0.3399									
2	0.6607	0.6797								
3	0.9829	0.9982	1.0196							
4	1.3053	1.3215	1.3413	1.3595						
5	1.6278	1.6444	1.6593	1.6771	1.6993					
6	1.9506	1.9658	1.9822	1.9964	2.0144	2.0392				
7	2.2754	2.2879	2.3082	2.3215	2.3377	2.3534	2.3791			
8	2.5950	2.6107	2.6283	2.6429	2.6532	2.6827	2.6916	2.7189		
9	2.9169	2.9331	2.9488	2.9654	2.9838	2.9947	3.0080	3.0286	3.0588	
10	3.2396	3.2557	3.2705	3.2888	3.3037	3.3185	3.3347	3.3542	3.3679	3.3987

plus sign in Eq. (11), in which case one finds

$$s=\pm\int[(1+\gamma_1^2-y^2)(2-y^2)]^{-\frac{1}{2}}[r(y)]^2dy. \quad (13)$$

The double sign reappears because of the freedom of choice of the sign in

$$1/r(y)=\gamma_1\pm(\gamma_1^2-y^2+1)^{\frac{1}{2}} \quad (14)$$

obtained from (12).

In the case of periodic orbits the values of r lie between $r_{\min}$ and $r_{\max}$, where

$$1/r_{\min}=\gamma_1+(\gamma_1^2+1)^{\frac{1}{2}}, \quad (15)$$

$$1/r_{\max}=\gamma_1+(\gamma_1^2-1)^{\frac{1}{2}}; \quad (16)$$

we must now use the plus sign in (14) and we obtain

$$s=2\gamma_1^2\int[(1+\gamma_1^2-y^2)(2-y^2)]^{-\frac{1}{2}}(y^2-1)^{-2}dy$$

$$-2\gamma_1\int(2-y^2)^{-\frac{1}{2}}(y^2-1)^{-2}dy$$

$$-\int[(1+\gamma_1^2-y^2)(2-y^2)]^{-\frac{1}{2}}(y^2-1)^{-1}dy. \quad (17)$$

The second integral represents an elementary function. If we measure s from a point where $r=r_{\min}$, the lower limit in each of the definite integrals corresponding to (17) is zero.

The third integral in (17) is an elliptic integral of the third kind which is reduced to

$$\int_0^u\frac{du}{sn^2u-\alpha}=(2sna\ cna\ dna)^{-1}$$

$$\times\left[ln\frac{H(a-u)}{H(a+u)}+2uZ(a)\right], \quad (18)$$

where

$$y=2^{\frac{1}{2}}sn\ u, \quad (19)$$

$$sn^2\ a=\alpha, \quad (20)$$

if $\alpha=\frac{1}{2}$.

Finally, we can evaluate the first integral in (17) by differentiating Eq. (18) with respect to α before setting $\alpha=\frac{1}{2}$; we obtain in this manner:

$$s=\tfrac{1}{2}(1+\gamma_1^2)^{\frac{1}{2}}\left[\frac{H'(a-u)}{H(a-u)}-\frac{H'(a+u)}{H(a+u)}\right.$$

$$\left.+2uZ'(a)\right]+\frac{\gamma_1snu\ cnu}{sn^2u-sn^2a}. \quad (21)$$

All the above functions of Jacobi are constructed with the modulus

$$k=[2/(1+\gamma_1^2)]^{\frac{1}{2}}. \quad (22)$$

We must note that the three integrals in (17) are improper and do not converge for the value $y=1$. Nevertheless, the sum of these integrals must be a continuous function in the neighborhood of $y=1$, since the integral (13) converges for this value of the upper limit of the corresponding definite integral. One can see that this is actually the case by transforming the right-hand side of Eq. (21) using the relation[6]

$$\frac{2sna\ cna\ dna}{sn^2u-sn^2a}=\frac{H'(u-a)}{H(u-a)}-\frac{H'(u+a)}{H(u+a)}+2Z(a), \quad (23)$$

[6] E. B. Wilson, *Advanced Calculus* (Ginn and Company, Boston, 1912), p. 513.

obtaining thus:

$$s=\gamma_1\frac{2snu\ cnu-1}{2sn^2u-1}-(1+\gamma_1^2)^{\frac{1}{2}}\times\left[\frac{H'(u+a)}{H(u+a)}-Z(a)-uZ'(a)\right]. \quad (24)$$

From this equation it follows also that when $u=0$, which corresponds to $r=r_{\min}$, then $s=0$, as we were expecting.

One can also write (24) in the form

$$s=\gamma_1\frac{2snu\ cnu-1}{2sn^2u-1}-(1+\gamma_1^2)^{\frac{1}{2}}\left[\frac{cn(u+a)\ dn(u+a)}{sn(u+a)}+Z(u+a)-Z(a)-uZ'(a)\right]. \quad (25)$$

Eliminating s from (9) and (10) one obtains the differential equation of the orbit, whose integral is

$$\varphi=am\ u+[\gamma_1 u/(1+\gamma_1^2)^{\frac{1}{2}}]. \quad (26)$$

The last two equations, together with

$$(r^2+2\gamma_1 r-1)^{\frac{1}{2}}(1/r)=2^{\frac{1}{2}}sn\ u, \quad (27)$$

obtained from (12) and (19), determine the motion completely.

IV. PERIOD

From (27) it follows that r is periodic in u with period $2K$. The increase in s when u increases from u to $u+2K$ is, according to Eq. (25),

$$s_1=2(1+\gamma_1^2)^{\frac{1}{2}}KZ'(a). \quad (28)$$

If the orbit has l loops, then its total length is

$$L=2l(1+\gamma_1^2)^{\frac{1}{2}}KZ'(a), \quad (29)$$

and the period in t is therefore

$$T=(c_1/v)L. \quad (30)$$

For numerical applications it is convenient to transform (29) by means of the formula[6]

$$dn^2\ u=Z'(u)+(E/K), \quad (31)$$

and we obtain in this way:

$$L=2l(1+\gamma_1^2)^{\frac{1}{2}}[(K\gamma_1/(1+\gamma_1^2))-E], \quad (32)$$

where K and E are the complete elliptic integrals of the first and second kinds, respectively.

V. NUMERICAL RESULTS AND APPLICATION TO COSMIC RADIATION

Using values of γ_1 corresponding to periodic orbits,[1] we have calculated L, using Eq. (32), for several values of l and for various values of the number n of turns. Furthermore, these results have been applied to the case of electrons moving in the equatorial plane of the magnetic field in the neighborhood of the earth, and by means of Eq. (30) the periods of motion in t have been calculated. The results are given in the Table I.

[6] E. T. Whittaker and G. N. Watson, *A Course of Modern Analysis* (Cambridge University Press, Teddington, 1940), fourth edition, p. 518.

Magnetostriction and Order-Disorder

J. E. GOLDMAN
Westinghouse Research Laboratories, East Pittsburgh, Pennsylvania

AND

R. SMOLUCHOWSKI
Metals Research Laboratory, Carnegie Institute of Technology, Pittsburgh, Pennsylvania

(Received July 1, 1948)

An experimental and theoretical study of the relationship between saturation magnetostriction and the order-disorder transformation in an iron-cobalt alloy has been carried out. For the experimental work Fe-Co alloys in the neighborhood of the 50 atomic percent composition containing 0.75 percent Cr were employed. Measurements of both electrical resistivity and neutron diffraction have been used to confirm the presence of the superlattice. Measurements of the magnetostriction were made with a resistance strain gauge technique. An increase in the saturation magnetostriction is observed on ordering. Theoretical analysis based on the influence of order on the fluctuation of local electron density predicts a variation in agreement with experiment and also accounts for the influence of composition.

INTRODUCTION

MANY magnetic phenomena depend very critically upon the fundamental magnetostrictive constants. Becker and Kersten[1] have shown that the coercive force and initial permeability should depend very markedly upon the saturation magnetostriction, λ_s. The high coercive force in such materials as cobalt magnet steel can be traced directly to this prediction.[2] It has been felt that many hitherto unexplainable anomalies in coercive force and permeability might become resolved if the magnitude of λ_s can be related to some fundamental structure characteristics of alloys. Since many of these anomalies are exhibited by binary alloys in which there is an order-disorder transformation, it was decided to investigate an alloy system of this type in order to ascertain whether there exists a relationship between order-disorder and magnetostriction. Theoretical analysis of the influence of order on local electron density and thus on magnetization and magnetostriction also indicated the possibility of an appreciable effect.

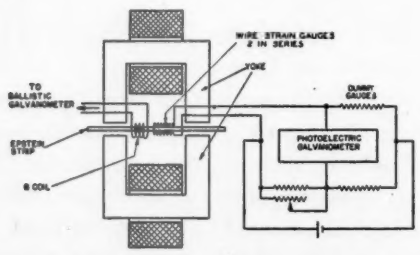

FIG. 1. Circuit diagram of magnetostriction measuring apparatus.

EXPERIMENTAL

Samples of the alloy were prepared by melting pure electrolytic iron and pure cobalt in a high-frequency vacuum furnace. 0.75 percent chromium was included in the melt in order to permit the material to be properly worked.[3] The ingot was then forged and cold-rolled into strip 0.038 cm in thickness and annealed for 10 hours at 850°C in wet hydrogen in order to remove any carbon that may be present and to further homogenize the material. In its final form, the amount of carbon present in the sample was less than 0.005 percent. The samples were prepared in the form of strips 15 cm×3 cm×0.038 cm. This is actually half of a conventional Epstein strip. All the strips were then heated to 900°C in a neutral atmosphere and quenched in cold water. In order to keep the samples flat, the annealing as well as the quenching was accomplished by placing the strip between two $\frac{1}{4}$-inch

[1] See, for example, the recently published compilation by Kersten, *Foundations of the Theory of Ferromagnetic Hysteresis and Coercive Force* (Edwards Brothers, Inc., Ann Arbor, Michigan, 1946), (in German).
[2] J. E. Goldman, Trans. A.S.M. **37**, 212 (1946).
[3] Subsequent measurements on chromium-free alloys indicated the effect of this addition to be negligible.

copper bars. The ordered samples were annealed for several hours at a temperature slightly below the critical temperature for order which is 732°C.

Magnetostriction measurements were made with the resistance strain gauge technique which was first suggested and employed for this purpose by one of us.[4] These strain gauges operate on the principle that if a thin wire is stretched, its resistance will undergo a change proportional to the degree of strain. The constant of proportionality, the gauge factor,

$$\text{G.F.} = \frac{\Delta R/R}{\Delta l/l},$$

varies from 1 to as much as 12.1 depending upon the material, the magnitude of the stress, and other factors. The fine wire is bonded to a small piece of treated paper which is in turn bonded to the member whose strain is to be measured. These experiments have been carried out with Type *A* gauges (advance) of the *SR*-4 series manufactured by the Baldwin-Southwark Division of the Baldwin-Locomotive Works. The isoelastic gauges although possessing a higher G.F. are unsuitable for this application—because of the magnetoresistance of the gauge material.

In order to obtain the desired sensitivity of 2×10^{-8} in the apparatus, it was necessary to measure $\Delta R/R$ of the order of 4×10^{-8}. This was accomplished by means of a conventional type d.c. Wheatstone bridge circuit with a Rubicon photoelectric galvanometer as the detecting device operating as a deflection instrument rather than as a null indicator. The effect of temperature or other electromagnetic and atmospheric variations is minimized by employing identical gauges in all four arms of the bridge, all mounted on or close to the sample under test, and a single shielded and thermally insulated decade resistance box in parallel with one arm for balancing and calibration. The active arm of the bridge consists of two gauges in series, one mounted on each side of the strip under test. This minimizes the error due to bending of the sample. The magnetizing field is supplied by a 'symmetrical Hipernik yoke. The yoke, sample, and bridge are kept in a large thermally insulated box to reduce still further the effect of air currents and

[4] J. E. Goldman, Phys. Rev. **72**, 529 (1947).

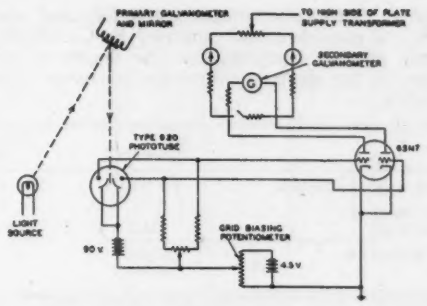

FIG. 2. Amplifying circuit for photoelectric galvanometer.

changes in ambient temperature. In order to minimize flux linkage by the gauge leads, all leads are twisted and brought out symmetrically. A schematic representation of the circuit is shown in Fig. 1. Details of the photo-galvanometer are shown in Fig. 2.

With this arrangement and with drift as well as pick-up reduced to a negligibly small value, a change in resistance corresponding to a strain of 10^{-6} gives a deflection on the secondary galvanometer of 46 mm. This corresponds, therefore, to a strain sensitivity, $\Delta l/l$ per mm $=2.15\times10^{-8}$. Since we can estimate without difficulty to a fraction of a mm, it is felt that measurements of strain down to 10^{-8} can be made with good accuracy and reproducibility. The maximum uncertainty due to drift during the course of a measurement is of the order of 0.25 mm.

Measurements of magnetostriction were made by saturating the strip in the yoke and measuring the change in length when the flux density in the strip was reduced to zero. Magnetic measurements were made with a search coil and ballistic galvanometer.

There are several inherent advantages in this type of measurement which it may be of value to point out. (1) The measurement of the magnetostrictive strain utilizes only a very small portion of the sample, usually no greater than 1 inch, and measures the magnetostriction over this region. This has the dual advantage of permitting the use of very small samples and eliminating end effects due to shearing strains, non-uniformity of flux, etc. (2) The nature of the method is such that the effect of temperature and other variables is essentially eliminated. (3) A closed magnetic path may be used, thus

TABLE I. Saturation magnetostriction and electrical resistivity of quenched and annealed Fe-Co alloys of the 50 atomic percent composition. The degree of order as evidenced by the neutron diffraction patterns is included in the table.

	Quenched	Annealed
Saturation magnetostriction	6.5×10^{-5}	9.2×10^{-5}
Electrical resistivity (micro-ohm-cm)	24.2	18.82
Neutron diffraction	Slightly ordered	Well ordered

assuring a greater uniformity of flux distribution and eliminating possible errors due to form effect. (4) Finally, and perhaps most significant, by using square samples and type AX gauges, measurements can be made quite readily in two perpendicular directions, thus eliminating to a great extent the uncertainty in the knowledge of the demagnetized state, and errors due to the possible non-randomness of the initial distribution of domain directions.

Resistivity measurements were made by the standard method of using a type K potentiometer and measuring the voltage drop across two fixed points in the sample as well as the potential drop in a standard cell in series with the sample, the latter measurement determining the current. To detect the state of order by direct means, samples were given to Dr. S. Siegel who used neutron diffraction techniques[5] at the Clinton pile of the Oak Ridge National Laboratory to detect superlattice lines in the alloy. The x-ray atomic scattering factors of iron and cobalt being so similar, it is difficult to employ the standard x-ray techniques for this purpose.

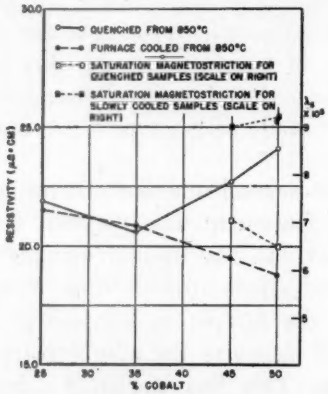
QUENCHED FROM 850°C
FURNACE COOLED FROM 850°C
SATURATION MAGNETOSTRICTION FOR QUENCHED SAMPLES (SCALE ON RIGHT)
SATURATION MAGNETOSTRICTION FOR SLOWLY COOLED SAMPLES (SCALE ON RIGHT)
RESISTIVITY (μΩ-CM)
% COBALT

FIG. 3. Resistivity of quenched and annealed Fe-Co alloys containing various amounts of cobalt (0.75 percent Cr). Saturation magnetostriction for the 45 and 50 percent alloys is shown by the dashed curve. Scale on the right indicates magnetostriction.

[5] S. Siegel and C. G. Shull, Bull. Am. Phys. Soc. **23**, No. 4, 5 (1948); also, S. Siegel, private communication to the authors.

RESULTS

The results of the investigation are shown in Table I. The values given are averages for several samples. The deviation for the magnetostriction values is in no case greater than ±10 percent for the quenched samples and only a few percent for the annealed samples.

It is seen that the magnetostriction at saturation increases by about 40 percent upon ordering. It must be pointed out, however, that the neutron-diffraction patterns indicate that even the quenched samples are seen to be to some extent ordered. Photomicrographic evidence precludes the possibility of this change as well as the change in electrical resistivity being due to any metallurgical effect such as a dispersed phase or grain size effect.

It may be of interest to point out the variation in electrical resistivity as a function of cobalt content for samples quenched and air cooled from 850°C. This data, shown in Fig. 3, appears to be consistent with the hypothesis proposed by Ellis and Greiner[6] that a certain amount of ordering takes place at 35 percent cobalt and increases in degree with increasing cobalt content. The saturation magnetostriction for the 45 and 50 percent Co alloy measured on the same samples has been included in the figure. It has already been pointed out above that the quenched samples are to some extent ordered and the state of order would therefore be quite sensitive to the quenching rate.

THEORY AND DISCUSSION

There are, in general, two ways of approach to the problems of magnetic properties within the domains of a ferromagnetic metal. In the case of volume properties one treats the whole domain as a unit without specified crystallographic directions, and the approach is partly based on the band theory of metals. The magnetization appears as strongly dependent upon the relative size of unfilled $3d$-shells as compared

[6] W. C. Ellis and E. G. Greiner, Trans. Am. Soc. Metals **29**, 415 (1941).

to the interatomic distances. This theory is particularly successful in explaining the saturation moments of the ferromagnetic metals, influence of alloying elements, volume magnetostriction, and other aspects[7] which depend upon the average electron density and do not involve explicit crystallographic directions. The notion of an average electron density in the 3*d*-shells in a metal, and in particular in an alloy, can be interpreted either in terms of a 3*d*-band or, perhaps preferably, in terms of an additive interaction between 3*d*-shells of individual atoms. The dependence of the interaction forces (exchange forces) between the 3*d* electrons upon the ratio of the interatomic distance to the radius of the 3*d*-shell has been pointed out by Slater[8] and later more quantitatively expressed by Néel[7] in his plot of the coefficient of molecular field against distance between the 3*d*-shells (see Fig. 4). This way of approach, however, is not suitable for the treatment of linear magnetostriction and a literal interpretation of the above curve, as representing interaction between a pair of atoms in the crystal lattice, is not immediately justified. As shown below, the magnetostriction of iron is due to the angular dependence of the interaction between the magnetic moments of the atoms rather than to the dependence of that interaction upon distance as one might like to infer from the curve in Fig. 4. Magnetostriction of iron estimated on the latter basis appears to have a wrong sign and a wrong order of magnitude. Also an attempt to explain the influence of order on magnetostriction, by taking into account the difference of the radii of the 3*d*-shells of iron and of cobalt and estimating the shift of the representative points on the curve in Fig. 4, fails.

The other type of approach which is much more successful in the treatment of the linear magnetostriction is that given by Becker.[9] Every atom is supposed to behave as a magnetic dipole and the interaction between parallel dipoles is given by the well-known formula

$$U=\frac{\mu^2}{r^3}(1-3\cos^2\alpha), \qquad (1)$$

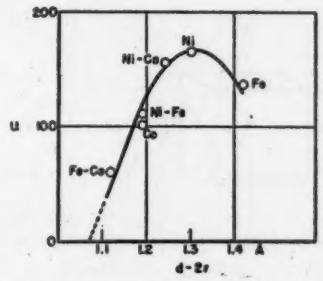

FIG. 4. Curve giving the molecular field coefficient as a function of the distance between 3d shells (after Néel).

where r is the distance and α the angle between the line joining the atoms and the direction of the dipoles. This model is clearly over-simplified; but, apart from a numerical factor, it describes the linear magnetostriction of iron satisfactorily, although it is less successful in the case of nickel. It gives, however, no clue as to the probable dependence of magnetostriction on composition of alloys and upon the various volume properties which lead to the curve shown in Fig. 4.

No attempt will be made to estimate theoretically the possible dependence of the exchange forces between unfilled 3*d*-shells upon the angle between the direction of magnetization and the line joining the two atoms. Instead, in our theory, which will be developed for a body-centered cubic lattice, we shall follow essentially the dipole approximation including, however, certain features of the other point of view. For simplicity we shall limit ourselves to the interactions between an atom and its nearest and second nearest neighbors, which in a body-centered lattice, are only about 15 percent further away. Also we shall limit ourselves to the magnetostriction in the direction of easy magnetization. Both these simplifications can be easily removed, but the treatment becomes then unnecessarily cumbersome. We shall consider the magnetostriction in the [100] direction, which is the direction of easy magnetization in iron and in some iron-cobalt alloys and is accounted for on the basis of Becker's theory. According to Shih,[10] there is indication that in a 50:50 iron-cobalt alloy the direction of easy magnetization is the [111] direction. This case has been examined in detail and it appears that all the results of our theory

[7] L. Néel, Ann. de physique **8**, 237 (1937). R. Smoluchowski, Phys. Rev. **59**, 309 (1941); **60**, 249 (1941).
[8] J. C. Slater, Phys. Rev. **36**, 57 (1930).
[9] R. Becker, Zeits. f. Physik **62**, 253 (1930).
[10] J. W. Shih, Phys. Rev. **46**, 139 (1934).

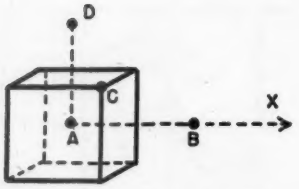

FIG. 5. The unit cell of a body-centered cube showing the three kinds of neighbors of an atom in a domain.

including the quantitative influence of ordering apply here also except for the difference in sign of the magnetostriction as in Becker's theory. Figure 5 represents an atom and its neighbors in a body-centered cubic lattice in a domain which is magnetized along the [100] direction which we chose as the direction of the X coordinate. The atom A has three kinds of neighbors: nearest neighbors of the type C; second nearest neighbors in the direction of magnetization, type B; and second nearest neighbors in the directions perpendicular to the direction of magnetization, type D. In iron and in iron-cobalt alloys the magnetostriction is positive; thus, in the magnetic condition the interatomic distances parallel to the direction X are increased by a factor $(1+\lambda)$. In the other two perpendicular directions the distances are decreased by a factor $(1-\lambda/2)$. Thus, we use the condition that magnetostriction occurs without a change of volume, although a correction could be easily introduced for the known Poisson's ratio. Differentiation of the expression (1) gives easily the following contributions of the three types of neighbors to the change of the magnetic interaction as the function of the parameter λ:

$$\Delta U_C = -\frac{16}{9}\sqrt{3}\frac{\mu^2}{a^3}\lambda; \quad \Delta U_B = 6\frac{\mu^2}{a^3}\lambda; \quad \Delta U_D = -\frac{3}{2}\frac{\mu^2}{a^3}\lambda$$

where a is the lattice constant. It is interesting to note that the only negative term is that due to the C type atoms. All other contributions to the magnetic energy are positive and oppose a positive magnetostriction. The distance AC remains unchanged within the approximation of terms linear in λ, and so the negative terms, and, thus, the positive magnetostriction is solely due to the angular displacement of the atom C.

Since we are going to consider ordering phenomena, we have to specify the contributions from atoms in the various positions, and we will use the subscripts AB, AC, and AD. The energy of the dipole interaction of one atom with its neighbors is thus:

$$\frac{2}{a^3}\left(6\mu_{AB}^2+3\mu_{AD}^2-\frac{64}{9}\sqrt{3}\mu_{AC}^2\right)\lambda, \tag{2}$$

which, for the assumption of all dipoles being identical, simplifies to

$$-6.6\frac{\mu^2}{a^3}\lambda.$$

The density of energy is then expressed by

$$E_d = -\frac{1}{2}N\frac{\mu^2}{a^3}6.6\lambda,$$

where N is the number of dipoles per cubic centimeter which, for a body-centered lattice, is equal to $2/a^3$ thus:

$$E_d = -1.65N^2\mu^2\lambda. \tag{3}$$

This decrease of magnetic energy is naturally opposed by an increase of the elastic energy. The latter, in our case, is given by

$$E_e = \tfrac{3}{2}G\lambda^2, \tag{4}$$

where G is the shear modulus. Thus, at equilibrium, magnetostriction will be obtained from the condition

$$\frac{\partial}{\partial\lambda}(E_d+E_e)=0,$$

which gives us

$$\lambda = \frac{N^2}{G}\frac{64\sqrt{3}\mu_1^2-81\mu_2^2}{54}, \tag{5}$$

where subscripts 1 and 2 indicate contributions from nearest and from second nearest neighbors, respectively. The numerical factor differs slightly from that given by Becker because of the summation which here extends only over the first two layers of neighbors. In the case of a random alloy, the average magnetic moments of nearest and second nearest neighbors are the same and the formula simplifies to

$$\lambda = \frac{N^2}{G}0.56\mu^2. \tag{6}$$

It is thus necessary to determine the influence of ordering on μ_1 and μ_2.

If we could consider the total magnetization as due to a sum of independent contributions of Fe-Fe, Co-Co, and Fe-Co pairs of neighbors, then we would obtain a quick qualitative estimate of the effect of ordering. Clearly, the pair Fe-Co would have to contribute more to the magnetization than the other two kinds. Inasmuch as in an ordered alloy all nearest neighbors are of the Fe-Co type, while in a random alloy only half of them are of that type, formula (5) would give a larger magnetostriction in an ordered state. However, such an assumption has many drawbacks and is difficult to reconcile with the present theory of magnetism which relates the magnetic moment to the electron density rather than to an interaction between pairs of atoms.

The dependence of magnetization per atom upon the electron concentration, as summarized in the well-known curve shown in Fig. 6, indicates a maximum around 8.3 valence electrons per atom, and is well explained on the basis of the band theory of metals.[11] The main fact underlying the theoretical interpretation of the curve in Fig. 6 is the fundamental importance of the electron density rather than the type of atoms which contribute electrons. We shall consider the total magnetization as being determined, not so much by an average electron density of the whole metal, but rather by a sum of contributions of local electron densities. Also we shall consider the curve in Fig. 6 as applying to local electron concentrations, although the experimental points on this curve, except for pure metals, were obtained for random alloys, and thus in that sense are average values. The local electron concentration naturally depends upon the neighboring atoms and these are influenced by the degree of order.

In order to make our theory quantitative, we have to take into account the fluctuations of the charge density in a random and in an ordered alloy and estimate the contributions of local electron densities to the final magnetic moment. The probability that an atom in a random 50–50 alloy will have r identical neighbors among its n neighbors is

$$\frac{1}{2^n}\binom{n}{r}. \tag{7}$$

From this we can easily compute the probability of finding a given average electron concentration among the eight neighbors of an atom. The magnetic moment characteristic of the given atom and its neighborhood is then determined by the arithmetical mean of the number of valence electrons of the atom in question and of the average valence electron density of its neighborhood. Thus, in the case of an iron atom with its eight valence electrons, the effective density will vary anywhere from 8, in case it is surrounded by 8 iron atoms, to 8.5 if it is surrounded by 8 cobalt atoms. Similarly, the effective electron density for a cobalt atom will vary from 8.5 to 9. The corresponding probability of the occurrence of these density fluctuations is obtained from the expression (7). The magnetic moment associated with each of the thus computed electronic densities is read off the curve in Fig. 6, in which we use a linear relationship, expected by theory, and somewhat more perfect than that given by experimental data. Thus the magnetization increases linearly from the value 2.22 for Fe to 2.53 at 35 percent Co, and then decreases linearly to the value for Co. Pure cobalt has a close-packed lattice so that the direct use of its moment, 1.7 in our case, may not be correct, since both iron and iron-cobalt alloys are body-centered cubic up to 75 percent Co. By extrapolating the magnetization values of body-centered iron-cobalt

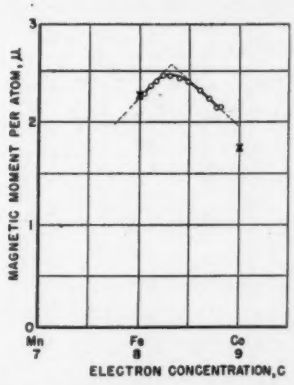

FIG. 6. Magnetic moment per atom in Bohr magnetons *vs.* electron concentration for iron, cobalt and their body centered alloys.

[11] See, for example, F. Seitz, *Physics of Metals* (McGraw-Hill Book Company, 1943), p. 308.

TABLE II. Comparison of the theoretical and experimentally observed percent increase of magnetostriction in the ordered state over the disordered state for the 45 and 50 percent cobalt alloys.

	50 Co	45 Co
Observed	40	30
Theoretical	85	70

alloys, we obtain the value 1.88 for pure body-centered cobalt. This correction is not important and it introduces only small numerical differences in the result. If we now add all the contributions of the various local electron concentrations with the proper probabilities, we obtain a magnetic moment of 2.27 which is about 4 percent smaller than the value 2.37 which we considered as characteristic of the average density of 8.5 electrons. In a perfectly ordered alloy, each iron atom is surrounded by 8 cobalt atoms and each cobalt atom by 8 iron atoms so that the local electron density will be everywhere 8.5 and, thus, the corresponding magnetic moment 2.37.

If we now try to compute the change of magnetostriction on ordering, we have to substitute the proper μ values in formulae 5 and 6. For a random alloy $\mu_1=\mu_2=\mu=2.27$; for an ordered alloy the magnetic moment for the nearest neighbors μ_1, according to the previous paragraph, will be 2.37; on the other hand, the magnetic moment for the second nearest neighbors, which are always of the same kind as the central atom, will be given by the average of the magnetic moments of pure iron and of pure cobalt, thus $\mu_2=2.05$. The ratio of the two magnetostrictions turns out to be 1.85, thus an increase of 85 percent. This is to be compared with the observed value of about 40 percent. It is important that the small change of 4 percent of the magnetic moment, μ, between the ordered and disordered state does not play a significant role in the change of magnetostriction. It is rather the change in the second nearest neighbors which produces the big difference.

It is perfectly understandable why the theoretical increase of magnetostriction is higher than the experimental result. One would not expect our experimental treatments to correspond so closely to a comparison of a perfectly random with a perfectly ordered state. As mentioned before, the results of neutron diffraction experiments confirm this explanation. Another important aspect is the fact that "random" alloy may have a certain degree of short-range order. On the basis of this theory, one might expect magnetostriction to be quite sensitive to short-range order.

The theory here outlined can be easily extended to the 55 percent Fe 45 percent Co alloy for which experimental data are available. First, for a random alloy, instead of formula (7) we have

$$\binom{n}{r}p^{n-r}q^r \qquad (8)$$

where p and q are the concentrations of cobalt and of iron, respectively. This gives us the statistical neighborhood of *any* atom in a random alloy. Among these atoms 45 percent are cobalt atoms and thus by averaging the electron densities we obtain the contributions of local neighborhoods around cobalt atoms to the total magnetization. A similar procedure gives the contributions of neighborhoods of iron atoms. The result is $\mu=2.26$ for a random alloy.

A perfectly ordered alloy containing 45 percent cobalt can be represented as a perfectly ordered 50:50 alloy in which 10 percent of the cobalt atoms are substituted by iron atoms. This substitution is random and all cobalt atoms have iron atoms as nearest neighbors. Among the iron atoms some have all nearest neighbors cobalt atoms, some have one iron atom among them, some two, three, and so on. The relative percentages are 21.5; 19; 7.4; etc. Finally the substitutionally dissolved iron atoms have all neighbors iron atoms. Computation of the local densities and the corresponding probabilities gives $\mu_1=2.33$. A similar calculation for the second neighbors gives $\mu_2=2.10$. The increase of magnetostriction as obtained from formula (5) is 70 percent which is to be compared with the experimental value of about 30 percent. Presumably the low observed value is, as in the previous case, due to incomplete order and imperfect randomness. The decrease of the influence of order on magnetostriction at lower cobalt content is accounted for satisfactorily by the theory. Table II summarizes the results.

Recent work of Fine and Ellis[12] indicates an interesting volume increase of ordered Fe-Co alloys. As indicated by one of us,[13] the increase of the average interatomic distance on ordering can be interpreted as an increase of repulsion between the partly filled 3*d*-shells. According to the theoretical explanation of the saturation moment in ferromagnetic alloys (Fig. 6), the 3*d*-shells consist of two parts, one of which is just filled up at the electron concentration corresponding to the maximum value of the magnetization. As we know from band theory of metals, full electronic shells produce strong repulsive forces. The apparent increase of repulsion between the iron and cobalt atoms can be interpreted as due to a more perfect filling of the lower part of the 3*d*-shells in both kinds of atoms in the state of perfect ordering. In the random state, as indicated before, only part of the atoms will have the proper neighborhood to assure the optimum local electron concentration, and the repulsion forces will be weaker.

[12] M. E. Fine and W. C. Ellis, to be published in Trans. A.I.M.E.

[13] R. Smoluchowski, discussion to paper in reference 12.

ACKNOWLEDGMENT

The authors are grateful to Dr. Sidney Siegel for discussions and for making the neutron diffraction studies, to Mr. R. K. McGeary for preparing the samples, to Mr. W. N. Johnson for capable assistance in making the measurements, and to the Westinghouse Research Laboratories for permission to publish these results.

Note added in proof: Preliminary calculations indicate that a similar mechanism might explain the rapid decrease of magnetostriction in Fe-Si alloys at the composition of about 12 at. percent Si, where ordering is known to take place. These results were reported by the authors at the National Research Council Conference on Phase Changes held at Cornell University in August, 1948.

PHYSICAL REVIEW VOLUME 75, NUMBER 1 JANUARY 1, 1949

Irreversible Magnetic Effects of Stress

WILLIAM FULLER BROWN, JR.*
Naval Ordnance Laboratory, White Oak, Maryland

(Received June 8, 1948)

When Rayleigh's law for small hysteresis loops is interpreted in terms of the elementary process of domain wall displacement, its generalization to include effects of stress becomes possible. In this way theoretical formulas have been derived for the behavior of a soft iron or steel specimen which is first put into a state of normal magnetization at small magnetizing force H and is then subjected to a small tension cycle. According to the theory the magnetization should increase upon application of tension T by an amount $g(4.00\times10^{-9}HT+9.86\times10^{-18}T^2)$ in c.g.s. e.m.u., where $4\pi g$ is the slope of the normal permeability *vs.* H curve, and should remain at the new value upon removal of the tension. An experimental test of the theory verified these predictions within the precision claimed for them. On the basis of the theoretical model, certain effects of diminishing alternating fields and stresses are analyzed quantitatively; the results are used to explain qualitatively the observed long-time magnetic behavior of ships.

INTRODUCTION

THE changes of magnetization produced by stress are cause for concern whenever magnetic devices are subject to uncontrollable mechanical disturbances. Such changes are characterized by hysteresis and are, therefore, difficult to treat analytically. However, the stresses usually encountered are magnetically equivalent to rather small fields (as compared with those necessary to erase the previous history completely), and this suggests that it would be useful to extend the analytical description of small hysteresis loops, known as Rayleigh's law,[1] to cases in which the independent variable is stress rather than magnetizing force. The legitimacy of such an extension and the form that it must take both follow at once if one merely assumes that Rayleigh's law, with appropriate changes in the

* Present address: Sun Physical Laboratory, Newtown Square, Pennsylvania.

[1] R. Becker and W. Döring, *Ferromagnetismus* (Verlag Julius Springer, Berlin, 1939), p. 218 ff.

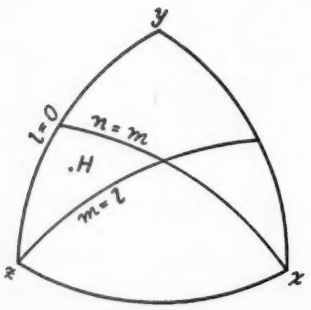

FIG. 1. Relation of field direction (H) to crystal axes. If labels (x, y, z) are assigned to the cubic axes of the individual crystals in a random manner, then with respect to the (x, y, z) axes the directions H will be distributed uniformly over the unit sphere. For present purposes the labels (x, y, z) are reassigned so that for half the crystals the relations are as shown here, with H somewhere in the indicated spherical triangle, and for the other half the axes are left-handed and the appropriate diagram is the mirror image of the one shown.

variables, applies to the elementary process of domain wall displacement[2] to which the macroscopic magnetization changes are due.

In 1945, at the Naval Ordnance Laboratory, the consequences of this assumption were developed theoretically and tested experimentally. The object was to arrive at a theoretical model capable of at least qualitative predictions, and therefore useful as a guide in planning experimental programs. From this point of view the theory was successful, for it predicted correctly the general behavior of the curves and the orders of magnitude of the constants deduced from them. Moreover, it did this on the basis of general crystal constants together with purely magnetic data on the particular specimen; no preliminary magnetomechanical data were required. Although the basic relations are simple, the detailed working out of their consequences is somewhat tedious, and therefore the results of this work—together with the experimental test of the theory—are of interest.

The theory presented here does not include an explanation of Rayleigh's law itself; that is a separate problem. For validity of the theory it is not necessary that Rayleigh's law hold for a single domain wall, provided it holds on the average for a group of many similar walls. The individual process is doubtless a discontinuous irreversible jump, but the jumps of different walls occur at different values of magnetizing force or stress. A derivation of Rayleigh's law, in the generalized form assumed here, therefore requires a statistical study of the behavior of domain walls. A derivation of this type has been given by Néel.[3]

[2] Reference 1, p. 105 ff.

THEORETICAL MODEL

The specimen is assumed to be a polycrystal wire or rod (of soft iron or steel) with field or tension or both applied along its axis. As is usual in domain theory, the magnetizing force and stress are assumed to be uniform. The polycrystalline specimen is furthermore assumed to consist of crystals whose axes are oriented at random. The results for it are therefore to be obtained by calculating for a single crystal in an arbitrary orientation and then averaging over all orientations.

In an iron crystal in which the internal stresses are not too high, each domain is (in the demagnetized state) magnetized to saturation along one of the "directions of easy magnetization," *viz.*, the [100] directions. Application of a magnetizing force or stress causes displacements of the walls separating adjacent domains, so that the more favorably magnetized domain grows at the expense of its neighbor. In the case of a magnetizing force, the more favorably magnetized domain is the one whose magnetization vector is closer, in direction and sense, to the magnetizing force; in the case of a tension, the more favorably magnetized domain is the one whose magnetization vector is closer in direction (without regard to sense) to the tension. Thus 90° walls, e.g. between [100] magnetization and [001], can be displaced either by magnetizing force or by tension; but 180° walls, e.g. between [100] and [$\bar{1}$00], are unaffected by tension. Furthermore, the 90° walls themselves may be grouped into two classes: those for which tension and positive magnetizing force produce displacements of the same sign and those for which they produce displacements of opposite signs.

In each crystal of the specimen, let the [100] axis closest to the positive field direction be labeled z, the one second closest y, and the one third closest x; then, for every crystal, the point on the unit sphere that represents the field direc-

[3] L. Néel, Cahiers de Physique, No. 12, p. 1 (Dec. 1942) and No. 13, p. 18 (Mar. 1943).

tion lies in the first octant and within (or on the boundary of) the spherical triangle bounded by the arcs $l=0$, $n=m$, and $m=l$, where (l, m, n) are the direction cosines of the field direction with respect to the (x, y, z) axes (Fig. 1). For an isotropic aggregate of crystals, the representative points are distributed at random over this spherical triangle; half the sets of axes are left-handed, but this is permissible in the present analysis.

An interdomain wall separates a domain magnetized along one of the directions z, y, x, $-x$, $-y$, $-z$ from one magnetized along another of these directions. Each possible pair of these symbols, with the above order preserved, represents a possible type of wall. Thus there are 15 types of wall:

Class A				Class B	
z, y	z, x	$z, -x$	$z, -y$	$z, -z$	
	y, x	$y, -x$	$y, -y$	$y, -z$	
		$x, -x$	$x, -y$	$x, -z$	Class
			$-x, -y$	$-x, -z$	C
				$-y, -z$	

Of these, the ones labeled "Class A" undergo displacements of the same sign under positive magnetizing force and tension; the ones labeled "Class C" undergo displacements of opposite signs; the ones labeled "Class B" are not affected by tension.

Either magnetizing force or tension is thermodynamically equivalent to a hydrostatic pressure within each domain, acting on its domain walls. This pressure is $HJ_s\cos(J, H)+\frac{3}{2}T\lambda_{100}\cos^2(J, H)$ for the case of magnetizing force H and tension T along the same direction. Here J_s is the saturation magnetization, and λ_{100} is the saturation magnetostriction for a crystal magnetized along [100]. Subtraction of the pressures on opposite sides of a wall gives the net pressure on the wall; for instance, for a (z, y) wall the pressure (considered positive if it tends to increase the z-magnetized domain) is

$$p_{z,y}=HJ_s(n-m)+\tfrac{3}{2}T\lambda_{100}(n^2-m^2). \qquad (1)$$

With the order of symbols used above, a positive field always favors the first member of the pair; a tension favors the first member of a class A pair and the second member of a class C pair.

It is usually assumed that small H and T produce a reversible displacement of each wall, proportional to the net pressure acting on it; and that the proportionality constant, averaged over all walls of a given type, has one value for the 12 types of 90° wall (classes A and C) and another value for the 3 types of 180° wall (class B). We now assume that in addition there is an irreversible displacement, governed, on the average for all walls of a given type, by a law similar to Rayleigh's; and that the constant in the irreversible term has one value for the 12 types of 90° wall and another value for the 3 types of 180° wall. Specifically, if v is the volume swept past by walls of any particular type (such as z, y) in unit volume of the crystal ($v=0$ in the demagnetized state) and if p is the net pressure determined by Eq. (1) or its appropriate modification, we assume:

(a) For a monotonic change from the demagnetized state, v has the sign of p, and

$$|v|=\alpha|p|+\beta p^2. \qquad (2)$$

(b) For a subsequent change Δp of opposite sign to the change immediately preceding it, Δv has the sign of Δp, and

$$|\Delta v|=\alpha|\Delta p|+\tfrac{1}{2}\beta(\Delta p)^2, \qquad (3)$$

provided $|\Delta p|$ is small enough so that the curve so calculated does not cross or touch the curve (2).

(c) For a change Δp larger than that specified in (b), (2) again holds.

(d) The constant α in the reversible term has one value α_1 for all wall types of classes A and C

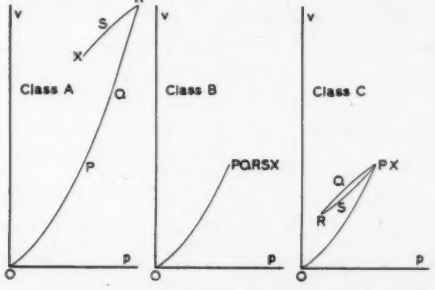

FIG. 2. Average behavior of a group of walls of one type. Class A, 90° walls for which tension is equivalent to positive magnetizing force; Class B, 180° walls; Class C, 90° walls for which tension is equivalent to negative magnetizing force. OP, magnetizing force applied; PQR, tension applied; RSX, tension removed. Abscissa p is hydrostatic pressure to which magnetizing force and tension are equivalent; ordinate v is volume swept out by walls of the specified type in unit volume of the specimen.

and another value α_2 for all wall types of class B. The constant β in the irreversible term has one value β_1 for all wall types of classes A and C and another value β_2 for all wall types of class B.

Assumptions (a) and (c) go somewhat beyond Rayleigh's law as it is usually stated, but they are at least approximately in accordance with experiment when the variables are magnetizing force and magnetization, and they also follow from Néel's theory. To the approximation adopted here, the normal and virgin states are identical and, more generally, any attainable pair of values (p, v) specifies a magnetic state uniquely.

Suppose, now, that an initially demagnetized specimen is subjected to the following treatment: (i) the magnetizing force is increased to a value H; (ii) a tension T is applied; (iii) the tension is removed. The behavior of each class of wall is illustrated in Fig. 2. In each of the three diagrams, curve OP corresponds to step (i), curve PQR to step (ii), and curve RSX to step (iii). The behavior of class B is simplest; Eq. (2) holds during step (i) and nothing happens thereafter. For class A, Eq. (2) holds during steps (i) and (ii), Eq. (3) during step (iii). For class C, Eq. (2) holds during step (i) and Eq. (3) during steps (ii) and (iii), which therefore cancel each other and return the walls to P after traversal of a Rayleigh loop. The net irreversible change of magnetization resulting from application and removal of the tension is entirely due to walls of class A.

Upon carrying out the details of the calculation and combining the contributions of all types of wall, we obtain the following formulas for the *irreversible* magnetization J_{ir} of a single crystal; the reversible part (determined by α_1 and α_2) is simply $\chi_0 H$, where χ_0 is the initial susceptibility.[4]

(i) H applied:

$$J_{ir}=J_s^3H^2(2\beta_1\phi_1+\beta_2\phi_2) \tag{4}$$

with

$$\phi_1=2(n^3+3nm^2+n^3+3nl^2+m^3+3ml^2), \tag{5}$$

$$\phi_2=8(n^3+m^3+l^3). \tag{6}$$

(ii) T applied—ΔJ_{ir} measured from the state with H at its final value and T zero:

$$\Delta J_{ir}=\beta_1(3J_s^2\lambda_{100}HT\psi_1+(9/8)J_s\lambda_{100}^2T^2\psi_2) \tag{7}$$

with

$$\psi_1=4(n^4-l^4), \tag{8}$$

$$\psi_2=2[n(n^2-m^2)^2+n(n^2-l^2)^2+m(m^2-l^2)^2]. \tag{9}$$

(iii) T removed—ΔJ_{ir} measured from the state at the end of step (ii):

$$\Delta J_{ir}=0. \tag{10}$$

The removal of tension causes no change of macroscopic magnetization because the displacements of walls of classes A and C produce equal and opposite changes of magnetization.

For an isotropic polycrystalline aggregate, the functions ϕ_1, ϕ_2, ψ_1, and ψ_2 must be averaged over the spherical triangle in Fig. 1. The averages are

$$\langle\phi_1\rangle=3\sqrt{2}=4.2426,$$
$$\langle\phi_2\rangle=6=6.0000,$$
$$\langle\psi_1\rangle=32/5\pi=2.0372,$$
$$\langle\psi_2\rangle=\sqrt{2}=1.4142.$$

I am indebted to Mr. Morton S. Raff for the carrying out of the integrations.

The variation of magnetization with tension during step (ii) is given, for the polycrystalline specimen, by

$$\Delta J=\gamma_1HT+\gamma_2T^2, \tag{11}$$

where

$$\gamma_1=3\beta_1J_s^2\lambda_{100}\langle\psi_1\rangle, \tag{12}$$

$$\gamma_2=(9/8)\beta_1J_s\lambda_{100}^2\langle\psi_2\rangle. \tag{13}$$

The normal magnetization curve at low magnetizing force is given by the equation for step (i) with the reversible term added; consequently, the normal permeability as a function of magnetizing force is given (in accordance with the original form of Rayleigh's law) by

$$\mu=\mu_0+cH, \tag{14}$$

where μ_0 is the initial permeability and

$$c/4\pi=J_s^3(2\beta_1\langle\phi_1\rangle+\beta_2\langle\phi_2\rangle)\equiv g. \tag{15}$$

If the ratio $f=\beta_2/\beta_1$ were known, β_1 could be evaluated from the slope of the μ *vs.* H curve. For lack of better knowledge, we tentatively assume $f=1$; this gives a tentative value for β_1,

$$\beta_1'=g/J_s^3(2\langle\phi_1\rangle+\langle\phi_2\rangle). \tag{16}$$

The ratio of the (unknown) correct value to this tentative value is

$$\beta_1/\beta_1'=(2\langle\phi_1\rangle+\langle\phi_2\rangle)/(2\langle\phi_1\rangle+f\langle\phi_2\rangle)$$
$$=1.707/(1+0.707f). \tag{17}$$

[4] Reference 1, p. 148 ff.

If $f<1$, the correct value of β_1 must be between β_1' and $1.707\beta_1'$. If $f>1$, the correct value will be smaller than β_1', but of the same order of magnitude if f is of order of magnitude unity. The error introduced by assuming $f=1$ therefore is probably no more serious than other errors inherent in our simplified model, and it does not affect either the form of the laws or the order of magnitude of the constants.

The assumption $f=1$ implies equal importance of 90° and 180° walls in phenomena attributable to irreversible wall displacements. If only 90° walls were important ($\beta_2=0$), the results would not be much different; but if only 180° walls were important ($\beta_1=0$), the phenomena under discussion would, according to our theory, not occur.

By setting $f=1$ and inserting the numerical values of the averages, we get

$$\gamma_1/g=0.42190\lambda_{100}/J_s, \tag{18}$$

$$\gamma_2/g=0.10983(\lambda_{100}/J_s)^2. \tag{19}$$

With $J_s=1710$ e.m.u. and $\lambda_{100}=16.2\times10^{-6}$,

$$\gamma_1/g=4.00\times10^{-9} \text{ e.m.u.}, \tag{20}$$

$$\gamma_2/g=9.86\times10^{-18} \text{ e.m.u.} \tag{21}$$

The theoretical model leads not only to a definite formula for the variation of magnetization with tension, but to definite values of the constants in the formula, and to evaluate them one needs only a set of purely magnetic data on the particular specimen—the variation of normal permeability with small magnetizing force. At this point, therefore, a series of measurements was carried out to test the predictions of the theory.

For validity of formula (11), the tension must not exceed a certain critical value, namely, the value at which the condition for validity of Eq. (3) ceases to hold during step (ii). This critical value is

$$T_c=(4/3\sqrt{2})(J_s/\lambda_{100})H=0.945(J_s/\lambda_{100})H. \tag{22}$$

If the critical value is exceeded, some walls of some of the crystals will cease to obey Eq. (3) and will obey, instead, Eq. (2). The effect on the behavior of the specimen will be small if the critical value is not greatly exceeded, since only a small fraction of all the walls will violate the condition for validity of Eq. (3).

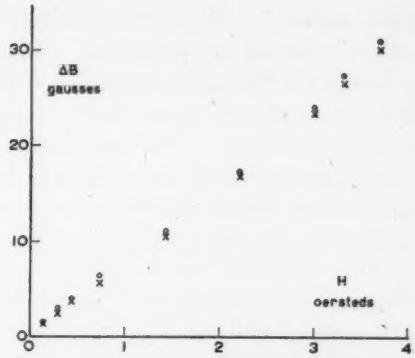

FIG. 3. Representative experimental data on irreversible change of flux density, ΔB, resulting from application and subsequent removal of tensile force 58.3 lb., with specimen initially in state of normal magnetization at magnetizing force H. Circles, change resulting from application of tension; crosses, net change resulting from application and subsequent removal of tension.

EXPERIMENTAL TEST

To test the theory, a steel specimen whose μ *vs.* H curve had been measured was put through the succession of steps analyzed in the preceding section, with various values of H and T. These measurements were carried out by Mr. E. L. Sanderson under the direction of Mr. J. R. Wright.

The specimen was a cylindrical rod 24″ long and 0.126″ in diameter. The correction for demagnetizing force is small and was neglected. For $H\leq4$ gauss, Eq. (14) holds with $\mu_0=75.2$ and $c=4.40$ gauss^{-1}. (The dimensional convention adopted here for e.m.u. is $[B]=[H]$.) The theoretical values of γ_1 and γ_2 are, therefore,

$$\gamma_1=1.40\times10^{-9} \text{ cm}^2 \text{ dyne}^{-1},$$
$$\gamma_2=3.45\times10^{-18} \text{ gauss cm}^4 \text{ dyne}^{-2}.$$

For the tension experiments, the magnetizing force was applied in the usual manner, with a solenoid. The ends of the sample were threaded into brass rods, one of which was connected to a weight and lever system for applying known tensions. The changes in flux density were measured by means of a 5000-turn, 252.6-ohm search coil connected to a fluxmeter (Leeds and Northrup galvanometer, Cat. No. 2290).

For each measurement, the specimen was demagnetized and put into a state of normal magnetization (the use of normal rather than virgin magnetization in step (i) makes Eq. (2) more certainly applicable). A known tension was

applied and the flux change observed; then the tension was removed and the flux change observed. The entire procedure was repeated for each pair of values of magnetizing force and tension.

According to Eq. (11), the flux change upon application of tension should be given by

$$\Delta B = \Gamma_1 F H + \Gamma_2 F^2, \tag{23}$$

where F is the force applied; the Γ's are simply related to the γ's and to the area of the cross section of the specimen. The flux change upon removal of the tension should be zero. Figure 3 shows representative data on the change of flux density produced (a) by application of tension and (b) by application and subsequent removal of tension. There is some change upon removal of the tension, but it is small.

The data were plotted and analyzed and the experimental values of the constants evaluated by Mr. Morton S. Raff.

To test Eq. (23), ΔB was first plotted against H, for each value of F. The data for each value of F fall on a straight line within the precision of the measurements. The slopes give values of Γ_1 ranging from 0.114 lb.$^{-1}$ for $F=23.1$ lb. to 0.154 lb.$^{-1}$ for $F=71.5$ lb. The intercepts $\Gamma_2 F^2$ are too small to be determined by this method.

The requirement $T \leq T_c$ becomes in this case $F/H \leq 18.0$ lb./gauss. For the smallest F, 23.1 lb., this condition is satisfied for $H \geq 1.28$ gauss; for the largest F, 71.5 lb., it is satisfied only for $H \geq 3.97$ gauss. The progressive change in the slopes of the curves indicates a progressively increasing importance of processes not correctly described by Eq. (3), and the best value of Γ_1 for comparison with theory is that for the smallest F, 0.114 lb.$^{-1}$. This gives

$$\gamma_1 = 1.64 \times 10^{-9} \text{ cm}^2 \text{ dyne}^{-1},$$

in satisfactory agreement with the theoretical value 1.40×10^{-9}. In fact, the agreement is better than one could legitimately expect in view of the simplifications made in the theory, such as uniformity of magnetizing force and stress and equality of the two β's.

To determine Γ_2, $\Delta B/F$ was plotted against F for each value of H. With this method of plotting, the requirement $T \leq T_c$ is satisfied over no part of the range at the lowest H, 0.148 gauss, but over all of it at the highest, 4.062. The straight line drawn for $H=4.062$ gauss gives $\Gamma_1 = 0.107$ lb.$^{-1}$, which agrees with the previous value 0.114 within the precision of the straight line representation of the badly scattered points, and it gives $\Gamma_2 = 0.00309$ gauss/lb.^{2}, whence

$$\gamma_2 = 8.03 \times 10^{-18} \text{ gauss cm}^4 \text{ dyne}^{-2}.$$

This agrees with the theoretical value, 3.45×10^{-18}, as well as could be expected. The theoretical value is affected by the approximations made in the derivation and by the uncertainty in the value of λ_{100} (which is squared here); the experimental value is deduced with difficulty from data which, plotted in this way, exhibit large scatter.

The experimental data confirm the predictions of the theory within the precision claimed for it.

DIMINISHING ALTERNATING FIELDS AND STRESSES

The same theoretical model can be used to calculate the behavior under other field and stress conditions. A few such results will be stated here for the case of a magnetic field or tension that undergoes alternations of sign with gradual diminution of amplitude, in the presence of a constant polarizing magnetizing force h. The results apply only to cases in which the instantaneous net magnetizing force or, more generally, the instantaneous "pressure" of Eq. (1) expressed as an equivalent magnetizing force is always considerably smaller than the coercive force, so that Rayleigh's law applies. Such a process can produce significant changes of magnetization, but it cannot bring about complete demagnetization in the case $h=0$ or establish the ideal magnetization corresponding to a value $h \neq 0$. Simple results are obtained only when h is small in comparison with the initial amplitude of the alternating component H; in view of the restrictions already placed on the net magnetizing force, the case $h \ll H$ may seem trivial, but actually it is not, for the presence of even a small biasing field can result in an appreciable magnetization when the process is of the type considered.

To a good approximation, the magnetization resulting from diminishing cycles of initial amplitude H in polarizing magnetizing force $h \ll H$ ("idealization in h by H") is

$$J = (\chi_0 + 2gH)h; \tag{24}$$

the susceptibility with respect to h is increased by the idealization process from χ_0 to χ_0+2gH. For diminishing tension cycles of initial amplitude T ("idealization in h by T"), gH is to be replaced by $\gamma_1 T$. If, as was assumed before, $\beta_2=\beta_1$, then an idealizing tension T is equivalent to an idealizing magnetizing force H given by

$$H/T=\gamma_1/g=0.4219(\lambda_{100}/J_s), \qquad (25)$$

or 1 dyne/cm^2 is equivalent to 4.00×10^{-9} gauss.

The effect of successive idealizations in h by H and in h' by H' depends on which is larger, H or H'. If the second idealization is weaker than the first, it produces a change of magnetization (from the value after the first)

$$\Delta J=(\chi_0+2gH')(h'-h); \qquad (26)$$

if it is stronger than the first, it erases it and produces a magnetization

$$J=(\chi_0+2gH')h'. \qquad (27)$$

More generally, in a series of idealizations, each produces a magnetization differing by the amount (26) from that after the most recent stronger idealization; any intermediate weaker ones are erased. For successive idealizations in h by T and in h' by T', gH' is to be replaced by $\gamma_1 T'$. Idealizations first by field and then by stress, or *vice versa*, are more complicated in their effects; walls of class B are affected by fields but not by stresses, and so complete erasure of the former by the latter does not occur.

The relations summarized above are in qualitative agreement with the experimentally known behavior. For instance, according to our simplified theory the first of a series of equal shocks (magnetic or mechanical) should produce a change of magnetization, and the subsequent ones should have no effect; what actually happens is that 90 percent or more of the change is produced by the first shock. No quantitative data are available to test the theory in the small-field range where, if anywhere, it should hold precisely. Shock amplitudes of practical interest are likely to lie somewhat beyond the range of validity of the theory, so that its chief practical usefulness is for approximate rather than precise predictions.

The results quoted here for tension are subject to an error not present in the purely magnetic case. The condition analogous to $h\ll H$, when H is replaced by a tension, is never satisfied by every wall of every crystal because of the geometrical factors in Eq. (1). However, if $J_s h\ll\lambda_{100}T$, the condition will be satisfied by most of the walls.

The foregoing results may be used to calculate, roughly, the behavior of a complex body, such as a ship, when it is subjected to irregular mechanical disturbances of the sort that occur in its normal history.[5] For this purpose we use a much simplified model. We suppose that the body consists of a large number of identical and mechanically independent parts and that these parts are also magnetically independent, except for a common demagnetizing field $-NJ$ determined by the average magnetization J of the body and by a demagnetizing factor N characteristic of the body as a whole. We suppose that the probability of receiving a shock of specified amplitude, in any specified time interval, is the same for each part, and we interpret a "shock" as a process similar to the "idealization in h by T" considered above.

We consider first the case in which the shocks all have the same amplitude T, but the applied field varies in an arbitrary manner. Suppose at first that the magnetizing force is a given function of time, $h(t)$. Let pdt be the probability that a part will be shocked during time interval dt, and choose the time scale so that p is constant. During dt, a fraction pdt of the parts receives a shock and changes from the existing magnetization to a magnetization χh, where $\chi=\chi_0+2\gamma_1 T$. Since these parts were selected at random, their average magnetization before the shock was the same as that of the whole body, J, and therefore the change of magnetization caused by shocks is $\chi h-J$ when averaged over the shocked parts and $(\chi h-J)pdt$ for the whole body. Meanwhile, all but an infinitesimal fraction pdt of the parts have changed their magnetization reversibly by $\chi_0 dh$. The total change is $dJ=(\chi h-J)pdt+\chi_0 dh$, or

$$dJ/dt+pJ=p\chi h+\chi_0 dh/dt. \qquad (28)$$

If the demagnetizing field is negligible, Eq. (28) shows that for constant applied field the magnetization approaches its final value according to

[5] The formulas to be given were derived by the author in 1942; the assumptions on which they rest had at that time only an experimental basis. A qualitative formulation of the theory, based on the same general picture and leading to similar conclusions, was arrived at independently at about the same time by Dr. S. Wolman and his collaborators at the Bureau of Ordnance.

an exponential law with a time constant $1/p$, which is easily seen to be the mean time that a part has to wait before receiving its first shock. If the demagnetizing field is not negligible, set $h=h_0-NJ$ in Eq. (28); the result is an equation of the same form, but with the susceptibilities replaced by the corresponding apparent susceptibilities and with p replaced by

$$p'=p(1+N\chi)/(1+N\chi_0). \tag{29}$$

Since $\chi>\chi_0$, the time constant is shortened by the demagnetizing field. For constant h_0 this may be interpreted as follows: the first changes occur at a larger h than is ultimately present; therefore, they take the average magnetization toward its ultimate value faster than if h were maintained constant and equal to its ultimate value.

We consider, second the case in which the demagnetizing field is negligible and $h=h_0=$ constant, with the body initially demagnetized, but the shocks have various amplitudes. Then in any part a shock produces an effect only if it is larger than every previous shock. We measure J from its initial value $\chi_0 h$ as zero, and we measure the shock amplitude by the J which it can produce. Let $p(J)dJdt$ be the probability that, in time dt, a part will receive a shock of amplitude between J and $J+dJ$. Then the probability per unit time of a shock greater than J is

$$F(J)=\int_J^{J_m} p(J)dJ, \tag{30}$$

where J_m corresponds to the largest shocks that ever occur. The fractional number of parts that escape shocks larger than J up to time t is, by familiar arguments, $e^{-F(J)t}$. The fractional number for which the largest shock experienced, up to time t, was one between J and $J+dJ$, is the differential of this with respect to J. The average magnetization at time t is therefore

$$\bar{J}=\int_0^{J_m} J(\partial/\partial J)[e^{-F(J)t}]dJ=Je^{-F(J)t}\Big|_0^{J_m}-\int_0^{J_m} e^{-F(J)t}dJ=J_m-\int_0^{J_m} e^{-F(J)t}dJ, \tag{31}$$

since $F(J_m)=0$.

For small t, Eq. (31) gives approximately

$$\bar{J}=t\int_0^{J_m} F(J)dJ. \tag{32}$$

Thus the initial rate of rise depends on the frequencies of shocks of all amplitudes. For large t, let $F(J)=u$; then the integrand in Eq. (31) may be written $e^{-ut}du/p(J)$, and if $p(J_m)\neq 0$ the result is approximately

$$\bar{J}=J_m-1/p(J_m)t. \tag{33}$$

Thus the asymptotic rate of approach to the final value depends only on the frequencies of the largest shocks: the smaller ones have already done all they can.

The results obtained here are formally very similar to those of Kittel's[6] phenomenological theory, but our interpretation is quite different from his. Kittel attributes the time constants to relaxation processes in the material, whereas in the present theory the time constants are properties not of the material but of its environment. Our calculation shows that magnetostrictive processes are capable of producing a behavior of the general type observed and therefore must be taken into account in any satisfactory theory of the phenomenon. On the other hand, slow mechanical and metallurgical changes in the material unquestionably do occur, and these may also contribute to the observed behavior; their effect would be primarily a change of magnetic *properties*, rather than merely of magnetic *state*.

The contributions made to this investigation by Messrs. Wright, Sanderson, and Raff have already been mentioned. I wish in addition to acknowledge my indebtedness to Dr. S. Wolman and to Mr. J. H. Sweer for many helpful discussions of this and related problems, and, finally, to Mr. J. A. Osborn for his careful carrying out of an earlier experimental program that formed the basis for many of the qualitative ideas presented here.

[6] Charles Kittel, Phys. Rev. 69, 640 (1946). The theory was first propounded in 1941.

PHYSICAL REVIEW VOLUME 75, NUMBER 1 JANUARY 1, 1949

Magnetic Domain Patterns on Single Crystals of Silicon Iron

H. J. WILLIAMS, R. M. BOZORTH, AND W. SHOCKLEY
Bell Telephone Laboratories, Murray Hill, New Jersey

(Received August 30, 1948)

Magnetic powder patterns have been obtained on electrolytically polished surfaces of single crystals of iron containing 3.8 weight percent silicon. Domains are easily visible, outlined by accumulations of colloidal magnetic particles. Several techniques have been developed that enable the direction of magnetization in each domain to be determined. Many types of domain patterns are observed, depending on the orientation of the surface with respect to the crystal axes. The simpler patterns can now be interpreted in some detail, and support the idea that the internal domain structure is relatively simple and is usually composed of a series of plates or slabs magnetized at 45° or 90° to the plate length. In one case it is verified that the plate thickness depends on plate length in approximate accordance with theory; and, for the more complicated "tree" patterns, comparison of theory with experiment shows that good agreement can be obtained using theoretical values of the wall energy. Further verification of the theory of Bloch walls is obtained by determining from experiment the change in spin orientation on traversing the wall.

INTRODUCTION

ALTHOUGH the domain theory of ferromagnetism has been found to be adequate in many respects, many details of domain structure, in particular the geometrical forms of the domains and their change with magnetization, have been lacking. It is generally recognized that the domains in an unmagnetized material are small regions, each saturated in a direction determined by the crystal axes or the local stresses. The change in magnetization, caused by the application of a magnetic field, takes place by movement of the boundaries between domains (in weak fields) or by rotation of the direction of magnetization (in strong fields). However, the shapes of the domains, and the ways in which the boundaries form and move with field and stress, have not heretofore been established experimentally.

In attempts to obtain visual evidence of domain structure, von Hámos and Thiessen[1] and Bitter[2] proposed independently that fine magnetic particles be spread over the surface of material to be investigated, in the hope that the inhomogeneities in the magnetization would be seen under the microscope in the same way that cracks and flaws in large pieces of iron have been detected for many years by sprinkling relatively coarse powder over the surface of the magnetized piece. This technique was developed by a number of investigators, and a considerable advance in knowledge and technique was made by Elmore and McKeehan[3] who applied a colloidal suspension of iron oxide to carefully polished specimens and observed the so-called "maze" patterns (see Fig. 2) in *unmagnetized* specimens of iron.

Later, Elmore[4] showed that the maze pattern is characteristic of the polished surface and not of the interior. He then removed the effects of mechanical polishing by electrolytic means and observed patterns on crystals magnetized at right angles to the surface. In our work we have used Elmore's method of electrolytic polishing and observed patterns on many crystal surfaces when the specimen is demagnetized and when it is magnetized to various extents parallel to the surface.

The basic theory of domains has been developed and extended by many writers. It is commonly assumed that in zero and low fields the magnetization in each domain is parallel to one or another of the directions of easy magnetization in the crystal (⟨100⟩ directions in iron). Recent progress in domain theory, particularly in domain geometry, has been made by Néel[5] using the assumption that there is a minimum number of magnetic poles at external and internal domain boundaries; this requires that the normal component of magnetization is

[1] L. v. Hámos and P. A. Thiessen, Zeits. f. Physik **71**, 442 (1931).
[2] F. Bitter, Phys. Rev. **38**, 1903 (1931).
[3] W. C. Elmore and L. W. McKeehan, Trans. A. I. Min. Met. Engrs. **120**, 236 (1936).
[4] W. C. Elmore, Phys. Rev. **51**, 982 (1937) and **53**, 757 (1938).
[5] L. Néel, J. de phys. [8] **5**, 241 (1944).

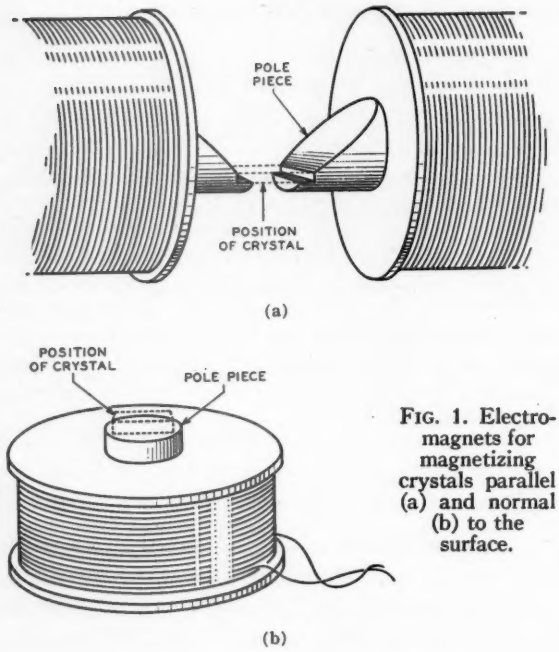

FIG. 1. Electromagnets for magnetizing crystals parallel (a) and normal (b) to the surface.

approximately constant across a boundary or "wall." The domain patterns described below are found to conform well to this principle of "flux closure" and, consequently, they represent configurations of low magnetostatic energy. The Bloch walls or transition regions which separate the domains also have energies of the order of 1 erg/cm^2; the stable arrangement of domains is the one which minimizes all the energies of which those of poles and domain walls are important.

In our work, the patterns on crystals of some orientations are simple and lead to definite conclusions regarding the domain structure of the whole crystal; with others they are very complex and little progress has been made in understanding them. In several instances the results confirm in a striking way the recent theoretical work of Néel.

EXPERIMENTAL PROCEDURE

Single crystals of iron containing 3.8 weight percent silicon were prepared by melting pure materials in pure hydrogen and solidifying very slowly, as previously described.[6] Specimens were cut with surfaces approximately parallel to (100), (110), or (111) planes. They were then deeply etched and annealed, some of them at 1300°C in pure hydrogen, and carefully polished using conventional metallographic technique.

The surfaces to be examined were electrolytically polished. This operation was carried out in a bath composed of 100 g of solid chromic acid and 900 g of an 85 percent solution of phosphoric acid. The bath was heated to 90°C and electrolyzed with the specimen as anode and a copper rod as cathode, with a current of 10 to 20 amperes. A specimen having an area of 1 or 2 cm^2 was immersed for about one minute, or until microscopic examination showed that all scratches were removed.

The colloidal suspension was made according to Elmore's directions:[7] 2 g of hydrated ferrous chloride ($FeCl_2 \cdot 4H_2O$) and 5.4 g of hydrated ferric chloride ($FeCl_3 \cdot 6H_2O$) were dissolved in 300 cm^3 of hot water, and a solution of 5 g of sodium hydroxide added to it with constant stirring; this was filtered, and the precipitate of Fe_3O_4 washed and added to one liter of 0.5 percent soap solution, and the whole boiled for a short time. A more concentrated colloidal suspension was also made by adding the precipitate of Fe_3O_4 to 100 cm^3 of soap solution.

Powder patterns were formed by placing a drop of the colloidal suspension on the crystal surface, then placing a thin microscope cover glass on the drop so that a thin layer of the colloidal suspension was left between the crystal and the cover glass. They were usually observed under the microscope with a magnification of

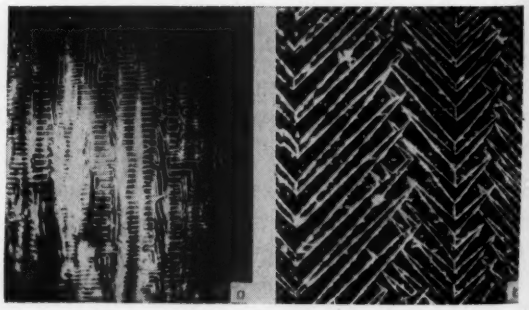

Mechanical polishing Electrolytic polishing

Crystal axes + →|0.1 mm|←

FIG. 2. Powder patterns obtained after mechanical polishing (a) and after electrolytic polishing (b) of the same surface area.

[6] H. J. Williams, Phys. Rev. **52**, 747 (1937).

[7] W. C. Elmore, Phys. Rev. **54**, 1092 (1938) and **62**, 486 (1942).

330 diameters. Ultropak dark field vertical illumination was used. Photographs were made with a Zeiss Ikon camera and Kodak Super XX 520 pack film.

When the usual colloidal suspension is used, the colloidal particles commonly form into lines, the rest of the area being almost free. On surfaces of certain crystallographic orientations, however, large portions of the field are covered with particles, other smaller portions being quite free. A pattern changes with application of field or stress, provided the solution has been freshly applied; but if it has remained undisturbed for some time—perhaps 10 minutes—it becomes "frozen" and immobile, each particle adhering to the same part of the surface in spite of change in magnetization. Before this occurs, Brownian motion of some of the particles can be observed.

Magnetization of the specimen in the plane of the surface was usually accomplished with the aid of the electromagnet sketched in Fig. 1a. Magnetization at right angles to the surface was carried out by placing the specimen on top of the iron core of an electromagnet having a vertical axis, Fig. 1b.

TECHNIQUES FOR DETERMINING DIRECTIONS OF MAGNETIZATION IN DOMAINS

A relatively simple pattern, and one having several features that we have been able to interpret, is formed on a surface almost parallel to the crystallographic planes (100). After the specimen has been polished mechanically, using conventional metallographic technique, but not yet polished electrolytically, the usual maze pattern of Fig. 2a, reported first by McKeehan and Elmore,[8] is obtained. After electrolytic polishing of the same area the pattern of Fig. 2b is observed, and repeated treatments do not change its character. The pattern resembles the outline of a tree with the branches pointing in two of the four directions that lie in the plane of the surface and are inclined 45° to the crystal axes. A similar "tree" pattern, but less well defined, was obtained on a surface prepared with a special wax-lap technique to be described in a forthcoming article by E. E. Thomas, of the Bell Telephone Laboratories.

[8] L. W McKeehan and W. C. Elmore, Phys. Rev **46**, 226 (1934).

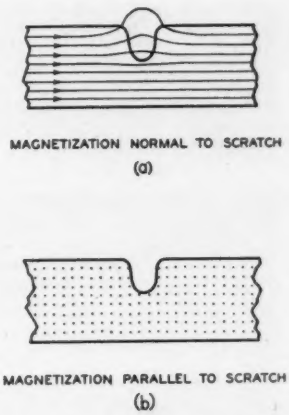

FIG. 3. (a) Illustrates how flux emerges from the metal while crossing a scratch which is normal to the magnetization in a domain; (b) shows that no flux emerges from the metal when the scratch is parallel to the magnetization in a domain.

It may be concluded that conventional mechanical polishing produces surface strains that affect the powder patterns, which cannot then be used to interpret domain structure in the interior. On the contrary, patterns on electrolytically polished surfaces are useful in obtaining information about the internal structure. This has been especially important in advancing our knowledge of domain geometry. Powder patterns can often be used to detect small surface strains.

The directions of magnetization in the various domains shown in the tree pattern have been determined by a technique involving (1) scratching the surface, and have been confirmed by (2) experiments on the effect of mechanical stress, and by (3) observation of peculiarities in the pattern obtained with the use of heavy colloid. The techniques which establish the nature of the magnetization pattern are described in the following sections, after which the theoretical explanation of the pattern is given.

Scratch Technique

If a scratch crosses a domain in which the magnetization is not parallel to the scratch, magnetic poles are formed when the flux emerges into the air where it crosses the scratch (Fig. 3a) and colloidal particles are attracted and enhance the visibility of the scratch. If the scratch is parallel to the magnetization, no disturbance of the flux occurs (Fig. 3b) and the scratch is almost or quite invisible. In practice it was found that the

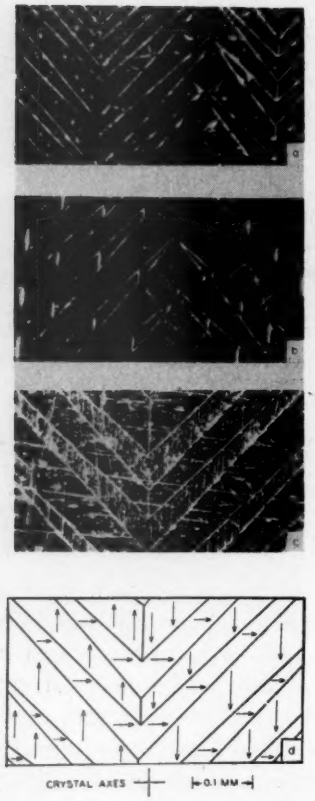

FIG. 4. (a) Typical "tree" pattern; (b) pattern on a surface having a series of parallel scratches made with a ruling engine; (c) pattern on a surface having vertical and horizontal scratches made with a brush of fine glass fibers; (d) directions of magnetization in pattern (c), as determined by the scratches.

scratch must not be so deep as to strain the surrounding material. After some experimenting, scratches were made in two ways: (i) by using a ruling engine with a conical sapphire stylus, the weight of which was carefully balanced to make a light scratch, and then polishing electrolytically to reduce the scratch still further, and (ii) by using a small brush made of fine glass fibers and passing it lightly over the surface. Scratches were always made approximately parallel to the known directions of easy magnetization, the [100] directions parallel to the sides of the figure. The results of the experiment are shown in Fig. 4. Here the first pattern is of the tree type and contains no scratches. The second was formed after vertical scratches had been made with a ruling engine. The third pattern shows two mutually perpendicular sets of scratches made with a brush having fine glass fibers, and the fourth part of the figure is a diagram showing the domain boundaries and directions of magnetization in the third pattern, deduced from the behavior of the colloid around the scratches. In the diagram the sense of the magnetization vector is chosen so that there is almost no change in the normal component of magnetization across a boundary, a condition*,[9,10] equivalent to the practical absence of magnetic poles at the boundary, and one which can be applied consistently throughout the whole pattern.

Striations of Colloid

It will be noted on many of the patterns (e.g., Figs. 6 and 10a) that between the domain boundaries there are irregular elongated masses or striations of colloidal particles which are larger and more numerous when the colloidal suspension is more concentrated. Such striations were observed repeatedly to be elongated in a direction at right angles to the direction of magnetization, as determined independently by other means, and so came themselves to be reliable indicators of direction of magnetization.

The reason for the orientation of the striations is not known with certainty, but a possible

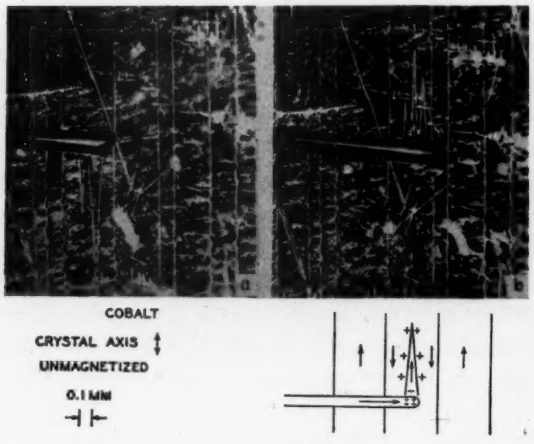

FIG. 5. Powder pattern showing regions of reversed magnetization induced by a permanent magnet probe, (a) before and (b) after moving the probe to the right so that it is above the adjacent domain. In (b) the regions of reversed magnetization are above the probe, in (a) they are below.

* The importance of this condition has been mentioned by Landau and Lifshitz (reference 9) and others, cf. references 7 and 10.

[9] L. Landau and E. Lifshitz, Physik Zeits. Sowjetunion 8, 153 (1935).

[10] L. Néel, J. de Phys. [8], 5, 241 (1944).

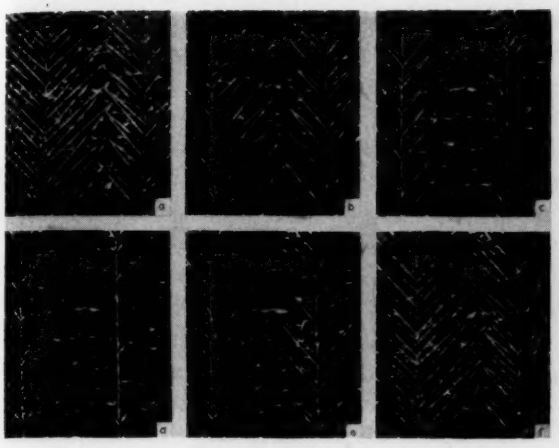

FIG. 6. (a) to (d), patterns all observed on the same area of a crystal, with tension increasing from zero to a maximum value. In (d) to (f) tension is decreasing from maximum value to zero.

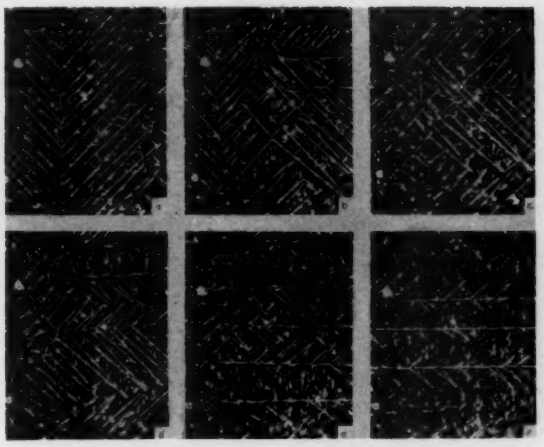

FIG. 7. Series of patterns, all observed on the same area of a crystal, as the compression was increased from zero to a maximum value.

explanation is as follows. The surface is not perfectly plane but has some irregularities that may be represented, for convenience, as a series of circular mounds. When the magnetization of the domain lies in the direction of the line connecting two mound centers, there will be magnetic poles produced in the valley between the mounds and the powder will collect in this region which will be elongated at right angles to the direction of magnetization ("transverse" striation). When the line between mounds lies at right angles to the direction of magnetization, no poles will lie in the valley between them and so no "longitudinal" striations will form. It is in a somewhat similar way that the colloid collects on mechanical scratches (see above) and is always elongated at right angles to the magnetization. The mound picture is supported by microscopic observation of a surface subjected to repeated electrolytic etching—the surface finally acquires an uneven appearance not unlike that of an orange peel. It is also supported by the fact that the striations form in the same places after successive demagnetizations. Imperfections in the structure completely below the surface might have a similar effect in producing striations.

Probe Technique

The direction and sense of the magnetization in a domain was determined with the aid of a long, thin probe consisting of a 0.015-cm wire of a permanent magnet material (Vicalloy), magnetized and placed on the surface to be examined while the colloid was present. The pole at the end of the probe produces a field in the underlying domain. If this field is in the same direction as the magnetization of the domain, this magnetization will not be affected. If it is in the opposite direction, it will cause a local reversal of magnetization within the domain, and one observes a number of pointed regions as depicted in Fig. 5a, immediately below the end of the probe. In Fig. 5b the probe has been moved to the right so that the end lies on the next domain; here it is noted that the pointed regions lie above the probe. These photographs (of cobalt) show that the domains mentioned are magnetized in antiparallel directions, and the sign of the pole on the probe (positive) proves that the first domain is magnetized toward the top and the second toward the bottom of the figure as indicated in the diagram.

Effect of Stress

Tension was applied to the upper surface of a thin single crystal, in a device that held the ends of the crystal fixed while a screw underneath the middle of the crystal pressed upwards. A series of patterns, obtained as the tension was first increased and then decreased in successive stages,

FIG. 8. Powder pattern on a surface having the lower half accurately parallel to a (100) plane, and the upper half inclined at an angle of 3° by rotation about a horizontal axis at the intersection of the two surfaces.

are reproduced in Fig. 6. According to domain theory, tension applied to a material having positive magnetostriction will increase the volume of the domains aligned parallel to the axis of the tension and decrease the volume of those making an angle of 90° with the axis. In the figure the areas of the tapered regions or "branches" are decreased and the areas having 180° boundaries are increased. In accordance with theory and with other considerations mentioned above, it is concluded that the tapered regions are magnetized at 90° to the (vertical) axis of tension and that for the highest tension (Fig. 6d) these regions practically vanish so that the material is then composed of domains oriented in the two senses of the tension axis. Thus the directions of magnetization deduced from the tension experiment agree with those determined by means of scratches and the striations of colloid.

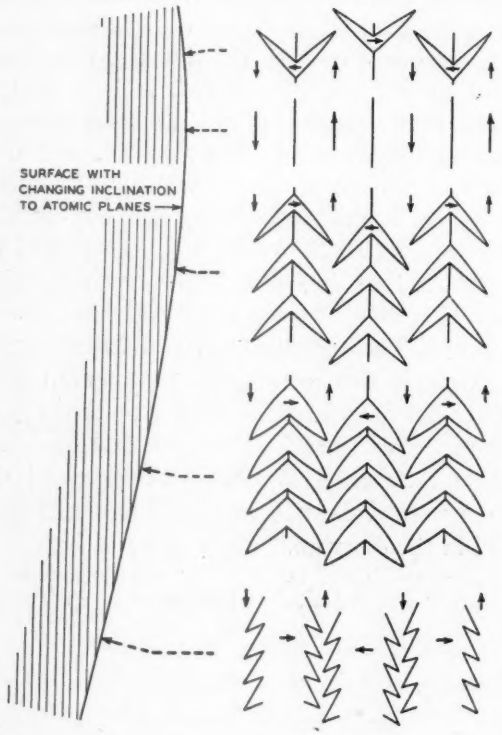

FIG. 9. Diagram showing the domains on a curved surface having a gradually varying inclination with respect to a (100) plane.

Compression was applied to the upper surface of the same specimen by clamping one end and forcing the other end upward with a screw. Results are shown in Fig. 7, with the compression axis now vertical (toward the top of the figure). One expects the pattern obtained with high elastic compression to be made of horizontal lines, 180° boundaries between domains pointing to the right and to the left. Since there are no horizontal boundaries in the pattern of the unstrained crystal in the portion of the specimen chosen for examination, these may be expected to form when a small compression is applied and to grow with increased compression until they constitute the whole pattern. These changes actually do occur, but not in a smooth way. Whole portions of the pattern change suddenly, even when the compression is increased slowly, in a way that cannot be followed by eye. With increasing compression the vertical 180° boundaries disappear, horizontal 180° boundaries form, and the 90° boundaries eventually disappear as expected (Fig. 7f).

SURFACES SLIGHTLY INCLINED TO (100)

The conditions under which the "tree" pattern forms, and the reasons for the formation of this particular kind of pattern, are fairly well understood and will now be described.

In a preliminary experiment a specimen was selected that had rounded edges, and colloid was deposited near these edges. The tree pattern appeared only when there was a slight inclination of the surface to (100) planes, and the branches were always oriented so that they pointed at ±45° to the "downhill" direction, the (100) planes being regarded as level.

On another specimen two plane surfaces were ground, one accurately parallel to (100) and the other inclined 3° thereto. Powder patterns were

then photographed over the ridge where the two surfaces join as shown in Fig. 8. Here again it was apparent that the tree pattern is characteristic of a surface inclined to (100) and that the branches point "down-hill."

In a more systematic experiment a curved surface was cut on a single crystal, as indicated schematically in Fig. 9. The pattern of Fig. 10(b) corresponds to the surface parallel to (100), (a) to a slope in one direction and (c) to (h) to increasing slope in the other direction. When the inclination between surface and crystal planes becomes relatively large the "branches" of the tree pattern become thick and are close together, until finally only the outlines of the end portions of the branches remain. At this stage most of the surface is magnetized transversely to the "tree trunks," and the remainder, on which most of the colloid collects, has the appearance of trees inverted from their original positions, as shown schematically in Fig. 9.

These observations can all be correlated on the basis of domain theory and, as is shown in detail in the appendix, the principal features can be understood semiquantitatively. The patterns represent minimum energy configuration in the form of a compromise between magnetostatic (pole) and domain wall energy.

Figure 11 shows the crystal surface which is tilted by an angle θ in respect to the crystal axes, XYZ. The underlying domains, which are magnetized parallel to [010] and [0$\bar{1}$0], produce a density of magnetic poles of $\pm I_s \sin\theta$ on the surfaces of alternating strips of width W. This gives rise to a magnetostatic energy, discussed in the Appendix, proportional to $W \sin^2\theta$ per unit area. When θ is larger than 1°, it is possible to reduce this energy by forming the tree patterns even though domain wall energy is added. Figures 12 and 13 show how this occurs. The branches are actually shallow domains about $\frac{1}{10}$ as thick as they are wide. They transport flux across the trunks of the trees and as they taper this flux is distributed as magnetic poles over the domain wall separating the branch from the underlying domain. The net result is to change the regions, on which there are poles, from strips of width W to strips approximately as wide as the branches, and so to reduce the magnetostatic energy about tenfold for the trees of Fig. 12. It would be reduced still more if the branches were narrower; however, to use narrower branches would require more domain wall surface. Using constants based on large-scale measured properties of the material, a minimum energy theory

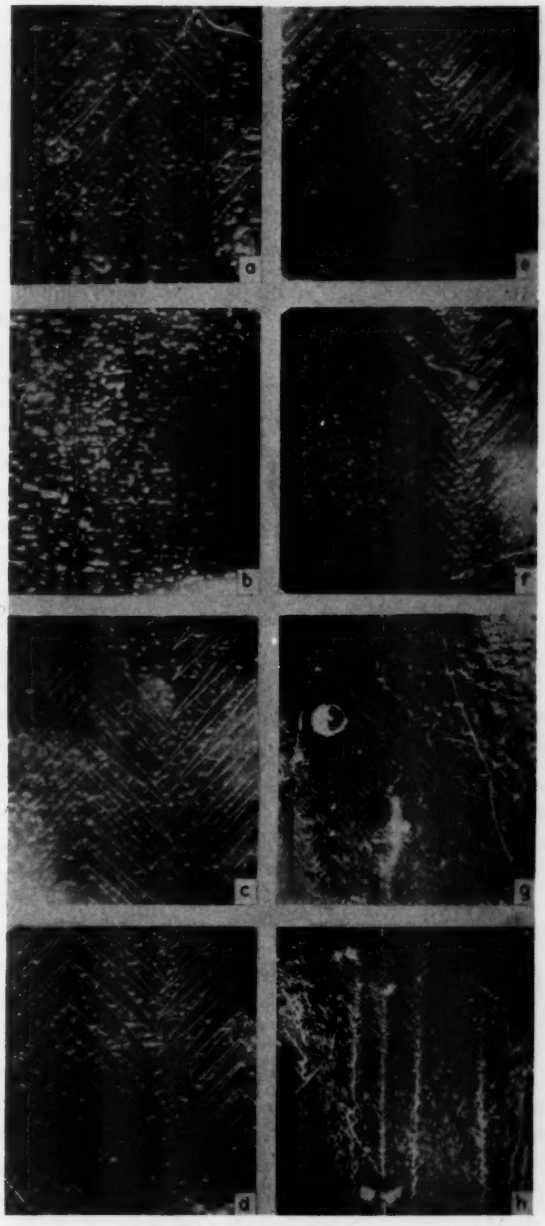

FIG. 10. Series of patterns observed at successive positions, (a) to (f), on a curved surface. Note correspondence to Fig. 9. Patterns in (g) and (h) were obtained with lower magnification, on surfaces corresponding to (b) to (d) and (d) to (f), respectively.

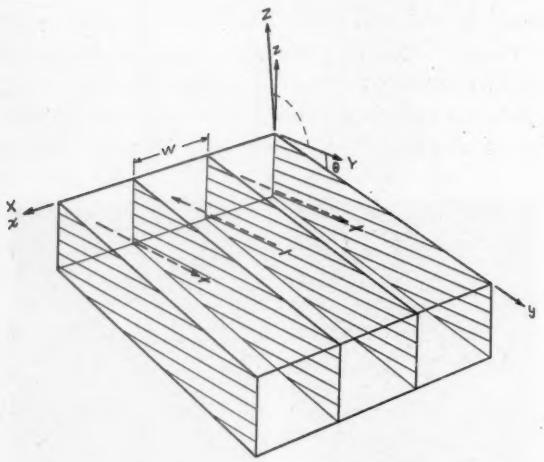

FIG. 11. Diagram showing the domain structure and distribution of poles as they would be if superficial domains ("branches") were absent.

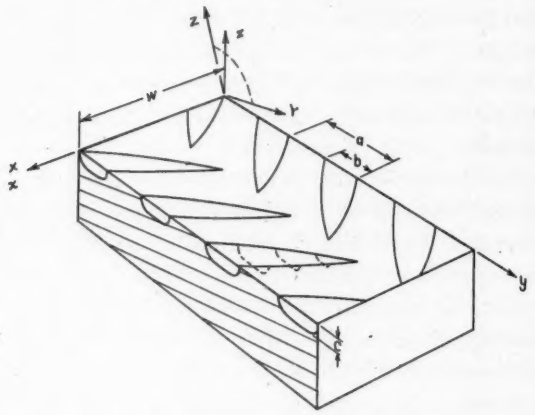

FIG. 12. Domain structure of the tree patterns.

has been worked out in the Appendix, and values for the dimensions a and b have been predicted. The computed values for a and b are about twice too large; considering the approximations involved in the theory, this may be regarded as a satisfactory confirmation of the model proposed.

The patterns at steeper slopes represent a continuous progression from the open tree patterns. From a theoretical viewpoint, however, it is simpler to regard them as modifications of the flux closure pattern of Fig. 14. In this pattern domains magnetized along [100] and [$\bar{1}$00] directions (the axes being as for Figs. 11 and 12) completely transport the flux which would otherwise emerge from the underlying domains. Figure 14a shows the arrangement of these domains with one of them removed and inverted at (b) to show its shape. It may be shown by calculation (i) that these domains can be constructed so that the geometrical pattern will be as indicated and (ii) that they do close flux correctly between [010] and [0$\bar{1}$0] domains. If the surface is tilted by θ in respect to the crystal axes, then the unit normal to the domain wall has direction cosines along X, Y, Z of $\pm\sin\theta/(1+\sin^2\theta)^{\frac{1}{2}}$, $\sin\theta/(1+\sin^2\theta)^{\frac{1}{2}}$, $\cos\theta/(1+\sin^2\theta)^{\frac{1}{2}}$. The The flux closure is indicated in (c) which is a view parallel to the surface of the specimen. Theory shows that this perfectly closed pattern is less stable than that shown in (d) for which the wall energy is somewhat less but, since magnetic poles are present as shown, there is some magnetostatic energy. The quantitative theory given in the appendix shows the same degree of agreement as for the tree patterns, the computed width of S which corresponds to the bright strips in Fig. 10(h) being about $\frac{1}{3}$ of the observed width. The dense deposit of colloid in Fig. 10(f) and (h) is readily understood on the basis of this model, since the pole density on the strips S and, consequently, the magnetic field are proportional to $\sin\theta$.

Effect of Vertical Field

A more direct confirmation of the pole density distribution of Fig. 13 has been obtained by

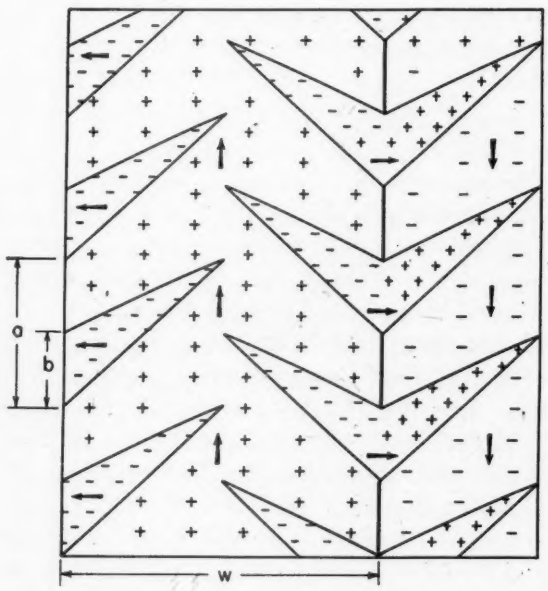

FIG. 13. Distribution of the magnetic poles on a tree pattern. Poles on branches are below surface level.

superposing a weak external vertical field (normal to the surface) which does not appreciably disturb the domain boundaries. This field adds to the underlying field in some areas and subtracts in others, depending on the sense of the underlying field, and thus gives rise to an unsymmetrical distribution of the colloid. The results of this experiment are shown in Fig. 15, and it may readily be seen that the patterns are just as predicted from the model of Figs. 12 and 13. Use of a vertical field thus permits determination of the sense of the magnetization vector in each domain.

It is to be noted that there is a very marked asymmetry in the intensity of the domain boundaries. In the next section we shall show that this is just what should be expected on the basis of the Bloch theory of the wall applied to the tree patterns.

Tree patterns of a somewhat different kind are observed on surfaces cut with the long dimension parallel to $[0\bar{1}1]$ and its surface inclined slightly to (100) in such a way that the $[0\bar{1}1]$ direction (instead of the [001] direction) lies accurately in the surface (Fig. 16). They can be interpreted satisfactorily in a way quite analogous to that just described.

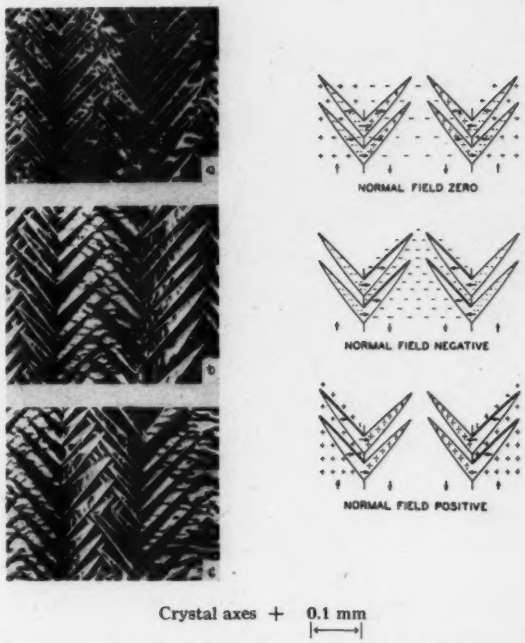

FIG. 15. Tree patterns showing the effect of applying a field of 30 Oersteds normal to the surface; (a) normal field zero, (b) normal field directed into the surface, (c) normal field directed outward from the surface.

SPIN ORIENTATION IN THE BLOCH WALLS

We shall next show that the theory of spin orientation, together with the domain model of Fig. 12, leads to precisely the observed asymmetry in the lines of the powder pattern. This involves describing the magnetization pattern in sufficient detail to include the variations within the walls themselves. Figure 17 represents this situation; (a) shows the tree pattern and (b) an enlarged portion of (a) showing the structure of the domain wall. The directions of magnetization in the branch and in the underlying domain are indicated by the arrows in the small cubes whose

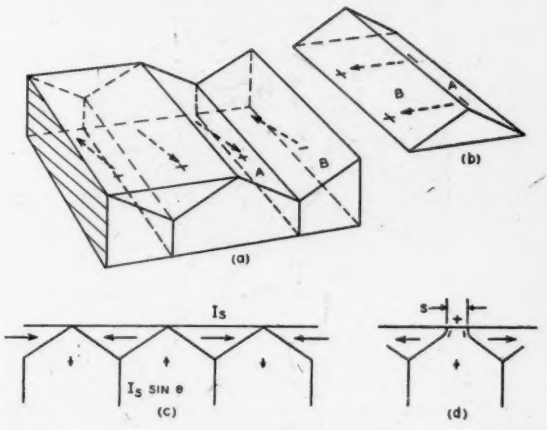

FIG. 14. (a), (b), and (c) show possible method of complete flux-closure for domain structure of Fig. 11; (d) shows structure modified to reduce wall energy and total energy.

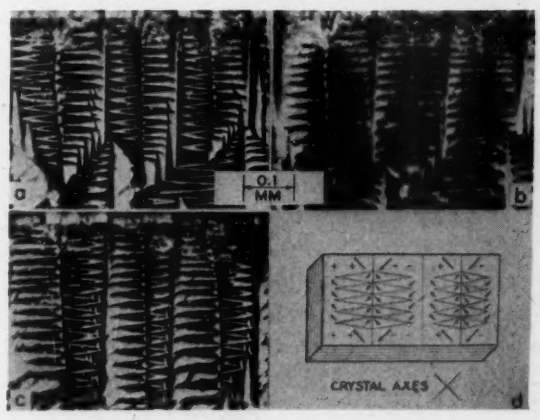

FIG. 16. Second kind of tree pattern; (a) field applied normal to the surface, (b) normal field zero, (c) normal field reversed, (d) diagram of directions of magnetization in the domains, crystal axes, and the inclination of the surface to the atomic planes (represented by lines on crystal edges).

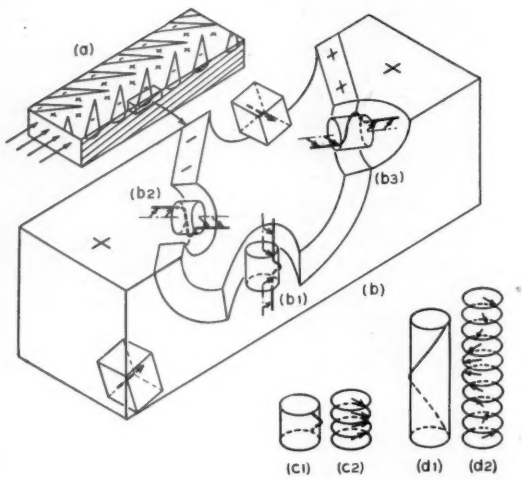

FIG. 17. The course of spin orientation during traversal of a domain wall in the tree pattern (see text).

edges are parallel to the crystal axes. The theory of domain walls requires that the component of magnetization along the normal to the wall remain substantially constant; thus attention can be concentrated on the component in the plane of the wall. The course of the spin orientation for the location (b1) is shown in (c2); here the magnetization vector is represented at the top, bottom and two intermediate points of the domain wall. The course of the component in the plane of the wall can thus be represented by a helical trace on a cylinder (c1); this convention is similarly employed in (b2) and (b3). It should be noted that this trace has the sense of a left-hand screw in all cases. This prediction is based on a consideration of the situation at (b1); if the screw were right-handed, the total angle turned through would be 270° as indicated in (d) rather than 90° as in (c). The right-hand screw would require about three times as much energy, and for that reason the left-hand screw is predicted for locations like (b1) near the bottom of the branch domain. Furthermore, if some parts of the wall have a left-handed course and others right-handed, lines of poles will be produced at boundaries between these parts and will add to the energy. Thus it is predicted that the entire wall will have a left-handed form. Within the wall itself there is a net flux from left to right in (b) which produces lines of poles where the wall strikes the surface of the specimen, and it is these lines of poles which cause the domain walls to capture colloid. The polarity of the poles, and hence the predicted course of spin orientation, can be verified by the vertical field experiments. The prediction from Fig. 17(b) can be summarized by saying that where the angle between the branch and the trunk is acute, the domain wall will have poles like those on the "sky" and where the angle is obtuse the domain wall will have poles like those on the branch. Inspection of Fig. 18 (an enlargement from Fig. 15(c)) shows that this prediction is born out in detail.** Considering that the domain wall is only about 500 to 1000A thick, it is especially gratifying that information on its internal structure can be obtained so directly.

EFFECT OF FIELD ON (100) PATTERNS

A specimen of a single crystal, $2.3\times0.6\times0.25$ cm^3, with edges approximately parallel to the cubic axes, was magnetized to various degrees with the electromagnet of Fig. 1(a). The direction of magnetization, [001], lay parallel to the long edge, and its intensity was determined with the use of a search coil and ballistic galvanometer. The patterns on one of the 2.3×0.6 cm^2 faces are shown in Fig. 19. The specimen was initially demagnetized, and the field then increased in steps to a high value ((a) to (f)), then again to zero (remanence). The tree pattern observed in the demagnetized state is consistent with the

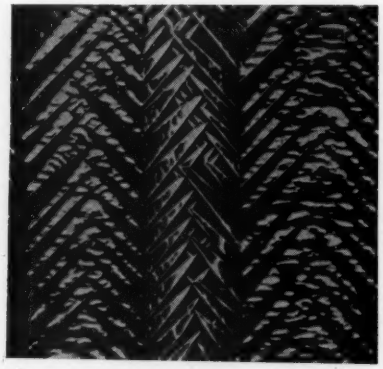

FIG. 18. Tree pattern with field applied normal to the surface, showing redistribution of colloid over the domains, intensification of some domain boundaries and disappearance of others, as compared with pattern obtained with no normal field (cf. Fig. 15).

** Except for some irregularities resulting from variations in illumination, focus, and uneven colloid distribution.

slight inclination, 1.5°, of the surface to the (100) plane.

In a preliminary experiment the specimen was demagnetized repeatedly and the pattern observed after each demagnetization. The general features of the patterns were always the same —that is, the pattern was of the tree type—but the details were never the same. In none of our experiments on electrolytically polished surfaces have we been able to reproduce a pattern of lines after a substantial change in magnetization. Careful observation shows that the lines do not tend to reform at the same place on the surface. This is in contrast to the maze patterns obtained after mechanical polishing; these can be reproduced accurately, and one concludes that they are determined by the mechanical condition of the surface, and not primarily by magnetic forces.

In Figs. 19(c) and (d) the character of the pattern is seen to be definitely different from that of (a); of the two sets of almost-parallel lines one set of lines is now predominant. When the magnetization is above 12,000 they have become so long that the whole field of view is crossed by only one set of lines.

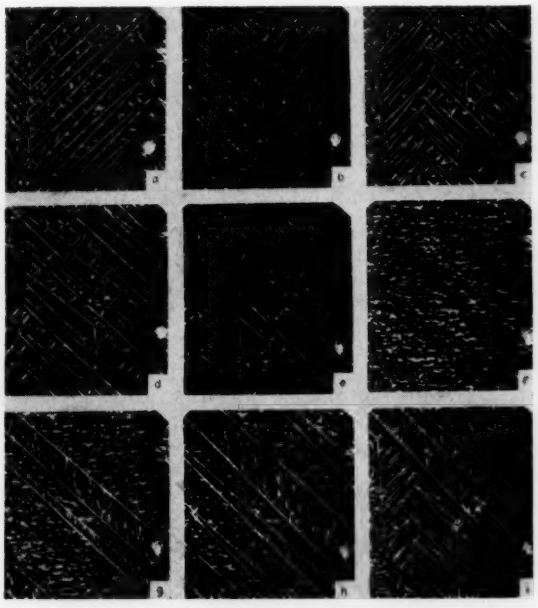

FIG. 19. Patterns on a surface inclined slightly to a (100) plane, with applied field and length of the crystal parallel to the [001] direction: (a) $B=0$, (b) $B=7000$, (c) $B=10{,}000$, (d) $B=11{,}600$, (e) $B=15{,}000$, (f) $B=18{,}600$, (g) $B=17{,}600$, (h) $B=17{,}400$, (i) $B=15{,}400$.

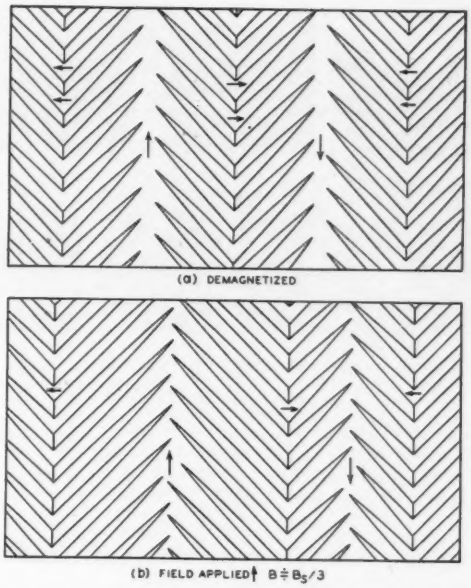

FIG. 20. Diagrams of the tree pattern showing the effect of applying a field.

Patterns of this kind were observed under lower magnification in order to be able to see a larger portion of the surface at once. It was then noticed that the whole tree pattern shifts with application of a field, the "trunks" moving sideways in one direction or the other so that the areas magnetized parallel to the field become larger and those antiparallel become smaller, and so more flux is permitted to travel in the direction of the field. This is shown schematically in Fig. 20. The "branches" of the trees extend to the middle of the domain, whatever its width, and when the specimen is magnetized the trees have branches that are usually longer on one side than on the other.

Experiments were carried out on a different specimen with the field applied parallel to a [011] direction lying in the specimen surface, a (100) plane. The patterns are reproduced in Fig. 21. When the magnetization is relatively low one notices some branch-like markings that are similar to those shown in Fig. 16 and, like them, may be attributed to a slight deviation of the surface from the (100) plane. The diagonal lines of Figs. 21(a) and (b) are 180° boundaries, similar to those shown in the pattern and diagram of Fig. 27 and referred to below in connection with

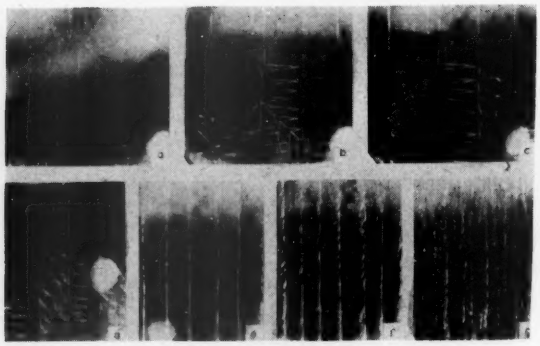

FIG. 21. Patterns on a (100) surface, with length of crystal and applied field parallel to the [011] direction. (a) $B=0$, (b) $B=9000$, (c) $B=14,500$, (d) $B=15,500$, (e) $B=15,900$, (f) $B=18,500$, (g) $B=20,000$.

that figure. Above these boundaries the magnetization goes in a zigzag manner from left to right with a component parallel to the direction of the applied field, whereas below these boundaries the net magnetization is from right to left. When the applied field is increased, the boundaries move toward the bottom of the figure (b) and finally out of the field of view (c), so that there is an increase in the areas magnetized more nearly parallel to the field at the expense of areas less favorably magnetized.

When the magnetization is relatively high ($B-H \doteqdot 16,000$) the pattern is simply a series of parallel lines, approximately equally spaced, and readily interpretable. When the field is so high (g) that the magnetization vectors are rotated out of the direction of easy magnetization and the angle between the local magnetization and the field is less than 45°, it is still true that there are no poles at domain boundaries and that the normal component of magnetization of the whole specimen is zero.

The decreasing distance between lines with increasing magnetization is in agreement with the reports of Kaya[11] and of Sixtus,[12] and with the theoretical work of Néel, as discussed below.

PATTERNS ON (110) AND (111) SURFACES

More complicated patterns have been observed on (110) and (111) surfaces. Figure 22 shows patterns taken with increasing magnetization on a surface parallel to (110), the field being applied in the $[1\bar{1}0]$ direction in the plane of the surface. These patterns will be discussed in the next section.

Patterns obtained on surfaces parallel to (111) planes are even more complicated than those on (110) surfaces. This may be expected, since no direction of easy magnetization lies in the surface. The effect of increasing field, applied in the $[1\bar{1}0]$ direction (lying parallel to the surface) is shown in Figs. 23(a) to (f). Figure 23(g) is a second pattern of material in the unmagnetized condition; it covers an area different from that of the other patterns and is chosen to show three sets of the stronger lines, each set making an angle of 120° with the others. This corresponds to the threefold symmetry of the crystal plane. The detail of the pattern is believed to be characteristic not of the interior but only of the surface, which probably has many poles and domains of closure of the kind discussed by Landau and Lifshitz.[9] No explanation of its detailed form has been given.

It appears that internal domain structures in an unmagnetized material are generally simple,

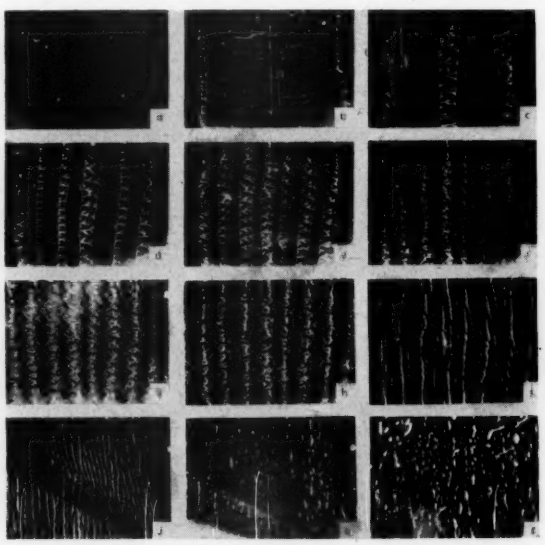

FIG. 22. Patterns on a (110) surface, with length of crystal and applied field parallel to the $[1\bar{1}0]$ direction. (a) $B=0$, (b) $B=14,800$, (c) $B=15,000$, (d) $B=15,200$, (e) $B=15,700$, (f) $B=16,400$, (g) $B=17,100$, (h) $B=18,200$, (i) $B=20,000$, (j) $B=20,200$, (k) $B=20,300$, (l) $B=20,500$.

[11] S. Kaya, Zeits. f. Physik **89**, 796 (1932) and **90**, 551 (1934).
[12] K. J. Sixtus, Phys. Rev. **51**, 870 (1937).

and that near the surface a more complicated structure is likely to occur. Domains of closure may form, or a fine-grained pattern may appear and give a distribution of poles with which a lower energy is associated. Only when a simple crystallographic plane and directions of easy magnetization are parallel to the surface has a simple structure, apparently representative of the interior, been observed.

Relation to Néel's Theory

Following the work of Landau and Lifshitz,[9] Néel[13] has investigated theoretically the domain structure of specimens of single crystals of various geometrical forms, oriented in different ways with respect to the crystallographic axes. He considers the energies associated with domain boundaries, crystal anisotropy, and magnetization, and selects the domain structure that has the lowest energy consistent with the assumption that there are no poles at internal domain boundaries.

A comparison of his theory with our experiments can be made when the specimen is a slab having its long dimension and magnetization parallel to a $[0\bar{1}1]$ direction, its large surface parallel to a (100) plane, and its sides parallel to (011). Figure 24(a) and (b) show the orientation with respect to the crystal axes, and the theoretical domain structure near remanence (a) when all of the domains are magnetized in directions making 90° or less with the direction of the applied field. The structures of (a) and (b) are composed primarily of domain sheets, S, oriented at right angles to the direction of the field. At the edges are domains P and Q, having a geometry that reduces the number of poles that would be present on the surface if the domain sheets constituted the whole of the specimen. Domains S and Q are magnetized parallel to directions of easy magnetization. Domains P, on the contrary, are directed about 45° from the nearest direction of easy magnetization and consequently possess some energy of anisotropy.

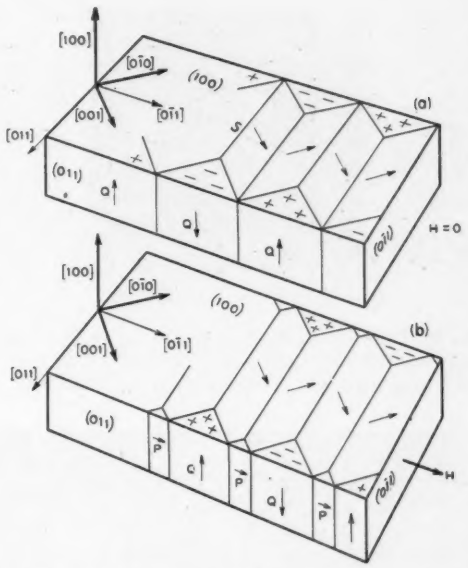

FIG. 24. Domain structure proposed by Néel; (a) without applied field, (b) with applied field.

The powder patterns observed on the top (100) surface of a specimen (see Fig. 21(c)), when the magnetic induction is above 14,000, correspond to the diagram of Fig. 24. The principal domain boundaries make an angle of 90°, and the directions of magnetization ±45°, to the direction of the field, and the absence of colloidal particles between lines suggests that there are no poles on this surface.

The patterns on the (011) surface (Fig. 22) also correspond in many of their features to the theoretical pattern. When the induction is less than about 15,000, the domains are magnetized at right angles to the direction of the field, and these regions may be identified with the Q domains of Fig. 24. At higher inductions the

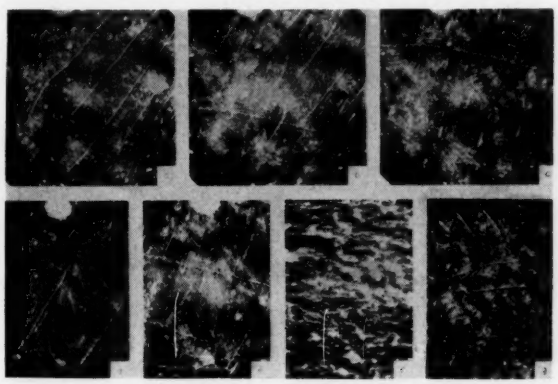

FIG. 23. Patterns on a (111) surface. (a) $B=0$, (b) $B=4000$, (c) $B=4800$, (d) $B=15{,}000$, (e) $B=15{,}500$, (f) $B=19{,}800$, (g) pattern on another area ($B=0$).

[13] L. Néel, J. de Phys. [8] **5**, 265 (1944).

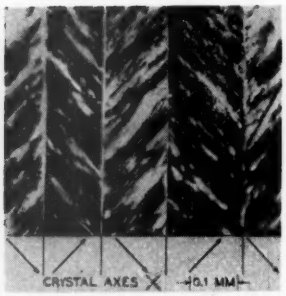

FIG. 25. Pattern obtained with a concentrated colloid on a (110) surface with striations of colloid indicating directions of magnetization (perpendicular to striations).

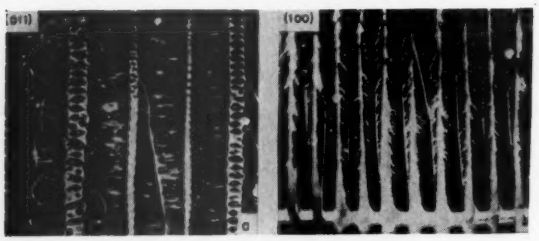

FIG. 26. Patterns obtained on the side and top surfaces of a crystal such as that shown by the drawing of Fig. 24: (a), (011) surface; (b), (100) surface. The lower part of the (b) pattern shows accumulations of colloid extending beyond the edge of the crystal.

boundaries seem to become wide (Fig. 22(c)), and new domains appear with complicated structure. These are the P domains of Fig. 24. As the induction increases the P domains grow at the expense of the Q domains, and at $B=18{,}000$ they cover practically the whole surface. This is in agreement with theory.

The fact that the P domains collect colloidal particles unevenly indicates that poles are present and that the surface has a complicated domain structure. The situation is then more complex than Néel's picture suggests. Apparently the magnetization in the P domains is not drawn out of the direction of easy magnetization and entirely into the [0$\bar{1}$1] direction, but some flux penetrates the surface to form poles. These facilitate the formation of small domains of reversed magnetization,[14] and effect a complicated pattern. Also, at high inductions the domain boundaries are not straight lines but are irregular in form.

[14] E. Lifshitz, J. Phys. U.S.S.R. 8, 337 (1944).

In order to check some of the conclusions derived from the patterns on (100) and (011) surfaces (Figs. 21 and 22), additional patterns were made with heavy colloid. Figure 25 corresponds to Fig. 21(e) in all respects except that the colloid was more concentrated, and the character of the striations of colloid confirms the previous conclusion that the directions of magnetization are inclined $\pm 45°$ to the direction of the field. Figure 26(a) corresponds to Fig. 22(c) and shows plainly that the Q regions are magnetized at 90° to the direction of the field. In Fig. 26(b) the edge of the crystal is in plain view, and the collection of particles at equally spaced regions shows that the poles here are quite strong; this is in agreement with Fig. 24(b).

Figure 27 is a pattern observed with low magnification on the (100) plane with zero magnetization. It is the same as Fig. 21(a), except that a larger area is visible. It corresponds in general features to the large top surface of Fig. 24(a) by having a prominent series of parallel lines at right angles to the long dimension, and having domains of closure near the

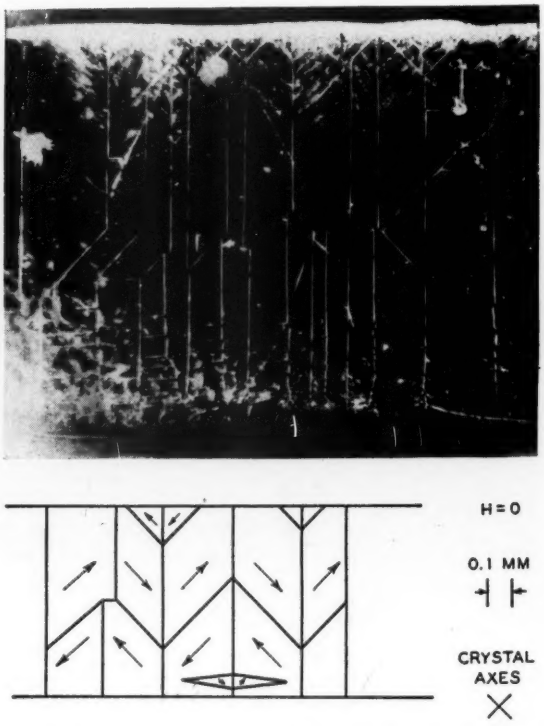

FIG. 27. Pattern on a (100) surface, and its interpretation.

edges. In addition it has, near the middle, some 180° boundaries inclined at 45° to the long dimension. Near the lower edge some tree-like patterns are formed. These have been previously commented on and are shown enlarged in Fig. 16.

Néel has related the distance between the lines of the pattern on the (100) surface, when the material as a whole is magnetized parallel to $[0\bar{1}1]$ (Fig. 21 (d) to (g)), to the intensity of magnetization, when this is more than 0.7 of saturation. The theoretical prediction of decreasing distance with increasing magnetization is confirmed by our experiments, as well as by those of Kaya and of Sixtus. According to theory this distance, W, is independent of the thickness and length of the specimen and is calculable if one knows the intensity of magnetization and the width, L, of the specimens—in our experiment 0.20 cm. Néel has calculated W for a specimen of iron having a width of 1 cm and an anisotropy constant, K, of 420,000, and has obtained a value of 50 microns for high magnetization ($\frac{3}{4}$ of saturation). In adapting this order-of-magnitude calculation to a crystal containing 3.8 percent silicon, the change in values of K and I_s can be disregarded. Using Néel's relation

$$W \propto (L)^{\frac{1}{2}},$$

it appears that W should be about 20 microns for $B=15{,}000$. This is somewhat smaller than that observed, 100 microns, but it is close enough to suggest that the assumptions underlying the calculations are essentially correct.

A change of domain thickness with domain width has been observed near the corner of a crystal in which the domains are magnetized at 45° to the specimen edges, which are of the form $\langle 110 \rangle$. This is shown in Fig. 28.

Although this pattern is not understood in complete detail, certain general features appear sufficiently well established to permit a comparison between theory and experiment. The domains consist of long slabs magnetized parallel to the domain boundaries as indicated by the striations, the direction of magnetization alternating from slab to slab. Where the slabs meet the [110] edges, there must be small domains of closure, magnetized in part vertically where they meet the surface and in part horizontally at right angles to the main domains so as to close

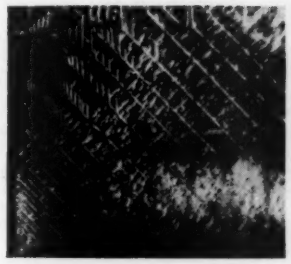

FIG. 28. Pattern on the corner of a crystal showing the increase in width of the domains as the length increases.

the flux pattern. Several possible domain structures have been devised to accomplish this closure using only easy directions and developing no poles; however, none of these has been verified directly from experiment. For all such patterns the closure domains extend inwards from the surface of the specimen to a depth roughly equal to the width W of the domains. Since the closure domains are magnetized at right angles to the main domains, they have magnetostrictive energy "s," (see Section 6 in the Appendix), giving each domain a magnetostrictive energy of about W^2s per unit depth. Each domain has a wall energy of γL per unit depth where γ is the wall energy per unit area and L the long dimension of the domain as seen in Fig. 29. Minimizing the total energy per unit volume of the specimen yields, in the usual way,[9,11,15] the result

$$W=(\gamma L/s)^{\frac{1}{2}},$$

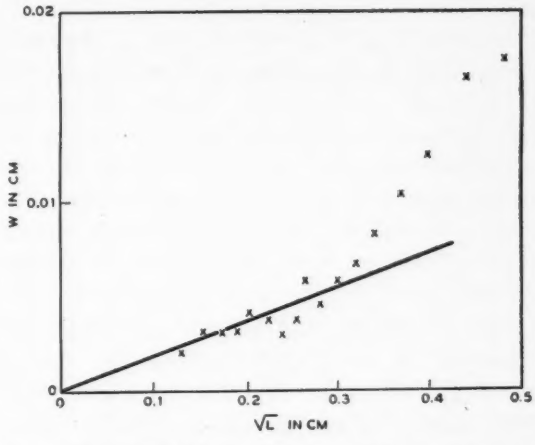

FIG. 29. Domain width as a function of the square root of the length for the pattern in Fig. 28.

[15] C. Kittel, Phys. Rev. **70**, 965 (1946).

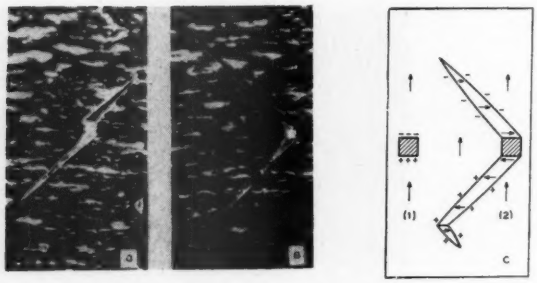

FIG. 30. Domain structure around holes in a crystal: (a) and (b), patterns observed; (c1) diagram showing a square hole with magnetic poles on opposite sides; (c2) diagram showing domains formed on opposite sides of a hole, as in (b), with consequent distribution of poles over tapered domains.

which is only approximate, since no detailed model of the domains of closure is employed. In order to test this relationship, values of W have been plotted against $(L)^{\frac{1}{2}}$ as measured from Fig. 28. The straight line corresponds to $\gamma/s = 3\times10^{-4}$ cm which may be considered in fair agreement with $\gamma=1.5$ ergs/cm^2 and $s=10^3$ ergs/cm^3 in the absence of a detailed theory of the domains of closure. Large deviations from the straight line occur at $(L)^{\frac{1}{2}}$ greater than 0.35; at this point the measured domain pattern intersects another and deviations from the simple formula might be expected.

DOMAIN STRUCTURE AROUND CAVITIES

Kersten's work[16] on the effect of cavities and nonmagnetic inclusions on the coercive force, and Néel's theoretical investigations[17] of the domain structure around them, prompted a search for powder patterns in such areas. Observation of a number of crystal surfaces under the microscope showed the presence of an occasional hole that had formed accidentally during the freezing or the etching or polishing of the crystal. The patterns around two holes in (100) surfaces are reproduced in Fig. 30. Careful examination of the character of the striations of colloidal particles indicates that the magnetization inside the long slender regions is oriented at 90° to that outside—that is, the lines are 90° boundaries. Many other patterns of similar form were observed.

[16] M. Kersten, Physik. Zeits. **44**, 63 (1943).
[17] L. Néel, Cahiers de Physique No. 25, 21 (1944).

Patterns of this type have been predicted by Néel on purely theoretical grounds and our patterns are a striking confirmation of his theory, which may be described as follows. Imagine a cubic or spherical hole in the middle of a domain, as indicated at (1) of Fig. 30(c). Then magnetic poles will exist on the surfaces normal to the direction of magnetization, and to these can be attributed a demagnetization energy,

$$E_0=(1/2)N_0I_s^2V_0.$$

N_0 is the demagnetizing factor, V_0 the volume of the hole, and I_s the saturation intensity of magnetization of the material around the cavity. If domain boundaries are formed as at (2), poles will not be present at the edges of the cavity, but will be distributed along the domain boundaries as indicated by plus and minus signs. In this case there will be energy associated both with the demagnetization (a volume effect) and with the boundaries (an area effect):

$$E_d=NI_s^2V, \quad E_\sigma=\gamma A.$$

Here N is the demagnetizing factor of the volume, V, enclosed by the domain boundaries and magnetized at right angles to the surrounding material, γ is the energy per unit area of boundary, and A the total area of the bounding surface or Bloch wall. According to theory, the size of the domain structure is defined by minimizing the sum of these two energies.

A rough calculation can easily be made of the size of domain to be expected around a hole of given size. Let the diameter of the hole (assumed spherical) be d, and let the shape of the domain be a rotational ellipsoid having minor axes d

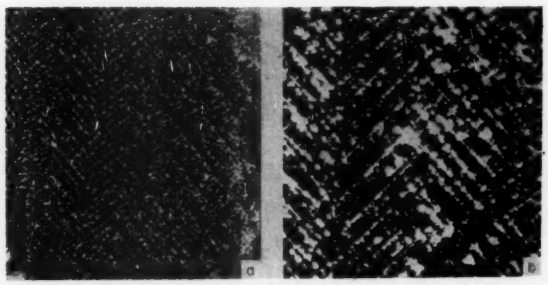

FIG. 31. (a) Pattern formed by air-blown carbonyl iron powder, after settling on a crystal; (b) pattern obtained by placing a drop of colloidal suspension on previously formed pattern of type (a).

and major axis l. When $l \gg d$, the demagnetizing factor of this ellipsoid is

$$N = 4\pi d^2[ln(2l/d) - 1]/l^2,$$

and the volume and surface are easily calculable. In estimating the magnetostatic energy, allowance should be made for the permeability of the domains themselves, resulting from the finite value of the anisotropy. This introduces a correction factor of about 1/25 as shown in Section 4 of the Appendix. Including this factor, the energies of the boundaries and the surface poles are

$$E_d = 16\pi^2 I_s^2 d^4[ln(2l/d) - 1]/75l,$$
$$E_\sigma = \pi^2 \gamma d l/4.$$

Using the numerical values $d = 0.001$ cm, $I_s = 1580$, $\gamma = 1.5$ ergs/cm^2, the value of l for which $E_d + E_\sigma$ is a minimum is 0.10 cm and the ratio l/d is approximately 100. The observed ratio of l/d for the domain of Fig. 30(b) is about 50, smaller by a factor of two—satisfactory agreement in view of the simplifications employed.

PATTERNS WITH DRY POWDER

Some patterns were formed by a different method. A fine grade of carbonyl iron powder, containing an appreciable number of particles less than 1μ in diameter, was placed under a bell jar and blown with a jet of high pressure air. This was allowed to settle for several minutes, the polished specimen was then placed under the bell jar and the finer particles allowed to settle on the specimen for several minutes more. The patterns so obtained are immobile and cannot be changed by changing magnetization or stress, and a separate pattern must be formed for each condition of the specimen. Figure 31(a) shows one pattern so obtained. In forming the pattern of Fig. 31(b) the powder was first allowed to settle as described and then colloidal solution was applied in the usual manner. The fine lines of colloidal magnetic particles are observed to coincide with the lines of coarser particles of carbonyl iron.

PLASTIC DEFORMATION OF CRYSTAL

In studying the effect of tension on domain patterns of crystals of iron containing some silicon, it was observed that the original "tree" type of pattern for zero stress could be obtained repeatedly after removal of the stress as long as it was within the elastic limit.

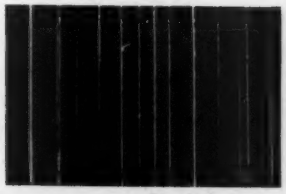

FIG. 32. Pattern on crystal of permalloy strained beyond elastic limit.

An attempt was made to find a domain pattern, with or without tension, on a single crystal containing 76 percent nickel and the remainder iron. No distinct pattern could be observed until rather high stress was applied, whereupon a series of parallel lines appeared as indicated in Fig. 32. These remained after repeated magnetization and demagnetization, and even after electrolytic polishing and re-application of colloid, always in the same place in the crystal. Without the presence of colloid they could not be detected under the microscope. The specimen had been stretched in a [110] direction. The lines are parallel to [1$\bar{1}$0], in the surface parallel to (001). Observation over the edge of the specimen, on the (1$\bar{1}$0) plane, showed two sets of lines making angles of ± 55 to 56° with the dege. There can be little doubt that the lines are caused by slip or incipient cleavage on (111) planes, for which the calculated angle is 54.7°.

This powder technique may be useful in observing plastic deformation or dislocations in the early stages, before their presence can be detected by other means.

We are indebted to Dr. C. Kittel for helpful discussions regarding domain theory, to Mr. J. G. Walker for valuable assistance with the photography and especially in the preparation of the specimens, and to Messrs. F. W. Ryan, R. A. Ehrhardt, and G. Bittrich for preparing the solution for electrolytic polishing and the ferromagnetic colloid.

APPENDIX

1. Remarks

In this appendix we shall give an approximate treatment of the energies involved for surfaces almost parallel to (100). In all cases we shall suppose that the underlying domains are magnetized along the [010] and [0$\bar{1}$0] directions while the outward normal to the surface is parallel to the direction [0, sinθ, cosθ].

Several steps are necessary in evaluating the magnetostatic energy. When magnetic fields are present, the magnetization is deflected slightly from the easy directions in the underlying domains. This effect is taken account of in Section 2 by assigning an effective permeability tensor to the underlying domains. For each assumed pattern the distribution of magnetic poles is estimated (Section 3). In most cases this distribution consists of one part where the [010] and [0$\bar{1}$0] domains strike the surface of the specimen plus another part where superficial [100] and [$\bar{1}$00] domains, like the tree branches, join the underlying domains. This latter part does not lie on the surface of the specimen but on the curved domain wall. However, since the superficial domains on the surface are relatively shallow, it is assumed for purposes of calculation that the pole lies on the surface also and that the effect of the superficial domain that lies over it can be neglected. (A rough estimate indicates that this approximation may lead to overestimating the energy by about 25 percent.) Finally all the pole distributions considered are approximated by infinite parallel strips. The energies for three such cases are worked out in Section 4: here Case I corresponds to the underlying domain pattern with no superficial domains, II to the tree pattern, and III to the steep slope pattern for which the strips are narrow compared to their spacing.

The areas of the domain walls present a simpler problem and are estimated on the basis of hypotheses on the shapes of the domains.

It may be worth pointing out that the mathematical problems involved in predicting the shapes of domain walls from first principles are of very considerable difficulty. This arises from the fact that the energy of the wall per unit area depends on the direction of its normal; the poles on the wall surface depend on its normal and on the field arising from other walls and surface poles. In this treatment, shapes observed in experiment have been used as a guide; it can be seen on the basis of general principles that these shapes are reasonable. Energy estimates are then based on the observed shapes and the sizes are determined by minimizing the energy in Sections 5 and 6; this leads to a set of predicted dimensions for the domains which compare within a factor of 2 to 3 with those observed.

A list of the principal symbols used in the equations is as follows (constants refer to 3.8 weight percent silicon iron):

$I_s = 1580$ gauss (saturation magnetization),
$K = 280{,}000$ ergs/cm^3 (anistropy constant),
$\gamma = 1.5$ ergs/cm^2 (Bloch Wall Energy),†
$C_{11} = 2.37\times10^{12}$, $C_{12} = 1.41\times10^{12}$ ergs/cm^3 (elastic constants),
$h_1 = 3.2\times10^{-5}$ magnetostrictive strain (taken the same as for iron),
μ^* = effective permeability of a domain (see Section 2),
χ^* = effective susceptibility of a domain,
s = magnetostrictive energy density (see Section 6),
ψ = magnetostatic potential for finite K,
φ = magnesostatic potential for infinite K,
W = spacing between parallel strips in Cases I, II, III (see Section 4),
S = width of strip (carrying poles) in Case III,
a, b, c = dimensions in tree patterns (Fig. 12),
e_1, e_2, e_3 = magnetostatic energies in ergs/cm^2 of surface (Eqs. of Section 4),
θ = tilt of surface with respect to crystal axes,
e_5 = energy per unit area of tree patterns (Section 5),
e_6 = energy per unit area for steep slope patterns (Section 6),
xyz = coordinates with respect to the surface of the specimen,
XYZ = coordinates with respect to crystal axes.

2. The μ^* Method for Magnetostatic Energies

When the magnetization is nearly parallel to an easy direction, the dependence of magnetization, I, upon field strength, H, within a domain may be taken into account by assigning a permeability tensor μ^* which takes a diagonal form when the easy directions are chosen for the axes. Parallel to the easy direction nearest the direction

† This value is a rough average for several crystallographic directions, based on the formulae of L. Néel, Cahiers de phys. 25, 1 (1944), using the constants for iron

of magnetization, $\mu=1$ since the saturation magnetization is practically independent of the field. The magnetization will be rotated slightly for H perpendicular to the easy direction, the equilibrium angle being given by minimizing the energy density

$$E=K[\alpha_2^2\alpha_3^2+\alpha_3^2\alpha_1^2+\alpha_1^2\alpha_2^2]-HI_s\alpha_1,$$

where K is the anistropy constant, α_1, α_2, α_3 are the direction cosines of the domain magnetization in respect to the XYZ crystal axes, I_s is the magnetization in the domain and H the field, taken as parallel to the X axis. If the domain is initially polarized parallel to z (i.e., $\alpha_3=1$, $\alpha_1=\alpha_2=0$) and if its direction is specified by conventional polar angles θ and φ, we have for small angles

$$\alpha_1=\sin\theta\cos\varphi,\quad \alpha_2=\sin\theta\sin\varphi,\quad \alpha_3=\cos\theta,$$

$$E=K[\cos^2\theta\sin^2\theta+\sin^4\theta\sin^2\varphi\cos^2\varphi]-HI_s\sin\theta\cos\varphi$$

$$\doteq K\theta^2-HI_s\theta\cos\varphi,$$

giving a minimum for $\varphi=0$ and $\theta=HI_s/2K$. The corresponding magnetization is thus $I_x=HI_s^2/2K$, $I_y=0$, $I_z=I_s$. This leads (by symmetry) to the conclusion that the tensor μ is diagonal for axes XYZ with components

$$\mu^*=1+4\pi I_s^2/2K$$

for X and Y and unity for Z. The values of μ^* and $\chi^*=I_s^2/2K$ for silicon iron are estimated as $\chi^2=(1580)^2/2\times280{,}000=4.5$ and $\mu^*=57$.

In order to discuss the energies in terms of μ^* and the surface poles, we introduce two sets of coordinates XYZ in respect to the crystal axes and xyz in respect to the surface of the specimen. We have

$$x=X,\quad y=Y\cos\theta-Z\sin\theta,$$
$$z=Y\sin\theta+Z\cos\theta.$$

The domains are assumed to be magnetized nearly parallel to the $\pm Y$ axis so that the axes of the permeability tensor μ are along XYZ with values μ^*, 1, μ^*. However, for small angles θ, no important error will be introduced by taking the axes of the μ^* tensor as along x,y,z.

An outline of the method of evaluating the magnetostatic plus anisotropy energy by the μ^* method†† is as follows (the mathematical details are given later): We first find the density of surface poles $\sigma_1(x,y)$ which would exist because of the tilt of the surface and the joining of superficial domains. Next we solve the magnetostatic problem which arises from placing $\sigma_1(x,y)$ on a block of material characterized by the μ^* tensor; this leads to a magnetostatic potential $\psi_1(x,y,z)$. Next we consider what internal magnetization I would result from the field corresponding to $\psi_1(x,y,z)$ and how this would change the net surface pole density from $\sigma_1(x,y)$ to $\sigma_2(x,y)$ and also produce a volume pole density equal to $-\nabla\cdot I$. Finally, we verify that these poles on the surface and throughout the volume simply give $\psi_1(x,y,z)$ so that $\psi_1(x,y,z)$ is a self-consistent potential distribution. The total magnetostatic energy distribution can be calculated either from

$$E_M=\tfrac{1}{2}\int\sigma_1(x,y)\psi_1(x,y,0)dxdy$$

or by adding the stored anisotropy energy and $\int(H^2/8\pi)dxdydz$, the two giving identical results.

Proof: ψ_1 as derived from σ_1 must satisfy the equations

$$\nabla^2\psi_1=0,\qquad z>0,$$

$$\mu^*[(\partial^2\psi_1/\partial x^2)+(\partial^2\psi_1/\partial z^2)]+[\partial^2\psi_1/\partial y^2]=0,\qquad z<0,$$

$$\mu^*[(\partial\psi_1/\partial z)_{z=-0}]-[(\partial\psi_1/\partial z)_{z=+0}]=4\pi\sigma_1,\qquad z=0.$$

For all cases of interest, the total number of poles on the surface, i.e., $\int\sigma_1dxdy$, is equal to zero. Hence these equations determine uniquely a ψ_1 which vanishes at $z=\pm\infty$. Now this ψ_1 will alter the magnetization inside the underlying domains from $I_0=(0,\pm I_s\cos\theta,\pm I_s\sin\theta)$, which corresponds to $K=\infty$, by a vector amount

$$\delta I=[-\chi^*(\partial\psi_1/\partial x),\,0,\,-\chi^*(\partial\psi_1/\partial z)].$$

This gives rise to an internal volume pole of

$$-\nabla\cdot(I_0+\delta I)=-\nabla\cdot\delta I=+\chi^*[(\partial^2\psi_1/\partial x^2)+(\partial^2\psi_1/\partial z^2)],$$

since the domains corresponding to the $K=\infty$ distribution give $\nabla\cdot I_0=0$ and an added surface pole of

$$\sigma_3(x,y)=-\chi^*(\partial\psi_1/\partial z)=z\text{ component of }\delta I.$$

The net volume pole $-\nabla\cdot I$ and surface pole $\sigma_2=\sigma_1+\sigma_3$ now give rise to a magnetostatic

†† For earlier treatments of similar problems see references 9, 11, and 17.

potential ψ_2 which must satisfy

$$\nabla^2\psi_2 = -4\pi(-\nabla\cdot I) = -4\pi\chi^*[(\partial^2\psi_1/\partial x^2)+(\partial^2\psi_1/\partial z^2)]$$

and

$$[(\partial\psi_2/\partial z)_{z=-0}-(\partial\psi_2/\partial z)_{z=+0}] = 4\pi[\sigma_1-\chi^*(\partial\psi_1/\partial z)_{z=-0}].$$

It is readily verified by substitution that these equations are satisfied by letting ψ_2 equal ψ_1. In other words, ψ_1 is the self-consistent solution desired. In addition, it may be verified by letting $B=H+4\pi\delta I$ (in keeping with the σ_1,μ^* model) and noting that stored anisotropy energy is $\delta I^2/2\chi^*$, that the following three expressions for E_M are equivalent:

$$E_M = \tfrac{1}{2}\int \sigma_1(x,y)\psi_1(x,y,0)dxdy$$

$$= \frac{1}{8\pi}\int H\cdot B dxdydz$$

$$= \int [(H^2/8\pi)+\delta I^2/2\chi^*]dxdydz.$$

We shall refer to this result as the μ^* method of calculating magnetostatic energies. It is obviously limited to cases for which θ and the deviations of magnetization from easy directions are all small.

3. Pole Density for $K=\infty$

When the magnetization is everywhere parallel to easy directions, the pole density on the surface or the domain walls is easily found. The density σ_1 on the surface of the [010] and [0$\bar{1}$0] domains is simply $\pm I_s\sin\theta$; this covers Case I and is one way of considering III.

For Case II, the tree patterns, the branches are [100] and [$\bar{1}$00] domains inserted in [010] and [0$\bar{1}$0] domains. The change in magnetization when [100] is inserted in [010] is equivalent to superimposing a new magnetization with components I_s, $-I_s$, 0. Thus, if the walls of the branches are parallel to [1$\bar{1}$0], no poles will be developed on the walls since they are parallel to the added magnetization; however, if they taper to a point, all of the flux entering the branch at the trunk eventually leaves through the wall. This is a particular example of a vector theorem relating to the poles appearing on the wall. If n is the unit normal drawn from a domain with magnetization I_1 into a domain of magnetization I_2, then the net surface pole density is

$$\sigma = n\cdot(I_1-I_2).$$

Hence, if n is perpendicular to I_1-I_2, i.e., if I_1-I_2 lies in the plane of the wall, the pole density is zero. For the case of the tree patterns the branches represent strips of varying width, having varying pole density cutting across a sky of uniform pole density (Fig. 13). This is approximated in Case II, treated below, by a pattern of strips of uniform pole density of equal width and alternating sign cutting at 45° across the specimen. This approximation tends to underestimate the actual energy and thus offsets the effect of neglecting the material in the branches lying above the wall surface as discussed in the introduction to the appendix.

4. Magnetostatic Energies for Special Cases

Case I

As shown in Fig. 11, the domains of width W are polarized approximately along $\pm Y$ so that the pole density for $K=\infty$ is $\sigma=\pm I_s\sin\theta$. For this structure, ψ_1 cannot depend on y so that the field H lies in the xz plane, in which the domains have permeability μ^*. Hence the potential ψ (omitting the subscript "1") needed in the expression for E_M (Section 2) must satisfy

$$\nabla^2\psi(x,z)=0,$$

$$+\frac{\mu^*\partial\psi}{\partial z}\Big]_{z=-0} - \frac{\partial\psi}{\partial z}\Big]_{z=+0} = 4\pi\sigma(x).$$

This solution is simply related to $\varphi(x,z)$, the solution of the simpler problem for $\mu^*=1$. It is readily verified that if $\varphi(x,z)$ is known, then the desired solution is

$$\psi(x,z)=2\varphi(x,z)/(1+\mu^*).$$

The energy E_M is then

$$E_M = \frac{2}{1+\mu^*}\int \varphi(x,0)\sigma(x)dxdy.$$

The integral has been evaluated by expanding $\varphi(x,z)$ in a series, $\exp[(n\pi/W)(\pm z\pm ix)]$, this

leading to

$$e_1 = 1.70 I_s^2 (\sin^2\theta) W/(1+\mu^*)$$

for the average energy per unit area, which in the limit $\mu^* = 1$ agrees with a result obtained by Kittel.[15]

Case II

For the case of the tree patterns we estimate the magnetostatic energy by replacing the branches and sky by parallel strips, each of width W having pole density $I_s \sin\theta$ running at 45° to x and y on the surface. For this case the surface pole density and potential may be taken to be $\sigma(x+y)$ and $\varphi(x+y,z)$ for $K = \infty$. For finite K we try the solution

$$\psi(x+y,z) = A\varphi(x+y,z), \quad z>0,$$
$$\psi(x+y,z) = A\varphi(x+y,az), \quad z<0.$$

The constant "a" is evaluated from $\nabla \cdot B = 0$ which gives

$$\mu^*(\partial^2\psi/\partial x^2) + (\partial^2\psi/\partial y^2) + \mu^*(\partial^2\psi/\partial z^2)$$
$$= (1+\mu^*)A(\partial^2\varphi/\partial x^2) + \mu^* a^2 A(\partial^2\varphi/\partial z^2) = 0,$$
$$a = ((1+\mu^*)/2\mu^*)^{\frac{1}{2}},$$

since $\nabla^2\varphi = 0$. A is then evaluated from the condition of surface poles and is found to be

$$A = 2/(1+(\mu^*(1+\mu^*)/2)^{\frac{1}{2}}) = 2/(1+40.7) = 1/20.8,$$

so that the energy per unit area of surface in this case

$$e_2 = 1.70 I_s^2 (\sin^2\theta) W/(1+(\mu^*(1+\mu^*)/2))^{\frac{1}{2}}.$$

Case III

For the case of patterns on steeply sloping surfaces, we shall initially neglect the jagged edges of the patterns and consider strips of uniform pole density σ and width S spaced with period W (when $S = W$ we have Case I). This case may be calculated by Fourier series or by an approximate method. According to the approximate method, we calculate φ at the center of one strip (at the origin of x and z) assuming that all the other strips are infinitely narrow. Taking the additive constant in the potential so that two unit lines of poles have potential $-2\ln r$, the potential at one strip due to all the others may be evaluated from

$$-2Re(\ln \tan\pi(x+iz)/2W) + 2\ln r.$$

This gives $-2\ln\pi/2W$ for the potential at the origin. The self-energy of the strip of unit pole density and width S at the origin is

$$(1/2S^2)\int_0^S\int_0^S -2\ln|x-y|\,dxdy = \tfrac{3}{2} - \ln S.$$

To get the total self-energy per strip, to its own self-energy we add one-half its energy of interaction with all the other strips and obtain

$$\tfrac{3}{2} - \ln S + \tfrac{1}{2}(-2\ln\pi/2W) = \tfrac{3}{2} + \ln 2W/\pi S.$$

For the case under consideration, the pole density on each strip is not unity but $SI_s \sin\theta$ and the length of strip per unit area is $1/W$ so the total energy per unit area is

$$e_3 = (3+2\ln 2W/\pi S) S^2 I_s^2 (\sin^2\theta)/W(1+\mu^*).$$

This expression should be quite accurate for $W \gg S$. As S approaches W an appreciable error will occur because the interaction between adjoining strips will differ from $+2\ln W$. However, even when $W = S$ the error is not great and the equation gives 2.16 instead of 1.70 for the numerical factor. (Introducing the correct energy for nearest neighbors reduces the error to less than 1 percent.)

5. Size Estimates for Patterns on Sloping Surface

In order to check the theory against experiment, a series of patterns was photographed on a uniformly curving surface varying in slope from $\theta = -5°$ to $\theta = +5°$. The patterns observed, which were similar to those of Fig. 10 but not as good photographically, could be classified as follows:

Simple parallel slabs: less than 0.5°; no branches.
Transition: 0.5° to 0.65°; trees form and branches grow to about $W/2$ in length.
Tree patterns: 0.65° to 1.30°; branches fill more of pattern finally eliminating trunk of tree.
Transition: 1.30° to 1.9°; branches begin to squeeze out sky.
Steep slope patterns: 1.9° to 3.9°; branches, cover all but a narrow strip of sky.

Except for the transition regions, it is possible to make rough estimates for the minimum energy configurations and check the dimensions with those obtained experimentally. The width W of the underlying domains is determined by the

TABLE I. Comparison of measured and calculated dimensions of tree pattern (Fig. 12).

Measured					
θ (degrees)	1.0	1.3	2.0	2.6	3.2
a (mm)	0.071	0.067			
b (mm)	0.067	0.067			
S (mm)			0.025	0.14	0.08
Computed					
c/b	0.05	0.07			
a (mm)	0.197	0.152			
b (mm)	0.115	0.115			
S (mm)			0.73	0.43	0.28

overall dimensions of the specimen and is considered a specified quantity. The dimensions measured for several angles are given in Table I. The quantities a, b, c are defined in Figs. 21 and 13 and S in Fig. 14. The value of W is 0.6 mm throughout.

In treating the tree patterns we assume that the branches of the trees nearly neutralize the net flux. This is reasonable since lack of neutralization is much more important for the wide strips between trunks ($W \doteq 0.2$ mm) compared to the branch width and spacing ($W \doteq 0.02$ mm). Starting with this assumption and assuming, furthermore, that the branches are elliptical cones, as indicated in Fig. 12, it is possible to determine the ratio of depth c to width b from the experimental data as follows. The flux carried by one branch is $I_s \pi bc/2$. Each branch neutralizes an area of $aW/2$ with pole density $I_s \sin\theta$. This gives

$$I_s \pi bc/2 = aWI_s(\sin\theta)/2,$$
$$c/b = aW(\sin\theta)/\pi b^2.$$

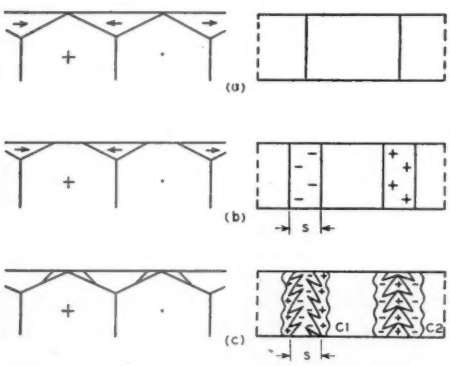

FIG. 33. Closure patterns for steeply sloping surface: (a) complete closure, (b) pattern with strips of alternating sign, (c) pattern with strip with no net pole density.

From these, the values of c/b have been computed and are tabulated in Table I. These indicate that taking c/b as 1/20 will be a satisfactory approximation. This gives

$$b = (20aW(\sin\theta)/\pi)^{\frac{1}{2}}.$$

We next start with the estimated values for θ, W and c/b and try to calculate a and b by minimizing the energy. The magnetostatic energy is estimated from Case II taking $W = a/2\sqrt{2}$; this introduces $\sqrt{8}$ into the denominator in e_4 (see below). Replacing the branch and sky pattern by parallel strips of equal width is obviously a crude approximation; also Case II corresponds to strips all lying in the xy plane, whereas the poles on the branches lie below the plane and are actually underneath permeable material. For these reasons we should regard the use of e_2 as being only a first approximation to the correct magnetostatic energy. If the cones were infinitely thin ($c/b = 0$) and the sides were straight, then the domain wall surface per unit area of the xy plane would be $b/2a$. Actually the branches have depth and are also slightly bulged, this increases the fraction; on the other hand they do not run to the center. We therefore compromise by using domain wall area per unit surface areas equal to

$$b/2a = (20W(\sin\theta)/4\pi a)^{\frac{1}{2}}.$$

The total energy for this case is, therefore,

$$e_4 = \frac{1.70aI_s^2 \sin^2\theta}{(1+(\mu^*(1+\mu^2)/2))^{\frac{1}{2}}(8)^{\frac{1}{2}}} + \gamma[20W(\sin\theta)/4\pi a]^{\frac{1}{2}}$$
$$= Aa \sin^2\theta + B(W \sin\theta/a)^{\frac{1}{2}},$$

where

$$A = \frac{1.70I_s^2}{(1+(\mu^*(1+\mu^*)/2)^{\frac{1}{2}}(8)^{\frac{1}{2}}} = \frac{1.70(1580)^2}{(41.7)(2.83)} = 3.60\times10^4,$$

$$B = \gamma(20/4\pi)^{\frac{1}{2}} = 1.5(5/\pi)^{\frac{1}{2}} = 1.89,$$

the units being c.g.s. The value of a which gives the least energy is readily found to be

$$a = (B/2A)^{\frac{2}{3}}W^{\frac{1}{3}}/\sin\theta = 8.83\times10^{-4}\times(0.06)^{\frac{1}{3}}/\sin\theta = 3.45\times10^{-4}/\sin\theta$$

from which the computed values of a in Table I are obtained. Combining these with the formula $b=(20aW)[(\sin\theta)/\pi]^{\frac{1}{2}}=1.15\times10^{-2}$ cm gives the value for b. The agreement between observation and calculation is fair, the calculated a and b being about 2.5 and 1.7 times the observed. The value for a depends upon $(b/c)^{\frac{1}{2}}$ power and is, therefore, insensitive to the assumed value. However, the agreement indicates the essential correctness of the physical picture.

The total energy per unit area is

$$e_5=\tfrac{3}{2}(2AB^2)^{\frac{1}{2}}W^{\frac{1}{2}}\sin\theta.$$

This formula should be fairly good for the range in which $b\cong a/2$, say from $b=a$ to $b=a/3$, corresponding to $\theta=0.6$ to $1.7°$.

6. Size Estimates for Steeper Slopes

Two models of the domain structure beneath the surface have been investigated. These are illustrated in Fig. 33: (a) represents the flux closure case, (b) shows the case discussed above for which there is a net pole density at the center of each [010] domain surface, (c) has no net pole density (since the transverse domains are deep enough to carry the required flux from each [010] to [0$\bar{1}$0] domain as in (a)); however, the walls have been pulled back to produce the type of pattern shown.

Calculations based on model (b) (but omitted from this appendix) lead to strip width 10 to 20 times narrower than observed, the reason being that the magnetostatic energy (see Section 4) of widely separated strips, on which lie poles, is high. Model (c) leads to widths about one third of the experimental values. On the basis of the interpretation of (c), the energy will be less for the staggered distribution c_1 than for c_2, since the former tends to move like poles farther apart; this is in agreement with the appearance of the patterns of Fig. 10(d), (e), and (f).

For slopes of 3° and widths of $W=0.6$ mm, the magnetostrictive energy in the transverse domains is comparable to the wall energy. The transversely magnetized domains are forced to fit the large underlying domains. This means the transverse domain is strained out of its equilibrium (i.e., zero stress) shape of strains of $\epsilon_{xx}=-\epsilon_{yy}=-h_1$, $\epsilon_{zz}=\epsilon_{xy}=\epsilon_{yz}=\epsilon_{zz}=0$, where h_1 is the fractional increase in length in the X direction in an unstressed domain when the magnetization is rotated from Y to X.[18] The energy density is thus

$$\tfrac{1}{2}c_{11}(\epsilon_{xx}^2+\epsilon_{yy}^2)+c_{12}\epsilon_{xx}\epsilon_{yy}=(c_{11}-c_{12})h_1^2.$$

The values of these constants for iron are[19]

$$c_{11}=2.37\times10^{12},\quad c_{12}=1.41\times10^{12}\ \text{ergs/cm}^3,$$
$$h_1=3.2\times10^{-5}$$

giving a magnetostrictive energy density of

$$s=0.96\times10^{12}\times(3.2)^2\times10^{-10}=0.98\times10^3\text{ergs/cm}^3.$$

The volume having this energy is $\sin\theta(W-S)^2/4$ per unit length along y and width W, hence the energy per unit area of surface is

$$s\sin\theta(W-S)^2/4W.$$

For $\theta=3°$ and $W=0.6$ mm this gives 0.75 erg/cm^2 which is comparable with the wall energy of about 1.5 ergs/cm^2.

In model (c), we treat each strip S as a pattern of alternating strips at 45°. This leads to using Case II with $W_2=S/4$ as an estimate from the pattern of Fig. 10 (f). A fraction S/W of the surface is covered with the strips. The reduction of wall surface per unit length of strips is about $1/2S$ based on the projected area and is perhaps $0.3S$ considering the fact that the wall boundary is curved. The average energy per unit area is

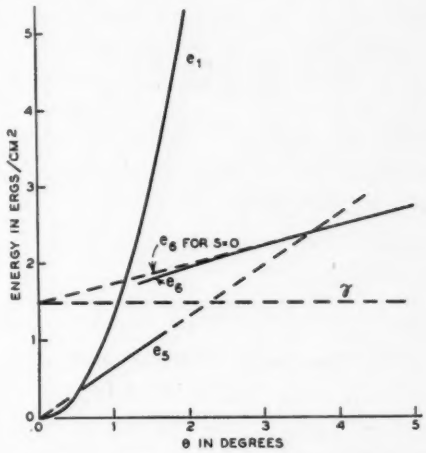

FIG. 34. Comparison of energies for simple parallel slabs (e_1), tree patterns (e_5), and various approximations for steep slope patterns (γ, $e_6(S=0)$, e_6).

[18] F. Bitter, *Introduction to Ferromagnetism* (McGraw-Hill Book Company, Inc., New York, 1937), p. 248.
[19] Reference 18, p. 254.

thus

$$e_6 = s(\sin\theta)W/4 + \gamma(1 - 0.3S/W) + 1.70S^2I_s^2(\sin^2\theta)/4W(1+(\mu^*(1+\mu^*)/2))^{\frac{1}{2}}.$$

This leads to a minimum energy for

$$S_{\min} = 0.3\gamma/[1.70I_s^2/2(1+(\mu^*(1+\mu^*)/2))^{\frac{1}{2}}]\sin^2\theta = 0.3\gamma/\sqrt{2}A\sin^2\theta,$$

where $A = 3.60\times10^4$ as defined in Section 5. The energy is then

$$e_6 = s(\sin\theta)W/4 + \gamma(1 - 0.15S_{\min}/W)$$

(neglecting the small correction to the magnetostatic energy). Values of $S_{\min}$ so calculated are given in Table I and are about 3 times the measured values.

7. Comparison of Total Energies

In Fig. 34, the three energy expressions are plotted as functions of θ. The e_1 curve is valid over the range of validity of the μ^* method; since the latter is limited by the condition that θ is small, this curve is certainly accurate to $\theta > 2°$. The e_5 approximation, however, depends on having $b \cong a/2$; the range of $b=a$ to $b=a/3$ is shown as heavy and represents an extension of e_5 somewhat beyond its range of validity. Three approximations to the steep slope patterns are shown: γ corresponds to placing $S=0$ and neglecting magnetostriction; e_6 for $S=0$ adds the effect of magnetostriction; e_6 shows the best approximation with $S=S_{\min}$. Figure 34 is seen to explain the general trend of one type of pattern to another satisfactorily, the incidence of tree patterns at $\theta \cong 0.5°$ being given correctly. The weakest feature is the e_5 curve which has not been treated accurately enough to give properly the transition from tree to steep slope patterns.

PHYSICAL REVIEW VOLUME 75, NUMBER 1 JANUARY 1, 1949

A Simple Domain Structure in an Iron Crystal Showing a Direct Correlation with the Magnetization

H. J. WILLIAMS AND W. SHOCKLEY
Bell Telephone Laboratories, Murray Hill, New Jersey

(Received August 30, 1948)

A hollow rectangle cut from a single crystal of 3.8 percent silicon iron has been studied with the aid of powder patterns and flux measurements. The edges and surfaces were all cut accurately parallel to ⟨100⟩, the directions of easy magnetization. The domain pattern consists of 8 domains, four forming an inner rectangle magnetized in one direction and the others forming an oppositely magnetized outer rectangle. Changes in magnetization occur by the growth of one set of domains at the expense of the other. In the saturated condition, each leg of the rectangle is one domain about 1.5×0.1×0.1 cm in size. Implications of these results in connection with Barkhausen effect are discussed, and a method of measuring the energy of the Bloch wall is proposed.

THE theory of magnetic domains has been developed over a period of years to explain the gross magnetic properties of matter in terms of the behavior of smaller regions of substantially uniform magnetization. However, except for certain artificially simplified cases such as fine stressed wires or very small particles, it has not been possible to obtain a complete picture of the domain structure in any actual specimen and to show how it explains the state of magnetization and variations thereof. The experiments described below furnish an example of correlation between domain structure and magnetization for a specimen having a dimension of the order of one centimeter.

This specimen was in the form of a hollow rectangle (or "picture frame") of 3.8 weight percent silicon iron cut from a single crystal so as to have all edges and surfaces substantially parallel to [100] or equivalent directions. It had origi-

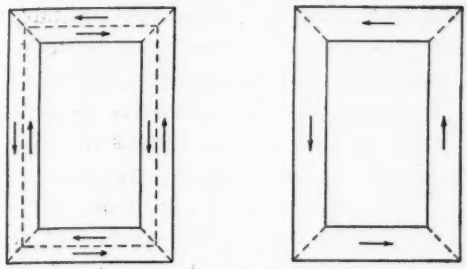

FIG. 1. Domain structure of the crystal with solid lines showing the outline of the crystal, dotted lines representing Bloch walls, and arrows indicating the directions of magnetization. (a) After applying a field; (b) after cooling from 1000°C.

nally been prepared and used for studies of magnetization along the [100] direction.[1] For these new experiments, the surfaces were carefully ground parallel to (001) planes so as to avoid the superficial "tree patterns"[2] and polished for use with the colloidal suspension used for observing domain patterns.[2,3]

The magnetization in the specimen has been determined by methods described below to consist essentially of eight domains arranged as shown in Fig. 1a. The domain walls shown by dashed lines are perpendicular to the paper and run through the specimen whose thickness is 0.074 cm. The width of the legs of the rectangle is 0.102 cm and the over-all dimensions are 1.9×1.3 cm. The pattern shown represents perfect flux closure in the sense that no magnetic poles are produced on any of the domain walls or external surfaces of the specimen. The magnetization changes by sidewise displacements of the walls so as to make the inner four domains, which represent flux in the clockwise sense, grow at the expense of the outer set, or vice versa.

Presumably the state of least energy can be obtained experimentally by heating the specimen above the Curie temperature and cooling it slowly. When this is done, it is found that the specimen is magnetized in four domains all running in one direction so that a state of saturation is produced (Fig. 1b). This domain structure would also seem to be theoretically the one of minimum energy. (It obviously has no magnetostatic or anisotropic energy and the wall energy is a minimum. There is some magnetostrictive energy; however, since the legs of the rectangle are long compared to their width, the stress will

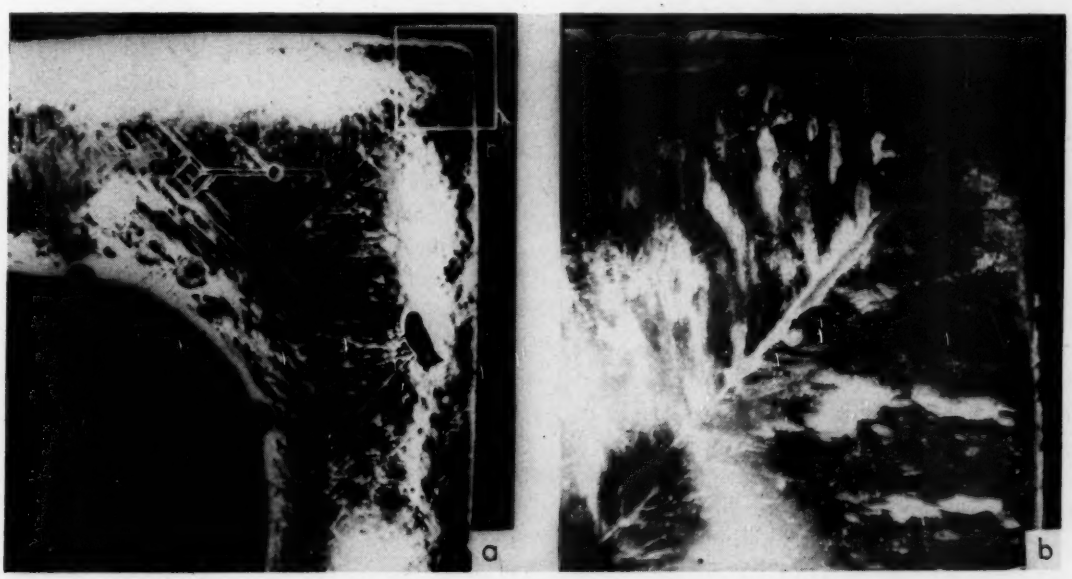

FIG. 2. (a) Pattern obtained on a corner of the crystal after cooling from 1000°C. (b) Small region shown in (a) obtained with greater magnification.

[1] H. J. Williams, Phys. Rev. **52**, 747–751 (1937).
[2] H. J. Williams, Phys. Rev. **71**, 646–647 (1947).
[3] H. J. Williams, R. M. Bozorth, and W. Shockley, Phys. Rev. **75**, 155 (1949).

thus

$$e_6 = s(\sin\theta)W/4 + \gamma(1 - 0.3S/W) + 1.70S^2I_s^2(\sin^2\theta)/4W(1+(\mu^*(1+\mu^*)/2))^{\frac{1}{2}}.$$

This leads to a minimum energy for

$$S_{\min} = 0.3\gamma/[1.70I_s^2/2(1+(\mu^*(1+\mu^*)/2))^{\frac{1}{2}}] \sin^2\theta = 0.3\gamma/\sqrt{2}A \sin^2\theta,$$

where $A = 3.60\times10^4$ as defined in Section 5. The energy is then

$$e_6 = s(\sin\theta)W/4 + \gamma(1 - 0.15S_{\min}/W)$$

(neglecting the small correction to the magnetostatic energy). Values of $S_{\min}$ so calculated are given in Table I and are about 3 times the measured values.

7. Comparison of Total Energies

In Fig. 34, the three energy expressions are plotted as functions of θ. The e_1 curve is valid over the range of validity of the μ^* method; since the latter is limited by the condition that θ is small, this curve is certainly accurate to $\theta > 2°$. The e_5 approximation, however, depends on having $b \cong a/2$; the range of $b = a$ to $b = a/3$ is shown as heavy and represents an extension of e_5 somewhat beyond its range of validity. Three approximations to the steep slope patterns are shown: γ corresponds to placing $S = 0$ and neglecting magnetostriction; e_6 for $S = 0$ adds the effect of magnetostriction; e_6 shows the best approximation with $S = S_{\min}$. Figure 34 is seen to explain the general trend of one type of pattern to another satisfactorily, the incidence of tree patterns at $\theta \cong 0.5°$ being given correctly. The weakest feature is the e_5 curve which has not been treated accurately enough to give properly the transition from tree to steep slope patterns.

PHYSICAL REVIEW VOLUME 75, NUMBER 1 JANUARY 1, 1949

A Simple Domain Structure in an Iron Crystal Showing a Direct Correlation with the Magnetization

H. J. WILLIAMS AND W. SHOCKLEY
Bell Telephone Laboratories, Murray Hill, New Jersey

(Received August 30, 1948)

A hollow rectangle cut from a single crystal of 3.8 percent silicon iron has been studied with the aid of powder patterns and flux measurements. The edges and surfaces were all cut accurately parallel to ⟨100⟩, the directions of easy magnetization. The domain pattern consists of 8 domains, four forming an inner rectangle magnetized in one direction and the others forming an oppositely magnetized outer rectangle. Changes in magnetization occur by the growth of one set of domains at the expense of the other. In the saturated condition, each leg of the rectangle is one domain about 1.5×0.1×0.1 cm in size. Implications of these results in connection with Barkhausen effect are discussed, and a method of measuring the energy of the Bloch wall is proposed.

THE theory of magnetic domains has been developed over a period of years to explain the gross magnetic properties of matter in terms of the behavior of smaller regions of substantially uniform magnetization. However, except for certain artificially simplified cases such as fine stressed wires or very small particles, it has not been possible to obtain a complete picture of the domain structure in any actual specimen and to show how it explains the state of magnetization and variations thereof. The experiments described below furnish an example of correlation between domain structure and magnetization for a specimen having a dimension of the order of one centimeter.

This specimen was in the form of a hollow rectangle (or "picture frame") of 3.8 weight percent silicon iron cut from a single crystal so as to have all edges and surfaces substantially parallel to [100] or equivalent directions. It had origi-

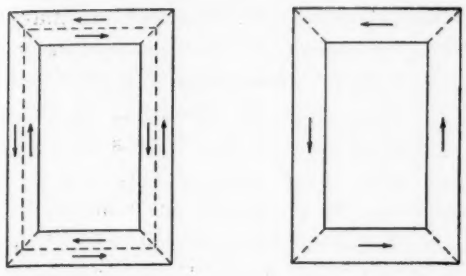

FIG. 1. Domain structure of the crystal with solid lines showing the outline of the crystal, dotted lines representing Bloch walls, and arrows indicating the directions of magnetization. (a) After applying a field; (b) after cooling from 1000°C.

nally been prepared and used for studies of magnetization along the [100] direction.[1] For these new experiments, the surfaces were carefully ground parallel to (001) planes so as to avoid the superficial "tree patterns"[2] and polished for use with the colloidal suspension used for observing domain patterns.[2,3]

The magnetization in the specimen has been determined by methods described below to consist essentially of eight domains arranged as shown in Fig. 1a. The domain walls shown by dashed lines are perpendicular to the paper and run through the specimen whose thickness is 0.074 cm. The width of the legs of the rectangle is 0.102 cm and the over-all dimensions are 1.9×1.3 cm. The pattern shown represents perfect flux closure in the sense that no magnetic poles are produced on any of the domain walls or external surfaces of the specimen. The magnetization changes by sidewise displacements of the walls so as to make the inner four domains, which represent flux in the clockwise sense, grow at the expense of the outer set, or vice versa.

Presumably the state of least energy can be obtained experimentally by heating the specimen above the Curie temperature and cooling it slowly. When this is done, it is found that the specimen is magnetized in four domains all running in one direction so that a state of saturation is produced (Fig. 1b). This domain structure would also seem to be theoretically the one of minimum energy. (It obviously has no magnetostatic or anisotropic energy and the wall energy is a minimum. There is some magnetostrictive energy; however, since the legs of the rectangle are long compared to their width, the stress will

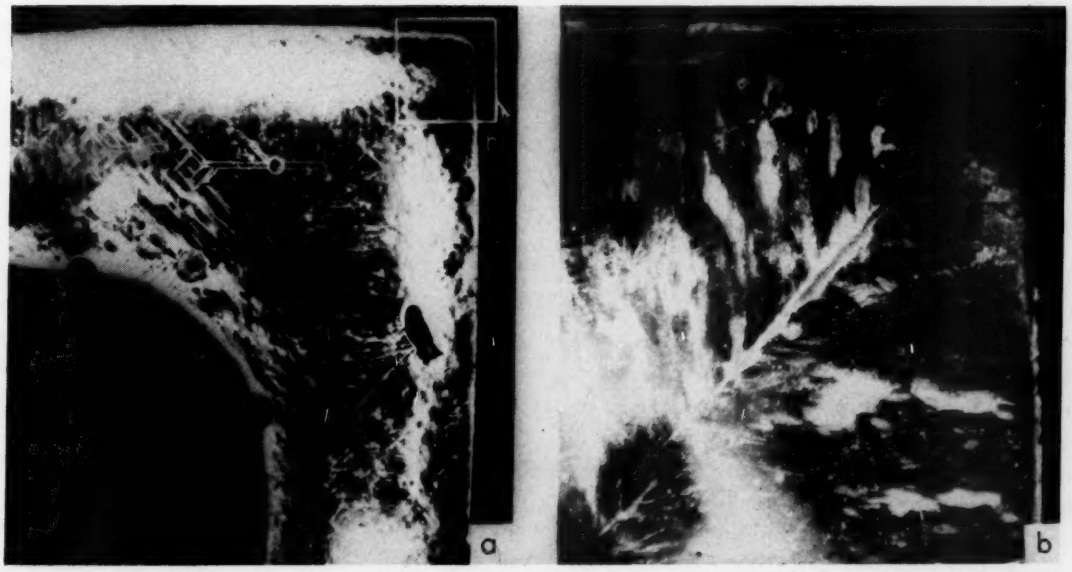

FIG. 2. (a) Pattern obtained on a corner of the crystal after cooling from 1000°C. (b) Small region shown in (a) obtained with greater magnification.

[1] H. J. Williams, Phys. Rev. **52**, 747–751 (1937).
[2] H. J. Williams, Phys. Rev. **71**, 646–647 (1947).
[3] H. J. Williams, R. M. Bozorth, and W. Shockley, Phys. Rev. **75**, 155 (1949).

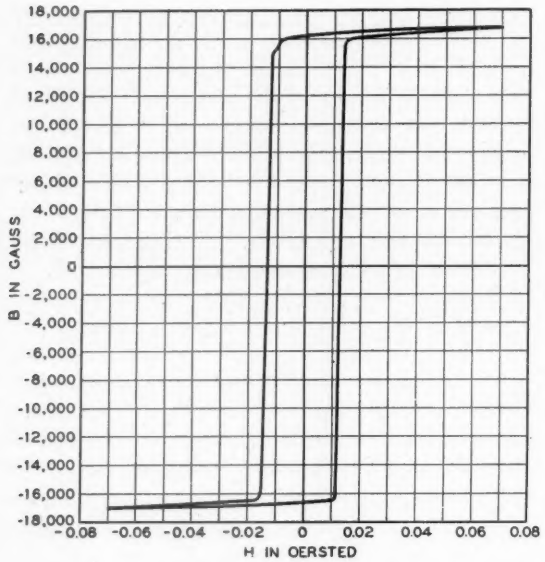

FIG. 3. Hysteresis loop traced on a Cioffi recording fluxmeter.

be much less than in a rectangle with a filled center. A rough estimate indicates that both the wall and magnetostrictive energy average about 1 erg/cm³ so that any increased complexity of domain structure to reduce magnetostrictive energy would result in a net increase in total energy due to added wall energy.[4])

The magnetization pattern just discussed has been established by using the powder pattern technique[2,3] combined with measurements of flux with the Cioffi recording fluxmeter.[5] In Fig. 2, a pattern is shown as obtained after cooling from 1000°C. Similar patterns were also observed on the other corners. This pattern shows a Bloch wall bisecting the 90° angle at the corner of the specimen. Figure 2b shows a portion of the same pattern taken with a larger magnification. This pattern shows the Bloch wall and a number of elongated clusters of colloidal magnetite. In previous work[2] the direction of magnetization has been shown to be normal to these elongated clusters. The powder patterns, observed over the entire crystal, showed that the domain structure, except for a few superficial details due to crystal imperfections and irregularities of cross section, was as shown in Fig. 2. This domain arrangement has a net magnetization equal to the saturation.

[4] See C. Kittel, Phys. Rev. **70**, 965 (1946), or reference (3) for a more general discussion of this subject.
[5] P. P. Cioffi, Phys. Rev. **67**, 200 (1945).

This feature was checked by putting primary and secondary windings around the specimen and then tracing a hysteresis loop (Fig. 3). Care was taken not to expose the specimen to magnetic fields previous to this. The results showed that the specimen had an initial magnetization, after cooling from above the Curie point of 17,000 gauss, in good agreement with the known saturation of the specimen, considering the uncertainty in exact cross section.

For intermediate states of magnetization the domain pattern of Fig. 4 was obtained. Figure 4 is a composite of three pictures of adjacent positions showing the wall at a corner and along part of a side of the crystal. The inner wall at the corner is due to excess material on the inside corner. The wall was easily traced along the specimen. Observation of the position of the wall on opposite sides of the crystal indicated that it extended straight through the specimen. According to this conclusion, the flux should vary linearly with position of the domain wall, varying from positive saturation to negative saturation, as the wall moves across the specimen. Within the

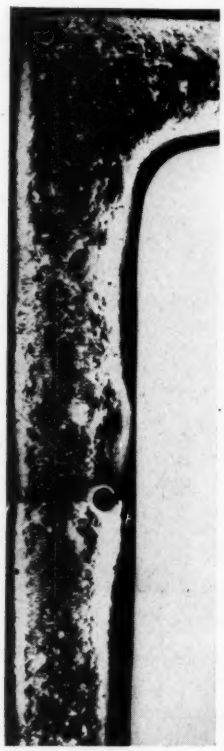

FIG. 4. Composite of patterns on three adjacent areas showing the domain structure represented in Fig. 1a.

|← 1 MM →|

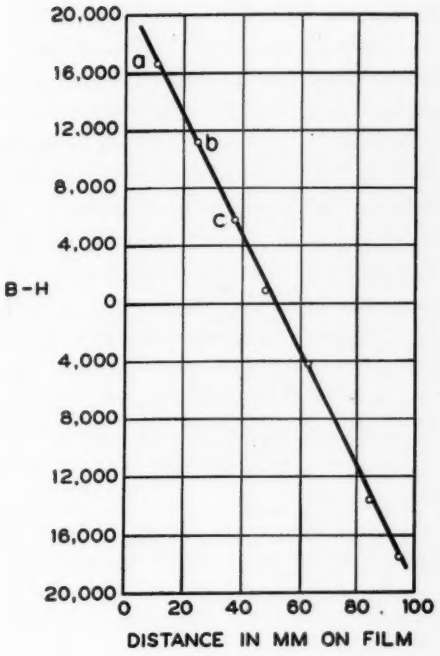

FIG. 5. Magnetization *vs.* displacement of the 180° Bloch wall, and patterns showing the Bloch wall in three different positions.

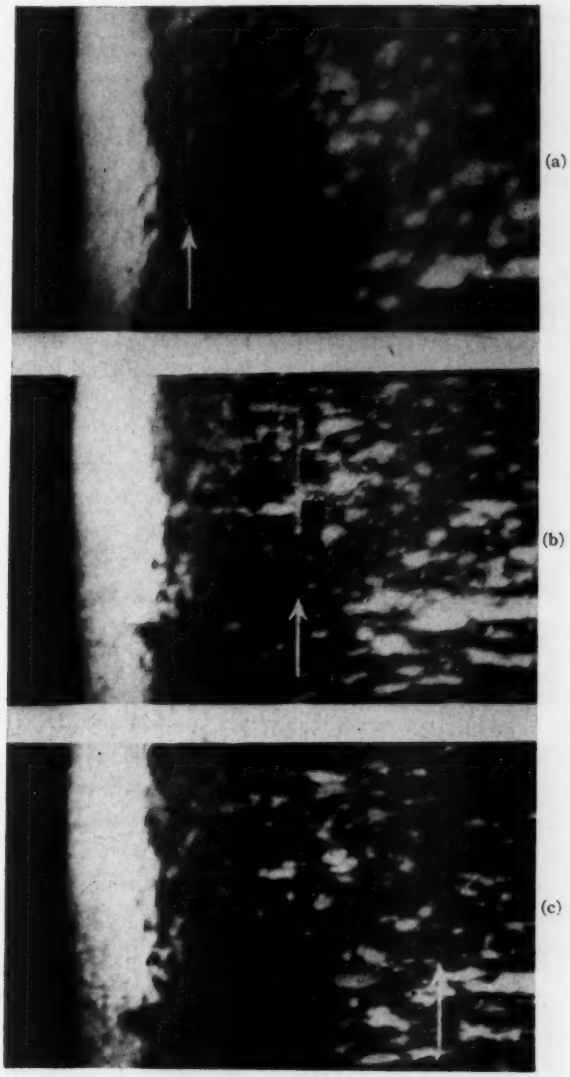

precision of measurement of the cross section, this was found to be the case. The wall was photographed at seven positions while tracing a hysteresis loop. Figure 5 shows the wall position for these photographs and the resultant plot of $B-H$ *vs.* wall position.

This experiment also throws light on the nature of the Barkhausen effect for specimens with large domains. According to early theories, the Barkhausen effect arises from the abrupt reversal of domains. In this specimen, on the contrary, a relatively steady progress of the domain boundary occurs. While this motion was being observed, however, the Barkhausen effect could be simultaneously heard over a loudspeaker and amplifier system. There are several possible mechanisms which may produce irregular or jerky motions of the Bloch wall. When the boundary moves past small holes or other slight imperfections appearing on the surface of the crystal, superficial domain structures around these regions unite with the wall, forming irregularities in it, a particular example of which is shown by the drawing in Fig. 6a. As the main wall continues to move, the walls extending from the holes to the main wall become more and more extended and finally break, suddenly forming a new structure

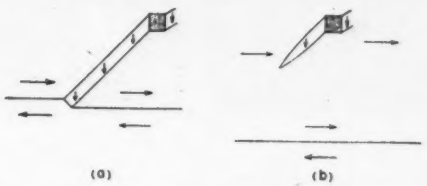

FIG. 6. (a) Drawing of the domain structure, around a square cavity, connected to the 180° Bloch wall. (b) Domain structure formed after breaking the connection between the cavity and the 180° Bloch wall.

around the hole, and the main wall straightens out (Fig. 6b). Figure 7 shows the actual patterns observed which correspond to the drawings of Fig. 6. Figure 7b is a superposition of the two patterns. The light lines show the original pattern (Fig. 7a) which was permitted to etch the surface, and the heavy lines show the final pattern corresponding to Fig. 6b. It is not possible at present to say whether the number and magnitude of Barkhausen impulses can be correlated with the behavior of these imperfections. However, it is evident that their behavior must account at least for some of the discontinuities observed in the magnetization process.

The same imperfections may possibly make important contributions to the coercive force of about 10^{-2} oersted observed for this specimen. From observations of patterns like those of Fig. 4 one estimates that there are about four such structures per cm showing on the surface. If there are other similar structures distributed uniformly in depth, there will, of course, be many more per unit area. Taking the diameter of the structure as 3×10^{-3} cm, we estimate that there will be about 10^3 per cm^2 of Bloch wall. Each of these exerts a force of about σC on the wall where $\sigma=2$ dynes/cm is the surface tension of the wall, and $C=\pi 3\times10^{-3}\doteq10^{-2}$ cm is the circumference of the contact with the wall. Thus the force on the wall due to these structures will be about $10^3\times2\times10^{-2}=20$ dynes/cm^2. When the wall is moved, there will be a tendency for all of the structures to pull back in one direction, giving a net force of this magnitude. The force per unit area on the wall due to a magnetizing field H is $2HI_s\doteq3000H$ for this material. Equating this force to the restoring force due to the structures leads to $H=0.006$ oersted, whereas the observed coercive force is about 0.012 oersted. At the present stage of these observations this agreement in order of magnitude may be fortuitous, and at most, all one can say is that the effect of surface tension on walls about imperfections may account for coercive force, and the abrupt changes when the walls break away may account for the Barkhausen effect.

Another explanation is that stresses produced during the formation of the crystal tend to hold certain small areas of the wall in position by interaction with the magnetostriction. This idea has previously been discussed by Kondorsky;[6] however, in that theory very considerable curvatures of the wall are assumed. In Fig. 4 it is seen that the wall is very nearly straight. This difference is due to the fact that the poles produced on a curved wall exert large forces on the wall and tend to make it plane. For this reason, even though the same forces may act as in the Kondorsky theory, the curvature of the wall will be small; however, some curvature is to be ex-

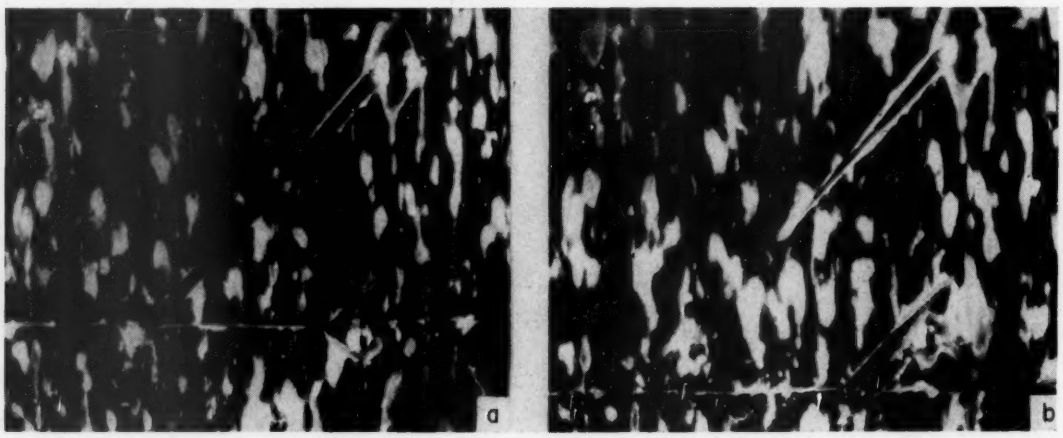

0.1 MM

FIG. 7. Patterns corresponding to the domain structure shown in Fig. 6.

[6] E. Kondorsky, Phys. Zeit. Sowiet. 11, 597 (1937); R. Becker and W. Döring, *Ferromagnetismus* (J. Springer, Berlin, 1939), p. 205.

pected and may be detectable in more precise experiments.

The domain structure in this specimen permits an experiment which will measure directly the domain wall energy. This may be accomplished with the arrangement shown in Fig. 8. Here a current, J, is passed horizontally through the specimen from one point contact to another. This is equivalent to winding the upper half of the specimen with a primary in one direction and the lower half with a primary in the opposite direction. This will produce a magnetic field around the hollow rectangle in opposite directions in the top and bottom halves, as indicated in (b), and will distort the wall, as indicated in (c). This distortion can be detected by comparing the wall positions on the two sides, or by comparing the wall position on one side with the total flux measured on the fluxmeter. The offset W of the wall from its average position will be linear in J to a first approximation. Assuming that the wall is the same shape all around the rectangle (if it were not, large magnetostatic fields would be produced), we may equate the surface tension force per unit length of the wall in the y direction to the magnetic force tending to move it. This force is obtained from the integral of H around the rectangle which gives

$$\int Hds = (4\pi/10)Jy/T,$$

assuming the current is uniformly spread throughout the height of the specimen at the wall position. Hence the force per unit height on the wall is

$$\int 2I_sHds = (8\pi/10)I_sJy/T$$

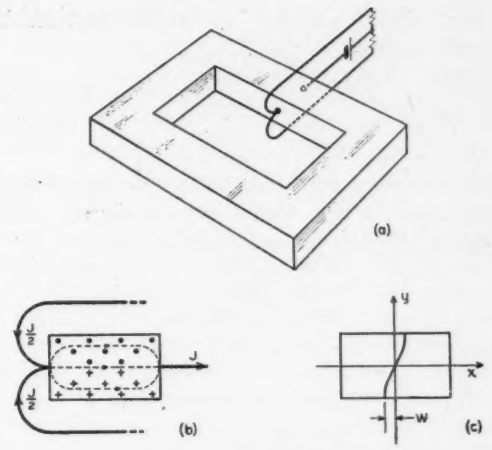

FIG. 8. Experimental arrangement proposed for a direct measurement of wall energy.

where I_s is the saturation magnetization. The force due to the surface energy of the wall is

$$L\sigma d^2x/dy^2$$

where L is the circumference around the rectangle. Equating these two forces and integrating subject to the boundary condition that $dx/dy=0$ at $y=\pm T/2$ gives

$$x=(2\pi/15)(I_sJ/L\sigma T)(y^3-3y(T/2)^2)$$

for the shape of the wall. The maximum value of x, shown as "W" in Fig. 8, is given by

$$W=(\pi/30)I_sJT^2/L\sigma.$$

Since I_s, J, T, and L are readily determined, this equation can be used to solve for σ as soon as W is measured. It is hoped that results of this experiment can be reported in the near future.

We are indebted to R. M. Bozorth and C. Kittel for suggestions and discussions, to W. L. Bond for assistance with an x-ray goniometer, and to J. G. Walker for assistance with the photography.

A Statistical Theory of Liquids. III

GEORGE JAFFÉ
Louisiana State University, Baton Rouge, Louisiana
(Received August 5, 1948)

In the present paper the author incorporates the dissipative processes of heat conduction and viscosity into his theory. In order to do that, he generalizes first the procedures of statistical mechanics in such a way that they might describe processes involving molecular flow. This is achieved in close analogy to Boltzmann's treatment for gases: Boltzmann's integro-differential equation is replaced by Gibbs' principle of "conservation of density-in-phase," and the solution is sought in form of a power series which modifies (slightly) the canonical ensemble. Finally the anisotropic distribution function in real space is obtained by integrating the multidimensional distribution function with regard to all coordinates and moments except those of one particle.

Section I gives the introduction and Section II the general outline of the theory. In Section III heat conduction is treated in form of the linear problem. The potential is smoothed out by making it dependent on the position of the center of mass only. With this simplification an asymptotic solution can be found which yields the time-dependent temperature gradient and heat current, and thereby the coefficient of heat conduction. In Section IV viscosity is treated in a similar way, and Section V treats the averaging processes involved in the evaluation of physical quantities. Finally, in Section VI, the coefficients of heat conduction and viscosity are calculated numerically for ten liquids from the potentials previously determined. The agreement is (with a few exceptions) about as good as might be anticipated from such a rigorous test. Thus, the same potentials, with their four available constants, have served now to calculate ten independent physical constants with a fair accuracy.

I. INTRODUCTION

A FEW years ago the author[1] developed a statistical theory of liquids which correlated in a satisfactory way the elastic and thermal behavior of liquids, including surface tension and vaporization. No attempt was made to incorporate the transport phenomena into the theory since, at that time, no method for treating these phenomena in liquid media existed.

It seemed evident to the author that his treatment of the liquid state had to be considered as incomplete as long as it was not shown that the dissipative properties can be derived from the same model. This is done in the present paper.

Though the first treatment of transport phenomena was based by Maxwell on his isotropic distribution law, Maxwell himself and Boltzmann repeatedly stressed the point that these phenomena necessarily involve anisotropic distribution functions. Therefore, all more rigorous treatments have been based on the determination of anisotropic distribution functions from Boltzmann's well-known integro-differential equation. This development has come to a satisfactory conclusion in the work of Enskog, Chapman, and others.[2] Unfortunately, Boltzmann's equation cannot serve as a starting point for the treatment of liquids, since it is essentially based on the concept of collisions and this concept breaks down in liquid media where neighboring molecules are constantly in interaction.

On the other hand, the powerful method of the partition sum which forms the foundation of all attempts of treatment of the liquid state is not directly applicable either. It became necessary to generalize this method first so that it might include non-isotropic and time-dependent distributions. In attempting to do this the author follows in a rather close way Boltzmann's original treatment for gases.[3] He replaces Boltzmann's integro-differential equation by Gibbs' principle of "conservation of density-in-phase" and Boltzmann's development in terms of velocities by a suitable generalization.

A first report of this treatment was given at the Cambridge meeting of the American Physical Society in April, 1946, and the method used was evident from the abstract given previously.[4]

[1] George Jaffé, Phys. Rev. **62**, 463 (1942); Phys. Rev. **63** 313 (1943). The text refers to these two papers as I and II.

[2] Compare S. Chapman and T. G. Cowling, *The Mathematical Theory of Non-Uniform Gases* (Cambridge University Press, Teddington, 1939).

[3] Ludwig Boltzmann, Wien. Ber. **66**, 275 (1872); Wiss. Abh. **I**, 316 (1909).

[4] George Jaffé, Phys. Rev. **69**, 688 (1946).

Slightly before (and without knowledge of the author) Kirkwood[5] had published the general outline of a very far-reaching statistical theory of transport, and somewhat later Born and Green[6] gave "A kinetic theory of liquids" which also includes transport phenomena. Both these theories are based essentially on the same principles as the author's approach, but they solve the problem of extending the statistical and kinetic methods to systems in motion in a much more general way than is attempted here.

In spite of this fact, it seems to the author that his own treatment is sufficiently different from Kirkwood's, as well as from Born and Green's theories, to be of interest.

Furthermore, only the author's developments are pushed to the actual calculation of thermal conductivities and viscosities of liquids *from potentials previously determined.* Though these numerical results are not altogether satisfactory, they definitely show that in the author's theory practically all properties of liquids can be coordinated by the same potential. It is this point—besides the general method—which appears to the author to be the principal result of the present investigation.

II. THE GENERAL METHOD

Boltzmann's integro-differential equation expresses the conservation of the number of molecules in a gas during their motion in space. In a similar way Gibbs' principle of conservation of density-in-phase expresses the fact that the number of systems is not affected by the motion of their representative points in phase space. If a multidimensional distribution function is to describe, in any way whatever, the motion of a real system, Gibbs' principle represents a necessary condition imposed on the distribution function. It will be seen that this principle is the only fundamental equation of our theory, in the same way as Boltzmann's integro-differential equation is the only fundamental equation for the corresponding development in the kinetic theory of gases.

We are considering a (virtual) ensemble of **N** systems. Each of the systems is supposed to consist of N identical mass points m.* Let q_i and p_i $(i=1, 2, \cdots, 3N)$ be the coordinates and moments, and let the forces be partly of internal, partly of external origin. Then, if we define the operator

$$D/Dt=(\partial/\partial t)+\sum_{i=1}^{3N}[(p_i/m)(\partial/\partial q_i)+\dot{p}_i(\partial/\partial p_i)]; \quad (2.01)$$

and call the distribution function $f(q_i, p_i, t)$, the principle of conservation of density-in-phase assumes the form

$$Df/Dt=0. \quad (2.02)$$

It is important to note that Eq. (2.02) holds not only for conservative systems but also for systems under the action of forces which are either functions of the coordinates alone, or of the coordinates and time.[7]

Equation (2.02) appears also in the theories of Kirkwood and of Born and Green,[8] but our treatment of it differs from theirs. Our object is to determine from (2.02) distribution functions which will eventually satisfy given initial and boundary conditions, when the internal and external forces are given. In this form, of course, the problem is hopelessly complicated. However, we simplify it by following Boltzmann's procedure more closely than the other authors. Boltzmann's method consists in treating the anisotropic distribution functions as only slightly different from the isotropic Maxwell distribution. This is done by multiplying the latter distribution function by a series which progresses by powers of the velocities.

In analogy to this concept we consider the anisotropic distribution functions which are to be determined as slight modifications of a canonical ensemble. Let ϵ_p be the kinetic energy, and let I_2, I_3, and I_4 be the resultant moments

$$I_2=\sum_{j=1}^{N} p_{jx}, \quad I_3=\sum_{j=1}^{N} p_{jy}, \quad I_4=\sum_{j=1}^{N} p_{jz}. \quad (2.03)$$

[5] John G. Kirkwood, J. Chem. Phys. **14**, 180 (1946).

[6] M. Born and H. S. Green, Nature **159**, 251 (1947); Proc. Roy. Soc. London **A188**, 10 (1946) and subsequent papers.

* This distinction between the letters **N** and N is maintained throughout the paper.

[7] J. Willard Gibbs, *Collected Works of J. Willard Gibbs* (Longmans Green and Company, New York, 1931), see Vol. II, p. 9.

[8] In Kirkwood's paper it is identical with his Eq. (3)—after division by the imaginary unit—and Born and Green's Eq. (3.5), paper I, reduces to our (2.02) if N is chosen for h and if the average accelerations are replaced by the actual accelerations.

Provided the forces derive from a potential ϵ_q we shall attempt to integrate (2.02) by a series of the type

$$f=\exp(-e(\epsilon_p+\epsilon_q)) \times(a+b_1I_2+b_2I_3+b_3I_4+c\epsilon_p+\cdots). \quad (2.04)$$

Here $a, b, c, e, \cdots$ are considered to be functions of t and the q_i, the dependence on the p_i being given by the series.

If, in addition to the forces deriving from ϵ_q, there are non-conservative forces, the form (2.04) for the distribution function may be retained, provided only that the p_i are determined from the complete set of forces. This means that neither $(\epsilon_p+\epsilon_q)$ nor the I's have to be invariants of motion, since it is by no means required that (2.04) represents a case of statistical equilibrium.

A few words must be said regarding the method by which a multidimensional distribution function, say of the type (2.04), may be used to derive the actual behavior of *one* system in real space. It is well known that this represents a problem of formidable difficulty which cannot be solved in an entirely satisfactory way, even for the canonical ensemble. However, we may be led by a heuristic principle. Since the canonical ensemble represents with adequate approximation the thermo-mechanical behavior of systems at rest, we may assume the same to be true for distributions which are only slightly different from the canonical ensemble at any moment of time, and which vary with time at a sufficiently slow rate. Expressed in a different way, we shall assume that the group averages over the **N** systems of the ensemble, taken at $t=t_0$, represent with sufficient accuracy the observable time averages taken in one system over a relatively short time interval that contains t_0. This need not be true under all circumstances,[9] but will be the more adequate the slower variable the process in question is.

III. HEAT CONDUCTION

Since our object is to derive the coefficients of heat conduction and of viscosity in the shortest way, we are going to follow Boltzmann's treatment in his original paper,[3] not the more general treatment given later in his *Lectures on Gas Theory*.[10] Correspondingly, we shall treat a linear problem which depends on the x direction only (besides depending on time). Furthermore, we shall assume that the internal forces, as well as the external ones, derive from potentials which may be time-dependent. Thus we set

$$\epsilon_q=\phi^{(i)}+\phi^{(e)}=\phi, \quad (3.01)$$

and call the total energy I_1

$$I_1=\epsilon_p+\epsilon_q=\epsilon_p+\phi. \quad (3.02)$$

Now we assume for the distribution function the form

$$f(q_i, p_i, t)=\exp(-eI_1) \times(a+bI_2+c\epsilon_p+dI_2\epsilon_p+\cdots), \quad (3.03)$$

where b, c, and d are supposed to be small and where all coefficients a to e depend on t and the q_{jx} only $(j=1, 2, \cdots, N)$.

In substituting (3.03) into our fundamental Eq. (2.02) we make use of the evident relation

$$D(\varphi\psi)/Dt=(D\varphi/Dt)\psi+\varphi(D\psi/Dt), \quad (3.04)$$

and obtain a set of partial differential equations from which the coefficients in (3.03) have to be determined. In order to save space we are not going to write down these equations, but we shall introduce first the simplification by which they become treatable. Namely, we are going to assume that ϕ depends on the coordinates only in the combination

$$q=(1/N)\sum_{j=1}^{N} q_{jx}. \quad (3.05)$$

This is a very far-reaching assumption since it means smoothing out the potential in such a way that it depends only on the position of the center of mass. Later we are going to introduce the more specific assumption that the internal potential is a function of density and temperature. Since in the linear problem density and temperature change in the x direction only, it seems an adequate expression of this fact that the internal potential is a function of (3.05) and, eventually, the time. However, it is evident that this assumption cannot be legitimate unless the physical system is sufficiently limited in the x direction. Therefore we assume that it extends

[9] See reference 5, pp. 184 to 185.

[10] Ludwig Boltzmann, *Vorlesungen über Gastheorie* (Johann Ambrosius Barth, Leipzig, 1896), cf. p. 184.

from $x=-l$ to $x=+l$. The ultimate justification of the form of potential adopted lies in the fact that it leads to physically acceptable results.

With ϕ depending on t and q only, the same will be true for a, b, c, d, and e. Furthermore, we have from the principle of linear momentum

$$DI_2/Dt=-\sum_{j=1}^{N}(\partial\phi^{(e)}/\partial q_{jx})=-\partial\phi^{(e)}/\partial q. \quad (3.06)$$

Hamilton's equations of motion yield

$$DI_1/Dt=\partial\phi/\partial t, \quad (3.07)$$

and

$$D\epsilon_p/Dt=-\sum_{j=1}^{N}p_{jx}(\partial\phi/\partial q_{jx})$$
$$=-(1/N)\sum_{j=1}^{N}p_{jx}(\partial\phi/\partial q). \quad (3.08)$$

Making use of all these relations and going to third-order terms in the moments, we finally find

$$(\partial a/\partial t)-a(\partial(e\phi)/\partial t)-b(\partial\phi^{(e)}/\partial q)=0, \quad (3.09)$$

$$(\partial b/\partial t)-b(\partial(e\phi)/\partial t)=-(1/Nm)$$
$$\times[(\partial a/\partial q)-c(\partial\phi/\partial q)-a\phi(\partial e/\partial q)], \quad (3.10)$$

$$(\partial c/\partial t)-c(\partial(e\phi)/\partial t)-a(\partial e/\partial t)$$
$$-d(\partial\phi^{(e)}/\partial q)=0, \quad (3.11)$$

$$(\partial b/\partial q)-b\phi(\partial e/\partial q)-d(\partial\phi/\partial q)=0, \quad (3.12)$$

$$(\partial d/\partial t)-d(\partial(e\phi)/\partial t)-b(\partial e/\partial t)$$
$$=-(1/Nm)[(\partial c/\partial q)-a(\partial e/\partial q)$$
$$-c\phi(\partial e/\partial q)]. \quad (3.13)$$

These are five equations which would be sufficient to determine the five coefficients a to e, if ϕ were known explicitly. However, this is not the case as ϕ depends in a rather involved way on those coefficients, as will be seen.

Let us first discuss the stationary state in the absence of boundaries. With all temporal differential coefficients vanishing, it follows from (3.09) that the resultant external force must be zero. There remain: Eq. (3.12), the two equations which are obtained by setting the right-hand sides of (3.10) and (3.13) equal to zero, and a fourth equation,

$$(\partial d/\partial q)-b(\partial e/\partial q)-d\phi(\partial e/\partial q)=0, \quad (3.14)$$

which results from fourth-order terms in the moments.

These remaining four equations split into two pairs, the one pair containing only a and c, and the other pair only b and d, besides e. As a result of this situation, it would be always possible to satisfy the equations by setting $b=d=0$, no matter how a, c, and e are determined. Now the mass current and the heat current become zero with b and d (see Section V, Eqs. (5.14), (5.15)) whereas the gradients of density and temperature depend on a, c, and e only (see Section V, Eqs. (5.09), (5.13)). It follows that, evidently by our radical assumption regarding the potential, the correlation between the two sets of physical quantities has been cut for the stationary state, and it is not possible to determine, say, the heat current as a function of the temperature gradient, from the solution of the stationary state. This does not exclude the possibility of determining this correlation from the treatment of non-stationary cases, since the complete equations (3.09) to (3.13) re-establish the connection.

We shall not discuss the solution of the stationary state in detail, but we shall draw one conclusion which will prove to be of importance. We are interested only in linear terms in q, and shall, therefore, set

$$a=a_0+a_1q, \quad (3.15)$$

with corresponding equations for c, e, and $\phi^{(i)}$. We then find

$$a_1=c_0\phi_1{}^{(i)}+a_0e_1\phi_0{}^{(i)}, \quad (3.16)$$

and

$$c_1=a_0e_1+c_0e_1\phi_0{}^{(i)}. \quad (3.17)$$

With these values the density gradient and the temperature gradient can be determined by the aid of the averaging processes discussed in Section V. The result is (with $n_0=N/V$, $V=$volume)

$$\alpha=(1/n_0)(\partial n/\partial q_{1x})=-(\phi_1{}^{(i)}e_0/N)(1-\gamma),$$
$$\text{(from (5.09))}, \quad (3.18)$$

and

$$\vartheta=(1/T_0)(\partial T/\partial q_{1x})=-(\phi_1{}^{(i)}e_0/N)(\gamma/Y),$$
$$\text{(from (5.13))}, \quad (3.19)$$

whereas the temperature T_0 (i.e., for $q_{1x}=0$) is given by

$$kT_0=Y/e_0, \quad \text{(from (5.11))}. \quad (3.20)$$

The following abbreviations for dimensionless

TABLE I. Constants calculated from potential: $\varphi(r)=fr^{-\lambda}-gr^{-\mu}$.

Liquid	$r_0\times10^8$	$\varphi''(r_0)$	$(c_p)_{liq}-(c_v)_{vap}$	$\tau\times10^{12}$	D'	B^*
Mercury	6.03	527	2.27	1.29	0.141	1.29
Bromine	11.0	6.37	8.64	2.96	0.391	4.73
Carbon disulfide	12.4	1.93	8.85	3.63	0.412	4.86
Acetone	14.7	1.04	12.0	3.60	0.465	6.49
Carbon tetrachloride	16.2	0.96	11.5	6.14	0.500	6.32
Chloroform	14.0	2.11	10.3	3.94	0.454	5.61
Ethyl ether	15.7	1.03	10.9	4.26	0.486	5.97
Benzene	16.9	0.588	12.4	5.32	0.522	6.78
Ethyl alcohol	15.4	0.93	16.1	2.86	0.510	8.63
Water	10.9	1.29	16.7	1.415	0.533	8.94

numbers have been introduced:

$$\gamma=c_0/(a_0e_0Z),\quad Z=1+3Nc_0/(2e_0a_0),\quad Y=1+\gamma. \tag{3.21}$$

The important result obtained thus consists in the fact that no temperature gradient can be described by our distribution function (3.03) unless $\phi_1^{(1)}\neq0$, nor unless $c_0\neq0$. On the other hand, e_1 enters neither into the expression of α nor of ϑ. Therefore, we may assume without loss of physical generality $e_1=0$, but we may not assume $c_0=0$.

Consequently, the problem arises of determining c_0 or c_0/a_0, since a further relation between a_0 and c_0 is imposed by the constancy of $\mathbf{N}$ (see Eq. (5.06)). The determination of c_0/a_0 is achieved in the following way.

The stationary state cannot be connected with a pressure gradient, since this pressure gradient would have to be balanced by a resultant external force which we have seen must be zero. Now the pressure gradient is determined by α and ϑ in the form

$$\partial p/\partial q_{1x}=(\partial p/\partial n)n_0\alpha+(\partial p/\partial T)T_0\vartheta, \tag{3.22}$$

and the condition $\partial p/\partial q_{1x}=0$ requires, therefore,

$$-\alpha/\vartheta=(\partial p/\partial T)T_0/(\partial p/\partial n)n_0=D. \tag{3.23}$$

The pure number D is calculable if the equation of state is known, and we are going to show in Section VI how D follows from our theory (Eq. (6.03)). It is a number smaller than 1 (see Table I) which assumes the limiting value $D=1$ for ideal gases.

Now c_0/a_0 becomes calculable by the substitution of (3.18) and (3.19) into (3.23). There are two solutions, but one has to be excluded on physical grounds. Setting

$$\zeta=D/2+[1+(D/2)^2]^{\frac{1}{2}}, \tag{3.24}$$

we find

$$\gamma=\zeta,\quad Y=1+\zeta,\quad Z=-(2/(3N\zeta))/(1-2/(3N\zeta)), \tag{3.25}$$

and, consequently,

$$c_0/a_0=-(2e_0/3N)/(1-2/(3N\zeta)). \tag{3.26}$$

We have the somewhat surprising result that c_0/a_0 turns out to be a constant which does not depend at all on the temperature gradient. Since this is so, this same value has to be used for the system in equilibrium when there is no density gradient nor a temperature gradient (i.e., when $\phi_1^{(1)}=0$). Calling a distribution function with $c_0\neq0$ a non-Maxwellian one, we see that our distribution function has to be non-Maxwellian in order to be, so to spreak, predestinated for describing temperature gradients. This feature distinguishes our multidimensional treatment from Boltzmann's where there was no necessity of introducing a coefficient corresponding to c_0.

Now we are prepared to approach the solution of the time-dependent Eqs. (3.09) to (3.13). It would, of course, be desirable to treat them with definite boundary conditions. This, however, would require going to terms of at least second order in q, and thereby the evaluation of the average values becomes extremely involved. For our purpose it is sufficient to find *any* solution which involves a heat flow. No such solution linear in q can be found which makes the resultant external force zero. This is physically evident, since any change in the density and temperature distribution will affect the position of the center of mass, and therefore requires external forces. In a realistic case those forces would be provided by the pressure reaction of the walls at $x=-l$ and $x=+l$. But we do not treat boundary conditions here, and therefore it is simpler to assume the external forces in the form of volume forces derivable from a potential, as we have done.

A simple way of producing molecular flow consists in subjecting the fluid to a time-dependent linear external potential (creation, or annihilation, of a gravitational field). It is in this form

that the problem was first treated.[4] However, the calculations become much simpler if the decay of any existing perturbation is studied, i.e., if a solution asymptotic in time is sought.

Thus we try to solve our equations by expressions of the form

$$a=a_0+a_1\exp(-t/\tau)q \tag{3.27}$$

for a, c, and $\phi^{(i)}$, and by expressions of the form

$$b=b_0\exp(-t/\tau) \tag{3.28}$$

for b and d. Here the coefficients a_0, a_1, $\cdots$ are supposed to be constants. Only for the external potential we assume the form

$$\phi^{(e)}=(1/2)\phi_2{}^{(e)}q^2. \tag{3.29}$$

Making $\phi^{(e)}$ of the order q^2 (which is otherwise neglected) represents an artifice that provides at the same time the required external force and does not otherwise interfere with the internal molecular processes. $\phi^{(e)}$ is only apparently independent of time, since q is itself of the order $\exp(-t/\tau)$ and disappears at the same rate as the density gradient.

Full generality would require to assume e also in the form indicated by (3.27). However, the subsequent averaging processes show that the heat current and the gradients of density and temperature come out independent of e_1. Therefore, much work of calculation can be saved by setting $e=e_0$ from the beginning.

The complete asymptotic solution becomes

$$a_1=(a_0e_0-rc_0)\phi_1{}^{(i)}/(1-r), \tag{3.30}$$

$$c_1=c_0e_0\phi_1{}^{(i)}/(1-r), \tag{3.31}$$

$$b_0=(\tau/Nm)(a_0e_0-c_0)\phi_1{}^{(i)}/(1-r), \tag{3.32}$$

$$d_0=(\tau/Nm)c_0e_0\phi_1{}^{(i)}/(1-r), \tag{3.33}$$

with

$$r=-\phi_2{}^{(e)}\tau^2/Nm. \tag{3.34}$$

Using these values we find from Section V, Eqs. (5.09) and (5.13)

$$\alpha=(r/(1-r))(\phi_1{}^{(i)}e_0/N)(1-\gamma)\exp(-t/\tau) \tag{3.35}$$

and

$$\vartheta=(r/(1-r))(\phi_1{}^{(i)}/N)(\gamma/Y)\exp(-t/\tau), \tag{3.36}$$

where γ, Z, and Y have been defined in (3.21).

A comparison between (3.18), (3.19) on the one hand, and (3.35), (3.36) on the other, shows that the parameter $D=-\alpha/\vartheta$ is the same in the case of the asymptotic solution as in the stationary case. Hence asymptotically there is no pressure gradient.

The heat current (Section V, Eq. (5.15)) becomes

$$H_x=(5/2)(N/Ve_0)(\phi_1{}^{(i)}\tau/Nm)\times(\gamma/(1-r))\exp(-t/\tau). \tag{3.37}$$

From (3.36) and (3.37) it is seen that the heat current and the temperature gradient have, asymptotically, the same time dependence, and consequently their ratio is a constant. The coefficient of heat conduction will be completely known as soon as r and τ are determined.

The number r can be obtained by correlating the internal potential $\phi^{(i)}$, as used until now in phase space, with the internal energy, $U=Nu$, of one of the systems in real space. To begin with the latter, we introduce now the assumption that it depends only on n and T. Therefore we have

$$U_1=\partial U/\partial q_{1x}=(\partial U/\partial n)n_0\alpha+(\partial U/\partial T)T_0\vartheta =[-Dn_0(\partial U/\partial n)+T_0(\partial U/\partial T)]\vartheta. \tag{3.38}$$

It will be convenient to introduce a dimensionless parameter

$$B^*=[-Dn_0(\partial U/\partial n)+T_0(\partial U/\partial T)]/(NkT_0), \tag{3.39}$$

and write (3.38) in the form

$$U_1=B^*NkT_0\vartheta. \tag{3.40}$$

If U is known as a function of n and T for the system in equilibrium, the parameter B^* is calculable. We shall show in Section VI how it can be determined in our theory (Eq. (6.07)). B^* is a positive number with values between 1 and 10 (see Table I).

According to the general statistical principles we obtain U_1 also by averaging $\phi_1{}^{(i)}\exp(-t/\tau)$ over all coordinates except q_{1x}. This yields, of course, $\phi_1{}^{(i)}\exp(-t/\tau)$ since $\phi_1{}^{(i)}$ is a constant.

However, there is a difference in sign between $\phi_1{}^{(i)}$ and U_1. This we see by comparing (3.40) with (3.19). If ϑ is positive, $\phi_1{}^{(i)}$ will be negative, but U_1 will be positive as all other quantities involved in the two equations are essentially positive. The reason for this difference is that (with ϑ positive) U_1 increases in the positive x direction, but the center of mass is displaced in the negative x direction.

Therefore, we have to equate

$$B^*NkT_0\vartheta = -\phi_1^{(i)} \exp(-t/\tau). \quad (3.41)$$

Substituting into this equation the value of ϑ from (3.36) and Y/e_0 from (3.20), we obtain an equation from which τ is easily determined as

$$\tau = -(1/Q), \quad Q = B^*\gamma - 1. \quad (3.42)$$

Q is a positive number of the order of 1 to 10.

With the value of τ just determined the coefficient of heat conduction, σ, becomes

$$\sigma = -H_x/(\partial T/\partial q_{1x}) = (5Q/2) \times (NkT/V)(R/\mu)(\tau/Y), \quad (3.43)$$

(μ = molecular weight).

Before we proceed to the determination of τ it may be of interest to go to the limit for ideal monatomic gases. In this case we have $D=1$, and therefore $\gamma = 1.62$, $Y = 2.62$ (from (3.24) and (3.25)), $B^* = \frac{3}{2}$ (from (3.39)), and $Q = 1.43$ (from (3.42)). Hence

$$\sigma = 3.57p(R/\mu)(\tau/Y), \quad (3.44)$$

and this might be compared with the corresponding formula in Maxwell's theory[11]

$$\sigma = 3.75p(R/\mu)\tau. \quad (3.45)$$

Both are identical in structure and almost coincide if Maxwell's time of relaxation (for second-order spherical harmonics) is identified with our τ/Y. Naturally, our formula (3.44) does not determine σ since τ is not known yet, and cannot be determined for gases unless we are willing to go back to Boltzmann's equation.[12] However, it is evident that if the internal potential is known, τ cannot remain undetermined, since the entire system is mechanically determined.

For liquids we may determine τ by specializing the perturbation which forms the initial state of our asymptotic solution. Let us assume, then, that we have a liquid under conditions of equilibrium, i.e., with uniform density and temperature. Now let us single out at random a large number, say N_1, of mass points which are supposed to be separated from each other by more than one average distance. The singled out mass points form a subsystem, and it is this subsystem which we are considering and to which we are applying our analysis. This is perfectly legitimate if the action of the other $(N-N_1)$ mass points on the N_1 distinguished ones is taken into account by an external, time-dependent potential, such as we have admitted throughout.

Finally, let us imagine that a perturbation is created in the following way. Let each of the particles of the subsystem be displaced in the positive x direction by a small distance ξ, and then all of them released at the same moment. This is, of course, a highly artificial perturbed state, and no procedures for actually producing it are available. However, if τ can be determined from any assumptions which are not contradictory in themselves, the value so obtained should have general validity. Our assumption is certainly not more artificial than Boltzmann's fiction of a "perfectly ideal case" where everywhere in a gas at a given moment the distribution function is supposed to be the same, but different from Maxwell's.[13]

We now proceed to calculate the average non-balanced force which will be active at the moment of release. Let us first consider one of the displaced N_1 mass points. We split its potential into two parts, φ and φ^*, where φ is due to the nearest neighbor only, and φ^* to the other $(N-2)$ mass points. The non-balanced force will be given, anyway with reasonable approximation, by φ alone, whereas φ^* causes the "damping" which leads to an exponential decrease.

As for φ, it may, again with reasonable approximation, be expressed by the first two terms of its development about the position of the minimum,[14] i.e., by

$$\varphi(r) = \varphi(r_0) + (1/2)\varphi''(r_0)r^2. \quad (3.46)$$

In consequence of the displacement ξ the potential (3.46) takes the form

$$\varphi(r) = \varphi(r_0) + (1/2)\varphi''(r_0)(r_1^2 + 2x_1\xi + \xi^2), \quad (3.47)$$

where r_1 and x_1 refer to the undisplaced position.

If now (3.47) is averaged over the N_1 displaced mass points, the first two terms will give

[11] Compare reference 10, Eqs. (219) and (239).

[12] Kirkwood and Born and Green have shown that the Boltzmann equation can be obtained from their general statistical treatment by suitable specialization. John G. Kirkwood, J. Chem. Phys. **15**, 72 (1947); M. Born and H. S. Green, Proc. Roy. Soc. London **A188**, 10 (1946), see Appendix I.

[13] Ludwig Boltzmann, reference 10, p. 164 and subs.

[14] Regarding this assumption, compare the discussion at the end of the paper.

rise to no resultant force since it was assumed that the liquid was in equilibrium before the displacements took place. The term $2x_1\xi$ cancels out because $\bar{x}_1=0$ if the N_1 mass points were picked out at random. Consequently, there remains only the last term which gives rise to an average non-balanced force, and this is an external force from the point of view of the subsystem. Hence this force derives from a potential (per particle) given by

$$\varphi^{(e)}=(1/2)\varphi''(r_0)\xi^2. \tag{3.48}$$

Since ξ is identical with the displacement of the center of mass of the subsystem, we have now for the subsystem exactly the situation that was assumed previously for the total system (see Eq. (3.29)).

There remains one important difference insofar as φ^* contains internal as well as external contributions. However, it follows from our Eqs. (3.09) to (3.13) that only the total potential enters into them. Therefore, this total potential may as well be split into the two parts $N_1\varphi$ and $\phi^*=N_1\varphi^*$, as into its internal and external parts. Consequently, our asymptotic solution (3.30) to (3.34) remains valid if we replace everywhere, N by N_1, q by ξ, $\phi^{(i)}$ by ϕ^*, and $\phi_2^{(e)}/N$ by $\varphi''(r_0)$. Thus we obtain finally (from (3.42) and (3.34))

$$\tau=[m/(Q\varphi''(r_0))]^{\frac{1}{2}}. \tag{3.49}$$

A few words have to be said regarding the validity of this derivation of τ. The procedure would be entirely legitimate if it might be assumed that the same pairs of mass points remain nearest neighbors. This, of course, is not the case for indefinite times, but for the short times involved in the decay of the perturbation the assumption seems plausible and should not lead to serious errors since only the *average* behavior is studied. The correlation between the local behavior (which determines τ), and the behavior of the liquid in bulk (as described by observable coefficients) is rigorously given by our theory.

It should be mentioned that our asymptotic solution involves a resultant mass current given, from (5.14), by

$$j_x=(nm/e_0a_0Z)(b_0+(3N+2)d_0/2e_0)\times\exp(-t/\tau). \tag{3.50}$$

The ordered velocity $u=\langle p_{1x}\rangle_{\text{av}}/m$ has to be taken into account in the calculation of the average values (Section V). It could be reduced to zero if a further term $g(\epsilon_p)^2$ is introduced into the distribution function (3.03).

IV. VISCOSITY

The treatment of viscosity is so similar to that of heat conduction that we can be short. There are only two points which have to be mentioned as being different. The first of them is that it does not seem to be possible to solve the complete set of equations without taking into account heat conduction at the same time. Thus, if there is a flow in the x direction and a velocity gradient in the y direction (which is the case we are going to treat), it becomes necessary to introduce a temperature gradient (and consequently a heat flow) in the y direction. This is evidently an expression of the fact that viscosity is a dissipative process, and that the heat generated has to be conducted away.

The second point of difference is that it becomes necessary to introduce non-conservative forces, since tangential surface forces cannot be represented by a potential.

These considerations lead to the following form of distribution function which is slightly different from the one used by Boltzmann in the case of viscosity:

$$f(q_i, p_i, t)=\exp(-eI_1)\times(a+bI_2+c\epsilon_p+fI_2I_3+dI_2\epsilon_p+\cdots). \tag{4.01}$$

To make the solution self-consistent[15] additional terms of the form $b'I_3+d'I_3\epsilon_p$ would have to be added in order to represent the heat current in the y-direction. However, this part of the problem has been treated in Section III. For simplicity we disregard the transverse heat current, though our solution will show a corresponding temperature gradient.

The assumptions regarding the forces are:

(a) There is an internal potential $\phi^{(i)}$ depending only on

$$q'=(1/N)\sum_{j=1}^{N}q_{jy}; \tag{4.02}$$

[15] We mean by this term that *all* equations at which we arrive by our procedure can be solved only with $b'\neq 0$ and $d'\neq 0$.

(b) There are non-conservative external forces in the x direction, X_j, equal on each mass point, and giving rise to a resultant external force X. These forces represent a convenient idealization of the external tangential surface forces which are required to maintain or produce a one-dimensional viscous flow;

(c) There are no forces in the z direction.

With these assumptions (3.07) and (3.08) are changed into

$$DI_1/Dt=(\partial\phi^{(i)}/\partial t)+(1/m)\sum_{j=1}^{N} p_{jz}X_j, \quad (4.03)$$

and

$$D\epsilon_p/Dt=(1/m)\times\sum_{j=1}^{N}[p_{jz}X_j-p_{jy}(\partial\phi^{(i)}/\partial q_{jy})]. \quad (4.04)$$

Otherwise the procedure remains the same as in Section III and we obtain five equations for the determination of our coefficients. Two of them are identical with (3.09) and (3.11), and the three additional equations are

$$(\partial b/\partial t)-b(\partial(e\phi)/\partial t)+(1/m)(c-ae)X_j=0, \quad (4.05)$$

$$(\partial f/\partial t)-f(\partial(e\phi)/\partial t)+(1/Nm)\times[(\partial b/\partial q')-b\phi^{(i)}(\partial e/\partial q')]=0, \quad (4.06)$$

and

$$(\partial d/\partial t)-d(\partial(e\phi)/\partial t)-b(\partial e/\partial t)-(ce/m)X_j=0. \quad (4.07)$$

In order to find an asymptotic solution we introduce expressions of the form

$$a=a_0+a_1\exp(-t/\tau)q' \quad (4.08)$$

for a, c, and $\phi^{(i)}$, and expressions of the form

$$b=b_0\exp(-t/\tau)+b_1\exp(-2t/\tau) \quad (4.09)$$

for b and d. Furthermore, we assume

$$X_j=X_0\exp(-t/\tau), \quad (4.10)$$

and

$$f=f_0\exp(-2t/\tau). \quad (4.11)$$

We simplify our treatment again by assuming $e=e_0=$const., since it can be shown that e_1 affects neither the velocity gradient, $\partial u/\partial y$, nor the tangential stress, X_y.

The asymptotic solution becomes

$$a_1=a_0e_0\phi_1^{(i)}+r'(c_0-a_0e_0), \quad (4.12)$$

$$c_1=c_0e_0\phi_1^{(i)}-r'c_0e_0, \quad (4.13)$$

$$b_0=(\tau/m)(c_0-a_0e_0)X_0, \quad (4.14)$$

$$b_1=b_0e_0\phi_1^{(i)}-(\tau/m)r'e_0(2c_0-a_0e_0)X_0, \quad (4.15)$$

$$d_0=-(\tau/m)c_0e_0X_0, \quad (4.16)$$

$$d_1=d_0e_0\phi_1^{(i)}+(\tau/m)r'c_0e_0^2X_0, \quad (4.17)$$

and

$$f_0=(\tau/2Nm)[b_0e_0\phi_1^{(i)}-(\tau/2m)r'e_0\times(2c_0-a_0e_0)X_0], \quad (4.18)$$

where r' is defined by

$$r'=X_0X\tau^2/mq'. \quad (4.19)$$

With the values (4.12) and (4.13) we find by the methods of Section V (Eqs. (5.09) and (5.13))

$$\alpha=-(r'e_0/N)(1-\gamma)\exp(-t/\tau), \quad (4.20)$$

and

$$\vartheta=-(r'e_0\gamma/NY)\exp(-t/\tau). \quad (4.21)$$

These expressions show that α/ϑ retains its previous value, $-D$, and that τ must be the same as in Section III. Furthermore, (4.20) and (4.21) lead to a determination of r' in a similar way as r was determined in Section III. We only have to substitute the new value of ϑ into (3.41), and obtain

$$r'=\phi^{(i)}/B^*\gamma. \quad (4.22)$$

In calculating $\partial u/\partial y$ (see Section V, Eq. (5.16)) we make use of b only, not of d, since X_y is also calculated in the first-order approximation, only f_0 being available. Thus we find

$$\partial u/\partial y=-(b_0/a_0Z)(\phi_1^{(i)}/NB^*)\times(1-\gamma/2)\exp(-2t/\tau), \quad (4.23)$$

and (from (5.19))

$$X_y=n_0(b_0/a_0e_0Z)(\phi_1^{(i)}/N)(\tau/2)\times(1-\gamma/2B^*)\exp(-2t/\tau). \quad (4.24)$$

Finally, we obtain for the coefficient of viscosity, η, the value

$$\eta=n_0kT(B^*\tau/2Y)(1-\gamma/2B^*)(1-\gamma/2). \quad (4.25)$$

In the limiting case of ideal gases this yields $\eta=1\cdot21p(\tau/Y)$ as compared with Maxwell's value $\eta=p\tau$. It might also be remarked that the

time of relaxation of a local disturbance involving a velocity gradient is half as large as that of a disturbance involving a temperature gradient (compare (4.24) with (3.36)). This also finds it counterpart in Maxwell's theory where the time of relaxation for second-order terms ($\partial u/\partial y$ and X_y) is only $\frac{2}{3}$ of the time of relaxation for third-order terms (as ϑ). Naturally Maxwell's results are exact for the force law adopted by him; ours are average values for any force law.

V. AVERAGE VALUES

According to the statistical method used here, distribution functions in phase space of the form (2.04) become distribution functions in real space—even if they are time-dependent—after integration with regard to all coordinates and moments, except those belonging to one mass point, say, the one with index 1. The integrations with regard to the moments can always be performed, those with regard to the coordinates become involved, even if our simplification is introduced that the potential depends only on the coordinates of the center of mass. However, the results become quite simple when all expressions are restricted to linear terms in the coordinates, as was done in our treatment so far.

A further important simplification arises if the coefficient e may be treated as a constant.[16]

The fundamental integral for all following calculations is

$$J_0=\int_{-\infty}^{+\infty}\exp(-e_0\epsilon_p)d\tau_p=(2\pi m/e_0)^{3N/2}. \quad (5.01)$$

From this, by the usual procedure of differentiation with regard to e_0, we obtain

$$J_1=\int_{-\infty}^{+\infty}\exp(-e_0\epsilon_p)\epsilon_p d\tau_p$$
$$=(3N/2e_0)(2\pi m/e_0)^{3N/2}, \quad (5.02)$$

and so forth. By the aid of these integrals and similar ones, all integrations with regard to the moments can easily be performed if it is remembered that all odd powers of moments yield zero upon integration.

We begin with our first distribution function (3.04). If we assume linear expressions of the form (3.15) for ϕ and the coefficients and if we develop to the first order in q, the number of systems in the cell $d\tau=d\tau_q d\tau_p$ will be given by

$$d\mathbf{N}_{p,q}=\exp(-e_0(\epsilon_p+\phi_0))$$
$$\times[a_0+a_1'q+(b_0+b_1'q)I_2$$
$$+(c_0+c_1'q)\epsilon_p+(d_0+d_1'q)I_2\epsilon_p]d\tau. \quad (5.03)$$

Here we have set

$$a_1'=a_1-a_0e_0\phi_1, \quad b_1'=b_1-b_0e_0\phi_1, \quad \cdots. \quad (5.04)$$

If we now integrate with regard to all moments and with regard to all coordinates except those of one mass point, we obtain *the number of systems in the ensemble* for which the first mass point is in the cell $d\tau_{q_1}$, namely

$$d\mathbf{N}_{q_1}=\exp(-e_0\phi_0)V^{N-1}(2\pi m/e_0)^{3N/2}$$
$$\times[(a_0+3Nc_0/2e_0)$$
$$+(a_1'+3Nc_1'/2e_0)q_{1x}/N]d\tau_{q_1}. \quad (5.05)$$

Performing the last three integrations we obtain the total number of systems

$$\mathbf{N}=\exp(-e_0\phi_0)V^N(2\pi m/e_0)^{3N/2}a_0Z, \quad (5.06)$$

where Z is defined in (3.21).

Now, from the basic assumption mentioned at the beginning of this section, we have

$$d\mathbf{N}_{q_1}/\mathbf{N}=dN_{q_1}/N, \quad (5.07)$$

where dN_{q_1} is *the number of mass points in one system* found in the cell $d\tau_{q_1}$ in real space. Equation (5.07) symbolizes the transition from the distribution function in phase space to the density distribution in real space. Thus we find, by dividing (5.05) by (5.06) and taking into account the definition of Z (3.21),

$$dN_{q_1}=n_0(1+\alpha q_{1x})d\tau_{q_1}, \quad (5.08)$$

where

$$\alpha=(1/(a_0ZN))(a_1'+3Nc_1'/2e_0) \quad (5.09)$$

is the local density coefficient previously used.

In calculating the temperature distribution, the mass current density j_x, and the heat current density, H_x, we have introduced a second viewpoint of approximation (besides limiting ourselves to first-order terms in q). Since the

[16] The result mentioned previously that the averages of physical significance such as α, ϑ, $\partial u/\partial y$, and X_y do *not* depend on e_1, is, of course, based on calculations which assume e in the form $e=e_0+e_1q$, etc. However, there is no reason to reproduce these more involved calculations, since the assumption $e_1=0$ leads to the same results.

deviation of our distribution function from the canonical form is supposed to be small, we have treated the coefficients, with the exception of a_0, as small quantities, products of which may be disregarded. This represents a first approximation only (since c_0 is finite, though small), and we have carried through the calculation for the temperature without this simplification. These calculations show that second-order terms having c_0 as one of their factors affect the results, leading to expressions for the constants (3.25) which are modified. However, the numerical difference does not amount to more than a few percent. Therefore, it seemed legitimate to accept the second viewpoint of approximation since, otherwise, it would have been necessary to introduce a further term, $g(\epsilon_p)^2$, into the distribution function, and this would have made the evaluation greatly more involved.

The temperature has to be defined by

$$3kT/2=(1/2m)\times\langle[(p_{1x}-\tilde{p}_{1x})^2+p_{1y}^2+p_{1z}^2]\rangle_N; \quad (5.10)$$

however, since $\tilde{p}_{1x}$ is a small quantity, it leads to a second order modification only and may be suppressed. We find (without neglected terms)

$$3kT/2=(3/2e_0)[1+(1/(a_0e_0Z))\times(c_0+c_1'q_{1x}/N)/(1+\alpha q_{1x})]. \quad (5.11)$$

From the second viewpoint of approximation the term in α may be neglected. This leads to

$$T=T_0(1+\vartheta q_{1x}), \quad (5.12)$$

where T_0 is given by (3.20) and ϑ by

$$\vartheta=\gamma c_1'/(c_0NY). \quad (5.13)$$

The constants γ and Y have been defined by (3.21), and have been determined previously (3.25).

As far as the mass current and the heat current are concerned, we require only the zero terms. By similar procedures as above, it is found in our approximation

$$j_x=n_0(m/(a_0e_0Z))(b_0+(3N+2)d_0/2e_0) \quad (5.14)$$

and

$$H_x=(5/2)n_0d_0/(e_0^3a_0Z). \quad (5.15)$$

In the calculation of H_x naturally everywhere $(p_{1x}-\tilde{p}_{1x})$ has to be substituted for the x-component of the moment. Furthermore, only that contribution has to be taken into account which is due to molecular motion whereas the contribution which is due to molecular interaction may be neglected. For the asymptotic solution of Section III (Eqs. (3.30) to (3.34)) the latter is of second order in $\exp(-t/\tau)$. In spite of this fact the heat current turns out to be essentially due to the existence of an internal potential since it vanishes with $\phi_1^{(i)}$ (see Eqs. (5.15) and (3.33)).

We now turn to the averages based on the distribution function (4.01). The calculations of density and temperature remain the same as above since (4.01) and (3.04) are identical as far as the terms contributing to the density and temperature are concerned. In determining $\partial u/\partial y$ and X_y we have to retain second-order terms in the small coefficients, since these quantities are of the second order themselves. However, the d term has not been considered for the reason given above (see p. 192). We find for the velocity gradient

$$\partial u/\partial y=(1/(a_0e_0Z))(b_1'/N-b_0\alpha). \quad (5.16)$$

The tangential stress, X_y, is defined by

$$X_y=\langle(n/m)(p_{1x}-\tilde{p}_{1x})(p_{1y}-\tilde{p}_{1y})\rangle_N. \quad (5.17)$$

Here again the term due to molecular interaction vanishes since the asymptotic solution of Section IV (Eqs. (4.12) to (4.17)) involves no *internal* forces in the x-direction. However, the tangential stress X_y has its origin in the internal and external forces (see Eqs. (5.19) and (4.18)).

Equation (5.17) may be replaced in our approximation by

$$X_y=(n_0/m)\langle p_{1x}p_{1y}\rangle_N \quad (5.18)$$

and leads to

$$X_y=n_0mf_0/(e_0^2a_0Z). \quad (5.19)$$

VI. COMPARISON WITH EXPERIMENT

In order to evaluate the coefficients of heat conduction and viscosity numerically, we still have to determine the dimensionless numbers D and B^* which have been introduced. They can be calculated if the equation of state of the liquid is known, and we are going to use the relations established in I.

The parameter D is defined by (3.23), and we take the partial differential coefficients from I,

Eqs. (6.04) to (6.06). Thus we find

$$\partial p/\partial T = nk - (\partial^2 U/\partial T^2) = aB \qquad (6.01)$$

and

$$(\partial p/\partial n)n = nkT + V(\partial^2 U/\partial V^2) = B, \qquad (6.02)$$

where a is the coefficient of thermal expansion, and B is the bulk coefficient.

Consequently D, given by (3.23) becomes, by the insertion of (6.01), (6.02),

$$D = aT. \qquad (6.03)$$

Hence D depends on the coefficient of expansion only. With D known our numbers γ, Z, and Y become calculable ((3.24) and (3.25)).

To determine B^* we first evaluate $\partial U/\partial n$ and $\partial U/\partial T$. From I, Eq. (6.04) we have

$$(\partial U/\partial n)n = -V(\partial U/\partial V) = -NkT(1-\delta), \qquad (6.04)$$

where δ is defined by

$$\delta = pV/(NkT) = p/(nkT), \qquad (6.05)$$

and is a very small number which has been neglected in the following calculations.

Furthermore, we have from I, Eq. (6.10)

$$(\partial U/\partial T)T = [(\partial/\partial T)(kN_0T - L^*)]T, \qquad (6.06)$$

where L^* is the molar heat of vaporization, provided N_0 refers to a mole of liquid. Consequently, from the definition (3.39)

$$B^* = D(1-\delta) + (1 - (\partial L^*/\partial T)/R). \qquad (6.07)$$

Thereby B^* is reduced to observable quantities, and so is Q (3.42).

We can express B^* still in another way. From a well-known relation we have

$$\partial U/\partial T = (c_p^*)_{\text{liq}} - (c_v^*)_{\text{vap}}, \qquad (6.08)$$

where $(c_p^*)_{\text{liq}}$ and $(c_v^*)_{\text{vap}}$ are the respective molar heats. That yields

$$B^* = D(1-\delta) + [(c_p^*)_{\text{liq}} - (c_v^*)_{\text{vap}}]/R, \qquad (6.09)$$

and this form is particularly suited for theoretical calculations since $[(c_p^*)_{\text{liq}} - (c_v^*)_{\text{vap}}]$ is directly given by our theory (I, Eqs. (6.09) and (8.16)).

So far, no special form for the potential of molecular interaction, $\varphi(r)$, had to be assumed, since the equations used are general consequences of our theory. The knowledge of $\varphi(r)$ is required only for the evaluation of τ, and, naturally, for the eventual theoretical calculation of the empirical constants involved in (6.03) and (6.09). The time of relaxation itself is calculable from (3.47), after r_0, the position of the minimum has been determined from the potential itself.[17]

TABLE II. Comparison of calculated and observed values of coefficients of heat conduction and viscosity.

Liquid	$\sigma\times10^4$ calc.	t°C	obs.	t°C	$\eta\times10^3$ calc.	t°C	obs.	t°C
Mercury	(0.2)	357	385	149	1.61	357	9.21	340
Bromine	1.03	58.8	—	—	2.56	58.8	7.21	56.4
Carbon disulfide	2.24	46.3	3.82	30	2.61	46.3	3.17	46
Acetone	3.45	56.5	4.14*	56.5	2.85	56.5	2.49	54
Carbon tetrachloride	1.73	76.8	2.4	68	3.68	76.8	4.86	77
Chloroform	1.44	61.2	2.88	12	2.48	61.2	4.67	40
Ethyl ether	2.02	34.6	3.28*	34.6	2.09	34.6	2.13*	35
Benzene	3.48	80.1	3.33	12	3.68	80.1	3.29	80
Ethyl alcohol	6.40	78.4	4.16	75	4.07	78.4	4.46	78.3
Water	32.6	100	16.3	100 23 atm.	7.04	100	2.85	100

* Numbers with asterisks are interpolated.

It might be pointed out that the ratio σ/η is free of τ and is reduced to observable data by (6.03) and (6.09). Hence σ/η can be evaluated from experimental evidence otherwise obtained. However, we intend to apply the much more rigorous test of calculating σ and η separately.

In Part I we have determined the potentials φ for 10 test liquids (Part I, Table II), so it becomes possible to calculate σ and η from these potentials without using any empirical data nor adapting any constant. Evidently this is the most severe test that can be put upon the theory.

In Table I we have collected the values of r_0, $\varphi''(r_0)$, $[(c_p^*)_{\text{liq}} - (c_v^*)_{\text{vap}}]$, τ, D, and B^* which are used in the further calculations. We stress once more the fact that the constants in Table I are exclusively based on theoretical values though these are, in some cases, affected by considerable errors, as may be seen from I, Table I.[18]

In Table II the theoretical values of σ and η are compared with the observed ones. The calculations refer to the "standard temperatures" used in Parts I and II, i.e. the temperatures of the boiling point at 1 atmos. Observed values are

[17] The position of the minimum, r_0, should be well distinguished from r_1, the average distance of two nearest neighbors for given density and temperature. The latter quantity was called σ_0 in I and II, and the difference between r_0 and $r_1 = \sigma_0$ appears from a comparison between Table I of this paper and Table II of I.

[18] The theoretical values for $[(c_p^*)_{\text{liq}} - (c_v^*)_{\text{vap}}]$ are not listed in I, but they were implied in the calculations which led to the evaluation of $(c_p)_{\text{liq}}$.

not in all cases known for these temperatures, and therefore the temperatures to which the observations refer are indicated. In some cases (marked by asterisks) the observed values are interpolated.

It will be observed that for seven of the 10 liquids the agreement, though far from quantitative, is about as good as might be expected from the approximate nature of some of the evaluations. Also, the strong temperature dependence of η should be taken into account. Water shows considerably larger deviations, as it did in the calculations of I and II and as might be accounted for by its anomalous nature. That the calculated values of η for Br and particularly for Hg are so much too small seems to indicate a systematic error in our final formulas (though not necessarily in our theory).

Table I shows that Br has a larger value of $\varphi''(r_0)$, and Hg a very much larger one, than any of the other liquids. In the opinion of the author this fact indicates that these high values of $\varphi''(r_0)$ account for the large deviations. These may be caused by one of two facts, or by both of them. On the one hand, the procedure of approximating the intermolecular potential by a parabola (see (3.48)) may be quite inadequate if the curvature is large. On the other hand, it may not be legitimate to neglect second-order terms in q when $\varphi''(r_0)$ is large. It must be recalled that the presence of the external potential was completely neglected in the calculations of the averages which were carried to the first order in q. Naturally, this omission will be the more serious the larger the second-order term $\varphi''(r_0)$ is.

It is regrettable that σ for Br is not observed, since from a comparison of σ/η between theory and experiment it might be inferred whether it is really the theoretical value of τ that causes the discrepancy. In the case of Hg the ratio σ/η does not teach us anything since the heat conduction is electronic for this metal. We have added the calculated value of σ in brackets to show how large the discrepancy becomes when our model does not represent the mechanism at all.

It might be pointed out in this connection that, of the seven liquids where the agreement is reasonably good, chloroform shows the largest deviations and the largest $\varphi''(r_0)$. Looking at Table I we see that this liquid falls somewhat out of line, particularly if it is compared with the related carbon tetrachloride. A value of $\varphi''(r_0)$ near 1 would appear much more probable, and would do away with a great part of the deviation. It was stated in I, p. 474 that the exponents λ and μ of the potential can be chosen within rather wide limits without affecting the results there obtained. Maybe the choice of λ and μ for chloroform was particularly unhappy.

The systematic deviations exhibited by Br and Hg show the desirability of extending the approximations to second-order terms (from both view points of approximation). This, however, means a rather formidable task.

If we summarize the results of our three papers on the statistical theory of liquids, it can be stated that it correlates practically the complete behavior of liquids. One and the same potential, with its four constants, represents in an almost quantitative way ten empirical constants: heat of vaporization, specific heat, coefficient of expansion, bulk coefficient, vapor pressure, surface tension, heat conduction, viscosity, and the Eötvös and Kamerling Onnes constants. Though the agreement is far from completely satisfactory in all instances, this is presumably due not to the fundamental features of our model but to the specific choice of the potential used and to the approximate evaluations carried through.

Letters to the Editor

PUBLICATION of brief reports of important discoveries in physics may be secured by addressing them to this department. The closing date for this department is five weeks prior to the date of issue. No proof will be sent to the authors. The Board of Editors does not hold itself responsible for the opinions expressed by the correspondents. Communications should not exceed 600 words in length.

On the Cs^{137} Disintegration Scheme

ALLAN C. G. MITCHELL AND CHARLES L. PEACOCK
Indiana University, Bloomington, Indiana
November 23, 1948

THE beta- and gamma-ray spectrum of Cs^{137} (33 yrs.) has been measured by Townsend, Owen, Cleland, and Hughes[1] who find that the beta-ray spectrum is simple with an end point at 0.550 Mev. In addition, there is only one gamma-ray of energy 0.663 Mev which is internally converted. Later, Townsend, Cleland, and Hughes[2] showed that there were no coincidences between the beta- and gamma-rays and proved that the beta-disintegration leads to a metastable state of Ba^{137} which has a half life of 158 ± 5 sec. The gamma-ray is emitted from this metastable state.

In this laboratory various groups have been using the Cs^{137} internal conversion line for calibration purposes and have some additional information to add to this problem.

We have confirmed (with J. L. Meem, Jr. and F. Maienschein) that there are no beta-gamma-coincidences. The half-life of the Ba^{137} metastable state has been measured and a value of 156 ± 3 secs. obtained, in agreement with the earlier work.

The K and L internal conversion lines of the 0.663 Mev gamma-ray have been resolved and the ratio N_K/N_L has been determined by several investigators. The best value for this ratio is 4.8 ± 0.3. In addition, the internal conversion coefficient α_K has been measured and is 11.8 percent.

From this information, the spin change connected with the transition from the metastable state of Ba^{137} to the ground state can be calculated. From the curves of Hebb and Nelson,[3] for the value of Z^2/E associated with this gamma-ray, a value of $N_K/N_L=4.8$ is obtained for a spin change $\Delta l=5$ and 6.6 for a spin change of 4. The experimental value $N_K/N_L=4.8$ indicates that the spin change is $\Delta l=5$.

The internal conversion coefficient can be calculated as a function of spin change from the theory of Dancoff and Morrison. One obtains the following values for $\alpha_K{}^l$, for electric multipole radiation: 2.19, 5.80, 15.15, 39.2 percent for $\Delta l=3$, 4, 5, and 6, respectively. For magnetic multipole radiation one obtains for $\beta_K{}^l$: 7.88 and 20.0 percent for $\Delta l=2$ and 3, respectively. The best agreement is obtained on the assumption that the radiation is electric 2^5 pole. This entails a spin change of 5 and a change of parity.

Finally the spin change can be roughly determined from the life-time of the metastable state. Using the formula given by Bethe[4]

$$\tau=5\times10^{-21}(l!)^2\left(\frac{20}{E_\gamma}\right)^{2l+1}\text{ sec.},$$

the following values of the half-life, $t_{\frac{1}{2}}$, we obtain: 4×10^{-5}, 0.9, and 2.8×10^4 secs. for $l=4$, 5, and 6, respectively. Here the theory is less exact. The half-life is consistent with $\Delta l=5$.

Since the spins and magnetic moments of Cs^{137} and Ba^{137} (ground state) are known,[5] one is tempted to draw an energy level diagram showing the spins of each level. If this be done, certain difficulties are encountered which we should like to point out. The spin of the ground state of Ba^{137} is 3/2 and magnetic moment 0.235. Three lines of evidence make it appear very probable that there is a spin change of 5 connected with the transition Ba^{137} (excited) to the ground state. This would require that the spin of Ba^{137} (excited) be 13/2. The spin of Cs^{137} is said to be[5] 7/2. We have calculated the (ft.) value for the beta-transition $Cs^{137}\rightarrow Ba^{137}$ (excited) and have found the value 0.3×10^{10}, which would place this transition in the third forbidden group. According to Gamow-Teller selection rules, this requires a parity change and a spin change $\Delta l=\pm3$, ±4. Fermi selection rules require a change of parity and $\Delta l=\pm2$, ±3. A value of $\Delta l=3$, should be chosen if the arguments advanced in this note for the spin of Ba^{137} (excited) are correct. It is very difficult to understand how the beta-transition $Cs^{137}\rightarrow Ba^{137}$ (ground state) can be more highly forbidden than that corresponding to $Cs^{137}\rightarrow Ba^{137}$ (excited) since the arguments advanced here would require a spin change of only 2 and no change of parity.

We are indebted to Professor E. J. Konopinski and Mr. J. R. Pruett for many helpful discussions. This research was supported jointly by the Office of Naval Research and the Atomic Energy Commission.

[1] J. Townsend, G. E. Owen, M. Cleland, and A. L. Hughes, Phys. Rev. **74**, 99 (1948).
[2] J. Townsend, M. Cleland, and A. L. Hughes, Phys. Rev. **74**, 499 (1948).
[3] M. H. Hebb and E. Nelson, Phys. Rev. **58**, 486 (1940).
[4] H. A. Bethe, Rev. Mod. Phys. **9**, 226 (1947).
[5] H. H. Goldsmith and D. R. Inglis, The Properties of Atomic Nuclei. I. Spins, Magnetic Moments, and Electrical Quadrupole Moments, Brookhaven National Laboratory, October 1, 1948.

Attenuation of Sound in Rarefied Helium*

MARTIN GREENSPAN
National Bureau of Standards, Washington, D. C.
November 16, 1948

THE attenuation of sound at 1 Mc/sec. in helium, at pressures ranging from 30 to 0.4 mm Hg, has been measured in an attempt to elucidate mean-free-path effects. At the lowest pressure reached the wave-length (about 1 mm) was two or three mean free paths.

The complex propagation constant, $K=\alpha+i(\omega/v)$, where α is the amplitude attenuation, ω the circular frequency, and v the phase velocity, is given for a viscous, heat con-

ducting hydrodynamic fluid by Kirchhoff's equation,[1]

$$\omega^2+\left[v_0^2+i\omega\left(\frac{4}{3}\mu'+\nu\right)\right]K^2+i\frac{\nu}{\omega}\left(\frac{v}{\gamma}{}_0^2+\frac{4}{3}i\omega\mu'\right)K^4=0. \quad (1)$$

Here v_0 is the Laplacian velocity, μ' the kinematic viscosity, ν the thermometric conductivity (diffusivity) and γ the ratio of specific heats. According to the kinetic theory of Maxwellian molecules, we have $\nu=(5/2)\mu'=(5/2)(\mu/\rho)$, where ρ is the density and μ the viscosity, which is independent of pressure. It appears that helium gas can be well represented by Maxwellian molecules.

The usual first approximation from Eq. (1) gives

$$\alpha\approx(7/10)(\omega/v_0)(\omega\mu/p), \quad (2)$$

in which p is the pressure of the gas, and γ has been taken as 5/3 (monatomic gas). Wang Chang and Uhlenbeck[2] have calculated the second approximation,

$$\alpha\approx\frac{7}{10}\frac{\omega}{v_0}\frac{\omega\mu}{p}\left[1-1.114\left(\frac{\omega\mu}{p}\right)^2\right], \quad (3)$$

as well as a value, to the same order of approximation, based on the Burnett equations for Maxwellian molecules which take mean-free-path effects into account. This value is

$$\alpha=\frac{7}{10}\frac{\omega}{v_0}\frac{\omega\mu}{p}\left[1-3.682\left(\frac{\omega\mu}{p}\right)^2\right]. \quad (4)$$

For a particular case the exact hydrodynamic value for α can be got from Eq. (1). This was done for He at 300°K using $\mu=1.974\times10^{-4}$, $v_0=1.017\times10^5$, $\gamma=5/3$, and $\omega=2\pi\times10^6$, all in c.g.s. units. The resulting equation is

$$K^2=2.28\times10^5 ip\frac{p+2.14i-(p^2-0.424+0.930ip)^{\frac{1}{2}}}{p+1.24i} \quad (5)$$

where p is in mm Hg.

The heavy full line in Fig. 1 shows the value of α computed from Eq. (5). The measured values, indicated by circles, are seen to be in substantial agreement with the classical hydrodynamic value down to the lowest pressure used, at which the wave-length was 2 or 3 mean-free-paths. The second approximations are shown in Fig. 1 by the dashed line for the hydrodynamic case and by the dotted line for the Burnett equation. To this order of approximation the Burnett equation is inferior to the hydrodynamic equation; however, the convergence of the expression represented approximately by Eq. (3) is obviously very poor, so that it is likely that the same is true of Eq. (4) and no conclusions as to the validity of the general methods of Chapman and Enskog can be drawn from the attenuation data. It appears that attenuation measurements at lower pressures or higher frequencies would be required to show mean-free-path effects. The experimental difficulties would be considerable. An estimate of the accuracy of the experimental data can be gained from the scatter of the points in Fig. 1. The measured values tend to be generally somewhat high indicating a systematic error or perhaps a slight lack of purity of the helium. Tank helium, purified by passage over outgassed charcoal refrigerated with liquid air, was used in the experiments.

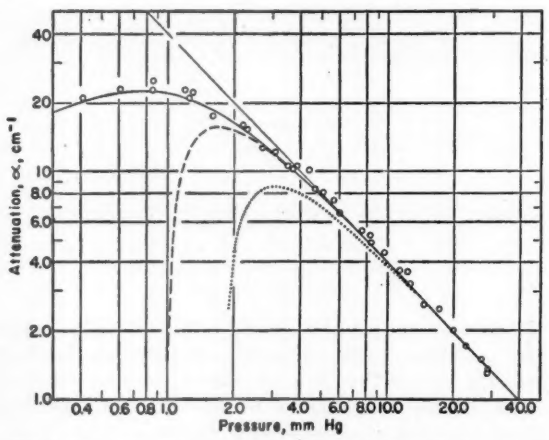

FIG. 1. Attenuation of sound at 1 Mc/sec. in helium. Circles—experimental results. Heavy full line—exact hydrodynamic. Light full line—first approximation, hydrodynamic and Burnett. Dashed line—second approximation, hydrodynamic. Dotted line—second approximation, Burnett.

It may be of interest to indicate the method of making the measurements of attenuation. The source was an X-cut quartz crystal driven in its fundamental thickness mode by a crystal-controlled, electron-coupled oscillator at constant voltage. The receiver was a similar crystal at an adjustable distance from the source. The output of the receiver was electronically processed and logarithmically recorded. The record consisted of a portion corresponding to small values of the separation between source and receiver which showed pronounced standing waves, a portion corresponding to large separations in which noise and unwanted signals due to electrical and mechanical leakage were evident, and an intermediate portion to which, for the pressures used, a straight line could be fitted, of which the slope was taken as the attenuation α. It was not found possible to calculate α from the amplitudes of the standing waves. Apparently the amplitudes are seriously affected by slight variations in the degree of parallelism of the source and receiver.

* This work was supported in part by the Office of Naval Research.

[1] Lord Rayleigh, *Theory of Sound* (Dover Publications, Inc., New York, 1945), Vol. II, p. 319.

[2] On the transport phenomena in rarefied gases, Applied Physics Laboratory, Johns Hopkins University. CM-443. UMH-3-F Feb. 20, 1948.

The Magnetic Moment of Aluminum[27]

JOHN R. ZIMMERMAN* AND DUDLEY WILLIAMS
The Ohio State University, Columbus, Ohio
November 18, 1948

SINCE our earlier reports[1,2] on super-regenerative oscillator techniques for determining the gyromagnetic ratios of nuclei by observation of magnetic resonance absorption frequencies, we have used these techniques to observe magnetic resonances of Al^{27} in aqueous solutions of the salts $AlCl_3$ and $Al_2(SO_4)_3$. The preliminary results obtained thus far for μ are in satisfactory agreement with the value reported by Millman and Kusch.[3] Their reported value is

$$\mu=3.628\pm0.010 \text{ nuclear magnetons},$$

and is based on a value of $I=5/2$ for the nuclear spin of Al^{27}. The work of Millman and Kusch involved the use of a molecular beam of $KCl \cdot AlCl_3$ molecules and their published curve shows a peak with a half-width of approximately 90 gauss with center at 1810 gauss; the frequency used was 1.996 megacycles/sec. The present work was done at a frequency in the neighborhood of 6.5 megacycles/sec. and the observed absorption peak was observed near 5900 gauss and had a half-width of 1 gauss. In view of the narrow half-width of the absorption peak as observed by the present method, it would appear that a more precise value for the magnetic moment of Al^{27} can be obtained as soon as certain refinements have been completed.[3] A more detailed report on the subject will be given later.

We should like to express our appreciation to the Graduate School and to the trustees of the University Development Fund at the Ohio State University for research grants used in this work.

* Charles A. Coffin Fellow, General Electric Company, Schnectady, New York.

[1] J. R. Zimmerman and D. Williams, Phys. Rev. **73**, 94 (1948).
[2] J. R. Zimmerman and D. Williams, Phys. Rev. **74**, 1885 (1948).
[3] S. Millman and P. Kusch, Phys. Rev. **56**, 303 (1939).

Doppler Broadening of a Gamma-Ray Line

V. K. RASMUSSEN, C. C. LAURITSEN, AND T. LAURITSEN
Kellogg Radiation Laboratory, California Institute of Technology, Pasadena, California

November 8, 1948

THE gamma-radiation observed in the bombardment of beryllium with deuterons consists of lines at 0.411, 0.477, and 0.715 Mev, as well as higher energy components.[1,2] The 0.411 and 0.715 Mev lines are attributed to excited B^{10} produced in the d, n reaction, while the 0.477 Mev line is attributed to the well-known first excited state of Li^7, produced in the d, α-reaction.

Using a magnetic lens spectrometer with a resolution of 1.47 percent (full width at half-maximum) instead of the 3 percent used in work previously reported, we have reexamined the secondary electron spectrum from these three gamma-rays. A target of 8.9 mg/cm² beryllium metal backed by a 7.0 mg/cm² thorium metal photoelectron converter at the source position in the spectrometer was bombarded with 1.19 Mev deuterons. The deuteron beam entered on the axis of the spectrometer; only secondary electrons ejected with angles between 14° and 16° to the axis were accepted by the diaphragm system. The secondary electron spectrum obtained is shown in Fig. 1, where the identification of the several peaks is indicated above the curve. The measured width of the 411 kev and 715 kev K conversion lines is 2.3 percent and 1.6 percent respectively, the increase over the instrumental width being due to the scattering and energy loss in the thorium converter, which is relatively more important at the lower energy. The greatly increased width (4.1 percent) of the K photoelectron peak from the 0.477 Mev line is attributed to Doppler broadening caused by the relatively high velocity of the excited Li^7 nucleus.

TABLE I.

Reaction	$E_{\text{bombarding}}$ (Mev)	V_{cm}	V_{Li^7} (in cm coord. system)	Δ_{max} (kev)	Δ_{min} (kev)	Δ_{cm} (kev)
$Li^7(p, p')Li^{7*}$	1.05	0.0059 c	0.0041 c	4.8	0.9	2.8
$Be^9(d, \alpha)Li^{7*}$	1.19	0.0065 c	0.029 c	16.9	−10.7	3.1

In order to compare directly the shape of the broadened line with the normal shape, we have studied the secondary electron spectrum from this gamma-ray when the Li^7 is excited by two other means; by the decay of Be^7, $Be^7(K)Li^{7*}$[3] and by the inelastic scattering of protons in lithium. The same thorium foil converter, and as nearly as possible the same source geometry were used throughout. The resulting K photoelectron peaks, after subtraction of backgrounds, division by the electron momentum and normalization to equal areas, are plotted in Fig. 2. The photoelectron peak from the gamma-ray resulting from the Be^7 decay is 2.1 ±0.1 percent wide at half maximum, the peak from the $Li^7(p, p')Li^{7*}$ reaction is 2.2±0.1 percent wide, and that from the $Be^9(d, \alpha)Li^7$ reaction is 4.1±0.1 percent wide. The peak of the $Li^7(p, p')$ distribution is displaced in the direction of higher energy by 1.6±0.5 kev from the Be^7 peak, and the $Be^9(d, \alpha)$ peak is displaced several kev downward. The latter curve is clearly asymmetric.

When excited Li^7 is left after the decay of Be^7, the emission of the gamma-radiation takes place from a system which is practically stationary; the maximum recoil of the Li^7 from the neutrino and gamma-ray is less than 67 ev. In the heavy particle reactions, however, the center of mass motions and the velocities of the emitting Li^7 are quite appreciable (Table I). The peak shift for a velocity of the center of mass, V_{cm}[4] will be approximately

$$\Delta_1 = E_\gamma (V_{cm}/c)(\cos\theta)_m$$

where $(\cos\theta)_m$ is the mean cosine of the angle between the gamma-rays and the photoelectrons accepted by the spectrometer. The value of this mean cosine depends on the

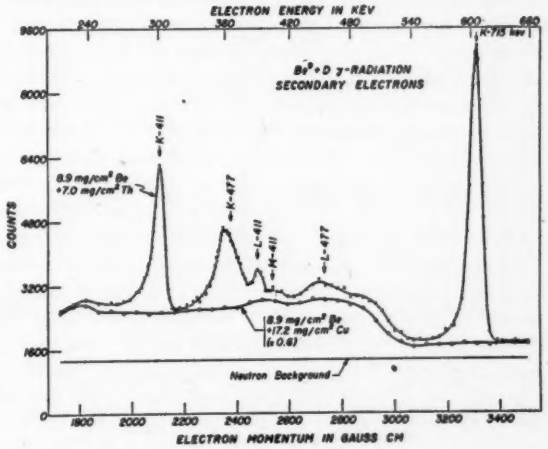

FIG. 1. Lower energy end of the spectrum of secondary electrons from the Be^9+d gamma-radiation.

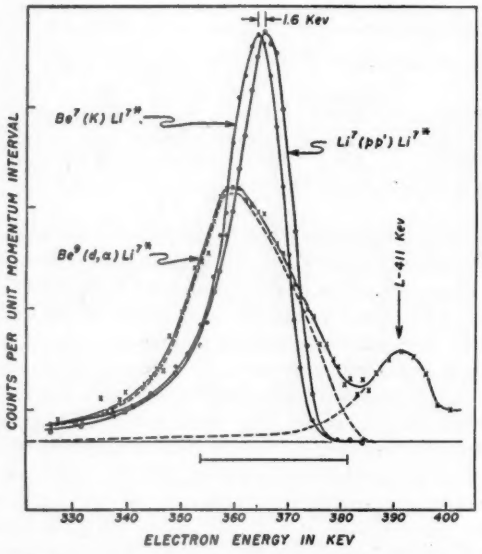

FIG. 2. K photoelectrons ejected from 7.0 mg/cm² of thorium by the 477 kev gamma-ray line from Li^7. The horizontal line just below the curves represents the maximum Doppler effect in the $Be^9(d,\alpha)Li^{7*}$ reaction.

angular distribution of the photoelectrons and on the target geometry; a rough estimate of these effects yields a value of about 0.8. Scattering in the converter will tend to lower the apparent shift and broaden the line. In the center of mass system, the motion of the Li^{7*} will tend to broaden the line, without shifting the peak, the amount of broadening being

$$\Delta_2 = 2E_\gamma(V_{cm}(Li^7)/c).$$

If the gamma-ray emission is isotropic and is not correlated with the Li^7 direction, the observed peak should be rectangular with the sides rounded off by the effect of finite resolution; translation to the laboratory system shifts the center of the rectangle toward higher energy by an amount Δ_1. It is quite clear from Fig. 2 that the observed curve deviates markedly from this simple shape.

Three possible explanations for the deviation suggest themselves: First, the Li^7 nuclei may not be isotropically emitted with respect to the bombarding beam or there may be some correlation between the direction of motion of a Li^7 nucleus and the gamma-ray it emits. Second, additional gamma-rays near 477 kev may be present, although this offers no convincing explanation of the shape observed. Third, some of the Li^{7*} nuclei may be stopped before they radiate. Since the gamma-ray transition involved is usually taken as $^2P_{1/2}-{}^2P_{3/2}$, magnetic dipole radiation is the most probable allowed radiation, and the half-life of the state should be of the order of 10^{-13} sec. The range of a 4 Mev Li^7 nucleus in beryllium is around 6×10^{-4} cm and the mean velocity[4] is 0.5×10^9 cm/sec. The Li^7 nuclei will therefore be stopped in a time comparable with the half-life of the excited state, except when they can escape from the target in the backwards direction. Since the yield of the $Be^9(d,\alpha)Li^7$ reaction is rising steeply at this energy, most of the Li^7 will be made in the first thin ($\sim10^{-4}$ cm) layer of the target. The stopping would result in a deficiency of nuclei emitting with the maximum forward velocity, while the number contributing to the "red shift" region would be much less affected.

The above considerations apply also to the shift and broadening of the peak obtained from the $Li^7(p,p')Li^{7*}$ reaction, although, in this case, the lower density of the Li^7 metal and its lower stopping power for the Li^{7*} nuclei result in a somewhat longer stopping time. The fact that a definite shift is observed indicates that the lifetime of Li^{7*} cannot be long compared to 10^{-12} sec.

We are much indebted to Professor R. F. Christy for assistance in the analysis of the problem. This work was assisted by the Joint Program of the Office of Naval Research and the Atomic Energy Commission.

[1] T. Lauritsen, W. A. Fowler, C. C. Lauritsen, and V. K. Rasmussen, Phys. Rev. **73**, 636 (1948).
[2] T. Lauritsen, C. B. Dougherty, and V. K. Rasmussen, Bull. Am. Phys. Soc. **23**, 5, 16 (1948).
[3] We are greatly indebted to Professor R. W. Richardson of the University of California at Los Angeles for making the Be^7 for us and to Professor D. M. Yost of the California Institute of Technology for making the chemical separations involved.
[4] Effects of order v^2/c^2 have been neglected.

Isotopic Weights of Medium Elements

K. OGATA
Department of Physics, Faculty of Science, Osaka University, Osaka, Japan
September 20, 1948

ISOTOPIC weights of all the isotopes of Cr, Fe, Zn, and Br were determined with a Bainbridge-Jordan type mass-spectrograph. Glow discharge in a cylindrical tube was used as the ion source. A brief account of the result is as follows:

1. *Chromium.* Discharge through the vapor mixture of n-CrH_{16} and chromyl chloride (CrO_2Cl_2) produced doublets, whose mass differences were as follows:

Doublets	Number of doublets measured	Mass differences ($\times10^{-4}$ M.U.)
$C^{12}_4H^1_{12}-Cr^{50}$	6	673.2±3.7
$C^{12}_4H^1_{14}-Cr^{52}$	17	920.3±4.2
$C^{12}_4H^1_{15}-Cr^{53}$	13	1008.7±4.1
$C^{12}_4H^1_{16}-Cr^{54}$	7	1100.0±4.6

2. *Iron.* Iron carbonile (Fe(CO)) was prepared as the volatile iron. Discharge was passed through the mixture of its vapor and normal heptane vapor. The measured doublets and their mass differences were as follows:

Doublets	Number of doublets measured	Mass differences ($\times10^{-4}$ M.U.)
$C^{12}_4H^1_{16}-Fe^{54}$	10	1065.3±4.7
$C^{12}_4H^1_{18}-Fe^{56}$	23	1271.3±2.3
$C^{12}_4H^1_{19}-Fe^{57}$	15	1338.1±5.0
$C^{12}_4H^1_{10}-Fe^{58}$	4	1458.8±4.7

3. *Zinc.* A small electric crucible which contained small pieces of Zn metal was introduced in the discharge tube. N-heptane vapor sustained the discharge, while the zinc was vaporized by electric heating. Doublets and mass differences obtained were as follows:

Doublets	Number of doublets measured	Mass differences ($\times 10^{-4}$ M.U.)
$C^{12}_5H^1_4-Zn^{64}$	13	982.3±6.4
$C^{12}_5H^1_6-Zn^{66}$	17	1213.8±3.9
$C^{12}_5H^1_7-Zn^{67}$	8	1280.1±6.3
$C^{12}_5H^1_8-Zn^{68}$	8	1355.5±6.3
$C^{12}_5H^1_{10}-Zn^{70}$	3	1346.0±16

4. *Bromine.* Discharge was operated through the mixture of normal heptane vapor and sublimated vapor of titanium tetrabromide crystals. Since doublets could not be obtained in this case, dispersion curves were drawn by the least square method with five hydrocarbon lines, $C^{12}_3H^1_2$, $C^{12}_3H^1_3$, $C^{12}_3H^1_4$, $C^{12}_3H^1_5$, and $C^{12}_3H^1_6$, which covered the doubly ionized region of Br. From these dispersion curves and the mass $H^1=1.0081$, the following mass differences were obtained:

Mass differences	Number measured
$\frac{1}{3}Br^{79}-C^{12}_3H^1_3=0.43618\pm2.3\times10^{-4}$	11
$\frac{1}{3}Br^{81}-C^{12}_3H^1_4=0.42700\pm1.6\times10^{-4}$	11

From these above results of the mass differences and the value $H^1=1.008131\pm0.033\times10^{-4}$, $C^{12}=12.003871\pm0.33\times10^{-4}$,[1] the isotopic weights of all these isotopes were calculated. The isotopic weights, the packing fractions, and the binding energies which were calculated from the mass of hydrogen (1.008131) and neutron (1.008945) are summarized in Table I. In the last column are given theoretical binding energies, calculated from Nakabayashi's formula of the binding energy,[2]

$$E=-15.2A+20(N-Z)^2/A+14.6A^{\frac{2}{3}}+0.62Z^2A^{-\frac{1}{3}}(10^{-3}\text{ M.U.})$$

TABLE I.

Element	Z	A	Isotopic weight	Packing fraction	Binding energy (10^{-4} M.U.) Exp.	Theor.
Cr	2	50	49.96443± 3.9×10⁻⁴	−7.11±0.08	463.3	463
		52	51.95598± 4.4×10⁻⁴	−8.47±0.08	489.6	485
		53	52.95527± 4.4×10⁻⁴	−8.44±0.08	499.3	495
		54	53.95427± 4.8×10⁻⁴	−8.47±0.09	509.2	504
Fe	26	54	53.95774± 4.8×10⁻⁴	−7.83±0.09	504.1	500
		56	55.95340± 2.7×10⁻⁴	−8.32±0.05	526.4	522
		57	56.95485± 5.2×10⁻⁴	−7.92±0.09	533.9	532
		58	57.95091± 4.9×10⁻⁴	−8.46±0.09	546.7	542
Zn	30	64	63.95365± 6.6×10⁻⁴	−7.24±0.10	594.4	594
		66	65.94676± 4.2×10⁻⁴	−8.07±0.06	619.2	616
		67	66.94826± 3.8×10⁻⁴	−7.71±0.06	626.6	625
		68	67.94885± 6.5×10⁻⁴	−7.53±0.09	635.0	635
		70	69.9461 ±17 ×10⁻⁴	−7.69±0.24	655.4	652
Br	35	79	78.94438± 5.0×10⁻⁴	−7.04±0.06	733.8	735
		81	80.94228± 3.8×10⁻⁴	−7.12±0.05	753.8	752

here, A is mass number, Z is number of protons, and N is number of neutrons.

The packing fraction curves were drawn in this region by using these results and the values of Ti[3] and Ni[4] reported in our previous paper.

It is seen from these curves (Fig. 1) that the packing fraction of the isotopes of the same elements differ considerably from each other. It is worth noticing especially that in the four pairs of isobars, $Ti^{50}-Cr^{50}$, $Cr^{54}-Fe^{54}$, $Fe^{58}-Ni^{58}$, and $Ni^{64}-Zn^{64}$, the packing fraction of larger atomic number elements is always larger algebraically than that of small atomic number elements. The dotted line in this figure shows the general tendency of the packing fraction curves in this region. It is seen from these curves that Dempster's packing fractions[5] in this region are slightly large, and that the minimum of our packing fraction curve is located about Cr or Fe, though in Dempster's curve it is located about Ti.

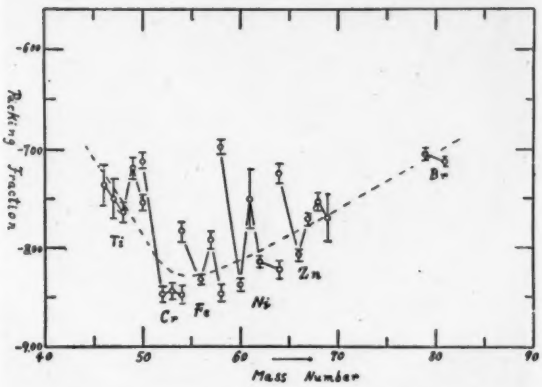

FIG. 1. Packing fraction curve in the region Ti to Br.

[1] K. Ogata, Proc. Phys.-Math. Soc. (Japan) **22**, 486 (1940).
[2] Private communication.
[3] T. Okuda and K. Ogata, Proc. Phys.-Math. Soc. (Japan) **25**, 374 (1943).
[4] T. Okuda, K. Ogata, H. Kuroda, S. Shindo, and S. Shima, Phys. Rev. **59**, 104 (1941).
[5] A. J. Dempster, Phys. Rev. **53**, 64 (1938).

Cloud-Chamber Evidence of a Meson-Nucleus Interaction*

G. E. VALLEY, C. P. LEAVITT, AND J. A. VITALE

Physics Department and Laboratory for Nuclear Science and Engineering, Massachusetts Institute of Technology, Cambridge, Massachusetts

November 12, 1948

IN September 1948 we successfully operated a cloud chamber filled with argon to a pressure of 105 atmospheres (at 15°C) in a magnetic field of 8800 gauss, and at an altitude of 12,730 feet above sea level (by Summit Lake on Mt. Evans in Colorado). Stereoscopic pictures

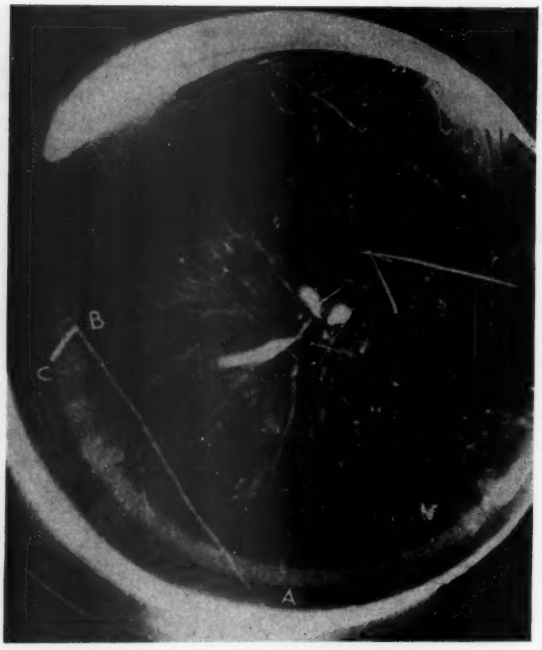

FIG. 1. High pressure cloud chamber picture showing a star produced by a non-ionizing particle, and a meson AB which produces a nucleon BC at the end of its path. The positive and negative ion tracks of the star are separated by the electric clearing field. The heavy plumes in the center of the picture are caused by corona from the clearing field electrode (6000 volts, 105 atmosphere argon, 8800 gauss, counter controlled).

were taken by means of two cameras, each inclined by 8° to the axis of symmetry.

The chamber was surrounded on top and sides by 11 cm of lead. During part of the experiment the instrument was triggered by hard showers produced by penetrating particles either in the lead or in the gas and walls of the chamber.

We observed the following phenomena:

(1) Production of positron-electron pairs in the gas.
(2) Particles apparently unaffected by the magnetic field which come to rest in the gas.
(3) Stars of one, two, three and four prongs produced in the gas by non-ionizing radiation. One of these is shown in Fig. 1.
(4) A comparatively high abundance of tracks similar to that marked ABC in Fig. 1. Here a long scattered track ends in a short straight section making a large angle with the original direction.

With counter control we observed five such tracks in 57 pictures. Without counter control we observed two such tracks in 135 pictures. Contrariwise the abundance of stars shows no dependence upon counter control at all. This is precisely what would be expected if the phenomena $A\ B\ C$ are locally produced and if the stars are produced by neutrons made in the atmosphere above. Locally produced neutrons are too few to have much probability of making a collision in the gas.

We have one picture which shows two such events in which the long components appear to emerge from a point just within the duralumin cloud-chamber wall. This we take to show that the particles which produce the long track proceed toward and not away from the juncture with the short track.

If it be assumed that the phenomenon represents the elastic or inelastic scattering of the particle which produced the long track, or that it represents the production of a single pronged star by virtue of the kinetic energy of that particle, then the total cross section for these processes is in excess of fifty barns. We calculate this by comparison of the abundance of these events with the abundance of tracks which stop in the gas and are also unaffected by the magnetic field.

Finally we have attempted in three cases to determine the mass of the "long" component by scattering-range measurements.

We set $\theta_1^2+\theta_2^2+\theta_3^2=\theta_4^2$ where θ_1 is the theoretical $R\,M\,S$ planar Coulomb scattering angle, θ_2 is the magnetic deflection angle over the same path and θ_3 is the "residual" or instrumental scattering of a very high energy track. The sum of the squares of these angles is then equal to the square of the angle actually measured, θ_4.

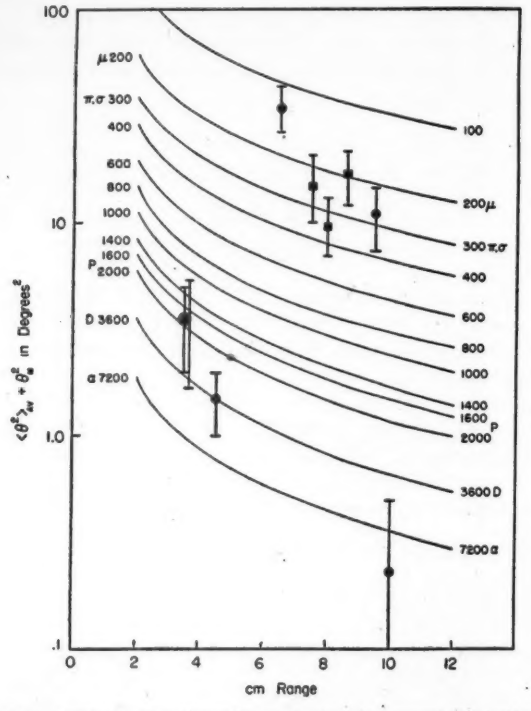

FIG. 2. Curves showing theoretical scattering plus magnetic deflection, for various masses over a range interval of 1 cm, against residual range in cm. Square points represent events like ABC in Fig. 1; round points represent heavily ionizing tracks which simply end in the gas.

In Fig. 2 we have plotted curves showing the sum $\theta_1^2+\theta_2^2$ *versus* range in cm under the conditions pertaining. We have superimposed, on this, points showing $\theta_4^2-\theta_3^2$ for several tracks. The square points are for the phenomena like $A\ B\ C$ of Fig. 1. The round points represent a random sample of heavy tracks which end in the gas. It is seen that these are well grouped into meson-like and nucleon-like particles and that in particular all of the phenomena like $A\ B\ C$ of Fig. 1 are mesons, whose precise mass we cannot here determine.

However, since these mesons are locally produced, they must be heavy, according to current ideas.

Unfortunately all our pictures of these events do not show so unequivocally that the short track is due to a nucleon or heavier particle. However, we have not observed any electrons to emerge from the ends of any of the short tracks.

We therefore conclude that these events show sigma-mesons which produce one-pronged stars, and for the present, put aside the less pleasant idea that μ-mesons rarely decay. Why we saw no π-μ-electron events remains to be investigated. It also must be investigated whether it is a property of argon alone, or of other of the lighter elements also, predominantly to boil off a single charged particle upon acceptance of a heavy meson.

We were ably and invaluably assisted in operating the heavy machinery by Thomas Mersereau. We are indebted to Professors B. B. Rossi and J. R. Zacharias for the advice and encouragement they gave us. We wish to express our appreciation to the many members of the staffs of M.I.T. and the Inter-University High-Altitude Laboratory, who helped us.

* This work was supported in part by the joint program of the Office of Naval Research and Atomic Energy Commission.

Temperature Dependence of Scintillations in Sodium Iodide Crystals

W. C. ELMORE
*Swarthmore College, Swarthmore, Pennsylvania**
AND
R. HOFSTADTER
*Princeton University, Princeton, New Jersey**
November 19, 1948

THE high speed "Microoscillograph"[1] and a new fast amplifier[2] have been employed in studying the temperature dependence of radium gamma-ray induced scintillations in thallium activated sodium iodide crystals.[3] In these studies light pulses were conducted by internal reflection along the length of a one-foot transparent fused quartz rod.[4] The crystal sample was placed, within a furnace, next to one polished end of the quartz rod. The photomultiplier was kept at room temperature and positioned at the other end of the quartz rod. After transformation of the light pulse to a current pulse, the photomultiplier signal was amplified approximately 200 times and brought to the plates of the Microoscillograph through short leads. Permanent records of the traces are obtained on the target photographic plates of the Microoscillograph. To obtain the records, a ten millicurie source was placed within a few inches of the crystals and random sweeps were used.

The polycrystalline NaI (Tl) samples were prepared by fusing in vacuum Baker and Adamson reagent grade sodium iodide together with 1 percent, by weight, of thallium iodide. The preparation is sealed off in a quartz tube in which the fusion takes place. Other samples were made containing 0.1 percent and 0.02 percent of Tl I.

At the present time the data allow only rough estimates to be made of the duration and pulse shape of the light emitted during a scintillation. This is due to the circumstance that the observed pulses do not show a unique shape or behavior. Some pulses, particularly the larger ones, rise as fast as the rise time of the amplifier ($\sim 2\times10^{-8}$ sec.), while others build up to a maximum value over an interval of perhaps 0.1 microsecond. Still others show only an irregular structure. It is probable that the number of quanta, detected by the photomultiplier in the average scintillation, is not large enough to smooth statistically the pulse shape to a recognizable form. A distortion of the true pulse form also occurs in the larger pulses since they drive the amplifier into a non-linear region.

The results for duration of the light pulse are the following. At room temperature most pulses, whatever their shape, terminate in about 0.4 to 0.7 microsecond. At 150°C the pulses are over in about 0.3 to 0.4 microsecond. At 345°C the larger pulses decay to zero in approximately 0.15 microsecond. These results do not preclude the occurrence of single electron pulses following the main pulse by a time of the order of twice the given pulse duration.

We have also examined pulses obtained with the 0.1 percent and 0.02 percent Tl I samples and, for the same excitation, have observed fewer pulses than in the 1 percent sample but have noticed no change in the duration or shape of the individual pulses. We have also compared the total amount of light detected by the photomultiplier in a large scintillation at room temperature and at 345°C. At room temperature from three to five times as many quanta are detected per scintillation as in the corresponding case at the higher temperature. It is not known whether this result corresponds to a real decrease in the number of emitted quanta or to a shift in frequency of the emitted light band, although it is suspected that the former is the case.

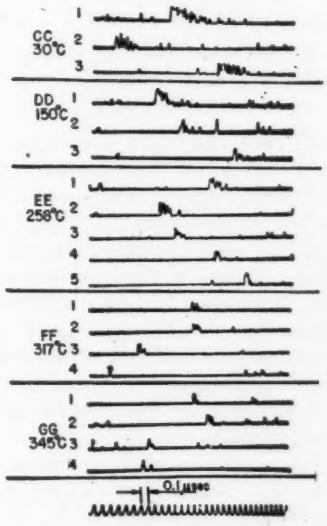

FIG. 1. Pulses showing sharp rise.

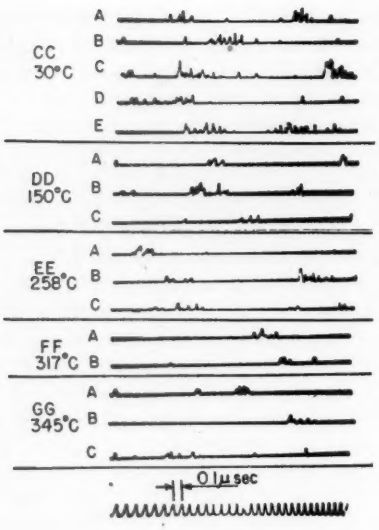

FIG. 2. "Irregular" pulses.

Figures 1 and 2 show typical pulses at the various temperatures. The pulses in these figures represent approximately the photomultiplier current (not integrated current). This is due to the low value of the anode load resistance at the photomultiplier.

* Research carried out at Brookhaven National Laboratory, Upton, Long Island, New York under the auspices of the Atomic Energy Commission.
[1] G. M. Lee, Proc. I.R.E. 34, 121W (1946).
[2] W. C. Elmore, to be published.
[3] R. Hofstadter, Phys. Rev. 74, 100 (1948).
[4] This technique has previously been used by G. B. Collins. We are indebted to Dr. Collins for loan of a quartz rod.

Energy of the Disintegration Product of a Light Mesotron*

J. C. FLETCHER** AND H. K. FORSTER***
California Institute of Technology, Pasadena, California
November 8, 1948

IN a series of cloud-chamber observations performed at sea level, a photograph was obtained which is interpreted as the disintegration of a negative mesotron which comes to rest in a graphite plate.

The experiments were performed with an Argon-filled cloud chamber 22 inches in diameter, with a lighted area 2-inches deep, illuminated from the sides by two Argon discharge tubes. The chamber was placed in a magnetic field of 4700 gauss, uniform to ±4 percent within the illuminated area. Three graphite plates, each 1.1 cm-thick (2.0 g/cm²) were inside the chamber; 33 cm of lead and two coincidence counters were placed above it. A schematic diagram of the apparatus, showing the arrangement of chamber, lights and cameras, is shown in Fig. 1.

On the photograph reproduced in Fig. 2, a particle is seen which enters the lower left-hand portion of the cloud chamber through the front glass and comes to rest in the bottom graphite plate. A lightly ionizing particle is seen to emerge from below the plate at an angle of about 90° with the entering particle. Its curvature and ionization indicate that it is a fast particle of negative charge. From comparison of the density of the track of the incoming particle with that of the outgoing particle it is quite apparent that the former is heavily ionizing. It should be pointed out that the difference in appearance of the tracks on the two photographs is characteristic for an arrangement of lights and cameras similar to that shown in Fig. 1, in which the light coming from the tracks must be scattered through widely different angles in order to reach the two cameras. The energy of the particle emerging below the plate is found to be 28.1±1.5 Mev by curvature measurement. This value is in very good agreement with the energy calculated from the energy loss in the several traversals of the graphite plates. The disintegration particle traverses the graphite plates five times and this affords a very good opportunity to obtain an upper limit for its mass. Extensive measurements of the energy loss of knock-on electrons of various energies in graphite plates were carried out.[1] It is well known that this energy loss is subject to statistical fluctuations; however, from statistics of the experimentally obtained values, the probability could be calculated that, in a specific case, the energy loss of an electron of a given energy in traversing 1 cm of graphite deviate from the mean (and theoretical) value by a given amount. Curvature measurements of the particle in the photograph before and after each traversal of a graphite plate together with the information obtained on the statistical fluctuation of the energy loss to be expected, allow then to place an upper limit on the mass of the particle: there is a probability larger than 0.95 that the mass of the particle is smaller than 7 electron masses. After careful measurement and reprojection of the two tracks it was concluded that they intersect 3 cm from the front glass, well within the illuminated region of the chamber. However the slight possibility that the two tracks pass within a small distance accidentally, cannot be excluded.

Interpretation of the event as the disintegration of a light mesotron and estimation of the point of intersection of the two tracks within the graphite leads to a value of

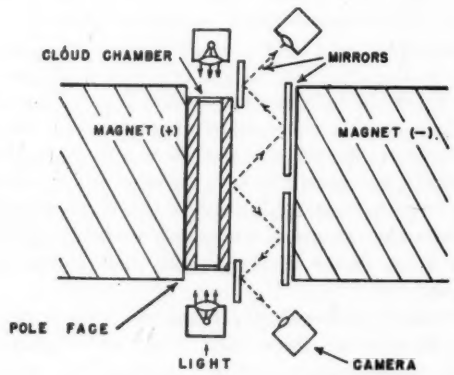

FIG. 1. Schematic diagram of apparatus.

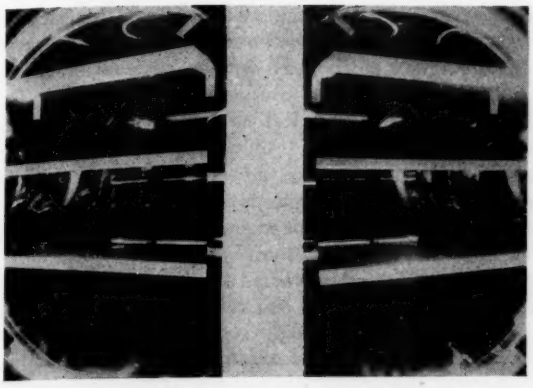

FIG. 2. Cloud-chamber photograph of a mesotron which stops in a graphite plate (lower left), and disintegrates with the emission of a lightly ionizing particle.

36 ± 3 Mev for the energy of the disintegration particle. This value for the energy is somewhat smaller than the average value of 45 Mev found by Thompson[2] and considerably larger than the value of 25 Mev found by Anderson *et al.*[3] The spread in disintegration energies indicates that more than 2 particles are created in the process of disintegration of the light mesotron.

The writers are indebted to Professor Carl D. Anderson who first suggested this problem and who rendered valuable aid during the progress of this work.

* Assisted by the Joint Program of the Office of Naval Research and the Atomic Energy Commission.

** Now at Hughes Aircraft Company, Culver City, California.
*** Now at the University of California, Los Angeles, California.

[1] J. C. Fletcher, thesis (Ph.D.), California Institute of Technology, June, 1948.
[2] R. W. Thompson, Phys. Rev. **74**, 490 (1948).
[3] Anderson, Adams, Lloyd, and Rau, Phys. Rev. **72**, 724 (1947).

Relative Sensitivities of Some Organic Compounds for Scintillation Counters*

H. T. GITTINGS, R. F. TASCHEK, A. R. RONZIO, E. JONES, AND W. J. MASILUN
Los Alamos Scientific Laboratory, Los Alamos, New Mexico
November 8, 1948

A SEARCH for organic materials which would serve as scintillation-type detectors similar to naphthalene[1] has resulted in establishing the sensitivities of nine compounds relative to naphthalene,[2,3] both for 1P21 and 1P28 photomultipliers. Recrystallized and sublimed samples of all compounds were used with the exception of one sample of commercial naphthalene for comparative purposes. 1.8 grams of each material were used, packed as nearly as possible at constant volume in quartz test tubes, the scintillations observed by four photo-multipliers in parallel surrounding the test tube. The pulses were amplified by a Los Alamos Model No. 500 pulse amplifier, voltage discriminated, and recorded on a scale of 4096 and register. The multipliers were not refrigerated. A 20 mc radium gamma-source placed at a standard distance of 71.5 cm was used for all tests.

Figures 1 and 2 show a series of integral, pulse height distributions for the compounds investigated as observed with 1P28s and 1P21s. In addition it is desired to call attention to the following features:

(1) Several compounds, in particular anthranilic acid, showed exceedingly strong fluorescence to ultraviolet excitation but were very poor as scintillating materials with radium gammas.

(2) The dynode power supply was arranged so that the supply voltage could be varied and also the voltages to the individual tubes could be separately adjusted. This made it possible to equalize the detection sensitivities of the parallel tubes and after adjustment to shift all the tubes together to any desired average dynode voltage. Dynode voltage on the 1P28s was so adjusted that for two bias values the purified naphthalene counts coincided with those using the 1P21s. Since this voltage was nearly identical with that used for the 1P21s, it appears from the RCA Handbook data that the 1P28 observes about ten times more luminous flux from the naphthalene radiation than the 1P21.

(3) The scintillation property appears to be connected with molecular structure since phenanthrene is a very poor material and its isomer anthracene a very good one.

(4) This property does not seem to be connected with condensed-ring systems in general, since 1,2-benzanthracene was exceedingly poor, but may possibly be more closely associated with the conjugate bonding observed in stilbene.

(5) The stilbene, at the high biases, is at least a factor of three better than anthracene which had been the best material found previously.[3]

(6) Although refrigeration was not used, the pulse height curves do not seem to extrapolate back to the same zero bias value for all the compounds. On the curves for naphthalene, anthracene and stilbene the zero bias values could possibly be the same, as shown in the figures, indicating that most of the betas arising from the gamma-radiation make enough photons to be counted. For most of the other materials, however, there seems to be some

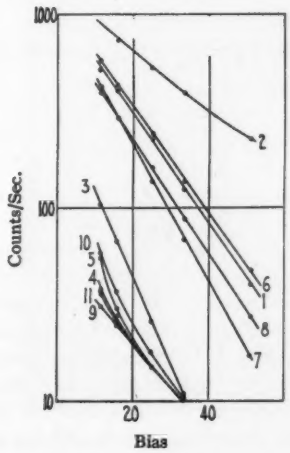

FIG. 1. Integral bias curves with 1P21s. 1—anthracene, 2—stilbene 3—phenanthrene, 4—phenyl benzal glyoxalidone, 5—triphenyl methane, 6—naphthalene, 7—naphthalene—stock, 8—fluorene, 9—anthranilic acid, 10—acenapthene, 11—benzanthracene, 12—diphenyl.

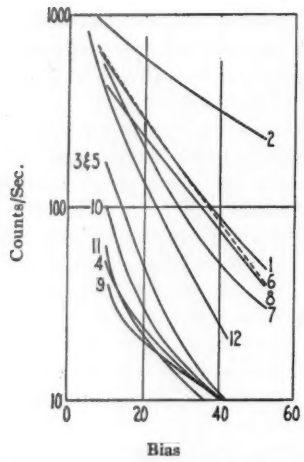

FIG. 2. Integral bias curves with 1P28s: 1—anthracene, 2—stilbene, 3—phenanthrene, 4—phenyl benzal glyoxalidone, 5—triphenyl methane, 6—naphthalene, 7—naphthalene—stock, 8—fluorene, 9—anthranilic acid, 10—acenapthene, 11—benzanthracene, 12—diphenyl.

indication that not all betas are counted even at zero bias. The great advantage of the stilbene is its high conversion efficiency, i.e. large number of photons per unit beta-energy loss, which is apparent at the large pulse heights. The flatness of the stilbene curve at low bias leads one to hope that a sufficiently good material may be found for which the extrapolation to zero pulse height can be made unambiguously without the use of refrigeration. Stilbene is at present being investigated with multiplier refrigeration.

* This document is based on work performed under government contract number W-7405-eng-36 for the Los Alamos Scientific Laboratory of the University of California.

[1] Martin Deutsch, Technical Report No. 3, Laboratory for Nuclear Science and Engineering, M.I.T. (1947); H. Kallman, Natur u. Technik, July (1947).

[2] Progress Report, Laboratory for Nuclear Science and Engineering, M.I.T., April (1948).

[3] P. R. Bell, Phys. Rev. **73**, 1405 (1948).

Radiation from Columbium 95

J. E. HUDGENS, JR. AND W. S. LYON
Chemistry Division, Oak Ridge National Laboratory, Oak Ridge, Tennessee

November 12, 1948

NEDZEL[1] using the beta-ray spectrometer in studying columbium 95 has reported one beta-ray (0.154 Mev) and one gamma-ray (0.77 Mev). In addition, he observed a conversion electron peak with energy of 0.224 Mev. Levinger[2] further studied this peak and assigned it to a short-lived columbium 95 isomer the gamma-ray of which is completely converted, and which undergoes isometric transition to 35-day columbium 95. Using a beta-ray spectrometer similar to that described by Deutsch *et al.*[3] we have recently examined both the 35-day and the short-lived nuclide of columbium 95.

From a hydrochloric acid solution containing columbium 95 and its parent zirconium 95, the zirconium was removed by repeated extractions with 0.5*M* thenoyltrifluoacetone benzene solution. From the pure aqueous solution, active columbium was precipitated by the addition of 0.5 mg of columbium carrier and evaporation in nitric acid. This material (~100 microcuries) was placed on a laminated Formvar-polystyrene film (~50 micrograms/cm²) and used as a source for the study of the beta-spectrum in the beta-ray spectrometer. From the data obtained, a plot of the counts per minute per unit momentum interval *versus* the current in amperes [(N/I) *vs.* I] has been made (Fig. 1). A conversion peak may be noted at 0.200 Mev, and another at 0.735 Mev. The Kurie plot (Fig. 2) indicates one beta-

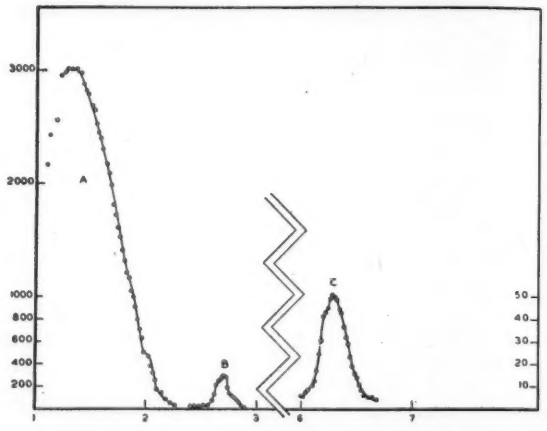

FIG. 1. The beta- and conversion-electron spectra of Cb^{95} (counts per minute per unit momentum interval plotted against coil current in amperes).
A is the continuous beta-spectrum of Cb^{95}; B is the conversion electron peak of the 90-hr. Cb^{95}; C is the conversion electron region of the 0.75 Mev gamma-ray.

ray of energy 0.146 Mev is associated with the decay of the 35-day columbium 95 nuclide. Using values for intensities obtained by graphical integration under the counts per minute per unit momentum interval *vs.* coil current plot, we find that the short lived isomer is present to the extent of 1.4 percent in a solution in which zirconium 95 and columbium 95 are in equilibrium. The decay of a columbium source has been followed on a standard bell-type thin-end window Geiger-Mueller counter equipped with continuous recorder. These data indicated the half-life to be 90 hours which is identical with the value reported by Steinberg.[4]

After extrapolation of the Kurie plot and a recalculation and replotting of a theoretical (N/I) *vs.* I curve, we have compared the areas under the continuous beta-spectrum and the areas under the two conversion electron regions. We find for 35-day columbium 95 the ratio of the conversion electrons to the continuous beta-particles is 2.4×10^{-3}.

A source for study of the gamma-spectrum was prepared in a manner similar to that described above. The amount of active columbium taken was increased ~50 fold, and the precipitated columbium oxide was mounted in the spectrometer and data obtained using first a uranium and

TABLE I. Energy values for columbium 95.

	35-day Cb^{95}	90-hour Cb^{95}
β-max.	0.146±0.01 Mev	
γ	0.758±0.02 Mev	0.216±0.01 Mev (100% converted)
Conv. electrons / Continuous beta-particles	2.4×10^{-3}	1.4×10^{-2}

later a lead radiator. These data indicate the presence of one gamma-ray of energy 0.758 Mev, which is in good agreement with the energy value obtained from the conversion electron region in the beta-spectrum.

A summary of the results obtained in this investigation is shown in Table I.

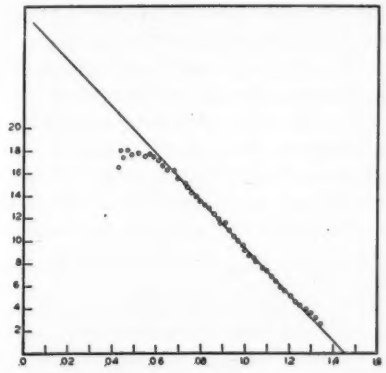

FIG. 2. Kurie plot of the beta-spectrum of Cb^{95}. (Kurie plot, $(N/FI^2)^{\frac{1}{2}}$ *vs.* energy E, where N is net counting rate, F is the Fermi function, and I is the coil current in amperes.)

This document is based on work performed under Contract No. W-7405 eng. 26 for the Atomic Energy Commission at the Oak Ridge National Laboratory.

[1] V. A. Nedzel, PPR Vol. 9B, 7.15.7 (1947). (The Plutonium Project Report (PPR) contains a complete report of Project information, Vol. 9B being entitled *Radiochemistry of the Fission Products*. This volume is in the process of being declassified and prepared for publication as part of the National Nuclear Energy Series under auspices of the United States Atomic Energy Commission.)
[2] J. S. Levinger, PPR Vol. 9B, 7.15.11 (1946).
[3] M. Deutsch, L. G. Elliott, and R. D. Evans, Rev. Sci. Inst. **15**, 178 (1944).
[4] E. P. Steinberg, PPR Vol. 9B, 7.15.10 (1946).

Observations on Large Cosmic-Ray Bursts at an Altitude of 3500 Meters*

EDWARD F. FAHY AND MARCEL SCHEIN
Department of Physics, University of Chicago, Chicago, Illinois
November 15, 1948

EXPERIMENTS on the frequency *versus* size of large bursts under great thicknesses of lead have been carried out at Climax, Colorado (altitude 3500 meters). The equipment used consisted of an ionization chamber (Carnegie Model "*C*" meter) filled to a pressure of 50 atmospheres of pure argon and surrounded by three different lead shields. These shields were (a) 10.7 cm Pb;

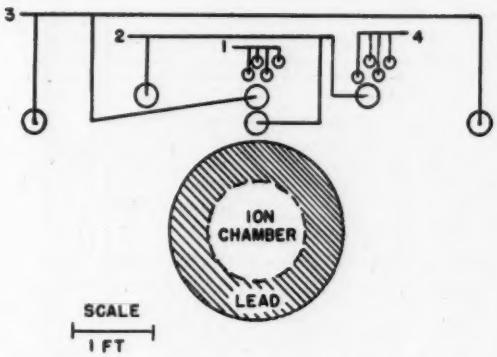

FIG. 1. A schematic drawing of the ionization chamber, 10.7-cm Pb shield and Geiger-Müller counters which are connected to four different coincidence circuits as shown.

(b) 26.7 cm Pb; (c) shield (b) plus a 30.5-cm lead slab covering a cone of approximately 45° semi-vertical angle with respect to the center of the ionization chamber. On a horizontal plane over the ionization chamber and the various lead shields was placed a number of Geiger-Müller counters which were connected to four different coincidence circuits. The Geiger-Müller counters were arranged relative to one another so that they would record large atmospheric showers of various spreads over the ionization chamber shield.

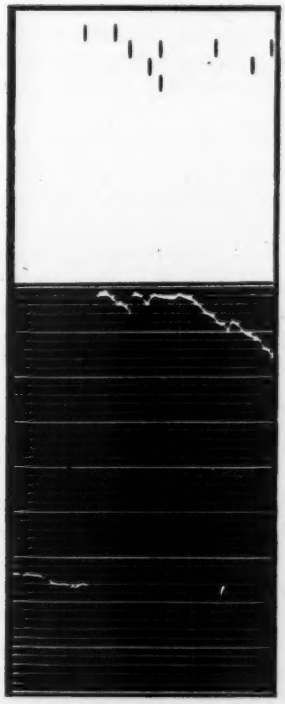

FIG. 2. Record of a burst which is equivalent to 3300 singly charged particles at minimum ionization passing through the ion chamber. The records of the recording lights of the coincidence circuits are above the electrometer trace. It can be seen clearly that this burst does not occur simultaneously with any of the four coincidences registering atmospheric showers.

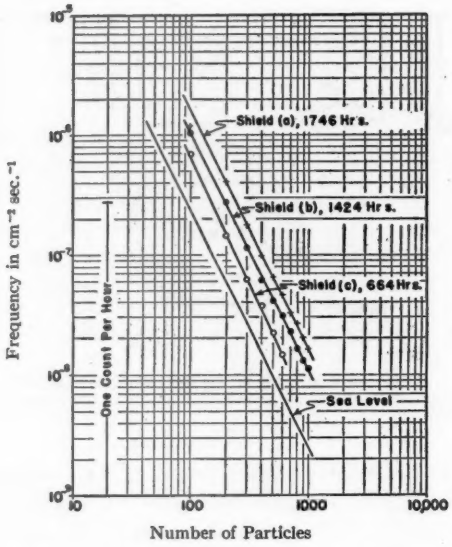

FIG. 3. Frequency *versus* size curves for large cosmic-ray bursts under several lead shields at an altitude of 3500 meters. The number of hours data obtained with each shield is shown in the figure. The sea level curve was obtained with a 10.7-cm Pb shield.

A schematic drawing of the ionization chamber, the 10.7-cm Pb shield, and the Geiger-Müller counters is shown in Fig. 1. This arrangement corresponding to the 10.7-cm Pb shield is similar to that used by Lapp[1] at sea level. Both the electrometer trace from the ionization chamber, which registers the cosmic-ray intensity and the bursts, and the recording lights of the coincidence circuits were recorded on the same 5-inch wide photographic paper as shown in Fig. 2.

By means of this arrangement, it was found that, within experimental error, less than 5 percent of the bursts were caused by air showers even with shield (a). It is very difficult to see any mechanism by which an atmospheric shower of very high energy could produce more than 100 particles below 10.7-cm Pb without tripping the shower recording arrangement. If we should assume that these bursts are produced by μ-mesons of energies greater than 10^{10} ev,[2,3] then we would expect that the burst producing radiation would exhibit no detectable absorption in lead and, also, that there would be very little, if any, absorption in the atmosphere from Climax to sea level. The experimental data in Fig. 3 shows that this is not the case, however. For burst sizes of more than 300 particles, corresponding to an energy of 4.5×10^{10} ev of the burst producing radiation,[3] there is clearly a decrease in frequency by a factor of approximately 6.7 on going from Climax to sea level. This fact demonstrates that these large bursts at high altitude are not produced by μ-mesons. The burst producing radiation is absorbed by a factor of 1.52 on increasing the lead shield from 10.7-cm to 26.7-cm Pb. This figure corresponds to a mean free path of 434 g/cm² in lead, assuming that the burst producing radiation is absorbed exponentially. This value is considerably larger than the mean free path of a high energy nucleon which is absorbed according to a cross section equal to the geometrical cross section of a lead nucleus which can be estimated to correspond to a mean free path of about 160 g/cm² in lead.

Some indication regarding the zenith angle dependence of the intensity per steradian of the burst producing radiation can be obtained from the data with shield (c). This shield is not hemispherically symmetrical and, therefore, the absorption in it, expected according to the above measured mean free path of 434 g/cm² in lead, is a function of the zenith angle dependence of the particles initiating the bursts. At 300 particles it can be seen from Fig. 2 that the burst frequency was changed by 1.83 on going from shield (b) to shield (c). Furthermore, this change in a spherical shield of 30.5-cm Pb, according to the mean free path of 434 g/cm², should be 2.22. This means that only 0.83 of the burst producing radiation encountered the flat absorber of shield (c). In order to make this so, it is necessary for the intensity per steradian of the radiation producing more than 300 particles to vary as between $\cos^5\theta$ and $\cos^6\theta$. This strong zenith angle dependence is further evidence for the fact that the burst producing radiation exhibits a strong absorption in the earth's atmosphere.

We wish to express our thanks to Dr. M. A. Tuve, Department of Terrestrial Magnetism, Carnegie Institution, for putting the Model "*C*" meter at our disposal.

* Assisted by the joint program of the Office of Naval Research and Atomic Energy Commission.

[1] R. E. Lapp, Phys. Rev. **69**, 333 (1946).
[2] Marcel Schein and Piara S. Gill, Rev. Mod. Phys. **2**, 267 (1939).
[3] R. F. Christy and S. Kusaka, Phys. Rev. **59**, 414 (1941).

Erratum: Nuclear Spins and Quadrupole Moments of B^{10} and B^{11}

[Phys. Rev. **74**, 1191 (1948)]

WALTER GORDY AND HAROLD RING
Department of Physics, Duke University, Durham, North Carolina
AND
ANTON B. BURG
Department of Chemistry, University of Southern California, Los Angeles, California

November 10, 1948

IN the above letter the nuclear quadrupole couplings of B^{10} and B^{11} in borine carbonyl were erroneously listed with negative signs. These constants are both positive.

Rock Magnetism as a Clue to Earth's Magnetic History

O. W. TORRESON, THOMAS MURPHY,* AND JOHN W. GRAHAM**
Department of Terrestrial Magnetism, Carnegie Institution of Washington, Washington, D. C.

November 15, 1948

DURING June, July, and August this past summer, an expedition to the western United States made measurements of the magnetization of rocks in several localities.

This work was undertaken on the supposition that fine-grained, undisturbed sedimentary rocks which had been laid down in tranquil water millions of years ago might still retain a magnetic polarization acquired as a result of the orientation of magnetic particles in the direction of the earth's field existing at the time of deposition.

Measurements were made at eight sites in Colorado, Utah, Washington, Idaho, Wyoming, and South Dakota. These sites, together with a number of others, were suggested as suitable for the work by members of the United States Geological Survey. The rocks range in age from Jurassic (100 million years) to Miocene (10 million years). Altogether sixteen sites were examined for suitability, the requirements being that the rock have a workable exposure, be fine-grained, be flat-lying, appear undeformed, lack any history of thermal disturbance, have sufficient cohesion to permit preparation of 3 cm cubic samples, and be sufficiently magnetic to be measurable (minimum measurable moment 10^{-7} c.g.s. units per cc).

The expedition had a staff of three, and utilized two six-by-six $2\frac{1}{2}$ ton trucks as mobile equipment. One of these was fitted as living quarters and the other was fully equipped to make complete determinations of magnetic polarization in the field.

At the eight sites a total of 94 samplings was made, the smallest number at a given site being two and the largest twenty-one.

The directions of magnetization for all 94 samples are used in plotting the frequency distribution curves in Fig. 1. At the eight sites the present magnetic declination ranges from 13° to 22° east of geographic north, and the inclination from 66° to 72°. It is seen from Fig. 1 that there is a marked tendency for the horizontal component of rock magnetism to center on geographic north rather than on the present geomagnetic north. This result is to be expected if, through geologic time, magnetic north has oscillated 30 to 40 degrees to either side of a mean which is geographic north, a cyclic pattern found from magnetic measurements made in 1947[1] on 5000 years of glacial clay deposits in New England (15,000 to 20,000 years old[2]) and on ocean bottom samples (1,000,000 years). The magnetic stability of glacial clays has been established by studies of folded strata.

The inclination values in the rocks are seen in Fig. 1 to be slightly less than the present inclination of the earth's field.

All the sites did not give equally concordant results. At Glenns Ferry, Idaho, for example, thirteen samples averaging 2° east of geographic north in declination gave a very small scatter of polarizations, whereas the 21 samples from the Badlands at South Dakota gave a very great scatter. Stream bedding may be one of the factors responsible for the scattered polarizations at the latter site.

At one site, studies of the polarizations of sedimentary pebbles in a conglomerate give evidence that fine-grained, water-deposited material can retain a direction of magnetization for millions of years. Polarizations of the same material in the undisturbed condition at this site are included in the data of Fig. 1.

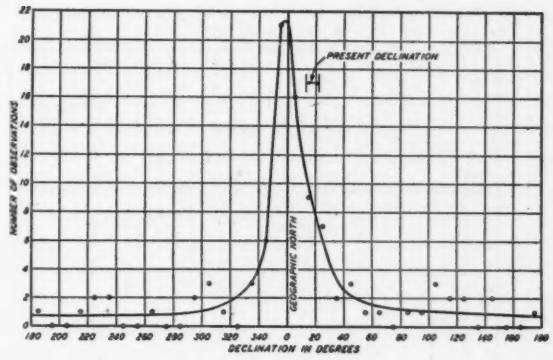

FIG. 1A. Frequency distribution of declination measurements on rock samples.

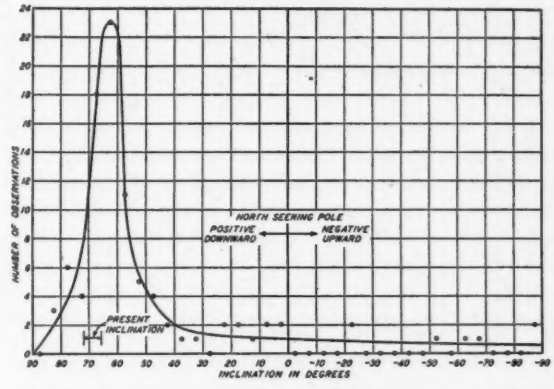

FIG. 1B. Frequency distribution of inclination measurements on rock samples.

These observations, with two-thirds of the declination values in a narrow band centered on geographic north and inclination values differing little from present inclination are consistent with the idea that, for the past 100 million years, the earth's magnetic field has been approximately centered on the earth's geographic axis. They do not support the contention, recently reiterated on the basis of measurements of the polarizations of 50-million year old igneous dikes in England,[3] that the earth's field in the past has had a reverse polarity.

* Trinity College, Dublin, Ireland; Fellow of the Carnegie Institution.
** Graduate student, Geology Department, Johns Hopkins University; Fellow of the Carnegie Institution.
[1] Terr. Mag. 53, December, 1948.
[2] Am. J. Sci. 246, 689–700 (1948).
[3] Nature 161, 462–464 (1948).

The Formation of U^{232} by Helium Ions on Thorium

AMOS S. NEWTON
Radiation Laboratory, University of California, Berkeley, California
September 27, 1948

GOFMAN and Seaborg first produced the isotope U^{232} by deuteron bombardment of thorium.[1] Studier and Hyde[2] have reported the occurrence of the α, $p3n$ reaction

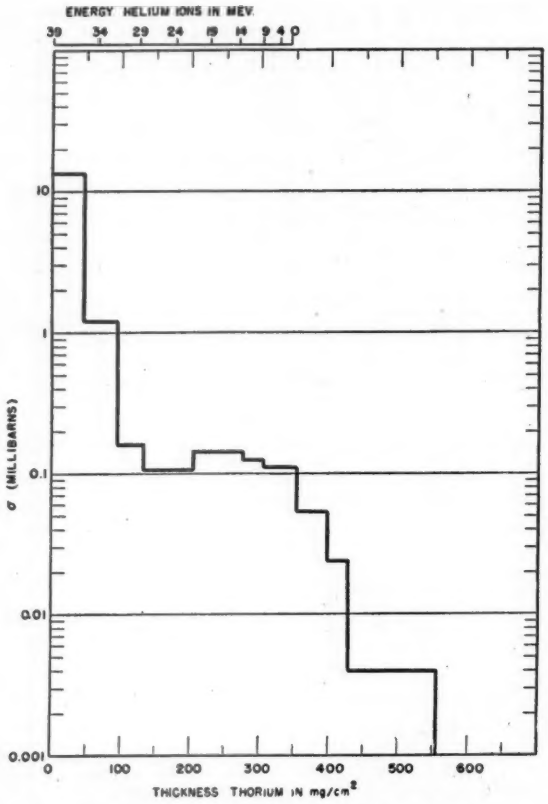

FIG. 1. Cross section for U^{232} production from thorium+helium ions.

on thorium to give Pa^{232} which decays by beta-emission to U^{232}. In neither of the above mentioned experiments was the cross section for formation of U^{232} determined.

In connection with work on the fission of thorium with helium ions,[3] a long bombardment of a thick target was obtained from which it was possible to calculate the cross section and measure roughly the threshold for the formation of U^{232} by helium ion bombardment of thorium. From the active area of this target thin layers were milled, the millings from each respective layer collected quantitatively, weighed, dissolved in hydrochloric acid, and diluted to a known volume. About six months after bombardment, uranium was extracted from aliquots of each of these solutions by ether extraction of uranyl nitrate. The thorium aliquot was added to 1 ml concentrated nitric acid in a 30 ml Kjeldahl flask and boiled until fumes of NOCl were no longer evolved. Then 3 ml of 10*M* ammonium nitrate were added and the solution extracted with 3 ml ether, the water phase being frozen in a dry ice-acetone bath to separate the phases. The ether was washed twice with 4 ml portions of 10*M* ammonium nitrate. Three successive extractions of the original sample were made and the ether extracts combined. To the combined ether extracts a few drops of concentrated nitric acid were added and the solution evaporated to eliminate the ether. The resulting solution was transferred to a platinum plate with a micropipette and the beaker and pipette washed three times with 3-drop portions of nitric acid. The solution on the platinum plate was evaporated under a heat lamp and then flamed to give samples for alpha-counting. This method gave reproducible results and was probably quantitative for the uranium since further extractions of the sample gave no activity.*

Since U^{232} decays by alpha-emission to $RdTh^{228}$ which has a 1.9-year half-life, measurements made soon after separation of the U^{232} are not contaminated with daughter products. To check for possible contamination from other alpha-emitters, samples from the first five layers were pulse analyzed and shown to contain no alphas of range differing from the 3.85-cm range of U^{232},[4] the range being checked against an ionium standard.

Table I contains the data used in calculating the cross sections. In these calculations the half-life of U^{232} was taken as 70 years from the work of James, Florin, Hopkins, and Ghiorso.[4] The initial 39-Mev energy of the alpha-particles is degraded to an average energy of 37.5 Mev in the first layer. At this energy the average cross section for formation of U^{232} is 13.2 millibarns, this figure representing the sum of the cross sections for the $\alpha, 4n$ and $\alpha, p3n$ reactions. No independent yields for these two modes of formation of U^{232} were obtained since the 1.4-day Pa^{232} had completely decayed at the time of the uranium separation.

In Fig. 1, in which the cross section for formation of U^{232} has been plotted against the thickness of thorium, it is seen that there is apparently a deuteron contamination of the helium ion beam causing the production of U^{232} beyond the threshold for the helium ion reaction. The indicated yield is a minimum in the fourth layer indicating that the $d, 2n$ reaction probably has a maximum yield in the fifth layer and some helium ion formation of U^{232} is still occurring in the third layer. This places a maximum value of 31.6 Mev and a minimum of 28 Mev on the threshold for the formation of U^{232} by helium ions, with an average value of 30 Mev. The yield from deuterons is observed to fall off rapidly when the thickness of thorium absorber becomes greater than 430 mg/cm² which corresponds to a reduction in energy of 20 Mev deuterons to about 10 Mev.

TABLE I. The yield of U^{232} from the bombardment of thorium with 39-Mev helium ions.*

Layer	Wt. Th in layer grams	Fraction of layer analyzed	α-Counting rate at 52% geometry c/m	σ (Units 10^{-27} cm²)	Thickness Th layer mg/cm²
1	0.380	.01	4544	13.4	44.2
		.01	4385	12.9	
2	0.408	.025	1336	1.2	47.4
		.025	1340	1.2	
3	0.332	.025	122	0.165	38.6
		.05	230	0.155	
4	0.640	.05	303	0.106	74.4
		.05	300	0.105	
5	0.612	.05	385	0.141	71.3
6	0.250	.05	140	0.125	29.1
7	0.411	0.1	401	0.11	47.8
8	0.396	0.1	187	0.053	46.1
9	0.252	0.1	55	0.024	29.3
10	1.082	0.1	38	0.004	126.0

* Area target = 8.60 cm²; Total bombardment = 3020 μah; $T_{\frac{1}{2}}U^{232}$ = 70 years.

The author wishes to thank Mr. A. Ghiorso for making pulse analyses of the samples and Dr. J. G. Hamilton and the crew of the Crocker Laboratory cyclotron for bombarding the sample.

This work was performed under the auspices of the Atomic Energy Commission and the Radiation Laboratory, University of California, Berkeley, California.

[1] J. W. Gofman and G. T. Seaborg, PPR Vol. 17B, No. 2.4 (to be issued). First reported in Report CN-332, October 20, 1942.
[2] M. Studier and E. Hyde, PPR Vol. 17B, No. 9.2 (to be issued).
[3] A. S. Newton, "The Fission of Thorium by Helium Ions," Phys. Rev. 75, 17 (1949).
* This chemical method is not original with the author but its development was due to the efforts of many individuals on several branches of the Manhattan Project.
[4] R. A. James, A. E. Florin, H. H. Hopkins, and A. Ghiorso, PPR Vol. 14B, No. 22.8 (to be issued).

The Gamma-Rays of W^{187} in the Low Energy Region*

LOUIS A. BEACH, CHARLES L. PEACOCK, AND ROGER G. WILKINSON
Indiana University, Bloomington, Indiana
November 16, 1948

THE use of a very thin window g-m tube detector in a small 180° spectrometer has made it possible to extend our study of W^{187} to energies of about 3 kev. The beta-ray source consisted of a thin deposit of finely divided WO_3 about one mg/cm² thick backed by a 0.06 mg/cm² Zapon film. The 24-hour W^{187} was obtained from Oak Ridge. Figure 1 shows the electron spectrum in the low energy region. Conversion lines are found at 7, 66, 127, and 136 kev. The first of these appears low in intensity since it is close to the window cut-off and corresponds to a gamma-ray at 0.078 Mev, if it is assumed to be a *K*-line. The remaining three lines are found to be the *K*, *L*, and *M* components associated with the conversion of a gamma-ray at 0.138 Mev. Using photographic plate detection, Valley[1] has found conversion lines in this region which he attributes to three gamma-rays at 0.086, 0.135, and 0.101 Mev. Our results are in accord with the assignment of two of these, with somewhat different energy values, but the presence of a gamma-ray at 0.101 Mev cannot be inferred from our data.

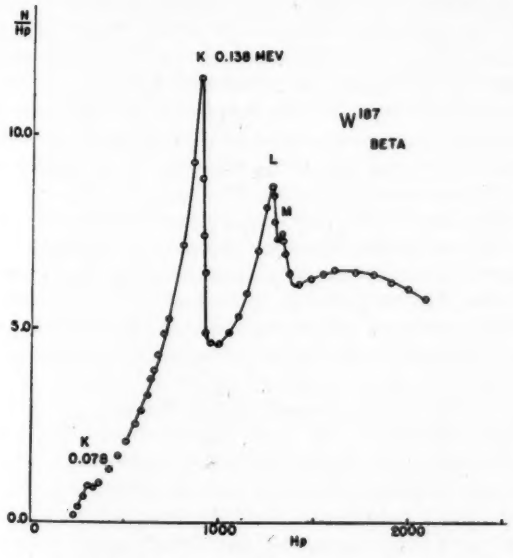

FIG. 1. Low energy electron spectrum of W^{187}.

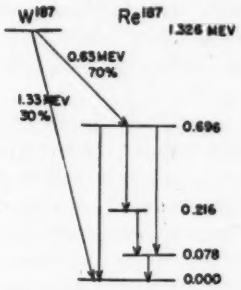

FIG. 2. Decay scheme of W^{187}.

From a study of the photoelectrons ejected from a thin lead radiator, gamma-rays at 0.14 and 0.21 Mev have been previously suggested.[2] The photoelectron line caused by the 0.14-Mev gamma-ray was very close to window cut-off and the energy assignment in doubt. It would now appear that the photoelectron line previously ascribed to a 0.21-Mev gamma-ray is really the *L* line of the 0.138-Mev gamma-ray. This correction makes the decay scheme previously given more consistent.[2] Figure 2 shows the decay scheme which is consistent with our earlier studies and the present low energy measurements. In addition, coincidence studies and an analysis of the relative intensities support this picture. However, since the decay is complex and cannot be inferred directly from the data, it is perhaps best to regard the scheme as a tentative one. In any case, Fig. 2 may be regarded as a summary of the radiations of W^{187} and their energies which we have obtained.

* Assisted by the joint program of the Office of Naval Research and Atomic Energy Commission.
[1] G. E. Valley, Phys. Rev. 59, 686 (1941).
[2] C. L. Peacock and R. G. Wilkinson, Phys. Rev. 74, 601 (1948).

The Possible Magnetic Field of a Rotating Metallic Body Containing a Stress Gradient

A. E. BENFIELD
Department of Engineering Sciences and Applied Physics, Cruft Laboratory, Harvard University, Cambridge, Massachusetts
November 12, 1948

IN view of the recent interest in the magnetic fields of the earth, the sun and other astronomical bodies, and in mechanisms for producing magnetic fields by rotation,[1]

it is perhaps worthwhile to draw attention to a possible mechanism for producing a *small* effect, which does not seem to have attracted much notice. The idea may be explained as follows.

Consider the possibility of separating a small amount of the electric charge in a solid metallic conductor, and hence establishing a small potential gradient in it, by compressing part of it. Such a separation of charge, caused by a stress gradient,* does not seem to have been directly observed. However, a closely related phenomenon was studied long ago by P. W. Bridgman,[2] when he found the Peltier heat between a number of compressed and uncompressed metals, by measuring the e.m.f. of a thermocouple consisting of a metal in its compressed and uncompressed state. The thermal e.m.f. E in a thermocouple is related to the Peltier heat π by the relation $\pi = T(dE/dT)$, where T is the absolute temperature. Thus, after measuring E as a function of T in the temperature range 0°C to 100°C, Professor Bridgman was able to calculate π at a number of pressures up to 12,000 kg/cm². This existence of π would seem to imply that some charge flows on compressing part of a conductor.

One may also discuss the possibility of a small charge separation in terms of the behavior of the electrons in a metal. Consider the maximum energy of the electrons constituting a degenerate Fermi-Dirac gas in a piece of metal at 0°K. This energy may be written[3]

$$E_{\max} = h/2m(3n/8\pi)^{\frac{1}{3}} \qquad (1)$$

where h = Planck's constant, m = the *effective* mass of the electron and n = the number of electrons per cm³. Suppose we now uniformly compress the whole piece of metal so that we have $n+\Delta n$ electrons per cm³. We can calculate the increase in $E_{\max}$ by differentiating Eq. (1) with respect to n, and on so doing we find that, if $\Delta n \ll n$,

$$\Delta E_{\max} = \tfrac{2}{3} E_{\max} \Delta n/n \qquad (2)$$

nearly, provided that m is a constant.

If we now imagine the compressed piece of metal to be directly connected to an uncompressed piece of the same material, all the metal being at the same temperature, electrons might be expected to flow from the compressed piece until a potential difference corresponding to $\Delta E_{\max}$ is established.[4] On computing $\Delta E_{\max}$, however, from Eq. (2), one finds predicted potential differences (for metals about as compressible as copper) of the order of 10^{-2} volts between uncompressed metal, and metal hydrostatically compressed to 10^4 kg/cm²; whereas the observed Peltier heats[2] never exceed 0.003 joules/coulomb (Bismuth) at this pressure, and are mostly a factor of 10 to 1000 less; some compressed metals even have a negative Peltier heat. However, the use of Eq. (2) for a *quantitative* estimate of $\Delta E_{\max}$ is unwise, possibly for a number of reasons. For example, m varies from metal to metal,[5] and on compressing a metal one might expect m to vary. In this connection it is worth pointing out that, should m vary on compressing in such a way that $dm/dn = \frac{2}{3}m/n$, $\Delta E_{\max}$ would be zero.

Also, there is some question to what extent the potential jump between the interiors of two dissimilar metals (or a metal in its compressed and uncompressed state), which are in contact, can be identified with the Peltier heat effect.[6]

However, if *some* charge separation occurs, it introduces the possibility of a magnetic field being associated with a rotating metallic body containing a stress gradient, and it gives rise to an interesting relationship between gravitation and electromagnetism. This may perhaps best be visualized by considering the possible existence, somewhere in space, of a cool metallic body having, say, the dimensions of a small planet or a large meteor. The interior of such a body, like the interior of the earth, would be under pressure, due to its own gravitational field. A small radial charge separation should occur, positive charge remaining, in general, near the center of the body. A static separation of electric charge would thus have been brought about in a conductor by its own steady gravitational field. And it has been shown that if a body containing such a radial charge distribution rotates, there will be an accompanying magnetic field.[7]

The connection described here between gravitation and electromagnetism would not, however, have the fundamental or general nature of the one which has been sought for so long. No time dependence nor "action at a distance" is involved. No new terms would appear in Maxwell's equations or the other fundamental equations of electromagnetism, for the same reasons that the fundamental equations do not contain special terms to account for the thermo-electric effects. Also, to be effective, the mass would have to conduct.

These ideas do not explain the primary magnetic fields of the earth and the sun. The magnetic field to be expected from the mechanism suggested here, for a cool metallic body of appropriate astronomical size, cannot be calculated without a quantitative knowledge of the charge distribution in the body, but it would clearly have an intensity many orders of magnitude less than the observed magnetic fields of the earth and sun, though it would in general have the right sign and shape. Nevertheless, the ideas may be of some interest at a time when considerable attention is being paid to the magnetic fields of the earth and various other astronomical bodies.

A measure of the lack of quantitative agreement may be seen by considering some papers of H. Haalck,[8] who also had the idea of a separation of charge due to a pressure gradient. He attempted to apply it to the hot interiors of the earth and the sun, in order to try to explain the magnetic fields of these bodies. But in so doing it was necessary for him to imagine electric fields of the order of 10^{18} or more times greater than are considered here, and a vast charge separation. The large electric charge separation that would be needed to explain the primary terrestrial and solar magnetic fields has been attacked and criticized as a serious weakness of Haalck's ideas, on the grounds that no known mechanism can quantitatively account for it.[9]

In conclusion, I wish to thank a number of colleagues, in particular Professor P. W. Bridgman and Professor E. M. Purcell, for several helpful discussions.

[1] H. W. Babcock, Astrophys. J. **108**, 191–200 (1948); S. J. Barnet Am. J. Phys. **16**, 140 (1948); P. M. S. Blackett, Nature **159**, 658–666 (1947); E. C. Bullard, Geophys. Suppl., Monthly Notices, Roy. Astron. Soc. **7**, 248 (1948); E. C. Bullard *et al.*, The Observatory **68**, 144 (1948); S. Chapman, Nature **161**, 52 (1948); Monthly Notices, Roy. Astron. Soc. **108**, 236 (1948); T. G. Cowling, Monthly Notices, Roy. Astron. Soc. **105**, 166 (1945); W. M. Elsasser, Phys. Rev. **72**, 821 (1947); A. L. Hales and D. I. Gough, Nature **160**, 746 (1947); J. Mariani, Phys. Rev. **73**, 78 (1948); Nature **162**, 612 (1948); H. T. H. Piaggio, Nature **161**, 450 (1948); A. D. Thackeray, Monthly Notices, Roy. Astron. Soc. **107**, 463 (1947); H. Y. Tzu, Nature **160**, 746 (1947); S. K. Runcorn and S. Chapman, Proc. Phys. Soc. **61**, 373 (1948).

[*] One may think of it as something like the Thomson Effect of thermoelectricity, with a stress gradient taking the place of a temperature gradient.

[2] P. W. Bridgman, Proc. Am. Acad. Arts and Sciences **53**, 269 (1918).

[3] See, for instance, Richtmeyer and Kennard, *Introduction to Modern Physics* (McGraw-Hill Book Company, Inc., New York, 1942), 3rd Ed., p. 116.

[4] See, for instance, K. K. Darrow, Rev. Mod. Phys. **1**, 149 (1929).

[5] F. Seitz, *Modern Theory of Solids* (McGraw-Hill Book Company, Inc., New York, 1940), Chap. 4.

[6] P. W. Bridgman, *The Thermodynamics of Electrical Phenomena in Metals* (The Macmillan Company, New York, 1934).

[7] W. Sutherland, Terrestrial Magnetism **5**, 73–83 (1900); **13**, 155–158 (1908); D. Brunt, Astronom. Nachricht. **196**, 169–184 (1913); G. Angenheister, Physik. Zeits. **26**, 305 (1925).

[8] H. Haalck, Gerlands Beiträge zur Geophysik **52**, 243 (1938); Zeits. f. Physik **105**, 81 (1937).

[9] T. Schlomka, Zeits. f. Geophysik **13**, 126 (1937).

On the Production of Nuclear Polarization*

M. E. Rose
Oak Ridge National Laboratory, Oak Ridge, Tennessee
November 8, 1948

THE spin dependence of nuclear forces (in particular, the $n-p$ interaction) has hitherto been investigated at thermal energies by the scattering of neutrons in ortho- and para-hydrogen.[1] For other nuclei the neutron interaction is ascertainable from neutron diffraction experiments.[2] A possible method of studying the spin dependence of the forces over the entire energy range so that the interactions for both spin orientations are, in principle, deducible, would involve the use of targets of polarized nuclei for scattering and absorption experiments with polarized neutrons.[3] The production of polarized neutrons at each energy above the thermal region may be achieved by using the target with aligned nuclear spins as polarizer as well as analyzer.

In the following we consider the process of aligning nuclear spins in order to estimate the expected order of magnitude of the nuclear paramagnetism.[4] In all cases except ordinary paramagnetic substances the alignment of the nuclear spins must be achieved by direct coupling of the nuclear moments with an external magnetic field H. The nuclear polarization factor f_N is given by

$$f_N=\frac{1}{I}\frac{\Sigma m_i \exp(-W(m_i)/kT)}{\Sigma \exp(-W(m_i)/kT)} \tag{1}$$

where I is the nuclear spin, m_i the component of spin in the direction of the field and the sums in (1) are over all magnetic substates of energy $W(m_i)$. For direct coupling $W(m_i)=-m_i\mu H/I$ where μ is the magnetic moment and f_N is given by the well-known Brillouin formula. For all practical cases ($\mu H/kT\ll 1$) we have

$$f_N=\frac{1}{3}\frac{I+1}{I}\frac{\mu H}{kT}. \tag{2}$$

To cite a few examples, the values of H/T in kilogauss/degree required to produce 20 percent nuclear polarization of H^1, H^3, He^3, Li^7, F^{19}, In^{115} all lie between 2000 and 3000 so that with a temperature of 0.01°K a reasonable magnetic field would suffice. For such nuclei a polarization of about 40 percent is perhaps within the realm of practical possibility if suitable arrangements are made for cooling by establishing thermal contact with the paramagnetic salt. Preliminary considerations indicate that a metallic contact between salt and nuclear sample may be entirely adequate from the point of view of both relaxation time and thermal conduction.[5]

In the case of nuclei in paramagnetic substances the field produced at the nucleus by hyperfine structure coupling should be sufficiently large, in some cases at least, to produce the required nuclear alignment in the range of temperature 0.1 to 0.01°K. The applied field is, therefore, used merely to align the electronic moments. If ΔW is the over-all splitting of the ground state multiplet and J_e the electronic angular momentum we find, in sufficient approximation,

$$f_N=\tfrac{1}{3}f_e\frac{I+1}{I}\frac{J_e}{2J_e+1}\frac{\Delta W}{kT};\quad J_e\geq I$$

$$f_N=\tfrac{1}{3}f_e\frac{I+1}{2I+1}\frac{\Delta W}{kT};\quad J_e<I \tag{3}$$

where f_e is the fractional saturation for the electronic moments. For present purposes we can take $f_e\sim 1$ so that $f_N=0.2$ requires $\Delta W/kT\sim 1$. Estimates of ΔW for the rare earth ions based on spectroscopic data for screening constants and average radius of the $4f$ shell (0.5A) indicate a splitting varying from 0.01 to 0.1 cm^{-1} so that the required temperature range would appear to be feasible. The situation in the case of the transuranic rare earths would appear to be about as favorable.

* This document is based on work performed under Contract No. W-7405 eng. 26 for the Atomic Energy Commission at the Oak Ridge National Laboratory.

[1] R. B. Sutton *et al.*, Phys. Rev. **72**, 1147 (1947).

[2] C. G. Shull, E. O. Wollan, G. A. Morton, and W. L. Davidson, Phys. Rev. **73**, 262 (1948). See also, J. M. Blatt, Phys. Rev. **74**, 92 (1948).

[3] Another possible method involves the depolarization of polarized neutrons by diffusion. See M. Hamermesh and J. Schwinger, Phys. Rev. **69**, 145 (1946); S. Borowitz and M. Hamermesh, unpublished.

[4] A consideration of the experiments with polarized nuclei and neutrons is given in M. E. Rose, Phys. Rev. **75**, 213 (1949).

[5] H. B. G. Casimir and E. M. Purcell, Oak Ridge Conference on Nuclear Physics and Low Temperatures, August 7, 1948.

Scattering and Absorption of Neutrons by Polarized Nuclei*

M. E. Rose
Oak Ridge National Laboratory, Oak Ridge, Tennessee
November 8, 1948

IN the following we consider scattering of S neutrons by a nucleus with spin I so that the interaction between neutron and nucleus is described by the two phase shifts η'

and η'' corresponding to the total angular momentum of the combined system $J=I-\frac{1}{2}$ and $I+\frac{1}{2}$, respectively. The scattering is then conveniently described in terms of the scattering amplitudes

$$a=\frac{4\pi}{k}\frac{I\eta'+(I+1)\eta''}{2I+1}$$

$$b=\frac{4\pi}{k}\frac{\eta''-\eta'}{2I+1} \tag{1}$$

so that b is a measure of the spin dependence of the forces. In (1), k is the wave-member of the neutron. The purpose of the scattering experiments is then to measure both η' and η'' as a function of energy.

For scattering above thermal energies, where scattering by a single nucleus only need be considered, we find for the elastic scattering cross section

$$\sigma=\sigma_0(1+\rho) \tag{2}$$

where $4\pi\sigma_0=a^2+I(I+1)b^2$ is the cross section without polarization of nuclei and/or neutrons. The relative change in cross section is[1]

$$\rho=2If_nf_N\frac{b}{a}\frac{1-b/2a}{1+I(I+1)b^2/a^2} \tag{3}$$

where f_n is the neutron polarization. The magnitude of the phase shifts are given in terms of measurable or calculable quantities by

$$4\pi\eta'^2=\sigma_0\left(1-\frac{I+1}{I}\frac{\rho}{f_nf_N}\right)$$

$$4\pi\eta''^2=\sigma_0(1+\rho/f_nf_N). \tag{4}$$

In the case of direct coupling the nuclear polarization f_N is most easily obtained from the Brillouin formula or Eq. (2) of the preceding letter. Since the neutrons would be polarized by transmission through a thickness x of the target of aligned nuclei, which implies that polarization of the nuclear spins will decrease the scattering ($\rho<0$), the neutron polarization is given by $f_n=-\tanh N\sigma_0x\rho/f_n$ or $f_n^2\approx-N\sigma_0x\rho$, where N is the volume density of scattering nuclei.

While the sign of both phase shifts cannot be determined in a purely nuclear scattering experiment, the relative sign of η' and η'' can be determined, in the thermal region, from the coherent scattering of polarized neutrons by aligned nuclei. The scattering per unit solid angle in the Bragg peaks will increase by a factor $1+\rho_c$ where, for a mono-isotopic lattice,

$$\rho_c=(I^2f_N^2b^2+2If_nf_Nab)/a^2. \tag{5}$$

It is seen that the sign of a/b, and, therefore, of η'/η'' (the magnitudes $|\eta'|$ and $|\eta''|$ are known), can be determined by observing the *direction* in which the coherent scattering changes when the neutron polarization is reversed or turned on. Here it is necessary and desirable to polarize the neutrons by transmission through magnetized iron so that the relative directions of polarization of nuclei and neutrons can be changed. For an idea as to the order of magnitude of the effect to be observed we consider the case of H^1 for which $b/a=-3.45$. With $f_N=0.2$, we have $\rho_c=-0.09$, 0.33 and 0.12 for $f_n=0.3$, -0.3 and 0, respectively.

Another interesting experiment would involve the absorption of polarized (S) neutrons by polarized nuclei for the purpose of determining the angular momentum J of levels of the compound nucleus. Whenever the absorption is predominantly due to a single level, as in the case of resonance, the value of J of this level can be determined by observing the *direction* in which the absorption changes when the neutron polarization is turned on. Under the condition cited, the cross section is given by (2) (with a different σ_0, of course) and

$$\begin{aligned}\rho&=f_nf_NI/I+1, &&\text{if } J=I+\tfrac{1}{2}\\ \rho&=-f_nf_N, &&\text{if } J=I-\tfrac{1}{2}.\end{aligned} \tag{6}$$

Again, it is necessary to vary the relative directions of polarization of neutrons and nuclei so that the neutrons must be polarized by ferromagnetic materials and, except in the case of thermal resonances, it is necessary to work in the $1/v$ region.

The investigation of the angular distribution of radiation emitted from polarized nuclei can yield further information concerning nuclear spectroscopy. This has been discussed by Spiers[2] who has given the angular distribution of dipole γ-rays around the direction of the polarizing magnetic field. A similar calculation for the angular distribution of quadrupole radiation shows that the anisotropy is of the same order of magnitude as for the dipole case but its sign is reversed. For $\Delta J=0$ the emission is preferentially in the direction of the field and for $\Delta J=\pm2$ the anti-parallel direction is preferred.

Details will be given in a subsequent publication.

* This document is based on work performed under Contract No. W-7405 eng. 26 for the Atomic Energy Commission at the Oak Ridge National Laboratory.

[1] For notation see M. E. Rose, Phys. Rev. **75**, 213 (1949).

[2] J. A. Spiers, Nature **161**, 807 (1948).

Proceedings of the American Physical Society

Minutes of the Meeting of the New England Section at Bowdoin College, Brunswick, Maine

October 23, 1948

THE thirty-first meeting of the New England Section of the American Physical Society was held at the Searles Science Building, Bowdoin College, Brunswick, Maine, on Saturday, October 23, 1948. Fifty-two members of the Section registered. The programme included four invited papers, three of which formed a symposium on low temperature physics. There follow the titles of the invited papers and the abstracts of the ten-minute contributed papers relating to research. Abstracts of the ten-minute contributed papers relating to the teaching of physics will appear in the American Journal of Physics.

At the business meeting, the following officers were elected for 1949:

Chairman: Mildred Allen, Mount Holyoke College.

Vice-Chairman: R. D. Evans, Massachusetts Institute of Technology.

Secretary-Treasurer: G. F. Hull, Jr., Dartmouth College.

Programme Committee: J. C. Street, Harvard University, and T. Soller, Amherst College.

Gordon F. Hull, Jr.
Secretary-Treasurer

Invited Papers

Isotopic Weights, K. T. Bainbridge, *Harvard University.*

Symposium on Low Temperature Physics

Fluid Properties of Liquid Helium, A. D. Misener, *University of Toronto.*

The Helium Three Isotope at Liquid Helium Temperature, H. A. Fairbank, *Yale University.*

The Surface Resistance of Superconductors at Microwave Frequencies, W. M. Fairbank, *Amherst College.*

Contributed Papers

Precise Measurements of the Molar Refraction of Carbon Dioxide and Its Variation with Density. Victor H. Coffin and Clarence E. Bennett, *University of Maine.**—Precise measurements of molar refraction for carbon dioxide have been made by displacement interferometry over a density range from zero to 0.06 gram/cc (approximately 32 atmospheres) at temperatures ranging from 32°C to 67°C. These were made at four wave-lengths, 5780A, 5461A, 4359A, and 4047A, thereby extending the work described in earlier papers by Bennett,[1] and Oleson and Bennett.[2] The molar refraction at zero frequency $[(A^2-1)/(A^2+2)][M/\rho]$ was calculated for each value of temperature and density by least squares analysis and was plotted as a function of density. Density values were calculated from pressure readings using the Beattie-Bridgeman equation of state, the pressure readings being obtained by the use of a Keyes deadweight gauge. The molar refraction thus determined decreases from 6.6 to 6.25 (c.g.s. units) as the density increases, in accord with earlier observations[2] but not in accord with molar polarization measurements reported by Keyes and Oncley.[3] The question is raised whether or not the discrepancy might in any way be due to a lack of consideration of infra-red absorption bands in the dispersion extrapolation. According to Van Vleck,[4] such a consideration seemed unnecessary, although a new dispersion formula by Fuch[5] takes these into account. Unfortunately, this formula is not applicable to displacement interferometry.

* Assisted by Contract N6-ori-181, Office of Naval Research.
[1] C. E. Bennett, Phys. Rev. **54**, 200 (1934).
[2] F. B. Oleson and C. E. Bennett, Bull. A. Ps. 16, No. 4 (June, 1941).
[3] F. G. Keyes and J. L. Oncley, Chem. Rev. **19**, 195 (1936).
[4] John H. Van Vleck, *Electric and Magnetic Susceptibilities* (Oxford University Press, London).
[5] O. Fuchs, Zeits. f. Physik **46**, 519 (1928).

A Method of Measurement of Small Periodic Displacements and Its Application to Determining the Piezoelectric Constants of Potassium Dihydrogen Arsenate. Thaddeus Niemiec, *Wesleyan University.* (Introduced by K. S. Van Dyke.)*—The periodic mechanical displacement of one end of a piezoelectric crystal bar of known properties, such as quartz, is compared with that of an unknown, in this case a crystalline bar of potassium dihydrogen arsenate (KDA). 60-cycle sinusoidal fields applied to the two crystals are adjusted in magnitude and phase until their displacements are equal. Equality is determined by a null method. Two metal plates fastened to the ends of the

crystal bars form a capacitor which is used as the tuning element of a high frequency oscillator (15 mc). The oscillator is frequency modulated by any changes which occur in the capacitance and detected by an f-m receiver. Absence of 60-cycle modulation indicates equality of amplitude. The sensitivity is sufficient, under some conditions, to detect changes in amplitude as small as 3A, and crystal amplitudes as small as 3×10^{-6} cm are measured to better than one percent. For KDA the piezoelectric constants are determined as follows at 0°C: $d_{14}=d_{25}=2.66\times10^{-11}$ and $d_{36}=2.24\times10^{-11}$ coulomb per newton. Their variation has been followed over a wide temperature range and the temperature coefficients determined. That of d_{14} is large, its value doubling in the range 20° to −125°C as a Curie point is approached. The crystals of KDA were furnished through the courtesy of the Brush Development Company.

* This work was supported by Contract No. W28-003 sc-1556 with The United States Army Signal Corps.

Fringing Field Corrections for Magnetic Sector Lenses and Prisms. KENNETH T. BAINBRIDGE, *Harvard University*.—The usual methods[1,2] for locating the image of a source are unsatisfactory when magnetic sector fields are used for focusing ions in a magnetic spectrometer. Essentially the effect of a fringing field is to change the focusing problem from one dealing with normal entry of the ions into the field to one involving oblique entry. One proceeds to calculate by Herzog's or Cartan's methods the focusing conditions for the oblique entry case at the real boundary of the poles and then displaces the source and its image by the amount determined from the experimentally measured fringing field distribution. The actual image is beyond the location predicted by Coggeshall's method,[1] which is based on an incorrect assumption for the optimum condition of focus. On the other hand, the location of the actual image is closer to the pole boundary than that predicted by Nier using Barber's rule.[2] The image can be brought to the desired location in practical spectrometers[2] by displacing the magnet in the direction of the sector apex. Under these conditions the median radius of curvature must be slightly increased.

[1] N. D. Coggeshall, J. App. Phys. 18, 855 (1947).
[2] A. O. Nier, Rev. Sci. Inst. 11, 212 (1940); 18, 398 (1947).

THE AMERICAN INSTITUTE OF PHYSICS

INCORPORATED

57 East 55 Street New York 22, N.Y.

MEMBER SOCIETIES:

American Physical Society
KARL K. DARROW, *Secretary*, Columbia University, New York 27, New York.

Optical Society of America
ARTHUR C. HARDY, *Secretary*, Massachusetts Institute of Technology, Cambridge 39, Massachusetts.

Acoustical Society of America
WALLACE WATERFALL, *Secretary*, 57 East 55th Street, New York 22, New York.

Society of Rheology
EARL K. FISCHER, *Secretary*, Institute of Textile Technology, Charlottesville, Virginia.

American Association of Physics Teachers
C. J. OVERBECK, *Secretary*, Northwestern University, Evanston, Illinois.

AFFILIATED SOCIETIES:

American Society for X-Ray and Electron Diffraction
Electron Microscope Society of America
Physical Society of Pittsburgh
Physics Club of Chicago
Physics Club of Philadelphia
Cleveland Physics Society
Physics Club of the Lehigh Valley

ASSOCIATES:

Over seventy-five leading industrial enterprises and other institutions which contribute to the support of the Institute.

JOURNALS:

The Physical Review
JOHN T. TATE, *Editor*, University of Minnesota, Minneapolis, Minnesota.

Reviews of Modern Physics
J. W. BUCHTA, *Editor*, University of Minnesota, Minneapolis, Minnesota.

Journal of the Optical Society of America
GEORGE R. HARRISON, *Editor*, Massachusetts Institute of Technology, Cambridge, Massachusetts.

The Journal of the Acoustical Society of America
FLOYD A. FIRESTONE, *Editor*, 3318 Forrester Street, N.W., Washington, D. C.

American Journal of Physics
THOMAS H. OSGOOD, *Editor*, Michigan State College, East Lansing, Michigan.

The Review of Scientific Instruments
GAYLORD P. HARNWELL, *Editor*, Randal Morgan Laboratory of Physics, University of Pennsylvania, Philadelphia, Pennsylvania.

The Journal of Chemical Physics
JOSEPH E. MAYER, *Editor*, Kent Chemical Laboratory, University of Chicago, Chicago 37, Illinois.

Journal of Applied Physics
ELMER HUTCHISSON, *Editor*, Case Institute of Technology, Cleveland 6, Ohio.

Physics Today
DAVID A. KANZLER, *Editor*, American Institute of Physics, 57 East 55 Street, New York 22, New York.

OFFICERS

GEORGE R. HARRISON, *Chairman*
Massachusetts Institute of Technology
WALLACE WATERFALL, *Secretary*
The Celotex Corporation
GEORGE B. PEGRAM, *Treasurer*
Columbia University
JOHN T. TATE,
Adviser on Publications
University of Minnesota

GOVERNING BOARD

LUIS W. ALVAREZ
ROBERT B. BRODE
E. U. CONDON
A. J. DEMPSTER
W. F. FAIR, JR.
HARVEY FLETCHER
R. C. GIBBS
GEORGE R. HARRISON
W. V. HOUSTON
PAUL E. KLOPSTEG
F. W. LOOMIS
PHILIP M. MORSE
GEORGE B. PEGRAM
A. H. PFUND
JOHN T. TATE
WALLACE WATERFALL
M. W. WHITE
A. G. WORTHING

Consultant on Printing
MELVIN LOOS

ADMINISTRATIVE STAFF

HENRY A. BARTON, *Director*
CLEVELAND NORCROSS,
Assistant Director
THEODORE VORBURGER,
Business Manager
RUTH F. BRYANS,
Publication Manager
BERTY HOFSTADTER, *Office Manager*
EILEEN B. NEUBERGER,
Circulation Manager

THE American Institute of Physics was founded in 1931 as a federation of leading societies in the field of Physics. It combines into one operating agency those functions on behalf of physics which can best be done by the Societies jointly. Its purpose is the advancement and diffusion of physics and its applications to human welfare. To this end it publishes for itself or the Societies the nine journals listed on this page; promotes unity and effectiveness of effort among all who are interested in physics; renders numerous direct services to physicists and to the public; and cooperates with government agencies, national associations, educational institutions, technical industries, and others in such manner as to realize the opportunities and fulfill the responsibilities of physics as an important and constructive human activity.

CONTENTS

THE PHYSICAL REVIEW SECOND SERIES, VOL. 75, NO. 1 JANUARY 1, 1949

Threshold and Resonances in $C^{13}(p,\alpha)B^{10}$ Reaction and Energy Levels of N^{14} . . . . . W. E. SHOUPP, B. JENNINGS, AND E. H. SUR 1

Total Cross Sections of Nuclei for 90-Mev Neutrons . . . . . LESLIE J. ECKE, EDWIN M. MCMILLAN, JACK M. PETERSON, AND DUANE C. SEWELL 7

On Simultaneous Beta-Gamma Emission from Nuclei . . . . . CONRAD L. LONGMIRE 13

Fission of Thorium with Alpha-Particles . . . . . AMOS S. NEWTON 17

Note on the One-Electron States of Diatomic Molecules . . . . . HENRY A. ERIKSON AND E. L. HILL 19

Note on the Bremsstrahlung Produced by Protons . . . . . JOHN L. POWELL 23

Radiations of Uranium Y . . . . . G. B. KNIGHT AND R. L. MACKLIN 25

Experiments on the Effect of Atomic Electrons on the Decay Constant of Be^7 . . . E. SEGRÈ AND C. E. WIEGAND 31

Secondary Emission of Electrons by High Energy Electrons . . . . . J. G. TRUMP AND R. J. VAN DE GRAAFF 44

On the He^3—He^4 Equilibrium below the λ-Point . . . . . C. T. LANE, HENRY A. FAIRBANK, L. T. ALDRICH, AND ALFRED O. NIER 46

Gamma-Rays from Deuteron Resonance . . . . . DAVID E. ALBURGER 51

Cosmic-Ray Intensity above the Atmosphere . . . . . A. V. GANGNES, J. F. JENKINS, JR., AND J. A. VAN ALLEN 57

Properties of Cosmic Radiation at Very High Altitudes . . . . . MARTIN A. POMERANTZ 69

Absorption Spectrum of Dense Lithium Vapor . . . . . CH'EN SHANG-YI AND CHANG CHIH-SAN 69

Isotope Shifts in Uranium Spectra . . . . . L. E. BURKHART, GEORGE STUKENBROEKER, AND SAM ADAMS 69

K Spectra of Element 61 . . . . . L. E. BURKHART, W. F. PEED, AND E. J. SPITZER 69

Electrostatic Interaction and Low Energy Particles in Alpha-Radioactivity . . . . . MELVIN A. PRESTON 70

Measurement of the Radioactive Decay Constant of ThC′ Using a Coincidence Method . . . F. W. VAN NAME, JR. 109

Observation of the Ferro-Electric Displacement Effect in Barium Titanate . . . . . R. R. NEWTON, A. J. AHEARN, AND K. G. MCKAY 120

Calculation of the Changes in the Conductivity of Metals Produced by Cold-Work . . . . . J. S. KOEHLER 128

Magnetic Susceptibility of Zinc at Liquid Helium Temperatures . . . . . S. G. SYDORIAK AND J. E. ROBINSON 118

Magnetic Internal Conversion Coefficient . . . . . S. D. DEELL 139

Periods of Motion in Periodic Orbits in the Equatorial Plane of a Magnetic Dipole . . . ANTONIO ROMERO JUÁREZ 137

Magnetostriction and Order-Disorder . . . . . J. E. GOLDMAN AND R. SMOLUCHOWSKI 140

Irreversible Magnetic Effects of Stress . . . . . WILLIAM FULLER BROWN, JR. 142

Magnetic Domain Patterns on Single Crystals of Silicon Iron . H. J. WILLIAMS, R. M. BOZORTH, AND W. SHOCKLEY 155

Simple Domain Structure in an Iron Crystal Showing a Direct Correlation with the Magnetization . . . . . H. J. WILLIAMS AND W. SHOCKLEY 170

Statistical Theory of Liquids. III . . . . . GEORGE JAFFÉ 178

Letters to the Editor:

On the Cs^{137} Disintegration Scheme . . . . . ALLAN C. G. MITCHELL AND CHARLES L. PEACOCK 197

Attenuation of Sound in Rarefied Helium . . . . . MARTIN GREENSPAN 197

Magnetic Moment of Aluminum[27] . . . . . JOHN R. ZIMMERMAN AND DUDLEY WILLIAMS 198

Doppler Broadening of a Gamma-Ray Line . V. K. RASMUSSEN, C. C. LAURITSEN, AND T. LAURITSEN 199

Isotopic Weights of Medium Elements . . . . . K. OGATA 200

Cloud-Chamber Evidence of a Meson-Nucleus Interaction . . . . . G. E. VALLEY, C. P. LEAVITT, AND J. A. VITALE 201

Temperature Dependence of Scintillations in Sodium Iodide Crystals . . . . . W. C. ELMORE AND R. HOFSTADTER 203

Energy of the Disintegration Product of a Light Mesotron . . J. C. FLETCHER AND H. K. FORSTER 204

Relative Sensitivities of Some Organic Compounds for Scintillation Counters . . . . . H. T. GITTINGS, R. F. TASCHEK, A. R. ROSSIO, E. JONES, AND W. J. MADIGAN 205

Radiation from Columbium 92 . . . . . J. E. HUDGENS, JR. AND W. S. LYON 206

Observations on Large Cosmic-Ray Bursts at an Altitude of 3500 Meters . . . . . EDWARD F. FANY AND MARCEL SCHEIN 207

Erratum: Nuclear Spins and Quadrupole Moments of P^{31} and P^{32} . . . . . WALTER GORDY, HAROLD RING, AND ANTON B. BURG 208

Rock Magnetism as a Clue to Earth's Magnetic History . . . . . O. W. TORRESON, THOMAS MURPHY, AND JOHN W. GRAHAM 208

Formation of U^{232} by Helium Ions on Thorium . . . . . AMOS S. NEWTON 209

Gamma-Rays of W^{187} in the Low Energy Region . . . . . LOUIS A. BEACH, CHARLES L. PEACOCK, AND ROGER G. WILKINSON 211

Possible Magnetic Field of a Rotating Metallic Body Containing a Stress Gradient . A. E. BENFIELD 211

On the Production of Nuclear Polarization . . . . . M. E. ROSE 213

Scattering and Absorption of Neutrons by Polarized Nuclei . . . . . M. E. ROSE 213

Proceedings of the American Physical Society:

Minutes of the Meeting of the New England Section at Bowdoin College, Brunswick, Maine, October 23, 1948 215

LANCASTER PRESS, INC., LANCASTER, PA.